Advances Related to United States and International Mineral Resources: Developing Frameworks and Exploration Technologies

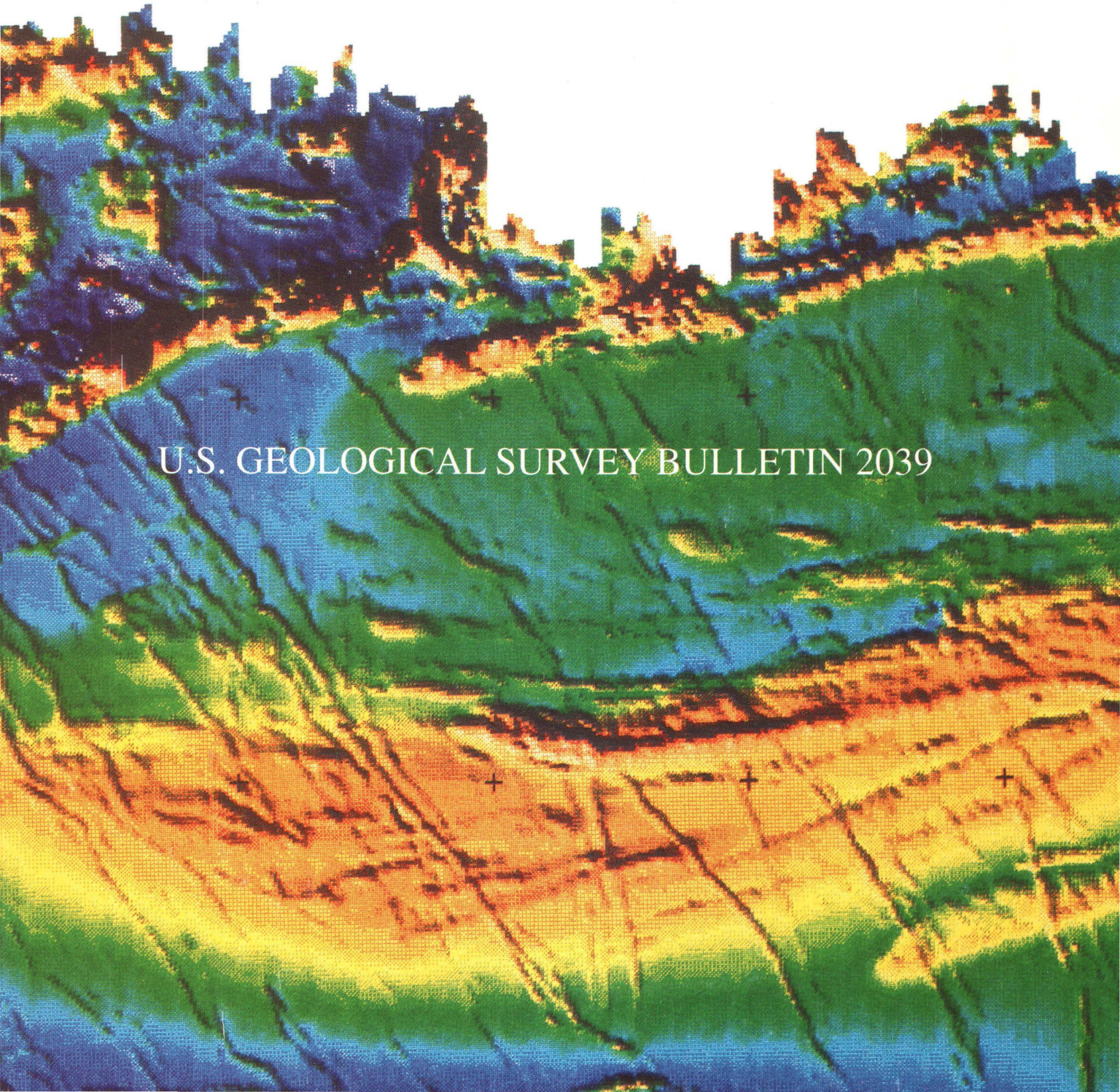

U.S. GEOLOGICAL SURVEY BULLETIN 2039

COVER.—Part of a color shaded relief aeromagnetic map of north-central Minnesota. Color changes represent broad changes in magnetic field strength. The warm colors (red, orange, and yellow) represent areas of magnetic field highs; the cool colors (green, blue, and purple) represent magnetic field lows.

Advances Related to United States and International Mineral Resources: Developing Frameworks and Exploration Technologies

Edited by RICHARD W. SCOTT, JR., PAMELA S. DETRA, *and* BYRON R. BERGER

U.S. GEOLOGICAL SURVEY BULLETIN 2039

The Bulletin reports some accomplishments of the U.S. Geological Survey in research on mineral resources in 1992

UNITED STATES GOVERNMENT PRINTING OFFICE WASHINGTON : 1993

U.S. DEPARTMENT OF THE INTERIOR
BRUCE BABBITT, Secretary

U.S. GEOLOGICAL SURVEY
Dallas L. Peck, Director

For sale by
USGS Map Distribution
Box 25286, Building 810
Denver Federal Center
Denver, CO 80225

Library of Congress Cataloging-in-Publication Data

Advances related to United States and international mineral resources : developing frameworks and exploration technologies / edited by Richard W. Scott, Jr., Pamela S. Detra, and Byron R. Berger.
p. cm. — (U.S. Geological Survey bulletin ; 2039)
Includes bibliographical references.
1. Prospecting—Equipment and supplies. 2. Mines and mineral resources—United States. I. Detra, Pamela S. II. Berger, Byron R. III. Series.
QE75.B9 no. 2039
[TN270]
557.3 s—dc20 92–43213
[622'.1'028] CIP

CONTENTS

[Letters designate chapters]

INTRODUCTION

USGS—MEETING OUR NATION'S NEED FOR MINERAL RESOURCES THROUGH APPLIED, BASIC, AND TECHNOLOGY RESEARCH

By Byron R. Berger[1] *and* Pamela S. Detra[1]

Mineral resources are an essential component of the foundation of a strong society and healthy economy. Providing information for the public good about the origin, quality, and quantity of mineral resources world-wide has been an important mission of the U.S. Geological Survey (USGS) since its creation in 1879. This information contributes to (1) the national security by assuring a supply of raw materials; (2) the economic well-being of the United States by maintaining a healthy minerals industry as well as other industries, such as aerospace and steel, that depend upon minerals; (3) public health by providing understanding of the occurrence of metals in the natural environment and the behavior of metals in potentially hazardous situations; (4) land-use decisions and land-use classification by public and private interests; and (5) government policy making.

To effectively accomplish a USGS goal of providing mineral resource information for the public good, the Office of Mineral Resources, Geologic Division of the USGS, seeks to quickly and effectively disseminate research results to government, commercial, and general public interests. This Bulletin, *Advances related to United States and international mineral resources: Developing frameworks and technologies*, reports progress on some of the current activities of the Office of Mineral Resources and reflects the necessity for an international perspective regarding mineral resources and resource technology.

The organization of this Bulletin is based on the philosophy that the needs of mineral-resource-information users are best met by (1) establishing a geologic framework for mineral deposits nationally and internationally, (2) developing technologies that will aid in the exploration and evaluation of mineral resources and mineral resource potential, and (3) providing tests of new technologies to provide measures of their utility. For many years, the USGS has used this programmatic approach to fulfill its mission of earth science in the public interest.

ESTABLISHING A GEOLOGIC FRAMEWORK FOR MINERAL DEPOSITS

The science of economic geology matured as a discipline within the earth sciences in the latter half of the 19th century. Whereas earlier engineers and geologists tended to classify ore deposits on the basis of form and (or) mineralogy, genetic concepts became the preferred underpinning of the field as it evolved from a practiced art to a science. Many USGS geologists contributed to the evolution of thought in this science in its infancy (e.g., Samuel F. Emmons, George Becker, Waldemar Lindgren, Raphael Pumpelly, Frederick Ransome, and Josiah Spurr). Each of these geologists and their colleagues believed that the genesis and occurrence of mineral deposits were best understood in the context of their geologic framework. The presumption that different deposit types reflect differing pressure and temperature environments has formed the intellectual framework of economic geology for most of the 20th century; this framework was established by the early years of the century.

During the past three decades, a new perceptual framework—plate tectonics, in conjunction with new research technologies—has revolutionized our understanding about the origin and occurrence of mineral deposits. But, as in the early years of this century, it is still a framework based on sound information about regional geology and detailed understanding about individual deposits.

[1]U.S. Geological Survey, Mail Stop 973, P.O. Box 25046, Denver Federal Center, Denver, CO 80225.

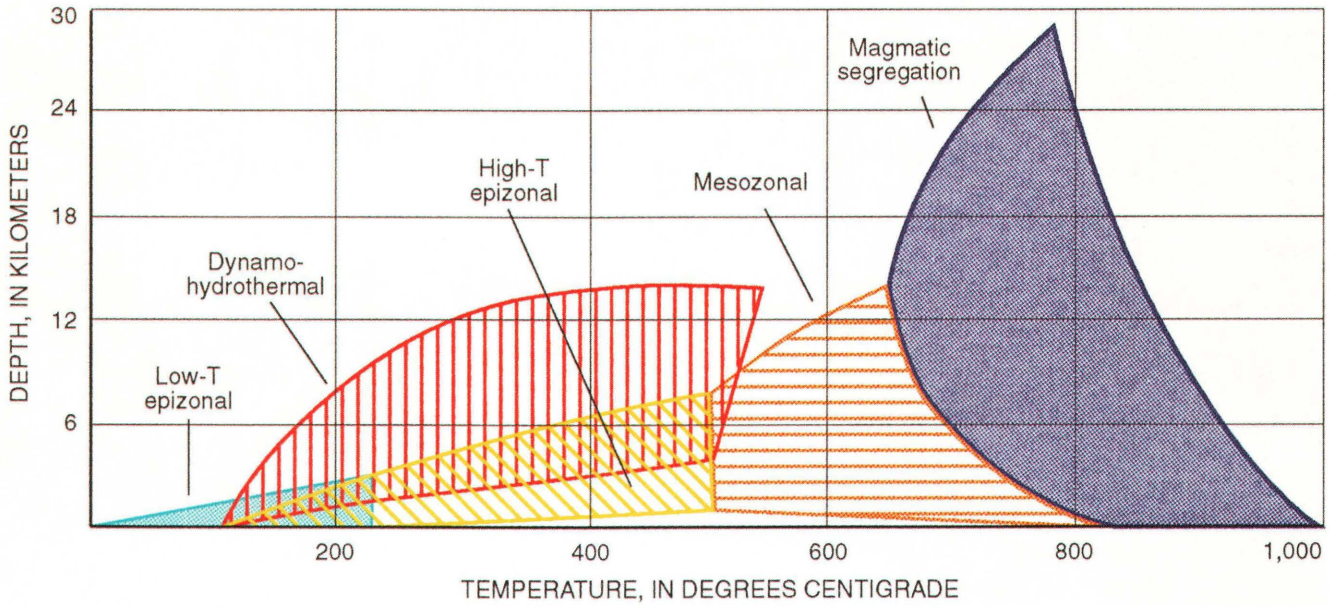

Figure 1. Classification of mineral deposits in terms of pressures and temperatures that exist in different tectonic settings where specific deposit types form (inferred from stable alteration mineral assemblages and geothermal gradients). The mineral-deposit styles are as follows: (1) magmatic segregation, (2) mesozonal, (3) high-temperature epizonal, (4) dynamo-hydrothermal, and (5) low-temperature epizonal. Selected, typical, mineral-deposit styles and examples for each of the deposit types are given in table 1.

With the advances in technology, scientists have achieved new insights into the pressure and temperature conditions under which mineral deposits are formed (fig. 1) and which mineral-deposit styles fit into the pressure-temperature types (table 1). As a result, scientists also now recognize the important relation between tectonic environment and deposit type. The USGS is actively participating in this revolution in technology and understanding. Several papers in parts 1 and 2 of this volume reflect our continuing attempt to understand the all-important geologic framework within which deposits occur. Contributions include Stoeser (Chapter A); Blank (Chapter B); Kleinkopf (Chapter C); Bradley (Chapter D); and Ludington and others (Chapter I). The remaining papers in parts 1 and 2 deal more specifically with mineral deposits or mining districts (see Ayuso and Foley (Chapter E); Offield and others (Chapter F); Staude (Chapter G); Wallace and others (Chapter H); Hofstra and others (Chapter J); Hammarstom (Chapter K); and Rytuba and others (Chapter L)).

DEVELOPING AND TESTING TECHNOLOGIES FOR MINERAL RESOURCE ASSESSMENT AND EXPLORATION

The development and utilization of appropriate and state-of-the-art technologies is integral to mineral resource assessments and exploration. Regional targeting of permissive mineral-resource terranes contributes to both of these ends. Larsen (Chapter Q) is developing a geologic model to target heavy mineral placers in the southeastern United States. New and improved technologies in remote sensing have resulted in major advances in the utility of this approach to regional analysis, particularly in arid and semiarid regions. Clark and others (Chapter N) and Knepper (Chapter O) describe important advances in technology development in this field.

Once a regional assessment or exploration analysis has been completed, follow-up technologies are useful for outlining specific mineralized areas. Whitney and Landis (Chapter M) are investigating volatiles in clay minerals as a tool for outlining permissive or prospective areas within sedimentary sequences. McKee and others (Chapter P) are investigating the utility of the thermochronology of fluid inclusions in mining-district-scale studies.

When technologies have been developed that appear to be useful, performance testing under normal field conditions is valuable both to document the conditions under which a technology is useful and to transfer that technology to other users. The papers in part 4 all take developed technologies and test them with such objectives in mind. Stream-sediment geochemistry is applied by Grosz (Chapter R) and lithogeochemistry by Thorman and Brooks (Chapter Y), and both are components in the multidisciplinary study described by Toth and others (Chapter V). Stressed vegetation is tested by Payás and others (Chapter S). Geophysical techniques are tested by Horton and others (Chapter T) and Grauch and Hoover (Chapter X).

Table 1. Selected, typical, mineral-deposit styles and examples for deposit types shown in figure 1.

Mineral-deposit style	Examples (locations)
Magmatic deposits	
Layered mafic intrusions	*Bushveld*
	Stillwater
Anorthosite titanium	*Allard Lake*
Kimberlite diamonds	*Kimberley*
Carbonatite rare-earth	*Mountain Pass*
Mesozonal deposits	
Pegmatites, lithium	*Kings Mountain*
	Manono-Kitole
Rhyolite tin	*Black Mountains*
High-heat-flow granites	*Cornwall*
High-temperature epizonal deposits	
Porphyry copper	*Bingham Canyon*
	El Salvador
Porphyry molybdenum (Climax style)	*Climax*
Epithermal gold-silver	*Comstock lode*
	Pachuca
Polymetallic veins, replacements	*Bingham Canyon*
	Bolivia
Skarn-related copper	*Bingham Canyon*
	Christmas
Cyprus massive	*Cyprus*
	Turner-Albright
Kuroko massive sulfide	*Kuroko*
	Kidd Creek
Dynamo-hydrothermal deposits	
Polymetallic veins	*Coeur d'Alene*
Low-sulfide quartz veins	*Mother Lode*
	Ballarat
	Muruntau
Low-temperature epizonal deposits	
Sedimentary iron	*Lake Superior*
	Clinton
Mississippi Valley Pb-Zn	*Viburnum*
	Cracoc-Silesia
Roll-front uranium	*Grants*
	Powder River

Mineralogy is utilized by Sidder and others (Chapter U) to provide genetic insights into the Pea Ridge deposit, and mineral chemistry is applied to gold placers by Desborough and others (Chapter Z).

GAPS IN THE INFORMATION BASE

Viewing mineral deposits from a "source" to "sink" perspective has long been the subject of academic science. However, detailed studies of natural abundances of trace elements in all varieties of rocks have failed thus far to elucidate which rocks unequivocally have served as metal sources for most types of mineral deposits. Therefore, source regimes have had little application in mineral resource assessment and exploration activities. Nevertheless, as Doe (Chapter AA) asserts, the investigation of characterizing source rocks should continue.

CHAPTER A

TERTIARY CALDERAS AND REGIONAL EXTENSION OF THE EAST-CENTRAL PART OF THE TINTIC–DEEP CREEK MINERAL BELT, EASTERN GREAT BASIN, UTAH

By DOUGLAS B. STOESER[1]

ABSTRACT

Caldera-related Oligocene (≈34 Ma) rhyolitic tuff and volcanic megabreccia occur at three localities in the east-central part of the Tintic–Deep Creek mineral belt in the Basin and Range of western Utah. The volcanic rocks at these localities (Maple Peak (West Tintic Mountains), south Cherry Creek, and Desert Mountain) are 8,000–10,000 ft, 4,200 ft, and > 5,000 ft thick, respectively. Megabreccia at Maple Peak and Desert Mountain contain blocks > 1,000 ft long, whereas, at south Cherry Creek, blocks are as much as 100 ft long. The tuff and megabreccia at the Maple Peak and Desert Mountain localities are interpreted to be intracaldera in origin and belong to the Maple Peak and Desert Mountain calderas. The megabreccia of the Maple Peak area had previously been interpreted to be large breccia pipes but here is considered to be intracaldera collapse breccia. The Maple Peak caldera had been previously unrecognized. The south Cherry Creek volcanic rocks may be either intracaldera or caldera proximal and are interpreted to be associated with the Maple Peak caldera. The relationship between the intracaldera Maple Peak section and volcanic rocks of the East Tintic Mountains, where a caldera (the Tintic caldera) has been proposed, remains unresolved, but the volcanic-rock sections between the two ranges do not appear to correlate.

The three sections of tuff and megabreccia dip an average of 40°–50° ENE. This structural orientation is interpreted as being caused by rotation of blocks above a westward-dipping detachment, named here the Tintic Valley detachment. Extensional deformation above the detachment dismembered at least two caldera complexes, the Maple Peak and Desert Mountain, segments of which were tectonically transported west on the detachment. Overall structural relationships are obscured by extensive alluvial cover in the study area.

INTRODUCTION

An east-west-trending belt of Tertiary igneous rocks and mineral deposits (the Tintic–Deep Creek mineral belt) extends from the Tintic district west to the Deep Creek Range in the northern part of the Delta 1°×2° quadrangle (figs. 1, 2) (Hilpert and Roberts, 1964; Shawe and Stewart, 1976). The Tintic–Deep Creek belt contains two suites of igneous rocks, a late Eocene to mid-Oligocene (42–34 Ma) suite of intermediate to rhyolitic volcanic and intrusive rocks (Lindsey and others, 1975; Morris and Lovering, 1979; Lindsey, 1982; Shubat and Snee, in press) and an early Miocene to Holocene suite (≈21 Ma) of basalts and highly evolved, high-silica and topaz rhyolite and granite (Turley and Nash, 1980; Lindsey, 1982; Christiansen and others, 1986). The Eocene-Oligocene igneous rocks align with the belt (the eastern part of which comprises the Thomas Range–Tintic volcanic field of Stokes, 1986), whereas the Miocene to Holocene igneous rocks are distributed throughout the Sevier Desert region roughly along a north-south axis. The Eocene-Oligocene volcanic rocks have traditionally been viewed as having formed prior to Basin-and-Range extension, whereas the younger group of igneous rocks is clearly related to it. Gans and others (1989), however, have interpreted volcanic rocks of mid-Oligocene age in east-central Nevada

[1]U.S. Geological Survey, Mail Stop 905, P.O. Box 25046, Denver Federal Center, Denver, CO 80225.

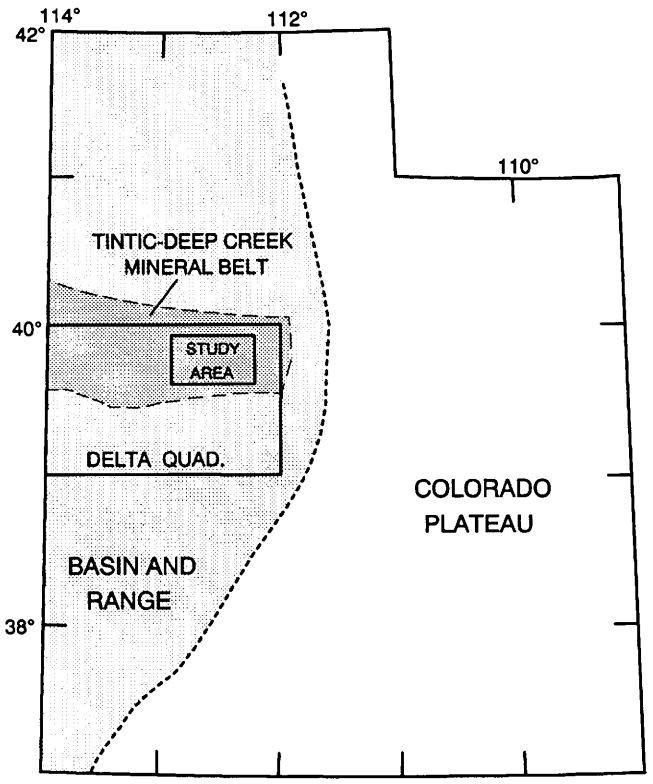

Figure 1. Index map of Utah showing the location of the study area and the Delta 1°×2° quadrangle.

(at the west end of the Tintic–Deep Creek belt) as being coeval with early Basin-and-Range extension.

This paper presents preliminary evidence that the igneous rocks and mineral deposits of the east-central part of the Tintic–Deep Creek belt belong to several calderas that have been disrupted and extended by large-scale extensional faulting. These conclusions are based on study of mid-Tertiary volcanic rocks at three localities: Maple Peak, south Cherry Creek, and Desert Mountain (fig. 3), where thick sections of tuff and megabreccia have been previously reported (Morris and Kopf, 1970a, 1970b; Kattelman, 1968; Walsh, 1987). This paper presents new mapping and stratigraphy for these rocks and interprets them as chiefly intracaldera in origin. Based on their structural setting, it is also proposed that these rocks lie within a highly extended terrane that is related to an underlying detachment fault. Geochronologic and petrologic studies of the igneous rocks from the study area are in progress, and cooperative mapping of the Maple Peak area is being conducted with the Utah Geologic Survey. This report is a product of the Delta CUSMAP (Conterminous United States Mineral Assessment Program) project of the Office of Mineral Resources of the U.S. Geological Survey. This paper benefited from reviews and critical comments by Daniel R. Shawe, David A. Lindsey, and Thomas A. Steven.

MAPLE PEAK

Maple Peak includes the highest point in the West Tintic Mountains and forms the southernmost mountain within that range (figs. 2, 4). Previous geologic mapping of the West Tintic Mountains shows the Maple Peak area as being underlain by Precambrian quartzite, Paleozoic limestone, a thick section of Tertiary undifferentiated volcanic rocks, Tertiary megabreccia, and Tertiary monzonitic intrusions, all of which are overlain by the Salt Lake Series of clastic sediments of late Tertiary age (Groff, 1959; Morris and Kopf, 1970a; Pampeyan, 1989). Morris and Kopf (1970a) described the undifferentiated volcanic rocks as being comprised chiefly of purplish-gray, medium-grained, porphyritic latite and quartz latite lava containing phenocrysts of andesine, sanidine, biotite, hornblende, and quartz in a fine-grained crystalline matrix. They also stated that the volcanic rocks locally include a "basal unit of white, fine-grained tuffs and buff unsorted tuff breccias." They estimated the total thickness of volcanic rocks to exceed 1,000 ft.

Morris and Kopf (1967) described three large breccia pipes in the southern part of the West Tintic Mountains, which they named the Maple Peak, Cherry Creek, and Hassel breccia pipes (fig. 4). These pipes were thought to consist of elongate bodies of coarse breccia cutting the Tertiary volcanic rocks as well as older sedimentary rocks. The megabreccias were described as consisting of a massive chaotic breccia with 65 percent silicified, calcitized, and chloritized felsic volcanic matrix and 35 percent inclusions, including blocks as much as 1,200 ft long. Inclusions in the breccia consist of quartzite, phyllite, argillite, conglomerate, limestone, shale, chert, latite, quartz latite, monzonite, quartz monzonite, and aplitic granite. The breccia matrix was described as containing unsorted angular and broken crystals of quartz, orthoclase, andesine, biotite, and lithic fragments, in a very fine grained groundmass.

Reexamination of the volcanic rocks and breccia along a northeast traverse across Maple Peak revealed a thick section of intercalated rhyolitic welded tuffs and coarse volcanic megabreccia capped by a lacustrine(?) sedimentary unit (fig. 4, table 1). The volcanic rocks at Maple Peak dip 20°–65° NE., with an average dip for the entire section of approximately 40°–45°.

The lower part of the volcanic-rock section at Maple Peak is approximately 6,500 ft thick and consists chiefly of altered rhyolitic welded tuffs (units t1–t5, fig. 4, table 1) (part of the lower section was not seen along the traverse where it is intruded by monzonite porphyry, fig. 4). The tuffs all contain phenocrysts of plagioclase, sanidine, quartz, and biotite and range from relatively crystal rich to crystal poor with abundant pumice fragments and few lithic clasts. Two massive latite units (f1 and f2, fig. 4) were

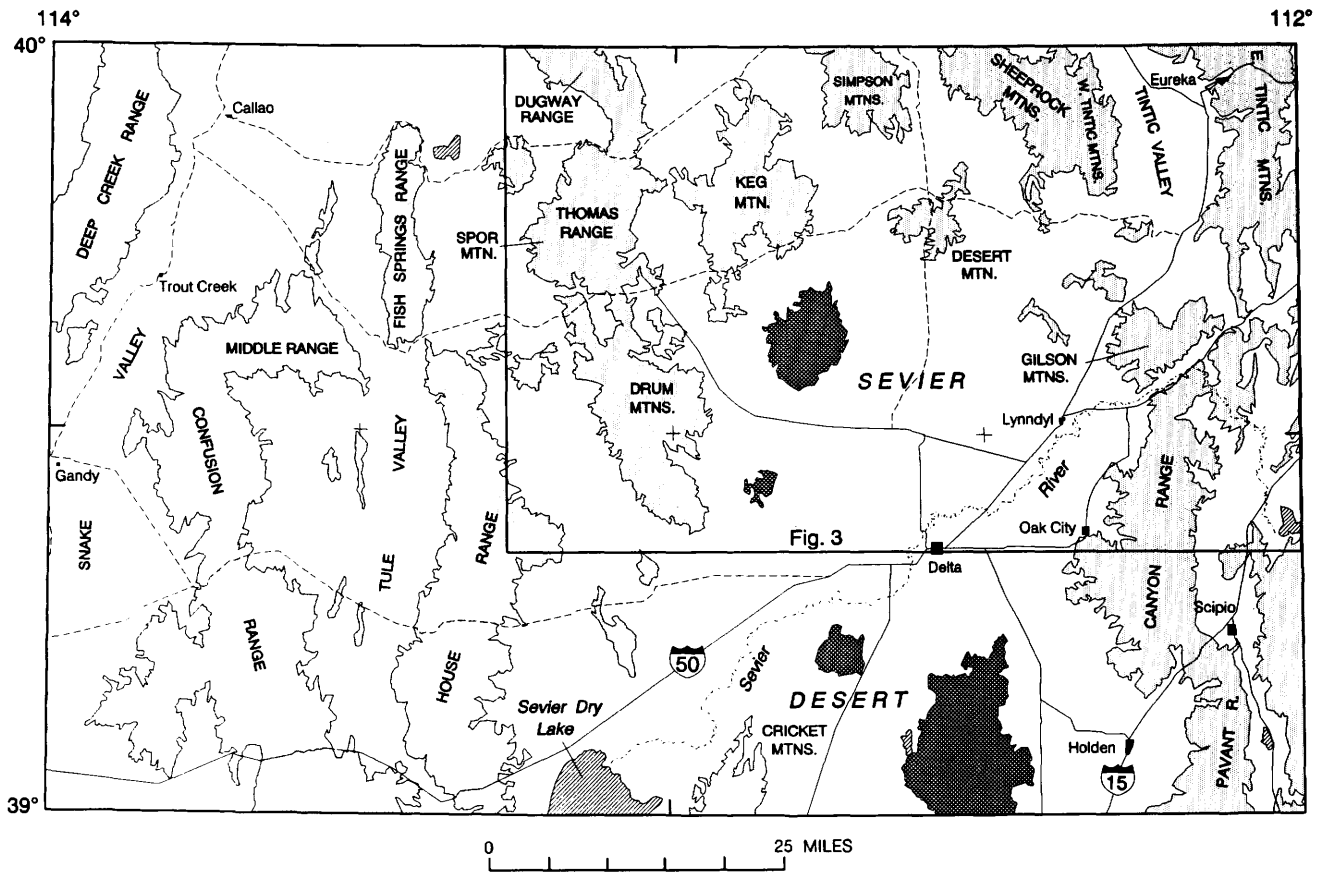

Figure 2. Index map to geographic features of the Delta 1°×2° quadrangle and to figure 3. Solid lines are paved highways and roads; dashed lines are improved dirt roads. Light-gray areas are ranges and areas of outcrop. White areas are intermontaine alluvium. Dark-gray areas within the Sevier Desert are Pliocene and Quaternary basaltic volcanic rocks that lie on basin fill. Areas with diagonal lines are lakes.

encountered on the traverse that may be either flows or flow domes intercalated in the section, allochthonous slabs of older volcanic rock incorporated within the t2 tuff unit, or hypabyssal intrusives. The hypabyssal-intrusion interpretation is based on the observation that monzonite and latite intrude mid-Tertiary volcanic rocks in the East and West Tintic Mountains and at Desert Mountain (see below).

The lower part of the traversed section contains several areas of dense phenocryst-poor andesite breccia (unit Tab, fig. 4). Morris and Kopf (1970a) described this breccia as consisting of fragments of fine-grained, dark-reddish-brown andesite; monzonite porphyry; quartzite; and carbonate rocks in a sparse matrix of hematite-stained, pulverized andesite. Where seen by the author, this unit consists of monomict breccia with fine-grained andesitic clasts in a fine-grained andesitic matrix. These rocks appear to have formed by brecciation of a massive andesite and may be flow breccia or agglomerate, or they may have been brecciated subsequent to cooling. The andesite breccia was interpreted by Morris and Kopf (1970a) to be breccia intruded into the volcanic rocks, but, to me, they appear to be inclusions of andesite breccia incorporated into the welded tuffs. I also found several 6- to 8-ft-diameter clasts of the andesite breccia in the lower Maple Peak megabreccia. These andesitic breccia bodies occur north and west of, but spatially near, a large mass of andesite at the southeastern part of Maple Peak (fig. 4)—these breccia bodies may represent older volcanic rock that was dismembered during formation of the tuffs and megabreccias.

The upper part of the Maple Peak section consists of rhyolitic welded tuffs and coarse megabreccia (fig. 4, table 1). Although Morris and Kopf (1967) indicated that the megabreccia of Maple Peak intrudes the volcanic rocks, I reinterpret the megabreccia as being volcanic megabreccia that is intercalated in the volcanic section and that overlies the lower tuff section. This reinterpretation is, in part, based on the observation that the central part of the Maple Peak megabreccia contains a clast-poor zone (fig. 4). The clast-poor zone is poorly exposed, but, where examined, it is a eutaxitic welded tuff. Furthermore, this tuff dips approximately 40° NE., indicating that this unit has a strike and dip conformable with the volcanic section above and below the megabreccia. Morris and Kopf (1970a) showed several 85° NE. dips for the megabreccia in the traverse area, but I was unable to replicate these measurements when I visited these locations, and they are

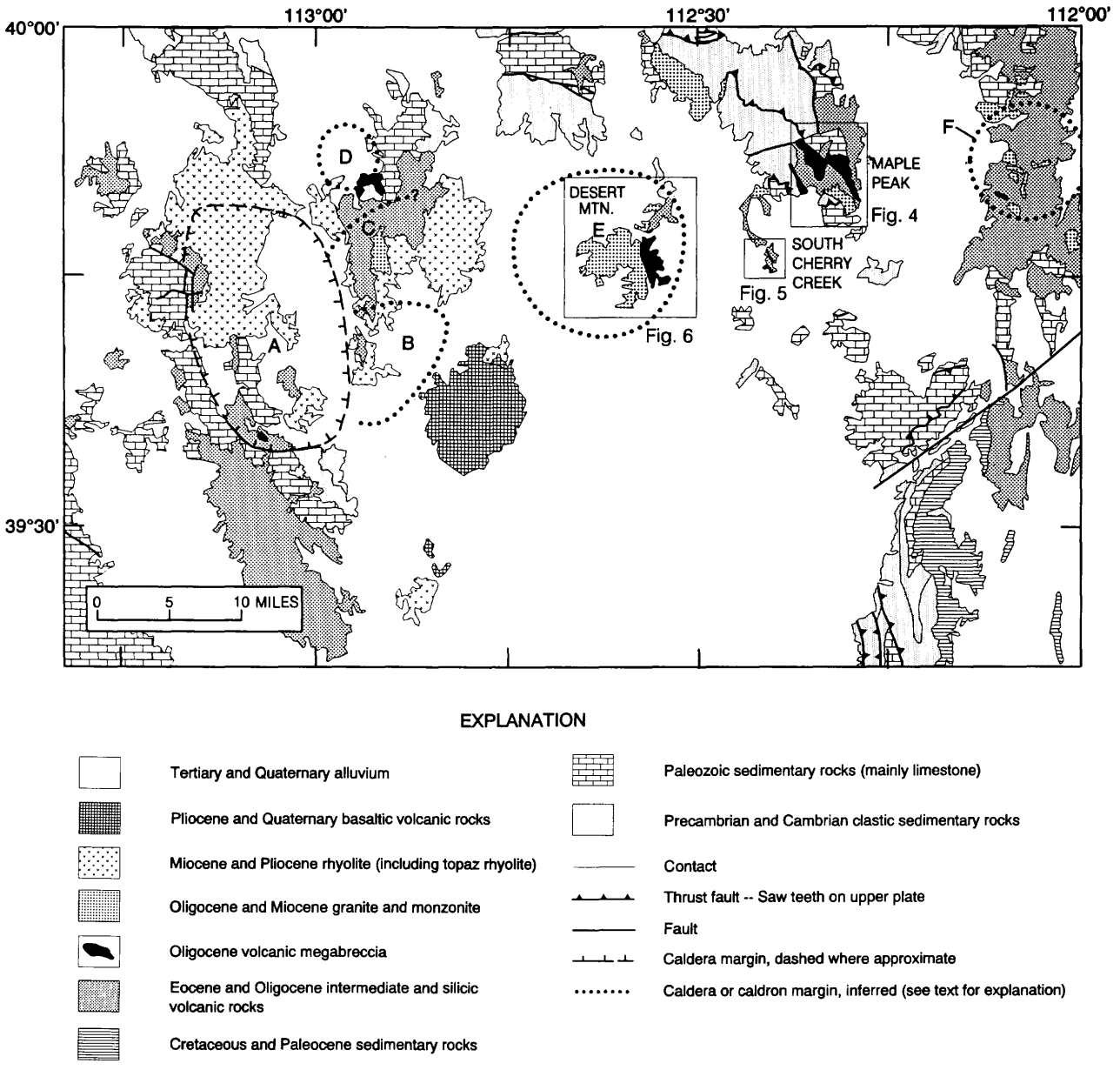

Figure 3. Simplified geologic map of the northeastern part of the Delta 1°×2° quadrangle and index map to figures 4, 5, and 6. Also shown are known and proposed calderas and caldrons as discussed in text: A, Thomas caldera; B, Picture Rock caldera; C, Keg caldron; D, Dead Ox caldron; E, Desert caldera; and F, Tintic caldera.

not shown on figure 4. Morris and Kopf (1967) were well aware of the clast-poor zone within the Maple Peak megabreccia stating on page C69 of their paper that "The central area of this pipe is dominantly composed of tuffaceous material and rare boulder-sized clasts of sedimentary rocks." They ascribed the clast-poor central area to zonation within the breccia pipe. It is also clear from their text that I am not the first to propose that the central zone of the megabreccia is a welded tuff: Morris and Kopf also note on the same page that "The central zone of the breccia pipes closely resembles ashfall arkosic tuffs and commonly has been mistaken for a pyroclastic deposit." They also stated in several places within their paper that the welded tuffs of the volcanic section "superficially resemble the tuffaceous and fragmental matrix of the pipes," but they did not state in what way the breccia-pipe matrix differs from the tuffs. If, indeed, the central part of the Maple Peak megabreccia is a welded tuff that is conformable with the rest of the section, it is difficult to retain the interpretation of Morris and Kopf (1967) that the megabreccia represents a breccia pipe that intrudes the volcanic rocks. The megabreccia of Maple Peak is here reinterpreted to be two volcanic megabreccia units that are intercalated in the welded tuff section. The lower megabreccia

Table 1. Description of stratigraphic units along traverse shown in figure 4.

[--, part of section not seen in interval now occupied by monzonite intrusion (Tm)]

Map unit	Thickness (feet)	Rock type	Description
sl	>590	sedimentary rocks	Calcareous shale, pumiceous(?) siltstone.
t7	1,360	rhyolitic welded tuff	Altered, tan to light-brown, pumice rich, lithic-clast poor, good eutaxitic texture, ~25% phenocrysts of quartz, feldspar, biotite and hornblende.
mb2	940	megabreccia	Altered crystal-rich rhyolitic matrix with phenocrysts of quartz, feldspar, and biotite.
t6	340	rhyolitic welded tuff	Light-gray, densely to poorly welded, weak layering with good eutaxitic texture, ~3-6% phenocrysts of sanidine, quartz, plagioclase and biotite.
mb1	630	megabreccia	Cream-colored rhyolitic matrix, with < 15% phenocrysts of sanidine, plagioclase, quartz, and biotite.
t5	0-170	rhyolitic welded tuff	Light-gray, massive, ~10-12% phenocrysts (sanidine, plagioclase, quartz, trace biotite), ~5% lithic clasts; wedges out to east.
t4	610	rhyolitic welded tuff	Medium-brown, very altered, flow banded with distinct eutaxitic texture (with greatly flattened pumice (fiamme); < 10% phenocrysts of quartz, feldspar, and biotite(?), sparse lithic clasts.
t3	1,260	rhyolitic welded tuff	Medium-gray, altered, massive, structureless, pumice rich, crystal poor (~10%, quartz, feldspar, biotite), ~35% lithic clasts.
f2	250	porphyritic latite(?)	Massive, with ~35% phenocrysts (plagioclase, hornblende, biotite, clinopyroxene) in devitrified groundmass; lower part of unit light-gray, upper part altered, mottled green and light-purple.
t2	1,540	rhyolitic welded tuff	Mostly massive, structureless, altered, crystal poor, cream to buff colored, ~15% phenocrysts plagioclase, quartz, sanidine, biotite, sparse small lithic clasts; dense, well-laminated zone near top with good eutaxitic texture.
fl	215	porphyritic latite(?)	Approximately 5% plagioclase phenocrysts in very fine grained, dense, light-gray groundmass.
--	2,020	--	Part of section not seen in interval now occupied by monzonite intrusion (Tm).
tl	420	rhyolitic welded tuff	Dark brown,~40% phenocrysts (plagioclase, sanidine, quartz, biotite), ~30% pumice fragments, sparse lithic fragments.
Total	10,345		

along the traverse is approximately 630 ft thick; the upper megabreccia is approximately 940 ft thick; and the intervening tuff is 340 ft thick (table 1). Preliminary $^{39}Ar/^{40}Ar$ biotite and sanidine ages for the tuff yield 34.6±0.1 and 34.4±0.05 Ma respectively (L.W. Snee, unpub. data).

Even without the evidence of a welded tuff unit within the Maple Peak megabreccia, it is difficult to accept the megabreccias of the study area as breccia pipes because of their size. Their approximate dimensions are: 1.5 by 3.5 mi for the Maple Peak megabreccia, 1 by 3 mi for the Cherry Creek megabreccia, and 0.5 by 1 mi for the Hassel megabreccia. Lipman (1984) noted that, although diatremes (breccia pipes) produce structures containing coarse breccias similar to the megabreccias of ash-flow

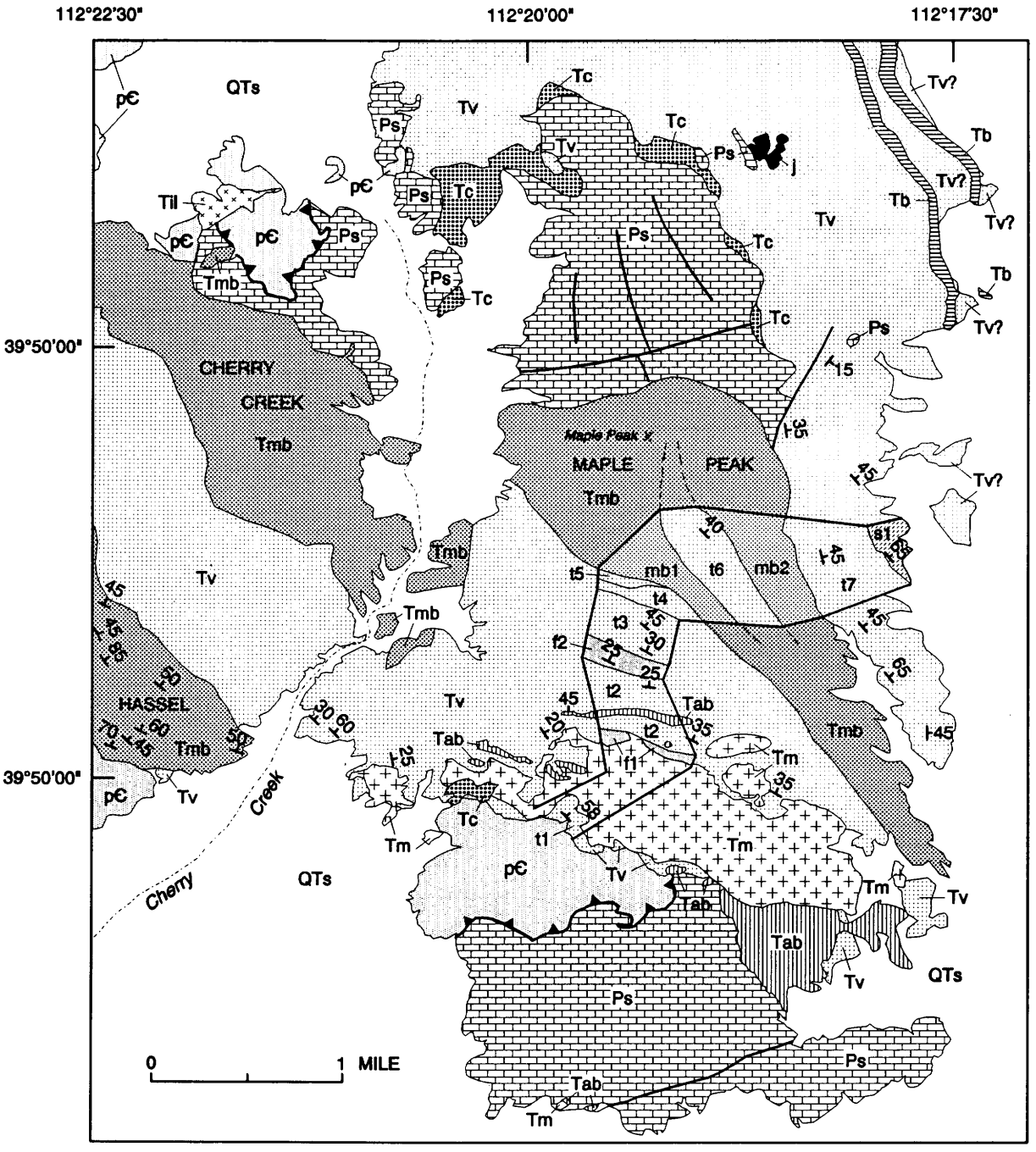

Figure 4 (explanation is on facing page). Geologic map of Maple Peak area, including detailed stratigraphy along a traverse across Maple Peak. Traverse location bounded by heavy lines in east-central part of map. Labeled rock units within traverse area are described in table 1. Map is modified from Morris and Kopf (1970a). Megabreccias are shown with names assigned by Morris and Kopf (1967).

calderas, the maximum known diameter of diatremes is less than 1 mi. Another feature of these megabreccias is their spatial association with the welded tuff section, which would easily be understood if they were layered units within that section. If the megabreccias are layered units within the section, the map pattern of the Cherry Creek and Maple Peak megabreccias shown on figure 4 suggests that they are continuous, and not separate, megabreccias.

A notable feature of the Hassel breccia pipe, as mapped by Morris and Kopf (1970a), is the large number of strike and dip measurements within the unit (only some of which are shown on fig. 4), most of which are 45°–85° NE. A well-defined, northeast-dipping layering is an odd

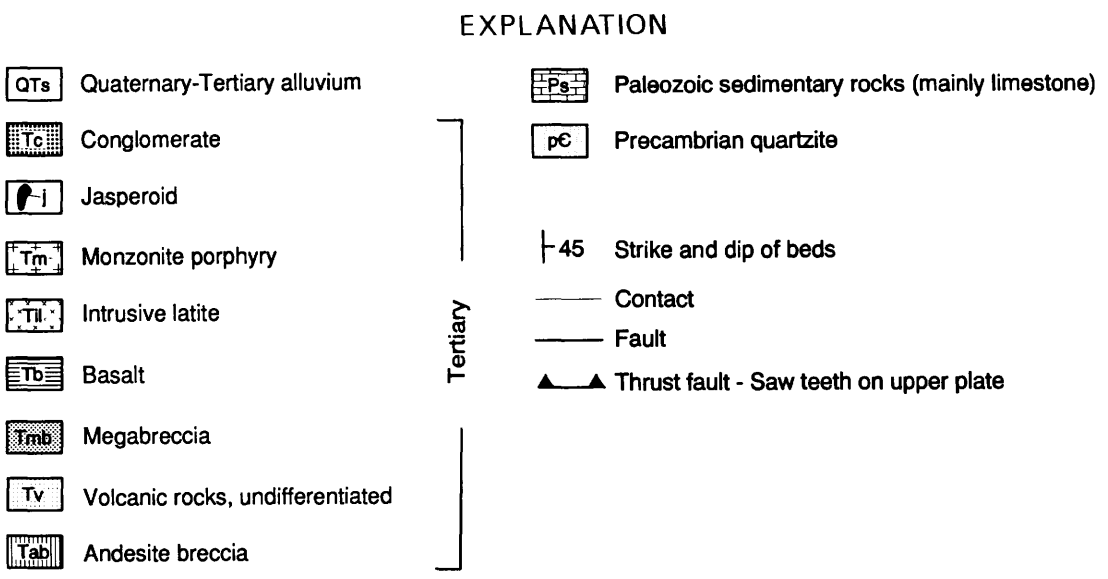

feature for a breccia pipe, but it is consistent if the Hassel unit is a layered unit within the volcanic section. I have examined only the southeasternmost part of the area mapped as the Hassel pipe and found it to be a massive, clast-poor, welded tuff.

Overlying the upper Maple Peak megabreccia is another thick (1,360 ft) rhyolitic tuff, which, in turn, is overlain by sedimentary rocks that are a minimum of 590 ft thick (table 1). These sedimentary rocks were not examined closely but, where observed on the traverse, consist of calcareous shale and siltstone. This unit was not recognized by Morris and Kopf (1970a) in their mapping. The relationship of the sedimentary rocks to the tuff is not known, but the attitude of the sedimentary rocks is approximately conformable with the tuff. Morris and Kopf (1970a) mapped several basalt units to the north of the traverse (fig. 4), and, based on stratigraphic relationships observed at the south Cherry Creek study area (discussed below), these may be basalt flows intercalated with the sedimentary rocks.

The occurrence of thousands of feet of very thick welded tuffs intercalated with very coarse volcanic megabreccia is distinctive of an intracaldera ash-flow sequence (Lipman, 1976, 1984; Best and others, 1989), and I, therefore, conclude that the tuff and megabreccia of the Maple Peak area were deposited within an ash-flow caldera. Given the fairly consistent dip to the northeast and lack of evidence for a repeat in the tuff-megabreccia section, the entire intracaldera sequence appears to be exposed in the Maple Peak area. The approximate thickness of 10,000 ft for the Maple Peak section suggests that the caldera was large.

The overall geometry of the proposed caldera is unclear, and resolution of its features must await further mapping; however, a few features of the caldera can be noted here. Best and others (1989) observed that, in other calderas, "lenses of landslide breccia within the intracaldera tuff thin away from the caldera wall from which they were derived, but can extend many kilometers into the center of the depression." The shape of the Maple Peak–Cherry Creek megabreccia fits this description (very thick to the northwest and wedging out to the southeast) and suggests that the collapsed-wall source of the megabreccia inclusions was to the northwest. Another notable feature of the Maple Peak sequence as mapped by Morris and Kopf (1967, 1970a) is the large mass of Paleozoic limestone that overlies the Maple Peak–Cherry Creek megabreccia and, in turn, appears to be overlain by tuff (fig. 4). This limestone may be a very large, intact block of the wall that slumped in as the caldera wall collapsed. The intact nature of the Maple Peak section suggests that the floor of the caldera is exposed to the southwest of the basal volcanic units and that the West Tintic mining district—immediately to the west of the Hassel megabreccia unit—and the intrusives contained in that district (Gardner, 1954; Stein and others, 1988) are located in the floor of the caldera. The sedimentary rocks that overlie the Maple Peak volcanic rocks may be late caldera fill or they may be part of a regional series of mid- to late-Tertiary sediments that are found throughout the region (Heylmun, 1965; McDonald, 1976).

SOUTH CHERRY CREEK

The south Cherry Creek study site (fig. 3) consists of a series of low hills south of the Sheeprock Mountains where Cherry Creek empties southwards into the Sevier Desert. The area was first mapped by Morris and Kopf (1970b), who recognized four stratigraphic units (from

bottom to top): Tertiary welded tuff and breccia, volcanic sandstone and limestone, gravel, and a basalt flow. Morris (1987, p. 4) later described the tuff and breccia unit as a massive to crudely layered rhyolitic tuff breccia that erupted from breccia pipes located in the southern part of the West Tintic and Sheeprock Mountains. He also presented a K-Ar biotite age for the tuff of 34.5 Ma (although Morris did not cite a source for this age determination, possibly it is derived from the 34.6±1.7-Ma K-Ar biotite age of Marvin and Dobson (1979) for a quartz-rich rhyolite tuff at the south Cherry Creek locality). Sanidine from one of the Cherry Creek tuffs yielded a preliminary $^{39}Ar/^{40}Ar$ age of 34.7±0.1 Ma (excess ^{40}Ar) (L.W. Snee, unpub. data).

In examining the tuff, I found vitrophyric layers within the tuff, some of which could be traced for more than one-half mile. Mapping these vitrophyres led to defining an internal stratigraphy for the tuff based on alternating vitrophyric and non-vitrophyric tuff zones (fig. 5). In addition, two megabreccia zones within the tuff section were also mapped (Tm_1 and Tm_2, fig. 5). The tuffs are pumice rich and lithic poor but highly variable in degree of induration and phenocryst content, and the non-vitrophyric tuffs are pervasively altered such that the mafic minerals have rarely survived. Dips within the tuff section vary from 20° to 65° NE. Based on an average dip of about 40° NE., the exposed tuff section is roughly 4,200 ft thick. Of particular note is the welded tuff above the upper megabreccia unit (Tm_2), which is an altered, tannish-brown, pumice-rich, phenocryst-poor tuff that is as much as 2,000 ft thick.

Vitrophyres occur throughout the tuff section and, in general, are relatively thin (about 1.5 to 5 ft) and uniform in thickness. Notable, however, is the vitrophyre at the top of the tuff section that, although its thickness appears to vary significantly along strike, is locally as much as 100 ft thick. Most of the vitrophyres can be traced for hundreds of feet or more, but some occur as thin lenses of only a few tens of feet in length. One angular discordancy is present in the lower part of the tuff section, where the lowest vitrophyre is sharply truncated by the overlying vitrophyre and tuff (fig. 5). The vitrophyres contain few to abundant lithic clasts and phenocrysts of sanidine, plagioclase, quartz, biotite, sparse hornblende, and trace clinopyroxene in a glassy matrix. In hand specimen, the vitrophyres are a dull black (perlitic) color, suggesting that the glass is hydrated.

The lower megabreccia (Tm_1), stratigraphically the lowest unit observed at south Cherry Creek, consists chiefly of large blocks of quartzite and limestone as much as 60–100 ft in diameter. The eastern two-thirds of the southernmost outcrop of the lower megabreccia consists of a very altered intermediate volcanic rock that I interpret to be a large block within the megabreccia. The matrix of the megabreccia was not observed, and thus, it is not known if this unit is a volcanic megabreccia. The upper megabreccia (Tm_2) forms a distinct layer within the tuff section. The clast content of the upper megabreccia changes along strike such that, in the southeast, it is a clast-rich breccia with a tuff matrix and blocks as much as about 40 ft in diameter, and, to the northwest, it passes into a tuff with sparse clasts (< 5 percent) that are mostly less than 6 ft in diameter. The breccia is polymict, with quartzite being the dominant clast type, but clasts of limestone and various types of volcanic rocks are also present, including crystal-rich rhyolite clasts similar to some of the underlying tuffs. The upper megabreccia is less than 100 ft thick in the southeast and thickens to the northwest. It includes a cap zone of purplish, clast-poor, crystal-rich, densely welded, agglomeratic tuff that grades downward into the megabreccia.

The tuff sequence is overlain by a poorly exposed section of sedimentary rocks composed of volcaniclastic sandstone, water-laid tuff(?), and minor limestone. A olivine-basalt flow overlies the sedimentary rocks. Both units dip to the northeast and appear to have about the same structural attitude; both are roughly conformable with the underlying tuff. The basalt may be intercalated with the sedimentary rocks, but no rock crops out above the basalt. Based on a dip of 30°–40° NE. for the sedimentary rocks, they are 600–1,000 ft thick. Morris and Kopf (1970b) mapped tuff above the sediments and basalt, but field examination failed to locate any tuff outcrops—the areas mapped as tuff by them is here remapped as part of the Tertiary pediment alluvium unit of figure 6.

The south Cherry Creek section bears an overall similarity to the Tertiary section found in the Maple Peak area. Both are composed of rhyolitic tuffs that include lower and upper megabreccias and are capped by a thick section of sedimentary rocks and associated basalt.

DESERT MOUNTAIN

Desert Mountain is a small, isolated range that consists of two main geological units: a rhyolitic tuff with megabreccia along the eastern margin and a granitic complex that forms the bulk of the range (fig. 6). Precambrian quartzite and diamictite of the Sheeprock Group also crop out at the northern end of the range (fig. 6). Desert Mountain has been mapped previously by Kattelman (1968), Shawe (1972), Rees and others (1973), and part of Desert Mountain along the Callao-Jericho road was mapped by Walsh (1987). Calkins (1972) also did a magnetic and gravity survey of Desert Mountain. The present report is based, in part, on a new map of Desert Mountain being prepared by D.B. Stoeser and D.A. Lindsey.

The tuff of Desert Mountain, as named by Walsh (1987), occurs along the entire eastern flank of Desert

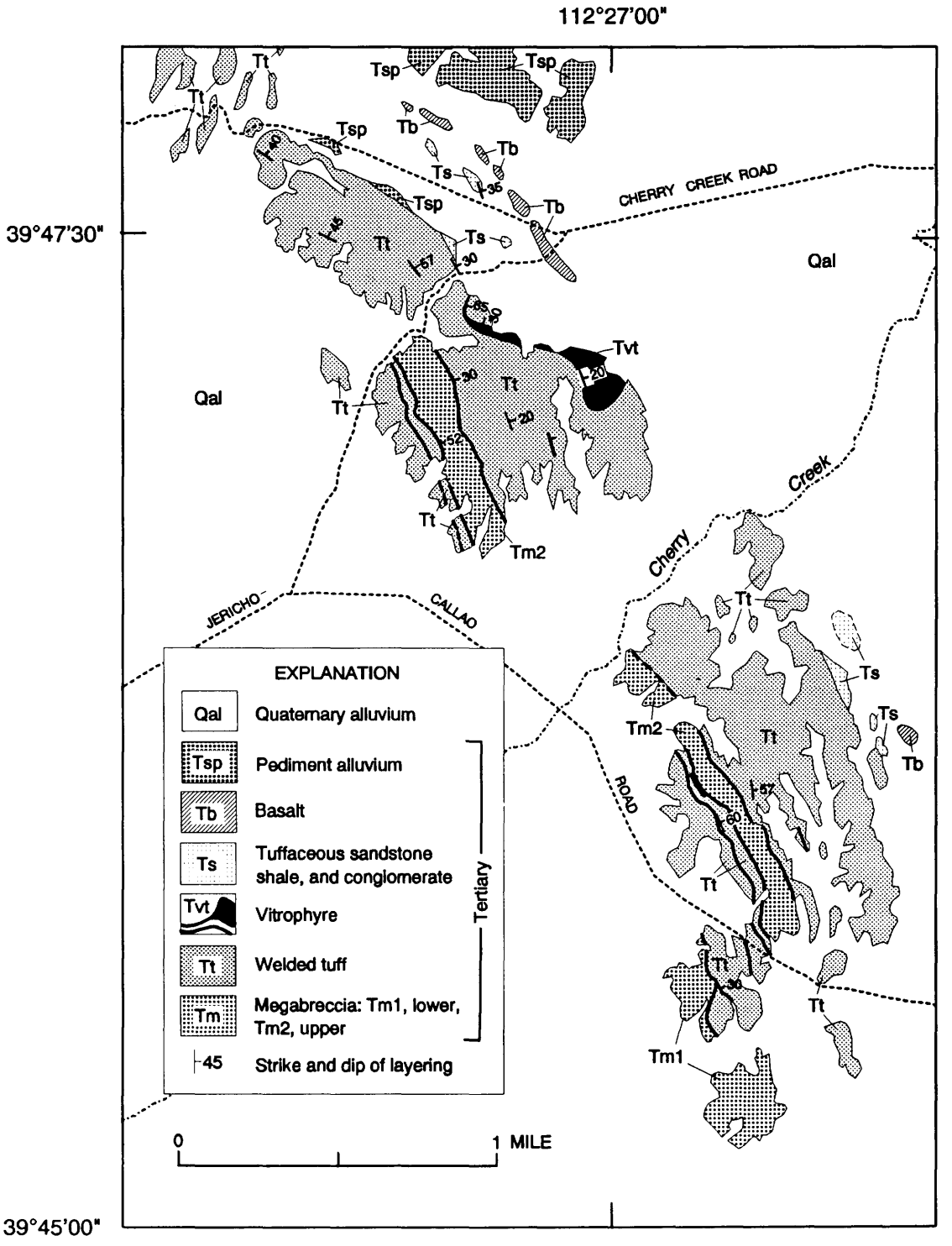

Figure 5. Geologic map of south Cherry Creek area. Based in part on mapping by Morris and Kopf (1970b).

Mountain. As described by Walsh, it consists of two facies: massive rhyolitic tuff and megabreccia with a rhyolitic matrix (the facies are gradational and simply reflect that the tuff ranges from clast rich to clast poor). The tuff is crystal rich, with phenocrysts of plagioclase, sanidine, quartz, biotite, and sparse hornblende in an aphanitic matrix that contains sparse, small, compacted pumice fragments and sparse to numerous lithic fragments. The tuff has been dated by Lindsey and others (1981) at 34.5±1.3 Ma (zircon fission track).

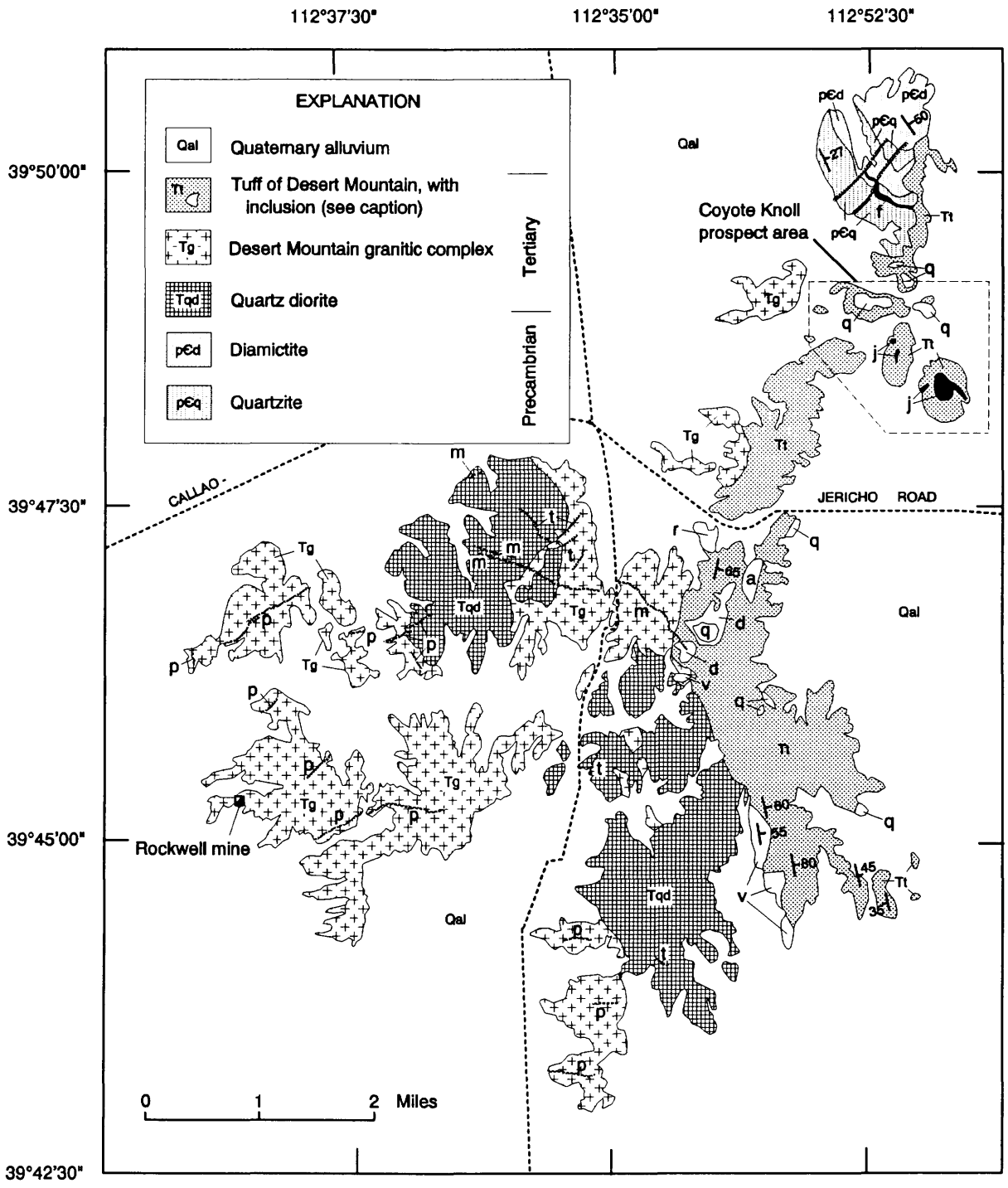

Figure 6. Geologic map of Desert Mountain. Main units described in explanation box within figure; other labeled units on map refer to either inclusions within the tuff of Desert Mountain or dikes within the granitic complex of Desert Mountain. Labeled inclusions are: a, Tertiary andesite; d, Precambrian diamictite; q, Precambrian quartzite; r, rhyolite; and v, andesite to dacitic volcanic rocks, lahar, and volcanogenic sedimentary rocks. Labeled dikes are: f, felsite; m, monzonite; p, lamprophyre; and t, latite. Also shown are areas of jasperoid (j) formed by replacement of tuff. Other symbols are the same as on figure 4.

Most of the megabreccia occurs south of the Callao-Jericho road (figs. 3, 6). The megabreccia is chaotic, matrix rich (> 80 percent), and contains a few blocks up to about 1,500 ft in length. Inclusions in the megabreccia zones are dominantly quartzite, with lesser amounts of diamictite, argillite, volcanic rocks, and sparse, small (< 10 cm) plutonic rocks. The volcanic-rock inclusions are comprised of andesite, latite, dacite, and sparse rhyolite.

The large volcanic blocks located at the southern end of the tuff outcrop (fig. 6) consist of intact sections of dacite, latite, lahar(?), and volcaniclastic sedimentary rock.

The structural attitude of the tuff is problematical because the tuff is massive and generally without well-defined layering so that determining attitudes in the field is very difficult. Based on local, weak layering and orientation of pumice lappilli, it appears that the tuff has an overall attitude of dipping steeply to the east (fig. 6). Shawe (1972) and Walsh (1987) also indicate that the tuff and megabreccia dip steeply east and is intruded by the granite. Based on dips shown in figure 6, the exposed section of tuff and megabreccia is approximately 5,000 ft thick.

The tuff of Desert Mountain is largely altered such that the mafic minerals are replaced by aggregates of opaque minerals, and hematite and feldspar are sericitized. In some places, the tuff is very dense and hard, as if silicified. Of approximately 50 samples of the tuff that I examined in thin section, primary mafic minerals were found only in three samples. In addition to the regional low-grade alteration of the tuff, most of the tuff north of the Callao-Jericho road has been argillically altered and locally silicified to form jasperoid (fig. 6). The most intensely altered area of tuff, the Coyote Knoll prospect area (fig. 6), was explored for gold by Freeport-McMoran during 1989–1990. The granite of Desert Mountain, north of the road, also has been weakly to strongly argillically altered, and, therefore, the alteration postdates the main igneous units of Desert Mountain.

The granitic complex of Desert Mountain consists of multiple intrusive units of biotite monzogranite (not shown on fig. 6) and includes large roof pendants of quartz diorite. Granite intrudes the tuff of Desert Mountain and is therefore younger. Although the granite has been dated several times, it is not clear what units were dated because previous workers recognized only a single granite at Desert Mountain. Armstrong (1970) dated the granite by the K-Ar method at 28.5±0.6 Ma (biotite) and 26.5±0.5 Ma (orthoclase). Lindsey and others (1975) using the fission-track method obtained ages of 28.2 Ma (sphene) and 32.4 Ma (zircon). Walsh (1987) also cites an unpublished Sr-Rb isochron age for the granite by E.H. Christiansen of 34.8±0.8 Ma. The granitic complex is intruded by dikes of lamprophyre, mafic-rich porphyritic monzonite and quartz monzonite, latite, and granitic felsite (fig. 6).

Both Kattleman (1968) and Rees and others (1973) interpreted the tuff to be a shallow intrusive; Rees and others, in particular, considered it to be a diatreme. Shawe (1972) and Walsh (1987) interpreted the tuff to be extrusive and intracaldera in origin. Given the great thickness of the tuff-megabreccia section and the large size of some inclusions in the megabreccia, I concur with the intracaldera interpretation.

DISCUSSION

CALDERAS

A number of calderas have been proposed to lie within the eastern half of the Tintic–Deep Creek belt (fig. 3). Of these, only the 38–36-Ma Thomas caldera is clearly defined and well accepted (Shawe, 1972; Lindsey, 1982). Other proposed calderas and caldrons include the Tintic caldera of the East Tintic Mountains (Morris, 1975), the Desert caldera (Shawe, 1972), the Dead Ox and Keg caldrons of the Keg Mountains (or Keg caldera of Shawe, 1972; Shubat and Snee, in press), and Picture Rock caldera, which is immediately south of the Keg Mountains (ARCO, unpub. report, Anaconda Geological Document Collection, University of Wyoming, Laramie; Shubat and Snee, in press). Only the Tintic caldera, the Desert caldera, and the Maple Peak caldera (a newly proposed caldera) are located within the study area and are discussed here.

TINTIC AND MAPLE PEAK CALDERAS

Morris (1975) first proposed the Tintic caldera primarily on the basis of the existence of a circular magnetic anomaly that coincided with a thick section of intermediate to rhyolitic volcanic rocks in the southern part of the East Tintic Mountains. The inferred caldera was approximately 8 mi in diameter. Magmatic rocks of the East Tintic Mountains were divided into two age groups by Morris and Lovering (1979); an older group of about 35–32 Ma and a younger group of about 18 Ma. The proposed Tintic caldera assemblage belongs to the older group and was thought to have included two major outflow units: the Fernow and Packard Quartz Latites. The existence of a caldera in the southern East Tintic Mountains has been supported by Hannah and Macbeth (1990), Hannah and others (1990, 1991), Macbeth (1990), and Keith and others (1989, 1991)—these workers felt that caldera formation was related to rocks assigned to the Copperopolis latite formation of Morris (1975) and Morris and Lovering (1979) rather than to the Fernow or Packard Quartz Latites.

Hannah and Macbeth (1990) and Macbeth (1990) mapped a section of volcanic tuffs and flows, approximately 3,200 ft thick, that they subdivided into lower and upper pyroclastic sequences. The lower pyroclastic sequence consists of andesitic tuff and tuff breccia that is overlain by andesitic flows. The lower tuffs include megabreccia with clasts exceeding 325 ft in diameter. The upper pyroclastic sequence contains a lower rhyolitic lapilli tuff overlain by lacustrine sediments and andesitic flows and agglomerate. The two pyroclastic sequences are overlain and underlain by thick sections of mafic (dominantly

andesitic) flow rocks. They propose two phases of caldera collapse based on the tuffs and tuff breccias in the lower part of each sequence. Available age dating of these rocks cited by Hannah and Macbeth (1990) indicate they were deposited at approximately 35–37 Ma. Although Hannah and Macbeth (1990) and Macbeth (1990) support a caldera interpretation for these rocks, they admit that most of the overt features of a caldera are absent due to complications induced by post-caldera cover and structural events, including the caldera being truncated and downdropped on the west by the Tintic Valley fault (Mabey and Morris, 1967). They also reduced the size of the proposed caldera to a diameter of approximately 6.5 mi.

Keith and others (1989, 1991) studied the upper pyroclastic sequence, which they described as members of the Copperopolis latite of Morris (1975) and Morris and Lovering (1979). They published $^{39}Ar/^{40}Ar$ geochronologic data that support an age of 35–37 Ma for these rocks. They also showed that overlying andesitic and rhyolitic rocks, as well as monzonite intrusions, were implaced between 34.5 and 33.6 Ma. Based on their work they concluded "that a large caldera related to the eruption of the younger Packard Quartz Latite and Fernow Quartz Latite is not present in this area." They continued on to conclude "that a smaller caldera related to the eruption of the tuff member of the Copperopolis latite may be present."

In the Tintic area, two caldera-related volcanic-rock sequences are now recognized: those previously assigned to the Tintic caldera in the southern East Tintic Mountains (Hannah and Macbeth, 1990; Keith and others 1989, 1991; Macbeth, 1990; and Morris, 1975) and those of the West Tintic Mountains as proposed in this paper. The two sequences are separated by the approximately 10-mi-wide Tintic Valley, and it appears that the rocks of both sequences extend beneath the cover of the valley. Based on the lack of correlation of the stratigraphy of the two sections (i.e., 3,200 ft of mostly andesitic rocks in the East Tintic Mountains versus 9,600 ft of rhyolitic tuff and megabreccia in the West Tintic Mountains), it seems unlikely that they represent the same calderas. In addition, the East Tintic caldera-related rocks appear to be somewhat older that those of the West Tintic Mountains (35–37 Ma as opposed to 34.5 Ma), although certainly more work is needed to resolve the age of formation of these rocks. They are close in age, however, and it seems likely that multiple caldera-forming events have occurred in the Tintic area during the early Oligocene. Because the caldera-related rocks of the West Tintic Mountains do not appear to correlate with those in the East Tintic Mountains, I propose recognizing a separate ash-flow caldera, the Maple Peak caldera, named after the location where the best and most complete exposures of the intracaldera rocks are found. A relationship between East Tintic volcanic rocks may exist based on: (a) the occurrence of magmatic events equivalent in age to the Maple Peak intracaldera rocks in the East Tintic Mountains, and (b), as proposed below, Tintic Valley may have formed by extension, and the two volcanic sequences may have initially been more in proximity than they are now. One interesting possibility is that the Fernow Quartz Latite may be outflow from the Maple Peak caldera. The Fernow is a large, welded, ash flow that occurs throughout the southern part of the East Tintic Mountains and for at least another 20 mi to the south. In spite of the quartz latite name, the Fernow is a rhyolite with 68–70 percent silica and contains abundant phenocrysts of plagioclase, quartz, biotite, and minor sanidine and hornblende (Morris, 1975; de Vries, 1990). The more recent works by Hannah and Macbeth (1990) and Keith and others (1989, 1991) have failed to identify a source for the Fernow in the East Tintic Mountains, but its lithology fits well with the rhyolitic tuffs of the Maple Peak intracaldra sequence (table1).

DESERT MOUNTAIN CALDERA

The Desert caldera was first proposed by Shawe (1972) based on the presence of "rhyolitic to quartz-latitic ash-flow tuff units" along the eastern margin of the range and on a circular magnetic high over the western part of the range. Shawe showed the caldera as including all of Desert Mountain and centered on the western part of the range (fig. 3). Both Shawe (1972) and Walsh (1987) interpreted the granite to be resurgent into the tuff, which is supported by available dating as shown by Walsh (1987) and by recent mapping. Although the Desert Mountain igneous rock assemblage has been assigned to the Desert caldera by Shawe, I recommend changing the name to the Desert Mountain caldera in order to make its name fit more appropriately with its type locality.

Structural complications induced by regional extension, as discussed below, indicate that calderas in the east-central part of the Tintic–Deep Creek belt have been dismembered and that the exposed parts of these calderas may not correspond with the locations of their root zones (that is, the upper parts of the calderas have been transported laterally away from their underlying intrusive zones). Another significant problem is that alluvial cover obscures most of the study area. As already noted, the great thicknesses of tuff and large size of the inclusions in the megabreccias at Maple Peak and Desert Mountain indicate that these rocks must be intracaldera in origin. Although a thick section of tuff and megabreccia occurs at south Cherry Creek, the clast size of the megabreccia is significantly less than for megabreccia at the other two localities, and the south Cherry Creek volcanic rock assemblage may be either intracaldera or very proximal in origin. If proximal rocks lie between the two intracaldera assemblages of Maple Peak and Desert Mountain, it is unlikely that the Desert Mountain assemblage belongs to

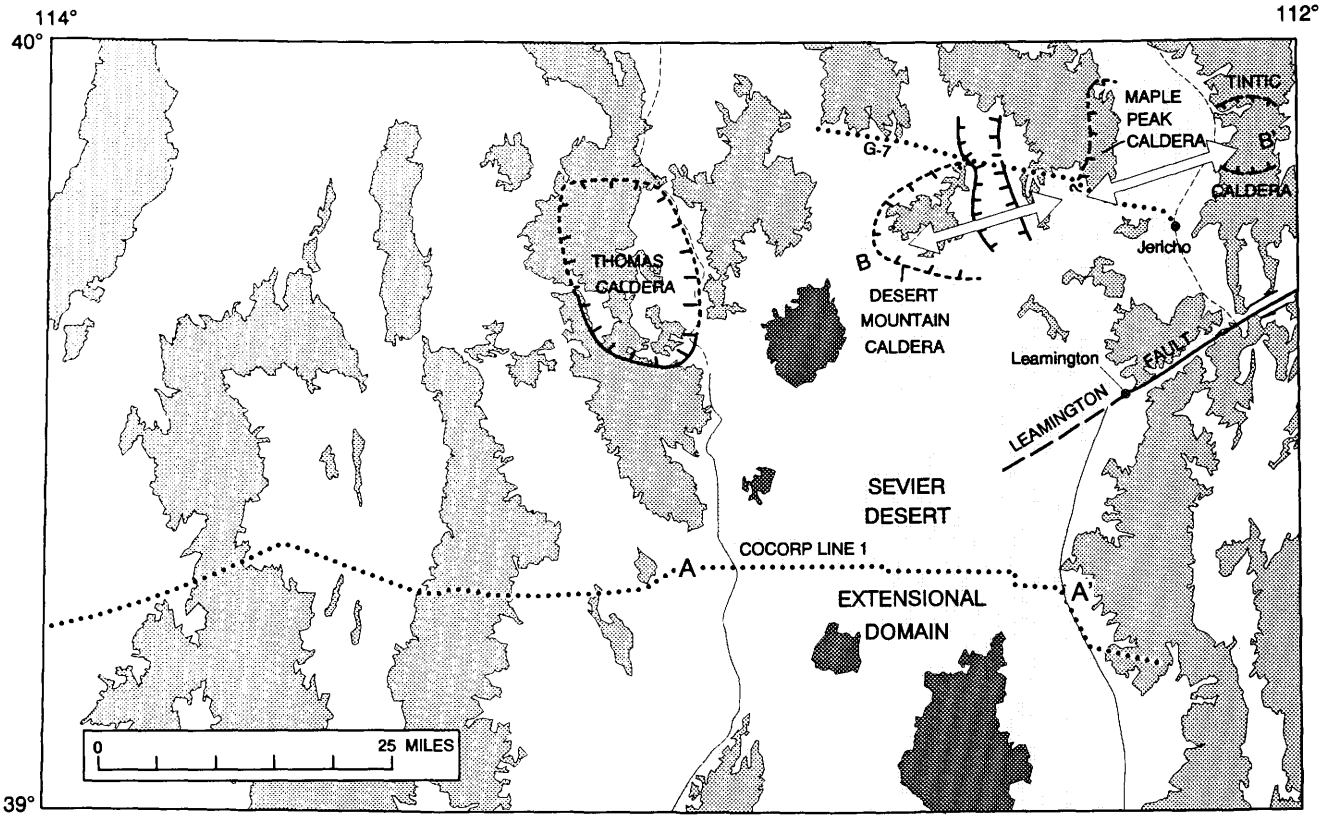

Figure 7. Map of the Delta 1°×2° quadrangle showing location of proposed calderas in the study area and the Sevier Desert extensional domain and related features. Tintic caldera as shown by Hannah and Macbeth (1990). White arrows show direction of proposed extension related to deformation of caldera-related volcanic rocks. Medium- and dark-gray areas are ranges and basaltic volcanic fields from figure 2. A–A′ marks location of cross section shown on figure 8. B–B′ marks location of cross section shown on figure 10. Dotted line labeled G–7 represents a seismic line described by Planke and Smith (1991).

the same caldera as that of Maple Peak. If it did, then the rocks of Desert Mountain were transported over 13 mi to the west from the site of the Tintic caldera—this requires that a deep part of that caldera was transported the farthest, a relation opposite to that expected. Thus, I conclude that the intracaldera rocks of Desert Mountain belong to a separate caldera from those of Maple Peak, and I support the caldera interpretation of Shawe (1972) for Desert Mountain (fig. 7).

REGIONAL EXTENSION

The study area lies north of the Sevier Desert Basin, which underlies the central part of the Sevier Desert (figs. 2, 8). The basin is located between the Canyon Range on the east and the Cricket and Drum Mountains on the west and is more than 10,000 ft deep (Planke and Smith, 1991). The Sevier Desert Basin is one of the major extensional features of the eastern Basin and Range and has received considerable study (McDonald, 1976; Lindsey, and others, 1981; Von Tish and others, 1985; Mitchell and McDonald, 1986; Planke and Smith, 1991), including COCORP seismic reflection profile line 1 (fig. 7) (Allmendinger and others, 1983, 1985). The basin was formed by extension on the Sevier Desert detachment, a low-angle normal fault that heads along the west flank of the Canyon Range, dips westward at about 10°–12°, and extends at least as far west as the House Range (Allmendinger and others, 1983; Smith and Bruhn, 1984). An interpretative cross section of the COCORP seismic data across the Sevier Desert extensional domain by Von Tish and others (1985) is shown on figure 8. Sharp (1984) has estimated that total displacement on the Sevier Desert detachment is between 28 and 38 km (17–24 mi). Extension on the Sevier Desert detachment occurred primarily during two episodes (Von Tish and others, 1985): the first episode began no later than the middle Oligocene (before 28 Ma) and continued into the middle Miocene, and the second episode began in the middle Pliocene and continues to the present.

The Sevier Desert extensional domain and the underlying Sevier Desert detachment have been mapped as far north as the latitude of Leamington (fig. 7) (Von Tish and others, 1985; Gans, 1987; Planke and Smith, 1991) or to

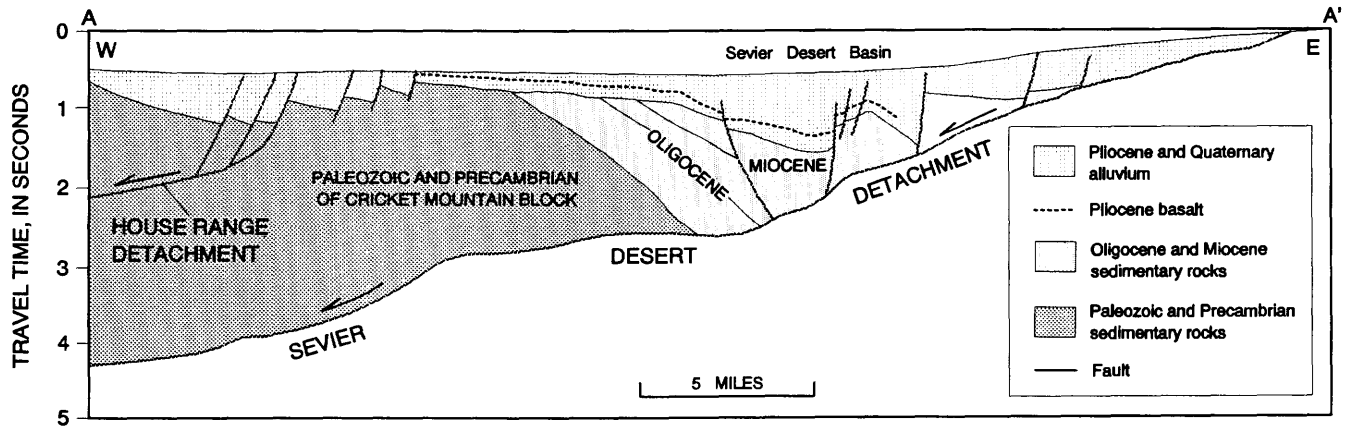

Figure 8. Interpretative cross section of Sevier Desert Basin along COCORP seismic reflection line 1, between A and A′ on figure 7 (2× vertical exaggeration) (from Von Tish and others, 1985).

about 12 mi south of Desert Mountain. Defining regional extension to the north is problematical. The presence of regional extension in the study area is suggested by attitudes of the Oligocene volcanic rocks within the eastern part of the Tintic–Deep Creek belt. The volcanic rocks of the West Tintic Mountains, south Cherry Creek, and Desert Mountain all have a consistent, moderately steep dip to the northeast, whereas volcanic rocks of similar age in the East Tintic Mountains, to the east of the study area, and those of the Keg Mountains, Thomas Range, and Drum Mountains to the west, are nearly flat-lying. That is, the Oligocene volcanic rocks that are north of and on the trend of the known Sevier Desert extensional domain are tilted and those to the flanks are not. The indicated area of regional extension, however, does continue eastward from the Sevier Desert extensional domain to Tintic Valley north of the Leamington fault (fig. 7). It should be noted that the eastern portion of the Sevier Desert detachment has been removed by erosion due to uplift in the area of the Canyon Range (Sharp, 1984). In addition to the structural evidence, Planke and Smith (1991) describe results from a seismic line that crosses the study area (dotted line labeled G7 on fig. 7), that indicates "a weak, discontinuous, westward-dipping reflector, whose projection intersects the surface just west of Jericho"—they propose that this may be the Sevier Desert detachment.

The occurrence of limestone xenoliths within the Desert Mountain intrusive complex may provide direct evidence for the Sevier Desert detachment beneath Desert Mountain. Late, mafic-rich, monzonite porphyry dikes in the northwestern part of the intrusive complex (fig. 6) contain blocks of limestone and marble as much as 50 ft in diameter (as well as large blocks of granite and small inclusions of various types of mafic intrusive rocks). Because it seems unlikely that these carbonate blocks could have been derived from above the emplacement level of the dikes, they must have come from below. This relationship indicates that there is a bottom or floor to the intrusive complex. The Desert Mountain intrusive complex may be laccolithic in form, or alternatively, a detachment may underlie the complex and the monzonite dikes postdate initiation of the detachment and sampled limestone from beneath the detachment.

Regional extension in the Sevier Desert region can be further defined by the gravity gradient map of the Delta 1°×2° quadrangle (fig. 9) (Bankey and Cook, 1989). This map shows the horizontal rate of change of the gravity field. Where the gravity field changes sharply over a short distance, it indicates boundaries between crustal domains with significant differences in density. Typically, these zones correlate with high-angle faults that bound basins; these zones are due to the sharp gravity contrast between alluvial basin fill and bedrock and, in most cases, locate faults formed during regional extension. In figure 9, lines have been drawn along these zones for emphasis.

The western margin of the Sevier Desert extensional domain, along the west flank of the Sevier Desert, is well defined by a steep gravity-gradient zone that runs west of the Cricket Mountains and along the east flank of the Drum Mountains (fig. 9). Based on figure 9, I have extended the western boundary of regional extension northward between the Thomas Range and Keg Mountain along an apparent, direct continuation of this zone. The eastern margin of the domain in the study area is drawn along the east margin of Tintic Valley where Mabey and Morris (1967) and Morris (1975, 1987) locate a major range-front fault. Tintic Valley exhibits a major gravity low that Mabey and Morris (1967) and Cook and others (1991, p. 18) have interpreted as indicating approximately 6,000 to 7,000 ft of fill, although some contribution to the gravity anomaly might be due to low-density caldera material beneath the valley. As previously stated, Planke and Smith (1991) indicate that a detachment heads at the location of Jericho, which lies on the

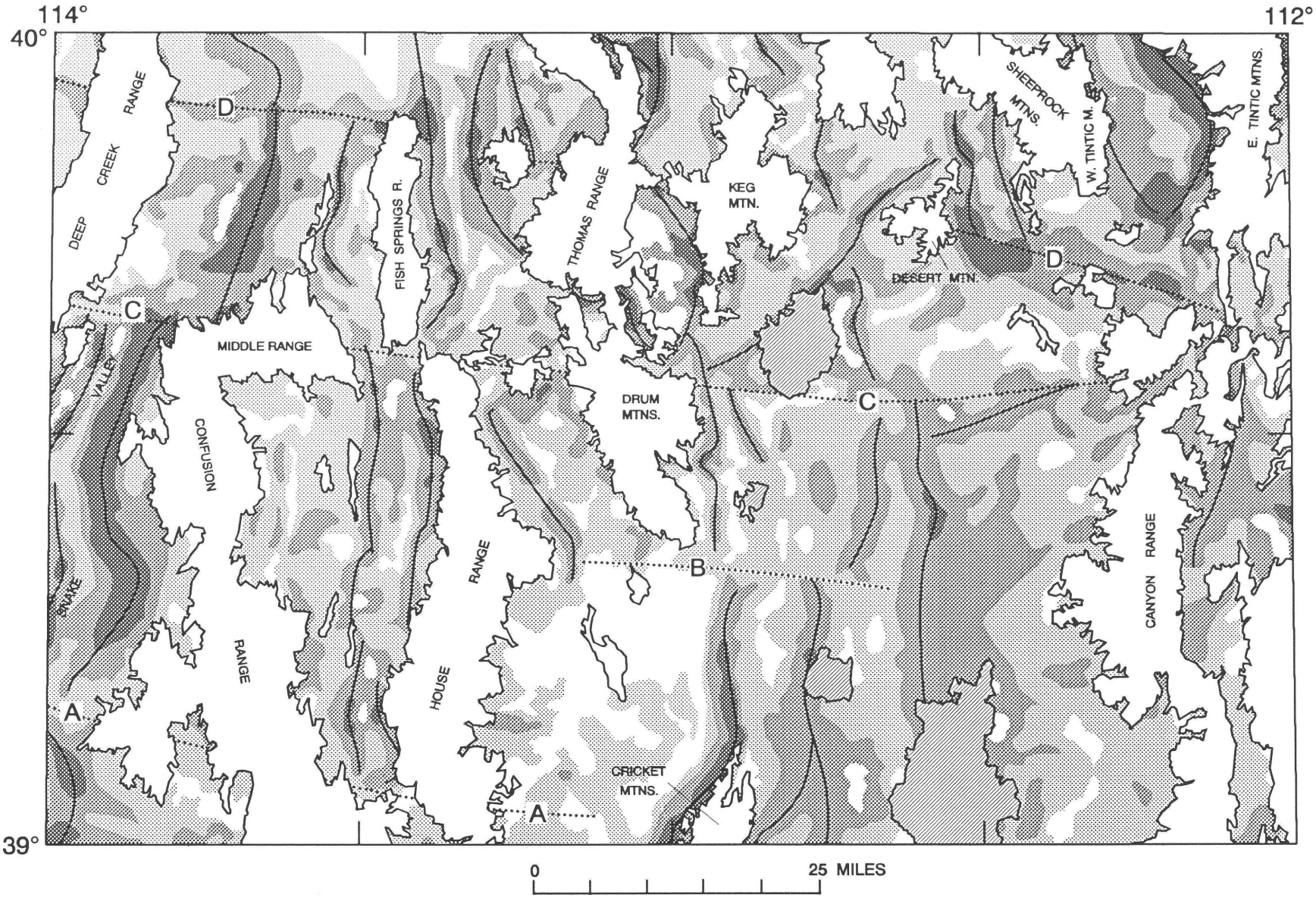

Figure 9. Simplified gravity gradient map of the Delta 1°×2° quadrangle adapted from original data of Bankey and Cook (1989). Range boundaries from figure 2 are superimposed over gravity gradients. Shades of gray represent magnitude of horizontal gradient of the gravity field (see Bankey and Cook, 1989, for explanation): white 0.0–0.7, light gray 0.7–1.5, medium gray 1.5–3.5, and dark gray > 3.5. Areas shown with diagonal pattern are Pliocene and Quaternary volcanic fields shown on figure 2. A, B, C, and D represent east-west lineaments that are discussed in the text.

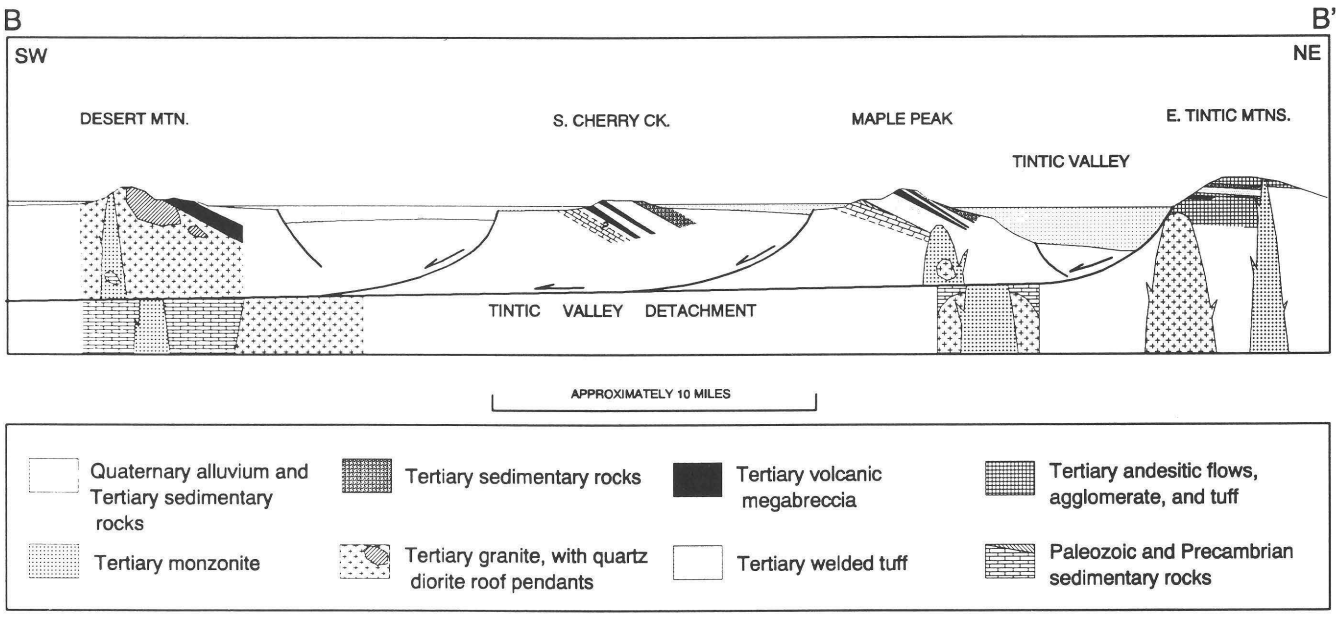

Figure 10. Generalized interpretive cross section of study area (along B–B′ on figure 7). Geology of the East Tintic Mountains adapted from Hannah and Macbeth (1990) and Macbeth (1990), Tintic Valley from a gravity interpretation by Cook and others (1991), Maple Peak from Morris and Kopf (1970a) and this paper, south Cherry Creek from this paper, and Desert Mountain from Walsh (1987) and this paper. Blank areas of the figure indicate parts for which the geology in unknown due to alluvial cover. No vertical exaggeration.

East Tintic range-front fault (fig. 8, 9). Tintic Valley is interpreted to be underlain by a major listric fault that forms a half-graben and that soles westward to form a detachment that underlies the study region (fig. 10).

The gravity gradient data for the Delta 1°×2° quadrangle also exhibits four east-west lineaments (labeled A, B, C, and D). The southern three lineaments, A, B, and C, all mark disruptions in the north-south grain of the data. These north-south features usually indicate extensional faults, either as range-front faults or intrabasinal extensional faults. Lineaments A and B simply mark such disruptions and do not have notable surface expression. Lineament C is discussed separately below. Lineament D is distinct from the other three in that it is a gravity-gradient lineament, which suggests that it may be a major fault. Lineament D appears to extend almost the complete length of the Delta 1°×2° quadrangle. It is disrupted by north-south-trending gravity-gradient features, indicating that it is older than regional extension.

Lineament C is a major feature within the north-central part of the quadrangle. Its main characteristics west of the Sevier Desert extensional domain are:

1. Disruption of north-south-trending gravity-gradient features and, therefore, presumably disruption of faults related to post mid-Tertiary extensional faulting,
2. Aligns with east-west strike-slip faults at the southern end of the Deep Creek range (Smith and others, 1991),
3. Aligns with topographic highs and anomalous range alignments as shown by the east-west-trending Middle Range and smaller positive areas west of the Drum Mountains; also aligns with truncations of the Deep Creek, Fish Springs, and House Ranges,
4. Corresponds to an inversion in dip of Paleozoic sedimentary rocks between the Fish Springs and House Ranges,
5. Aligns with intrusions in the area of Sand Pass, which is located at the join between the Fish Springs and House Ranges, and
6. Aligns with the southern margin of the Thomas caldera and the flaring of the topography of the northern part of the Drum Mountains.

East of the Drum Mountains, the projection of the lineament is largely under alluvial cover, but on the gravity gradient map (fig. 9), there is a change from north-south-trending gravity-gradient features to the south of the lineament to east-west-trending ones to the north. Because of the features defining the lineament at Sand Pass at the join between the Fish Springs and House Ranges, the lineament is informally named here the Sand Pass lineament. A major feature of the Sand Pass lineament is that it forms the southern boundary for the Oligocene magmatism of the Tintic–Deep Creek belt. With few exceptions, all intrusions and vents of this age are near or north of the Sand Pass lineament. Altogether, the features associated with the Sand Pass lineament indicate that crust to the north of the lineament reacted differently to regional extension compared to crust to the south. East-west lineaments with similar features have also been reported in southwestern Utah and southern Nevada (Ekren and others, 1976; Rowley and others, 1978). The nature of the Sand Pass lineament is

unclear: it may mark a major crustal discontinuity in the basement between Proterozoic terranes or between Archean and Proterozoic terranes, or more simply, it may represent a transition zone between two extensional domains. Based on the evidence for regional extension and a detachment beneath the study area and because features of the Sevier Desert detachment are truncated at the Sand Pass lineament, I conclude that a separate and probably coeval detachment, named here the Tintic Valley detachment, and a related extensional domain underlie the east-central part of the Tintic–Deep Creek belt (fig. 10).

REFERENCES CITED

Allmendinger, R.W., Sharp, J.W., Von Tish, D., Oliver, J., and Kaufman, S., 1985, COCORP profile across the Cordilleran hingeline, west-central Utah, *in* Gries, R.R. and Dyer, R.C., eds., Seismic Exploration of the Rocky Mountain Region: Rocky Mountain Association of Geologists, p. 23–30.

Allmendinger, R.W., Sharp, J.W., Von Tish, D., Serpa, L., Brown, W., Kaufman, S., Oliver, J.E., and Smith, R.B., 1983, Cenozoic and Mesozoic structure of the eastern Basin and Range Province, Utah, from COCORP seismic relection data: Geology, v. 11, p. 532–536.

Armstrong, R.L., 1970, Geochronology of Tertiary igneous rocks, eastern Basin and Range Province, western Utah, eastern Nevada, and vicinity, U.S.A.: Geochimica et Cosmochimica Atca, v. 34, p. 202–232.

Bankey, Viki, and Cook, K.L., 1989, Complete Bouguer gravity map and related geophysical maps of the Delta 1°×2° quadrangle, Utah: U.S. Geological Survey Miscellaneous Field Studies Map MF–2081–A, scale 1:250,000.

Best, M.G., Christiansen, E.H., Deino, A.L., Gromme, C.S., McKee E.H., and Noble, D.C., 1989, Excursion 3A—Eocene through Miocene volcanism in the Great Basin of the western United States, *in* Chapin, C.E. and Zidek, Jiri, eds., Field Excursions to Volcanic Terranes in the Western United States, Volume II: Cascades and Intermountain West: New Mexico Bureau of Mines and Mineral Resources Memoir 47, p. 91–133.

Calkins, W.G., 1972, Magnetic and gravity study of Desert Mountain, Juab County, Utah: Utah Geological and Mineralogical Survey Bulletin 95, 21 p., 1 plate.

Christiansen, E.H., Sheridan, M.F., and Burt, D.M., 1986, The geology and geochemistry of Cenozoic topaz rhyolites from the western United States: Geological Society of America Special Paper 205, 82 p.

Cook, K.L., Mabey, D.R., and Bankey, Viki, 1991, The new gravity map of Utah—An overview of its usefulness for geologic studies: Utah Geological Survey, Survey Notes, v. 24, no. 4, p. 12–21.

Ekren, E.B., Bucknam, R.C., Carr, W.J., Dixon, G.L., and Quinlivan, W.D., 1976, East-trending structural lineaments in central Nevada: U.S. Geological Survey Professional Paper 986, 16 p.

Gans, P.B., 1987, An open-system, two-layer crustal stretching model for the eastern Great Basin: Tectonics, v. 6, p. 1–12.

Gans, P.B., Mahood, G.A., and Schermer, Elizabeth, 1989, Synextensional magmatism in the Basin and Range Province; a case study from the eastern Great Basin: Geological Society of America Special Paper 233, 53 p.

Gardner, W.C., 1954, Geology of the West Tintic mining district and vicinity, Juab County, Utah: Salt Lake City, University of Utah, unpub. M.S. thesis, 43 p.

Groff, S.L., 1959, Geology of the West Tintic Range and vicinity, Tooele and Juab Counties: Salt Lake City, University of Utah, unpub. Ph.D. thesis, 183 p., map scale 1:20,439.

Hannah, J.L., and Macbeth, Alec, 1990, Magmatic history of the East Tintic Mountains, Utah: U.S. Geological Survey Open-File Report 90–0095, 24 p., 1 plate, scale 1:24,000.

Hannah, J.L., Stein, H.J., and Macbeth, Alec, 1990, A caldera in the East Tintic Mountains, Utah—Field relations between Tertiary magmatism and Tintic-type ore deposits [abs.], *in* Geology and Ore Deposits of the Great Basin, Reno/Sparks, Nevada: Geological Society of Nevada and U.S. Geological Survey, 1990 Program with Abstracts, p. 63.

Hannah, J.L., Stein, H.J., and Macbeth, A.P., 1991, Field relations between Tertiary magmatism and Tintic-type ore deposits, East Tintic Mountains, Utah, *in* Raines, G.L., Lisle, R.E., Schafter, R.W., and Wilkinston, W.H., eds., Geology and Ore Deposits of the Great Basin: Geological Society of Nevada, Symposium Proceedings, v. 1, p. 485–489.

Hilpert, L.S., and Roberts, R.J., 1964, Economic Geology, *in* Mineral and water resources of Utah: Washington, D.C., 88th U.S. Congress, 2nd. Session, Committee Print, p. 28–34.

Heylmun, E.B., 1965, Reconnaissance of the Tertiary sedimentary rocks in western Utah: Utah Geological and Mineral Survey Bulletin 75, 38 p.

Kattelman, D.F., 1968, Geology of the Desert Mountain intrusives, Juab County, Utah: Brigham Young University Geology Studies, v. 15, pt. 1, p. 85–107.

Keith, J.D., Dallmeyer, R.D., Kim, Choon-Sik, and Kowallis, B.J., 1989, A reevaluation of the volcanic history and mineral potential of the central East Tintic Mountains, Utah: Utah Geological and Mineral Survey Open-File Report 166, 74 p.

Keith, J.D., Dallmeyer, R.D., Kim, Choon-Sik, and Kowallis, B.J., 1991, The volcanic history and magmatic sulfide mineralogy of latites of the central East Tintic Mountains, Utah, *in* Raines, G.L., Lisle, R.E., Schafter, R.W., and Wilkinston, W.H., eds., Geology and Ore Deposits of the Great Basin: Geological Society of Nevada, Symposium Proceedings, v. 1, p. 461–483.

Lindsey, D.A., 1982, Tertiary volcanic rocks and uranium in the Thomas Range and northern Drum Mountains, Juab County, Utah: U.S. Geological Survey Professional Paper 1221, p. 1–57.

Lindsey, D.A., Glanzman, R.K., Naeser, C.W., and Nichols, D.J., 1981, Upper Oligocene evaporites in basin fill of Sevier Desert region, western Utah: Bulletin of the American Association of Petroleum Geologists, v. 65, p. 251–260.

Lindsey, D.A., Naeser, C.W., and Shawe, D.R., 1975, Age of volcanism, intrusion, and mineralization in the Thomas Range, Keg Mountain, and Desert Mountain, western Utah: U.S. Geological Survey Journal of Research, v. 3, no. 5, p. 597–604.

Lipman, P.W., 1976, Caldera-collapse breccias in the western San Juan Mountains, Colorado: Geological Society of America Bulletin, v. 87, p. 1397–1410.

Lipman, P.W., 1984, The roots of ash flow calderas in western North America—Windows into the tops of granitic batholiths: Journal of Geophysical Research, v. 89, p. 8801–8841.

Mabey, D.R., and Morris, H.T., 1967, Geologic interpretation of gravity and aeromagnetic maps of Tintic Valley and adjacent areas, Tooele and Juab Counties, Utah: U.S. Geological Survey Professional Paper 516–D, 10 p.

Macbeth, A.P., 1990, Geology of the southwestern East Tintic Mountains, central Utah: University of Vermont, unpub. M.S. thesis, 164 p.

Maciulaitis, P.E., 1991a, Jericho property, Juab County, Utah: Boulder, Colorado, Euro-Nevada Mining Corporation, Inc., unpub. report, 28 p.

_____1991b, Rockwell/Sahara property, Juab County, Utah: Boulder, Colorado, Euro-Nevada Mining Corporation, Inc., unpub. report, 24 p.

Marvin, R.F., and Dobson, S.W., 1979, Radiometric ages: Compilation B, U.S. Geological Survey: Isochron/West, no. 26, p. 3–32.

McDonald, R.E., 1976, Tertiary tectonic and sedimentary rocks along the transition—Basin and Range province to plateau and thrust belt province, Utah, *in* Newman, G.W. and Goode, H.D., eds., Basin and Range Symposium and Great Basin Field Conference: Rocky Mountain Association Geologist Guidebook, p. 503–514.

Mitchell, G.C., and McDonald, R.E., 1986, History of Cenozoic extension in central Sevier Desert, west-central Utah, from COCORP seismic reflection data—Discussion: Bulletin of the American Association of Petroleum Geologists, p. 1015–1021.

Morris, H.T., 1975, Geologic map and sections of the Tintic Mountain quadrangle and adjacent part of the McIntyre quadrange, Juab and Utah Counties, Utah: U.S. Geological Survey Miscellaneous Investigations Series Map I–883, scale 1:24,000.

Morris, H.T., 1982, Regional relations of Wah Wah–Frisco thrust fault in western Utah: U.S. Geological Survey Professional Paper 1150, 64 p.

_____1983, Interrelations of thrust and transcurrent faults in the central Sevier orogenic belt near Leamington, Utah, *in* Miller, D.M., Tood, V.R., and Howard, K.A., eds., Tectonic and Stratigraphic Studies in the Eastern Great Basin: Geological Society of America Memoir 157, p. 75–81.

_____1987, Preliminary geologic map of the Delta 2° quadrangle Tooele, Juab, Millard, and Utah Counties, Utah: U.S. Geological Survey Open-File Report 87–185, 18 p., scale 1:250,000.

Morris, H.T., and Kopf, R.W., 1967, Breccia pipes in the West Tintic and Sheeprock Mountains, Utah: U.S. Geological Survey Professional Paper 575–C, p. C66–C71.

_____1970a, Preliminary geologic map and cross sections of the Maple Peak quadrangle and adjacent part of the Sabie Mountain quadrangle, Juab County, Utah: U.S. Geological Survey Open-File Report 70–234, scale 1:24,000.

_____1970b, Preliminary geologic map and cross sections of the Cherry Creek quadrangle and adjacent part of the Dutch Peak quadrangle, Juab County, Utah: U.S. Geological Survey Open-File Report 70–233, scale 1:24,000.

Morris, H.T., and Lovering, T.S., 1979, General geology and mines of the East Tintic mining district, Utah and Juab counties, Utah: U.S. Geological Survey Professional Paper 1024, 203 p.

Pampeyan, E.H., 1989, Geologic map of the Lynndyl 30- by 60-minute quadrangle, west-central Utah: U.S. Geological Survey Miscellanceous Investigations Series Map I–1830, scale 1:100,000.

Planke, Sverre, and Smith, R.B., 1991, Cenozoic extension and evolution of the Sevier Desert Basin, Utah, from seismic reflection, gravity, and well log data: Tectonics, v. 10, p. 345–366.

Rees, D.C., Erickson, M.P., and Whelan, J.A., 1973, Geology and diatremes of Desert Mountain, Utah: Utah Geological and Mineralogical Survey, Special Studies 42, 12 p., 1 plate.

Rowley, P.D., Lipman, P.W., Mehnert, H.H., Lindsey, D.A., and Anderson, J.J., 1978, Blue Ribbon lineament, an east-trending structural zone within the Pioche mineral belt of soutwestern Utah and eastern Nevada: U.S. Geological Survey Journal of Research, v. 6, no. 2, p. 175–192.

Sharp, J.W., 1984, West-central Utah: palinspastically restored sections constrained by COCORP seismic reflection data: Ithaca, New York, Cornell University, unpub. M.S. thesis, 60 p.

Shawe, D.R., 1972, Reconnaissance geology and mineral potential of Thomas, Keg, and Desert calderas, central Juab County, Utah, *in* Geological Survey Research 1972: U.S. Geological Survey Professional Paper 800–B, p. B67–B77.

Shawe, D.R., and Stewart, J.H., 1976, Ore deposits as related to tectonics and magmatism, Nevada and Utah: American Institute of Mining Engineers, Transactions, 1977 Annual Meeting, Las Vegas, Nevada, v. 260, p. 225–232.

Shubat, M.A., and Snee, L.W., in press, High-precision $^{40}Ar/^{39}Ar$ geochronology, volcanic stratigraphy, and mineral deposits of Keg Mountain, west-central Utah: U.S. Geological Survey Bulletin 2012, Chapter G.

Smith, D.L., Gans, P.B., and Miller, E.L., 1991, Palinspastic restoration of Cenozoic extension in the central and eastern Basin and Range Province at latitude 39–40°N., *in* Raines, G.L., Lisle, R.E., Schafter, R.W., and Wilkinston, W.H., eds., Geology and Ore Deposits of the Great Basin: Geological Society of Nevada, Symposium Proceedings, v. 1, p. 75–86.

Smith, R.B., and Bruhn, R.L., 1984, Intraplate extensional tectonics of the eastern Basin-Range—Inferences on structural style from seismic reflection data, regional tectonics, and thermal-mechanical models of brittle-ductile deformation: Journal of Geophysical Research, v. 89, p. 5733–5762.

Spenser, J.E., and Welty, J.W., 1986, Possible controls of base- and precious-metal mineralization associated with Tertiary detachment faults in the lower Colorado River trough, Arizona and California: Geology, v. 14, p. 195–198.

Stein, H.J., Kelley, D.L., Kaminsky, J.F., and Gordon, I.R., 1988, Field trip guide for the West Tinitic mining district, western Utah: U.S. Geological Survey Open-File Report 88–0558, 12 p.

Stokes, W.E., 1986, Geology of Utah: Salt Lake City, Utah Geological and Mineral Survey, 280 p.

Turley, C.H., and Nash, W.P., 1980, Petrology of late Tertiary and Quaternary volcanism in western Juab and Millard Counties, Utah: Utah Geological and Mineral Survey Special Study 52, p. 1–33.

Von Tish, D.B., Allmendinger, R.W., and Sharp, J.W., 1985, History of Cenozoic extension in central Sevier Desert, west-central Utah, from COCORP seismic reflection data: Bulletin of the American Association of Petroleum Geologists, v. 69, no. 7, p. 1077–1087.

Vries, R.D. de, 1990, Tales of Tertiary tuffs in central Utah: De Kalb, Northern Illinois University, unpub. M.S. thesis, 160 p.

Walsh, D.V., 1987, Geological and geochemical relationships of the Desert Mountain igneous complex rocks: Salt Lake City, University of Utah, unpub. M.S. thesis, 64 p.

Wilkins, J., Jr., Beane, R.E., and Heidrick, T.L., 1986, Mineralization related to detachments faults—A model, *in* Beatty, B., and Wilkinson, P.A.K., eds., Frontiers in Geology and Ore Deposits of Arizona and the Southwest: Arizona Geological Society Digest, v. 16, p. 108–117.

CHAPTER B

BASEMENT STRUCTURE IN THE RAILROAD VALLEY–GRANT RANGE REGION, EAST-CENTRAL NEVADA, FROM INTERPRETATION OF POTENTIAL-FIELD ANOMALIES

By H. RICHARD BLANK[1]

Regional gravity and aeromagnetic anomaly maps are widely used to delineate first-order structural features expressed by marked density and magnetization contrasts. In east-central Nevada and elsewhere in the miogeoclinal domain of the Basin and Range extensional province, the gravity method is especially effective for distinguishing areas where the bedrock is veneered by pediment gravels (or by Cenozoic volcanic and volcaniclastic rocks) from areas underlain by relatively thick, low-density valley fill. The density "basement" is generally rock of the miogeoclinal carbonate succession or Mesozoic and Cenozoic intrusive rock. The aeromagnetic method, on the other hand, detects magnetic crystalline rock beneath the nonmagnetic carbonates. This "basement" may be either Phanerozoic intrusives or the Precambrian igneous-metamorphic complex. Signatures of strongly magnetic volcanic rocks of the Cenozoic section are typically distinguished by their shorter spatial wavelengths, which result from greater proximity to the detector and lesser depth extent.

The original objective of recent U.S. Geological Survey (USGS) gravity and aeromagnetic investigations in east-central Nevada was to aid in mineral resource assessment of Bureau of Land Management Wilderness Study Areas. Later, the scope of investigation was expanded to include a study of the structural framework of sedimentary basins with known or potential hydrocarbon deposits. Studies of basement structure in the Railroad Valley–Grant Range region (fig. 1) focus on both objectives and involve integration of potential-field, seismic, drilling, and geologic-map data. Railroad Valley has a strike length of nearly 175 km, with an average north-northeasterly trend. Its maximum width of about 25 km occurs where it is flanked on the east by the Grant Range. This central sector is the locus of oil production in the valley. The nearby Troy district, in the southern Grant Range, achieved prominence in the past as a producer of gold, silver, and tungsten.

Figure 2 shows the complete-Bouguer gravity anomaly field of the Railroad Valley–Grant Range region. The color interval on the map is 2 milligals (mGal), and the absolute anomaly level at Currant is –210 mGal. Primary gravity data were obtained from files of the National Center for Geophysical and Solar-Terrestrial Data (Boulder, Colorado 80303), supplemented by several dozen stations recorded by the USGS in conjunction with current programs. A reduction density of 2.67 g/cm^3 was employed, and all stations have been terrain-corrected out to a radius of 167 km (see Cordell and others, 1982, for a description of standard USGS gravity-reduction procedures). Stratiform geologic units shown on the figure are: Paleozoic sedimentary rocks, chiefly miogeoclinal carbonates (Pz), Tertiary volcanic and sedimentary rocks (T), and Quaternary surficial deposits (Qa). Granitic intrusive rocks of Cretaceous and Tertiary age (KTi) are represented by a diagonal pattern; the largest such body exposed is the Troy pluton. Also shown is the Shell No. 1 discovery hole in Railroad Valley, which intersected quartz monzonite at a depth of 10,330 ft (3.15 km). Quartz monzonite has been intersected in several other drill holes at shallower depths in the valley.

[1]U.S. Geological Survey, Mail Stop 964, P.O. Box 25046, Denver Federal Center, Denver, CO 80225.

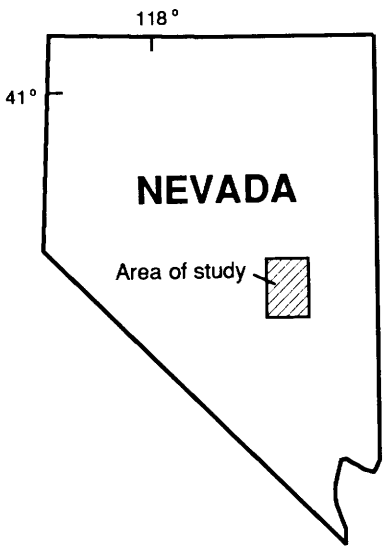

Figure 1. Index map of Great Basin showing Railroad Valley–Grant Range region, east-central Nevada.

The Bouguer anomaly map shows a north-northeast-trending anomaly depression in Railroad Valley that is narrower than the full width of the valley and that contains two collinear axial lows separated by a weak rise. All six of the producing oil fields are situated on the margins of the northern low, which has a residual amplitude of –43 mGal. Exploration drilling has established that the thickness of valley fill (Tertiary and Quaternary deposits, including Tertiary volcanic rocks) in this area exceeds 4.2 km (see Garside and others, 1988, for a recent compendium of drilling data). At such depths, the prevailing geothermal gradient may be sufficient to convert organic material to oil (Hulen and others, 1991), and the presence of high-angle faults on the margins of the deep could have facilitated upward migration to suitable traps and reservoirs. The mean density contrast corresponding to a 43-mGal anomaly produced by 4–5 km of valley fill is much less than the 0.40–0.45 g/cm^3 predicted for fill relative to Paleozoic carbonates (Guion and Pearson, 1979) or to igneous intrusive rock. This discrepancy is probably attributable to an abundance of high-density carbonate materials in the Tertiary and Quaternary valley fill, as suggested by down-hole sonic and lithologic logs. Megaclasts of Paleozoic carbonate rocks are locally present and, in some places, have been detected by detailed, high-precision, commercial gravity surveys.

The 43-mGal anomaly low has horizontal gradients along its eastern flank of as much as 11 mGal/km, whereas those on the western flank are about half as strong. Accordingly, the bedrock surface beneath Railroad Valley can be modeled as an asymmetric graben or half graben with its floor tilted down to the east—this is in agreement with seismic-reflection results (Bortz and Murray, 1979; Vreeland and Berrong, 1979; Foster and others, 1985; Effimoff and Pinezich, 1986). The eastern marginal gradient is a continuous, well-constrained gravity feature that follows the trend of the range front for a distance of 65 km, from near Currant to the southwest corner of the map area (fig. 2). The locus of *maximum* gradients in this belt is a line 2–10 km west (basinward) of the nearest bedrock outcrops. The line of maxima roughly coincides with a line of springs and groundwater seepage and is believed to mark the approximate trace of the main boundary fault (range-front fault) on the west side of the Grant Range (Foster, 1979). Opposite the two gravity lows, where the gradient is steepest, the fault or fault zone is probably a high-angle structure, but in the intervening segment (in the vicinity of the Troy pluton), dips as low as 20° have been interpreted from seismic data (Potter and others, 1991). Either flatter dip or deeper burial of a specific density discontinuity would weaken the gradient. Down-hole logs show the rocks immediately east of the gradient maxima, just north of the Troy pluton, to be predominantly high-velocity, high-density, Paleozoic carbonate sand/gravel and breccia (identified as valley fill) below the uppermost 400 m or so of section. A transverse seismic profile in this area reveals east-dipping reflectors abutting an underlying, gently west-dipping reflector that is interpreted as a low-angle normal fault. Thus, where the gravity gradients are weaker, the range-front fault apparently truncates sections that include detached and rotated allochthonous Paleozoic strata (either megaclasts in "valley fill" or strata that form the hanging wall of a low-angle normal fault).

Residual aeromagnetic total-field intensity for the Railroad Valley–Grant Range region is shown on figure 3. This map was prepared in the USGS Branch of Geophysics by merging data from several different surveys (after removing the International Geomagnetic Reference Field corresponding to the date of each survey, draping to an elevation of 1,000 ft (305 m) above terrain, and reducing to the pole). The generalized geologic units on this figure are the same as those of figure 2, and, in addition, the locus of maximum horizontal gradients of the Bouguer anomaly field on the east side of Railroad Valley (range-front fault; see above) is indicated by a heavy dashed line. The color interval on the map is 10 nanoteslas (nT), and the absolute residual field intensity over the Shell No. 1 discovery hole is about +12 nT.

The main aeromagnetic feature of interest is a broad positive anomaly with three principal crests that encompasses the northern half of Railroad Valley (most of the sector shown on fig. 3) and most of the Grant Range. The axis of this anomaly tends to parallel that of the negative gravity anomaly associated with Railroad Valley: both extend N.-S. across the area of figure 3 and are convex eastward. No offset of the aeromagnetic feature is observed where it is transected by the line of maximum

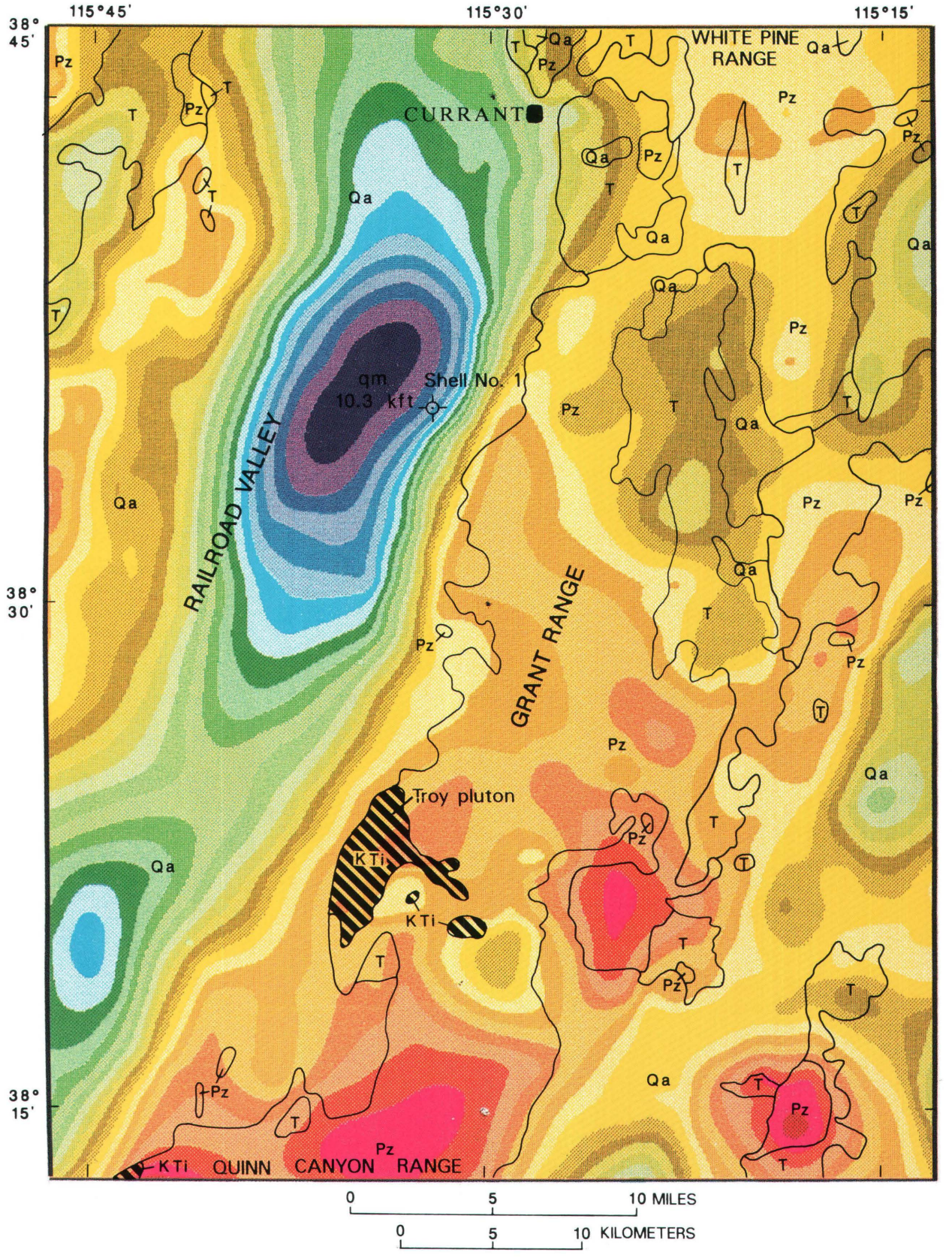

Figure 2. Complete-Bouguer gravity anomaly map of Railroad Valley–Grant Range region, east-central Nevada. Color interval 2 mGal. Pz, Paleozoic sedimentary rocks; KTi, Cretaceous and Tertiary granitic intrusive rocks; T, Tertiary volcanic and sedimentary rocks; Qa, Quaternary surficial deposits. Quartz monzonite (qm) was penetrated at 10,330 ft in Shell No. 1 discovery hole.

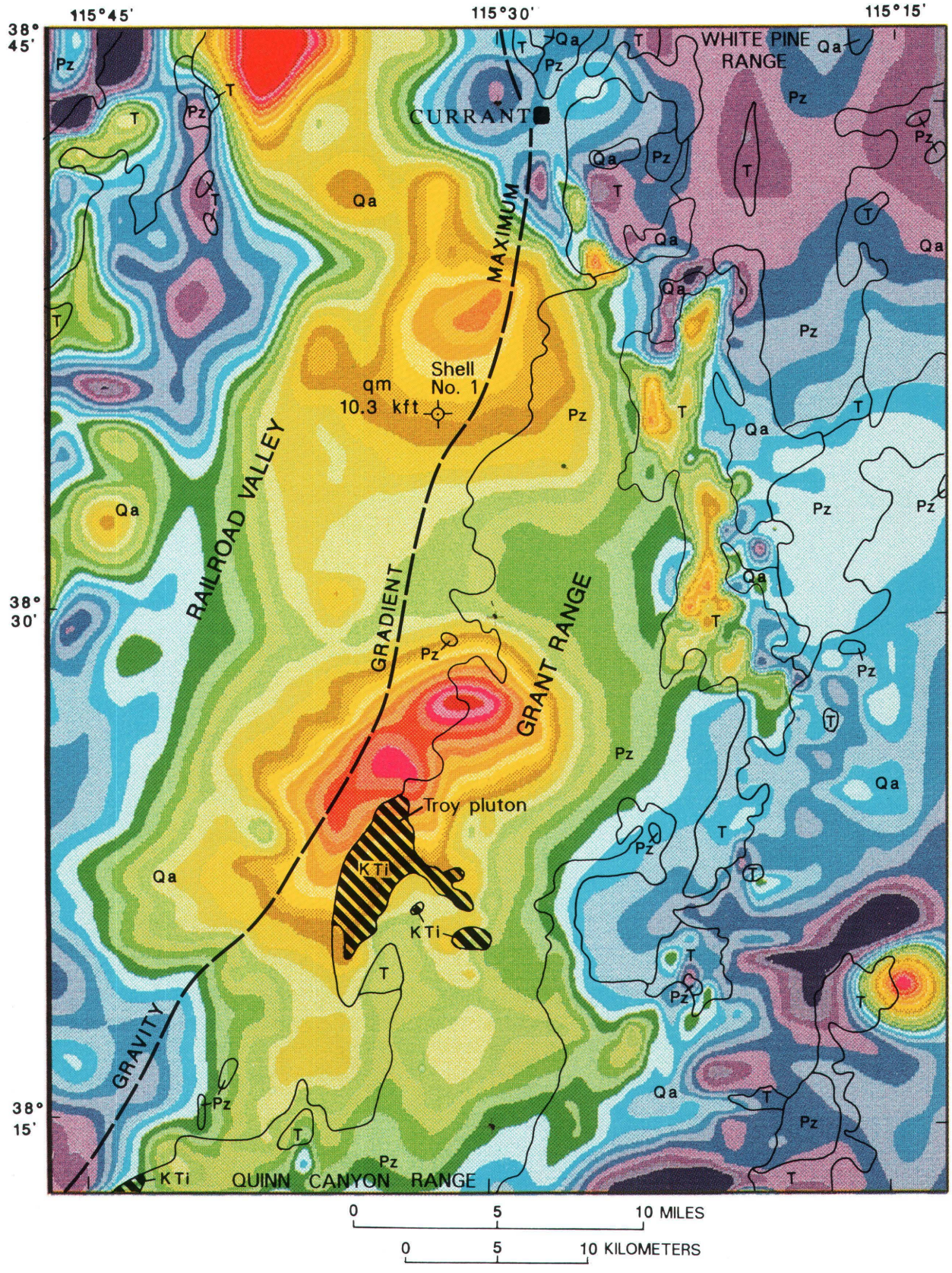

Figure 3. Residual aeromagnetic total-field intensity map of Railroad Valley–Grant Range region, east-central Nevada. Color interval 10 nT. Symbols are the same as for figure 2.

gravity gradients, which nearly bisects it. Therefore, the range-front fault must be listric with respect to, or terminate at, a low-angle structure at or near the surface of the magnetic body. This structure may be the low-angle normal fault north of the Troy pluton that is interpreted from seismic data. Mississippian Chainman Shale, a source rock for the hydrocarbons (Barker and Peterson, 1991), could locally have served as the zone of detachment. The question of whether the low-angle fault passes beneath the Grant Range at depth or connects with a low-angle fault exposed on the west side of the Grant Range (as inferred by Lund and others, 1991, and Potter and others, 1991) is not likely to be resolved from the potential-field data.

Because no strongly magnetic Paleozoic or Late Proterozoic strata are known from geologic mapping in the region, possible sources of the broad aeromagnetic anomaly are limited to the Precambrian igneous-metamorphic crystalline basement complex and Phanerozoic intrusive bodies. The most likely source is considered to be a Phanerozoic granitic batholith. Granitic plutons are exposed in the southwestern White Pine Range, in the southern Grant Range, and in the northern Quinn Canyon Range, and, as noted above, quartz monzonite has been penetrated in several drill holes in Railroad Valley. All of these occurrences are spatially associated with the broad anomaly, although typical rock of the Troy pluton (two-mica granite) is known to be only very weakly magnetic (M.R. Hudson, oral commun., 1992). Potassium-argon ages for biotite of the plutons range from 23 to 36 Ma, according to Kleinhampl and Ziony (1985), who cite Schilling (1965) and Armstrong (1970). Yet a 70-Ma minimum age of crystallization has been determined for the Troy pluton by Fryxell (1988) on the basis of whole-rock Rb/Sr analysis. These apparently contradictory results can be reconciled by postulating that the aeromagnetic anomaly source is a composite body consisting of weakly magnetic granite that was emplaced during Late Cretaceous time and strongly magnetic monzonitic rock emplaced during an episode of renewed heating and magmatism in the Tertiary.

The batholith, if present, must have had a major role in the tectonic evolution of the Railroad Valley–Grant Range region. Initial emplacement would have occurred during a late stage of synkinematic regional metamorphism that is recorded in lower Paleozoic rocks of the southern Grant Range (Kleinhampl and Ziony, 1985). Renewed magmatism in Oligocene-Miocene time may have contributed to arching of the range, as well as to high heat flow in Railroad Valley. Also, a structural parallelism indicates that the batholith may have influenced the configuration of youthful extensional structures, such as the Railroad Valley graben.

Some implications of the batholith for mineral resource exploration have been discussed in detail elsewhere (Lund and others, 1987, 1988). Of special interest are the prominent anomaly crestal areas north of the Troy pluton and north of the Shell No. 1 discovery hole (fig. 3). Such highs superimposed on the broad positive anomaly could be expressions of structural relief, or locally enhanced magnetization, or both. (A third prominent high on the broad anomaly, centered 15 km west of Currant at the north edge of the map, is much more intense and sharply bounded than the other two and could be due to a buried mafic volcanic complex. Unlike the others, it has no apophysis beneath Paleozoic rocks.) If these highs are produced by intrusive rock, they flag potential loci of hydrothermal alteration and mineralization. Moreover, the gravity data strongly suggest that much of the area beneath the two aeromagnetic highs is pedimented bedrock and is therefore possibly accessible for exploitation, should mineral deposits be proved.

REFERENCES CITED

Armstrong, R.L., 1970, Geochronology of Tertiary igneous rocks, eastern Basin and Range Province, western Utah, eastern Nevada, and vicinity: Geochimica et Cosmochimica Acta, v. 34, p. 203–232.

Barker, C.E., and Peterson, J.A., 1991, Burial history of the Mississippian Chainman Shale and the Eocene Sheep Pass Formation, Railroad and White River Valleys, eastern Nevada, *in* Flanigan, D.M.H., Hansen, M., and Flanigan, T.E., eds., Geology of White River Valley, the Grant Range, Eastern Railroad Valley and Western Egan Range, Nevada: Reno, Nevada Petroleum Society, 1991 Field Trip Guidebook, p. 37–46.

Bortz, L.C., and Murray, D.K., 1979, Eagle Springs oil field, Nye County, Nevada, *in* Newman, G.W., and Goode, H.D., eds., 1979 Basin and Range Symposium: Denver and Salt Lake City, Rocky Mountain Association of Geologists and Utah Geological Association, p. 441–454.

Cordell, L.E., Keller, G.R., and Hildenbrand, T.G., 1982, Bouguer gravity map of the Rio Grande rift, Colorado, New Mexico, and Texas: U.S. Geological Survey Geophysical Investigations Map GP-949, scale 1:1,000,000.

Effimoff, I., and Pinezich, A.R., 1986, Tertiary structural development of selected basins—Basin and Range Province, northeastern Nevada, *in* Mayer, L., ed., Extensional Tectonics of the Southwestern United States—A perspective on Processes and Kinematics: Geological Society of America Special Paper 208, p. 31–42.

Foster, N.H., 1979, Geomorphic exploration used in the discovery of the Trap Spring field, Nye County, Nevada, *in* Newman, G.W., and Goode, H.D., eds., 1979 Basin and Range Symposium: Denver and Salt Lake City, Rocky Mountain Association of Geologists and Utah Geological Association, p. 477–488.

Foster, N.H., Vreeland, J.H., and Dolly, E.D., 1985, Basin and Range seismic profiles in Railroad Valley, Nye County, Nevada, *in* Gries, R.R., and Dyer, R.C., eds., Seismic Exploration of the Rocky Mountain Region: Denver, Rocky Mountain Association of Geologists and Denver Geophysical Society, p. 283–288.

Fryxell, J.E., 1988, Geologic map and descriptions of stratigraphy and structure of the west-central Grant Range, Nye County, Nevada: Geological Society of America and Chart Series MCH 064, scale 1:24,000, 16 p.

Garside, L.J., Hess, R.H., Fleming, R.C, and Weimer, B.S., 1988, Oil and gas developments in Nevada: Nevada Bureau of Mines and Geology Bulletin 104, 136 p.

Guion, D.J., and Pearson, W.C., 1979, Gravity exploration for petroleum in Railroad Valley, Nevada, *in* Newman, G.W., and Goode, H.D., eds., 1979 Basin and Range Symposium: Denver and Salt Lake City, Rocky Mountain Association of Geologists and Utah Geological Association, p. 544–556.

Hulen, J.B., Bortz, L.C., and Bereskin, S.R., 1991, Geothermal processes in evolution of the Grant Canyon and Bacon Flat oil reservoirs, Railroad Valley, Nye County, Nevada, *in* Flanigan, D.M.H., Hansen, M., and Flanigan, T.E., eds., Geology of White River Valley, the Grant Range, Eastern Railroad Valley and Western Egan Range, Nevada: Reno, Nevada Petroleum Society, 1991 Field Trip Guidebook, p. 47–54.

Kleinhampl, F.J., and Ziony, J.I., 1985, Geology of northern Nye County, Nevada: Nevada Bureau of Mines and Geology Bulletin 99A, [including geologic map, scale 1:250,000], 172 p.

Lund, Karen, Beard, L.S., Blank, H.R., Jr., Hofstra, A.H., and Hamilton, M.M., 1988, Mineral resources of the Riordens Well Wilderness Study Area, Nye County, Nevada: U.S. Geological Survey Bulletin 1731–H, 16 p.

Lund, Karen, Beard, L.S., and Perry, W.J., Jr., 1991, Structures of the northern Grant Range and Railroad Valley, Nye County, Nevada—Implications for oil occurrences, *in* Flanigan, D.M.H., Hansen, M., and Flanigan, T.E., eds., Geology of White River Valley, the Grant Range, Eastern Railroad Valley and Western Egan Range, Nevada: Reno, Nevada Petroleum Society, 1991 Field Trip Guidebook, p. 1–6.

Lund, Karen, Nash, J.T., Beard, L.S., Blank, H.R., Jr., and Tuftin, S.E., 1987, Mineral resources of the Blue Eagle Wilderness Study Area, Nye County, Nevada: U.S. Geological Survey Bulletin 1731–D, 19 p.

Potter, C.J., Grow, J.A., Lund, K., Perry, W.J., Jr., Miller, J.J., and Lee, M.W., 1991, Comparison of basin geometry and faulting styles along a regional seismic-reflection profile from Railroad Valley to Lake Valley, Nevada, *in* Flanigan, D.M.H., Hansen, M., and Flanigan, T.E., eds., Geology of White River Valley, the Grant Range, Eastern Railroad Valley and Western Egan Range, Nevada: Reno, Nevada Petroleum Society, 1991 Field Trip Guidebook, Reno, p. 59–60.

Schilling, J.H., 1965, Isotopic age determinations of Nevada rocks: Nevada Bureau of Mines and Geology Report 10.

Vreeland, J.H., and Berrong, B.H., 1979, Seismic exploration in Railroad Valley, Nevada, *in* Newman, G.W., and Goode, H.D., eds., 1979 Basin and Range Symposium: Denver and Salt Lake City, Rocky Mountain Association of Geologists and Utah Geological Association, p. 557–572.

CHAPTER C

MAGNETIC INTERPRETATION OF A MINERALIZED SHEAR ZONE IN THE SOUTHERN PART OF THE IDAHO BATHOLITH

By M. DEAN KLEINKOPF[1]

In the northwestern part of the Hailey 1°×2° quadrangle, located in the southern part of the Idaho batholith, magnetic-anomaly data that is displayed in shaded relief reveal a conspicuous northeast-trending linear belt of steep magnetic gradient (fig. 1). This belt is interpreted as a buried shear zone that may have influenced emplacement of mineral deposits in this area.

Analyses of magnetic-anomaly data were made as part of a multidisciplinary team effort under CUSMAP (Conterminous United States Mineral Assessment Program) to assess the mineral resource potential of the Hailey and western Idaho Idaho Falls 1°×2° quadrangles. The aeromagnetic-anomaly data are applicable for direct detection of mineralized features and are applied in conjunction with other geophysical, geological, and geochemical investigations to delineate major fault and shear zones, map buried intrusive complexes, and identify localities that might be hydrothermally altered or mineralized.

The bulk of the rocks of the Cretaceous Idaho batholith are biotite granodiorites or two-mica granites (Kiilsgaard and Lewis, 1985; Lewis and Kiilsgaard, 1991). The batholithic terrane exhibits exceptionally uniformly low magnetization and shows few distinctive anomalies, except for those associated with minor occurrences of diorite intrusions and border facies of tonalite, which are more strongly magnetized than the main mass of the batholith. The Tertiary granitic batholiths and stocks are considerably more magnetic than the granitic rocks of the Cretaceous Idaho batholith. The highest magnetic values on the map (fig. 1) correlate spatially with high-elevation, Tertiary, epizonal plutons such as the granitic intrusions of the Sawtooth batholith (S); the stock at Steele Mountain (SM); and the Sheep Mountain batholith (SHM). The magnetic-anomaly data indicate that these composite intrusive complexes are more extensive in the subsurface than in outcrop. The belt of steep magnetic gradient is nearly continuous along the southeastern side of the Sawtooth, Steele Mountain, and Sheep Mountain intrusions.

The southern part of the Idaho batholith is broken into a series of rhombic blocks (Bennett and Lewis, 1989) resulting from intersections of northeast- and northwest-trending faults. Northeast-trending faults parallel the trans-Challis fault system (TCFS), which is related to Eocene extension. Northwest-trending faults relate to basin-and-range extension in the Miocene. Many of the faults are reflected in the magnetic-anomaly data as contour alignments and deflections of contours across the magnetic grain. In particular, the belts of steep magnetic gradient often are seen to correlate with faults or postulated faults and shear zones. The prominent example in the study area (fig. 1) is the northeast-trending belt of steep magnetic gradient that occurs near Atlanta and is interpreted to reflect a buried shear zone, probably part of the trans-Challis fault system (TCFS). Other evidence supports the interpretation that the belt of steep magnetic gradient may be a tectonic feature. Two regional basin-and-range faults, the Deer Park (DPF) and Montezuma (MF) faults and correlative magnetic trends, systematically change strike from south-southeast north of the belt of steep magnetic gradient to southeast on the south side of the belt (fig. 1).

Northeast of Atlanta, a number of gold deposits are clustered along the belt of high magnetic gradient (fig. 1). Additional undiscovered mineral deposits may occur along the belt to the northeast and southwest of Atlanta. If the

[1]U.S. Geological Survey, Mail Stop 964, P.O. Box 25046, Denver Federal Center, Denver, CO 80225.

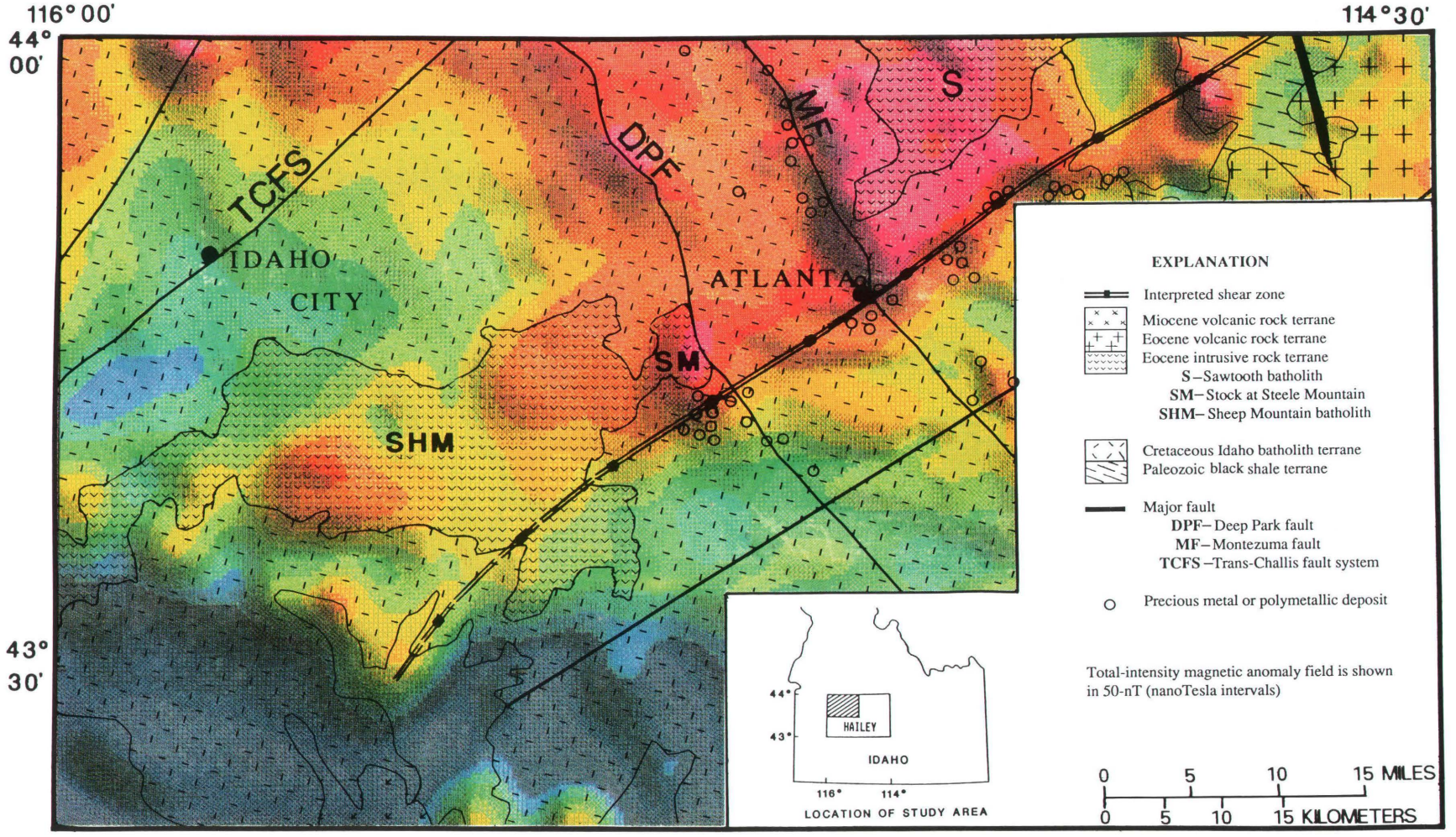

Figure 1. Map of northwestern part of the Hailey, Idaho, 1°×2° quadrangle showing residual, total-intensity aeromagnetic anomalies in shaded relief; generalized geology; interpreted shear zone; and distribution of precious metals and polymetallic deposits. For sources of aeromagnetic anomaly data see Kleinkopf and others (1989); geology and distribution of mineral deposits modified from Worl and Johnson (1989).

trend is part of the TCFS, it may hold potential for extensive epithermal gold mineralization, which is characteristic of the TCFS (Bennett, 1984; Kiilsgaard and others, 1986). In order to study spatial relationships between the geophysical anomalies and the occurrence of precious metals and polymetallic deposits, a generalized summary of plots taken from Worl and Johnson (1989) was prepared that combines distribution of precious-metal and polymetallic-vein, stockwork, and skarn deposits. The deposit types correspond to mineral deposit models, or modifications of models, found in Cox and Singer (1986).

In summary, new potential areas for undiscovered mineral resources may be located northeast and southwest of Atlanta along the belt of steep magnetic gradient. For detailed mineral resource exploration that might be considered in the future, closely spaced magnetic data collected by aircraft or on the ground may be used to detect segments of fault zones or granitic intrusions that are hydrothermally altered and possibly mineralized. Detection is based on the assumption that the magnetic susceptibilities of the hydrothermally altered areas would be perceptibly reduced relative to the unaltered parts of the features.

REFERENCES CITED

Bennett, E.H., 1984, The trans-Challis fault zone: A major crustal discontinuity in central Idaho [abs.]: Geological Society of America Abstracts with Programs v. 16, no. 6, p. 442.

Bennett, E.H., and Lewis, R.S., 1989, The geology and ore deposits of the Idaho batholith in the Hailey 1°×2° quadrangle, Idaho, *in* Winkler, G.R., and others, eds., Geology and Mineral Deposits of the Hailey and Western Idaho Falls 1°×2° Quadrangles, Idaho: U.S. Geological Survey Open-File Report 89–639, p. 26–32.

Cox, D.P, and Singer, D.A., eds., 1986, Mineral deposit models: U.S. Geological Survey Bulletin 1693, 379 p.

Kiilsgaard, T.H., and Lewis, R.S., 1985, Plutonic rocks of Cretaceous age and faults of the Atlanta Lobe of the Idaho batholith, *in* McIntyre, D.H., ed., Symposium on the Geology and Mineral Deposits of the Challis Quadrangle, Idaho: U.S. Geological Survey Bulletin 1658–B, p 29–42.

Kiilsgaard, T.H., Fisher, F.S., and Bennett, E.H., 1986, The trans-Challis fault system and associated precious metal deposits, Idaho: Economic Geology, v.81, p. 721–724.

Kleinkopf, M.D., Bankey, Viki, and McCafferty, A.E., 1989, Gravity and magnetic anomaly patterns applied to mineral resource exploration, Hailey 1°×2° quadrangle, Idaho, *in* Winkler, G.R., and others, eds., Geology and Mineral Deposits of the Hailey and Western Idaho Falls 1°×2° Quadrangles, Idaho: U.S. Geological Survey Open-File Report 89–639, p. 26–32.

Lewis, R.S., and Kiilsgaard, T.H., 1991, Eocene plutonic rocks in south-central Idaho: Journal of Geophysical Research, v. 96, no. B8, p. 13295–13311.

Worl, R.G., and Johnson, K.M., 1989, Geologic terranes and mineral deposit types in the Hailey and western Idaho Falls 1°×2° quadrangles, Idaho, *in* Winkler, G.R., and others, eds., Geology and Mineral Deposits of the Hailey and Western Idaho Falls 1°×2° Quadrangles, Idaho: U.S. Geological Survey Open-File Report 89–639, p. 3–16.

CHAPTER D

ROLE OF LITHOSPHERIC FLEXURE AND PLATE CONVERGENCE IN THE GENESIS OF SOME MISSISSIPPI-VALLEY-TYPE ZINC DEPOSITS IN THE APPALACHIANS

By DWIGHT C. BRADLEY[1]

INTRODUCTION

Ordovician-hosted Mississippi-Valley-type (MVT) zinc deposits in the Appalachian fold-thrust belt and foreland basin (fig. 1) generally are regarded as having formed from basinal brines that migrated cratonward from the orogen or its foreland basin (Oliver, 1986; Bethke and Marshak, 1990; Kesler and Van der Pluijm, 1990). The age of mineralization, however, has been subject to much debate, and as a consequence, mineralization has been linked only in very general terms to Appalachian plate-tectonic history. Various researchers have argued that mineralization occurred during Middle Ordovician (Hoagland and others, 1965; Callahan, 1968; Bradley, 1989a), Late Ordovician to Devonian (Kesler and Van der Pluijm, 1990), and late Paleozoic (Hearn and others, 1987). Depending on the age of mineralization, any connections between metallogenesis and plate-tectonic events would be sought in either the Alleghanian, Acadian, or Taconic orogenies.

One aspect of ore deposit geology that can be linked in detail to Appalachian plate tectonics is the geologic history of host strata. In this paper, I discuss geologic effects of the Taconic arc–passive margin collision (Bradley and Kusky, 1986; Bradley, 1989b) that now control, in part, the distribution of many MVT deposits. Two related processes are of particular interest. Lithospheric flexure caused forebulge uplift and normal faulting; both were instrumental in ground preparation. Flexure also drove subsidence of a foredeep basin that probably expelled mineralizing fluids. Plate convergence drove the Taconic thrust belt over the foredeep and forebulge and caused these belts to migrate toward the craton. This paper documents an association noted by Mitchell (1985) and Kaiser and Ohmoto (1988) between economic MVT deposits and flexure-induced features related to an arc–passive margin collision. Exploration for MVT deposits in some frontier regions may benefit from similar plate-tectonic considerations.

[1]U.S. Geological Survey, Branch of Alaskan Geology, 4200 University Drive, Anchorage, AK 99508.

THE TACONIC OROGENY AND LATER TECTONIC EVENTS

The early Paleozoic evolution of the Appalachians was a Wilson cycle of opening, then partial closing, of the Iapetus ocean basin. Late Proterozoic rifting of Proterozoic basement was followed by Cambrian and Early Ordovician subsidence of a passive margin with two components: (1) a miogeoclinal wedge of mainly platformal carbonate rocks up to 3.5 km thick, which now host the MVT deposits, and (2) farther east, a much thinner apron of slope and rise facies, now preserved in far-traveled thrust sheets.

This passive margin endured until its collision with an arc complex during the Ordovician Taconic orogeny (Rowley and Kidd, 1981; Bradley, 1989b) (fig. 2). The earliest stratigraphic record of collision is an Early to Middle Ordovician influx of orogen-derived flysch, which conformably overlies older slope and rise deposits. The arrival of flysch from the east was synchronous with gentle uplift of the platform. Uplift, therefore, can be viewed as a distal effect of collision. In the carbonate rocks that now host the MVT deposits, this uplift is recorded by an unconformity:

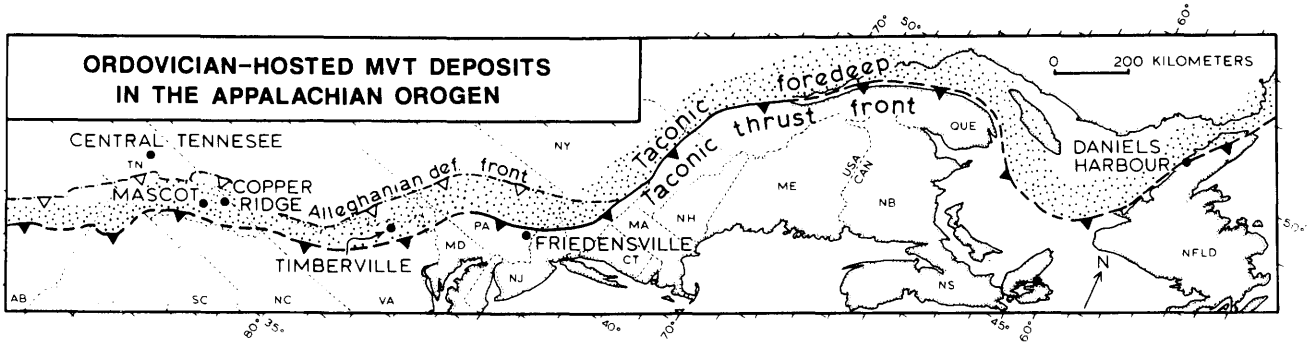

Figure 1. Map of Appalachian orogen showing main MVT deposits or districts (black dots). Taconic foredeep (foreland basin) formerly occupied stippled area but has been partially eroded away. Late Paleozoic Alleghanian deformation front (open barbs) lies cratonward of Taconic thrust front (solid barbs) in central and southern Appalachians.

the post-Knox unconformity in the southern Appalachians (Mussman and Read, 1986), the post-Beekmantown unconformity in Pennsylvania and New York (Lash, 1989), and the St. George unconformity in Newfoundland (Knight and others, 1991). Mussman and Read (1986) reported erosional relief in Virginia up to 140 m; they also reported sinkholes and caves extending down to 65 m below the unconformity. Knight and others (1991) reported erosional relief in Newfoundland up to 50 m and karst features to depths of 120 m. Comparable erosional relief and depth of karst features have been reported from all of the MVT districts discussed below. The unconformity has been widely attributed to passage of a forebulge (Jacobi, 1981; Rowley and Kidd, 1981; Bradley and Kusky, 1986; Lash, 1989; Knight and others, 1991) because uplift was synchronous with flysch sedimentation farther east and was followed immediately by collision-induced drowning of the platform and progradation of flysch. The unconformity and subsequent events vary in age along the orogen (Bradley, 1989b), indicating that eustatic fall in sea level cannot have been the sole cause of emergence.

Overlying the unconformity is an upward-deepening, diachronous succession of carbonates, black shales, and turbidites. The shales and turbidites comprise the synorogenic clastic fill of the Taconic foredeep, a basin that migrated cratonward through time across the former continental shelf (Rowley and Kidd, 1981; Bradley, 1989b). Normal faulting, induced by lithospheric flexure, accompanied foredeep subsidence (Bradley and Kidd, 1991). Paleogeographic relations across the Taconic foredeep are summarized in figure 3. This cross section depicts a quasi-steady-state configuration that migrated cratonward through time; it is appropriate for a given transect until thrusting ceased.

Two younger collisions—the Acadian in the Devonian (Osberg and others, 1989) and the Alleghanian in the Mississippian to Permian (Hatcher and others, 1989)—had markedly different effects on Taconic paleogeographic elements in the northern versus the southern parts of the orogen. In the northern Appalachians, the Taconic thrust front is the cratonward limit of significant shortening in the northern Appalachians (fig. 1); Ordovician foredeep deposits west of the Taconic thrusts are subhorizontal. In the northern Appalachians, the Taconic front is accurately located by fossiliferous wildflysch deposits (olistostromes and tectonic melange) that immediately flank far-traveled allochthons. In the southern and central Appalachians, late Paleozoic thrusts and folds deform a broad region to the west of the Taconic thrust front; this region includes Ordovician foredeep strata as well as MVT deposits in older carbonate rocks. In the central and southern Appalachians, the position of the Taconic thrust front is not known precisely, but it can be estimated by assuming that Ordovician facies belts in the foredeep (black shales, turbidites) were the same width and distance from the thrust front as in the northern Appalachians (Bradley, 1989b).

ORDOVICIAN-HOSTED MVT DEPOSITS

Ordovician-hosted MVT deposits in the Appalachian fold-thrust belt and (or) foreland basin (Clark, 1987) are hosted by strata that were laid down only a few million years before the Taconic orogeny. Mineralized areas discussed below include the Elmwood and nearby deposits of the Central Tennessee district, the Mascot–Jefferson City and Copper Ridge deposits of the East Tennessee district, the Timberville deposit in Virginia, the Friedensville deposit in Pennsylvania, and the Daniel's Harbour deposit in Newfoundland. The deposits can be divided into three groups on the basis of the state and age of deformation of the host strata: (1) flat-lying strata, (2) deformed strata that were flat-lying until the late Paleozoic Alleghanian orogeny, and (3) deformed strata that were overthrust during the Taconic orogeny.

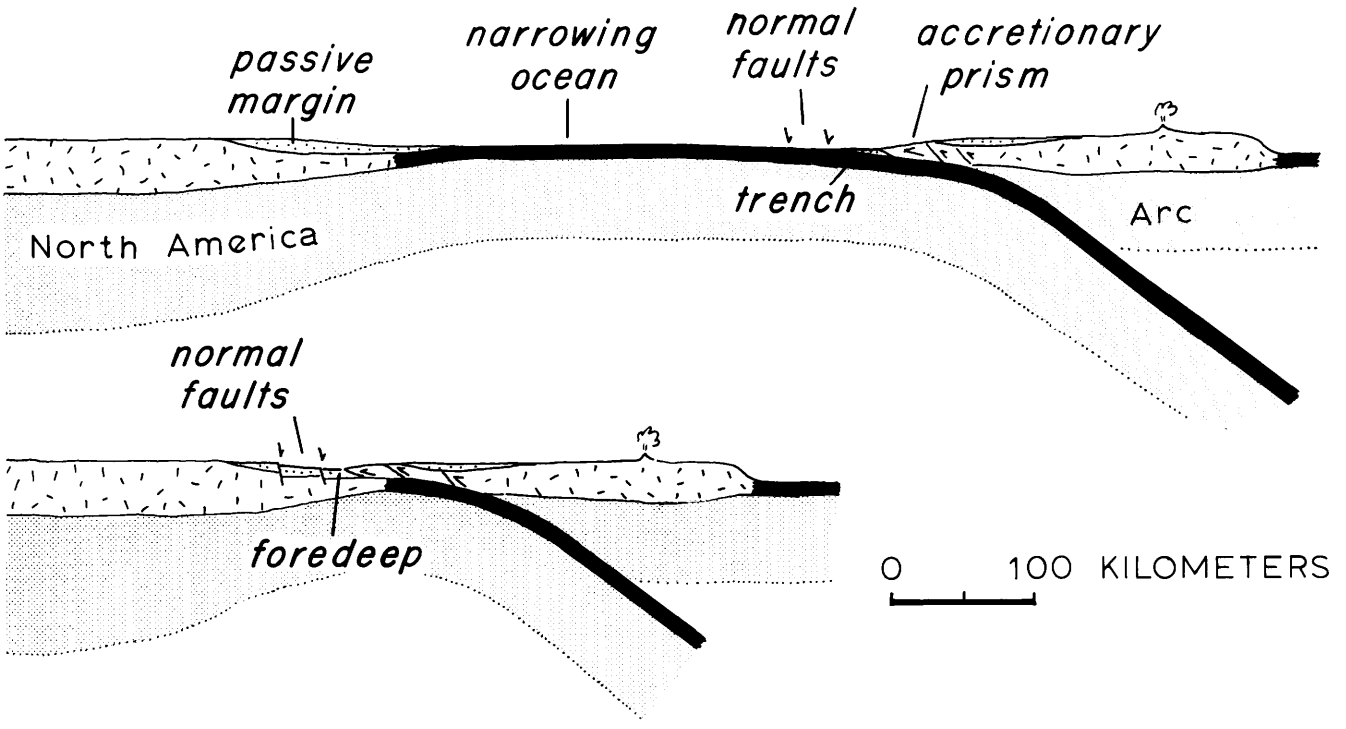

Figure 2. Schematic model of Taconic orogeny as an arc–passive margin collision. Plate convergence shown in top part of figure inevitably led to collision illustrated in bottom part of figure. Rise of Taconic forebulge and subsidence of Taconic foredeep were secondary effects of collision.

DEPOSITS IN FLAT-LYING STRATA

MVT deposits of this group are exemplified by the Central Tennessee district, on the Nashville dome (fig. 1). Lower Ordovician carbonate rocks of the Knox Group host the mineralization, which was controlled by solution-collapse breccias formed during karst formation along the post-Knox unconformity (Gaylord and Briskey, 1983). The Nashville dome and Cincinnati arch together comprise part of an elongate uplift that flanks the southern and central Appalachian thrust belt (Quinlan and Beaumont, 1984). During Ordovician time, the axis of the Nashville dome was located about 65 km east of the Devonian axis (Stearns and Reesman, 1986). The position next to the orogenic belt, the magnitude of uplift, and the cratonward shift of the arch between Ordovician and Devonian times together suggest that the Nashville dome–Cincinnati arch began as a flexural effect of Taconic loading (Quinlan and Beaumont, 1984).

Figure 3 shows the reconstructed position of the Central Tennessee district as projected onto the schematic cross section through the Taconic foredeep at the time when Ordovician thrusting ceased. This distance was estimated by summing (1) the present distance from the Elmwood deposit on the Nashville dome to the Chattanooga thrust, (2) the pre-late-Paleozoic palinspastic distance from the Chattanooga to the Knoxville thrust (Woodward and Gray, 1985), and (3) the palinspastic distance (Walker and others, 1983) from the Knoxville thrust to the eastern margin of the Sevier Basin (a local depocenter of the Taconic foredeep) (Shanmugam and Walker, 1980). At the close of the Taconic orogeny, the Central Tennessee MVT district lay about 275 km cratonward of the thrust front.

DEPOSITS IN STRATA DEFORMED DURING THE LATE PALEOZOIC

MVT deposits of this group include Mascot–Jefferson City, Copper Ridge, and Timberville. These deposits are hosted in folded and thrust-faulted Ordovician carbonate rocks within the late Paleozoic southern Appalachian fold-thrust belt. As in the Central Tennessee district, mineralization is localized by karst-related solution-collapse breccias that lie immediately below the post-Knox unconformity. In the East Tennessee district, detrital sphalerite sands in solution-collapse deposits, described by Kendall (1960) and Hoagland and others (1965), have dips comparable to the bedding dips of the host strata, proving that mineralization preceded Alleghanian deformation.

When thrusting ended in the Ordovician, the host strata of the Mascot–Jefferson City, Copper Ridge, and Timberville deposits were located on the undeformed cratonic flank of the Taconic foredeep (fig. 3). The positions

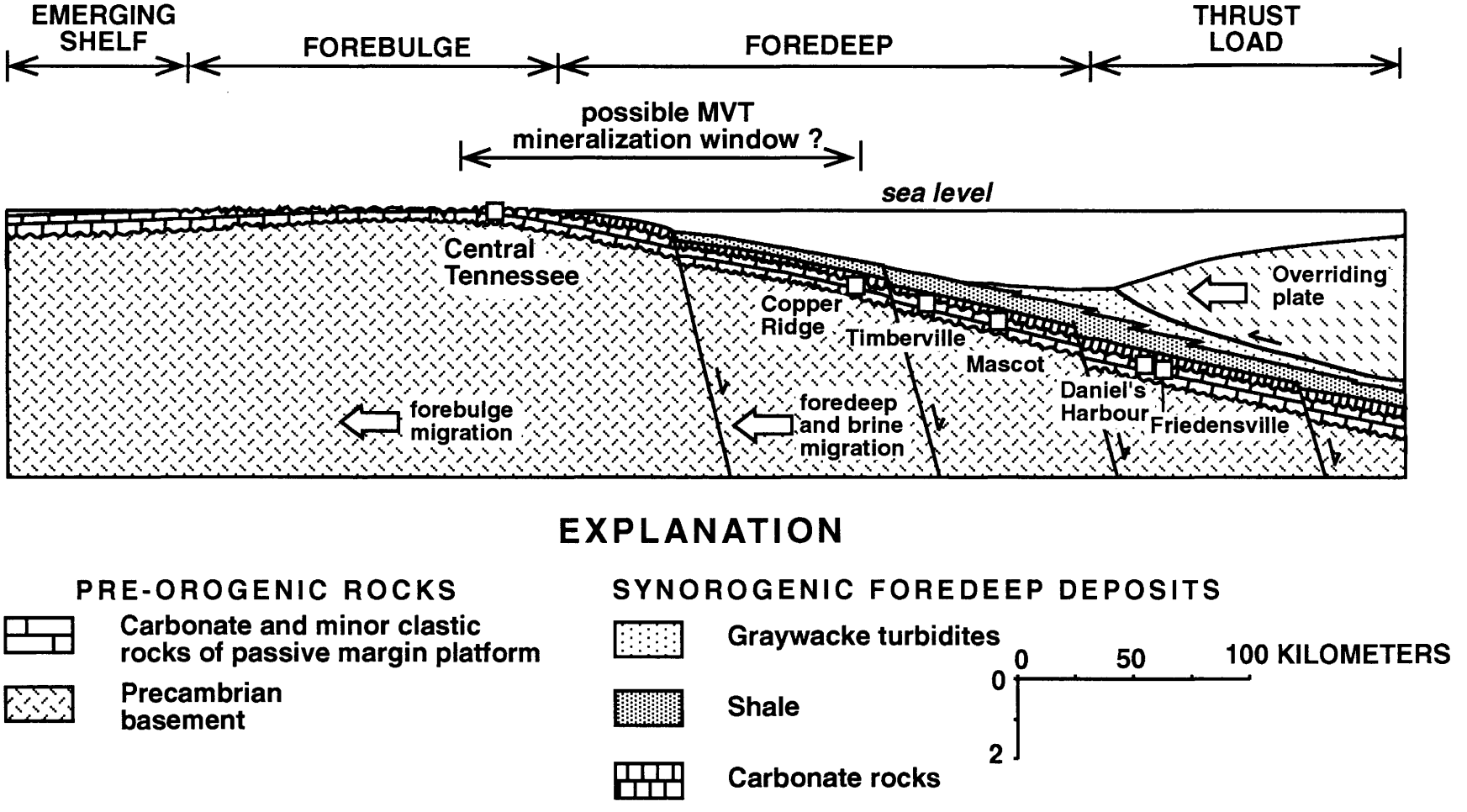

Figure 3. Generalized cross section through Taconic foredeep. Positions of Ordovician-hosted MVT deposits are projected onto section relative to paleogeographic elements when plate convergence ceased. Two locations where MVT deposits now occur (Friedensville and Daniel's Harbour) were tectonically buried beneath Taconic thrust sheets during the Ordovician.

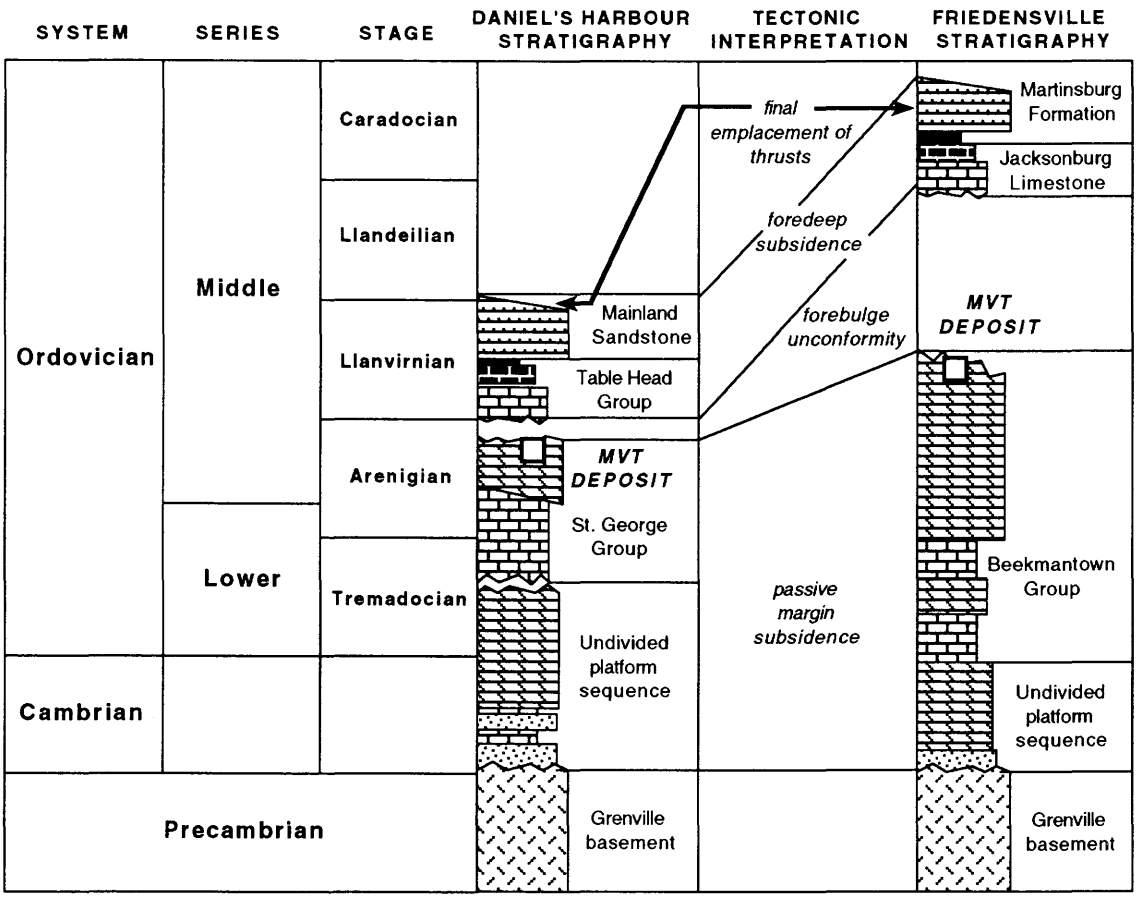

Figure 4. Cambrian and Ordovician stratigraphy at Daniel's Harbour and Friedensville deposits. Forebulge unconformity, foredeep deposits, and Taconic thrusting differ in age between the two sections, but the relative order of events is the same.

of the Mascot–Jefferson City and Copper Ridge deposits were estimated from a palinspastic cross section of the Sevier Basin (Walker and others, 1983, p. 705, upper section). The position of Timberville was estimated from a palinspastic cross section through northern Virginia (Read, 1980, p. 1582, section A). Estimated palinspastic distances to the Taconic thrust front are 55 km for the Mascot–Jefferson City deposit, 85 km for the Timberville deposit, and 115 km for the Copper Ridge deposit.

DEPOSITS IN STRATA TECTONICALLY BURIED DURING THE ORDOVICIAN

The Daniel's Harbour and Friedensville deposits (fig. 1) have the most intriguing connection to Taconic paleogeography. The Daniel's Harbour deposit in western Newfoundland is hosted by Lower Ordovician platform carbonates of the St. George Group, and the ore bodies occur immediately beneath a major karsted unconformity at the top of the St. George Group (fig. 4). Ore postdates, but is spatially associated with, dolomitic breccia bodies and Ordovician sinkholes formed by karst processes (Lane, 1984). These breccia bodies are elongate parallel to orogenic strike, and they appear to have nucleated along orogen-parallel normal faults that were active during and immediately after forebulge uplift (Knight and others, 1991). Lane (1989) reported "rotated geopetal sediments in ore-stage cavities and displaced ore bodies along faults" as evidence that mineralization preceded contractional deformation. Host rocks at the Daniel's Harbour deposit are part of the gently dipping, parautochthonous platformal sequence that was tectonically buried beneath the Humber Arm allochthon during the Middle Ordovician (Cawood and Williams, 1988). When thrusting ceased, the deposit lay at least 10 km to the east of (behind) the thrust front. In figure 3, the position of the Daniel's Harbour deposit was estimated by extrapolation 20 km along strike to the south, where the Humber Arm allochthon has not been eroded away and extends at least as far west as the coast. According to Cawood and Williams (1988), the parautochthonous ore-hosting strata at the Daniel's Harbour deposit were not penetratively deformed during emplacement of the allochthon; gentle bedding dips and

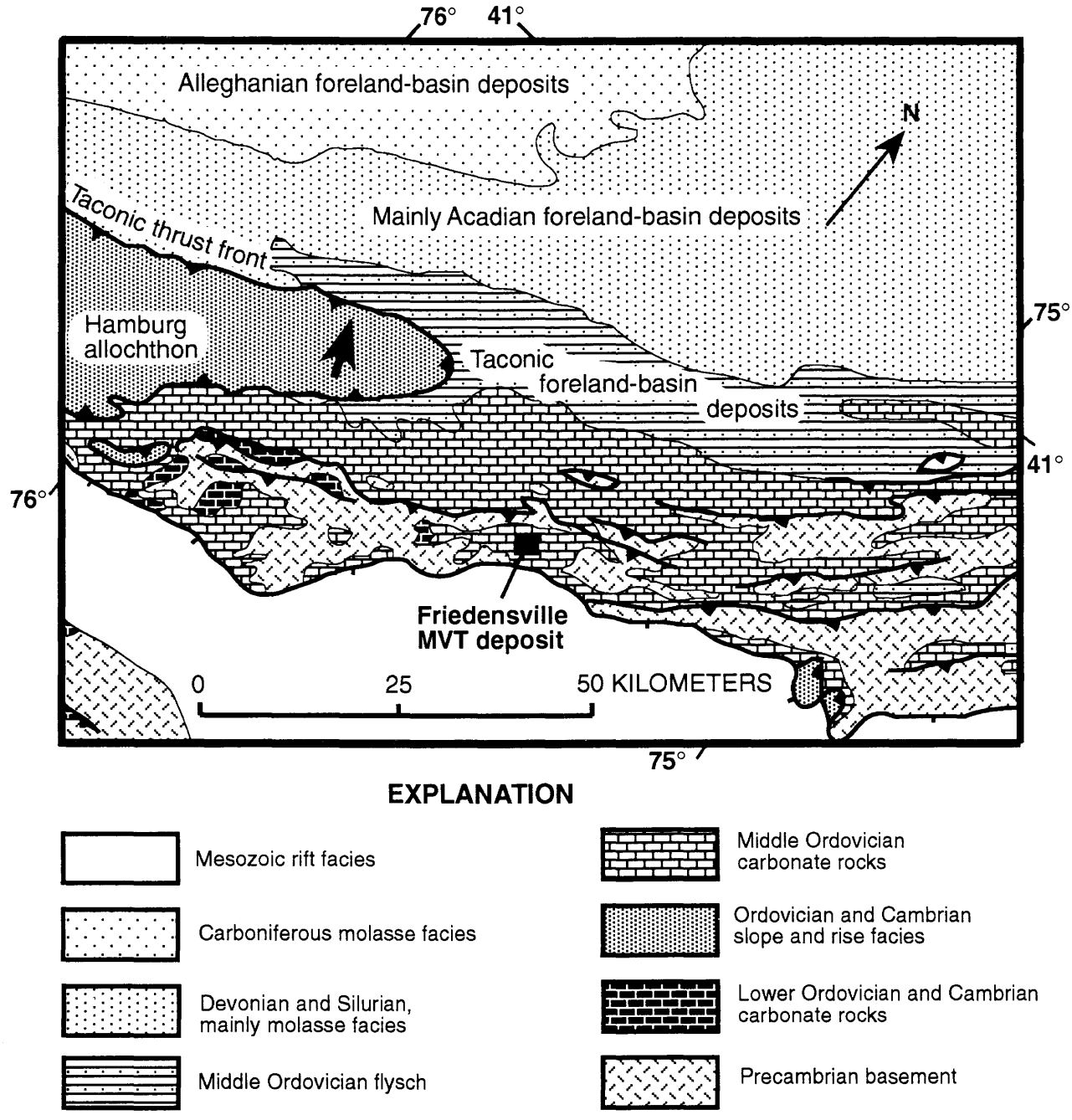

Figure 5. Generalized geologic map of Friedensville, Pennsylvania, and vicinity. Friedensville was tectonically buried during the Taconic orogeny by the Hamburg allochthon, which advanced toward N. 18° W. (large arrow; Lash and Drake, 1984). Present erosional front of Hamburg klippe lies about 20 km cratonward of Friedensville.

high-angle reverse faults in the Daniel's Harbour area date from the Devonian Acadian orogeny.

The MVT deposit at Friedensville, Pennsylvania (fig. 5) is hosted by platformal carbonate rocks of the Lower and Middle Ordovician Beekmantown Group. The ore occurs in tabular, solution-collapse breccias that lie just below the post-Beekmantown unconformity (fig. 4). Stratabound ore bodies at the Friedensville deposit are folded and faulted along with enclosing strata, and hence, mineralization predated deformation (Callahan, 1968, p. 103). As at the Daniel's Harbour deposit, host rocks at the Friedensville deposit are part of the parautochthonous platformal sequence that was tectonically buried beneath the Hamburg allochthon during the Middle Ordovician (Lash and Drake, 1984). When thrusting ceased, the Friedensville deposit lay about 20 km to the east of (behind) the

thrust front. In figure 3, the position of Friedensville was estimated by extrapolation 20 km along strike to the south, where the Ordovician thrust front is marked by a belt of Ordovician wildflysch immediately west of the leading edge of the Hamburg klippe (Root and MacLachlan, 1978). Ore-hosting strata at Friedensville are folded and cut by several generations of faults. Deformation is either Taconic (Lash and Drake, 1984, p. 32) or Alleghanian.

DISCUSSION

Events leading up to and including the Taconic orogeny in the Appalachians provided many of the conditions necessary for MVT mineralization. During the Cambrian and Early Ordovician in the Appalachians, carbonate host rocks were deposited along a thermally subsiding passive margin in a seaward-thickening miogeoclinal wedge. During the earliest stages of collision, uplift of the platform at a forebulge resulted in widespread ground preparation, and much ground was prepared in this fashion because plate convergence caused the forebulge to migrate. Passive-margin subsidence and collision at low latitudes is a key factor because forebulge uplift exposed carbonate rocks to karst formation. In contrast, karsted forebulge unconformities are unlikely to form during high-latitude collisions, such as the Brooks Range orogeny, involving a clastic rather than a carbonate platform. Collision drove the subsidence of a shale- and turbidite-filled foreland basin and also caused the basin to migrate cratonward. The migration of facies belts capped the permeable carbonate platform with an impermeable shale aquitard. Evidence from the Daniel's Harbour deposit suggests that flexure-induced normal faults dating from early collision played a role in ground preparation. Normal faults also appear to have helped to focus mineralizing fluids in the Northern Arkansas MVT district in the Ouachita foredeep (Bradley and Kidd, 1991) and the Taconic foredeep of New York (Bradley and Kidd, 1991). Mitchell (1985) suggested a similar fluid-focusing mechanism for the Irish base-metal district in the Variscan foreland. Flexure-induced normal faults in other foredeeps, therefore, are promising exploration targets.

When Taconic thrusting ceased, six MVT localities were distributed across a 300-km-wide belt that stretched from forebulge to thrust belt (fig. 3): the Central Tennessee district on the forebulge; the Copper Ridge, Timberville, and Mascot–Jefferson City deposits on the cratonic flank of the foredeep; and the Daniel's Harbour and Friedensville deposits beneath thrust sheets. A simple explanation for this distribution is that mineralization occurred during the Middle Ordovician by foreland basin dewatering, as discussed below. But if so, then there were at least two episodes of MVT mineralization in the Appalachian foreland, a second event being necessary to explain numerous MVT occurrences and small deposits in the Appalachian foreland in rocks as young as Silurian, Devonian, and even Pennsylvanian (Clark, 1987).

The case for Middle Ordovician mineralization is summarized here. The prevailing view of Appalachian MVT mineralization as a product of foreland basin dewatering (Kesler and others, 1988) can be reconciled with the distribution of deposits in figure 3 only if mineralization occurred during the Middle Ordovician. The last time the Daniel's Harbour or Friedensville deposits could have been connected in any hydrologically simple way to a foreland basin was immediately before tectonic burial during the Middle Ordovician. Younger (Acadian and Alleghanian) foreland basins may have existed to the east of the Daniel's Harbour and Friedensville deposits, but any such basins would have been superimposed on the eroded roots of the Taconic thrust belt and not on the more deeply buried parautochthon within which the ore bodies occur. Younger foreland basins certainly existed west of the Daniel's Harbour and Friedensville deposits (fig. 5), but they are unlikely to have expelled large quantities of fluid toward and beneath the frontal thrusts. Foreland basin brines could only have migrated through the Daniel's Harbour and Friedensville areas during the brief (5–10 m.y.) Middle Ordovician interval between the time of karst-related ground preparation at the forebulge and the time of tectonic burial by thrusts. If this scenario is valid, the 300-km width of the belt of MVT localities records the end of plate convergence—this halted an ore-deposit "production line" that had MVT deposits at various places along it (fig. 3). Each deposit would have formed on the forebulge or cratonic flank of the foredeep; post-mineralization plate convergence would have conveyed the earlier formed deposits away from the relative position at which they formed, toward or beneath the orogen. This orogenic-foreland setting for mineralization differs slightly from the setting proposed for MVT deposits of the Ozarks in the foreland of the Ouachita orogen (Leach and Rowan, 1986) and those in the foreland of the Canadian Rockies (Garven, 1985). In the latter two regions, mineralizing fluids are believed to have been driven by gravity across a sediment-filled foreland basin that had a surface that sloped down toward the craton. In contrast, Middle Ordovician mineralizing fluids in the Appalachians would necessarily have migrated across a foredeep that sloped up toward the craton and had a deep axial depression (as in fig. 3).

Mineralization of the Ordovician-hosted deposits could be younger than Middle Ordovician; but if so, two very different genetic models must apply to six similar deposits: one mechanism for the Daniel's Harbour and Friedensville deposits, and another for the Central Tennessee district and the Copper Ridge, Mascot–Jefferson City, and Timberville deposits. These last four could have been

formed from Acadian or early Alleghanian foreland-basin brines sometime after the Middle Ordovician. Post-Middle-Ordovician mineralization at the Daniel's Harbour and Friedensville deposits, however, could only have taken place beneath the Taconic thrust belt, and the mineralizing fluids would have been something other than foreland-basin brines.

The distribution of deposits in figure 3, therefore, highlights an unanswered question in Appalachian metallogenesis that future studies should address. One possibility is that there were two or more mineralizing events: an earlier one during the Middle Ordovician and a later one during the late Paleozoic. The other possibility is that there was a single late Paleozoic mineralizing event but two very different environments of mineralization: subthrust and orogenic foreland. Future research should indicate whether the Daniel's Harbour and Friedensville deposits have textural, isotopic, fluid-inclusion, or other properties that set them apart from the other Ordovician-hosted MVT deposits.

REFERENCES CITED

Bethke, C.M., and Marshak, S. 1990, Brine migrations across North America—The plate tectonics of groundwater: Annual Reviews of Earth and Planetary Science, v. 18, p. 228–315.

Bradley, D.C., 1989a, Mississippi Valley-type Pb-Zn mineralization during Ordovician arc-continent collision in the Appalachians: Geological Society of America, Abstracts with Programs, v. 21, p. A8.

———1989b, Taconic plate kinematics as revealed by foredeep stratigraphy, Appalachian orogen: Tectonics, v. 8, p. 1037–1049.

Bradley, D.C., and Kidd, W.S.F., 1991, Flexural extension of the upper continental crust in collisional foredeeps: Geological Society of America Bulletin, v. 103, p. 1416–1438.

Bradley, D.C., and Kusky, T.M., 1986, Geologic evidence for rate of plate convergence during the Taconic arc-continent collision: Journal of Geology, v. 94, p. 667–681.

Callahan, W.H., 1968, Geology of the Friedensville zinc mine, Lehigh County, Pennsylvania, *in* Ridge, J.D., ed., Ore Deposits of the United States, 1933–1967 [The Graton-Sales Volume, v. 1]: American Institute of Mining, Metallurgy, and Petroleum Engineers, p. 95–107.

Cawood, P.A., and Williams, H.S., 1988, Acadian basement thrusting, crustal delamination, and structural styles in and around the Humber Arm allochthon, western Newfoundland: Geology, v. 16, p. 370–373.

Clark, S.H.B., 1987, Metallogenic map of zinc, lead, and barium deposits and occurrences in Paleozoic sedimentary rocks, east-central United States: U.S. Geological Survey Miscellaneous Investigations Series Map I–773, scale 1:2,500,000.

Garven, G., 1985, The role of regional fluid flow in the genesis of the Pine Point deposit, western Canada sedimentary basin: Economic Geology, v. 80, p. 307–324.

Gaylord, W.B., and Briskey, J.A., 1983, Geology of the Elmwood and Gordonsville mines, Central Tennessee zinc district, *in* Tennessee Zinc Deposits Field Trip Guide Book: Blacksburg, Virginia, Virginia Tech Department of Geological Sciences, Guide Book Number 9, p. 116–151.

Hatcher, R.D., Jr., Thomas, W.A., Geiser, P.A., Snoke, A.W., Mosher, S., and Wiltschko, D.V., 1989, Alleghanian Orogen, *in* Hatcher, R.D., Jr., Thomas, W.A., and Viele, G.W., eds., The Appalachian-Ouachita Orogen in the United States: Boulder, Colorado, Geological Society of America, The Geology of North America, v. F–2, p. 233–318.

Hearn, P.P., Sutter, J.F., and Belkin, H.E., 1987, Evidence for late Paleozoic brine migration in Cambrian carbonate rocks of the central and southern Appalachians: Implications for Mississippi Valley-type mineralization: Geochimica et Cosmochimica Acta, v. 51, p. 1323–1334.

Hoagland, A.D., Hill, W.T., and Fulweiler, R.E., 1965, Genesis of the Ordovician zinc deposits in East Tennessee: Economic Geology, v. 60, p. 693–714.

Jacobi, R.D., 1981, Peripheral bulge—A causal mechanism for the Lower/Middle Ordovician unconformity along the western margin of the northern Appalachians: Earth and Planetary Science Letters, v. 56, p. 245–251.

Kaiser, C.J. and Ohmoto, H., 1988, Ore-controlling structures of Mississippi valley-type mineralization on the North American midcontinent as products of late Paleozoic convergent plate tectonism, *in* Kisvarsanyi, G., and Grant, S.K., eds., North American Conference on the Tectonic Control of Ore Deposits and the Vertical and Horizontal Extent of Ore Systems, Proceedings Volume: Rolla, Missouri, University of Missouri—Rolla, p. 424–430.

Kendall, D.L., 1960, Ore deposits and sedimentary features, Jefferson City mine, Tennessee: Economic Geology, v. 55, p. 985–1003.

Kesler, S.E., Jones, L.M., and Ruiz, J., 1988, Strontium-isotopic geochemistry of Mississippi Valley-type deposits, east Tennessee: Implications for age and source of mineralizing brines: Geological Society of America Bulletin, v. 100, p. 1300–1307.

Kesler, S.E., and Van der Pluijm, B.A., 1990, Timing of Mississippi Valley-type mineralization: Relation to Appalachian orogenic events: Geology, v. 18, p. 1115–1118.

Knight, I., James, N.P., and Lane, T.E., 1991, The Ordovician St. George unconformity, northern Appalachians: The relationship of plate convergence at the St. Lawrence Promontory to the Sauk-Tippecanoe sequence boundary: Geological Society of America Bulletin, v. 103, p. 1200–1225.

Lane, T.E., 1984, Preliminary classification of carbonate breccias, Newfoundland Zinc mines, Daniel's Harbour, Newfoundland: Geological Survey of Canada Paper 84–1A, p. 505–512.

Lane, T.E., 1989, Sphalerite/dolomite stratigraphy and the tectonic origin of an MVT deposit, Daniel's Harbour, western Newfoundland, Canada: Geological Society of America, Abstracts with Programs, v. 21, p. A8.

Lash, G.G., 1989, Middle and Late Ordovician shelf activation and foredeep evolution, central Appalachian orogen, *in* Keith, B.D., ed., The Trenton Group (Upper Ordovician Series) of Eastern North America: Deposition, Diagenesis, and Petroleum: American Association of Petroleum Geologists, Studies in Geology 29, p. 37–53.

Lash, G.G., and Drake, A.A., Jr., 1984, The Richmond and Greenwich slices of the Hamburg klippe in eastern Pennsylvania—Stratigraphy, sedimentology, structure, and plate tectonic

implications: U.S. Geological Survey Professional Paper 1312, 40 p.

Leach, D.L., and Rowan, E.L., 1986, Genetic link between Ouachita foldbelt tectonism and the Mississippi Valley-type lead-zinc deposits of the Ozarks: Geology, v. 14, p. 931–935.

Mitchell, A.H.G., 1985, Mineral deposits related to tectonic events accompanying arc-continent collision: Institute for Mining and Metallurgy Transactions, Section B, v. 94, p. B115–B127.

Mussman, W.J., and Read, J.F., 1986, Sedimentology and development of a passive- to convergent-margin unconformity: Middle Ordovician Knox unconformity, Virginia Appalachians: Geological Society of America Bulletin, v. 97, p. 282–295.

Oliver, J., 1986, Fluids expelled tectonically from orogenic belts: Their role in hydrocarbon migration and other geologic phenomena: Geology, v. 14, p. 99–102.

Osberg, P.H., Tull, J.F., Robinson, P., Hon, R., and Butler, J.R., 1989, The Acadian Orogen, *in* Hatcher, R.D., Jr., Thomas, W.A., and Viele, G.W., eds., The Appalachian-Ouachita Orogen in the United States: Boulder, Colorado, Geological Society of America, The Geology of North America, v. F–2, p. 179–232.

Quinlan, G.M., and Beaumont, C., 1984, Appalachian thrusting, lithospheric flexure, and the Paleozoic stratigraphy of the eastern interior of North America: Canadian Journal of Earth Science, v. 21, p. 973–996.

Read, J.F., 1980, Carbonate ramp-to-basin transitions and foreland basin evolution, Middle Ordovician, Virginia Appalachians: American Association of Petroleum Geologists Bulletin, v. 64, p. 1575–1612.

Root, S.I, and MacLachlan, D.B., 1978, Western limit of Taconic allochthons in Pennsylvania: Geological Society of America Bulletin, v. 89, p. 1515–1528.

Rowley, D.B., and Kidd, W.S.F., 1981, Stratigraphic relationships and detrital composition of the medial Ordovician flysch of western New England: Implications for the tectonic evolution of the Taconic orogeny: Journal of Geology, v. 89, p. 199–218.

Shanmugam, G., and Walker, K.R., 1980, Sedimentation, subsidence, and evolution of a foredeep basin in the Middle Ordovician, southern Appalachians: American Journal of Science, v. 280, p. 479–496.

Stearns, R.G., and Reesman, A.L., 1986, Cambrian to Holocene structural and burial history of Nashville dome: American Association of Petroleum Geologists Bulletin, v. 70, p. 143–154.

Walker, K.R., Shanmugam, G., and Ruppel, S.C., 1983, A model for carbonate to terregenous clastic sequences: Geological Society of America Bulletin, v. 94, p, 700–712.

Woodward, N.B., and Gray, D.R., 1985, Southwest Virginia, Tennessee, and northern Georgia sections, *in* Woodward, N.B., ed., Valley and Ridge Thrust Belt: Balanced Structural Sections, Pennsylvania to Alabama: Knoxville, University of Tennessee, Studies in Geology, v. 12.

CHAPTER E

Rb-Sr ISOTOPIC REDISTRIBUTION AND CHARACTER OF HYDROTHERMAL FLUIDS IN THE CATHEART MOUNTAIN Cu-Mo DEPOSIT, MAINE

By ROBERT A. AYUSO[1] *and* NORA K. FOLEY[2]

ABSTRACT

The Catheart Mountain porphyry Cu-Mo deposit is composed of hydrothermally altered equigranular granodiorite and porphyritic dikes that contain as much as 4 weight percent sulfides (pyrite, molybdenite, chalcopyrite, galena, and sphalerite). Propylitic to potassic alteration produced a succession of mineral assemblages: biotite was replaced by chlorite and then by muscovite; plagioclase by albite + epidote; chlorite by muscovite; K-feldspar by muscovite; and sphene by rutile. All rocks in the hydrothermal system can be systematically arranged in terms of a relative measure of alteration intensity (alteration index) that depends on the sum of the total abundances of K-feldspar, muscovite, and quartz. Up to 6.9 weight percent K_2O, 3,900 ppm Cu, and 320 ppm Mo are found in rocks with high alteration indices; these rocks also have lower contents of CaO and Na_2O, higher values of Fe^{3+}/Fe^{2+} and K/Na, and higher abundances of Cu and Mo relative to rocks with lower alteration indices. Sr contents decreased (from about 900 to 50 ppm), and Rb contents generally increased to as much as 250 ppm in rocks with high alteration indices; this resulted in generally higher values of Rb/Sr (as much as 3.5). Rb-Sr whole-rock isotopic analyses of nine Catheart Mountain samples from the equigranular granodiorite hosts and porphyritic dikes that vary widely in their indices of alteration (from 40 to 74) yield an apparent isochron age of 422±15 Ma and Sr_i (strontium initial ratio) = 0.70603±0.00019 (2 σ). The bulk of the geochemical data indicate that the Rb-Sr isotopic system was reset as a result of alteration, that the isochron age is not the crystallization age of the stock or of the mineralization, and that the Sr_i of the fluids involved during alteration modified the magmatic Sr_i value. Fluid-inclusion studies indicate that late mineralizing fluids responsible for Cu mineralization were pervasive throughout the system; they were of moderate temperatures (< 300°C); and they were characterized by generally low salinities (up to 5 equivalent weight percent NaCl) and moderate CO_2 contents (5–15 mole percent). Widely varying CO_2/H_2O values of inclusions in quartz veins suggest that CO_2 effervescence may have contributed to deposition of the second stage of mineralization that produced chalcopyrite + sphalerite + galena + quartz ± pyrite ± calcite.

INTRODUCTION

The Catheart Mountain stock is associated with one of the best examples of porphyry-style Cu-Mo mineralization in the New England Appalachian Mountains. Together with the nearby molybdenite occurrence at Sally Mountain, they belong to the northern Appalachian porphyry Cu-Mo province (Hollister and others, 1974). The Catheart Mountain stock and granitic rocks at Sally Mountain intruded the Attean pluton in the Chain Lakes massif and are part of an allochthonous block that rests on Proterozoic Grenville basement (fig. 1) (Stewart and others, 1985). The purpose of this study is to investigate the response of the Rb-Sr isotopic system to the hydrothermal alteration at Catheart Mountain and to present a

[1]U.S. Geological Survey, Mail Stop 954, 12201 Sunrise Valley Drive, National Center, Reston, VA 22092.

[2]U.S. Geological Survey, Mail Stop 959, 12201 Sunrise Valley Drive, National Center, Reston, VA 22092.

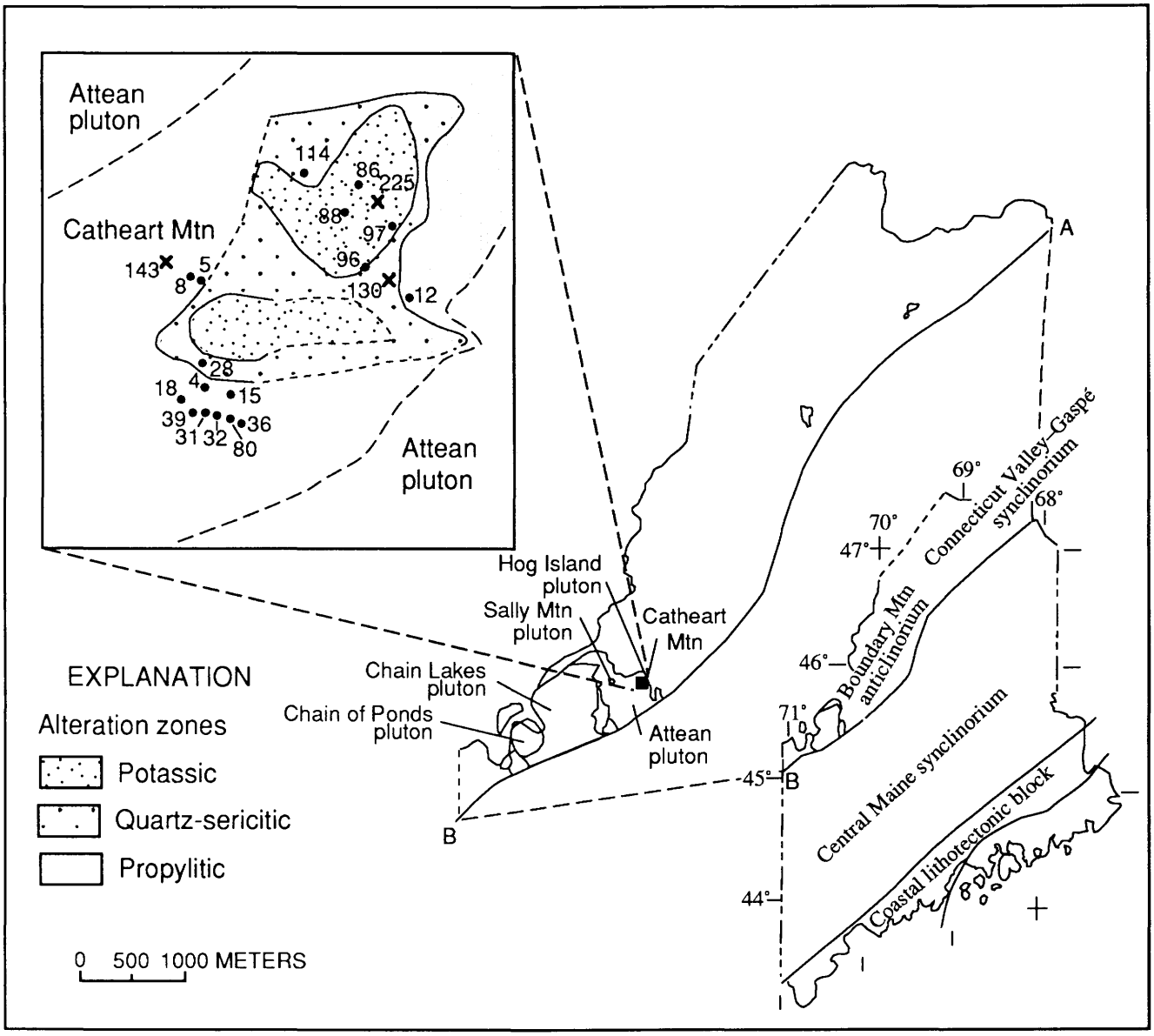

Figure 1. Map showing the generalized hydrothermal alteration areas and location of the drill core samples used at Catheart Mountain (modified after Schmidt, 1974). Line A–B represents the southernmost extension of the North American basement (Grenville) proposed by Zen (1983). Numbered dots identify drill hole locations; numbered X's show locations of outcrops.

preliminary characterization of the fluid inclusions associated with the alteration.

Schmidt (1974) determined the extent of the regional alteration zones at Catheart Mountain. He proposed that the stock was associated with a porphyry Cu-Mo system similar to that described in the classical porphyry model (Lowell and Guilbert, 1970). Atkinson (1977) identified breccia pipes and proposed that the alteration also included a silicic, fluorite-rich phase. Ayuso (1987) established compositional variations in white micas from all the alteration zones and attempted to relate white-mica chemistry to the Cu and Mo content of the bulk rocks; Ayuso and others (1988) determined the range in O and Pb isotopic compositions, and Ayuso (1989) presented results of a study of the geochemistry of the Catheart Mountain stock. Recently, in an effort to systematically characterize the chemical and mineralogical changes during hydrothermal alteration, an index of alteration was developed for samples at varying stages of alteration at Catheart Mountain (Molling and Ayuso, 1990).

ANALYTICAL PROCEDURES

One hundred and sixteen holes were drilled on Catheart Mountain by the Scott Paper Company, and 45 sam-

from these holes were obtained for geochemical studies. Modal abundances were estimated by point counting and used a computational technique that employed whole-rock data and microprobe compositions of minerals of each rock (Molling and Ayuso, 1990) in a scheme first proposed by Ferry (1985). A suite of samples containing abundant fluid inclusions in quartz phenocrysts and in narrow quartz + muscovite + sulfide veins was selected from 19 core locations within and adjacent to the two mineralized centers at Catheart Mountain (fig. 1). Fluid inclusions in samples of the Attean pluton and of nearby plutons, including Sally Mountain, Hog Island, and Chain of Ponds, were also examined for comparison. Petrographic studies of fluid inclusions were made on over 35 thin sections of material from the equigranular and porphyritic parts of the stock. The thermometry data were collected using equipment marketed by Fluid, Inc. of Denver, Colorado. The stage was calibrated using the melting point of ice, synthetic fluid inclusions prepared by Fluid, Inc., and various other standards of known melting point. A small number of samples were crushed in oil, with a crushing stage constructed by Chaixmeca, Ltd. (France), to confirm the presence of noncompressible gas in some inclusions. The distribution of all types of inclusions in phenocrystic quartz and vein quartz and calcite was characterized, and heating and freezing studies were conducted on representative inclusions; initial results are summarized in table 1 and compared with data for other granite-related mineral deposits of the northern Appalachian Mountains and with porphyry Cu deposits in the Western United States and Canada.

Whole-rock splits of nine samples from Catheart Mountain were analyzed by isotope dilution for Rb and Sr using a 6-inch, 60-degree-sector, NBS-type mass spectrometer at the U.S. Geological Survey in Reston, Virginia. A special effort was made to obtain the least altered samples available from drill core in an attempt to estimate the original isotopic composition of the Catheart Mountain stock. Five of the samples from Catheart Mountain are from the porphyritic dikes, and four are from equigranular host rocks. Three outcrop samples from the nearby Sally Mountain Mo occurrence were also analyzed for comparison with the Catheart Mountain stock. The ratio of $^{86}Sr/^{88}Sr$ of 0.1194 was used for normalizing the Sr isotopic measurements. Sr blanks are less than 2 ng and those for Rb are 0.2 ng or less. Replicate analyses of NBS SRM 987 give an averge $^{87}Sr/^{86}Sr$ of 0.71016±0.00006 (95 percent confidence level). The precision of individual samples at the 95 percent confidence level is 0.022 percent for $^{87}Sr/^{86}Sr$, 1.2 percent for Rb, and 2.0 percent for Sr. The isotopic and decay constants recommended by Steiger and Jager (1977) were used for all the isotopic calculations. The regression and uncertainty calculation of York (1966) was used to determine ages and their uncertainty at the 2-sigma level.

GEOLOGIC SETTING

The Catheart Mountain stock lies within the Attean pluton on the southeast flank of the Boundary Mountains anticlinorium (Albee and Boudette, 1972) in the Chain Lakes massif, an allochthonous crustal block consisting for the most part of a thick sequence of diamictite, metasedimentary rocks (quartzites, feldspathic metasandstone), and sparse mafic metavolcanic rocks (Boone and others, 1970). The Chain Lakes massif was regionally metamorphosed to sillimanite grade and retrograded to chlorite facies in the middle Paleozoic. Granitic rocks exposed at Sally Mountain also contain molybdenite mineralization (Albee and Boudette, 1972), but the extent of mineralization is minor relative to Catheart Mountain, and the regional alteration zones are not well developed.

CATHEART MOUNTAIN PETROLOGY

The Catheart Mountain stock consists of equigranular, fine- to medium-grained granitic to granodioritic rocks (referred to as quartz monzonites by Schmidt, 1974) and irregular dikes of porphyritic granodiorite and granite (quartz porphyries of Schmidt, 1974). Sulfide mineralization is found in both the dikes and host rocks, in contrast to the Attean pluton, which is generally sulfide free. Schmidt (1974) delineated two main centers of hydrothermal alteration and five major gradational regional alteration zones. In relative order of increasing intensity of alteration, they consist of the propylitic, outer phyllic, phyllic, quartzose potassic, and potassic alteration zones (fig. 1 shows a summary of the alteration zones). Sulfide minerals are found within siliceous veinlets (stockwork) and are disseminated in the granodiorites and dikes; these veinlets are oriented generally east-west, especially within the potassic alteration zone. Some of the veinlets in the propylitically altered zone consist of a central zone, containing ore minerals and quartz-sericite (phyllic) alteration, surrounded by a K-feldspar-rich alteration zone (potassic) (Ayuso, 1987); this is in agreement with the zonal arrangement in many porphyry Cu deposits (e.g., Titley, 1975; Titley, 1982; Gustafson and Hunt, 1975; Brimhall, 1977).

Granitic rocks at Catheart Mountain, which have preserved textural remnants of probable magmatic origin, consist of alkali feldspar and plagioclase, quartz, biotite, and accessory minerals (sphene, zircon, allanite, apatite, and magnetite) (Ayuso, 1987). Hornblende may have been originally present; virtually all rocks contain large amounts of secondary minerals, predominantly secondary K-feldspar, quartz and muscovite; epidote and chlorite are also ubiquitous, as are calcite, pyrite, and hematite. Trace amounts of gypsum were also found. Together with the paragenetic relations established by textural studies on the

Table 1. Characteristics of selected granite-related mineral deposits of the Eastern and Western United States and Canada.

[Th, homogenization temperature in °C]

Deposit location	Metals	Th, initial (°C)	Th, late (°C)	Inclusion types[1] I	II	III	IV	V	CO_2 content[2] (~mole %)	References
Eastern United States and Canada										
Maine:										
Sally Mountain	Cu-Mo	?[3]	~200	X	X		X		L	(This study)
Catheart	Cu-Mo	>300	199	X	X	X	X	X	L(~20–>50)	(This study; Nash, 1976)
Quebec:										
Mines Gaspé	Cu-Mo	506	110	X	X	X	X		L(~5–15 vol)	(Shelton, 1983)
Madeleine Gaspé	Cu	420	120	X		X	X	X	L(~5–90)[4]	(Williams-Jones and others, 1989)
Manitoba:										
Tanco	Ta-Sn-Li-Cs	327	265				X		Variable	(Thomas and Spooner, 1985)
New Brunswick:										
Mount Pleasant	W-Mo-Sn-F	490	100	X	X	X				(Samson, 1990)
Lake George	Sb-W-Mo	405	142	X			X	X	L(~17–100)	(Seal and others, 1987)
Western United States and Canada										
Arizona:										
Bagdad	Cu			X	X	X	X		L	(Nash and Cunningham, 1974)
Sierrita	Cu	440	120	X	X	X				(Preece and Beane, 1982)
Nevada:										
Copper Canyon	Cu	500	150	X	X	X	X	X	L(~5 vol)	(Nash and Theodore, 1971; Theodore and Nash, 1973)
New Mexico:										
Santa Rita	Cu	+800	220	X		X	X		V	(Reynolds and Beane, 1985; Beane and Titley, 1981)
Utah:										
Park City	Cu-Au	+600	185	X	X	X				(John, 1989)
British Columbia :										
Granisle/Bell	Cu	+1,000	200	X	X	X				(Wilson and others, 1980)

[1] Inclusion types modified from Nash (1976): I, H_2O-rich; III, halite-bearing; IV, mixed H_2O-CO_2; V, L-V CO_2.

[2] Approximate contents given for types IV and V inclusions only; L, liquid; V, vapor; all given in mole percent unless noted; vol, volume percent.

[3] ?, temperature unknown.

[4] Combined CO_2+CH_4+N_2 expressed as equivalent CH_4.

basis of fracture density and alteration intensity (Ayuso, 1987), the alteration index (*AI*) defined by Molling and Ayuso (1990), which consists of the sum of the abundances of K-feldspar + muscovite + quartz (weight percent), can be used to monitor the relative degree of alteration in these rocks. This alteration index uses minerals that are normally produced during potassic and quartz-sericite alteration in classical porphyry Cu systems—these minerals are usually abundant and are normally associated with rocks containing variable amounts of alteration, up to the highest grades of mineralization. Values for the alteration index are thus thought to provide useful, systematic estimates of the relative alteration intensity in this hydrothermal system because virtually all rocks can be expressed in terms of different combinations of K-feldspar, muscovite, and quartz.

Most mineralized samples are characterized by a high density of quartz veins and a high abundance of sulfide minerals and especially by the occurrence of abundant, turbid K-feldspars (Molling and Ayuso, 1990); the turbidity is thought to represent very small fluid inclusions and (or) a network of grain boundaries produced during exsolution (Ferry, 1985). In fact, tiny fluid inclusions have been found in some hydrothermal K-feldspars that exchanged their oxygen isotopic composition during alteration (O'Neil and Taylor, 1967). In general, turbid K-feldspars at Catheart Mountain are particularly abundant in rocks with the highest values of *AI* and have much lower contents of Na and Ba relative to non-turbid K-feldspars—this is consistent with the suggestion that these elements are removed from igneous rocks as a result of hydrothermal alteration (Molling and Ayuso, 1990). Plagioclase is found as sparse phenocrysts in the granodiorite, but it is most abundant in the matrix where it has been replaced by muscovite, epidote, and calcite; plagioclase was replaced by hydrothermal K-feldspar in the strongly altered samples. Reaction of feldspars and fluids has also produced albitic rims surrounding plagioclase and turbid K-feldspar; plagioclase compositions are increasingly more potassic as a function of alteration, again indicating wholesale removal of Ca and Na and influx of K during alteration and mineralization of the system. Biotite was first altered to chlorite and sphene and, subsequently, to complexly intergrown epidote and chlorite. Clusters of rutile in biotite are thought to represent exsolution of Ti during recrystallization. Epidote compositions depend almost exclusively on the composition of the mineral undergoing replacement. In fact, epidote compositional variability at Catheart Mountain may indicate availability of Fe^{+3} as controlled by the prevailing O fugacity. Chlorite ranges from chlinochlore to pycnochlorite and is strongly dependent on the composition of the precursor mineral (Molling and Ayuso, 1990).

Two generations of muscovite that differ in size, abundance, and sulfide mineral association were produced as a result of the hydrothermal event (Molling and Ayuso, 1990). In addition, deuteric, fine- to medium-grained muscovite, as found in most evolved granitic rocks, is found as elongated blades oriented along cleavage planes replacing plagioclase. Growth of deuteric muscovite was not accompanied by significant addition of sulfide minerals. Infiltration of hydrothermal fluids at the onset of the hydrothermal event reequilibrated the deuteric muscovite and produced coarse-grained muscovite during the first stage of mineralization (pyrite + molybdenite). This first influx of sulfides was overprinted in the porphyritic dike rocks by an assemblage that included fine-grained muscovite and quartz—this is broadly equivalent to quartz-sericite alteration (sericitic) in classical porphyry-type Cu deposits. Fine-grained muscovite thus replaced all other minerals, and in particular, fine-grained muscovite was produced as a result of recrystallization and reequilibration of coarser grained muscovite contemporaneously with the second influx of sulfide minerals into the veins (chalcopyrite + sphalerite + galena + quartz ± pyrite ± calcite). Muscovites have a wide range in octahedral cation contents, and average compositions of coarse-grained muscovites are more aluminous adjacent to molybdenite than the finer grained muscovites in contact with pyrite and chalcopyrite (Ayuso, 1987; Molling and Ayuso, 1990). This trend may reflect temperature of formation because more aluminous muscovites reflect higher temperatures (Velde, 1965; McDowell and Elders, 1980), and because, in general, in many porphyry systems, molybdenite is associated with higher temperatures and earlier episodes of mineralization and chalcopyrite is associated with lower temperatures and later episodes of mineralization (e.g., Brimhall, 1977; Gustafson and Hunt, 1975).

Preliminary temperature estimates obtained by a two-feldspar geothermometer (Haselton and others, 1983), a plagioclase-muscovite geothermometer (Green and Usdansky, 1986), and chlorite geothermometers (e.g., Cathelineau, 1988) indicate temperatures in the range of about 300±50°C. Molling and Ayuso (1990) suggested that mineral compositions recorded progressive reequilibration during hydrothermal activity at Catheart Mountain, consistent with a system initially dominated by magmatic water with temperatures of approximately 400°C. Subsequent alteration may have resulted from influx of meteoric water at temperatures as low as 200–250°C (generally in the temperature range found in many other porphyry Cu systems: 200–350°C at Butte (Brimhall, 1979); less than 350°C in El Salvador (Gustafson and Hunt, 1975)). In most porphyry Cu deposits, temperatures of later stages of mineralization reported from fluid-inclusion studies are near 200°C (e.g., table 1), and salinities are low. P-T ranges typical of later mineralizing stages of many Cu porphyry deposits (less than 400°C and less than 4 kb) are shown on figure 2; fluids responsible for most Cu-porphyry deposits are CO_2 poor and highly saline, at least initially (table 1) (e.g., Hollister, 1978; Nash, 1976).

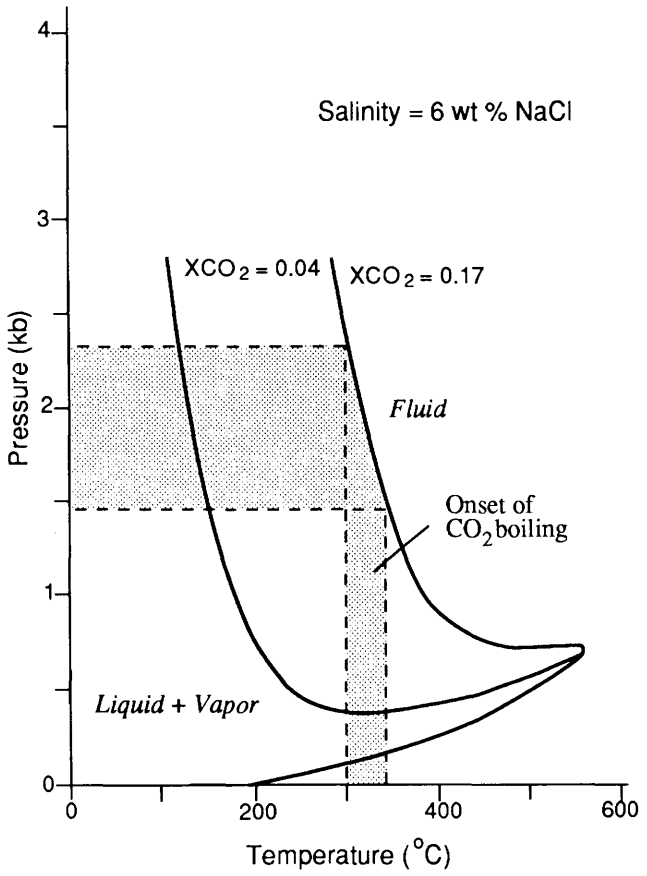

Figure 2. Phase relations in the system H_2O-CO_2-NaCl, from Bowers and Helgeson (1983). P-T diagram of CO_2 in 6 percent NaCl solutions at mole fraction CO_2 of 0.04 and 0.17. Modified from Seal and others (1987). Probable P-T range for late mineralization of Catheart Cu-Mo porphyry based on geologic constraints is shown by dashed lines and shaded area.

Virtually all elements at Catheart Mountain have been strongly affected by metasomatic changes, but Al, Ti, and P are among those that appear to be relatively immobile (Ayuso, 1989). Rocks containing a progressively higher *AI* are relatively depleted in CaO, Na_2O, FeO, and Sr among others and have relatively higher contents for K_2O, Fe_2O_3, H_2O, CO_2, Rb, S, etc. The least altered rocks have Cu contents as low as 10 ppm and Mo as low as 0.2 ppm; with increasing alteration, Cu content is up to 3,900 ppm, and Mo is up to 320 ppm. According to Molling and Ayuso (1990), samples with $AI < 50$ represent the stage at which coarse-grained muscovite and K-feldspar had developed—this stage predates the production of fine-grained muscovite. Samples with $AI > 50$ invariably contain fine-grained muscovite in the alteration assemblage; in these samples, the Ti-bearing mineral is rutile instead of sphene. Moreover, with increasing *AI*, plagioclase content declines, as does the content of epidote, calcite, and pyrite.

FLUID INCLUSIONS AND THE NATURE OF THE HYDROTHERMAL FLUIDS

Fluid inclusions found in quartz and calcite from the Catheart Mountain porphyry (fig. 1) fall into groups based on textural relationships and bulk fluid chemistry. Primary vapor-rich (V) inclusions coexist with liquid-vapor (L-V), and liquid-vapor-solid (L-V-S) inclusions predominantly occur in vein quartz (fig. 3*A*, 3*B*). The L-V-S inclusions contain a variable number of daughter minerals. Halite, and possibly sylvite, occur as rare daughter minerals, mainly in small inclusions in quartz phenocrysts; these may have formed during the early Mo-bearing stage of mineralization because they are not found in vein quartz associated with chalcopyrite. Small flakes of muscovite are a common solid inclusion occurring both in host quartz and in fluid inclusions (fig. 3*C*). When muscovite occurs in fluid inclusions, the mica appears to have acted as a trap for inclusion fluids during crystal growth and signifies the primary nature of the inclusions. In addition, one or two minute unidentified birefringent solids also occur, as do small opaque solids that may be chalcopyrite (fig. 3*D*). Calcite also contains some apparently primary liquid-vapor inclusions (fig. 3*E*) that are large relative to the secondary inclusions and aligned generally parallel to growth zones. These inclusions also have regular liquid-to-vapor ratios and lack trapped or daughter solids.

Numerous inclusions containing two liquids and a gas (L_1-L_2-V) at room temperature are present in both vein and phenocrystic quartz. The second liquid, identified as CO_2 on the basis of crushing and thermometry studies, is readily visible in most larger inclusions. L_1-L_2-V

Figure 3 (facing page). Photomicrographs of fluid-inclusion types that characterize phenocrystic and vein quartz of the Catheart Mountain stock. *A,* Primary vapor-rich inclusions (v) coexist with liquid-vapor (2l+v, l+v) and liquid-vapor-solid inclusions in quartz. Field of view equals 150 μm. *B,* Predominant solids in inclusions contained in quartz are tentatively identified as muscovite, halite, and sylvite. Field of view equals 250 μm. *C,* Muscovite flakes (m) occur in many inclusions in quartz. Field of view is 150 μm. *D,* Opaque solids, possibly chalcopyrite (c?), are also found with other solids in inclusions in quartz. Field of view ≅ 150 μm. *E,* Primary and secondary liquid-vapor inclusions in calcite. The larger primary inclusions parallel a crystal face, whereas secondary inclusions are aligned along a healed microfracture at an angle to the growth surface. Field of view equals 1.5 mm. *F,* Inclusions containing two liquids and a gas (2l+v) coexisting with vapor-rich inclusions (v) are present in both vein and phenocrystic quartz. Field of view equals 150 μm. *G,* CO_2-bearing inclusions that have variable ratios and that contain muscovite flakes (m) are found in quartz. Field of view equals 200 μm. *H,* L_1+L_2+V inclusions that have regular H_2O/CO_2 values and that contain solids (2l+v+s) occur in quartz grains encased in chalcopyrite. Field of view equals 150 μm.

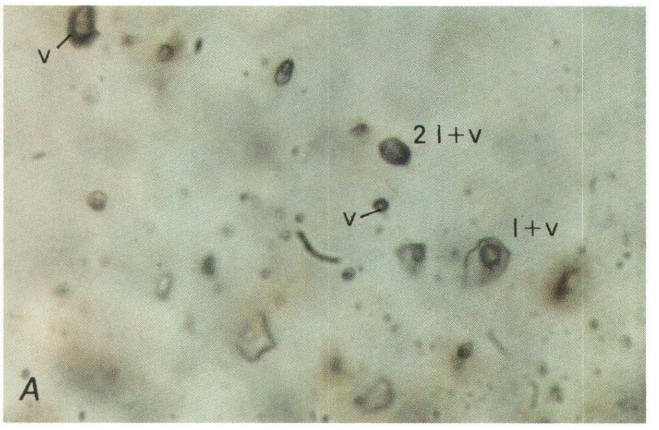
v
2 l+v
v
l+v
A

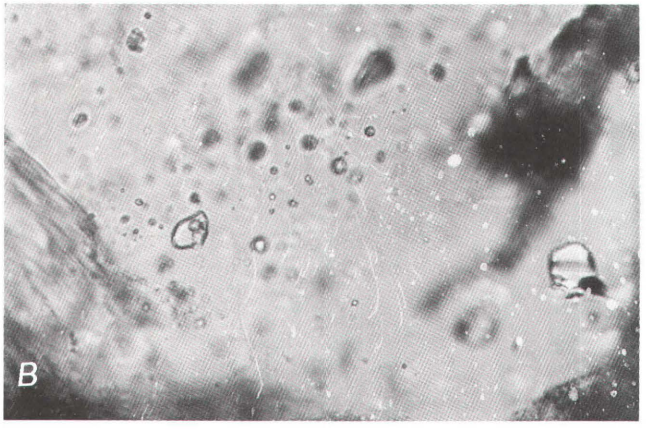
B

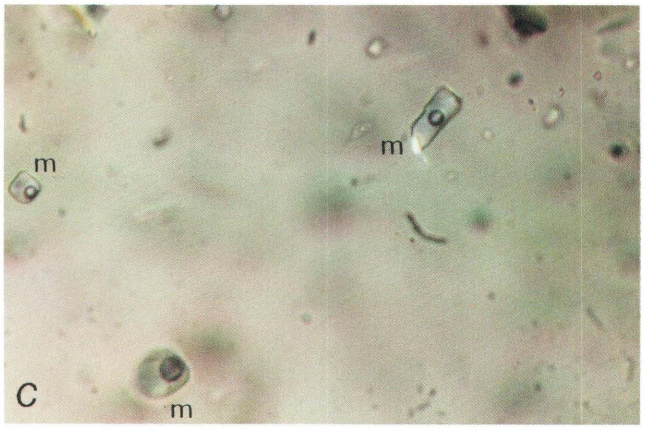
m
m
m
C


c?
D

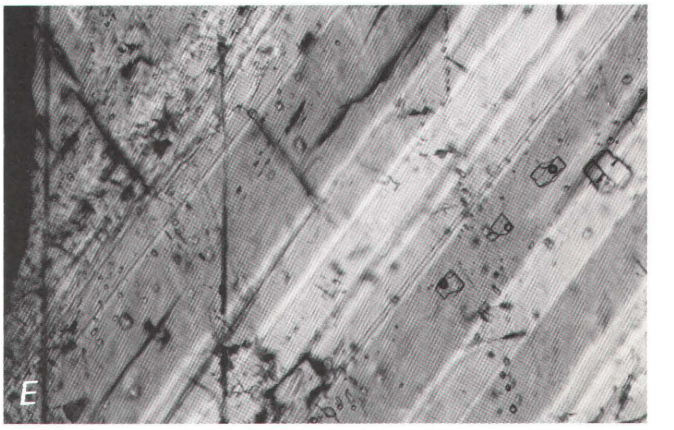
E


v
2l+v
F

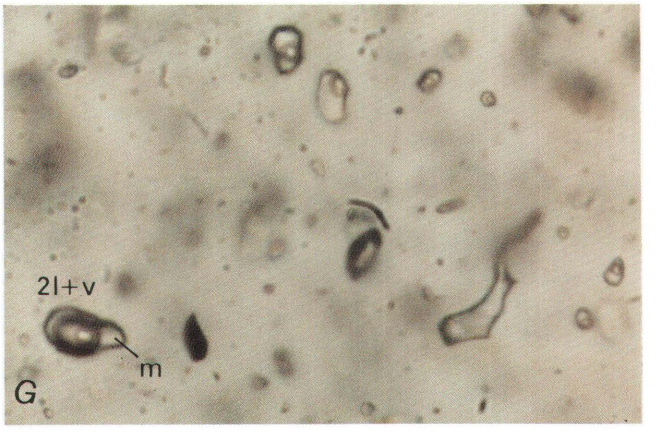
2l+v
m
G

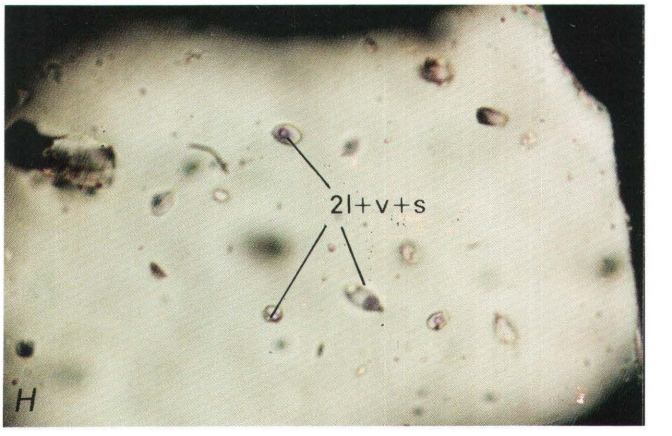
2l+v+s
H

inclusions with highly variable volumetric proportions predominate in the coarse vein quartz (fig. 3*F*). Vapor-rich inclusions also occur with L_1-L_2-V inclusions; however, they are less common. The three-phase inclusions have visually estimated $C_2O_2/(H_2O+CO_2)$ ratios that range from 5 to 47 percent; gas-rich inclusions are also present. The majority of these inclusions have $CO_2/(H_2O+CO_2)$ of 30–45 percent. Some L_1-L_2-V inclusions also contain one or two solids (fig. 3*G*); these inclusions are found in the narrower sulfide-bearing quartz veins that cut the core of the stock. Some of these liquid CO_2-bearing inclusions are attached to muscovite blades partially imbedded in quartz; hence, they are probably primary in origin (fig. 3*H*). The volumetric proportions of CO_2 and H_2O in these inclusions are more regular than those found in the coarse quartz veins, volume percent CO_2 ranges from 5 to 15 for the larger, more readily visible inclusions.

Secondary L-V inclusions and inclusions of an ambiguous nature are abundant in quartz phenocrysts and in vein quartz and calcite. These inclusions occur in numerous curved and linear arrays that cut across aggregates of the host mineral. The inclusions are generally small and have regular liquid-to-vapor ratios; they rarely contain trapped solids.

Preliminary optical study of selected samples of molybdenite-bearing rocks in the Sally Mountain stock indicates that L-V, V, and L-V-S are the predominant types of inclusions. Only one single inclusion has been found containing two liquids plus vapor (L_1-L_2-V) in samples from Sally Mountain. Quartz phenocrysts in the Attean pluton also contain L-V, V, and L-V-S inclusions, and it apparently contains no two-liquid-plus-vapor inclusions. Quartz phenocrysts in samples of the nearby Devonian Hog Island and Chain of Ponds plutons (Albee and Boudette, 1972; Heizler and Lux, 1984) also contain mainly inclusions of L-V, V, and L-V-S types. A single inclusion in quartz from the Chain of Ponds pluton is possibly of the L_1-L_2-V type. Further studies are in progress to place more quantitative limits on the temperature distribution, salinities, gas contents, and daughter minerals or trapped solids present in primary and secondary inclusions occurring in these plutons.

At the present time, the data suggest that the liquid, CO_2-bearing inclusions are restricted predominantly to the granitic rocks associated with mineralization at Catheart Mountain. The generally uniform spatial distribution of inclusion types in vein quartz and in quartz phenocrysts, and the large number of L_1-L_2-V inclusions compared to other plutonic rocks in the region, suggests that the ore fluids were localized in and around the Catheart Mountain stock. The regular distribution of inclusion types (all types are generally found at all depths in all drill core) also suggests that fractures and veinlets were open to most fluids, at least during the later stages of the evolution of the hydrothermal system, and that the fluid flow in the hydrothermal system generally was pervasive, occurring throughout the pluton.

Homogenization temperatures of primary and secondary inclusions in quartz from Catheart Mountain range from 199°C to 305°C. Visual estimates of low liquid-to-vapor ratios for some other inclusions (e.g., vapor-rich inclusions in fig. 3*A*, 3*B*) suggest that the actual temperature range may be even higher. Many CO_2-bearing inclusions decrepitated prior to homogenization. CO_2 effervescence is suggested by inclusions in coarse vein quartz that have highly variable H_2O/CO_2 values and coexisting L-V, L_1-L_2-V, and V-rich inclusions. Estimates of the salinity of measured inclusions based on last melting temperatures of solids (ice or clathrate-hydrate) range from about 0 to 5 weight percent NaCl according to data summarized by Collins (1979). Methane is assumed to be virtually absent based on melting temperatures of solid CO_2 to liquid CO_2 in the presence of vapor of about -56 ± 1°C.

Most of the inclusion data presented here are representative of the later hydrothermal fluid that resulted in the second pervasive influx of sulfide minerals into the system consisting of veins of chalcopyrite + sphalerite + galena + quartz ± pyrite ± calcite and fine-grained muscovite. The preliminary results suggest a model whereby a hydrothermal fluid of moderate temperature and salinity (1), gradually became saturated in CO_2 with decreasing temperature and (2), began to effervesce and deposited quartz, chalcopyrite, and a second generation of muscovite in veins. This effervescence due to CO_2 followed an initial phase of mineralization that deposited quartz, molybdenite, and the first generation of muscovite in veins at Catheart Mountain. Magmatic feldspars, the primary sinks for Rb and Sr in the granodioritic rocks, were systematically destroyed during this alteration, and, in their place, hydrothermal albite and K-feldspar were formed. Figure 2 shows the probable P-T range for formation of the second stage of sulfide mineralization; an onset of CO_2 effervescence occurring at about 300–340°C would yield pressures in the range of about 1.4–2.3 kb, consistent with geologic estimates of a shallow depth of emplacement for the Catheart Mountain stock (3–5 km). CO_2 is not typical of Cu-Mo porphyry systems, although it has been identified in some deposits (table 1). For deposits where CO_2 is present, amounts of CO_2 may range from as low as about 3 mole percent CO_2 (limits of optical detection) to more than 30 mole percent in CO_2-rich inclusions; some inclusions may have no optically detectable CO_2 but may have large CO_2 pressures at room temperature (Nash, 1976). Liquid, CO_2-bearing inclusions are thought to be associated with relatively low-temperature porphyry-type deposits or the low-temperature stages of such deposits (Nash, 1976). Unlike H_2O boiling of a brine, CO_2 effervescence generally results in an inital drop in total salinity due to loss of CO_2 to the vapor phase; this is followed by a

Table 2. Rb-Sr isotopic data and alteration indices of the Catheart Mountain porphyry Cu-Mo deposit and Sally Mountain Cu-Mo occurrence, Maine.

[--, data not available]

Sample[1]	Rb	Sr	Rb/Sr	$^{87}Rb/^{86}Sr$	$^{87}Sr/^{86}Sr$	*AI*[2]
CATHEART MOUNTAIN						
Porphyritic dikes						
114-494	94.0	861	0.1092	0.3164	0.70750	49
12-370	136.0	498	0.2731	0.7915	0.71079	56
5-680	127.0	379	0.3351	0.9695	0.71191	65
5-740	143.0	249	0.5743	1.6674	0.71685	73
31-282	210.0	168	1.2500	3.6300	0.72674	74
CATHEART MOUNTAIN						
Equigranular granodiorite host						
114-442	96.9	680	0.1425	0.4121	0.70854	40
31-210	126.0	621	0.2029	0.5868	0.70961	46
31-52	87.4	736	0.1188	0.3435	0.70816	48
18-190	110.0	486	0.2263	0.6530	0.71003	50
SALLY MOUNTAIN						
AT-05	147.4	104	1.4173	4.1095	0.73286	--
AT-06	174.1	69	2.5232	7.3251	0.74871	--
AT-07	213.9	51	4.1615	12.1247	0.77885	--

[1] Sample numbers correspond to drill hole number and depth.

[2] Alteration index, (*AI*) consists of the sum of the abundances (in weight percent) of K-feldspar, muscovite, and quartz (Molling and Ayuso, 1990).

gradual increase in salinity with continued boiling as salts are concentrated in the fluid. The low and variable salinities of the late hydrothermal fluid may reflect this process in part. In the Eastern United States and Canada, CO_2 is a more commonly reported constituent of inclusions in quartz from granite-related mineral deposits compared to deposits from the Western United States and Canada (table 1). However, compared to such granite-related deposits, those from the East have a distinct metallogenic association, are possibly more deeply eroded, are generally older, and have penetrated fundamentally different basement rocks. Other explanations are also possible, and further interpretation must await a more comprehensive database.

RUBIDIUM AND STRONTIUM GEOCHEMISTRY

Isotopic data for Rb and Sr are given in table 2 and are plotted in figure 4. Whole-rock data for nine samples from both petrographic units of Catheart Mountain plot on or near the regression line within analytical uncertainty and indicate an age of 422±15 Ma (fig. 4). The initial $^{87}Sr/^{86}Sr$ is 0.70603±0.00019. Two samples of the porphyritic dikes and one from the equigranular host fall off the regression line, suggesting that they were geochemically disturbed in a different manner than the rest of the samples. If these three samples were eliminated from the age calculation, the remaining six samples would indicate an age of 420±4 Ma for the Catheart Mountain stock; the initial $^{87}Sr/^{86}Sr$ ratio for these six samples is 0.70609±0.00003—these results are very similar to the entire set of data.

In a general way, measured Sr isotopic ratios are higher in rocks with higher alteration indices—this is consistent with the idea that the fluids associated with alteration were enriched in radiogenic Sr. The fluids could have acquired their isotopic composition by leaching of older minerals with high Rb/Sr values, such as biotite. The resulting isotopic composition, thus, would have been enriched in radiogenic ^{87}Sr, and this mechanism would have produced enrichment of radiogenic Sr in newly precipitated albite rims and epidote involved in the destruction of magmatic plagioclase.

Rb and Sr abundances in the Catheart Mountain stock are directly related to the extent of alteration of the rock (fig. 5). With increasing alteration, as indicated by *AI* values, Rb contents are relatively enhanced and Sr contents are relatively lowered (fig. 5*A*, 5*B*). The coherent changes in Rb and Sr contents reflect the progressive destruction of plagioclase by hydrothermal fluids. As a result of this alteration, relatively calcic magmatic plagioclase eventually disappeared, and this also resulted in a net removal of Sr from the whole rocks. Although rims of albite and epidote were also formed as a result of the alteration, these minerals are Sr poor (e.g., Dickin and Jones, 1983; Andre

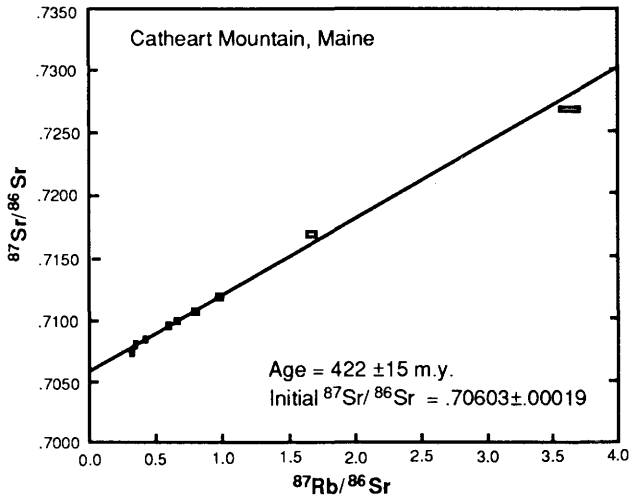

Figure 4. Rb-Sr isochron diagram for the Catheart Mountain pluton. Size of individual data points reflects the 95 percent confidence level.

and Deutsch, 1986). $^{87}Rb/^{86}Sr$ isotopic values are generally low at Catheart Mountain (fig. 4), from about 0.3 to 3.5, and broadly increase with higher *AI* in both the equigranular host rocks and porphyritic dikes, consistent with the suggestion that the low values of $^{87}Rb/^{86}Sr$ are best interpreted as the result of hydrothermal leaching. Rb/Sr values increased up to about 3.5 in the most altered rocks (fig. 5).

The three samples analyzed for their isotopic compositions from Sally Mountain do not plot on the regression line for the Catheart Mountain stock but broadly indicate an age of 393±29 Ma and initial $^{87}Sr/^{86}Sr$ value of 0.70949 (table 2). Values of the $^{87}Rb/^{86}Sr$ ratio range from 4.1 to 12.1, and Sr content is as low as 51.4 ppm in these samples. Thus, the isotopic data do not indicate that Sally Mountain and Catheart Mountain belong to a common isotopic system—this is consistent with the suggestion that the two hydrothermal systems did not share the same type of mineralizing fluids.

SUMMARY AND DISCUSSION

The whole-rock Rb-Sr isochron age and initial $^{87}Sr/^{86}Sr$ of the porphyritic dikes and equigranular rocks at Catheart Mountain can be interpreted in at least two ways: (1) The isotopic compositions survived the hydrothermal event, and they are magmatic. In this interpretation, the whole-rock Rb/Sr age of about 422 Ma and the Sr initial value of about 0.70603 are primary; or (2) the isotopic compositions in the Catheart Mountain pluton formed under the influence of the hydrothermal event. In this interpretation, the isochron age is not the crystallization age but reflects an open isotopic system and probably mixing of different isotopic reservoirs (e.g., a magmatic

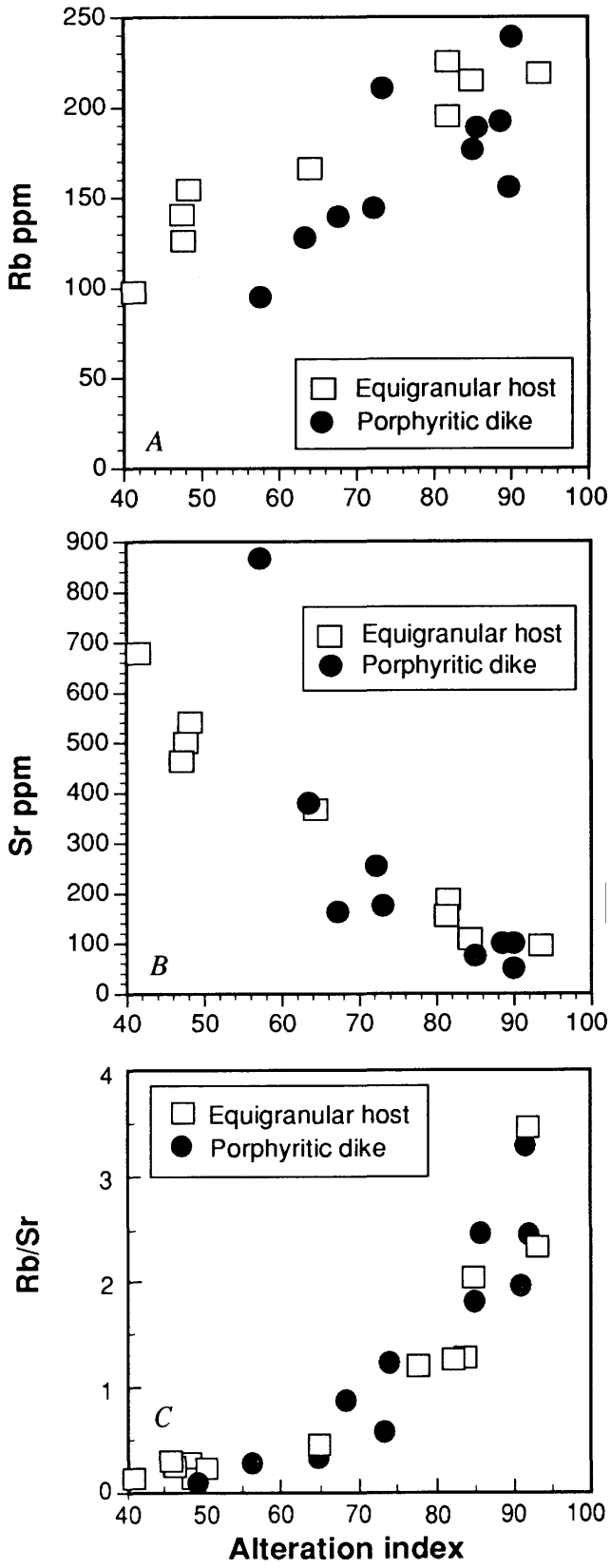

Figure 5. Abundances of *A*, Rb; *B*, Sr; and *C*, values of Rb/Sr plotted as a function of hydrothermal alteration as represented by the alteration index, *AI*= K-feldspar + muscovite + quartz (in weight percent). Figure shows all samples analyzed in this study and samples analyzed by Ayuso (1989).

component plus an assimilation component). These two alternatives are explored in more detail below.

In the event that new Rb-Sr heterogeneities were established by the remobilization of Rb and Sr isotopes and a common initial Sr ratio developed at the onset of alteration (perhaps by mechanisms similar to those found in other altered systems elsewhere (Zeck and Wallin, 1980)), it is conceivable that whole-rock Rb-Sr ages reported in this study approximate the age of crystallization (and mineralization) of the Catheart Mountain stock. In this case, the whole-rock Rb-Sr isochron would provide a minimum estimate of the crystallization age—an estimate that would be aproximately similar to the mineralization age because mineralization usually occurs shortly after crystallization of the pluton, in a way similar to that of other porphyry Cu systems (Norton, 1978).

This interpretation of the Rb-Sr isotopic data, however, does not appear to be viable because the hydrothermal system was open to migration of Rb (resulting in a net gain in Rb content) and Sr (net loss of Sr) as both the original fabric and mineralogy of the pluton were drastically modified. A net loss of Sr in the system implies that radiogenic Sr was also lost. Moreover, a magmatic interpretation of the whole-rock Rb-Sr age is in conflict with previously reported age determinations on muscovite from molybdenite veins from Catheart Mountain that yielded somewhat older ages (K-Ar = 441±8 Ma; Rb-Sr model age = 447±10 Ma) (Lyons and others, 1986); the analytical uncertainties of these determinations, however, indicate that all of these ages are roughly equivalent. Lyons and others (1986) indicated that the Rb-Sr model age (447±10 Ma) obtained on Catheart Mountain was similar to the zircon age of 443±4 Ma of the Attean pluton; they also suggested that the Attean and the Catheart Mountain stock were comagmatic—we do not favor this interpretation on the basis of geochemical contrasts between the Attean and the Catheart Mountain stock (Ayuso, 1989). In fact, the K-Ar muscovite age and Rb-Sr model age (Lyons and others, 1986) contrast with preliminary results of our ongoing Ar-Ar dating study, indicating that muscovites in textural equilibrium with molybdenite and chalcopyrite have Ar-Ar plateau ages of about 435±2 Ma (Ayuso and Kunk, unpub. data). If this Ar-Ar muscovite age is meaningful, the implication is that neither our whole-rock Rb-Sr results (422±15 Ma) nor the previously determined Rb-Sr model ages and K-Ar ages (447±10 Ma and 441±8 Ma, respectively; Lyons and others, 1986) give a precise estimate of the age of the hydrothermal event. However, one important and unexpected result of this study is that, despite the strong alteration effects at Catheart Mountain, the whole-rock Rb-Sr age differs by less than 3 percent from our preliminary Ar-Ar age.

There is no direct way to recover the original $^{87}Sr/^{86}Sr$ value, unless contamination throughout the life of the hydrothermal event was produced by magmatic fluids containing the same $^{87}Sr/^{86}Sr$ ratio as the rocks. The samples would have lost Sr (higher Rb/Sr values only), but the initial $^{87}Sr/^{86}Sr$ signature would have been preserved, and the estimated age would be a general approximation of the age of the hydrothermal event.

Age-corrected Sr initial ratios at 434 Ma, which is the suggested Ar-Ar age of muscovite associated with the mineralization at Catheart Mountain (Ayuso and Kunk, unpub. data), range from about 0.7055 to about 0.7066. The only striking exception is from a highly altered sample (31–282; *AI* = 74) that does not contain epidote and that has a value of initial Sr of about 0.7044. In contrast to hydrothermal alteration systems elsewhere (Andre and Deutsch, 1986), epidote-poor rocks (higher alteration index) at Catheart Mountain are the most intensely altered, and we think that they are unlikely to contain primary isotopic features. If, as we think, the hydrothermal fluids differed from the magmatic fluids and were probably more radiogenic than the rocks, the resulting Sr initial ratio represents a mixture of the magmatic Sr initial ratio and the radiogenic ratio of the contaminating fluid, although the end-member compositions cannot be established at this time. In fact, the plot of age-corrected initial Sr versus 1/Sr (not shown) demonstrates that the porphyritic dikes and the equigranular host rocks can be separated into two general fields and that, at least in the porphyritic dikes, there is a hint that the higher initial Sr values are in the Sr-poor rocks (high *AI*).

At the height of hydrothermal activity at Catheart Mountain, the fluid was probably moderately hot (at least as hot as 300°C), oxidizing (high values of Fe^{3+}/Fe^{2+}), and saline (occurrence of halite, table 1). The hydrothermal fluid progressively became saturated in CO_2 with decreasing temperature, effervesced, and deposited quartz, chalcopyrite, and fine-grained muscovite in veins. Effervescence may indicate a period of second boiling as a result of CO_2—a period subsequent to the event that deposited quartz, molybdenite, and coarser muscovite. Destruction of biotite accounts for the loss of Mg in the whole rock. Igneous plagioclase released Ca and Na (and Sr) to the fluid, and reactions with the fluid ultimately precipitated hydrothermal K-feldspar and produced an enrichment in K and Rb; these reactions also produced high values of K/Na and Fe^{3+}/Fe^{2+} in hydrothermally altered rocks by base-exchange reactions (Hemley and Jones, 1964)—this also lowered the KCl/HCl ratio in the aqueous phase (Burnham, 1979). The fluid was thus probably enriched in radiogenic Sr as a result of these reactions. Hydrothermally produced K-feldspar and muscovite account for the bulk of the K and H_2O influx into the system; albitic plagioclase accounts for the Na and at least some of the Sr retained in the rock after alteration. Epidote and chlorite formed during alteration also partially account for the Ca, Fe, Mg, and Sr in the rock, and the sulfide minerals account for the influx of Cu, Mo, and S. Toward the end of the alteration events, hydrolysis reactions increased values of the KCl/HCl ratio and formed muscovite from K-feldspar (Burnham and Ohmoto, 1980).

ACKNOWLEDGMENTS

This study benefitted from the generous help of R.G. Schmidt during selection of core samples and through discussions on the nature of the mineralization and alteration in the Catheart Mountain area. We thank J.G. Arth for his critical help and advice in the isotope laboratory and for discussions on the geochemistry of granitic rocks. The paper benefitted greatly from reviews by B.R. Doe and R. Seal.

REFERENCES CITED

Albee, A., and Boudette, E.L., 1972, Geology of the Attean quadrangle, Somerset County, Maine: U.S. Geological Survey Bulletin 1297, 110 p.

Andre, L. and Deutsch, S., 1986, Magmatic $^{87}Sr/^{86}Sr$ relicts in hydrothermally altered quartz diorites (Brabant Massif, Belgium) and the role of epidote as a Sr filter: Contributions to Mineralogy and Petrology, v. 92, p. 104–112.

Atkinson, D., 1977, Catheart Mountain, an Ordovician porphyry copper molybdenum occurrence in northern Appalachia: London, Ontario, University of Western Ontario, Ph.D. dissertation, 192 p.

Ayuso, R.A., 1987, Mineralized rocks of the Catheart Mountain Cu-Mo porphyry, Maine: Aluminous white micas as indices of mineralization: U.S. Geological Survey Bulletin 1803, 16 p.

Ayuso, R.A., 1989, Geochemistry of the Catheart Mountain porphyry copper deposit, Maine: Maine Geologcial Survey, Studies in Maine Geology, Jackson Volume, p. 139–162.

Ayuso, R.A., Horan, M., and Criss, R.E., 1988, Pb and O isotopic geochemistry of granitic plutons from northern Maine: American Journal of Science, v. 288, p. 421–460

Beane, R.E., and Titley, S.R., 1981, Porphyry copper deposits, Part II. Hydrothermal alteration and mineralization: Economic Geology, 75th Anniversary Volume, p. 214–269.

Boone, G.M., Boudette, E.L., and Moench, R.H., 1970, Bedrock geology of the Rangeley Lakes–Dead River basin region, western Maine, *in* New England Intercollegiate Geologic Conference, 62nd Annual Meeting, Rangeley Maine: Guidebooks for Field Trips in the Rangeley Lakes–Dead River Basin, Western Maine, p. 1–24.

Bowers, T.S., and Helgeson, H.C., 1983, Calculation of the thermodynamic and geochemical consequences of nonideal mixing in the system H_2O-CO_2-NaCl on phase relations in geologic systems—Equation of state for H_2O-CO_2-NaCl fluids at high pressures and temperatures: Geochimica et Cosmochimica Acta, v. 47, p. 1247–1275.

Brimhall, G.H., 1979, Lithologic determination of mass transfer mechanisms of multiple stage porphyry copper mineralization at Butte, Montana: Vein formation of hypogene leaching and enrichment of potassium-silicate proto-ore: Economic Geology, v. 74, p. 556–589.

Brimhall, G.H., 1977, Early fracture-controlled disseminated mineralization at Butte, MT: Economic Geology, v. 72, p. 37–59.

Burnham, C.W., 1979, Magmas and hydrothermal fluids, *in* Barnes, H.L., ed., Geochemistry of Hydrothermal Ore Deposits, 2nd edition: John Wiley and Sons, p. 71–136.

Burnham, C.W., and Ohmoto, H., 1980, Late-stage processes of felsic magmatism: Mining Geology Special Issue No. 8, p. 1–11.

Cathelineau, M., 1988, Cation site occupancy in chlorites and illites as a function of temperature: Clay minerals, v. 23, p. 471–485.

Collins, P.L.F., 1979, Gas hydrates in CO_2-bearing fluid inclusions and the use of freezing data for estimation of salinity: Economic Geology, v. 74, p. 1435–1444.

Dickin, A.P., and Jones, N.W., 1983, Relative element mobility during hydrothermal alteration of a basic sill, Isle of Skye, N.W. Scotland: Contributions to Mineralogy and Petrology, v. 82, p. 147–153.

Ferry, J., 1985, Hydrothermal alteration of Tertiary igneous rocks from the isle of Skye, northwest Scotland: II. Granites: Contributions to Mineralogy and Petrology, v. 91, p. 283–304.

Green, N.L., and Usdansky, S.I., 1986, Ternary feldspar mixing relations and thermobarometry: American Mineralogist, v. 71, p. 1100–1108.

Gustafson, L.B., and Hunt, J.P., 1975, The porphyry copper deposits at El Salvador, Chile: Economic Geology, v. 70, p. 857–912.

Haselton, H.T., Jr., Hovis, G.L., Hemingway, B.S., and Robie, R.A., 1983, Calorimetric investigation of the excess entropy of mixing in analbite-sanidine solid solutions—lack of evidence for Na, K, short range order and implications for two-feldspar geothermometry: American Mineralogist, v. 68, p. 398–413.

Heizler, M.T., and Lux, D.R., 1984 $^{40}Ar/^{39}Ar$ incremental release geochronology on hornblende-biotite pairs for the Chain of Ponds pluton, west-central Maine [abs.]: Geological Society of America, Abstract with Programs, v. 16, p. 22–23.

Hemley, J.J., and Jones, W.R., 1964, Chemical aspects of hydrothermal alteration with emphasis on hydrogen metsomatism: Economic Geology, v. 59, p. 538–569.

Hollister, L.S., 1978, Geology of the Porphyry Copper Deposits of the Western Hemisphere: New York, American Institute of Mining, Metallurgical, and Petroleum Engineers, 219 p.

Hollister, V.F., Potter, R.R., and Barker, A.L., 1974, Porphyry-type deposits of the Appalachian orogen: Economic Geology, v. 69, p. 618–630.

John, D.A., 1989, Evolution of hydrothermal fluids in the Park Premier stock, central Wasatch Mountains, Utah: Economic Geology, v. 84, p. 879–902.

Lowell, J.D., and Guilbert, J.M., 1970, Lateral and vertical alteration-mineralization zoning in porphyry ore deposits: Economic Geology, v. 63, p. 645–654.

Lyons, J.B., Aleinikoff, J.N., and Zartman, R.E., 1986, Uranium-thorium-lead ages of the Highlandcroft plutonic suite, northern New England: American Journal of Science, v. 286, p. 489–509.

McDowell, S.D., and Elders, W.A., 1980, Layer silicate mineralogy in borehole Elmore 1, Salton Sea geothermal field, California, USA: Contributions to Mineralogy and Petrology, v. 74, p. 293–310.

Molling, P. and Ayuso, R.A., 1990, Mineral paragenesis and hydrothermal alteration in the Catheart Mountain porphyry Cu-Mo deposit [abs.]: Geological Society of America, Abstracts with Programs, v. 22, p. 57–58.

Nash, J.T., 1976, Fluid inclusion petrology—Data from porphyry copper deposits and applications to exploration: U.S. Geological Survey Professional Paper 907–D, 16 p.

Nash, J.T., and Cunningham, C.G., Jr., 1974, Fluid-inclusion studies of the porphyry copper deposit at Bagdad, Arizona: U.S. Geological Survey Journal Research, v. 2, p. 31–34.

Nash, J.T., and Theodore, T.G., 1971, Ore fluids in a porphyry copper deposit at Copper Canyon, Nevada: Economic Geology, v. 66, p. 385–399.

Norton, D., 1978, Source lines, source regions, and path lines for fluids in hydrothermal systems related to cooling plutons: Economic Geology, v. 73, p. 21–28.

O'Neil, J.R. and Taylor, H.P., 1967, The oxygen isotope and cation exchange chemistry of feldspars: American Mineralogist, v. 52, p. 1414–1437.

Preece, R.K., III, and Beane, R.E., 1982, Contrasting evolutions of hydrothermal alteration in quartz monzonite and quartz diorite wall rocks at the Sierrita porphyry copper deposit, Arizona: Economic Geology, v. 77, p. 1621–1641.

Reynolds, T.J., and Beane, R.E., 1985, Evolution of hydrothermal fluid characteristics at the Santa Rita, New Mexico, porphyry copper deposit: Economic Geology, v. 80, p. 1328–1347.

Samson, I.M., 1990, Fluid evolution and mineralization in a subvolcanic granitic stock: The Mount Pleasant W-Mo-Sn deposits, New Brunswick, Canada: Economic Geology, v. 85, p. 145–163.

Schmidt, R.G., 1974, Preliminary study of rock alteration in the Catheart Mountain molybdenum-copper deposit, Maine: U.S. Geological Survey Journal Research, v. 2, p. 189–194.

Seal, R.R., II, Clark, A.H., and Morrissy, C.J., 1987, Stockwork tungsten (scheelite)-molybdenum mineralization, Lake George, southwestern New Brunswick: Economic Geology, v. 82, p. 1259–1282.

Shelton, K.L., 1983, Composition and origin of ore-forming fluids in a carbonate-hosted porphyry copper and skarn deposit: A fluid inclusions and stable isotope study of mines, Gaspé, Quebec: Economic Geology, v. 78, p. 387–421.

Steiger, R.H., and Jager, E., 1977, Convention on the use of decay constants in geo- and cosmochronology: Earth and Planetary Science Letters, v. 36, p. 359–362.

Stewart, D. B., Luetgert, J.H., Unger, J.D., and Phillips, J.D., 1985, Characterization of the crust of Maine by seismic reflection and refraction [abs.]: Geological Society of America, Abstracts with Programs, v. 17, p. 727.

Theodore, T.G., and Nash, J.T., 1973, Geochemical and fluid zonation at Copper Canyon, Lander County, Nevada: Economic Geology, v. 68, p. 565–570.

Thomas, A.V., and Spooner, E.T.C., 1985, Occurrence, petrology, and fluid inclusion characteristics of tantalum mineralization in the Tanco granitic pegmatite, S.E. Manitoba, *in* Taylor, R.P., and Strong, D.F., eds., Granite-Related Mineral Deposits, [extended abstracts of papers presented at the CIM conference on granite-related mineral deposits]: Halifax, Canada, CIM Geology Division, p. 274–278.

Titley, S.R., 1982, The style and progress of mineralization and alteration in porphyry copper systems, *in* Titley, S.R., ed., Advances in Geology of the Porphyry Copper Deposits, Southwestern North America: Tucson, Arizona, University of Arizona, p. 93–116.

Titley, S. R., 1975, Geological characteristics and environment of some porphyry copper occurrences in the southwestern Pacific: Economic Geology, v. 70, p. 499–514.

Velde, B., 1965, Phengite micas: Synthesis, stability, and natural occurrence: American Journal of Science, v. 263, p. 886–913.

Williams-Jones, A.E., Samson, I.M., and Linnen, R.L., 1989, Fluid evolution and its role in the genesis of the granite-related Madeleine copper deposit, Gaspé, Quebec: Economic Geology, v. 84, p. 1515–1524.

Wilson, J.W.J., Kessler, S.E., Cloke, P.L., and Kelly, W.C., 1980, Fluid inclusion geochemistry of the Granisle and Bell porphyry copper deposits, British Columbia: Economic Geology, v. 75, p. 456–61.

York, D., 1966, Least squares fitting of a straight line: Canadian Journal of Physics, v. 44, p. 1079–1086.

Zeck, H.P., and Wallin, B., 1980, A 1,220±60 m.y. Rb-Sr isochron age representing a Taylor-convection caused recrystallization event in a granitic rocks suite: Contributions to Mineralogy and Petrology, v. 74, p. 45–53.

Zen, E-an, 1983, Exotic terranes in the New England Appalachians—Limits, candidates, and ages: A speculative essay: Geological Society of America Memoir 158, p. 55–81.

CHAPTER F

STRUCTURE AND ORIGIN OF THE ELY COPPER DEPOSIT, EAST-CENTRAL VERMONT

By TERRY W. OFFIELD,[1] JOHN F. SLACK,[1] *and* SARAH A. WITTINBRINK[2]

ABSTRACT

The Ely copper deposit, in the Orange County copper district, east-central Vermont, occurs within pelitic and psammitic schist of the Middle Silurian(?) to Lower Devonian Gile Mountain Formation in a stratigraphic zone containing relatively abundant amphibolite. Stratabound layers and lenses of massive sulfide are concentrated near the crest of a prominent regional fold and are distributed en echelon down the plunge of the fold. The sulfide is interpreted to be of exhalative volcanogenic origin, formed in association with sea-floor basalts. Subsequent to deposition on or near the sea floor, layer-parallel foliation developed during intense isoclinal folding (F_1). This was followed by open to isoclinal folding (F_2) that produced reclined folds; the latest deformational episode consisted of regional arching and local structural doming (F_3). Each tectonic episode was accompanied by regional metamorphism. Sulfide layers were tectonically thickened and thinned, folded, and repeated by ductile thrust faulting. The present distribution of sulfide largely is controlled by the geometry of F_2 parasitic folds. Folding and shearing were intensified by ductility contrast and mobilization of the sulfide during deformation and metamorphism.

INTRODUCTION

The Ely mine, also known as the Copperfield or Vershire mine, is located about 5 km southeast of the town of Vershire Center in the Orange County copper district of east-central Vermont (fig. 1). Ely was discovered in 1820, and for a time during the 1850's, was the largest copper producer in the United States (Stevens, 1911, p. 1772). The mine closed in 1892 after producing approximately 35,000,000 pounds of copper from about 500,000 tons of ore that had an average grade of 3.5 percent Cu (White and Eric, 1944). Attempts at production around the turn of the century had little success, and the mine was abandoned in 1903.

Geologic studies of the mine area are limited. An unpublished thesis by Smith (1905) included observations made while most of the mine workings were accessible as well as descriptions of the ore by mine supervisors. The history and production of the mine and descriptions of the orebodies were presented by Wheeler (1883), Smyth and Smith (1904), and Weed (1911); Buerger (1935) described the ore and gangue mineralogy. White and Eric (1944) provided cross sections of the workings accessible above flooding level, a map of foliations and lineations measured at the surface around the mine, and a brief description of the local geology. The regional geology was outlined by Hitchcock (1912) and Doll (1944). Hermance and others (1949) reported on the findings from nine holes drilled in the mine area by the Bureau of Mines.

The present study is part of work in progress to determine the regional and local structural setting and deformational history of the sulfide deposits of the district. Results so far differ from those of prior studies in two important regards: (1) With one exception, earlier workers recognized only two episodes of deformation; we find good evidence of three deformational events in which the regional folds of the study area formed in an episode between the two deformational events recognized earlier; and (2) prior interpretations involved syn- to post-metamorphic introduction of sulfide into structural loci, following the conventional epigenetic model of the times, whereas we interpret the origin

[1]U.S. Geological Survey, Mail Stop 954, 12201 Sunrise Valley Drive, National Center, Reston, VA 22092.

[2]Department of Geological Sciences, Northwestern University, Evanston, IL 60208.

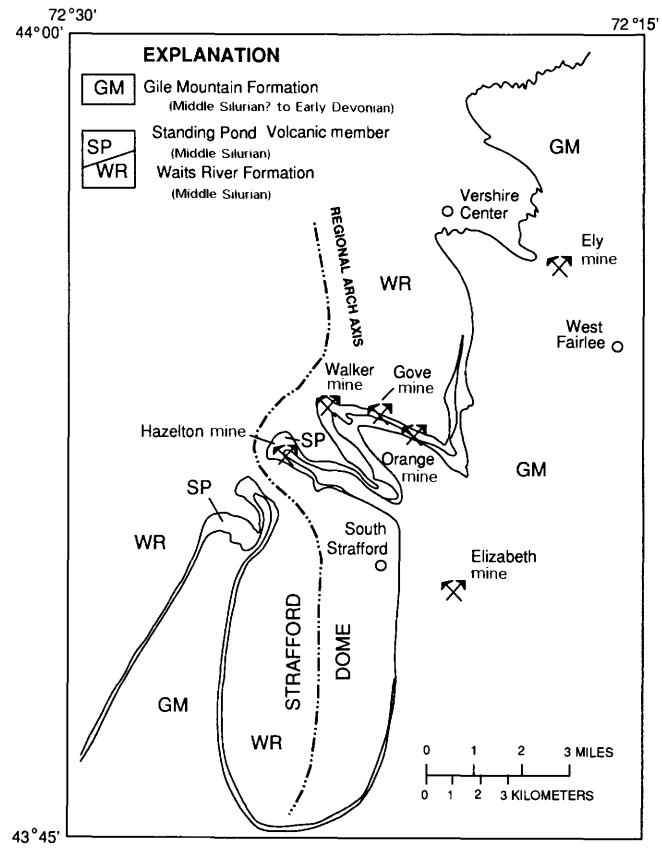

Figure 1. Map showing structural pattern and Ely and Elizabeth deposits in the Orange County copper district. Geology after Howard (1969).

of the sulfide syngenetic (volcanogenic) with deposition of sulfide prior to deformation and metamorphism.

GEOLOGIC SETTING

The rock units in the study area make up the Connecticut Valley trough sequence, which extends nearly 400 km from western Massachusetts to southeastern Quebec (Hatch, 1988). The Gile Mountain Formation, stratigraphically at the top of the sequence, consists predominantly of pelitic schist, with minor quartzite and amphibolite in places. It is considered to be, in part, Early Devonian on the basis of plant fossils found in rocks in Quebec that are believed, but not proven, to be equivalent (Hueber and others, 1990). The Gile Mountain overlies calcareous metapelite and minor quartzose marble of the Waits River Formation in apparent lithologic transition, suggesting a transgressive facies boundary (e.g., Lyons, 1955). The Standing Pond Volcanic Member of the Waits River occurs mainly along the mapped Waits River–Gile Mountain contact but departs slightly from it to the north of the Strafford dome (fig. 1). The Standing Pond consists largely of hornblende-plagioclase amphibolite, with a local tholeiitic chemistry (Hepburn, 1984; J.F. Slack, unpub. data) and generally has been interpreted as a series of basalt flows transgressing a regional pelite-carbonate facies boundary (see Annis and others, 1983). Near Springfield, Vermont, 70 km south of Ely, a felsic dike that cuts the Standing Pond has been dated as Middle Silurian (423±4 Ma) by Aleinikoff and Karabinos (1990)—this requires that the underlying Waits River Formation be no younger than Middle Silurian in age. The Gile Mountain Formation is here given an age of Middle Silurian(?) to Early Devonian. The Connecticut Valley trough sequence, therefore, is apparently Silurian and Devonian in age, deposited shortly before the Devonian Acadian orogeny.

Most structural studies of the region identified two stages of deformation that were assumed to be products of the Acadian orogeny (e.g., White and Jahns, 1950; Lyons, 1955; Chang and others, 1965; Fisher and Karabinos, 1980). These and other workers considered the deformation to have involved pervasive isoclinal folding followed by an episode of regional arching that included the formation of local structural domes. This arching broadly warped the older foliation about an axis that trends approximately north-south along the west side of the copper district. Large folds (the "zigzag folds" of Doll, 1944) outlined by the Standing Pond Volcanic Member (fig. 1) were believed to have formed in the arching episode and were interpreted by White and Jahns (1950) as reverse drags that cascaded off the rising Strafford dome (fig. 1). The earlier studies also concluded that the two deformations each were accompanied by episodes of metamorphism to garnet grade or higher.

Our recent geologic studies indicate, instead, that at least three episodes of deformation occurred and that the regional arching and structural doming warped rocks already deformed by two episodes of intense folding. This more complicated deformational history was also recognized by Woodland (1977) in an area about 18 km southwest of the Ely mine, and evidence documenting it has been found consistently throughout the Connecticut Valley trough sequence of east-central Vermont by the authors (Offield and Slack, 1990). The metamorphic history associated with this series of deformations has been documented and described by Menard (1991) and Menard and Spear (1991). D_1, evidenced by abundant, small-scale isoclines and layer-parallel axial-surface foliation, was accompanied by biotite-grade metamorphism. D_2 formed open to isoclinal folds with highly variable development of axial-surface foliation, depending on rock type and structural locus. D_2 was associated with garnet-grade metamorphism during a significant increase in pressure. D_3, the regional arching event, was associated with the development of metamorphic grades up to sillimanite in the Ely area, decreasing in grade to the east and west.

The zigzag folds are present only on the east side of the Connecticut Valley trough and only in the copper district. These folds, which are reclined folds of the D_2/F_2 generation, are increasingly tighter and steeper in plunge the closer they are to the Strafford dome. They occur along the east flank of the D_3 regional arch and were tilted perhaps 10 to 30 degrees by a combination of the arching and formation of the Strafford dome (fig. 1). Our work indicates that the zigzag folds predate the doming and were deformed by it. The zigzag folds are of interest in the context of mineral resources because both the Ely and Elizabeth orebodies occur near the crests of anticlines (interpreted facing direction) in this group of folds and because the F_2 folding was important in shaping the sulfide deposit at Ely.

Figure 2. Block of psammitic schist showing asymmetric F_2 Z-folds and almost complete lack of S_2 foliation.

GEOLOGY OF THE ELY MINE AREA

The Ely mine exploited stratabound, massive sulfide deposits within the lower part of the Gile Mountain Formation, about 800 m stratigraphically (apparent thickness) above the Standing Pond Volcanic Member. Throughout eastern Vermont and the copper district, the Gile Mountain Formation is composed predominantly of pelitic schist. In the Ely mine area, however, a large proportion of the exposed rocks is psammitic (quartzose) schist. Wheeler (1883) first recognized this relation and noted the contrast with the setting of the Elizabeth orebody, which is mainly within pelitic schist and altered amphibolite (Howard, 1969; Annis and others, 1983). Drill cores from the Ely mine area examined by the authors (Offield and Slack) show the psammitic schist in gradational contact and interleaved with pelitic schist and lesser amphibolite. The psammitic schist is mainly composed of quartz, with minor plagioclase, mica, and garnet; some samples display a mylonitic fabric. The pelitic schist contains abundant muscovite and biotite, minor quartz and plagioclase, and local concentrations of staurolite and kyanite. Garnets in the pelitic schist commonly show inclusion-rich, anhedral, rolled cores and clear euhedral rims that reflect the complex deformation and metamorphism in the area (see also Menard, 1991).

Schistose amphibolite layers are not generally exposed at the surface but are seen in drill cores. The amphibolites are common in a 300-m-thick zone (apparent stratigraphic thickness) that hosts the Ely deposit. This zone maintains the same stratigraphic/structural position above the Waits River–Gile Mountain contact for at least 12 km to the south, where it contains the larger massive sulfide deposits of the Elizabeth mine (fig. 1). The amphibolite layers occur in both the pelitic and psammitic schists and, like the Standing Pond Volcanic Member, are believed to represent basaltic flows emplaced across locally transgressive facies of shaly and sandy sediments. In at least two places at Ely, the amphibolites are closely associated with coticules, which are also found at Elizabeth (Annis and others, 1983). The coticules consist of fine-grained, Mn-rich garnet and quartz in multiple layers less than 1 cm thick, which in places display complex, tight to isoclinal folds.

Throughout the area, mesoscopic folds are common in most outcrops. These folds are especially well displayed in the psammitic schist, where they range in form from attenuated isoclines to "V" shapes with one limb longer than the other and with wavelengths up to 40 cm (fig. 2). These are F_2 folds that deform a prominent foliation parallel to compositional layering ($S_{1=0}$). Tight to isoclinal F_1 folds only millimeters in wavelength, and to which the dominant S_1 foliation is axial planar, are common on F_2 fold limbs and crests, as can be seen by close inspection of structures in drill cores (fig. 3*A*). S_2 axial-surface foliation tends to be poorly developed in most F_2 folds; it consists of alignments of biotite and quartz that form surfaces nearly parallel to the long limbs of the folds, rather than in a bisecting position. In some more schistose rocks, S_2 foliation is defined by a well-developed crenulation cleavage. The same geometry of folds and foliation is seen in pelitic schist and amphibolite, except that fold crests in those lithologies tend to be marked by a series of small, rounded plications of highly variable shape (fig. 3*B*). Mineral lineations consisting of weak alignments of quartz and biotite grains commonly are present, oriented parallel to the axes of F_2 folds. In places, similar lineations parallel the axes of small F_1 folds and wrap over the crests of F_2 folds.

White and Eric (1944) did not specify what foliation is portrayed on their map, but because S_2 foliation is uncommon and the foliation varies in strike and dip (suggesting that it has been deformed), their measured foliations are likely to be mainly, if not entirely, S_1. A

Figure 3. Core from drillhole E-9, showing style of F_2 folds outlined by $S_{1=0}$. *A*, Amphibolite displays what are probably plications on the crest of a larger F_2 fold. The folded foliation is S_1, axial planar to very small, tight to isoclinal folds. No S_2 foliation is developed. *B*, Mixed pelitic-psammitic schist shows irregular F_2 folds in $S_{1=0}$, with partial, local development of S_2 axial-planar foliation. Diameter of core is 3 cm.

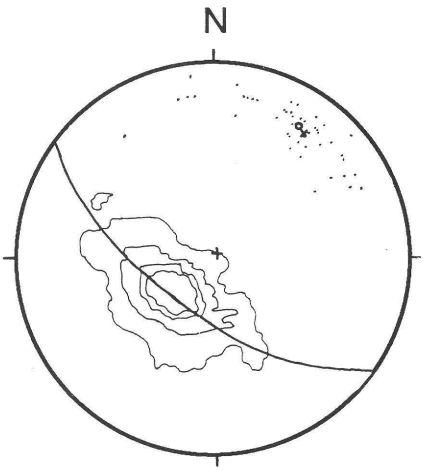

Figure 4. Stereographic plot of $S_{1=0}$ (contoured; n=717) and F_2 fold axes and cleavage-bedding intersection lineations (dots; n=50) of White and Eric (1944, pl. 2). X, ß-axis N. 37° E. 25°; o, mean lineation N. 35° E. 24°. Contours of foliation density 0.1, 5, 10, 25 percent (maximum density is 42 percent).

stereographic plot of the White and Eric (1944) map data (fig. 4) shows the foliation distribution to define a -axis of N. 37° E., 25°. Axes of small F_2 folds and "cleavage-bedding" intersection lineations (White and Eric, 1944, p. 6) on the plot are scattered, with a mean orientation of N. 35° E. 24°, very close to the β-axis. These lineations should all relate to F_2 axes; the meaning of the scatter in orientation is not entirely clear. Although it is possible that some of the fold-axis lineations plotted on figure 4 are of F_1 rather than F_2 generation, it is unlikely that this explains the scatter. F_1 folds are relatively scarce, and also the scatter of data for 13 folds we confidently identified as F_2 is as great as that shown by the lineations plotted on figure 4. The event that produced the scatter did not reorient the foliation as much as it did the fold lineations, suggesting post-F_2 rotational slip on foliation surfaces around axes steeply inclined to those surfaces. The scatter of the lineations is approximately on a great circle, suggesting dispersal by conical slip folding. The geometry is consistent with reshaping of F_2 structures during the D_3 formation of the Strafford dome.

Small-scale F_2 folds also show systematic changes in the sense of asymmetry, indicating the presence and geometry of larger scale folds in the mine area. Most workings are clustered about halfway up the ridge that contains the mine (fig. 5), in a zone of mostly pelitic schist with minor layers of psammitic schist and amphibolite. Mesoscopic folds in surface outcrops in this zone either are symmetric (M) or alternate in asymmetry (Z or S) on a scale of centimeters to meters, indicative of the axial zone of a larger fold. From 15 m above the main workings almost to the ridge crest, 70 m higher, is a zone of well-developed Z-folds in psammitic schist that includes a few interbeds of amphibolite. Just below the crest, the asymmetry reverses (S-folds), indicating the axial surface of a larger fold.

White and Eric (1944) noted the location of the Ely deposit on or near the axial plane of one of the regional zigzag folds but stressed the importance of local cleavage rolls (which they believed postdated the folds) as the main features controlling the occurrence of ore. Smith (1905) referred to such structures as "stepdowns" and believed

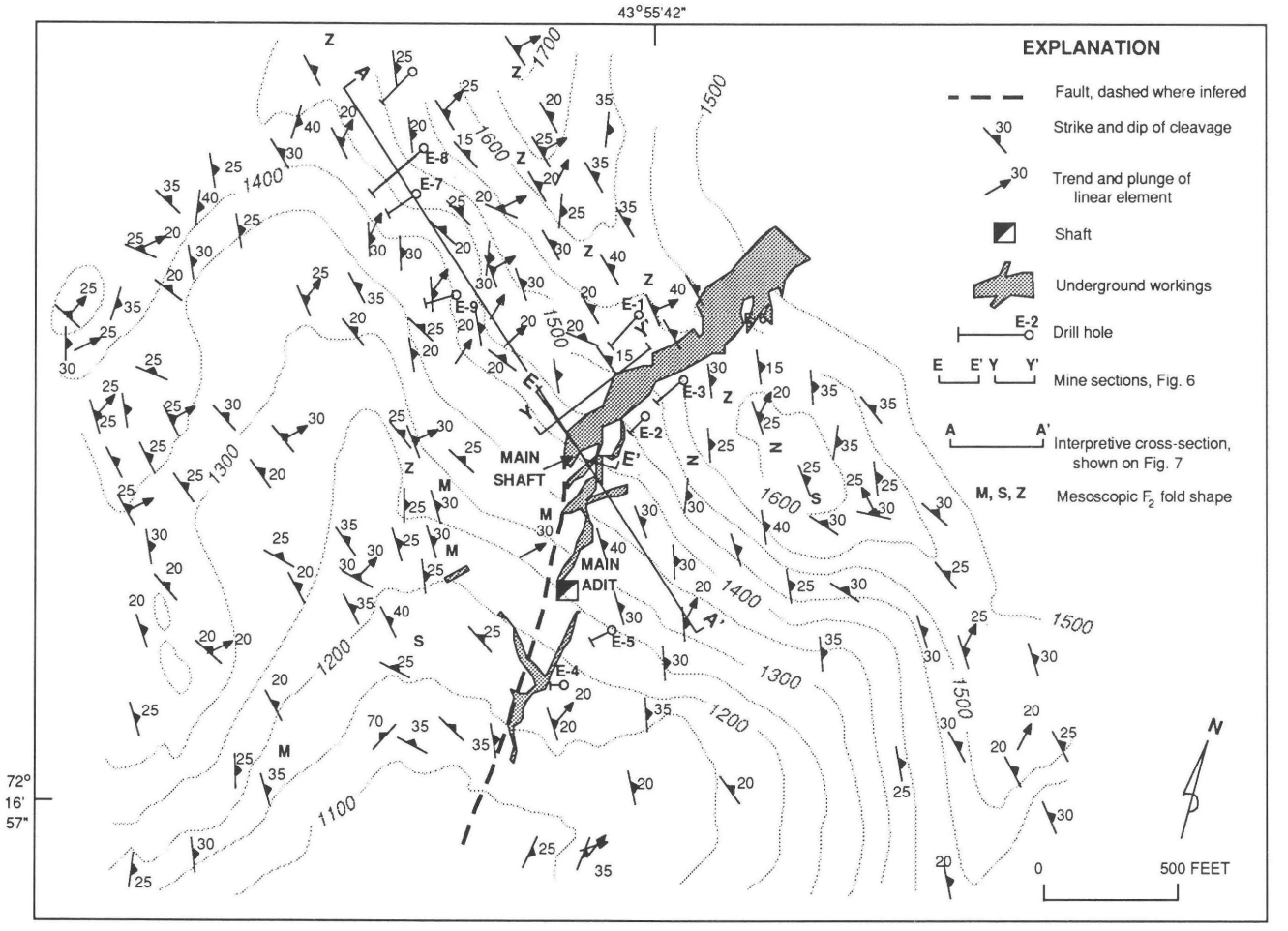

Figure 5. Map showing mine-area topography, mine workings, and structural elements in the area of the Ely deposit (after White and Eric, 1944, pl. 2). A–A′ is section line for face of block diagram shown on figure 7. E–E′ and Y–Y′ are mine sections shown on figure 6. Contour interval is 50 ft.

they had localized epigenetically introduced sulfides. The structures are not specifically delineated on the map of White and Eric (1944) and are not readily discernible in the pattern of 717 foliation readings shown on their map. White and Eric (1944) may have interpreted bends in ore layers and curved ore connections from one stope to another, shown on their mine sections, as indicating these cleavage rolls. Because warps of foliation would be expected from both inhomogeneous F_2 folding and the effects of D_3/F_3 deformation, we cannot assign the "cleavage rolls" or "stepdowns" to one or the other of these events.

All three phases of deformation involved shear that resulted in the rotation or offset of marker layers and any earlier structures. Discrete thrust faults are rarely exposed, however. One excellent example of an exposed thrust is in a small adit halfway between the two main mine openings. The contact zone between psammitic schist in the roof of the adit and pelitic schist containing considerable sulfide below is marked by an intense shear fabric and structural truncations. This thrust contact appears to represent a structure associated with F_1 isoclinal folding and foliation development because it is deformed by tight F_2 folds on the east side of the adit. In an adit about 25 m below this locality, White and Eric (1944) described a thrust fault that bounded sulfide ore. Their map shows the thrust connecting both adits (see fig. 5), but this connection seems doubtful unless there is structural repetition of the thrust by F_2 folding.

Mining was done primarily in tunnels and stopes off a "main shaft" (actually an inclined adit that followed the ore down plunge in the crestal area of a structurally complex system of folds). It was driven about N. 40° E. more than 1,000 m down an incline of about 25°, approximately on the trend and plunge of the mesoscopic F_2 folds (fig. 5). Figure 6 presents mine sections drawn by White and Eric (1944) of workings off the upper part of the main shaft. They show that ore occurs in thin layers, commonly

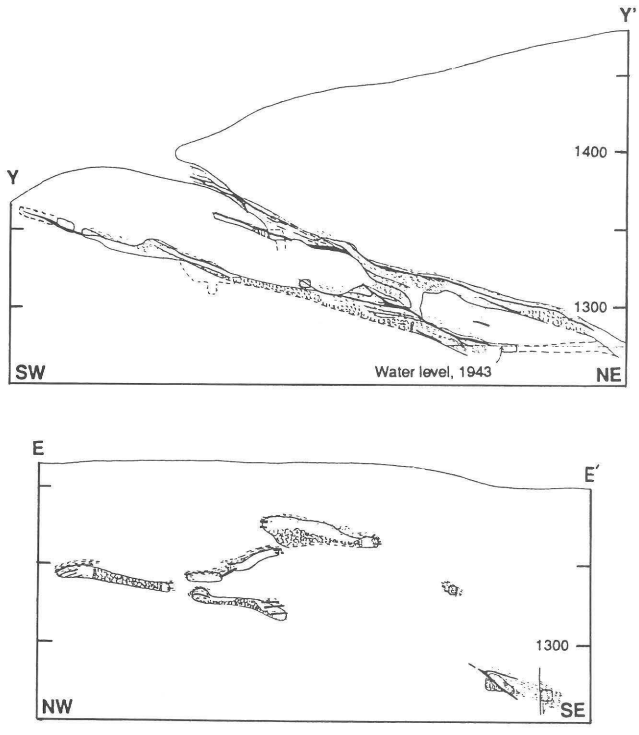

Figure 6. Mine section drawings from White and Eric (1944, pl. 6). Heavy black is "massive sulfide including schist with abundant disseminated sulfide"; light dashed lines are foliation. Displacement sense shown on small vertical fault. Adits, stopes, mine rubble indicated. E–E′, Y–Y′ located on figure 5. Numbers on vertical axes indicate elevation.

in stacks or sets of two to as many as six. In several parts of the mine workings shown, two or three of the layer sets occur, separated by up to 10 m of largely barren country rock. Although the mine sections reveal truncation and convergence of ore-layer sets and of layers within sets, they are especially important in showing that the ore layers are nearly everywhere parallel to schistosity (noted earlier by Wheeler, 1883). The few folds portrayed on the sections deform both ore and foliation. The sections also show disjunctive relations with one ore layer truncating another, apparently along small thrust faults.

Wheeler (1883, p. 221) provides a detailed description of the occurrence of ore in the mine:

> The vein really consists of two parallel ore sheets or strata of pyritic matter which are separated by an intervening layer of schist from ten to twenty-five feet thick. The lower vein or ore sheet is from one to eight feet in thickness, averaging about four feet, and on the whole is richer and more regular than the upper vein. The upper vein fluctuates very widely both in size and richness, as it will widen out from a one-foot vein of mundic [magnetic pyrite], assaying say one per cent [sic] in copper, to a twenty-five foot vein that will average over ten per cent [sic]. This great variation in the strength of the lode, more particularly the upper vein, is due to its highly lenticular character, as it really consists of a series of lenses or ore bodies extending both laterally and vertically, that are united by connecting sheets of ore. These connecting sheets will range from one to four feet in thickness, while the bonanzas or ore bodies will range from six to thirty feet in thickness. In addition to the great increase in strength at the ore bodies, these lenses are usually composed of high grade ore, so that they are veritable bonanzas, especially as they are apt to be nearly solid ore, with few or no bands of quartz or country rock. The connecting sheets are usually either mundic having very little copper pyrites mixed through it, or else are small mixed veins of nearly pure copper pyrites, intermixed through sheets of quartz. There are frequently one or more sheets of schist running through the ore, and these, when of large size, have frequently been mistaken for the hanging- and foot-walls of the vein, as no true or defined walls exist, though the ore is usually encased between quite even and regular surfaces.

This description from mine exposures is especially valuable, because many of the ore faces were not available for study even when Smith worked there in 1905. Smith's observations, and those of the miners he interviewed, led him to emphasize the distribution of ore in lenses. These lenses were described as being strung out en echelon down the inclined main shaft. Lenses to the north occurred 7 to 10 m below the lenses to their south, generally with overlaps of about 17 m but with one example of about 65 m of overlap. Individual lenses tended to be about 100 m long down plunge, about 17 to 80 m wide, and up to 10 m thick (average 3 m). Smith (1905) described the ore lenses as ending variously in sharp terminations associated with crushed quartz; or grading into disseminated, uneconomic ore; or fraying into unminable stringers. The ores consist of pyrrhotite, chalcopyrite, minor pyrite, and sphalerite in a gangue of quartz, mica, carbonate, feldspar, and minor tourmaline (Wheeler, 1883; Weed, 1911; Buerger, 1935). Reference by Wheeler (1883, p. 222) to quartz schist that is "highly garnetiferous, on the hanging side of the vein" may indicate the presence of coticules in the wallrocks of the sulfide ores.

Rare vertical faults that displace ore as much as 3 m typically are filled by carbonate and local barite (Smith, 1905; White and Eric, 1944). These faults apparently postdate all of the deformation described above and probably are a product of the Mesozoic deformation in the region. Similar late faults at the Elizabeth mine are filled by diabase and lamprophyre dikes of presumed Mesozoic age (Howard, 1969; Annis and others, 1983).

DISCUSSION AND INTERPRETATION

Previous workers considered the Ely deposit to have formed by epigenetic replacement during or following

regional metamorphism (Wheeler, 1883; Smith, 1905; Weed, 1911; White and Eric, 1944). Their interpretations were influenced greatly by theories, popular at the time, of epigenetic ore genesis and were supported by the fact that the sulfide bodies at Ely in places crosscut previously deformed silicate wallrocks (Smyth and Smith, 1904, p. 678; Smith, 1905, p. 127). Mine sections of White and Eric (1944) also show sulfide layers that appear to lie in the axial planes of F_2 folds, indicating emplacement of some sulfide after D_2 deformation. We consider such occurrences to be misleading, however, and believe that they represent minor tectonic repositioning or mobilization of sulfides, like those recognized in many other deformed and metamorphosed massive sulfide deposits throughout the world (e.g., Vokes, 1971; Gilligan and Marshall, 1987).

We suggest that the massive sulfide deposits at Ely are largely of exhalative volcanogenic origin and that the majority of the sulfide lenses originally formed more or less synchronously with deposition of the Gile Mountain Formation. Evidence for an early volcanogenic origin of the sulfides at Ely includes their overall stratabound geometry, their association with mafic metavolcanic rocks, and their deformation by two periods of folding; a photograph of folded, alternating layers of pyrrhotite and chalcopyrite shown by Weed (1911, pl. IV) clearly documents a predeformational age for the sulfides. Similar arguments can be made with respect to the other massive sulfides of the Orange County copper district, which also are believed to be of submarine volcanogenic origin. The largely sediment-hosted copper deposits of the district are considered excellent examples of the Besshi class of massive sulfide deposits (Slack, in press).

Because of the intense deformation in the mine area, we cannot distinguish between a purely exhalative origin for the sulfides and an origin involving replacement of permeable sediments during sedimentation or diagenesis. Although sub-sea-floor replacement, in part or whole, cannot be ruled out, we prefer a largely exhalative origin, particularly because of the layered association of sulfide deposits with amphibolite (metabasalt) and coticule. Coticules are believed to represent metamorphosed mixtures of detrital, clastic sediments and exhalative metalliferous precipitates enriched in iron and manganese (e.g., Spry, 1990) that formed directly on the sea floor.

Diagenetic mineralization seems less likely, based on the massive character of most of the ores and their similarity in composition and setting to the massive sulfide deposits that are actively forming on sediment-covered ridge crests. Modern analogs in such settings are at Guaymas Basin in the Gulf of California (Koski and others, 1985; Peter and Scott, 1988) and Middle Valley and Escanaba Trough, off the coasts of Washington and California, respectively (Goodfellow and Blaise, 1988; Koski and others, in press).

In modern submarine vent areas, sulfides can be irregularly distributed in layers, lenses, and talus flows on the sea floor. Sulfides may also occur irregularly below the sea floor, a product of the movement of hydrothermal fluids though permeable sediments. In the Orange County copper district, such inferred complexities have been compounded by intense deformation and metamorphism. Most of the small-scale structures evident in the mine sections portrayed by White and Eric (1944) involve folding and faulting of ore layers and $S_{1=0}$ foliation; they thus must be part of the F_2 folding event. Much of the detail of individual ore layers, however, and perhaps even the occurrence of ore in lenses, may be due to F_1 folding or to the original configuration of syngenetic (or synsedimentary) sulfides.

From Wheeler's (1883) description given above, it seems likely that the two main ore layers are stratigraphically separate and distinct and not a single layer repeated by folding. The abundance of tiny F_1 isoclines distributed throughout the host rocks, however, virtually requires the sulfide layers to have been deformed and reconfigured by F_1. Because such tight isoclinal folding seldom occurs without shearing and thrust faulting, the ore lenses described as having internal septa of schist may be isoclinal F_1 fold forms, sheared or offset by layer-parallel thrust faults so as to make fold crests difficult to recognize. On the other hand, the shaping of ore in lenses by a combination of original sea floor accumulation and F_1 deformation does not readily account for the en echelon distribution of those lenses down the plunge of the first-order F_2 fold structure. We believe that this geometry is a result of the configuration of F_2 parasitic folds, perhaps with later modification of trends and plunges by rotation and shear during D_3.

Concentration of sulfide in semi-massive to massive sulfide bodies would offer a conspicuous ductility contrast with silicate wallrocks and promote mobility during deformation (e.g., Vokes, 1971; Gilligan and Marshall, 1987). This ductility contrast locally would influence and accentuate deformation, and these effects probably would be heightened by the accompanying regional metamorphism. Both F_1 and F_2 folding would produce or exaggerate the lenticular shape of ore layers on fold limbs and result in prominent lensing of sulfide in fold crests. Ore layers would readily serve as slip surfaces in thrust dislocations, and sulfides under high P-T metamorpic conditions would be subject to remobilization, including injection as vein-like bodies into adjacent rock. Such injected sulfide was observed in the mine (e.g., Wheeler, 1883; Weed, 1911) and was considered evidence of ore localization in open space and for the structurally controlled, epigenetic introduction of sulfides.

Using surface structural observations and lithologic information from a fence of nine drill holes, we interpret the setting of the Ely deposit as shown in figure 7. The ore occurs principally in a stratigraphic section of pelitic schist

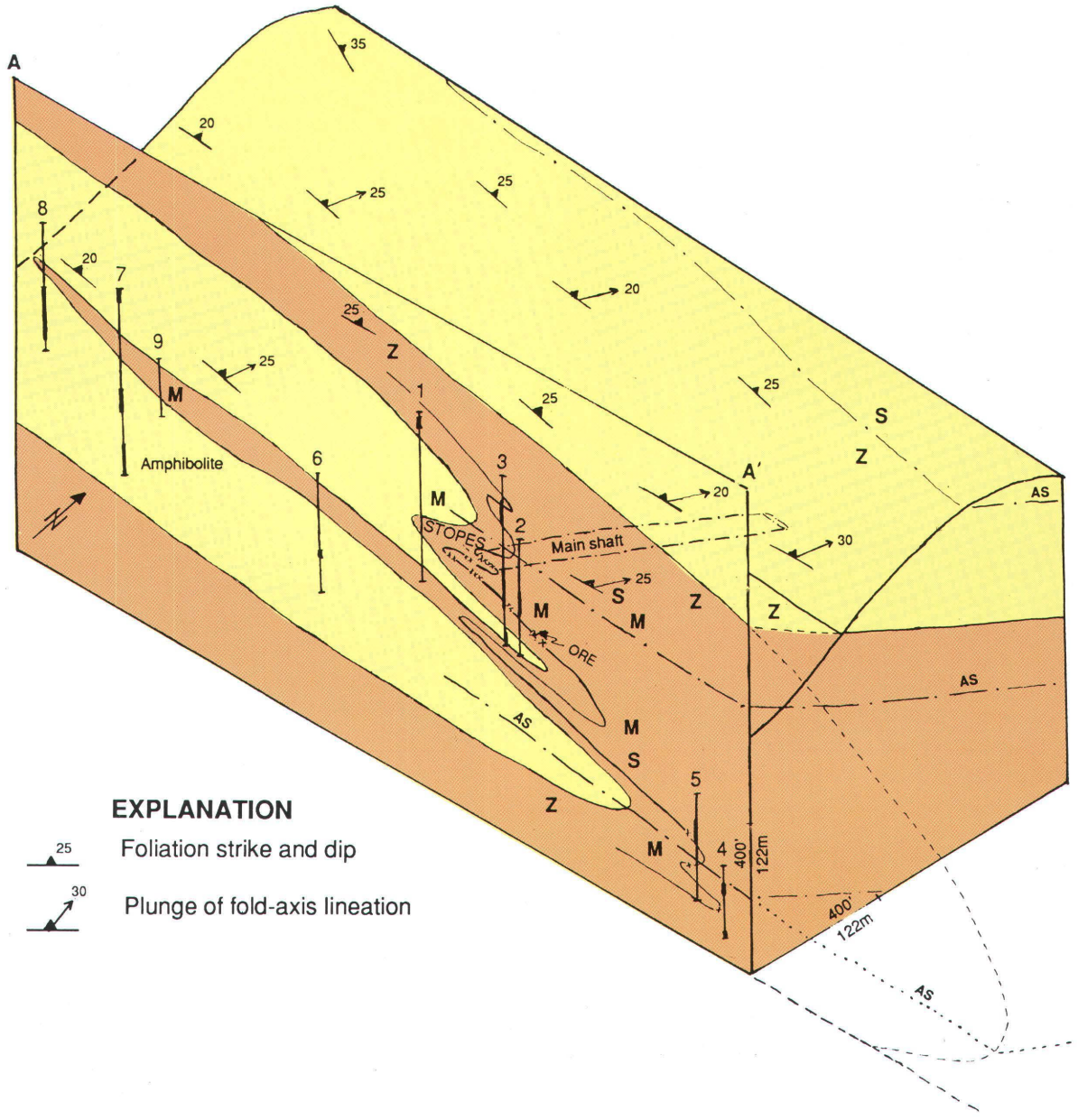

Figure 7. Block diagram showing interpreted position of ore zone on F_2 fold structure, location of main shaft, drill-hole information (drill holes shown by circled numbers), small-scale fold shapes observed in outcrop and drill holes (M, Z, S), and representative surface measurements of foliations and F_2 axial lineations. The drill holes lie off the section drawn on the front face of the block by as much as 200 m (in front and behind) and are presented in assumed simple updip and downdip projections to the face. Brown, dominantly pelitic schist with subordinate psammitic schist and amphibolite. Yellow, dominantly psammitic schist with subordinate pelitic schist and amphibolite. Thick black portions of drill holes, significant amphibolite layers. xx, sulfide in stopes and adits; x, significant sulfide occurrence in drill hole. AS, axial surface of large F_2 fold. Front face is section A–A′ on figure 5.

and amphibolite between sections of mixed psammitic schist and amphibolite. Ore lenses are localized in small folds on the flank and crest of a much larger fold (F_2). The drill-hole information indicates little likelihood for ore layers to occur on the upper flank of the large fold. If sulfide layers originally extended laterally beyond the small area explored by mining, however, our interpretation suggests that the most favorable structural locus for thickening and repetition of sulfide layers would be in the crestal zone of the large fold. Projection of drill holes 4 and 5 downdip

puts sulfide occurrences exactly in that crestal zone on the cross section illustrated. Assuming continuity of the original sea-floor distribution of sulfides, lenses of ore may occur far down the plunge of the main F_2 fold.

A more general conclusion regarding mineral deposits in the district is that massive sulfide bodies might reasonably be expected anywhere within amphibolite-rich stratigraphic intervals in the Gile Mountain Formation. Within those intervals, the axial zones of the reclined folds would be sites where sulfide layers, if present, could have been thickened and perhaps enhanced by the polyphase deformation recognized in the area (Offield and Slack, 1990). These stratigraphic and structural considerations, together with recent geochemical data (Watts, 1990; Slack and others, 1990), provide guidelines in the exploration for new massive sulfide deposits in the district.

REFERENCES CITED

Aleinikoff J.N., and Karabinos, Paul, 1990, Zircon U-Pb data for the Moretown and Barnard Volcanic Members of the Missisquoi Formation and a dike cutting the Standing Pond Volcanics, Southeastern Vermont, *in* Slack, J.F., ed., Summary Results of the Glens Falls CUSMAP Project, New York, Vermont, and New Hampshire: U.S. Geological Survey Bulletin 1887, p. D1–D10.

Annis, M.P., Slack, J.F., and Rolph, A.L., 1983, Stratabound massive sulphide deposits of the Elizabeth mine, Orange County, Vermont, *in* Sangster, D.F., ed., Field Trip Guidebook to Stratabound Sulphide Deposits, Bathurst Area, N.B., Canada and West-Central New England, U.S.A.: Geological Survey of Canada Miscellaneous Report 36, p. 41–51.

Buerger, N.W., 1935, The copper ores of Orange County, Vermont: Economic Geology, v. 30, p. 434–443.

Chang, P.H., Ern, E.H., Jr., and Thompson, J.B., Jr., 1965, Bedrock geology of the Woodstock quadrangle, Vermont: Vermont Geological Survey Bulletin 29, 65 p.

Doll, C.G., 1944, A preliminary report on the geology of the Strafford quadrangle, Vermont: Vermont Geological Survey, Report of the State Geologist, 24th, 1943–1944, p. 14–28.

Fisher, G.W., and Karabinos, Paul, 1980, Stratigraphic sequence of the Gile Mountain and Waits River Formations near Royalton, Vermont: Geological Society of America Bulletin, v. 91, p. 282–286.

Gilligan, L.B., and Marshall, Brian, 1987, Textural evidence for remobilization in metamorphic environments: Ore Geology Reviews, v. 2, p. 205–229.

Goodfellow, W.D., and Blaise, Bertrand, 1988, Sulfide formation and hydrothermal alteration of hemipelagic sediment in Middle Valley, northern Juan de Fuca Ridge: Canadian Mineralogist, v. 26, p. 675–696.

Hatch, N.L., Jr., 1988, Some revisions to the stratigraphy and structure of the Connecticut Valley trough, eastern Vermont: American Journal of Science, v. 288, p. 1041–1059.

Hepburn, J.C., 1984, Geochemical evidence for the origin of the Standing Pond Volcanics, eastern Vermont [abs.]: Geological Society of America, Abstracts with Programs, v. 16, no. 1, p. 23.

Hermance, H.P., Neumann, G.L., and Mosier, McHenry, 1949, Investigation of Ely mine copper deposit, Orange County, Vt.: U.S. Bureau of Mines Report of Investigations 4395, 11 p.

Hitchcock, C.H., 1912, The Strafford quadrangle: Vermont Geological Survey, Report of the State Geologist, 8th, 1911–1912, p. 100–45.

Howard, P.F., 1969, The geology of the Elizabeth mine, Vermont: Vermont Geological Survey, Economic Geology No. 5, 73 p.

Hueber, F.M., Bothner, W.A., Hatch, N.L., Jr., Finney, S.C., and Aleinikoff, J.N., 1990, Devonian plants from southern Quebec and northern New Hampshire and the age of the Connecticut Valley trough: American Journal of Science, v. 290, p. 360–395.

Koski, R.A., Benninger, L.M., Zierenberg, R.A., and Jonasson, I.R., in press, Composition and growth history of hydrothermal deposits in Escanaba Trough, southern Gorda Ridge, *in* Morton, J.L., Zierenberg, R.A., and Reiss, C.A., eds., Geologic, Hydrothermal, and Biologic Studies at Escanaba Trough, Gorda Ridge, Offshore Northern California: U.S. Geological Survey Bulletin 2022.

Koski, R.A., Lonsdale, P.F., Shanks, W.C., Berndt, M.E., and Howe, S.S., 1985, Mineralogy and geochemistry of a sediment-hosted hydrothermal sulfide deposit from the southern trough of Guaymas Basin, Gulf of California: Journal of Geophysical Research, v.90, p. 6695–6707.

Lyons, J.B., 1955, Geology of the Hanover quadrangle, New Hampshire–Vermont: Geological Society of America Bulletin, v. 66, p. 105–145.

Menard, Thomas, 1991, Metamorphism of calcitic pelitic schists, Strafford dome, Vermont: Rensselaer Polytechnic Institute, unpub. Ph.D. thesis, 295 p.

Menard, Thomas, and Spear, F.S., 1991, Metamorphic history of the Strafford dome, Vermont: An update [abs.]: Geological Society of America, Abstracts with Programs, v. 23, no.1, p. 103.

Offield, T.W., and Slack, J.F., 1990, Polyphase folding and thrust faulting in the Vermont copper belt [abs.]: Geological Society of America, Abstracts with Programs, v. 22, no. 2, p. 61.

Peter, J.M., and Scott, S.D., 1988, Mineralogy, composition, and fluid-inclusion microthermometry of seafloor hydrothermal deposits in the southern trough of Guaymas Basin, Gulf of California: Canadian Mineralogist, v. 26, p. 567–587.

Slack, J.F., in press, Descriptive and grade-tonnage models for Besshi-type massive sulphide deposits, *in* Kirkham, R.V., Sinclair, W.D., Thorpe, R.I., and Duke, J.M., eds., Ore Deposit Models: Geological Association of Canada Special Publication.

Slack, J.F., Atelsek, P.J., and Whitlow, J.W., 1990, Geochemistry of stream sediments and heavy-mineral concentrates from the Orange County copper district, east-central Vermont, *in* Slack, J.F., ed., Summary Results of the Glens Falls CUSMAP Project, New York, Vermont, and New Hampshire: U.S. Geological Survey Bulletin 1887, p. Q1–Q21.

Smith, P.S., 1905, Orange County copper district, Vermont: Harvard University, unpub. Ph.D. thesis, 177 p.

Smyth, H.L., and Smith, P.S., 1904, The copper deposits of Orange County, Vermont: Engineering and Mining Journal, v. 77, p. 667–678.

Spry, P.G., 1990, Geochemistry and origin of coticules (spessartine-quartz rocks) associated with metamorphosed massive sulfide deposits, *in* Spry, P.G., and Bryndzia, L.T., eds., Regional Metamorphism of Ore Deposits and Genetic Implications: Ultrecht, The Netherlands, VSP Publishers, p. 49–75.

Stevens, H.J., 1911, The copper handbook [1910–1911]: Houghton, Michigan, H.J. Stevens, Publisher, v. 10, 1902 p.

Vokes, F.M., 1971, Some aspects of the regional metamorphic mobilization of pre-existing sulphide deposits: Mineralium Deposita, v. 6, p. 122–129.

Watts, K.C., Jr., 1990, Regional exploration geochemistry of the Glens Falls 1°×2° quadrangle, New York, Vermont, and New Hampshire, *in* Slack, J.F., ed., Summary Results of the Glens Falls CUSMAP Project, New York, Vermont, and New Hampshire: U.S. Geological Survey Bulletin 1887, p. F1–F70.

Weed, W.H., 1911, Copper deposits of the Appalachian States: U.S. Geological Survey Bulletin 455, 166 p.

Wheeler, H.A., 1883, The copper deposits of Vermont: School of Mines Quarterly, Columbia College, New York, v. 4, p. 219–224.

White, W.S., and Eric, J.H., 1944, Preliminary report, Geology of the Orange County copper district, Vermont: U.S. Geological Survey Open-File Report, 37p.

White, W.S., and Jahns, R.H., 1950, Structure of central and east-central Vermont: Journal of Geology, v. 58, p. 179–220.

Woodland, B.G., 1977, Structural analysis of the Silurian-Devonian rocks of the Royalton area, Vermont: Geological Society of America Bulletin, v. 88, p. 1111–1123.

CHAPTER G

GOLD, SILVER, AND BASE METAL EPITHERMAL MINERAL DEPOSITS AROUND THE GULF OF CALIFORNIA, MEXICO: RELATIONSHIP BETWEEN MINERALIZATION AND MAJOR STRUCTURES

By JOHN-MARK G. STAUDE[1]

ABSTRACT

A compilation of epithermal precious-metal occurrences and major tectonic structures around the Gulf of California indicates that there is a regional correspondence and control of mineral deposits. This analysis is a regional evaluation rather than a mine- or district-specific study, and it permits better assessment of the overall correlation between locations and types of structures and their relative mineral endowment.

Compilation of 133 lode-gold, base-metal (Ag + Pb + Zn), and copper occurrences from western and northwestern Mexico shows that most of the deposits are structurally controlled. The structural controls vary in style and size as do the types of deposits hosted throughout the Gulf extensional province. Systematic trends in mineralization types, fault directions, and fault offsets indicate that the correspondence is not uniform throughout western Mexico and that different regions have varying types of deposits and degrees of correspondence to ma jor tectonic features.

The percentage of deposits occurring along major faults is highest in Sonora and North Baja and lowest in western mainland Mexico. The map compilation indicates a control of deposit type by different basement regions and by proximity to rift centers. Deposits close to the rift axis (i.e., northeastern Baja) are more gold rich and are of the hot-spring type, whereas those around the periphery of the Gulf are fissure veins and quartz-adularia-sericite veins. The compilation also shows that deposits are more gold dominated in the northwest part of the Gulf of California and more base metal and silver rich in the southeast portion of the Gulf of California region. These compositional differences may indicate differences in hydrothermal fluid chemistries, different source-rock compositions, or different degrees of magmatic gas input into the epithermal system. The deposits are diachronous around the Gulf: the hot-spring-type deposits in Baja formed more recently than the Late Cretaceous–early Tertiary (Laramide) and middle Tertiary (Oligocene-Miocene) epithermal vein systems.

Regional mineral exploration in transform-fault-tectonic settings should not only focus on following the main tectonic suture but also upon sampling, mapping, and determining the associated fault splays off the main suture. Few known deposits in the area studied are located directly on the major transform (i.e., San Andreas); instead, most structurally associated metal occurrences are along splays associated with smaller extensional and strike-slip faults.

INTRODUCTION

Structural control of ore deposits is by no means a new topic. Agricola (1556) recognized the importance of fractures for permitting metal-bearing fluids to infiltrate the host rock and to deposit metals in open spaces. Early in this century Spurr (1916), Hulin (1925), and Lindgren (1933) suggested that structural features were keys to ore deposition. Recently, the merging of structural interpretation with

[1]U.S. Geological Survey, Center for InterAmerican Mineral Resources Investigations, Tucson, AZ 85705.

mineral deposits has become significant: many new ore deposit discoveries have been made from structural analyses (e.g., Mesquite mine, McLaughlin mine, etc.). Most recent studies concentrate on theoretical models (Sibson, 1981, 1986) or individual occurrences, including such work as the investigation of the Henderson mine by Guha and others (1983) and the Sigma mine study by Robert and Brown (1986). Regional studies of Proterozoic ductile shear in the Canadian Abitibi Belt (Poulsen and Robert, 1989; Robert, 1990) and Archean ductile domains such as the Norseman-Wiluna Belt of Western Australia (Barley and Groves, 1988; Groves and Barley, 1988) have contributed to an overall understanding of the regional association of mineralization in ductile environments. However, comparatively little analysis of regional data with precise mine and structure locations has been done for brittle environments; the relation between plate margins and structurally controlled epithermal ore deposits has, likewise, received preliminary analysis. In the Gulf of California region, tectonic exposures are mostly shallow and expose cataclastic shear zones, making this area ideal for a regional study of structures and mineralization.

The Gulf of California region is a distinguishing feature of the North American Cordilleran orogenic system because of its unique tectonic history and complex geologic relations. The Gulf extends over 1,700 km south from the U.S.-Mexico border to Jalisco, Mexico (JA on fig. 1). A simplified compilation of the geologic structures and mineral occurrences is presented on plate 1 (plate 1 is in the pocket on cover 3 of this volume). The Gulf is long and narrow, forming an actively extending graben between the 5,000-ft-high peaks of the Sierra Pedro Martir (Baja California batholith) and the Basin and Range province of western Sonora (Stock and Hodges, 1989). Proposed models that attempt to explain the tectonic relations and implications of gulf formation and rifting are varied in their interpretations of age, mechanisms, and rate of opening.

In 1980, Homestake Mining Company discovered the McLaughlin orebody in Calistoga, California, and in 1984, Gold Fields Mining Company found a large orebody that they developed into the Mesquite mine near Yuma, Arizona. Both of these large gold deposits occur along faults associated with the San Andreas fault system. Other precious metal discoveries at the Picacho and Temco mines, near Mesquite, have led to increased interest in mineral deposits associated with transtensional faulting and rifting, especially around the mouth of the Gulf of California (plate 1). Recently, structural geologists and economic geologists have joined forces to work out kinematic-control and fluid-flow models for structurally associated ore deposits; these models have direct application to regional structural analyses (Sibson, 1987).

The abundance of gold deposits in southeastern California that parallel the San Andreas fault suggests the likelihood of undiscovered deposits in northwest Mexico. The San Andreas structural system continues southward from California into North Baja, California and Sonora, eventually becoming obscured by the Colorado River delta and the sedimentary basins of the Gulf. The main transform goes into the Gulf north of Puerto Penasco (PP on plate 1), but tensional graben faults and transtensional shear zones can be traced on land for over 1,200 km down both sides of the Gulf. Splays like the Imperial Valley fault and Laguna Salada fault host active hydrothermal centers like those at Cerro Prieto (CP on plate 1).

The continuation of the transform fault system in the submarine environment has been studied by means of bathymetric mapping, seismic reflection, and direct submarine observations (e.g., Von Damm and others, 1985; Lonsdale, 1989; and many others). Few geologic maps compare this detailed submarine information with surface mapping on both sides of the Gulf. The relations between submarine and subaerial tectonics need to be integrated to look at the structures of the entire Gulf extensional region. Analysis of tectonic features in the Gulf gives insight into the principle stresses, styles of faulting, and relative timing of offset. The results of this analysis can then be used to assess and predict ore deposit occurrences around the Gulf region. The map (plate 1) differs from previously published maps of the Gulf of California because it combines mineral deposit locations with detailed structures. By compiling structures and ore deposits on the same map, it becomes possible to determine which deposits occur along faults—this compilation is useful for regional geologic studies.

This paper (1) investigates the dip orientation and types of faults most commonly hosting mineralization around the Gulf of California, (2) quantifies the percentage of the known occurrences that are associated with different types of faults, (3) discusses how plate tectonics and mineral-deposit studies together can be used to determine the geologic history of the Gulf, and (4) presents data showing that submarine rift-graben faults and strike-slip splays from transform faults can be matched with documented structures on land.

PRINCIPAL DATA SOURCES AND STUDY-AREA BOUNDARIES

Compilation of faults from bathymetric and seismic reflection studies across the Gulf of California provides excellent data to compile the portion of the map covering the floor of the Gulf. In general, the Gulf is shallow, and tectonic features are rapidly blanketed by sediment, making it difficult to map the exact location of faults (Larson, 1972). Abundant submarine pull-apart basins like the Guaymas and Huatabampo Basins (GU and HU on plate 1) define zones of extension along the transform margin. Submarine dives, discussed by Lonsdale and others

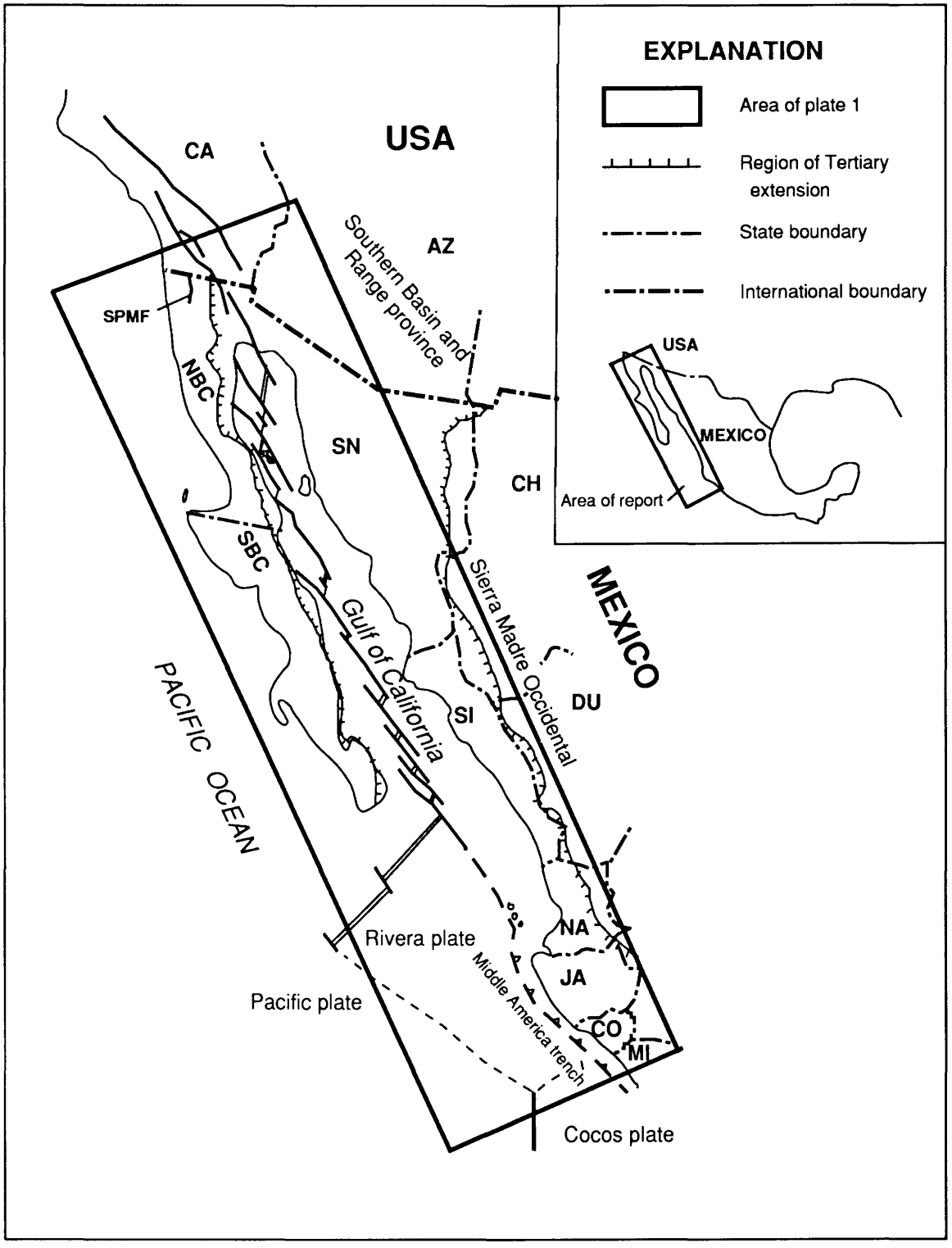

Figure 1. Gulf of California extended region and area covered in plate 1. The solid line outlines the limits of the structural and mineral deposit compilation. Abbreviations are Arizona (AZ), California (CA), Chihuahua (CH), Colima (CO), Durango (DU), Jalisco (JA), Nayarit (NA), Michoacan (MI), North Baja California (NBC), Sierra Pedro Martir fault (SPMF), Sonora (SN), and South Baja California (SBC).

(1980), aid in defining submarine topography and hydrothermal-fluid characteristics. Deep sea drilling results and maps published in deep sea drilling reports add significant tectonic-structural data useful in compiling maps (Curray and Moore, 1982). Heat flow studies by Lawyer and Williams (1979) provide data that can be used to verify asymmetric extension and general structural regimes.

Published tectonic maps from eastern Baja California by Rangin (1986), Hamilton (1971), Stock and Hodges (1989), Lonsdale (1989), de Cserna (1989), Dokka and Merriam (1982), Gastil and others (1975), Lopez Ramos (1982), and Sociedad Programación and Presupuesto (a Mexican governmental agency) were combined with maps showing mineral deposits from Wisser (1954), de la Fuente Moises (1985), and Leonard (1989) to generate plate 1. Additional field mapping and visits to mineral deposit sites by the author where conducted from 1987 through 1992.

The map compilation for the western Mexican mainland combines data from Gastil and Krummenacher (1977), Henry and Fredrikson (1987), Wahl (1973), and Swanson and McDowell (1984) in addition to information from the Baja California maps listed above. Mineral resource maps by Leonard (1989), Gonzalez Reyna (1956), Wisser (1966), Salas (1975), Consejo de Recursos Minerales (1985, 1987), Consejo de Recursos Minerales and State of Durango (1980), Universidad Autonima de Mexico (1974–77), Anaconda Mining Company (unpub. data), as well as files from the USGS Center for Mineral Resource Investigations and mines shown on the geotectonic maps listed above were used to construct plate 1.

The boundaries of the Gulf extensional province are difficult to define (see Stock and Hodges, 1989, for discussion) but are important for identifying the scope of this study. The western limit is defined by the eastern range-front fault of the Peninsular batholith (SPMF, fig. 1). West of the major range-front normal fault, there is considerably less faulting, and the batholith acts as a coherent block. The range-front fault system continues south along the east coast of the Baja Peninsula for nearly 800 km. In central Baja, the boundary becomes more difficult to define because, in many places, normal and strike-slip faults are covered by young volcanics, and where exposed, fault scarps often become diffuse (e.g., Bahia de Los Angeles (BL, plate 1), Santa Rosalia (SR, plate 1)).

In southern Baja, the escarpment follows the coast, and, in places, the sea cliffs themselves mark the escarpment. Faulting at the southern tip of Baja likely occurred before the early Miocene strike-slip motion that is associated with oblique subduction west of the Baja Peninsula (Spencer and Normack, 1979) and was not part of the late Miocene opening of the Gulf. Faults extending from La Paz to Cabo San Lucas are older than the rift faults but may have been reactivated and further mineralized during the rift-extensional events.

The eastern limit of extensional structures is also difficult to define. On the east, the transition grades into the Basin and Range province, and there is no single escarpment or main tectonic feature separating the Gulf from the entire Basin and Range. Geologically, the Gulf with its transtensional faulting is a continuation of basin-and-range extension. The Sierra Madre Occidental is a comparatively stable block and, in the southern part of the study area (Sinaloa and points further south), it is the eastern limit of the Gulf extensional province. In the northern part of the study area, the boundary is limited to within 200 km east of the eastern edge of the Gulf of California. This definition is necessary to confine the study area to the Gulf region and not the entire Basin and Range province.

DATA ANALYSIS

By comparing the tectonic features, hot springs, and mineralization around the Gulf on the map compilation, certain spatial and temporal correlations become apparent. The mineral occurrences can be quantified by counting the number of mineral occurrences that occur along major faults versus those not on regionally mapped faults. For the occurrences on faults, the direction and style (either normal or strike-slip) can be tabulated. For all occurrences, the principal commodities (gold, base metals, or copper) are distinguished for later comparison among deposit types.

The circum-Gulf region can be divided into 5 regions based on geographic position and State in order to facilitate comparison of structural and other data. North Baja California, South Baja California, and Sonora are each treated independently. Sinaloa and Durango comprise the fourth region, and the southern mainland States of Nayarit, Jalisco, and Colima are grouped as the fifth region. A tabulation of the number of mineral occurrences associated with strike-slip faults, normal faults, and those not associated with any fault using the five geographic groups is presented in table 1. Histograms based on this data table showing comparative features of structural control and mineral deposits around the Gulf are presented in figures that follow.

Comparing the various types of regional information highlights some broad correlations. Firstly, the percentage of mineral occurrences located on mapped faults differs throughout the Gulf of California region, as shown on figure 2. In North Baja and Sonora, the number of mineral occurrences on faults greatly exceeds those not coincident with structural features. However, in the southern part of the study area (South Baja, Sonora, and Sinaloa-Durango), the correspondence is only 50 percent, and in the southern mainland region, only about 30 percent of the mineral occurrences are on faults. The difference in mineralization and structural control around the Gulf indicates that there

Table 1. Number of mineral deposits associated with each type of structure in the Gulf of California extended region.

[The southern mainland Mexico group (S. mainland Mex.) includes the States of Nayarit, Jalisco, and Colima]

	Strike-slip fault	Normal fault	Not on fault	Total number
Au–Ag–base-metal deposits				
N. Baja	2	6	1	9
S. Baja	1	3	2	6
Sonora	7	2	4	13
Sinaloa-Durango	7	4	8	19
S. mainland Mex.	6	0	19	25
Gold-dominated deposits				
N. Baja	9	8	4	21
S. Baja	2	1	0	3
Sonora	6	2	3	11
Sinaloa-Durango	2	0	0	2
S. mainland Mex.	0	0	0	0
Copper deposits				
N. Baja	2	3	1	6
S. Baja	0	1	5	6
Sonora	3	0	7	10
Sinaloa-Durango	0	0	1	1
S. mainland Mex.	0	1	0	1
Totals:	47	31	55	133

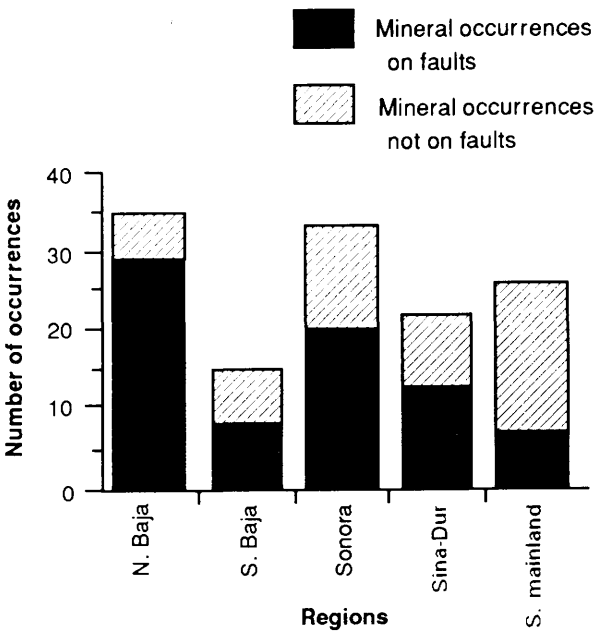

Figure 2. Comparison of mineral occurrences on faults to those not on faults in each of five regions: North Baja (N. Baja); South Baja (S. Baja); Sonora; Sinaloa and Durango (Sina-Dur); and the southern mainland group of Nayarit, Jalisco, and Colima, (S. mainland).

is a variation in the importance of structural control and a corresponding difference in deposit type. In North Baja and Sonora, the higher correspondence suggests that mineralization has a first-order correspondence to faulting such that fluids may be channeled through structures, whereas south of North Baja and Sonora, the occurrences do not correspond with major fault structures and, instead, are found throughout the area. Part of this disparity could be due to the varying quality of the data but, because maps were used of comparable scales and from similar sources, the observations are clearly not simply an artifact of the source mapping.

Combining all 133 occurrences and looking at the overall picture, 58 percent of the mineral occurrences are associated with some structure; 35 percent occur on normal faults; and 23 percent occur on strike-slip faults. The "Not on fault" column in table 1 indicates the number of mineral occurrences not coincident with a mapped fault. These percentages are important because they show that, over the entire Gulf region, a large percentage of the precious- and base-metal deposits are associated with major mapped structures and that the association between structures and deposits is particularly high in North Baja and Sonora.

A comparison of different deposits by region shows that base-metal occurrences are highly concentrated on the southern mainland and that gold deposits are concentrated in the northern Gulf region, especially in North Baja (fig. 3). The relation between mineral-deposit composition and region can be compared with the earlier observation that structural association with mineral occurrence is highest in North Baja California and Sonora. From the compilation, it appears that the gold deposits lie along major strike-slip structures more often than do the Ag-Pb-Zn veins.

The direction of dip of the faults that host mineral occurrences is independent of the side of the Gulf. In the simple extensional model often proposed for rift areas, the structures are drawn dipping toward the center of the rift. But in the Gulf of California, mineral occurrences are present in approximately equal numbers on east- and west-dipping structures on both sides of the Gulf. Figure 4 is a plot of number of mineral occurrences on east-dipping normal faults plotted next to the number of occurrences on west-dipping faults. The number of occurrences on east-dipping normal faults and west-dipping normal faults is nearly identical for each region. An interesting idea that may be drawn from this is that mineralizing fluids may not be derived from near the center of the rift and flow outward along faults, and instead, they may be regionally dispersed and localized near individual hydrothermal centers.

Most of the hot springs in the Gulf extensional province occur along the western margin of the Gulf and within the Gulf, along the rift transform and associated extensional grabens. Hot springs on the eastern coast of

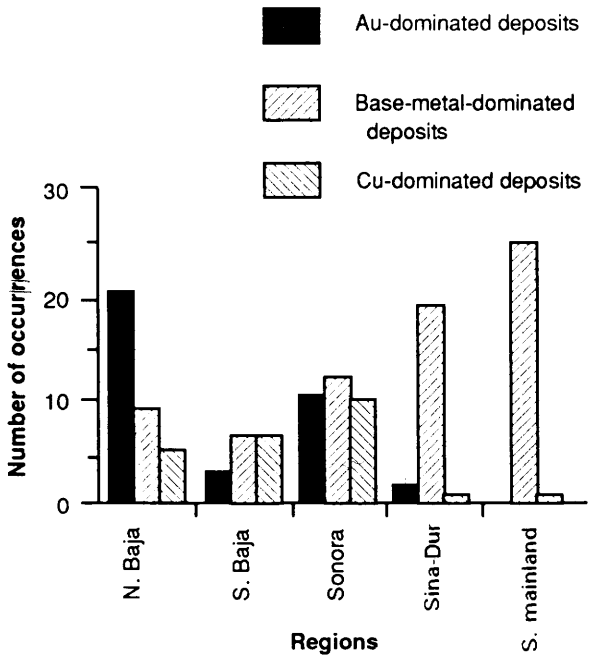

Figure 3. Comparison of mineralization types (showing the major metallic element) in each of five regions.

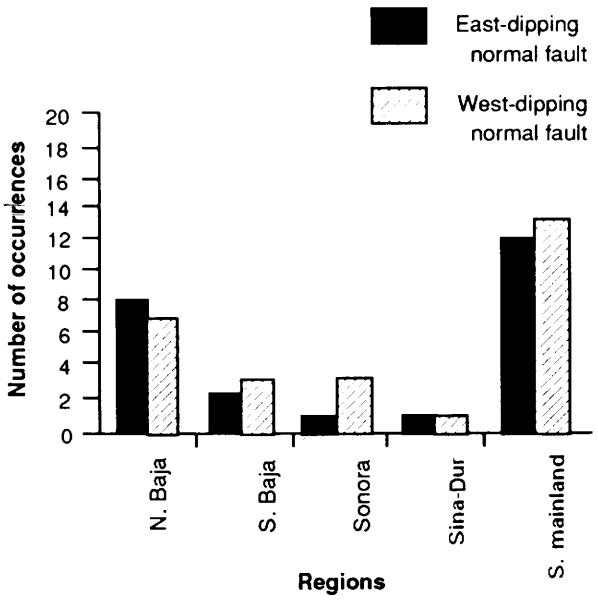

Figure 4. Diagram of dip directions of mineralized normal faults around the Gulf of California.

Baja occur along faults that can be traced back to active transforms in the Gulf. Cerro Prieto (CP) and other hot-spring areas have mineralized areas at the surface and extensive alteration along local structures (Elders and others, 1981). A simplified hot-spring location map is presented to show the location of geothermal fields (fig. 5).

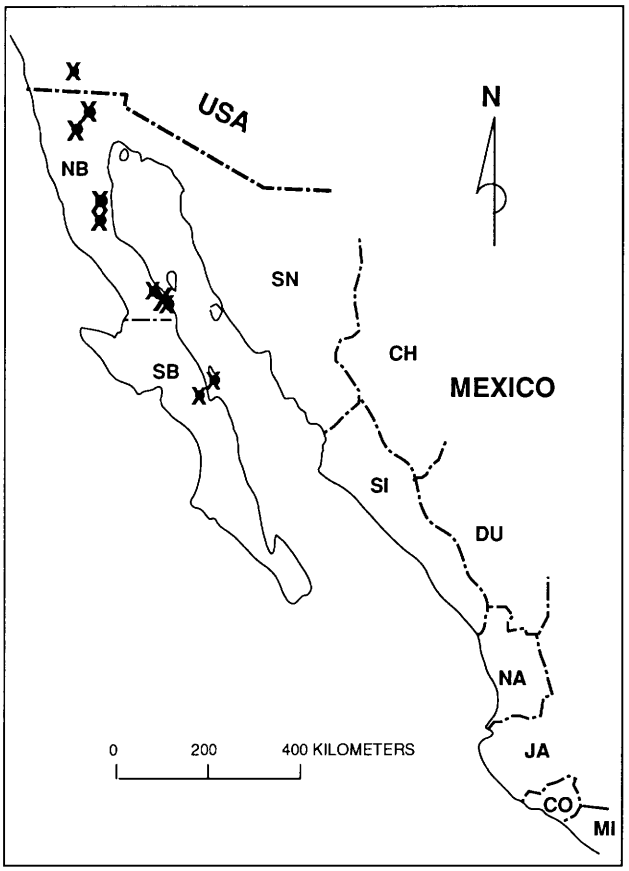

Figure 5. Generalized locations of active and recently active hot springs around the Gulf of California that are shown on plate 1. Hot springs are marked by star; abbreviations are: North Baja (NB), South Baja (SB), Sonora (SN), Chihuahua (CH), Sinaloa (SI), Durango (DU), Nayarit (NA), Jalisco (JA), Colima (CO), Michoacan (MI).

Eight of the 11 hot-spring areas that occur on land around the Gulf are along faults. The other three possibly connect with structures at depth, but no fault is identified on the surface. The springs are important because they could be a modern analog to the formation of epithermal mineral deposits and they are usually associated with a major fault.

TECTONIC ANALYSIS

The geology of the Gulf of California has been studied in detail, and the references cited in the Principal Data Sources and Study-Area Boundaries section of this report provide many of the basic observations used in outlining the geologic history of the Gulf. However, from the map and data presented in this compilation, several newly observed features become apparent. To put these in the tectonic context, we will first briefly summarize the salient tectonic events.

Baja California was originally part of mainland Mexico, with subduction extending along the eastern Pacific Ocean margin for over 5,000 km from northwestern Alaska to Central America. The continental crust surrounding the Gulf lies near the edge of the North American craton and is inherently weak due to its long and complex history of continental-margin sedimentation, tectonic accretion, and magmatism. These inherited weaknesses became future zones of failure and eventually gave rise to the Gulf and the development of a transtensional continental margin. During the Miocene, much of the future site of the Gulf was occupied by andesitic arc volcanoes overlying lithosphere that was subducted along the western margin of Baja California. To the east, the southern Cordillera was extending and low-angle detachments extended the Gulf region, forming a graben known as the protogulf. Differing accounts of the events leading to the opening of the protogulf are proposed by Karig and Jensky (1972), and Moore (1973). More recently, Gastil and others (1975, 1981), Spencer and Normack (1979), and Atwater (1989) brought new insights into the timing and order of events that led to the opening of the protogulf, and these events continue to open the Gulf today. Originally, the protogulf concept was proposed to explain the anomalously old oceanic crust in the mouth of the Gulf adjacent to the Mexican margin (Moore and Buffington, 1968). More recently, this concept has been expanded to include late Miocene extensional faulting, magmatism, and marine sedimentation in north and central Gulf areas (McLean and others, 1987).

Subduction along the western Baja California continental margin ceased 12–10 Ma, and east-west extension marked by basin-and-range faulting and alkali-basalt volcanism increased. The structurally weak zone, which was already developing inland of the continental margin, subsided even more, and the principal plate boundary shifted 250 km eastward into the extended continental crust at 6 Ma. Over the past 6 m.y., the Gulf has opened approximately 300 km. Figure 6 is a reconstruction of the position of Baja relative to North America at 6 Ma. The reconstruction closes some of the extension and is tied by similar conglomerate and volcanic sequences across the now open Gulf. The Pacific and North American plates were moving 10°–20° obliquely to the early San Andreas transform—this caused opening of small intra-Gulf pull-apart basins linked by en echelon faults (Atwater, 1989). These faults not only opened basins but also propagated on land, offsetting upper Miocene sedimentary and volcanic rocks. According to Atwater (1989), by 6 to 4 m.y. ago, the margin strengthened, probably cooled and became more rigid, and a weaker inland zone began to accommodate shearing between the two plates. Elevated heat flow and hydrothermal waters were liberated due to newly formed crustal-scale transform shears. It is these transform faults, associated pull-apart graben faults, and reactivation of normal

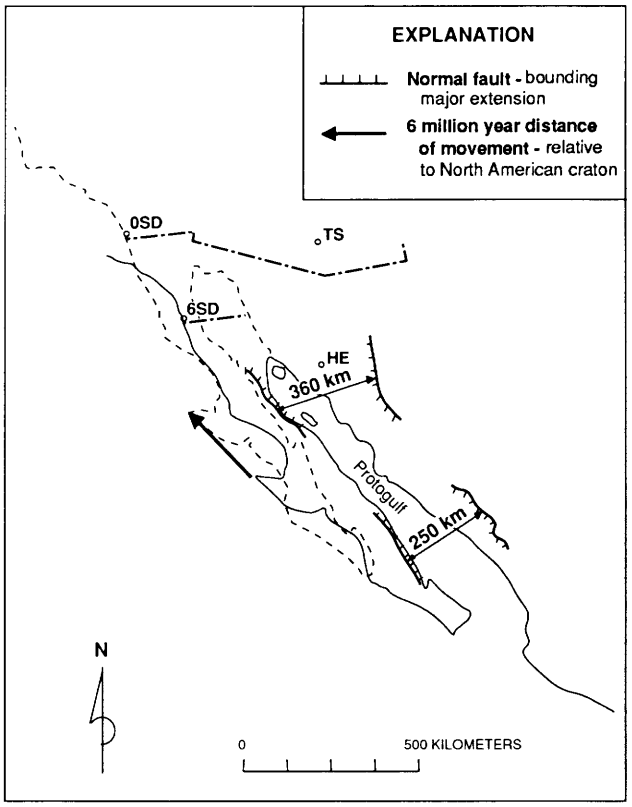

Figure 6. Reconstruction of proto–Gulf of California, showing width of gulf at 6 Ma and direction and distance moved in the last 6 million years relative to the North American plate. Diagram shows extent of study area within the extensional regime of northwest Mexico. The solid line outlines the geographic shape of the Gulf at 6 Ma, and the dotted line outlines the present-day geographic position. 6SD, location of San Diego 6 million years ago; 0SD, present location of San Diego. Tucson (TS) and Hermosillo (HE) are reference cities.

faults that host many of the high-angle, fault-related epithermal deposits in Sonora and Baja California.

Represented on the map of structures (plate 1) are varying stages of superimposed extension and strike-slip faults. In the Laguna Salada Fault zone (LSF on plate 1), strike-slip faults cut the normal faults in some areas, whereas in other areas normal faults displace strike-slip shear zones. The compilation also shows that splays off the main submarine transform can be traced onto land along the eastern edge of the Baja Peninsula. Finally, further study of the volcanic sequences and age determinations on the volcanosedimentary stratigraphy can be used with this compilation of structures to constrain the complex paleo-stress history.

DISCUSSION AND CONCLUSIONS

This paper presents a structural and mineral-occurrence compilation that is useful in connecting submarine

and subaerial geologic mapping. From this structural comparison, it is apparent that fault splays and en echelon transform faults extend significant distances away from the main transform plate boundary (e.g., Puertocitos, Isla La Guardia, etc.) and act as conduit structures for mineralizing fluids. The Gulf region plate boundary is a zone of rifting and transtensional shear through which heat is convected and hydrothermal fluids evolve. These fluids may transport metals, carrying them into and along fault structures in over 50 percent of the known epithermal mineral occurrences. Present-day geothermal activity in the Gulf seems to be continuing this production and convection of enriched fluids in the Gulf province. Compiled mineral occurrences show that structural control is a significant factor for epithermal mineral deposits, particularly in the gold-dominated deposits and especially in Sonora and northern Baja California.

Oxide and sulfide copper deposits, such as those at Boleo and southwest of Caborca, may be related at depth to large structures, but these structures are not mapped at the surface. Perhaps additional geophysics and satellite-image interpretation will be useful in not only locating alteration areas but also major faults. Copper porphyries are older than the Gulf extension and are not included in this project. Detailed maps for El Arco and porphyries in Sonora and Sinaloa show that major structures play a critical role in magma emplacement and hydrothermal fluid flow.

The greater abundances of hot springs in the western Gulf rather than in the eastern Gulf indicates that an asymmetry exists across the Gulf. This suggests the possibility of hotter crust and more active tectonics to the west. Heat-flow studies by Lawyer and Williams (1979) support this idea by showing increased heat flow in the western Gulf. Another observation of apparent asymmetry is that faulting on the western side of the Gulf is confined to a narrow strip, within a few tens of kilometers of the coastline. Faulting in western mainland Mexico, on the other hand, extends from the Gulf extensional region hundreds of kilometers eastward into the southern Basin and Range extensional regime (plate 1). The Gulf of California is also asymmetric in that it has a thinner crust in the west compared to that in the east (Gastil and others, 1975). The thinner crust has higher heat flow, which may drive the geothermal anomalies and which may concentrate the hot-spring-type gold mineralization along the western side of the Gulf, particularly in North Baja, where the transform comes on land (i.e., Imperial fault, Laguna Salada fault, etc.).

Another significant observation based on the map compilation (plate 1) is that faults originating at or near the transform extend long distances away from transforms and can be matched with faults mapped on land, thus tying the submarine-seafloor maps with circum-Gulf land maps. For example, in the Bahía Los Angeles area (BL on plate 1), strike-slip faults come on land and host small gold concentrations in Pliocene sandstones. And at Puertocitos (PU on plate 1), the Puertocitos fault (a splay off the main transform) comes on land and hosts the hot-spring-type Au occurrence. In Puertocitos, active hot springs in Pliocene and Quaternary volcanics are localized along this same splay. This has important implications for mineral exploration in the Gulf of California and other similar regions where submarine faults could be traced on land to discover new deposits.

Other transtensional settings, like the Red Sea, also show regional structural variations, and these appear to be controlled by preexisting structurally weak zones. In the Red Sea, the rift is superimposed upon deformed Precambrian basement. The preexisting weaknesses control the location of later structural failure. The Gulf of California inhabits a structurally weak trough, and the asymmetries can be explained from preexisting structures. Along the Atacama fault in western Chile, brittle transtensional shear structures host many gold deposits, yet, unlike the Gulf of California, the Atacama fault does not have hot-spring-type features (Brown and others, 1991).

Around the Gulf of California, the epithermal metal systems are gold dominated in the north and base metal dominated in the south—this could be caused by vertical zoning, crustal contamination, fluid chemistries, or timing and spatial relations to fluid and heat sources. The chemical variations might be due to preferential metal complexing and carrying of different metals or fluid dynamics and water-rock interactions. The fluid chemistry could likely be constrained by fluid-inclusion studies and detailed petrographic analyses of deposits throughout the region; however, this information is not available. Other options, such as differences in basement composition or magmatic sources could explain the variation. In North Baja and Sonora, mineralization is commonly very shallow, with aprons of hot-spring cinter, open-space cavities, and reed and plant detritus that is silicified in auriferous hematitic silica in the Tertiary volcanic and sediment-hosted occurrences. In the eastern Baja Peninsula, mesothermal quartz veins are common in metamorphosed Paleozoic volcanosedimentary rocks and granitic intrusions. These veins are probably related to mid to late Mesozoic batholithic plutonism and not to the waning stages of Tertiary subduction and the onset of extension in the Gulf of California. The mesothermal veins are not included in this study because they likely predate Gulf extension. The vein deposits on the mainland are of a higher temperature type than those that commonly contain tourmaline, quartz, pyrite and minor sericite. These veins are, in general, breccia zones with a quartz ± carbonate matrix, and their orientation varies as does their age. In this preliminary analysis, the veins and ore breccias are simply compared

in terms of their metal association. Further age dating will help constrain the relative timing of different mineralization events.

In conclusion, the map compilation (plate 1) provides a timely summary of existing tectonic data and correlates this data with a new mineral deposit map for western Mexico. Many of the epithermal mineral deposits are structurally controlled, particularly the gold-rich deposits in North Baja and Sonora. The type of mineralization changes from gold rich in the north to base metal rich in the south. Finally, gold deposits are most often associated with strike-slip faults, whereas the base-metal deposits occur in roughly equal numbers on both normal and strike-slip structures.

ACKNOWLEDGMENTS

This paper has benefited from careful review by Geoff Plumlee, Robert Kamilli, and Floyd Gray. Earlier drafts were reviewed by Peter Coney and Spencer Titley of the University of Arizona. Acknowledgments are extended to Mark Barton, Joaquin Ruiz, and Norm Page, who have contributed to discussions of the data and interpretations. Felipe Rendon, Porfirio Padilla, Dave Johnson, and Ryan Mouser accompanied me in the field and helped obtain hard-to-find Mexican geologic data. Thanks are due to Perry Durning of Fisher-Watt Gold Company and to the many other property owners who allowed access to their properties over the past five years while this study was completed.

REFERENCES CITED

Agricola, G., 1556, De Re Metallica, [English translation by H.C. Hoover and L.H. Hoover, 1950], New York, Dover Publications, 130 p.

Atwater, T., 1989, Plate tectonic history of the northeast Pacific and western North America: Geological Society of America, Decade of North American Geology, Geology of North America, Volume N, p. 21–72.

Barley, M.E., and Groves, D.I., 1988, Geological setting of gold mineralization in the Norseman-Wiluna Belt, Eastern Goldfields Province, Western Australia: Geological Society of Australia, Bicentennial Gold 88, Excursion no. 6, p. 18–46.

Brown, M., Daíz, F., and Grocott, J., 1991, Atacama Fault system; history of displacement and tectonic significance for the Mesozoic-Recent evolution of northern Chile: Santiago, Chile, Congreso Geologico Chileno, Resumenes Ampliados, p. 129–132.

Consejo de Recursos Minerales, 1985, Geologic and mineral district map of Durango: Consejo Recursos Minerales Publication, scale 1:500,000, 2 sheets.

Consejo de Recursos Minerales, 1987, Plano de recursos mineros activos y potenciales del Estado de Nayarit: Consejo Recursos Minerales unpub. map, scale 1:400,000.

Consejo de Recursos Minerales and State of Durango, 1980, Topographic and mineral commodities map of Durango, [1st ed.]: Consejo Recursos Minerales Publication, scale 1:500,000.

Cserna, Z. de, 1989, An outline of the geology of Mexico: Geological Society of America, Decade of North American Geology, Geology of North America, Volume A., p. 233–264.

Curray, J.R., and Moore, D.G., eds., 1982, Reports of the Deep Sea Drilling Project, v. 64, Parts I and II: Washington, U.S. Government Printing Office, 260 p.

Dokka, R.K., and Merriam, R.H., 1982, Late Cenozoic extension of northeastern Baja California, Mexico: Geological Society of America Bulletin, v. 93, p. 371–378.

Elders, W.A., Hoagland, J.R., and Williams, A.E., 1981, Distribution of hydrothermal mineral zones in the Cerro Prieto geothermal field of Baja California, Mexico: Geothermics, v. 10, p. 245–253.

Fuente Moises, M. de la, 1985, Analisis metalogenetico regional de la Peninsula de Baja California: Mexico City, Universidad Autonima de Mexico, unpub. thesis, 156 p.

Gastil, R.G., and Krummenacher, D., 1977, Reconnaissance geology of coastal Sonora between Puerto Lobos and Bahia Kino: Geological Society of America Bulletin, v. 88, p. 189–198.

Gastil, R.G., Morgan, G.J., and Krummenacher, D., 1981, The tectonic history of peninsular California and adjacent Mexico, *in* Ernst, W.G., ed., The Geotectonic Development of California, Rubey Volume 1: Englewood Cliffs, N.J., Prentice-Hall, p. 284–306.

Gastil, R.G., Phillips, R.P., and Allison, E.C., 1975, Reconnaissance geology of the State of Baja California: Geological Society of America Memoir 140, 170 p.

Gonzalez Reyna, J., 1956 [updated in 1966], Los criadores de Au, Ag, Pb, Zn, Cu en la Republica Mexicana: Mexico City, Twentieth International Geologic Congress, scale 1:2,000,000.

Groves, D.I., and Barley, M.E., 1988, Part 2: Gold mineralization in the Norseman-Wiluna Belt, Eastern Goldfields Province, Western Australia: Geological Society of Australia, Bicentennial Gold 88, Excursion no. 6, p. 48–66.

Guha, J., Archambault, G., and Leroy, J., 1983, A correlation between the evolution of mineralizing fluids and the geomechanical development of a shear zone as illustrated by the Henderson 2 mine, Quebec: Economic Geology, v. 78, p. 1605–1618.

Hamilton, W., 1971, Recognition on space photographs of structural elements of Baja California: U.S. Geological Survey Professional Paper 718, 26 p.

Henry, C.D., and Fredrikson, G., 1987, Geology of part of southern Sinaloa, Mexico adjacent to the Gulf of California: Geological Society of America, Map and Chart Series MCH063, [text and map], scale 1:250,000.

Hulin, C.D., 1925, Structural control of ore deposition: Economic Geology, v. 24, p. 15–49.

Karig, D.E., and Jensky, W., 1972, The proto–Gulf of California: Earth and Planetary Science Letters, v. 17, p. 169–174.

Larson, R.L., 1972, Bathymetry, magnetic anomalies, and plate tectonic history of the mouth of the Gulf of California: Geological Society of America Bulletin, v. 83, p. 3345–3360.

Lawyer, L.A., and Williams, D.L., 1979, Heat flow in the central Gulf of California: Journal of Geophysical Research, v. 84, p. 3465–3478.

Leonard, K.R., 1989, Preliminary deposit-type map of northwestern Mexico: U.S. Geological Survey Open-File Report 89–158, 330 p.

Lindgren, W., 1933, Mineral Deposits: New York, McGraw-Hill, 930 p.

Lonsdale, P.F., 1989, Geology and tectonic history of the Gulf of California: Geological Society of America, Decade of North American Geology, The Geology of North America, Volume N, p. 499–521.

Lonsdale, P.F., Bischoff, J.L., Burns, V.M., Kastner, M., and Sweeney, R.E., 1980, A high-temperature hydrothermal deposit on the seabed at a Gulf of California spreading center: Earth and Planetary Science Letters, v. 49, p. 8–20.

Lopez Ramos, E., 1982, Geologia de Mexico, [3rd ed.]: Mexico City, Universidad Autonima de Mexico, 454 p.

McLean, H., Hausback, B.P., and Knapp. J.H., 1987, The geology of west-central Baja California Sur, Mexico: U.S. Geological Survey Bulletin 1579, 16 p.

Moore, D.G., 1973, Plate-edge deformation and crustal growth, Gulf of California structural province: Geological Society of America Bulletin, v. 84, p. 1883–1906.

Moore, D.G., and Buffington, E.C., 1968, Transform faulting and growth of the Gulf of California since the late Pliocene: Science, v. 161, p. 1238–1241.

Poulsen, K.H., and Robert, F., 1989, Shear zones and gold—practical examples from the southern Canadian Shield, *in* Bursnall, J.T., ed., Mineralization and Shear Zones: Geological Association of Canada, Short Course Notes 6, p. 239–266.

Rangin, C., 1986, Contribution a L'etude geologique du systeme Cordillerain Mesozoique du nord-ouest du Mexique; Une coupe de la Basse Californie centrale a la Sierra Madre occidentale en Sonora: Paris, Memoires de la Societe Geologique de France, Memoire no. 148, 133 p.

Robert, F., 1990, Structural setting and control of gold-quartz veins of the Val D'Or area, southeastern Abitibi Subprovince, *in* Ho, S.E., Robert, F., Groves, D.I., eds., Gold and Base-Metal Mineralization in the Abitibi Subprovince, Canada, with Emphasis on the Quebec Segment: The University of Western Australia, Short Course, p. 167–209.

Robert, F., and Brown, A.C., 1986, Archean gold-bearing quartz veins at the Sigma Mine, Abitibi greenstone belt, Quebec; Part 1. Geologic relations and formation of the vein system: Economic Geology, v. 81, p. 578–592.

Salas, G.P., 1975, Carta y provincias metalogeneticas de la Republica Mexicana: Consejo de Recursos Minerales, Publication 21 E., scale 1:2,000,000.

Sibson, R.H., 1981, Fluid flow accompanying faulting; field evidence and models, *in* Simpson, D.W., Richards, P.G., eds., Earthquake Prediction, an International Review: American Geophysical Union, Maurice Ewing Series, v. 4, p. 593–603.

Sibson, R.H., 1986, Brecciation processes in fault zones: Pure and Applied Geophysics, v. 124, p. 159–175.

Sibson, R.H., 1987, Earthquake rupturing as a mineralizing agent in hydrothermal systems: Geology, v. 15, p. 701–704.

Spencer, J.E., and Normack, W.R., 1979, Tosco-Abreojos fault zone; a Neogene transform plate boundary within the Pacific margin of southern Baja California, Mexico: Geology, v. 7, p. 554–557.

Spurr, J.E., 1916, The relation of ore-deposition to faulting: Economic Geology, v. 11, p. 601–622.

Stock, J.M., and Hodges, K.V., 1989, Pre-Pliocene extension around the Gulf of California and the transfer of Baja California to the Pacific plate: Tectonics, v. 8, no. 1, p. 99–115.

Swanson, E.R., and McDowell, F.W., 1984, Calderas of the Sierra Madre Occidental volcanic field, western Mexico: Journal of Geophysical Research, v. 89, p. 8787–8799.

Universidad Autonima de Mexico, 1974–1977, Carta Geologica de Sinaloa, Mexico: U.N.A.M. Instituto de Geologia, scale 1:100,000, [series of 32 maps].

Von Damm, K.L., Edmond, J.M., Measures, C.I., and Grant, B., 1985, Chemistry of submarine hydrothermal solutions at Guaymas Basin, Gulf of California: Geochimica et Cosmochimica Acta, v. 49, p. 2221–2237.

Wahl, D.E., 1973, Geology of the El Salto strip, Durango, Mexico: Austin, University of Texas, unpub. M.S. thesis, 112 p.

Wisser, E., 1954, Geology and ore deposits of Baja California, Mexico: Economic Geology, v. 49, no. 1, p. 44–76.

Wisser, E., 1966, The epithermal precious-metal province of northwest Mexico: Nevada Bureau Mines Geological Report No. 13, p. 63–92.

CHAPTER H

CENOZOIC GEOLOGY AND MINERAL DEPOSITS OF THE BERENGUELA DISTRICT, NORTHWESTERN BOLIVIA

By ALAN R. WALLACE,[1] RICHARD F. HARDYMAN,[2] RICHARD M. TOSDAL,[3] NESTOR JIMENEZ,[4] JOSÉ LUÍS LIZECA,[4] *and* FERNANDO MURILLO[4]

ABSTRACT

The Berenguela Ag-Pb-Zn-Cd district of the northwestern Bolivian Altiplano was the site of episodic mid to late Tertiary deformation during basin sedimentation and explosive volcanism. Oligocene continental sedimentation produced the Berenguela Formation and the lower member of the Mauri Formation, both of which were buried by ignimbrites and volcaniclastic sediments of the Miocene upper member of the Mauri Formation. Dacitic to rhyolitic domes, lahars, and ash-flow tuffs were emplaced during middle Miocene to Pliocene time. Episodic tectonism and associated broad folding and high-angle faulting produced major unconformities in the sedimentary record.

The district contains two types of base- and precious-metal deposits. Late Oligocene–early Miocene(?) cadmium-rich veins formed along fractures in the Berenguela and lower member of the Mauri Formations, and middle Miocene or younger cadmium-poor veins formed in Miocene volcaniclastic and intrusive rocks. The different chemistries and mineralogies suggest different ages and metal sources for the two vein systems. Distinct thorogenic Pb isotopic compositions for galena in the two types of veins are consistent with this interpretation.

INTRODUCTION

The Berenguela district, approximately 160 km southwest of La Paz, Bolivia (fig. 1), consists of a network of mineralized faults that have been mined intermittently since Spanish colonial times, in the 1500's. The ores are hosted by Cenozoic continental sedimentary rocks, inviting comparison with the Corocoro district to the east, and by Miocene volcanic and intrusive rocks. Although the Berenguela district is of only minor economic importance, geologic relations provide many clues to the Cenozoic history of the northwestern Altiplano. Recent mapping by U.S. Geological Survey (USGS) and the Servicio Geológico de Bolivia (GEOBOL) geologists redefined the stratigraphic and tectonic history of the region and placed the mineral deposits in a more regional geologic framework.

REGIONAL GEOLOGIC SETTING

The Berenguela district, which surrounds the small town of the same name, is in the western Altiplano (fig. 1), the middle of three Andean morphotectonic elements that formed in response to subduction of the Nazca plate beneath the South American craton along the western margin of the continent (Baranzagi and Isacks, 1976). To the west, the Cordillera Occidental is underlain by Proterozoic to Tertiary metamorphic, igneous, and sedimentary rocks and is capped by a chain of Oligocene to Holocene stratovolcanoes. To the east, the Cordillera Oriental is dominated by thin-skinned thrust belts (Jordan and others, 1983; Sheffels, 1990). The Altiplano is underlain by an easterly thickening section of Tertiary sedimentary rocks that overlie, at varying depths, Proterozoic to Mesozoic sedimentary and crystalline rocks.

[1]U.S. Geological Survey, Mail Stop 905, P.O. Box 25046, Denver Federal Center, Denver, CO 80225.

[2]U.S. Geological Survey, University of Nevada, Mackay Building, Reno, NV 89557.

[3]U.S. Geological Survey, Mail Stop 901, 345 Middlefield Road, Menlo Park, CA 94025.

[4]Servicio Geológico de Bolivia, Calle Frederico Zuazo No. 1673, Casilla 2729, La Paz, Bolivia.

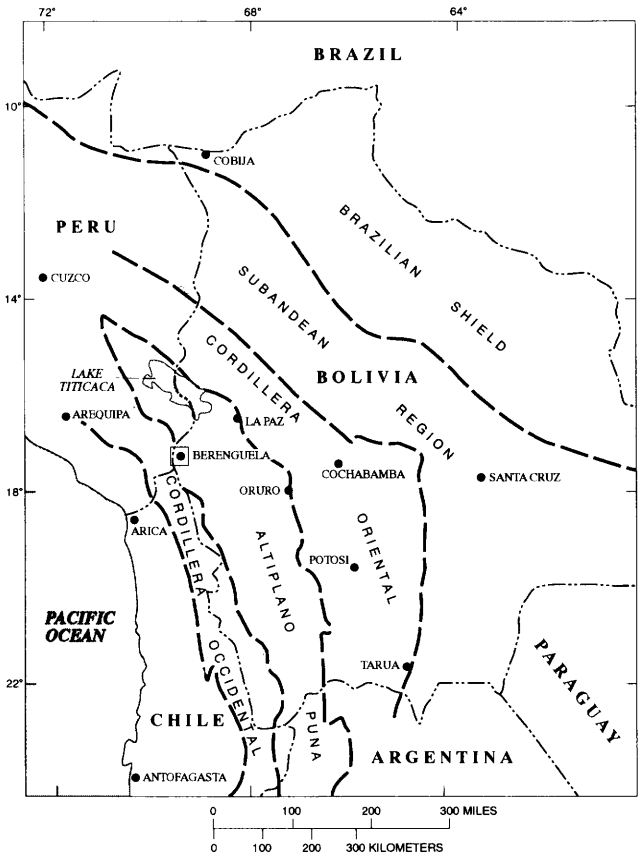

Figure 1. Location of the Berenguela, Bolivia, area with respect to major morphotectonic features of the central Andes. Heavy dashed lines separate morphotectonic elements.

Arc-related igneous activity related to the Andean cycle has persisted since Mesozoic time. Jurassic, Late Cretaceous, and Paleocene magmas were emplaced along the western cratonic margin, west of the modern chain of volcanoes. After a period of igneous and tectonic quiescence, magmatic activity was renewed in the late Oligocene, producing the "central volcanic zone," which extends from southern Peru into Chile (Thorpe, 1984). The western part of the zone is a chain of Miocene to Holocene andesitic stratovolcanoes along the crest of the Cordillera Occidental.

Many of the identified structures in the Altiplano region are products of late Oligocene and younger contraction and uplift related to subduction and formation of the Andean orocline. The region was tectonically inactive from the late Eocene until the late Oligocene, and continental clastic sediments were shed from the eroding Cordillera Occidental to produce a subdued landscape (Tosdal and others, 1984; Jordan and Alonso, 1987). Renewed episodic tectonism produced folds and thrusts in the eastern Altiplano (Jordan and others, 1983) and rapid uplift and multiple stages of pedimentation in the western Altiplano (Tosdal and others, 1984; McKee and Noble, 1989).

SEDIMENTARY AND IGNEOUS ROCK UNITS

The rocks of the Berenguela district record Oligocene and younger clastic sedimentation and plutonic and volcanic igneous activity. The oldest rocks exposed in the area are continental redbeds of the Oligocene Berenguela Formation (fig. 2), which includes more than 1,000 m of red quartz arenite, siltstone, and mudstone. Thin conglomerate beds are present locally, and they contain subrounded clasts of granite, gneiss, chert, and quartzite (1–10 cm in diameter), which were presumably derived from either a pre-Tertiary source or reworked from older Tertiary conglomerate layers. Bedding is generally parallel, although channelling is locally common beneath massive sandstone layers. The uppermost unit of the Berenguela exposed in the district is a massive sandstone. The red coloration is a product of diagenetic to post-diagenetic alteration of whatever mafic minerals (biotite, hornblende, and magnetite) may have been present in the sediments. The Berenguela Formation has been correlated with redbeds of the Tihuanacu Formation north of La Paz, the upper part of which has an age of 29 Ma (Swanson and others, 1987), and the Corocoro Formation, which has a late Oligocene to early Miocene age (17–25 Ma; data from A.H. Clark, cited in Flint, 1990). Therefore, the Berenguela Formation is probably of Oligocene age as well.

The Mauri Formation overlies the Berenguela Formation, and it reflects a progressive change from continental clastic sedimentation with a distal crystalline source (lower member) to volcaniclastic sedimentation with a nearby volcanic-arc source for the sediments and intercalated ignimbrites (upper member). The lower member (Mauri 1 and 3 of Sirvas C., 1964) is arkosic sandstone to siltstone, with a biotite- (and, near the base, plagioclase-) rich mineralogy that is distinct from that of the Berenguela Formation. Rare conglomerate units near the base of the Mauri contain subrounded pebbles to boulders of gneiss and granite (some with Late Proterozoic U-Pb-isotopic ages; R. Tosdal, unpub. data, 1991). Higher in the section, conglomerates are common and contain cobbles of distinctive basaltic volcanic rocks and minor sandstones in addition to clasts of gneiss and granite. The volcanic rocks are petrologically similar to those in the Abaroa Formation, which crops out some 50 km to the west and southwest. The conglomerate is coarser to the southwest of the town of Berenguela and must reflect source-region uplift to the west and south. Andesitic dikes and sills occur within the lower member (Mauri 2 and 4 of Sirvas C., 1964); these have been dated at 25.2±1.0 Ma (lava flow in Mauri 2; Lavenu and others, 1989) and 25.6 Ma (lava flow in Mauri 4; Evernden and others, 1977).

The upper member of the Mauri Formation is composed of a heterogeneous sequence of principally volcaniclastic tuffaceous sandstone and conglomerate and

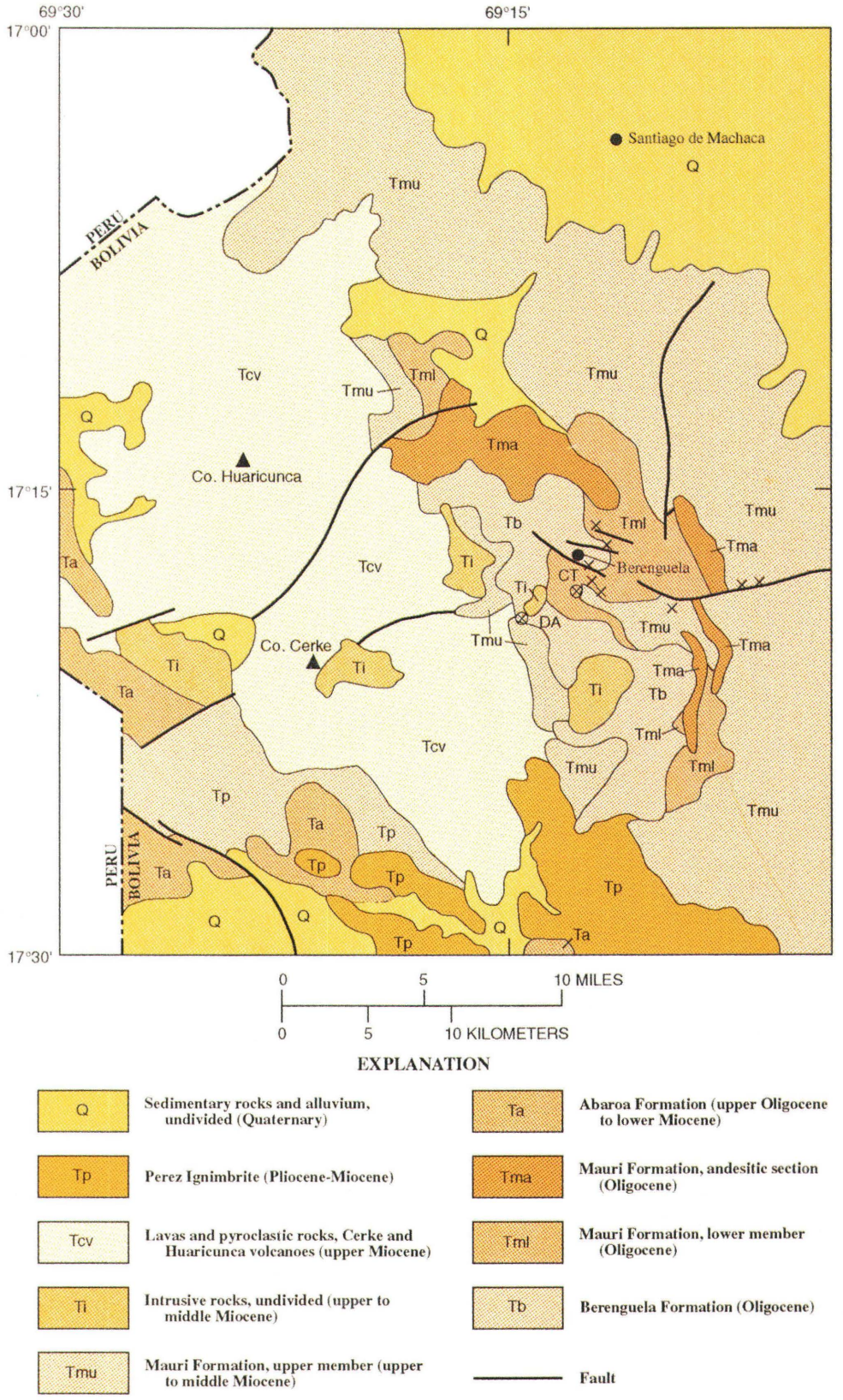

Figure 2. Generalized geologic map of the Berenguela region. CT, Cerro Tatitocollo prospect; DA, Dos Amigos prospect; X, mine or group of mines. Based on unpublished mapping (1990) by the authors of this paper.

ignimbrite. As such, the upper member represents a profound change in type and source of sedimentation from the rocks of the lower member. The units in the upper member, previously included as Mauri 5 and 6 on the east side of the area and the Cerke Formation to the west (Sirvas C., 1964), represent dynamic and rapid basin filling east of an active, explosive volcanic source. Units on the east side of the Berenguela district include interbedded sandstone, conglomerate, reworked tuffaceous sediments, and pyroclastic airfall deposits. To the west, the section is composed of predominantly pyroclastic deposits derived from a chain of volcanoes that include the modern Cerros Cerke and Huaricunca. Basalt-rich conglomerates in the Mauri east of Berenguela probably were derived from the late Oligocene to middle Miocene Abaroa Formation to the south. To the east, the younger rocks disconformably overlie the upper part of the lower member of the Mauri, and to the west, they unconformably overlie the Berenguela and lower part of the lower member of the Mauri Formations. In the central part of the Berenguela district, isolated remnants of a locally derived, trough-filling sedimentary breccia overlie the Berenguela and the lowermost part of the Mauri Formations. A tuff in the upper member of the Mauri, northeast of Berenguela, has been dated at about 10.5 Ma (Evernden and others, 1977). Constructional dacitic to andesitic volcanic activity along the Cerke-Huaricunca chain buried the older, more felsic pyroclastic material with flows and extensive mudflow breccias. These andesites and dacites were erupted at 5.7±0.5 Ma (Lavenu and others, 1989).

Subvolcanic intrusive bodies of rhyolite to dacite were emplaced along a north-northwest-trending belt in the western part of the study area. The stocks intrude the Berenguela Formation and both the lower and upper members of the Mauri Formation, but they are overlain by mudflow breccias of Cerro Cerke. Therefore, intrusive ages probably range from about 15 to 5 Ma, based upon existing geochronologic data and new stratigraphic relations.

The youngest unit in the area is the Perez ignimbrite, a moderately welded, quartz-phenocrystic tuff that was erupted at 2.2–3.3 Ma (Evernden and others, 1977; Lavenu and others, 1989). The tuff sheet extends for perhaps 100 km south of Berenguela and west to near the borders with Peru and Chile; it represents at least 250 km^3 of erupted magma.

STRUCTURAL GEOLOGY

Major unconformities and changes in sediment grain size and composition record regional tectonic events. Major unconformities occur between the Berenguela and lower member of the Mauri, between the lower and upper members of the Mauri, and between the upper member of the Mauri and the 5-Ma dacitic volcanic rocks of Cerro Cerke. The contact between the Berenguela and lower member of the Mauri is essentially parallel in the center of the district, but south of Berenguela, it is an angular unconformity of as much as 10°; also, the thick, prominent sandstone bed at the top of the Berenguela Formation was locally eroded prior to Mauri deposition. This indicates broad folding and erosion of the Berenguela prior to Mauri time, and the distinct change in lithology between the two formations indicates a profound change in source terranes. Regional stratigraphic correlations and limited geochronologic data indicate that this unconformity probably developed in the late Oligocene, perhaps between about 30 and 26 Ma. This time is regionally correlative with the onset of Cordilleran uplift and formation of the Bolivian orocline (Sempere and others, 1990; Isacks, 1988).

The second major disconformity occurs below the upper member of the Mauri Formation and related pyroclastic rocks. These sediments and tuffs were deposited on various eroded levels of the lower member of the Mauri and, in places, the Berenguela. The disconformity separates the dominantly continental clastic sedimentary rocks of the lower member of the Mauri and Berenguela Formations from the dominantly volcanic and volcaniclastic rocks of the upper member of the Mauri Formation. The age of the disconformity can only generally be placed between 26 Ma (the age of basalt flows in the lower member of the Mauri) and 10 Ma (the age of a tuff in the upper member of the Mauri). This major unconformity likely correlates with a regionally extensive period of Neogene deformation, perhaps broadly equivalent to the Quechua period of deformation (McKee and Noble, 1989). This episode, recognized in Peru, peaked at about 19 Ma.

The third unconformity is between the upper member of the Mauri/Cerke sequence and the dacitic volcanic rocks and mudflows derived from Cerros Cerke and Huaricunca. The older rocks, including the 10-Ma tuff, are broadly folded and faulted, and some erosion occurred prior to deposition of the dacitic material at about 5 Ma. This event reflects deformation throughout the region—this event is referred to as the late Miocene Quechua II deformational event in Peru (McKee and Noble, 1982, 1989). The flat-lying 2-Ma Perez ignimbrite indicates that the region has been tectonically quiet since that time.

Deformational structures within the Berenguela district include broad, open folds and high-angle faults. Polyphase brittle structures in the Berenguela Formation formed during four distinct deformation events. Open folds with westerly trending fold axes (N. 90° W.–N. 70° W.) that deform the Berenguela Formation but not the overlying Mauri Formation formed during the oldest event. This event records mild north-south-oriented contraction and was responsible for the observed unconformity between the Berenguela and Mauri Formations.

The second event is recorded by high-angle faults that are best exposed north of the town of Berenguela. Here, faults cut the sedimentary rocks and basalt intrusions of the Berenguela and lower Mauri Formations and the previously open folds. Two major trends of steeply dipping (60°–90°) faults are evident. One set is dominated by conjugate faults that strike generally east-west and dip to the north and south; less common faults trend northwesterly, N. 20°–50° W., and commonly link longer strike segments of the more westerly striking faults. A second fault set strikes northeasterly, N. 20°–50° E., and cuts and is cut by the westerly striking faults; this mutually crosscutting relationship indicates that the faults are contemporaneous. Slickensides on exhumed fault planes indicate multiple stages of movement on the faults, and most faults show evidence of normal-slip, oblique-slip, and (or) locally strike-slip movements, with both dextral and sinistral sense of shear. Fracture and microfault geometries in the sandstones of the Berenguela Formation are identical to the map-scale fault geometry, and these structures are commonly filled with silica and control the bleaching alteration of the red sandstones. Moreover, the cadmium-rich veins are localized along these faults and fractures, and they probably formed during this second faulting event.

The conjugate, westerly striking faults of the older fault set bound grabens in which the contact between the lower member of the Mauri Formation and the underlying Berenguela Formation has been downdropped with respect to the bounding mesas. The evidence for oblique slip on the faults indicates that the grabens formed during limited horizontal shearing, and the geometry of the grabens and the slickslides indicates that the regional tectonic regime was dextral shear. In this interpretation, the westerly striking faults are analogous to Riedel shears, which form early in the development of a strike-slip fault system (Tchalenko, 1970; Wilcox and others, 1973), and the northwesterly striking faults, veins, and fractures formed as normal or extensional structures. Shortening at this time would have been oriented approximately northwest-southeast, and extension would have been oriented northeast-southwest.

A third event is recorded by broad, open folds with north-trending (N. 0° E.–N. 15° E.) axes that deform the upper member of the Mauri Formation and subjacent rocks. The folds record mild west-east-oriented contraction. Near the town of Berenguela, the conjugate westerly striking faults that formed during the previous event were reactivated; the cadmium-rich veins were extensively brecciated during this deformation. Sinistral oblique movement on the conjugate faults is suggested by the slickslides along the exhumed fault planes. This sense of movement is consistent with the inferred direction of contraction. The superposition of folds and faults that developed during the first three deformations formed the broad structural dome in the Berenguela region.

A fourth episode of deformation is recorded by northerly striking, high-angle faults that cut Mauri and Berenguela Formation. Movement on faults is consistently normal. Faults cutting the Pliocene volcanic rocks west of Berenguela (Sirvas C., 1964) perhaps formed at this time.

MINERAL DEPOSITS

The Berenguela district includes two similar, but nevertheless distinct, types of silver-bearing mineral deposits: cadmium-rich, quartz-poor, base-metal veins in the Berenguela and lower member of the Mauri Formations, and cadmium-poor, quartz-rich veins associated with Miocene volcanic rocks. These were previously described by Schneider-Scherbina (1962) and Sirvas C. (1964).

DEPOSITS HOSTED BY SEDIMENTARY ROCKS

Silver- and base-metal-rich veins occur in steeply dipping fractures in the upper part of the Berenguela Formation, in the lower member of the Mauri sedimentary rocks, and occasionally in the andesites in the lower member of the Mauri (fig. 2). Many of the veins were exposed at the surface; concealed or buried veins were exploited in Colonial times by "piques" (steep, narrow, stone-lined declines that lead to drifts along the veins).

The veins formed along east-northeast- and northwest-trending faults in the sedimentary rocks, and major ore intercepts occur at the intersections of these two fault sets. Slickensides along fault surfaces cut the ore, indicating that fault movement continued after mineralization. The depth of oxidation is shallow (10–20 m), and most of the dumps from the shallow workings contain minor amounts of sulfides that could not be processed during Colonial times. Therefore, the veins likely continue to greater depths than those reached by historical mining. Topographic relations indicate that veins extend at least 200 m above and at least 100 m below the Berenguela-Mauri contact.

As exposed in surface workings, the veins are generally less than 10 cm wide, although millimeter-wide, silica-filled fractures cut altered wallrocks on either side of some veins. Rocks for a few centimeters to a meter on either side of the vein are bleached; in some areas of greater fracture density, the entire mass of host rock has been bleached. Some beds, especially massive sandstones bounded by mudstones, are preferentially bleached as much a 20 meters from the vein. Petrographic observations indicate that the major apparent chemical change is wholesale removal of iron during alteration. In some zones, barite has completely replaced the original quartz cement of the sandstones, and secondary copper carbonates and sulfates indicate that

copper (and other elements?) was deposited in the altered rocks. Evidence of silicification and carbonatization is notably absent in the alteration halo.

Vein minerals, as identified in samples collected from dumps, include galena, greenockite, barite, and sphalerite, with minor amounts of chalcopyrite, chalcocite, and rare marcasite. Paragenetic relations indicate that bleaching and minor dissemination of sulfides into the wallrock was the earliest paragenetic event. Barite was then deposited as a cement in the wallrocks, and the rock was then cut locally by thin chalcedonic veinlets. Bladed barite was the first major mineral to be deposited in the veins, followed by minor marcasite. Subsequently, sphalerite, galena, and greenockite were deposited in the vein. Galena and sphalerite are intergrown with delicately banded, yellowish, colloform minerals; in part, these might be secondary anglesite derived from the galena, but textures indicate that many of these bands are primary. The ores, both primary and secondary, are texturally and paragenetically similar throughout the district, and no systematic zoning was noted.

Much of the silver-rich ore mined from the oxidized parts of the veins was selectively hand sorted by Colonial miners and is therefore largely unavailable for study. Secondary iron oxides are primarily orangish goethite, with considerably less hematite and even less jarosite. Secondary copper carbonates and sulfates, including malachite, azurite, and possibly antlerite, form ubiquitous coatings on fractures. These secondary iron and copper minerals suggest that chalcocite was the primary copper sulfide in the veins and that pyrite, chalcopyrite, and the total volume of iron and copper sulfides were relatively minor (Anderson, 1982).

A number of prospects occur along a fault that is in the upper part of the lower member of the Mauri and that continues into the upper member of the Mauri, east of Berenguela. These deposits are characterized by abundant malachite, tenorite, milky quartz, and chalcedony, and textures are very different from those in the Berenguela district. This striking difference may indicate that these deposits are products of a mineralizing event unrelated to and possibly younger than the "typical" Berenguela ores. Conversely, the veins may represent a distal silica- and copper-rich zonation of the Berenguela mineralizing system.

DEPOSITS ASSOCIATED WITH VOLCANIC ROCKS

The mineral deposits that are associated with volcanic rocks occur in Miocene volcaniclastic and volcanic rocks at the Dos Amigos and Cerro Tatitocollo prospects. In contrast to the sedimentary-rock-hosted deposits, these deposits contain abundant silicified rock and, as indicated by preliminary geochemical data, very little cadmium (a few tens of parts per million versus several percent; J.L. Lizeca, unpub. data, 1991). Dos Amigos, a vein 2 km southwest of Berenguela, is along a fault that trends N. 70° W. in the Berenguela Formation along which a premineralization rhyolite dike was emplaced; slickensides in ore indicate subsequent fault movement. All rocks are altered to a quartz-sericite assemblage, and quartz is the dominant gangue mineral. Galena, pyrite, and sphalerite were observed on the dumps; Sirvas C. (1964) reported tennantite and pearceite. Both fault and hydrothermal breccias are common along the vein. Recent carbonate-bearing, low-temperature waters have formed a line of travertine aprons along the fault zone.

At Cerro Tatitocollo, 1 km south of Berenguela, rocks of the lowermost part of the lower member of the Mauri are unconformably overlain by volcaniclastic rocks of the upper member of the Mauri. The dominant host rock is an epiclastic breccia to pebble conglomerate of the upper member of the Mauri that is composed largely of subangular rhyolite fragments in a coarse-sand matrix. These rocks were intruded by flow-banded rhyolite plugs. Mineralization was concentrated along north-trending fractures; hydrothermal fumarolic breccias were localized along the fractures, and silicification increased towards the breccias. Silver, copper, arsenic, zinc, lead, and antimony have been reported from this zone, which has a maximum dimension of no more than a few hundred meters; gold occurs in a small area southwest of the silver and base-metal zone.

AGES AND GENESIS OF THE DEPOSITS

The distinct differences in cadmium and silica in the two types of ore deposits suggest two ages of mineralization and different sources of fluids and metals. The relatively more radiogenic thorogenic Pb isotopic compositions in the cadmium-rich veins ($^{208}Pb/^{204}Pb$ = 38.73–38.84; 4 deposits, 8 samples) relative to the volcanic rock and associated veins ($^{208}Pb/^{204}Pb$ = 38.36; 1 deposit, 1 sample) furthermore suggest that the two fluids interacted, or were derived from, two reservoirs of slightly different Pb isotopic compositions. Veins in the Berenguela and lower member of the Mauri Formations formed after deposition of at least the lower member of the Mauri and emplacement of the basalt—these events have been dated at 25 Ma. Sparse field relations suggest that veins in the Berenguela are unconformably overlain by unmineralized volcaniclastic rocks of the upper member of the Mauri Formation, thereby placing an upper age limit on the mineralization. In contrast, the volcanic-associated, cadmium-poor deposits are no older than middle Miocene, the inferred age of the igneous host rocks. The copper-silica deposits, for which no cadmium data are available,

in the upper member of the Mauri east of Berenguela, are likely less than 10 m.y. old, the same age as the tuff unit in the upper member.

Mineralizing fluids and contained metals could have been derived from more than one source. Unlike ores in the Corocoro district to the east, which formed in host rocks during diagenesis and were later remobilized into fractures (Flint, 1990), the ores at Berenguela are epigenetic. As a result, these deposits may not have formed in a manner like those at Corocoro, where the metals were remobilized by basin fluids from copper-rich basalts or copper deposits in the Cordillera Occidental (Flint, 1990). However, cadmium-rich ores are typically derived from basin fluids; fluids of demonstrable igneous derivation rarely contain abundant cadmium. Therefore, the abundance of cadmium in the Berenguela-hosted ores strongly suggests a basin fluid-origin for some or all of the metals—the difference between the deposits at Berenguela and Corocoro might be the presence or absence of fracture permeability at the time of initial fluid migration. If indeed the deposits formed before deposition of upper member of the Mauri volcaniclastic sediments, then mineralization might have occurred during the early to middle Miocene deformational event.

In contrast, the fluids involved in the formation of the igneous-hosted deposits formed during or after late Mauri sedimentation and related igneous activity. Metals may have been derived from an igneous source during Miocene volcanic activity; as with many volcanic-hosted epithermal systems, much of the mineralizing fluid may have been heated meteoric water. Remobilization of some of the older mineral deposits cannot be discounted; however, the relative absence of cadmium in the volcanic-hosted veins relative to silver and zinc, which have very similar mobilities (Rose and others, 1979), argues against significant remobilization of the metals in the older Zn-Cd-Ag-Pb veins.

ACKNOWLEDGMENTS

The field work for this study was part of a joint project, funded by the Interamerican Development Bank, between the USGS and GEOBOL to study precious-metal deposits in the Altiplano. C.G. Cunningham of the USGS served as overall project coordinator; Marcello Claure and Franz Tavera of GEOBOL were invaluable for their coordinating efforts in Bolivia. We thank Compañía Minera del Sur (COMSUR) and Rio Tinto Zinc for the use of their facilities in Berenguela.

REFERENCES CITED

Anderson, J.A., 1982, Characteristics of leached capping and techniques of appraisal, *in* Titley, S.R., ed., Advances in Geology of the Porphyry Copper Deposits, Southwestern North America: Tucson, University of Arizona Press, p. 275–295.

Barazangi, M., and Isacks, B.L., 1976, Spatial distribution of earthquakes and subduction of the Nazca plate beneath South America: Geology, v. 4, p. 686–692.

Evernden, J.F., Kriz, S.J., and Cherroni M.C., 1977, Potassium-argon ages of some Bolivian rocks: Economic Geology, v. 72, p. 1042–1061.

Flint, S.S., 1990, Sediment-hosted stratabound copper deposits of the central Andes, *in* Boyle, R.W., Brown, A.C., Jefferson, C.W., Jowett, E.C., and Kirkham, R.V., eds., Sediment-Hosted Stratiform Copper Deposits: St. John's Geological Association of Canada, p. 371–398.

Isacks, B.L., 1988, Uplift of the central Andean plateau and bending of the Bolivian orocline: Journal of Geophysical Research, v. 93, p. 3211–3231.

Jordan, T.E., and Alonso, R.N., 1987, Cenozoic stratigraphy and basin tectonics of the Andes Mountains, 20°–28° south latitude: American Association of Petroleum Geologists Bulletin, v. 71, p. 49–64.

Jordan, T.E., Isacks, B.L., Allmendinger, R.W., Brewer, J.A., Ramos, V.A., and Ando, C.J., 1983, Andean tectonics related to geometry of subducted Nazca plate: Geological Society of America Bulletin, v. 94, p. 341–361.

Lavenu, A., Bonhomme, M.G., Vatin-Perignon, N., and De Pachtere, P., 1989, Neogene magmatism in the Bolivian Andes between 16° S. and 18° S.: Stratigraphy and K/Ar geochronology: Journal of Latin American Geosciences, v. 2, p. 35–47.

McKee, E.H., and Noble, D.C., 1982, Miocene volcanism and deformation in the western Cordillera and high plateaus of south-central Peru: Geological Society of America Bulletin, v. 93, p. 657–662.

McKee, E.H., and Noble, D.C., 1989, Cenozoic tectonic events, magmatic pulses, and base- and precious-metal mineralization in the central Andes, *in* Ericksen, G.E., Canas Pinochet, M.T., and Reinemund, J.A., eds., Geology of the Andes and its Relation to Hydrocarbon and Mineral Resources: Circum-Pacific Council for Energy and Mineral Resources Earth Science Series, v. 11, p. 189–194.

Rose, A.W., Hawkes, H.E., and Webb, J.S., 1979, Geochemistry in Mineral Exploration, [2nd ed.]: New York, Academic Press, 657 p.

Schneider-Scherbina, A., 1962, Los yacimientos polimetalicos de Berenguela: Departmento Nacionál de Geologia, Informe No. 39 de la Misión Geologica Alemana en Bolivia, 54 p.

Sempere, T., Herail, G., Oller, J., and Bonhomme, M.G., 1990, Late Oligocene–early Miocene major tectonic crisis and related basins in Bolivia: Geology, v. 18, p. 946–949.

Sheffels, Barbara M., 1990, Lower bound on the amount of crustal shortening in the central Andes: Geology, v. 18, p. 812–815.

Sirvas C., J.F., 1964, Estudio geológico de la región Tambo Mauri-Berenguela, Provincia Pacajes del Departamento de La Paz, Republica de Bolivia: unpub. thesis, Universidad Mayor de San Andreas.

Swanson, K.E., Noble, D.C., McKee, E.H., Sempere, T., Martinez, C., and Cirbian, M., 1987, Major revisions in the age of rock units and tectonic events in the northern Altiplano basin of Bolivia [abs.]: Geological Society of America Abstracts Programs, v. 19, no. 6, p. 456.

Tchalenko, J.S., 1970, Similarities between shear zones of different magnitudes: Geological Society of America Bulletin, v. 81, p. 1625–640.

Thorpe, R.S., 1984, The tectonic setting of active Andean magmatism, *in* Harmon, R.S., and Barreiro, B.A., eds., Andean Magmatism: Chemical and Isotopic Constraints: Nantwhich, United Kingdom, Shiva Publishing Limited, p. 4–8.

Tosdal, R.M., Clark, A.H., and Farrar, E., 1984, Cenozoic polyphase landscape and tectonic evolution of the Cordillera Occidental, southernmost Peru: Geological Society of America Bulletin, v. 95, p. 1318–1332.

Wilcox, R.E., Harding, T.P., and Seely, D.R., 1973, Basic wrench tectonics: American Association of Petroleum Geologists Bulletin, v. 57, p. 74–96.

CHAPTER I

K-Ar AGES OF BOLIVIAN TERTIARY POLYMETALLIC VEIN DEPOSITS

By STEVE LUDINGTON,[1] EDWIN H. MCKEE,[2] *and* NORA SHEW[3]

INTRODUCTION

Silver and tin mining has been a mainstay of the Bolivian economy for over four centuries. In the Andes, south of the capital city of La Paz, dozens of large mines and hundreds of small mines and prospects occur in the Cordilleras Oriental and Occidental and on the Altiplano (fig. 1). Production has been mainly from the Cordillera Oriental.

Many of the mines in the Bolivian Andes are polymetallic vein deposits that are closely related to subvolcanic dacitic intrusions, and, as far as is known, most of these Tertiary intrusions and their associated polymetallic vein deposits are Miocene in age. The intrusions are emplaced in two distinct host-rock types: (1) Paleozoic marine sedimentary and metasedimentary rocks, primarily in the Cordillera Oriental, and (2) Tertiary continental sedimentary and volcanic rocks in the Cordillera Occidental and on the Altiplano.

The polymetallic veins consist primarily of sulfide minerals, chiefly pyrite, marcasite, and pyrrhotite. Lesser amounts of sphalerite, galena, cassiterite, arsenopyrite, chalcopyrite, stibnite, tetrahedrite, wolframite, bismuthinite, argentite, native bismuth, native gold, and complex sulfosalt minerals occur in various combinations. There is a notable scarcity of nonsulfide gangue, although quartz, barite, or manganese carbonate occur locally in the veins, primarily in the upper parts of the hydrothermal systems. Sericite, or white mica, is the most common alteration mineral, along with kaolinite. Alunite also occurs in a few deposits.

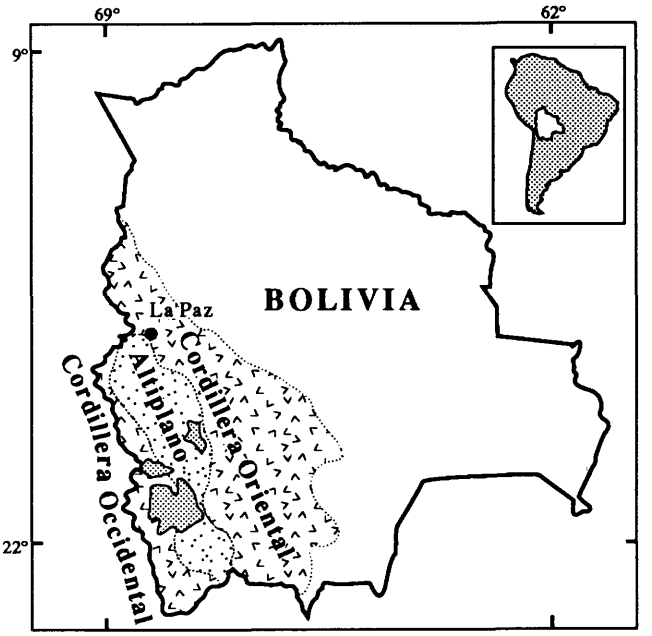

Figure 1. Index map showing location of physiographic provinces of Bolivia referred to in text.

This report summarizes the results of geochronologic studies of samples collected during 1990 and 1991 during a general study of the mineral deposits of the Altiplano of Bolivia.

K-Ar AGE DETERMINATIONS

Twelve new conventional K-Ar age determinations, from ten mineral deposits in the Cordillera Occidental and on the Altiplano of Bolivia, were performed during this study. The ages and analytical data are presented in table 1. Five of the ages directly date mineralization and (or)

[1]U.S. Geological Survey, Mail Stop 984, 345 Middlefield Road, Menlo Park, CA 94025.

[2]U.S. Geological Survey, Mail Stop 901, 345 Middlefield Road, Menlo Park, CA 94025.

[3]U.S. Geological Survey, Branch of Alaskan Geology, 4200 University Drive, Anchorage, AK 99508.

Table 1. K-Ar ages and analytical data for samples from the Altiplano and Cordillera Occidental, Bolivia.

[rad, radiogenic. Constants used were $^{40}K/K=1.167\times10^{-4}$ mol/mol; $l_b=4.962\times10^{-1}$/yr; $l_e+l_e'=0.581\times10^{-1}$/yr. Samples 90BSL014, 109, 110, 90BDR010, 90BBR004a, 10, 14, and 90BBG024 were analyzed by E.H. McKee. Samples 90BDR030, 35, 53, and 55 were analyzed in duplicate for argon by Nora Shew, yielding a single age. Potassium measurements by S.T. Pribble. Mass spectrometry by J.Y. Saburomaru, J.C. Von Essen]

Sample no.	Locality	Type of rock	Mineral analyzed	K_2O (weight percent)	$^{40}Ar_{rad}$ (mol/g x10^{-11})	$^{40}Ar_{rad}$ (percent of total)	Age (Ma)
Direct dates on mineral deposits							
90BDR010	San Cristobal (Toldos)	Dacite in pit	Biotite	7.47	9.136	54	8.5+0.3
90BBG024	Carangas	Rhyolite flow	Biotite	8.12	18.03	59	15.4±0.5
90BSL014	Buena Vista	Vein wallrock	Sericite	4.57	7.306	55	11.1±0.3
90BSL109	Kiska	Late vein	Alunite	8.19	16.08	36	13.6±0.5
90BSL110	Kori Kollo	Late vein	Alunite	9.59	6.555	50	4.7±0.2
Dates on intrusions, lavas, and ash-flow tuffs that constrain mineral deposit ages							
90BBR004a	Todos Santos	Dacite	Biotite	5.42	4.739	17	6.1±0.2
90BBR010	Negrillos	Ash-flow tuff	Biotite	8.46	26.61	75	21.7±0.7
90BBR014	María Elena	Andesite dike	Hornblende	.783	.7091	17	6.3±0.2
90BDR030	San Cristobal	Dacite stock	Biotite	8.90	10.32	49	8.0±0.1
				8.91	10.34	56	
90BDR035	Eskapa (Cuidado)	Dacite	Biotite	8.46	7.696	37	6.3±0.1
				8.51	7.727	44	
90BDR053	Mina Escala	Dacite debris flow	Biotite	8.08	21.43	60	18.2±0.3
				8.09	21.07	53	
90BDR055	Mina Escala	Rhyolite stock	Biotite	9.02	23.43	60	18.0±0.2
				9.04	23.62	73	

alteration events. The other seven ages are on intrusions, tuffs, or lava flows at five additional localities and indirectly aid in constraining the time of mineralization. The mineral deposits dated during this study were selected because they are broadly representative of Bolivian mineral deposits in the central Andes and little was known of their geochronology. Samples from the deposits dated directly yielded alunite, biotite, or sericite for dating; biotite and hornblende from the intrusions, ash-flow tuffs, and lava flows were used for age determination (table 1).

K-Ar analyses were performed using standard isotope-dilution techniques similar to those described by Dalrymple and Lanphere (1969). The mineral concentrates were made by heavy-liquid, magnetic, electrostatic, and hand-picking procedures. Potassium analyses were by lithium-metaborate-flux-fusion flame photometry, the lithium serving as an internal standard (Ingamells, 1970). Argon analyses were done using a five-collector mass spectrometer (Stacy and others, 1981). The precision of the data, shown as the "value" in table 1, is the estimated analytical uncertainty at one standard deviation (Cox and Dalrymple, 1967). It represents uncertainties in the measurement of radiogenic ^{40}Ar and K_2O based on experience with hundreds of replicated analyses in the Menlo Park laboratories of the U.S. Geological Survey. Mass discrimination of the spectrometer is routinely determined on the basis of multiple analyses of purified air. The constants used in age determination are those from the Subcommission on Geochronology (Steiger and Jaeger, 1977).

The new ages, along with brief descriptions of the mineral deposits, are given below. More detailed deposit descriptions can be found in a report on the mineral resources of the Bolivian Cordillera Occidental and Altiplano (U.S. Geological Survey and Servicio Geológico de Bolivia, 1991). Locations of the studied deposits together with all known major polymetallic vein deposits are shown on figure 2, which includes the new K-Ar ages reported here and all known previously reported ages (Ludington, Orris, and others, 1991) for polymetallic vein deposits.

KORI KOLLO DEPOSIT

The La Joya district includes several polymetallic vein deposits. Principal among them is the one at Cerro Kori Kollo, which contains about 150 tonnes of gold and 1,000 tonnes of silver and is the first Bolivian polymetallic vein deposit to produce substantial amounts of gold (Long and others, 1991). Cerro Kori Kollo is one of four hills in the district that are apparently cupolas on a large dacitic intrusive body that intrudes siltstone and sandstone of Silurian age. The ore consists of sulfide and oxide veins that cut a sericitized dacite porphyry.

The age of the La Joya dacite intrusion, based on a biotite K-Ar date, is 14.3±0.4 Ma, whereas an age determined on sericite from the orebody at Kori Kollo was 15.7±0.5 Ma (Redwood, 1987). These dates, although

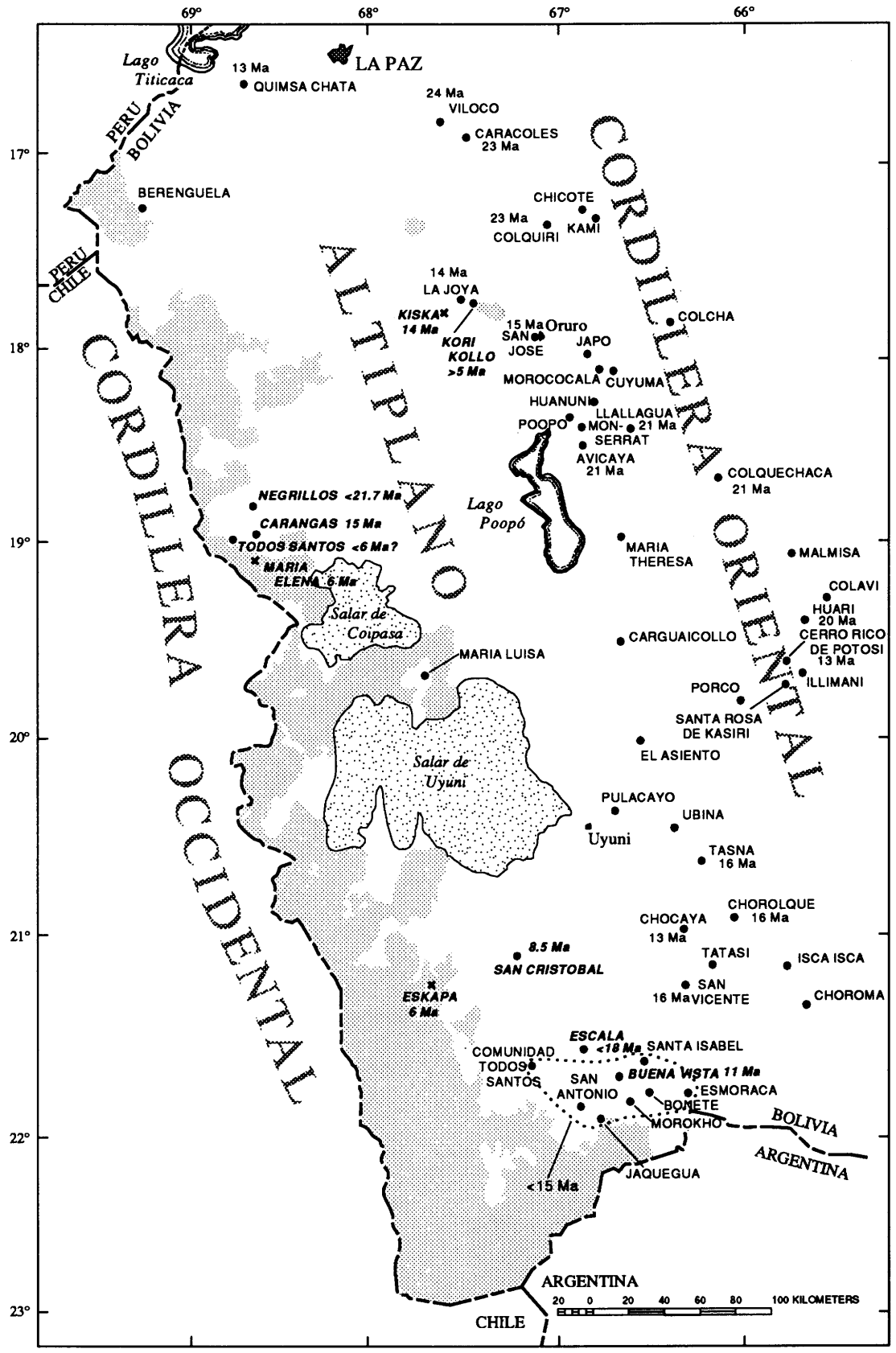

Figure 2. Map showing locations and ages of mineral deposits discussed in this study and additional polymetallic vein deposits in western Bolivia. Solid circles are polymetallic vein deposits; X's are other types of deposits. Names and dates in bold italics indicate deposits specifically studied. Shaded area indicates the young volcanic rocks of the Cordillera Occidental, which are post-mineral cover to the polymetallic vein deposits.

discordant in detail, are consistent with field evidence that indicates that intrusion of the dacite bodies and mineralization are closely related. We dated a quartz-alunite vein that crosscuts mineralized structures in the Kori Kollo mine and obtained a K-Ar age of 4.7±0.2 Ma (table 1). If all the dates are accurate, they indicate that the hydrothermal system was extremely long lived. Additional studies are needed to eliminate the possibility that the alunite age documents either a later hydrothermal event that is unrelated to the Miocene intrusion or supergene alteration.

NEGRILLOS AREA

In the Negrillos area, silver-bearing polymetallic veins are emplaced in a series of andesitic lava flows and volcanic breccias (Gamble and others, 1991). These rock units appear to be stratigraphically above an ash-flow tuff dated at 21.7±0.7 Ma (table 1), suggesting that the veins at Negrillos are younger than 21.7 Ma.

CARANGAS AREA

In the Carangas area, silver-bearing polymetallic veins are emplaced in altered tuffs of the Tertiary Carangas Formation (Gamble and others, 1991). The most significant deposits appear to be on Cerro Espíritu Santo, where zones of intense hydrothermal alteration are present. A distinctive rhyolite porphyry is found both as dikes and small plutons that intrude the hydrothermally altered rocks on the hill and as clasts within hydrothermal(?) mineralized breccias. Analysis of biotite from a dike in this rhyolite porphyry gave an age of 15.4±0.5 Ma (table 1). Although the field relations that constrain the meaning of this date are equivocal, the age of mineralization may be about 15 Ma.

TODOS SANTOS DEPOSIT

The deposit at the Todo Santos mine is related to a rhyolite dome complex that intrudes rock of the Tertiary Carangas Formation (Gamble and others, 1991). The main Todos Santos dome consists of flow-banded rhyolite that intrudes its own carapace of tuffs and breccias. The associated mineral deposit consists of a group of veins and disseminations in and near a fault that cuts the dome and its carapace of pyroclastic rocks. The prospect is of interest primarily for its precious-metal values, but base-metal values are also appreciable. Biotite from a coarse block-and-ash flow of pumiceous rhyodacite yielded a K-Ar age of 6.1±0.2 Ma (table 1); the block-and-ash flow is intruded by a small rhyolite dome, similar in appearance to the main dome at Todos Santos. If the two domes are temporally equivalent, the mineralization at Todos Santos may have formed less than 6.1 m.y. ago.

SAN CRISTOBAL DISTRICT (TOLDOS MINE)

Mineral deposits in the San Cristobal district occur near the center of a deeply eroded late Tertiary volcanic complex that consists of a number of subvolcanic stocks that intrude siltstone, sandstone, and conglomerate of probable Eocene and Oligocene age and younger volcanic and volcaniclastic rocks of probable Miocene age (Richter, Brooks, Ludington, and others, 1991). Currently, the most important mineral deposit in the district is being exploited at the Toldos mine, where an open-pit, heap-leach operation recovers silver from an orebody of approximately 3,000,000 tonnes at about 120 grams/tonne (g/t) silver.

The district is typical of many Altiplano polymetallic vein districts in that tin and gold are found in very low concentrations. In the Toldos deposit, alteration envelopes around silver-bearing pyrite veins are primarily composed of sericite. The dacite porphyry that hosts the deposit and others in the district have been affected by a form of potassic alteration that has resulted in whole-rock K_2O contents greater than 8 weight percent, even though petrographic studies have been unable to document and clarify the nature of the alteration. Fresh biotite phenocrysts are a distinctive characteristic of these altered rocks, and K-Ar ages on these biotites yielded ages of 8.0±0.1 Ma (90BDR030) and 8.5±0.3 Ma (90BDR010) (table 1). Sample 90BDR010 is from the open pit at the Toldos mine, whereas sample 90BDR030 is from an outcrop of a separate intrusion, several kilometers to the north. Thus, 8.5 Ma would appear to be the maximum age of mineralization.

ESCALA DEPOSIT

The Escala deposit consists of a series of silver-bearing polymetallic veins emplaced in a subvolcanic rhyolite porphyry stock (Richter, Brooks, Cox, and others, 1991). The rhyolite stock intrudes a series of dacitic ash-flow tuffs and debris flows. Near the deposit, a date of 18.2±0.3 Ma was obtained from biotite in a dacitic debris flow in the upper part of this volcanic series (table 1). Biotite from fresh intrusive rhyolite porphyry a few kilometers north of the Escala deposit yielded an age of 18.0±0.2 Ma. These dates constrain the age of the Escala deposit to be less than 18 Ma (table 1).

BUENA VISTA DEPOSIT

In the Buena Vista area, several polymetallic veins are emplaced in Miocene dacitic ash-flow tuffs, lava flows, and volcanic breccias (Ludington, Czamanske, and others, 1991). Unlike most of the Bolivian polymetallic vein

deposits, they have no obvious association with dacitic intrusive bodies. The veins contain lead, zinc, silver, antimony, and gold; the principal ore minerals are stibnite, galena, sphalerite, chalcopyrite, argentite, and various silver sulfosalts. Alteration sericite that is part of a quartz-sericite-pyrite envelope around a vein yields a K-Ar age of 11.1±0.3 Ma (table 1). This confirms an earlier determination of 11.3±0.6 Ma (Instituto de Geología Económica, 1985). This age is considered to be the age of mineralization at Buena Vista; it is considerably younger than the enclosing pyroclastic rocks, which appear to have been erupted between about 24 Ma and 15 Ma (Kussmaul and others, 1975).

MARÍA ELENA PROSPECT

Anomalous values of gold and silver are reported from a small, rhyolitic intrusive body near the top of Cerro Culebra, a composite stratovolcano about 6.5 km south of Todos Santos (Ratté and others, 1991). This intrusive is extensively silicified as are lava flows surrounding and overlying it. Base metals are generally absent from this mineralized system, which is probably an epithermal vein deposit rather than a polymetallic vein. The altered rocks at Cerro Culebra are cut by an unaltered hornblende-bearing andesite dike that yields a K-Ar age of 6.3±0.2 Ma (table 1), which provides a minimum age for the deposit.

CERRO ESKAPA AREA (CUIDADO MINE)

Cerro Eskapa is part of a large field of late Tertiary and Quaternary stratovolcanoes in the Cordillera Occidental and is about 125 km southwest of Uyuni. Two mineral deposits are hosted in the lavas of this volcano. One, the Cuidado mine, is near the summit of the volcano and consists of an area of conspicuous epithermal, chiefly argillic, hydrothermally altered dacitic breccias that contains anomalous values of gold, silver, arsenic, antimony, and tellurium. The other is on the flanks of the volcano and consists of copper veins in a massive dacitic lava dome-flow that contains phenocrysts of sanidine, plagioclase, biotite, and some quartz (Richter, Brooks, Shew, and others, 1991). Biotite from this rock yielded a K-Ar age of 6.3±0.1 Ma (table 1)—this serves as a maximum age of mineralization for the copper deposit.

KISKA PROSPECT

The Kiska gold-silver prospect is on an isolated hill southwest of the Kori Kollo deposit in the La Joya district (Ludington, du Bray, and others, 1991). The entire hill, which is composed primarily of Paleozoic sedimentary rocks, has been hydrothermally altered, primarily by strong silicification, and intruded by a dacite porphyry. The mineralized rock is a stockwork that consists of at least two generations of veins that contain fine silica, jarosite, hematite, and alunite . Alunite from the youngest and apparently unmineralized set of veins yielded an age of 13.6±0.5 Ma (table 1), providing a minimum age for the deposit.

Table 2. Ages of mineral deposits on the Altiplano and in the Cordillera Occidental, Bolivia.

[Deposits followed by an asterisk (*) are not polymetallic vein deposits; María Elena and the Cuidado mine on Cerro Eskapa are probably epithermal precious-metal deposits; Kiska is not assignable at present]

Mineral deposit	Age
Kori Kollo	>5 Ma
Negrillos	<21.7 Ma
Carangas	15 Ma
Todos Santos	<6 Ma
San Cristobal (Toldos mine)	8.5 Ma
Mina Escala	<18 Ma
Buena Vista	11 Ma
María Elena*	>6 Ma
Eskapa (Cuidado mine)*	<6 Ma
Kiska*	>14 Ma

DISCUSSION

The available radiometric ages of minerals associated with Tertiary polymetallic vein deposits in the Bolivian Andes south of La Paz are latest Oligocene or Miocene. This includes 14 ages taken from published sources (Ludington, Orris, and others, 1991) and the ages determined or constrained during this study (table 2, fig. 2). The ages range from about 24 Ma to about 5 Ma and span the entire Miocene with no apparent temporal maxima in mineralization. Three other deposits (María Elena, Eskapa, Kiska), which are not polymetallic vein deposits, also have comparable ages.

There do seem, however, to be spatial patterns in time-of-mineralization in this region. Deposits in the Cordillera Oriental are older than in the Altiplano and Cordillera Occidental, and deposits become progressively younger southward in both Cordilleras and in the Altiplano.

In the Cordillera Oriental, over a distance of about 500 km, the deposits decrease in age from about 24 Ma, at Viloco in the north, to about 16 Ma, at San Vicente in the south (Cerro Rico de Potosí appears to be an exception at 13 Ma).

A similar but less well-defined pattern of westward younging of polymetallic vein deposits is seen in the

Cordillera Occidental and on the Altiplano of Bolivia. The ages of deposits in this belt are significantly younger than in the Cordillera Oriental to the east: from about 15 Ma at Kori Kollo to less than 6 Ma at Todos Santos.

RELATIONSHIP OF MINERAL DEPOSITS TO ANDEAN VOLCANISM

The Andean Cordillera of western South America is commonly referred to as the classic example of a convergent continental plate margin (Dewey and Bird, 1970). The area of this report, southwestern Bolivia, lies in the central Andes, astride a major oroclinal bend in the Cordillera. Differences in the tectonic and igneous history of different parts of the Andes are the result of different rates and (or) angles of subduction between the Pacific Nazca plate and the continental South American plate, as well as to varying crustal thickness. Offshore from Bolivia and northern Chile, a segment of the subducting Nazca plate is bounded on the north by the Easter fault zone (subparallel to the Nazca Ridge) and on the south by the Challenger fault zone (Schweller and others, 1981). This Nazca plate segment is directly related to tectonism and volcanism in the Bolivian portion of the Andes.

In Bolivia, the Cordillera consists of three contiguous morphotectonic provinces, which are, from east to west, the Cordillera Oriental, Altiplano, and the Cordillera Occidental (figs. 1 and 2). Built across these provinces is the "central volcanic zone" (Thorpe and others, 1982), the largest of the three active volcanic chains in the Andean Cordillera. Here, volcanism has also been voluminous during most of the latter half of the Cenozoic, especially during the last 27 million years. The sites of former volcanoes define two arcs that merge at the southern end of the Altiplano. The eastern arc lies primarily in the Cordillera Oriental and consists of eroded calc-alkaline volcanoes that are late Oligocene and early to middle Miocene in age (27 to 11 Ma). The western arc (primarily in the Cordillera Occidental) forms the high crest of the Andes and is comprised of late Miocene to Holocene andesitic stratovolcanoes and voluminous ignimbrite sheets (Francis and others, 1983).

Calc-alkaline volcanic and intrusive rocks in the eastern arc (Cordillera Oriental) are the host for most of the Cenozoic polymetallic vein deposits in Bolivia and are closely associated with the hydrothermal activity that formed the veins. The volcanic and intrusive rocks range in age from about 27 to 11 Ma. Mineralization dates coincide with this time interval, with an apparent concentration between about 25 Ma and 15 Ma. In most mineralized areas, the age of mineralization is only slightly younger than intrusive and extrusive ages, confirming the observation that hydrothermal activity is fundamentally a late-stage part of the igneous system (McKee and Noble, 1990).

Bolivian polymetallic vein deposits appear to be smaller and less common on the Altiplano and in the Cordillera Occidental than in the Cordillera Oriental. This may be more apparent than real and could be the result of the relative lack of erosion of the younger volcanoes in the west or burial of older, mineralized hydrothermal systems by young, unaltered lava flows and ash-flow tuffs. Because it is much less deeply eroded, the western arc (Cordillera Occidental) appears to be more likely to host epithermal precious-metal deposits than polymetallic vein deposits. Because of the generally younger age of the igneous rocks, mineralization there is also younger.

REFERENCES CITED

Cox, Allan, and Dalrymple, G.B., 1967, Statistical analysis of geomagnetic reversal data and the precision of potassium-argon dating: Journal of Geophysical Research, v. 72, no. 10, p. 2603–2614.

Dalrymple, G.B., and Lanphere, M.A., 1969, Potassium-argon dating—Principles, techniques, and applications to geochronology: San Francisco, W.H. Freeman, 258 p.

Dewey, J.F., and Bird, J.M., 1970, Mountain belts and new global tectonics: Journal of Geophsyical Research, v. 75, p. 2625–2647.

Francis, P.W., Halls, C., and Baker, M.C.W., 1983, Relationships between mineralization and silicic volcanism in the central Andes: Journal of Volcanology and Geothermal Research, v. 18, p. 165–190.

Gamble, B.M., Ratté, J.C., Carrasco, Raul, Soria-Escalante, Eduardo, and McKee, E.H., 1991, Todos Santos district, *in* U.S. Geological Survey and Servicio Geológico de Bolivia, Geology and mineral resources of the Altiplano and Cordillera Occidental, Bolivia, *with a section on* Application of economic evaluations to mineral deposit models, by D.I. Bleiwas and R.G. Christiansen, U.S. Bureau of Mines: U.S. Geological Survey Bulletin 1975, p. 136–143.

Ingamells, C.O., 1970, Lithium metaborate flux in silicate analysis: Analytica Chimica Acta, v. 52, p. 323–334.

Instituto de Geología Económica, 1985, K-Ar ages of mineralization at the Caracoles, Siglo XX, Colquechaca, Colavi, Huari Huari, Unificada, Tasna, Inocentes, and Buena Vista mines in Bolivia: La Paz, Universidad Mayor de San Andres de Bolivia, Instituto de Geología Económica, Publicación Especial No. 2, p. 270–281.

Kussmaul, S., Jordan, L., and Ploskonka, E., 1975, Isotopic ages of Tertiary volcanic rocks of SW. Bolivia: Bundesanstalt für Bodenforschung und geologischen Landesämter, Geologische Jahrbuch, part B, v. 14, p. 111–120.

Long, K.R., Ludington, Steve, du Bray, E.A., André-Ramos, Orlando, and McKee, E.H., 1991, La Joya district, *in* U.S. Geological Survey and Servicio Geológico de Bolivia, Geology and mineral resources of the Altiplano and Cordillera Occidental, Bolivia, *with a section on* Application of economic evaluations to mineral deposit models, by D.I.

Bleiwas and R.G. Christiansen, U.S. Bureau of Mines: U.S. Geological Survey Bulletin 1975, p. 131–136

Ludington, Steve, Czamanske, G.K., Carrasco, Raul, Hinojosa-Velasco, Alberto, and McKee, E.H., 1991, Buena Vista area, *in* U.S. Geological Survey and Servicio Geológico de Bolivia, Geology and mineral resources of the Altiplano and Cordillera Occidental, Bolivia, *with a section on* Application of economic evaluations to mineral deposit models, by D.I. Bleiwas and R.G. Christiansen, U.S. Bureau of Mines: U.S. Geological Survey Bulletin 1975, p. 164–174.

Ludington, Steve, du Bray, E.A., and McKee, E.H., 1991, Kiska prospect, *in* U.S. Geological Survey and Servicio Geológico de Bolivia, Geology and mineral resources of the Altiplano and Cordillera Occidental, Bolivia, *with a section on* Application of economic evaluations to mineral deposit models, by D.I. Bleiwas and R.G. Christiansen, U.S. Bureau of Mines: U.S. Geological Survey Bulletin 1975, p. 191–192.

Ludington, Steve, Orris, G.J., Cox, D.P., and Asher-Bolinder, Sigrid, 1991, Mineral deposit models, *in* U.S. Geological Survey and Servicio Geológico de Bolivia, Geology and mineral resources of the Altiplano and Cordillera Occidental, Bolivia, *with a section* on Application of economic evaluations to mineral deposit models, by D.I. Bleiwas and R.G. Christiansen, U.S. Bureau of Mines: U.S. Geological Survey Bulletin 1975, p. 64–90.

McKee, E.H., and Noble, D.C., 1990, Cenozoic tectonic events, magmatic pulses, and base- and precious-metal mineralization in the central Andes, *in* Ericksen, G.E., Pinochet, Maria Teresa Cañaas, and Reinemund, J.A., eds., Geology of the Andes and its relation to hydrocarbon and mineral resources: Circum-Pacific Council for Energy and Mineral Resources Earth Science Series, v. 11, p. 189–194.

Ratté, J.C., Gamble, B.M., McKee, E.H., Soria-Escalante, Eduardo, and Carrasco, Raul, 1991, María Elena prospect (Cerro Culebra), *in* U.S. Geological Survey and Servicio Geológico de Bolivia, Geology and mineral resources of the Altiplano and Cordillera Occidental, Bolivia, *with a section on* Application of economic evaluations to mineral deposit models, by D.I. Bleiwas and R.G. Christiansen, U.S. Bureau of Mines: U.S. Geological Survey Bulletin 1975, p. 110–112.

Redwood, S.D., 1987, The Soledad Caldera, Bolivia—A Miocene caldera with associated epithermal Au-Ag-Cu-Pb-Zn mineralization: Geological Society of America Bulletin, v. 99, p. 395–404.

Richter, D.H., Brooks, W.E., Cox, D.P., Shew, Nora, Bailey, Elizabeth, Hinojosa-Velasco, Alberto, and Escobar-Diaz, Angel, 1991, Escala district, *in* U.S. Geological Survey and Servicio Geológico de Bolivia, Geology and mineral resources of the Altiplano and Cordillera Occidental, Bolivia, *with a section on* Application of economic evaluations to mineral deposit models, by D.I. Bleiwas and R.G. Christiansen, U.S. Bureau of Mines: U.S. Geological Survey Bulletin 1975, p. 159–161.

Richter, D.H., Brooks, W.E., Ludington, Steve, Hinojosa-Velasco, Alberto, Escobar-Diaz, Angel, McKee, E.H., and Shew, Nora, 1991, San Cristobal district, *in* U.S. Geological Survey and Servicio Geológico de Bolivia, Geology and mineral resources of the Altiplano and Cordillera Occidental, Bolivia, *with a section on* Application of economic evaluations to mineral deposit models, by D.I. Bleiwas and R.G. Christiansen, U.S. Bureau of Mines: U.S. Geological Survey Bulletin 1975, p. 153–156.

Richter, D.H., Brooks, W.E., Shew, Nora, Hinojosa-Velasco, Alberto, and Escobar-Diaz, Angel, 1991, Cerro Eskapa, *in* U.S. Geological Survey and Servicio Geológico de Bolivia, Geology and mineral resources of the Altiplano and Cordillera Occidental, Bolivia, *with a section on* Application of economic evaluations to mineral deposit models, by D.I. Bleiwas and R.G. Christiansen, U.S. Bureau of Mines: U.S. Geological Survey Bulletin 1975, p. 116–118.

Schweller, W.J., Kulm, L.D., and Prince, R.A., 1981, Tectonics, structure, and sedimentary framework of the Peru-Chile trench, *in* Kulm, L.D., Dymend, E.J., Dasch, E.J., and Hussong, D.M., eds., Nazca plate—Crustal formation and Andean convergence: Geological Society of America Memoir 154, p. 323–349.

Stacey, J.S., Sherrill, N.D., Dalrymple, G.B., Lanphere, M.A., and Carpenter, N.V., 1981, A five-collector system for the simultaneous measurement of argon isotopic ratios in a static mass spectrometer: International Journal of Mass Spectrometry and Ion Physics, v. 39, p. 167–180.

Steiger, R.H. and Jaeger, E., 1977, Subcommission on Geochronology—Convention on the use of decay constants in geo- and cosmochronology: Earth and Planetary Science Letters, v. 36, p. 359–362.

Thorpe, R.S., Francis, P.W., Hammill, M., and Baker, M.C.W., 1982, The Andes, *in* Thorpe, R.S., ed., Andesites: New York, John Wiley and Sons, p. 187–205.

U.S. Geological Survey and Servicio Geológico de Bolivia, 1991, Geology and mineral resources of the Altiplano and Cordillera Occidental, Bolivia, *with a section on* Application of economic evaluations to mineral deposit models, by D.I. Bleiwas and R.G. Christiansen, U.S. Bureau of Mines: U.S. Geological Survey Bulletin 1975, 365 p.

CHAPTER J

GOLD AND SILVER IN ACID-SULFATE ALTERATION AND QUARTZ-SERICITE-PYRITE STOCKWORKS, LA ESPAÑOLA PROSPECT, NORTHWESTERN ALTIPLANO, BOLIVIA

By ALBERT HOFSTRA,[1] RICHARD F. HARDYMAN,[2] LUIS BARRERA,[3] *and* ORLANDO SANJINES[3]

ABSTRACT

La Española prospect is located in the Bolivian portion of the Neogene to Quaternary magmatic arc of the central Andes. La Española was selected for study because it is the most intense color anomaly recognized on remote sensing imagery in the region. Field mapping and preliminary laboratory studies were conducted by geologists from GEOBOL (Servicio Geológico de Bolivia) and the USGS (U.S. Geological Survey) as part of a training program in volcanic-hosted precious metal deposits that was funded by the Inter-American Development Bank.

The hydrothermal system is centered on a 1.5 by 3 km composite dacite porphyry stock that intrudes upper Oligocene to middle Miocene andesitic to dacitic flows, lahars, and volcaniclastic sedimentary rocks. The stock consists of at least four intrusive phases that are sericitically altered, including one distinguished by an abundance of miarolitic cavities. Several small unaltered dacite porphyry dikes and plugs intrude altered dacite porphyry. K-Ar determinations on hornblende in pre-mineralization dacite flows (11.2±0.7 Ma) and on biotite from a pre-mineralization intrusive phase in the composite dacite porphyry stock (11.8±0.8 Ma) have similar ages. A K-Ar determination on alunite yielded an age of 10.3±0.3 Ma. The hydrothermal system is therefore about 1 Ma younger than the host composite dacite porphyry stock.

La Española prospect contains three types of mineral occurrences: (1) epithermal acid-sulfate-type mineralization characterized by an early stage of vuggy silica and quartz-alunite alteration and a second stage of silicification with pyrite-barite ± enargite ± galena ± sphalerite ± gold ± silver; (2) gold- and silver-bearing quartz-sericite-pyrite stockwork veinlets in the sericitic zone of a dacite porphyry stock; and (3) epithermal adularia-sericite-type quartz-pyrite-chalcopyrite-sphalerite veins on the margins of the stock.

Gold potential is believed to lie primarily in low-grade stockwork zones within the stock and in epithermal acid-sulfate mineralization along structures within and adjacent to the stock. Bulk samples from stockwork zones yield gold values of 50 to 1,700 ppb, and values of 2,000 ppb have been measured in hand samples of acid-sulfate mineralization. Potential for undiscovered stockwork and (or) acid-sulfate mineralization exists at depth within the system.

INTRODUCTION

La Española prospect is located at 17°14′ south latitude and 69°31′ west longitude in the Bolivian Andes, 187 km southwest of the capitol city of La Paz (fig. 1). The prospect is on the northwest margin of the Altiplano where it meets the eastern flank of the Cordillera Occidental. The elevation of the valley floor in this part of the Altiplano is about 4,000 m, and many of the volcanic summits in the area rise over 5,000 m. The prospect is

[1]U.S. Geological Survey, Mail Stop 973, P.O. Box 25046, Denver Federal Center, Denver, CO 80225.

[2]U.S. Geological Survey, University of Nevada, Makay Building, RMSM 101A, Reno, NV 89557.

[3]Servicio Geológico de Bolivia, Calle Frederico Zuazo No. 1673, Casilla 2729, La Paz, Bolivia.

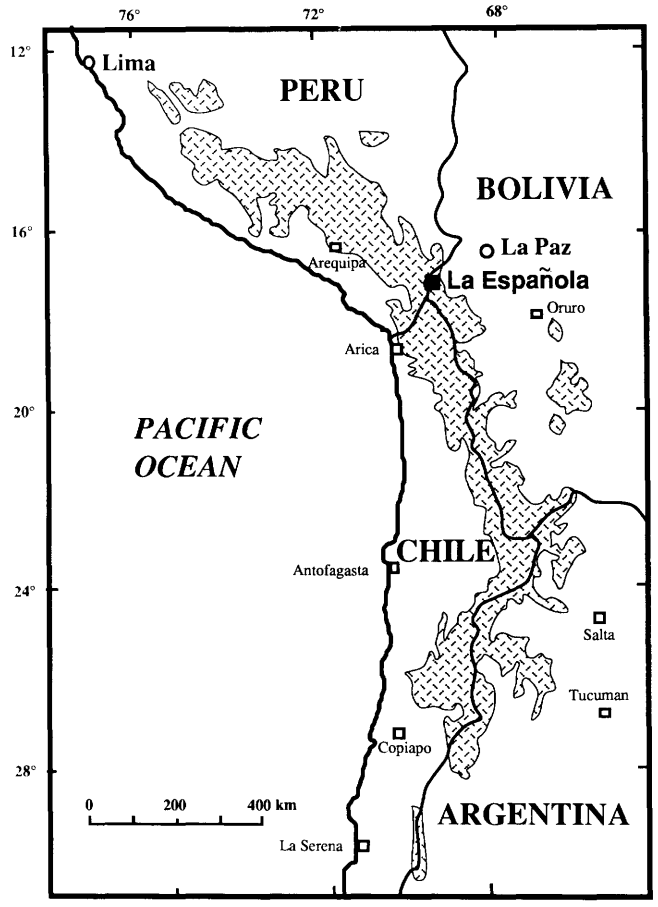

Figure 1. Location map showing the position of La Española prospect within the Neogene to Quaternary volcanic arc of the central Andes (stippled pattern). Adapted from Ericksen and others (1986).

within the Neogene to Quaternary volcanic arc of the central Andes (fig. 1). Much of the exploration effort in the region has focused on the numerous prominent alteration zones that are spatially associated with eruptive centers, especially stratovolcanoes, caldera complexes, and dome fields. Ore types present in this setting include Ag-Au veins and disseminations; polymetallic Ag–base metal veins; polymetallic Sn veins; porphyry Au-Cu, Ag-Cu, and Sn deposits; and numerous geothermal springs (Ericksen and others, 1986; Cunningham and others, 1991). Recent discoveries of large, low-grade precious metal deposits include La Joya (Bolivia) and La Coipa (Chile), which are mined by open-pit methods.

This report is an outgrowth of a two-year training project funded by the Inter-American Development Bank. The project is directed at training geologists from the national geological institutions of Bolivia, Chile, and Peru in modern techniques for studying and evaluating precious-metal deposits in volcanic rocks of the central Andes. The project included initial training in remote sensing, volcanology, and hydrothermal systems, followed by field and laboratory studies of several anomalous areas.

Processing of the remote-sensing imagery during the first year lead to the discovery of a strong color anomaly at the La Española prospect that is indicative of iron oxides and sericite (Jimenez and others, 1991). This is the largest and most intense anomaly recognized in the region. During the second year, the La Española prospect was the site of preliminary geologic mapping at scales of 1:50,000 and 1:10,000 by geologists at GEOBOL. Much of the mapping was conducted by Luis Barrera of GEOBOL as part of his senior thesis at the University of San Andres in La Paz. Since 1988, the potential for bulk minable precious-metal deposits at La Española has been under investigation by Expromin S.R.L. of La Paz.

This report is based on three days of field work spent reviewing the geology, alteration, and mineralization at La Española and builds on the geologic framework studies of geologists at GEOBOL and Expromin. Two days were also spent collecting samples for geochemical studies that will be the subject of another report. Several thin sections and X-ray diffraction spectra were also studied in the laboratory. The purpose of this preliminary report is to provide brief descriptions of some of the different types of alteration and mineralization present at La Española and to evaluate the significance of these features within the context of modern ore deposit models. Future field and laboratory studies are planned to test the validity of these first impressions.

LOCAL GEOLOGY

All of the rocks exposed in the La Española area (fig. 2) are late Oligocene or younger in age and were deposited in a volcanic-chain depositional environment (Wallace and others, 1991). The geology consists of an upper Oligocene to middle Miocene sequence of andesitic to dacitic volcanic flows, volcaniclastic sedimentary rocks, and lahars that were intruded by a composite dacite porphyry stock at about 11 Ma. Alteration and mineralization are centered on the dacite porphyry intrusive complex and appears to be about the same age. Figure 3 is a view looking southwest of the La Española prospect. The two light-colored hills in the foreground, San Geronimo and Jichu Cunca, are composed of the altered dacite porphyry intrusive complex. The major lithologic units are described below.

MAURI FORMATION

Rocks of the upper Oligocene to middle Miocene Mauri Formation crop out along the east and south sides

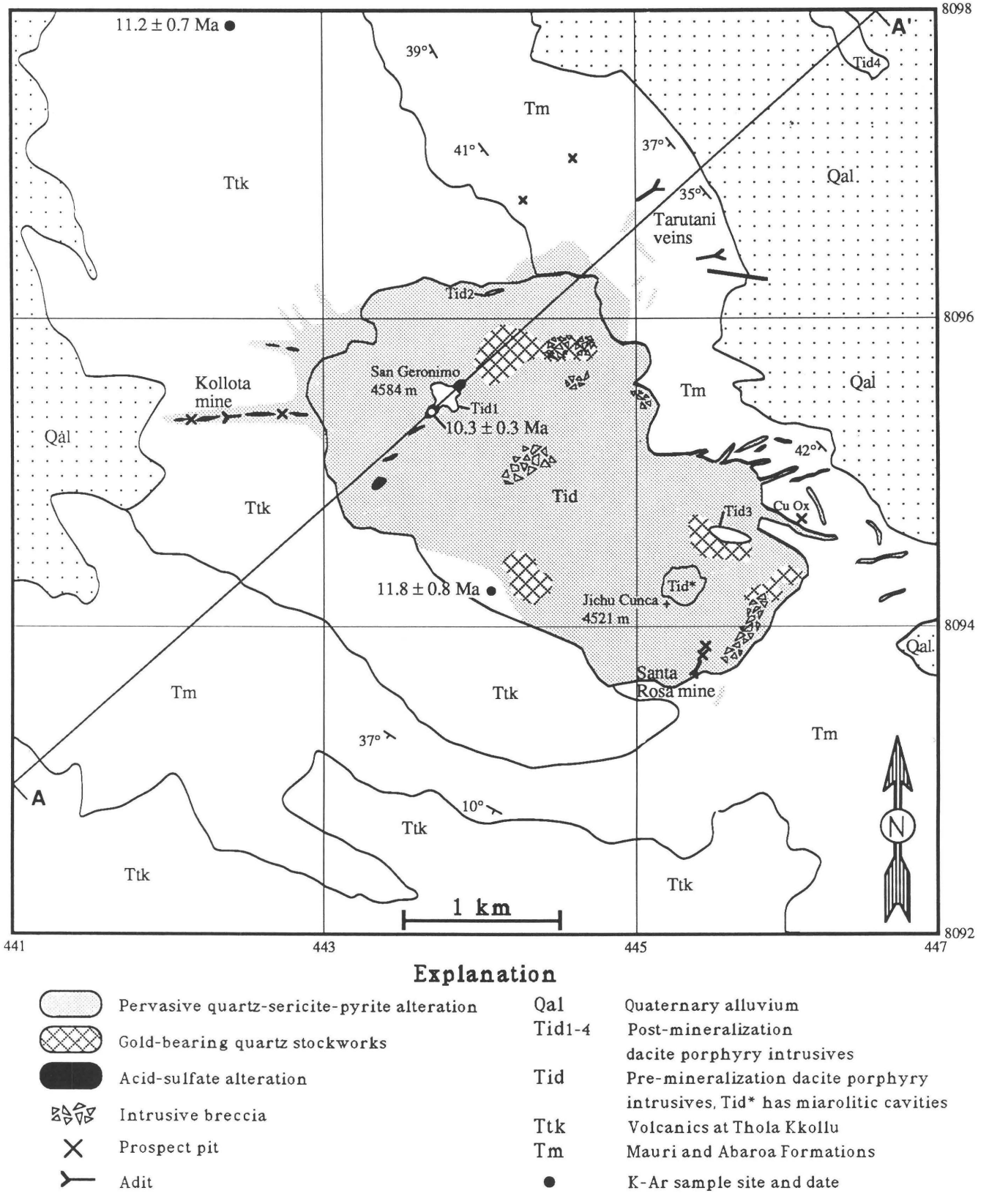

Figure 2. Simplified geologic map of La Española prospect, modified from mapping by L. Barrera and Expromin geologists. A–A′ is the line of cross section for figure 11. Coordinates in thousands of meters are from zone 19 of the transverse Mercator projection, international spheroid.

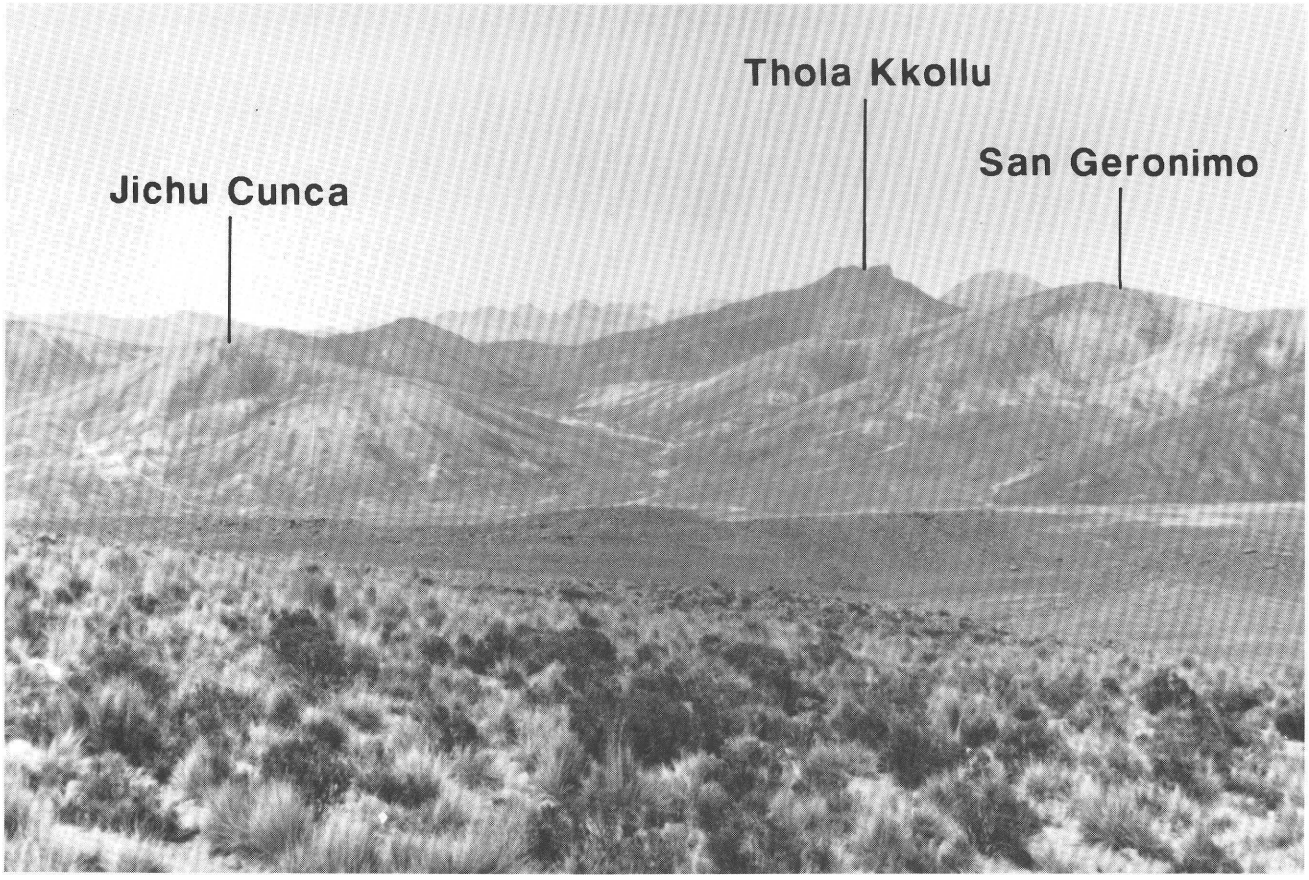

Figure 3. Photograph of La Española prospect looking southwest. San Geromino hill (4,584 m) and Jichu Cunca hill (4,521 m) are comprised of the altered dacite porphyry intrusive complex. Thola Kkollu hill (4,842 m) is visible in the background, and the crest of the Cordillera Occidental is in the far background.

of La Española and strike approximately N. 30° W. and dip to the west at about 40° (fig. 2). The steep dips are probably due to block faulting associated with an episode of middle Miocene uplift that affected this part of the Altiplano (Wallace and others, 1991). The base of the Mauri Formation is not exposed at La Española, although, about 20 km to the east, it lies unconformably on red arkosic sandstones of the middle Oligocene Berenguela Formation (Jimenez and others, 1991; Wallace and others, 1991). In the Berenguela area, the Mauri Formation has been divided into upper and lower parts. The upper part is not present in the La Española area. The lower part consists of purple and green volcaniclastic conglomerate, sandstone, siltstone, and mudstones deposited in an alluvial-fan environment. These rock units are overlain by the Abaroa Formation, which consists of volcaniclastic breccias and lahars that contain blocks of pyroxene andesite in a volcaniclastic matrix. Small pyroxene andesite flows and dikes are also present. Recent mapping by GEOBOL and USGS geologists indicate that the Abaroa Formation is the time-equivalent western facies of the lower Mauri in the Berenguela area. The Mauri and Abaroa Formations have therefore been combined on figure 2 (area labeled Tm). The upper age limit of the lower Mauri is constrained by a K-Ar age on biotite from a tuff near Berenguela that yielded an age of 13.6±1.1 Ma (Carlos Perez de Arce R., Laboratorio De Geocronologia, Servicio Nacional De Geologia Y Mineria—Chile, unpub. data). Evernden and others (1977) and Lavenu and others (1989) report ages for the Abaroa Formation that range from 21.6 to 13.5 Ma.

VOLCANICS AT THOLA KKOLLU

At La Española, the Mauri Formation is unconformably overlain by a sequence of nearly flat-lying lahars and dacite flows informally named here the volcanics at Thola Kkollu (Ttk on fig. 2). Some of the flows appear to be derived from a volcanic center at Thola Kkollu hill (fig. 3), 1 km southwest of the map area on figure 2, although this remains to be confirmed. Dips measured in these units are less than 12°, suggesting that there has been little or no tilting since deposition. The age of the rocks is constrained by two K-Ar determinations. Hornblende

from a dacite dike that crosscuts one of the lahars yielded an age of 11.2±2.4 Ma (Carlos Perez de Arce R. at the Laboratorio De Geocronologia, Servicio Nacional De Geologia Y Mineria—Chile, unpub. data). Another hornblende from a dacite flow from the same area yielded and age of 11.2±0.7 Ma (M. Macintyre, Scottish Universities Research Reactor Center, SURRC, U.K., unpub. data).

DACITE INTRUSIVE COMPLEX

A composite dacite porphyry stock was emplaced into the Mauri Formation and the volcanics at Thola Kkollu prior to mineralization (Tid and Tid* on fig. 2). From existing exposures it was impossible to determine whether the intrusive reached the surface, although if it did, all remnants of the overlying volcanic edifice have been removed. The stock measures about 1.5 km by 3 km in plan, is sericitically altered, and locally hosts some of the gold mineralization. Intrusive breccias are present at a few localities within the complex (fig. 2). Five or more intrusive phases are recognized, based on differences in phenocryst assemblages or abundance of miarolitic cavities. The contacts between all of the different intrusive phases have not yet been mapped. The intrusive dacite porphyry, labeled Tid on figure 2, is thought to consist of four or more intrusive phases. Most of the composite intrusive (Tid) is composed of two intrusive phases; one that contains greater than 20 percent phenocrysts and another that contains less than 5 percent phenocrysts. In both, seriate zoned plagioclase (1–7 mm) and hornblende (0.5–4 mm) are the most prominent phenocrysts. Biotite (< 1 mm) is usually visible in thin section. Another phenocryst-rich intrusive phase on the southwest side of Jichu Cunca hill can be distinguished by the presence of embayed (~ 1 mm) phenocrysts of quartz. The dacite porphyry intrusion mapped on top of Jichu Cunca hill (Tid* on fig. 2) is a phenocryst-rich plagioclase-hornblende dacite that is distinguished by the presence of abundant miarolitic cavities, 5 mm to 3 cm in size, lined with drusy quartz.

On the west side of the complex is another dacite intrusive phase that can be distinguished by the presence of 3 to 6 mm phenocrysts of biotite. This intrusive is sericitically altered except near its westernmost contact where it is nearly fresh. Biotite from this locality (fig. 2) yielded a K-Ar age of 11.8±0.8 Ma (M. Macintyre, Scottish Universities Research Reactor Center, SURRC, U.K., unpub. data).

Several near-vertical dacite porphyry dikes emanate from the south side of the main intrusive body and appear to occupy a radial fracture system (fig. 2). Some are phenocryst rich, and some are phenocryst poor. Two of the dikes dip toward the main intrusive body at about 45° and may have been emplaced along ring fractures or, more likely, along the steeply dipping bedding of the Mauri Formation. The contact between the dacite porphyry and the Mauri Formation is well exposed in this area and is knife sharp.

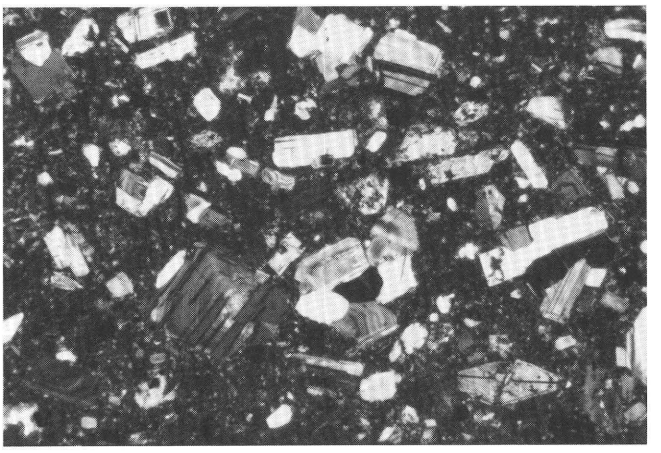

Figure 4. Photomicrograph of unaltered plagioclase-hornblende dacite porphyry from the top of San Geronimo hill (Tid1 on fig. 2). Note the seriate zoned plagioclase, twinned hornblende, and aphanitic groundmass. Field of view is 16 mm wide, crossed polars.

The early-altered dacites (Tid and Tid*) are intruded by several small dacite porphyry dikes and plugs that are fresh or exhibit weak propylitic alteration. A small plagioclase-hornblende dacite porphyry plug is present (Tid1 on fig. 2) on top of San Geronimo hill that is mineralogically and texturally very similar to the pre-mineralization phenocryst-rich dacite except that it is unaltered and lacks miarolitic cavities. The close similarity of this plug to the early-altered dacites (Tid and Tid*) suggests that both were derived from the same parent magma. Figure 4 is a photomicrograph of a sample from this intrusive (Tid*) showing seriate zoned plagioclase and twinned hornblende in an aphanitic groundmass. This plug crosscuts quartz-sericite-pyrite (QSP) and acid-sulfate-altered dacite porphyry (fig. 2). Also present are green- and brown-colored plagioclase-hornblende dikes (Tid2 and Tid3 on fig. 2) that contain about 10 percent phenocrysts and have much smaller phenocrysts (< 3 mm) than the other dacite intrusions. Some of these dikes cut QSP alteration and gold-bearing stockwork zones. Another unaltered phenocryst-rich plagioclase-hornblende dacite porphyry projects through alluvial cover in the northeast part of the map area (Tid4 on fig. 2). Miarolitic cavities were not observed in any of the post-mineralization intrusives.

The K-Ar ages suggest that the volcanics at Thola Kkollu and the pre-mineralization dacite porphyry stock are about the same age, 11 Ma. Mineralization is younger than the volcanics at Thola Kkollu (11.2±0.7 Ma) that are altered and mineralized and younger than the biotite-rich intrusive phase of the composite dacite porphyry stock that is also altered and mineralized (11.8±0.8 Ma).

ALTERATION AND MINERALIZATION

Several types of alteration and mineralization are present in and around the intrusive complex. Some exhibit characteristics of porphyry-style mineralization and others exhibit characteristics of epithermal acid-sulfate- and adularia-sericite-type mineralization. Descriptions of these rocks and the genetic implications of some of the features present are discussed below.

DRUSY QUARTZ VUGS

Vugs lined with drusy quartz that are up to 3 cm in diameter (e.g., fig. 5*A*) occur sporadically throughout the intrusive complex but are most common in the dacite porphyry exposed near the summit of Jichu Cunca hill (Tid* on fig. 2). At some localities, pyrite and chalcopyrite are associated with quartz. Quartz crystals in these cavities contain secondary vapor-dominant inclusions and aqueous inclusions that contain halite daughter minerals (figs. 5*B* and 5*C*). The fluid inclusions are characteristic of the porphyry environment and provide evidence of boiling. In some cases, the quartz also contains microscopic inclusions of rutile (fig. 5*D*), another feature commonly found in porphyry systems (Rose and Burt, 1979; Cox, 1986). Vugs lined with drusy quartz occur regardless of alteration zone and appear in vuggy silica, quartz-alunite, and QSP-altered rocks. Alunite encrustations on top of the drusy quartz clearly show that acid-sulfate alteration postdates the drusy quartz. The vugs of drusy quartz are thought to be miarolitic cavities or segregations that formed from a residual, immiscible, low-density fluid as the dacite porphyry intrusions cooled. The presence of miarolitic cavities in the pre-mineralization intrusives attests to the high volatile content of the magmas.

PERVASIVE ALTERATION

The dacite porphyry intrusive complex and portions of the surrounding volcanic host rocks are pervasively altered to an assemblage of quartz, sericite, and pyrite (QSP) (fig. 2). Thin sections show that, in the least altered samples, mafic minerals are destroyed and plagioclase is partially altered to very fine grained (< 20 microns) sericite. In the most intensely altered samples, all of the rock-forming minerals have been converted to an assemblage of quartz, sericite, and pyrite, and the sericite is coarser, ranging up to 1 mm (fig. 6). In a few samples, crystals of potassium feldspar are present that locally are partially to completely replaced by sericite (fig. 6). X-ray diffraction studies of samples from Jichu Cunca hill and San Geronimo hill show that QSP-altered dacite often contains gypsum and occasionally kaolinite or potassium feldspar in addition to sericite. The gypsum is thought to be the secondary hydration product of primary anhydrite. The kaolinite may be hydrothermal in origin or, more likely, is a supergene alteration product related to the oxidation of pyrite.

QSP alteration is largely restricted to the dacite porphyry intrusive complex, although locally, the surrounding host rocks are also altered (fig. 2), especially along

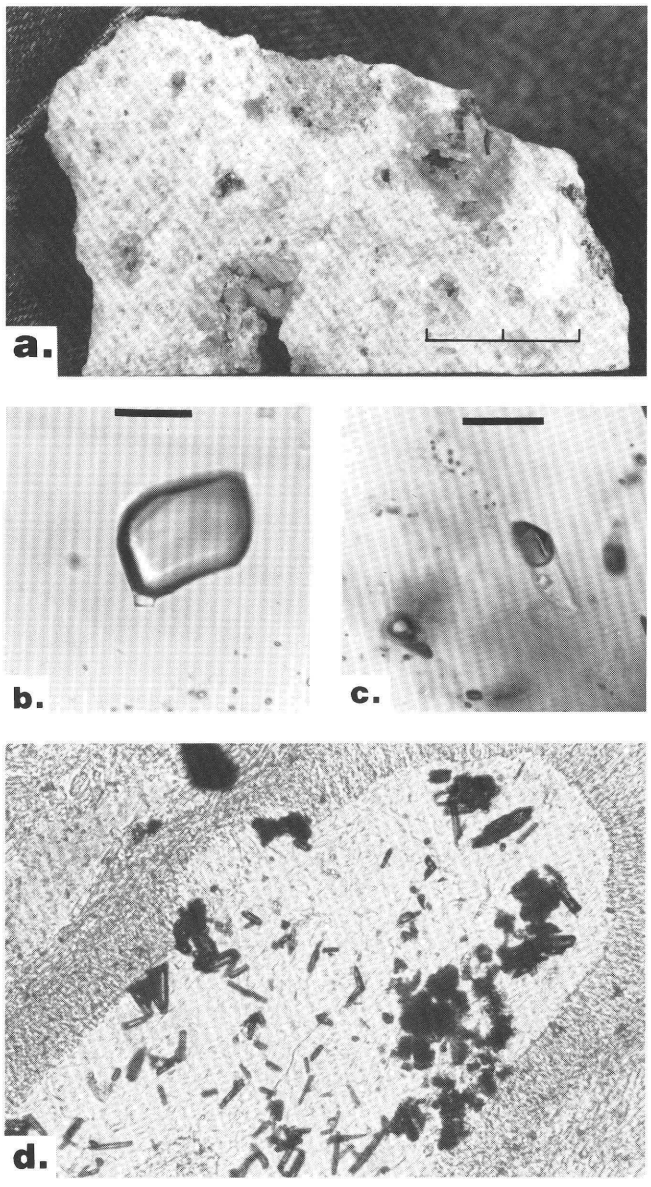

Figure 5. *A*, Photograph of miarolitic cavities in dacite porphyry from Jichu Cunca hill (Tid*). The scale is in centimeters. *B*, Photomicrograph of secondary gas-dominant inclusion with halite daughter mineral. *C*, Photomicrograph of secondary aqueous inclusion with halite daughter mineral. The fluid inclusions are in quartz from a miarolitic cavity. The black bar is 12 microns long. *D*, Photomicrograph of miarolitic cavity filled with quartz containing inclusions of rutile. Field of view is 1 mm wide, plane polarized light.

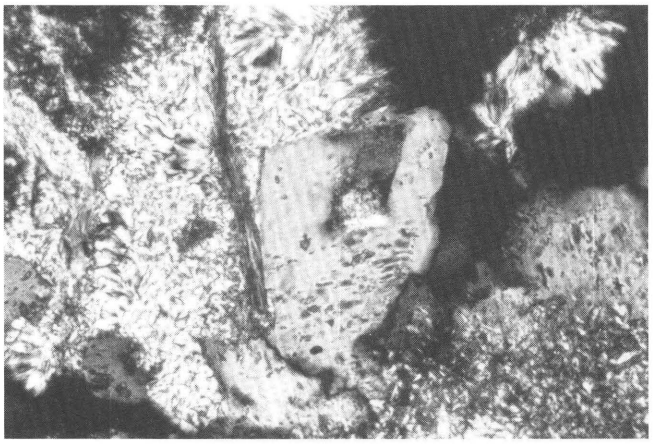

Figure 6. Photomicrograph of fibrous sericite, rhomb-shaped potassium feldspar, and opaque pyrite in a sample from the southwest side of Jichu Cunca hill. Fluid inclusions are visible in the potassium feldspar. Field of view is 4 mm wide, crossed polars.

fracture zones. For example, the dacite porphyry dikes emanating from the south side of the intrusive complex exhibit weak QSP alteration even though some of the dikes are less than 1 m in width. The host upper Mauri Formation at this locality is only propylitically altered even when in direct contact with QSP-altered dacite porphyry. However, on the north and west sides of the main intrusion, the volcanic host rocks exhibit pervasive QSP alteration that grades outward into propylitic alteration.

Within 0.5 to 1 km of the intrusive complex, the Mauri Formation and volcanics at Thola Kkollu are propylitically altered and contain chlorite, variable amounts of disseminated pyrite, calcite ± quartz veinlets, disseminated calcite, and disseminated epidote. On the northeast side of the intrusive, in the vicinity of the Tarutani veins, disseminated hematite in the Mauri Formation is present that may be hydrothermal in origin.

The presence of relict potassium feldspar and gypsum (after anhydrite) is important because K-spar and anhydrite are characteristic of the high-temperature, potassic zone of porphyry systems (Rose and Burt, 1979). The pervasive QSP alteration zone apparently collapsed inward, overprinting the earlier potassic alteration at La Española—this is common in many porphyry systems.

STOCKWORK MINERALIZATION

Previous to our field work, Expromin geologists identified three areas of stockwork mineralization that contain gold. Each of the stockwork zones is located near the margin of the dacite porphyry intrusive complex (fig. 2). Figure 7*A* is a photograph of stockwork mineralization outcropping on the east side of San Geronimo hill. Figure 7*B* is a closer view of the stockworks that occur throughout

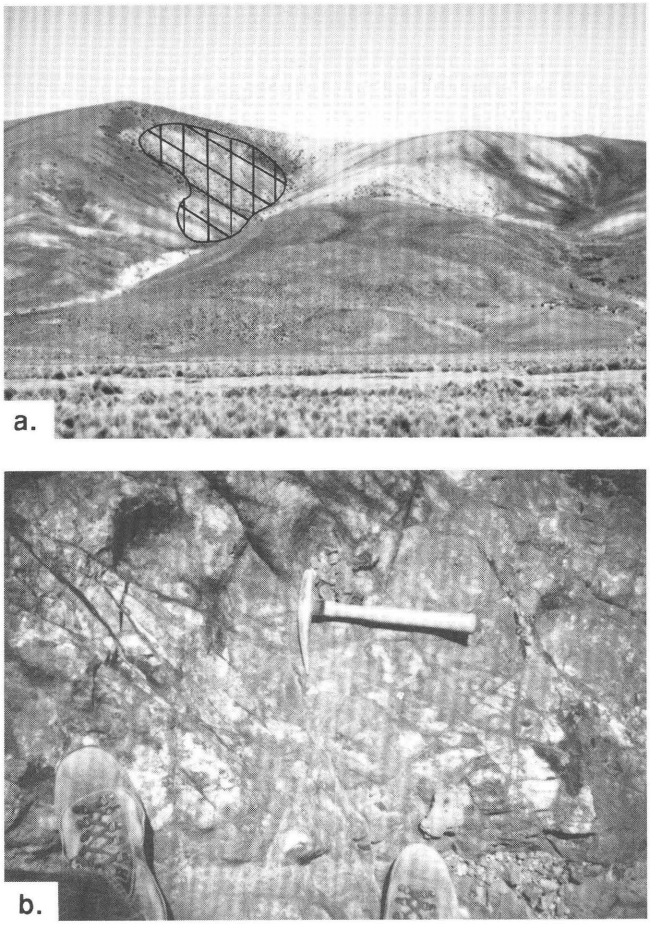

Figure 7. *A,* Photograph of gold-bearing stockwork zone on the east side of San Geronimo hill. *B,* Outcrop of stockwork zone that contains 1.2 ppm gold. Each veinlet contains quartz, sericite, and iron oxides after pyrite.

this zone. The stockworks consist of several generations of quartz veinlets, typically less than 2 mm in width, that also contain sericite and pyrite. Greater concentrations of disseminated pyrite are observed in and around the stockwork zones. The fracture density is around 10 fractures per square meter, and the fractures lack a strong preferred orientation. The intensity of gold mineralization in the stockwork zones correlates with the amount of quartz introduction; i.e., the more prominent the quartz veinlets, the higher the gold values (R. Terrazas, Expromin, oral commun., 1991). Fracture density is less important. Chemical analyses of channel samples (~ 0.1 m wide by 3 m long) and of bulk samples from prospect pits in stockwork zones yield gold values of 50 to 1,700 ppb (R. Terrazas, Expromin, oral commun., 1991). High gold values correlate spatially with high copper values. Silver values range between about 0.5 and 20 ppm, and copper values of up to 0.16 percent were encountered. The Ag/Au ratios in all three areas are generally less than 10. Arsenic, antimony, silver, lead, and zinc concentrations are sporadically

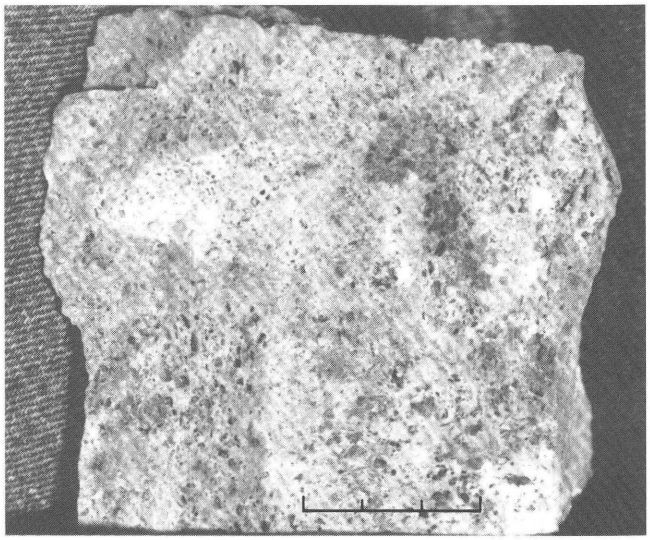

Figure 8. Photograph of hand specimen showing vuggy silica alteration developed in brecciated dacite porphyry from the southwest side of San Geronimo hill. The dark material is geothite and hematite after pyrite. Scale is in centimeters.

anomalous, but mercury is not (R. Terrazas, Expromin, oral commun., 1991). Drainage sediments below stockwork mineralization on the northeast side of San Geronimo contain gold flakes up to 3 mm in maximum dimension, with 1 mm flakes being relatively common. This suggests that the gold in the stockwork zones is fairly coarse grained. The geologic setting, mineralogy, and geochemical signature of the stockwork mineralization at La Española is similar to the gold-rich porphyry systems of the Maricunga belt of Chile (Vila and Sillitoe, 1991) and to other gold-rich porphyry systems on the Pacific Rim (Rytuba and Cox, 1991).

ACID-SULFATE ALTERATION ON SAN GEROMINO HILL

Several zones of acid-sulfate alteration are present on top of San Geronimo hill (fig. 2). These rocks form prominent blocky outcrops resistant to erosion. Two types of acid-sulfate alteration are present that are superimposed on the earlier, pervasive QSP alteration. Vuggy silica alteration consists of the residual silica left over after extreme acid leaching of the host rock and variable amounts of sugary quartz introduced by the hydrothermal fluids (fig. 8). Quartz-alunite alteration consists of a fine-grained intergrowth of quartz, alunite, and pyrite that locally contains clots of bladed alunite up to 2 mm in size (e.g., fig. 9*B*). The vuggy silica and quartz-alunite-altered rocks usually contain abundant red and brown iron oxides after pyrite. Occasionally vuggy silica can be observed to grade outward into quartz-alunite alteration, but more often it grades abruptly into QSP alteration. No barite or

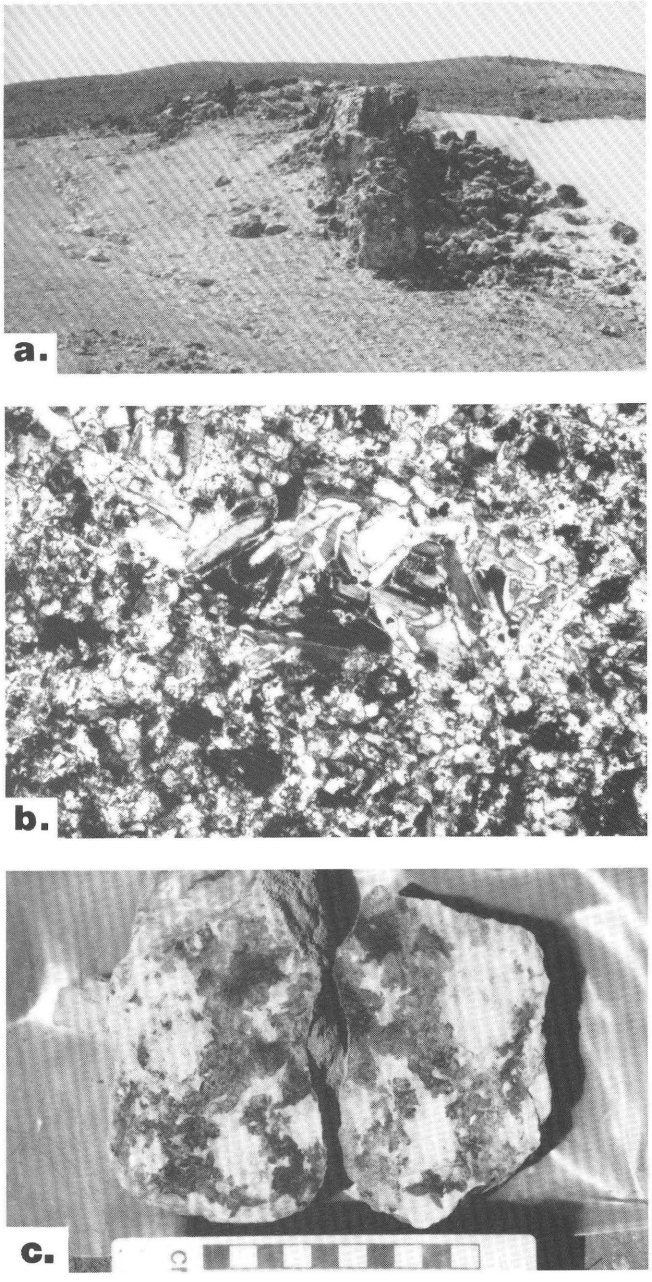

Figure 9. *A,* View looking east of vuggy silica and quartz-alunite altered dacite flow at the Kollota mine. Vuggy silica rubble on top of San Geronimo hill is visible in the upper right. *B,* Photomicrograph of quartz-alunite alteration. Lath-shaped crystals are alunite; ground mass is predominantly quartz. Field of view is 5 mm wide, crossed polars. *C,* Barite-enargite veinlet in quartz-alunite-altered dacite flow from the Kollota mine dump.

sulfides other than pyrite were observed in these outcrops. X-ray diffraction studies of samples from this locality show that kaolinite and pyrophyllite are also present. Some of the vuggy silica zones form dike-like bodies with a strong vertical aspect. Float boulders of vuggy silica

were also observed on Jichu Cunca hill, suggesting that acid-sulfate alteration is present in the southern part of the intrusive complex.

The geologic setting, presence of vuggy silica with quartz-alunite alteration, and the dike-like morphology of the altered zones are characteristic of magmatic hydrothermal acid-sulfate systems (Rye and others, 1991). This type of acid-sulfate alteration typically develops at shallow levels some distance above the mineralized portions of porphyry systems (Vila and Sillitoe, 1991). These rocks are also often the site of subsequent precious-metal mineralization (Heald and others, 1987; Hedenquist, 1987). The textural characteristics of the acid-sulfate alteration preserved on San Geronimo suggest that it formed at some distance below the surface and that there has been significant erosion since its formation. Opaline silica and chalcedonic quartz are absent; quartz and alunite are relatively coarsely crystalline; pyrophyllite is present, suggesting temperatures of 260°C or more (White and Hedenquist, 1990); and no flat-lying paleosurface or paleo-water-table features are preserved.

A sample of coarsely crystalline (1–2 mm) alunite from the acid-sulfate-altered zone on top of San Geronimo hill (fig. 2) was dated by the K-Ar method and yielded an age of 10.3±0.3 Ma (E.H. McKee, unpub. data). This is about 1 m.y. younger than the age (11.8±0.8 Ma) of the biotite-rich phase of the host intrusive complex.

KOLLOTA MINE

The Kollota mine is located on the west side of the intrusive complex where several prospect pits and an adit are developed along an east-west-striking fracture zone (fig. 2). The volcanic dacite flows along the structure are pervasively altered in a 2- to 4-m-wide zone to vuggy silica, quartz-alunite, or quartz-kaolinite that are resistant to erosion (fig. 9*A*). Figure 9*B* is a photomicrograph of quartz-alunite alteration from this outcrop. The acid-sulfate alteration is surrounded by a 10- to 25-m-wide envelope of quartz-sericite-pyrite alteration that abruptly grades into the propylitically altered volcanics. Locally, the fracture zone is brecciated and partially cemented with sugary, fine-grained quartz and pyrite. Unoxidized samples of vuggy silica often contain as much as 10 percent disseminated pyrite (< 1 mm size), and barite crystals up to 2 cm long are locally present in open spaces. Some of the acid-sulfate-altered dump samples are also crosscut by barite-enargite veinlets. Figure 9*C* is a photo of a hand sample that split along a barite-enargite veinlet. A rock sample containing barite-enargite veinlets contained 2 ppm gold (R. Terrazas, Expromin, oral commun., 1991). X-ray diffraction studies of samples from the Kollota mine dumps confirmed the field identification of alunite, barite, kaolinite, and sericite. A small, dark reddish-brown gossan about 1 by 3 m in size was also observed at this locality, suggesting that larger concentrations of sulfides are present locally within this zone.

The geologic features of the Kollota mine are characteristic of epithermal acid-sulfate or high-sulfidation systems (Heald and others, 1987; Hedenquist, 1987). The geologic setting, mineral assemblages, and two-stage paragenesis characterized by early acid-sulfate alteration followed by later quartz-pyrite-barite-enargite-gold precipitation is typical of these systems.

SANTA ROSA MINE

On the south side of Jichu Cunca hill are several prospect pits and adits of the Santa Rosa mine that date from Spanish Colonial times. The workings are along a pyritic, silicified fracture zone that contains high silver values. The structure strikes approximately N. 45° E. within QSP-altered dacite porphyry (fig. 2). Many of the rocks on the dump are breccias that contain fragments of vuggy-silica-altered dacite porphyry that are cemented by sugary, fine-grained quartz and pyrite. However, no alunite or kaolinite alteration was recognized in the field. Some of the breccias are cemented by a later stage of fine-grained quartz containing pyrite, barite, sphalerite, galena, and a relatively abundant, unidentified, dark-gray sulfosalt mineral. The sulfides and sulfosalt minerals are generally less than 2 mm in size, whereas barite crystals range up to 1 cm. A later stage of silicification consists of gray to white chalcedonic quartz that locally fills the remaining porosity in the breccia. Mineralization and silicification at Santa Rosa appears to be younger than the pervasive QSP alteration in the host dacite porphyry.

The mineralization at Santa Rosa has many similarities to the epithermal acid-sulfate mineralization at Kollota, except that alunite and kaolinite alteration is poorly developed, and greater amounts of silica and base-metals were introduced. The breccia fragments of vuggy silica, intense silification, abundance of pyrite and barite, and the relatively small amounts of open-space filling are characteristic of epithermal acid-sulfate systems.

TARUTANI VEINS

On the northeast flank of the main intrusive body, the lower Mauri Formation is host to Cu-Zn-bearing quartz veins of the adularia-sericite type (figs. 2 and 10). All of the Tarutani veins fill open spaces along fractures with little or no silicification of the wallrock. Pyrite, chalcopyrite, and sphalerite are the main sulfides present. To date, no geochemistry has been done to determine whether the veins carry significant gold or silver values. Figure 2

shows two prospect pits that were developed on two veins, 1 to 3 cm in width, each enclosed within a narrow 1–3 cm envelope of QSP alteration. Mine adits were developed on the two largest veins. The northern adit exploited a 6- to 10-cm-wide vein that strikes N. 62° E. and dips 70° to the north (fig. 10*A*). It is composed of several generations of 1- to 3-mm-size quartz that contains 1 to 10 volume percent sulfides. The vein is locally brecciated. The sulfides in the vein are generally less than 5 mm in size. Some of the vein material on the dump consists of quartz that contains about 5 volume percent chalcopyrite. This vein is surrounded by a symmetrical 2- to 4-cm envelope of QSP alteration that abruptly grades outward into propylitic alteration (fig. 10*B*). The southern adit exploited a 1-m-wide vein that strikes N. 70° E. and dips 85° to the north. This vein is mineralogically similar to the others except that it is brecciated and contains fragments of wallrock. The QSP alteration envelope around this vein is 4 to 10 cm wide. Although adularia was not identified in any of the Tarutani veins or alteration, the mineralization is very similar to adularia-sericite-type veins commonly found on the margins of porphyry systems (Margolis and others, 1991).

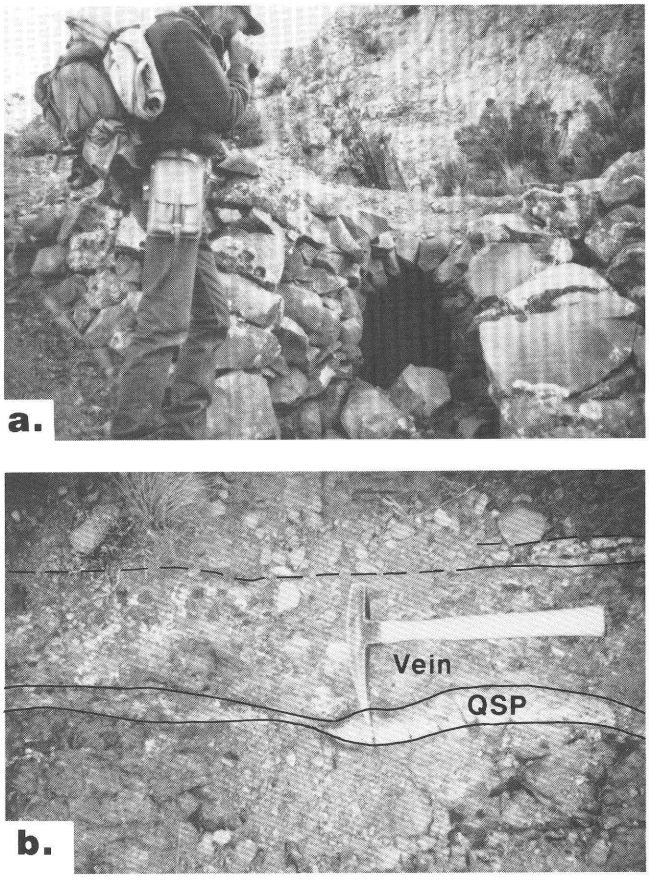

Figure 10. *A*, View along strike of the northern Tarutani vein. *B*, Photograph showing the narrow QSP alteration halo around the quartz-pyrite-chalcopyrite-sphalerite vein.

SUPERGENE ALTERATION

Supergene processes resulted in oxidation and leaching of sulfides to depths of generally less than 3–5 m. Recent prospect pits and trenches often reveal fresh rock with unoxidized sulfides a few meters below the surface. Geothite, hematite, and locally jarosite are the primary oxidation products of pyrite. Sulfuric acid produced by this process locally altered silicates to form kaolinite. Hydration of anhydrite produced gypsum. Supergene copper minerals including digenite, chalcocite, malachite, and azurite are present in dump material from the Tarutani veins. The lack of intense supergene oxidation is probably due to the arid climatic conditions that existed in the region since the middle Miocene (Vila and Sillitoe, 1991). The lack of deep oxidation is important because the pyrite and other sulfides present in unoxidized rock can have a deleterious affect on the recovery of gold by heap-leaching methods.

DISCUSSION

A preliminary hypothesis that is consistent with our observations is that La Española represents the juxtaposition of a magmatic-hydrothermal, acid-sulfate system on an earlier, gold-rich porphyry system with development of adularia-sericite-type veins on the periphery. Although we do not yet have the data to fully support these speculations, they provide a starting point for further field and laboratory studies. We envision a sequence of igneous and hydrothermal events as follows.

After deposition of the Mauri and Abaroa Formations, during late Oligocene to middle Miocene time, and after a period of uplift and erosion in the middle Miocene, the La Española area became the site of renewed volcanism. Eruption of dacite flows and fragmental volcanics at about 11 Ma, from a volcanic center at Thola Kkollu and from other volcanic centers nearby, resulted in the formation of the volcanics at Thola Kkollu. During the latter part of this episode, igneous activity commenced at La Española and produced the dacite porphyry intrusive complex. The geologic relations suggest that La Española was the site of repeated intrusive activity before, during, and after mineralization. As some of the more volatile-rich dacite porphyry intrusions cooled and crystallized, a low-density fluid or vapor separated to form miarolitic cavities. As other volatile-rich intrusions crystallized, dense magmatic brines separated, moved into surrounding fracture systems, and boiled to produce potassic alteration containing pyrite, chalcopyrite, ± gold. As the generation of

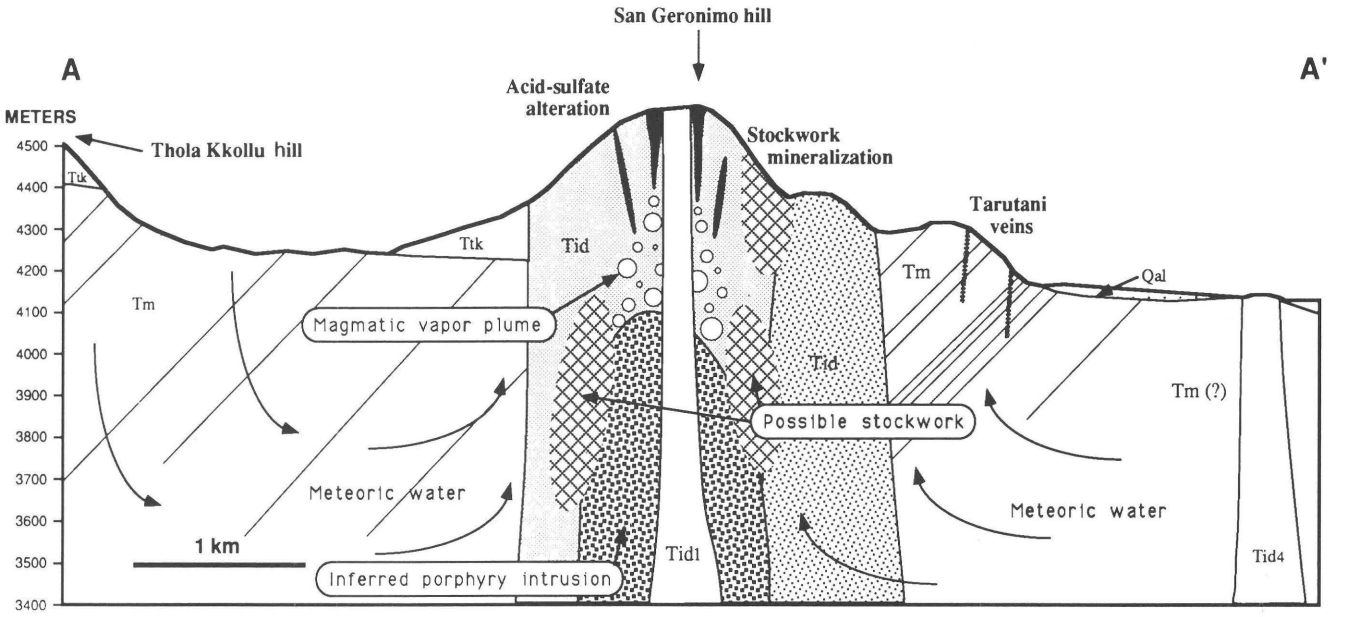

Figure 11. Schematic cross section along the line of section A–A′ on figure 2 showing the major features of La Española prospect. Two phases of the dacite porphyry stock (Tid) are shown, although the position of the contact between the two intrusive phases is only approximate. One or the other of these intrusive phases is thought to be responsible for the stockwork zone observed at the surface. Also shown is an inferred porphyry intrusion that is thought to be the source of the magmatic volatiles that produced the acid-sulfate alteration on San Geronimo hill and at the Kollota mine. The inferred porphyry intrusion may also have produced stockwork mineralization similar to that observed at the surface. The curved arrows represent possible flow paths of convecting meteoric water. See figure 2 for explanation of map symbols. See the Discussion section of the text for more details.

magmatic fluids waned, convectively circulating cells of meteoric water collapsed into the earlier formed zone of potassic alteration to produce pervasive quartz-sericite-pyrite alteration. The QSP stockwork zones may have formed outboard of the potassic zone as magmatic brines cooled and mixed with meteoric water. This sequence of intrusion, magmatic fluid generation and escape, and collapse of meteoric fluids into the system may have occurred several times. The three stockwork zones discovered at La Española may have been produced by separate intrusive events.

Magmatic hydrothermal acid-sulfate alteration formed at shallower levels in the system. The vuggy silica and quartz-alunite alteration observed on San Geronimo hill, at the Kollota mine, and at the Santa Rosa mine typically forms at the top of the magmatic vapor plume (fig. 11) where volatiles such as HCl, HF, and SO_2 condense and where SO_2 disproportionates to H_2SO_4 and H_2S (Rye and others, 1991). In the zone of condensation above the vapor plume, small volumes of extremely acidic fluid are generated that are progressively neutralized by reaction with the host rocks and by dilution with meteoric water. The acid-sulfate-altered rocks produced by this process are usually permeable and often are the site of subsequent quartz-pyrite-barite ± enargite ± gold ± silver ± base-metal mineralization such as that observed at the Kollota and Santa Rosa mines. Ore deposition in acid-sulfate systems has been attributed to cooling, to pH increases associated with progressive mixing between magmatic and meteoric waters, and to boiling (White and Hedenquist, 1990).

Acid-sulfate alteration and mineralization typically forms well above the level of potassic alteration in porphyry systems (often 500–700 m). The presence of acid-sulfate alteration within rocks formerly subjected to potassic alteration at La Española suggests that the hydrology of the system changed significantly. A drop in the water table or erosional unroofing during the life span of the igneous-hydrothermal system has been called upon to explain the lowering of magmatic-hydrothermal acid-sulfate alteration into the sericitic and potassic zones of porphyry systems (White and Hedenquist, 1990; Vila and Sillitoe, 1991). Further, based on the magmatic hydrothermal acid-sulfate model (Rye and others, 1991), it is possible to infer the presence of an unexposed intrusion at depth (e.g., fig. 11) that was the source of the magmatic volatiles necessary to produce the acid-sulfate alteration observed at the surface. The inferred intrusion may also have produced stockwork mineralization similar to that observed at the surface (fig. 11).

The dacite porphyry intrusive complex provided the thermal drive for convecting cells of meteoric water (fig. 11) that produced widespread propylitic alteration in the surrounding host rocks. Locally, these fluids were focused along high-angle faults and fractures in the

upwelling part of the cell to produce adularia-sericite-type veins, such as the Tarutani veins (fig. 11). Ore deposition in these veins may have occurred by mixing of meteoric water and fluids emanating from the intrusive or by boiling. The predominance of base-metal sulfides and lack of adularia in the veins suggests that fluid mixing was more important.

After the early dacite porphyry intrusions cooled and the hydrothermal system collapsed, La Española continued to be the site of intrusive activity. Numerous small plugs and dikes were emplaced into rocks that had previously been the site of hydrothermal activity. The later dacite porphyry intrusions probably remained unaltered because they contained lower concentrations of volatiles or were too small to drive convecting cells of meteoric water.

Uplift and erosion over the last 10 million years exposed the altered and mineralized rocks and produced the topographic relief observed today. Gold-bearing rock, which likely was present in the shallower parts of the system, was removed by erosion. Potential for placer gold may therefore exist in alluvial valley fill on the flanks of the La Española prospect.

ACKNOWLEDGMENTS

The authors would like to acknowledge our colleges, F. Tavera, N. Jimenez, J.L. Lizeca, F. Murillo, O. Flores, and R. Learned for stimulating discussions in the field that improved our understanding of La Española. We thank our drivers W. Mallea, W. Nina, J. Valdez, and R. Tapia for their help and support in camp. Publication was encouraged by F. Tavera and authorized by GEOBOL. Special thanks are offered to R. Terrazas of Expromin S.R.L. for allowing us to examine geologic maps and geochemical data collected during the course of exploration at La Española and for discussions regarding the origin of the mineralization. We are grateful to S. Sutley and T. Botinelly for help with the identification of minerals from X-ray diffraction spectra. And lastly, we thank the Inter-American Development Bank for funding.

REFERENCES CITED

Cox, D.P., 1986, Descriptive model of porphyry Cu-Au, *in* Cox, D.P., and Singer, D.A., eds., Mineral Deposit Models: U.S. Geological Survey Bulletin 1693, p. 110–114.

Cunningham, C.G., McNamee, J., Vasquez, J.P., and Ericksen, G.E., 1991, A model of volcanic dome-hosted precious metal deposits in Bolivia: Economic Geology, v. 86, p. 415–421.

Ericksen, G.E., Eyzaguirre, V.R., Urquidi, F., and Salas, R., 1986, Neogene-Quaternary volcanism and mineralization in the central Andes, *in* Horn, M.K., ed., Transactions of the Fourth Circum-Pacific Energy and Mineral Resources Conference, Singapore, p. 537–550.

Evernden, J.F., Kriz, J.S., and Cherroni, C., 1977, Potassium-argon ages of some Bolivian rocks: Economic Geology, v. 72, p. 1042–1061.

Heald, P.W., Foley, N.K., and Hayba, D.O., 1987, Comparative anatomy of volcanic-hosted epithermal deposits: Acid-sulfate and adularia-sericite types: Economic Geology, v. 82, p. 1–25.

Hedenquist, J.W., 1987, Mineralization associated with volcanic-related hydrothermal systems in the circum-Pacific basin, *in* Horn, M.K., ed., Transactions of the Fourth Circum-Pacific Energy and Mineral Resources Conference, Singapore, p. 513–524.

Jimenez, N., Lizeca, J.L., Murillo, F., Sanjines, O., Barrera, L., and Flores, O., 1991, Aplicacion de metodos de percepcion remota en el estudio geológico del area Berenguela-Charana, Bolivia [Workshop—Remote sensing applied to geological investigations]: Sevicio Geológico de Bolivia, Proyecto BID - USGS - GEOBOL,12–21 de Agosto de 1991, 8 p.

Lavenu, A., Bonhomme, M.G., Vatin-Perignon, N, and de Pachtere, P., 1989, Neogene magmatism in the Bolivian Andes between 16° S. and 18° S: Stratigraphy and K/Ar geochronology: Journal of South American Earth Sciences, v. 2, p. 35–47.

Margolis, J., Reed, M.H., and Albino, G.V., 1991, A process oriented classification of epithermal systems: Magmatic volatile-rich versus volatile-poor fluid paths [abs.]: Geological Society of America, Abstracts with Programs, v. 23, no. 5, p. A230.

Rose, A.W., and Burt, D.M., 1979, Hydrothermal alteration, *in* Barnes, H.L., ed., Geochemistry of Hydrothermal Ore Deposits, 2nd ed., New York, John Wiley and Sons, p. 173–235.

Rye, R.O., Bethke, P.M., and Wasserman, M.D., 1991, The stable isotope geochemistry of acid-sulfate alteration and vein forming alunite: U.S. Geological Survey Open-File Report 91–257, 58 p.

Rytuba, J.J., and Cox, D.P., 1991, Porphyry gold: A supplement to U.S. Geological Survey Bulletin 1693: U.S. Geological Survey Open-File Report 91–116, 7 p.

Vila, T., and Sillitoe, R.H., 1991, Gold-rich porphyry systems in the Maricunga belt, northern Chile: Economic Geology, v. 86, p. 1238–1260.

Wallace, A.R., Hardyman, R.F., Tosdal, R.M., Jimenez, N., Lizeca, J.L., and Murillo, F., 1991, Episodic mid–late Tertiary deformation during basin sedimentation and explosive volcanism, northwestern Altiplano, Bolivia [abs.]: Geological Society of America, Abstracts with Programs, v. 23, no. 5, p. A132.

White, N.C., and Hedenquist, J.W., 1990, Epithermal environments and styles of mineralization: Variations and their causes, and guidelines for exploration: Journal of Geochemical Exploration, v. 36, p. 445–474.

CHAPTER K

MINERALOGY AND CHEMISTRY OF GOLD-ASSOCIATED SKARN FROM NAMBIJA, ZAMORA PROVINCE, ECUADOR: A RECONNAISSANCE STUDY

By JANE M. HAMMARSTROM[1]

ABSTRACT

Gold mineralization is associated with skarn formed in a heterogeneous xenolith or roof pendant within the Jurassic Zamora batholith in southeastern Ecuador. Petrographic descriptions, electron microprobe data for minerals, and geochemical data for rock samples are presented for a suite of 16 samples collected as part of a reconnaissance study of the Nambija gold deposit (McKelvey, 1991). Hydrothermal alteration affected all the lithologies present at Nambija, including syenite porphyry, volcanic rocks and tuffs, and breccias. Zoned, anisotropic grossular-andradite garnet partially replaces phenocrysts and groundmass in breccia and is the dominant mineral in massive skarn; isotropic, pure andradite is locally developed. Other minerals present in skarn include diopsidic pyroxene, epidote, K-feldspar, actinolite, chlorite, quartz, apatite, calcite, pyrite, and traces of chalcopyrite. Free gold is present as electrum in quartz within massive garnet skarn and in garnet-rich breccia; gold is not associated with sulfide minerals in the sample suite studied. Temperature estimates from chlorite geothermometry are compatible with a < 300°C retrograde skarn stage. The Nambija deposit has some characteristics of relatively oxidized gold-bearing skarn deposits elsewhere but is unusually gold rich and copper poor.

INTRODUCTION

Gold has been mined in the Zamora Province of southeastern Ecuador since the 16th century. In the early 1980's, the gold potential of the area was "rediscovered," initiating a modern gold rush centered around the town of Nambija, which is along the eastern edge of the Cordillera de Nanguipa (Barragán, 1989). Gold deposits at Nambija, and nearby at Campana and Campanilla (fig. 1), form a north-south belt of structurally controlled mineralization hosted by a polylithologic xenolith or roof pendant within the Jurassic Zamora batholith. The xenolith rocks are tentatively correlated with the Jurassic Santiago and Macuma Formations (Salazar, 1988). McKelvey (1991) described the general geology of the Nambija deposits and showed that the host rocks at Nambija include limestone, shale, sandstone, and volcanic tuffs and flows, all of which are variably altered to skarn. Mineralization appears to be concentrated in a structurally controlled zone that extends for 1.5 km along strike, especially where breccias, faults, and dikes cut the skarn assemblages. The extremely high gold grade of the Nambija ore, purported to be in excess of 50 g/t (grams per tonne), has previously attracted intensive, small-scale, unorganized mining activities and, recently, the attention of the international mining industry. The coarse-grained nature of the gold at Nambija and also at Campanilla makes it difficult, due to nugget effects, to assess ore grades based on reconnaissance sampling. No reliable grade or tonnage data are available, but geologists visiting the area in the late 1980's speculated that the Nambija deposit has a potential ore tonnage of 25,000,000 short tons (23,000,000 metric tonnes) or more and that grade estimates for the active mining at the time of their visit were probably on the order of 0.5 to 1 oz Au/short

[1]U.S. Geological Survey, Mail Stop 959, 12201 Sunrise Valley Drive, National Center, Reston, VA 22092.

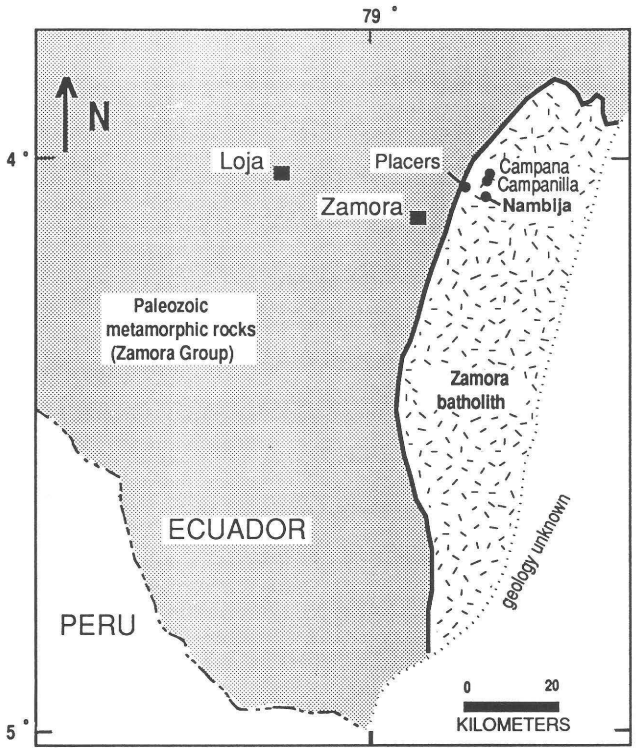

Figure 1. Location map for the Nambija, Campanilla, Campana, and placer gold deposits, Zamora Province, Ecuador. Geology from Mapa Geológico Nacional de la República del Ecuador (1982).

ton (14 to 484 g/t) (Mineral Resources Data System, 1991, record number TC00085).

Campanilla, a gold deposit recently developed by Plateau Mining Plc., reportedly has a significant tonnage of ore with gold grades of 0.5 oz/ton or more (Mining Magazine, 1990). The deposit at Campanilla is hosted by andesitic volcanic tuff. The tuff is locally altered to skarn; gold is associated with late quartz-carbonate veins that cut the skarn. Campanilla is classified as a vein-type gold deposit (Mining Magazine, 1990) that postdates skarn formation. Nambija has been described (Salazar, 1988) as a complex skarn deposit that cannot be readily classified using the criteria for different classes of calcic skarns defined by Einaudi and others (1981). Among the unusual features of the skarn at Nambija, Salazar (1988) noted that gold is present in a variety of textures and lithologies, that scheelite is present with sulfides, and that gold is deposited late in the paragenesis and may have been remobilized.

Mineral assemblages are one of the most useful guides for classifying skarn deposits and for understanding the environment of ore deposition. In this study, new data on mineral chemistry are presented for samples collected by McKelvey (1991) from Nambija, and the data are evaluated in terms of recent models for gold skarns (Meinert, 1989; Theodore and others, 1991; Ettlinger and Ray, 1989). The apparent size and grade of the Nambija deposit are well above the median values of 213,000 metric tonnes and 8.6 g/t Au, respectively, calculated for 39 gold-bearing skarns by Theodore and others (1991). If Nambija is a deposit of this type, it is certainly one of the most significant gold-bearing skarns in the world.

METHODS OF STUDY

Petrographic descriptions reported here are based on examination of hand specimens and thin sections for 16 samples collected by McKelvey (1991). Polished thin sections were prepared for 11 samples; several sections were prepared for some samples to include variations in texture within individual specimens. Minerals were analyzed by the author using an ARL-SEMQ electron microprobe at the U.S. Geological Survey in Reston, Va. Natural and synthetic mineral standards were used for silicate minerals; synthetic electrum standards were used for precious-metal analyses. The number of analyses determined for a given mineral reflects the modal abundances of that mineral in the sample suite. A scanning electron microscope was used for qualitative analyses and identification of submicroscopic minerals. Fifteen 2-kg bulk-rock samples (fig. 2, NAM-1 through NAM-15) were analyzed for a suite of 44 elements in U.S. Geological Survey analytical laboratories in Denver.

SAMPLE DESCRIPTIONS

Lithologies sampled include altered syenite porphyry, tuff, breccia, chlorite skarn, and garnet skarn. Sample locations and the distribution of lithologies are shown in figure 2. McKelvey's (1991) sketch map of the district shows the distribution of outcrops; it also shows a central zone of garnet skarn cut by dikes and breccias that is flanked by an outer zone of chlorite skarn. Mining activity is concentrated along the central zone. The distribution of rock types on figure 2 is generalized; the distribution of garnet-rich versus chlorite-rich skarn in this sample suite is much more erratic. This relation is not surprising in light of the heterogeneous skarn protolith and the extent of shearing and brecciation in the immediate area of the deposit.

Rock types (field names assigned by McKelvey, 1991) and mineral assemblages for samples studied by electron microprobe are summarized in table 1. A number of minerals reported from Nambija were not observed in the samples examined for this study, including scheelite, arsenopyrite, rhodochrosite, and brochantite.

SYENITE PORPHYRY

The predominant rock type in the Zamora batholith is a quartz-plagioclase-K-feldspar-hornblende tonalite

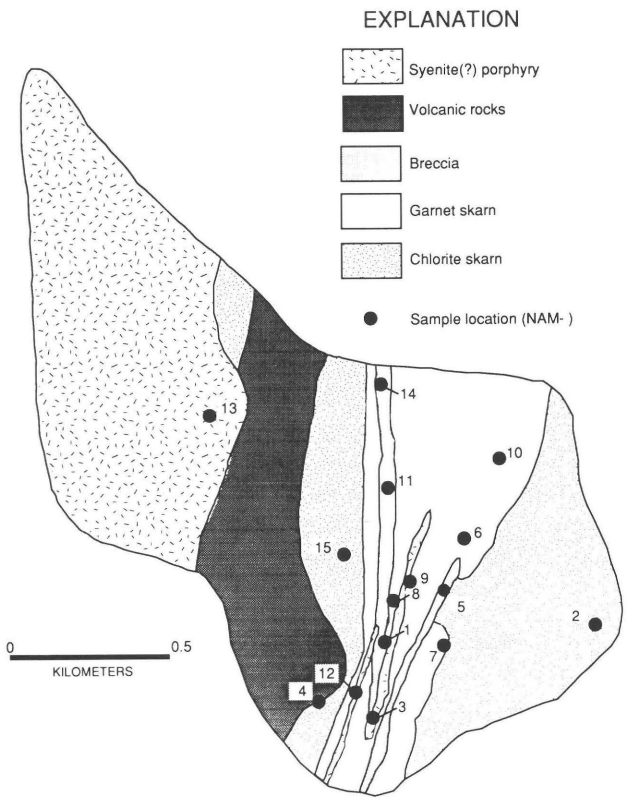

Figure 2. Generalized geologic map of the Nambija area showing sample locations. Modified from McKelvey (1991).

(Salazar, 1988) or granodiorite. Granite occurs locally. McKelvey (1991) described sample NAM-13 as a syenite porphyry, based on the absence of quartz, the abundance of K-feldspar phenocrysts, and the presence of relict mafic silicate minerals. The relation of this rock, and the two syenite porphyry dikes (fig. 2) that are associated with the main mineralized zone, to the main body of the batholith is unknown. The syenite porphyry is extensively hydrothermally altered throughout the mapped area. In hand sample, syenite-porphyry sample NAM-13 is a medium-grained, even-textured rock composed of chalky white 1–2-mm-long phenocrysts set in a buff-colored groundmass. Rusty clots mark the locus of oxidized, hydrated iron-oxide minerals. Phenocrysts are plagioclase (now pure albite) or orthoclase, clouded by alteration to sericite and clays. Shreddy, brown biotite is present in the groundmass. No calc-silicate minerals or sulfides are present.

TUFF

Sample NAM-10 is a distinctive black rock, described as a tuff (McKelvey, 1991), from an outcrop in the garnet skarn zone on figure 1. Based on thin-section study, the rock is composed of a dense swarm of plagioclase laths (0.5 mm wide by 2 mm long) altered to clays. Irregular patches of chlorite, typically 2 mm across, enclose blocky, 0.55 mm and smaller, disseminated magnetite grains that are partly oxidized to hematite; chlorite also fills in between plagioclase laths. These chlorite patches replace most of the igneous mafic silicate minerals in the rock; some biotite (table 2, analysis 9) is preserved. Epidote is the only calc-silicate mineral in this rock; pyrite and chalcopyrite are observed in chlorite. This rock represents endoskarn formed in an igneous protolith that was more mafic than the syenite porphyry.

BRECCIA AND SKARN

McKelvey (1991) noted that mineralization at Nambija appears to be concentrated in a linear, structurally controlled zone of multi-clastic intrusion and tectonic breccias that crosscut skarn assemblages. The distinction between breccia and skarn is based on outcrop texture; in thin section the distinction is less clear. Breccia samples (table 1) all contain altered feldspar phenocrysts, igneous clasts having porphyritic textures, and fine-grained volcanic(?) clasts. The groundmass is replaced by skarn minerals to varying degrees. Garnet partially replaces altered feldspar phenocrysts and groundmass in breccia. Epidote is locally developed in a few samples, and fibrous actinolite is present in veins, in groundmass, and as pseudomorphs that replace phenocrysts. Skarn samples NAM-3, 8, 12, and 14 are predominantly igneous rocks partly veined by (or locally altered to) skarn, whereas samples NAM-7, 9, and 15 are massive garnetites. In the few samples that contain both pyroxene and garnet, garnet is coarser, more abundant, and appears to be paragenetically later than pyroxene. Green and brownish chlorite pods, interstitial to massive garnet, are cut by blebby veinlets (fig. 3*A*) that are opaque in transmitted light. These blebs are fine-grained mixtures of quartz and iron oxides and form chains that appear as veinlets, or they line the walls of late calcite veins. In some samples, a brown, biotite-like material forms a spidery network of veinlets and patches throughout the rock. Microprobe analyses show that, although this material can be chemically homogeneous on the scale of tens of microns, it generally is heterogeneous across a single grain or along a veinlet. This material probably represents a mixture of several mineral phases, but in some cases, it has a composition intermediate between a biotite and a chlorite—i.e., low totals that suggest a hydrous mineral, significant but variable K_2O content (0.5 to 5 weight percent), and a highly variable silica content.

K-feldspar is ubiquitous in breccia and in skarn. In some samples, K-feldspar grew along or selectively replaced zones in garnet, imparting a "bullseye" texture to the garnet. K-feldspar forms monomineralic veinlets, or veinlets cored by calcite, and some K-feldspar appears to

Table 1. Summary of mineral assemblages present in 13 samples from Nambija that were studied by electron microprobe.

[Numbers under rock-type headings (skarn, breccia, tuff, porphyry) are sample numbers. X, mineral present; Tr, trace amount present; ---, mineral not observed; %Ad, mole percent andradite; %Hd, mole percent hedenbergite; %Ps, mole percent pistacite]

	Skarn							Breccia				Tuff	Porphyry
Mineral	NAM-3	NAM-7	NAM-8	NAM-9	NAM-12	NAM-14	NAM-15	NAM-1	NAM-5	NAM-11	89TT1	NAM-10	NAM-13
Electrum	---	---	---	---	---	---	X	---	---	---	X	---	---
Garnet (%Ad)	29-45	33-58	44-69	32-72	48-62	---	34-55; 98	21-63	X	---	58-65	---	---
Pyroxene (%Hd)	16-17	---	22	---	21-34	28	---	24	---	---	---	---	---
Epidote (%Ps)	---	---	---	---	24-30	---	---	---	X	---	X	26-36	---
Plagioclase	---	X	---	---	X	---	---	X	X	X	X	X	---
K-feldspar	X	---	---	X	X	---	---	---	X	X	X	---	X
Amphibole	---	---	---	---	---	---	---	---	---	X	---	---	---
Biotite	---	---	---	---	---	---	---	---	---	---	---	X	---
Chlorite	---	X	X	X	---	X	---	X	---	---	X	X	X
Biotite/chlorite	X	X	---	X	---	X	X	---	---	---	---	X	---
Calcite	---	X	X	X	X	X	X	X	---	---	X	---	---
Quartz	X	X	X	X	---	X	X	X	X	---	X	X	---
Sphene	---	---	---	---	X	---	---	---	---	---	X	---	---
Apatite	---	X	X	---	---	---	X	---	---	---	---	---	---
Magnetite	---	X	---	---	---	---	---	---	---	---	---	X	X
Pyrite	X	Tr	---	X	---	X	X	---	X	---	X	X	---
Chalcopyrite	X	---	---	X	---	---	X	---	---	---	---	---	---
Other[1]	X	---	---	---	---	---	---	---	---	---	---	---	---

[1] "Other" includes zircon, galena, sphalerite, and barite.

Table 2. Microprobe data for chlorite and biotite.

[Total iron reported as FeO; water computed assuming full hydroxyl site occupancy; -, no data. Explanation of "analysis numbers:" 1 and 2, sample NAM-1, green chlorite, 2 different grains; 3, sample NAM-7, average of 5 points taken along a 0.8-mm-long clot of pale-green chlorite in rosettes, interstitial to garnet; 4, sample NAM-7, brown chlorite, average of 2; 5, sample NAM-8, green chlorite, average of 2; 6, sample NAM-9, average of 3 points on pale, brownish-green chlorite in K-feldspar, interstitial to garnet; 7 and 8, sample NAM-10, averages of 3 points on each of 2 grains of green chlorite adjacent to epidote; 9, sample NAM-10, average of 4 points from a coarse-grained (1 mm across) diffuse patch of biotite (patches are mixtures of biotite- and green-chlorite-rich areas; they are riddled with magnetite inclusions and appear to represent alteration of relict mafic silicate minerals in the volcanic protolith)]

	Analysis number								
	1	2	3	4	5	6	7	8	9
(Results shown in weight percent)									
SiO_2	29.26	31.64	28.95	32.62	28.19	33.33	26.96	26.25	34.76
TiO_2	-	-	-	0.03	0.02	0.00	0.04	0.06	1.14
Al_2O_3	17.05	15.58	17.43	16.81	17.67	15.01	20.08	20.73	17.70
FeO	14.84	14.27	17.26	15.19	14.99	13.49	17.54	17.41	15.66
MnO	1.23	1.16	3.23	1.07	3.61	0.71	0.63	0.71	0.41
MgO	23.31	22.59	19.71	21.58	21.38	24.20	21.07	21.75	14.23
CaO	0.25	0.66	0.14	0.28	0.05	0.41	0.06	0.03	0.01
Na_2O	-	0.01	0.02	0.02	0.02	0.06	0.01	0.00	0.09
K_2O	0.03	0.10	0.14	0.47	0.01	0.17	0.61	0.08	9.63
H_2O	12.02	12.10	11.74	12.03	11.81	12.06	11.85	11.87	3.95
F	-	-	0.09	0.12	0.05	0.25	-	0.00	0.08
Cl	-	-	-	-	-	0.01	0.01	0.00	0.05
O=F	-	-	0.04	0.05	0.02	0.11	-	0.00	0.03
O=Cl	-	-	-	-	-	0.00	0.00	0.00	0.01
Total	98.0	98.1	98.7	100.0	98.5	99.8	98.9	98.9	97.6
(Results shown as number of cations—14 O equivalents for chlorite; 22 O equivalents for biotite)									
Si IV	2.99	3.21	2.99	3.23	2.91	3.29	2.76	2.68	5.33
Al IV	1.01	0.79	1.01	0.77	1.09	0.71	1.24	1.32	2.67
T site	4.00	4.00	4.00	4.00	4.00	4.00	4.00	4.00	8.00
Al VI	1.04	1.07	1.11	1.19	1.06	1.04	1.19	1.18	0.53
Ti	-	-	-	0.00	0.00	0.00	0.00	0.00	0.13
Fe^{2+}	1.27	1.21	1.49	1.26	1.35	1.11	1.50	1.49	2.01
Mn	0.11	0.10	0.28	0.09	0.32	0.06	0.05	0.06	0.05
Mg	3.55	3.41	3.04	3.19	3.29	3.56	3.22	3.32	3.25
O site[1]	5.96	5.79	5.92	5.72	6.01	5.77	5.97	6.05	5.97
Ca	0.03	0.07	0.02	0.03	0.01	0.04	0.01	0.00	0.00
Na	-	0.00	0.00	0.00	0.00	0.01	0.00	0.00	0.03
K	0.00	0.01	0.02	0.06	0.00	0.02	0.08	0.01	1.88
OH	8.00	8.00	7.97	7.96	7.99	7.92	8.00	8.00	3.95
F	-	-	0.03	0.04	0.01	0.08	-	0.00	0.04
Cl	-	-	-	-	-	0.00	0.00	0.00	0.01
Mg/(Mg+Fe)	0.74	0.73	0.67	0.72	0.71	0.76	0.68	0.69	0.62
Fe/(Fe+Mg)	0.26	0.27	0.33	0.28	0.29	0.24	0.32	0.31	0.38
T (°C)[2]	261	192	264	186	288	165	337	362	---

[1] Octahedral site sum exclusive of Ti for chlorite, includes Ti for biotite.

[2] Temperature estimates computed from Jowett's (1991) equation for chlorite geothemometry, $T\ (°C)=319(Al^{IV}_c) - 69$, where $Al^{IV}_c=Al^{IV}+0.1(Fe/Fe+Mg)$.

have grown unimpeded into open space before infilling by calcite (fig. 3*B*). Calcite veinlets, generally on the order of 0.2 mm in width, crosscut all other assemblages and appear to record the latest mineral deposition within these rocks.

Pyrite is sparsely disseminated throughout most of the samples; however, only one sample, NAM-3, can be described as sulfide rich where pyrite forms a network of massive and mottled grains that enclose rounded crystals of garnet and other silicates. This mottling results from incomplete replacement of preexisting silicate minerals. Chalcopyrite is the second most abundant sulfide present, and micron-size blebs of galena, pyrrhotite, and barite were identified in pyrite by scanning electron miscroscopy.

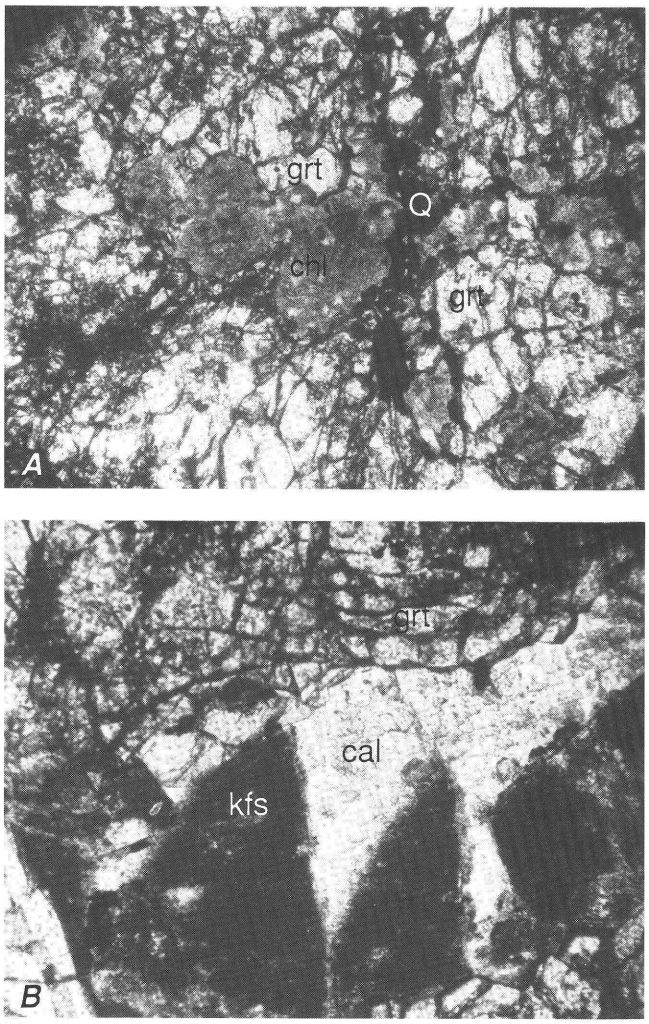

Figure 3. Photomicrographs showing skarn mineral textures in sample NAM-9, plane polarized light, field of view 1 mm across. *A*, Blebby, opaque quartz vein (Q) cutting chlorite (chl) interstitial to massive garnet (grt). *B*, Potassium feldspar (kfs) and calcite (cal) vein in garnet (grt).

Pyrite grains are brecciated and veined by late silicate minerals and calcite.

GOLD MINERALIZATION

Salazar (1988) described six types of gold occurrences at Nambija: (1) an interstitial, late phase between garnet crystals in assemblages with quartz, K-feldspar, calcite, and plagioclase; (2) with disseminated pyrite in calc-silicate minerals and volcanic breccias; (3) on K-feldspar grain boundaries; (4) in siliceous sedimentary rocks; (5) in quartz veins and veinlets; and (6) in fractures in shear zones. He concluded that gold was deposited after garnet and perhaps after K-feldspar and probably had a protracted history of deposition and remobilization that spanned skarn alteration, brecciation, and quartz veining in the district. Geochemical data for 15 samples representing various lithologies at Nambija show the highest gold values (as much as 47 ppm) are associated with quartz in garnet-rich skarn (table 3).

Macroscopic free gold is present as electrum in quartz within garnet-skarn sample NAM-15 and in sample 89TT1, a brecciated skarn from a locality just north of the area shown in figure 1. Both samples contain abundant garnet and neither show evidence for extensive retrograde alteration or sulfide deposition. Relatively rare, two-phase (liquid + vapor) fluid inclusions are present in quartz surrounding electrum and more commonly in calcite throughout the sample suite, but the fluid inclusions in the samples available are too small (< 10 microns) and too sparse for conventional geothermometry.

Electrum forms discrete grains and parts of discontinuous veinlets up to 0.6 mm long (fig. 4). Within each sample, electrum is compositionally homogeneous, but electrum in the breccia is enriched in gold (Au_{92} Ag_8) relative to electrum in garnet skarn (Au_{77} Ag_{23}). Given the limited number of samples available for study, it is impossible to determine how typical these values are for the entire district; the electrum compositions may reflect secondary gold enrichment through remobilization of precious metals, late in the life of the hydrothermal system.

MINERAL CHEMISTRY

GARNET

Most of the garnet at Nambija is yellowish green to green in hand sample. In thin section, the garnet is colorless or locally yellow in plane polarized light. Garnet varies in texture from patchy, to veins, to massive and is sector twinned, mostly anisotropic, and shows delicate, oscillatory growth zoning. Microprobe data for garnet were recalculated in terms of ideal garnet stoichiometry (8 cations per 12 oxygens and assuming no hydrogarnet component) for the estimation of ferric and ferrous iron contents and the calculation of molecular proportions of end members. Most Nambija garnets are intermediate in composition between grossular and andradite, and the sums of the pyrope, almandine, and spessartine components are less than or equal to 10 mole percent (fig. 5*A*). Garnet rims tend to be cleaner (inclusion-free) and enriched in iron (i.e., normally zoned) relative to cores, despite fine-scale oscillations in composition (see McKelvey and Hammarstrom, 1991, fig. 1). In gold-bearing garnet skarn sample NAM-15, however, cores, zones, and irregular patches of yellow, isotropic, nearly pure andradite are locally developed. Andradite is rimmed by garnet of intermediate composition, typically in coarse-grained pods. Hammarstrom (in Theodore and others, 1992) noted similar

Table 3. Analytical data for rock samples from Nambija.

[Numbers under rock-type headings (breccia, skarn, tuff, porphyry) are sample numbers. N, not detected at the concentration specified]

Element analyzed	Breccia NAM-1	Skarn NAM-2	Skarn NAM-3	Skarn NAM-4	Breccia NAM-5	Skarn NAM-6	Skarn NAM-7	Skarn NAM-8	Skarn NAM-9	Tuff NAM-10	Breccia NAM-11	Skarn NAM-12	Porphyry NAM-13	Skarn NAM-14	Skarn NAM-15
Trace element analysis[1] (in parts per million)															
Au	0.034	0.028	0.012	<0.002	0.008	1.20	0.024	7.30	0.012	<0.002	N0.002	0.90	0.002	1.65	47.0
Hg	0.04	0.08	0.20	0.04	0.18	0.28	N0.02	0.08	0.36	0.02	0.02	0.04	0.04	0.08	0.12
W	1.0	6.0	0.5	0.5	2.0	1.0	2.0	11.0	1.0	N0.5	6.0	0.5	1.0	0.5	2.0
Te	0.05	0.30	2.80	0.10	0.15	0.35	N0.05	0.10	<0.05	N0.05	N0.05	0.50	0.05	N0.05	N0.05
Optical spectroscopy[2] (in weight percent)															
Al	8.14	6.84	6.12	10.7	9.53	10.3	5.43	5.93	8.26	10.0	8.04	8.65	9.95	7.94	5.56
Ca	8.57	0.11	11.0	0.61	2.12	1.29	21.0	15.3	5.60	1.74	10.1	1.93	0.49	6.89	15.3
Fe	3.26	3.47	12.3	1.14	2.43	7.18	9.74	7.40	3.73	7.91	4.32	6.03	1.78	3.65	6.68
K	3.97	6.77	0.75	5.79	3.48	3.32	0.80	0.14	1.79	3.49	0.13	1.23	6.64	0.87	1.33
Mg	0.49	0.06	0.10	0.91	0.70	4.85	0.62	0.27	3.18	3.62	0.48	2.79	0.45	2.47	0.56
Na	2.92	0.23	0.02	3.56	4.40	0.85	0.04	2.31	3.54	3.33	4.66	4.78	3.17	4.88	0.89
P	0.06	0.04	0.03	0.07	0.09	0.06	0.58	0.41	0.11	0.09	0.09	0.06	0.09	0.07	0.14
Ti	0.32	0.35	0.26	0.38	0.42	0.54	0.28	0.21	0.34	0.62	0.28	0.53	0.31	0.49	0.34
Optical spectroscopy[2] (in parts per million)															
Ag	N0.045	N0.045	1.1	N0.045	0.28	0.58	N0.045	0.25	N0.045	N0.045	N0.045	0.55	0.051	0.30	2.9
As	3.6	N0.60	12	1.6	N0.60	N0.60	20	48	2.5	0.68	7.3	9.4	3.6	4.1	8.6
Ba	772	853	120	2,070	625	602	57	14	597	685	16	200	1,880	196	103
Be	<1	<1	<1	2	<1	<1	<1	<1	<1	<1	<1	<1	<1	2	<1
Ce	10	8	<4	27	17	15	14	7	28	21	63	11	31	56	18
Co	6	2	17	9	7	28	2	2	8	20	2	118	18	31	4
Cr	10	13	15	38	15	77	34	36	29	4	35	22	3	17	33
Cu	54	62	745	239	117	250	2	6	9	111	2	646	50	203	2
Ga	16	16	27	19	17	26	32	24	16	20	18	18	16	17	23
La	9	4	5	14	10	10	11	6	18	13	48	7	23	40	13
Li	6	5	7	17	10	76	11	7	8	46	7	37	4	11	12
Mn	4,480	135	8,320	1,350	2,630	4,320	8,630	6,770	2,570	2,660	4,860	4,440	1,130	5,910	7,550
Mo	<2	<2	<2	<2	4	8	<2	<2	<2	<2	<2	3	<2	<2	<2
Nb	<4	8	5	6	<4	5	5	<4	<4	<4	<4	5	8	<4	<4
Nd	9	<4	5	17	11	11	21	14	16	12	35	8	22	33	17
Ni	21	<2	5	21	5	42	10	9	10	7	9	24	5	21	15
Pb	5	13	16	14	22	24	4	8	7	18	<4	13	12	14	<4
Sb	<5	<5	<5	7	5	10	<5	<5	9	8	<5	8	<5	8	5
Sc	18	12	10	20	19	33	9	10	19	23	16	30	8	30	16
Sr	65	31	4	261	178	62	18	39	195	509	61	166	92	110	45
Th	5	6	7	5	<4	5	9	6	5	<4	<4	5	10	4	7
V	128	59	172	84	138	302	239	133	154	298	97	200	80	123	147
Y	17	6	17	26	16	11	40	38	22	15	21	10	26	11	28
Yb	2	2	3	3	2	2	4	3	3	2	3	1	3	1	3
Zn	13	8	210	223	125	239	26	36	83	171	15	35	36	69	19

[1] Trace elements determined by following methods (Arbogast, 1990): Hg, atomic absorption cold vapor method; W, visible absorption spectroscopy; Au, graphite furnace atomic absorption; Te, atomic absorption. P.L. Hageman, B.H. Roushey, and T.A. Roumer; analysts.

[2] Forty-element inductively coupled plasma—atomic emission spectroscopy analytical package (Lichte and others, 1987; Crock and others, 1983) with partial analysis for Ag, As, Bi, Cd, Cu, Mo, Pb, Sb, and Zn (Motooka, 1988). Bi < 10 ppm and Cd < 2 ppm for all samples. D.L. Fey, analyst.

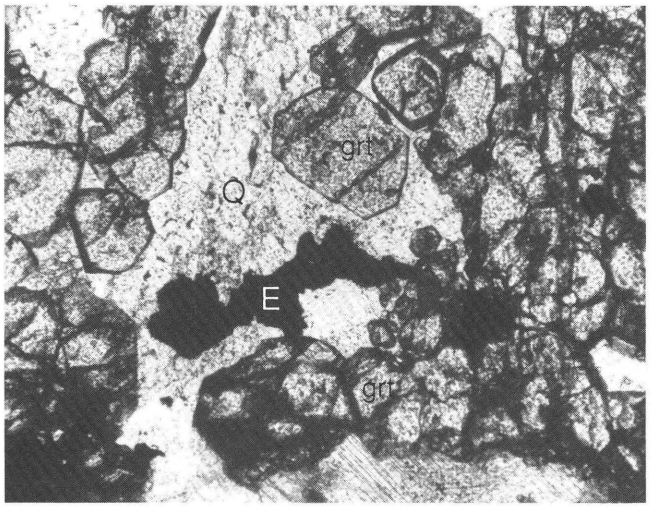

Figure 4. Photomicrograph showing coarse electrum (E) in quartz (Q) with zoned garnet (grt). Sample NAM-15, plane polarized light, field of view 2 mm across.

occurrences of multiple generations of garnet, including a break in composition between isotropic and anisotropic varieties, in skarn associated with gold mineralization in the Battle Mountain mining district of north-central Nevada. Meinert (1989) stated that pure andradite is relatively uncommon in gold skarns compared to intermediate grossular-andradite compositions. In five of the Nevada deposits, however, a stage of nearly pure andradite garnet growth appears to correlate with gold mineralization in skarn (Theodore and others, 1991, fig. 10) and may represent a stage of iron influx or remobilization. This influx of iron could be related to sulfide breakdown during late retrograde skarn stages within the hydrothermal system. It is conceivable that gold, originally deposited with sulfide minerals, may have been remobilized and concentrated as part of such a process. Therefore, samples that only contain garnet populations of a uniform composition may be less prospective than samples with more complex garnet populations.

TiO_2 contents of the pure andradites are negligible. Garnets in the two breccia samples (open symbols in figure 5*B*) are more titaniferous than those in massive skarn, which is typical of skarn developed in an igneous rather than a carbonate-rock protolith. Titanium content of garnet does not reflect the whole-rock titanium concentrations (table 3); the least titaniferous garnets are in pyroxene- and sphene-bearing samples.

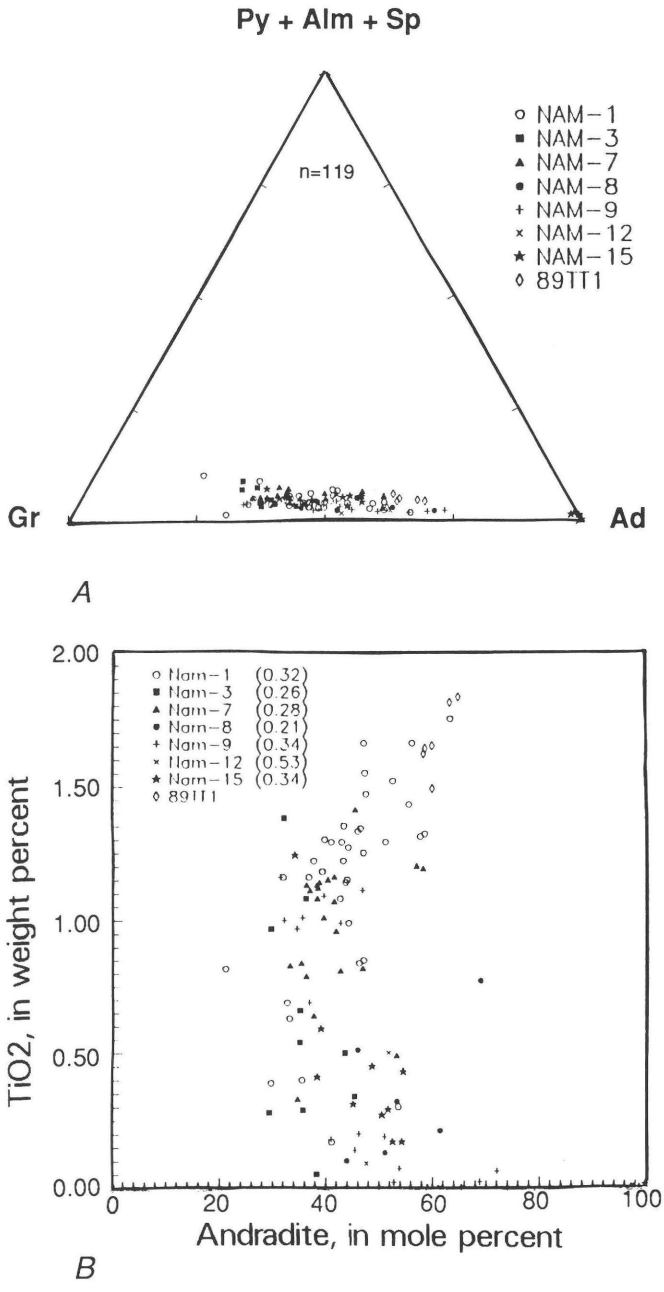

Figure 5. *A*, Ternary diagram showing Nambija garnet compositions plotted in terms of pyrope (Py) + almandine (Alm) + spessartine (Sp) components, grossular (Gr) component, and andradite (Ad) component. *B*, Variation of TiO_2 contents of Nambija garnets as a function of andradite content. Numbers in parentheses refer to whole-rock Ti content reported by McKelvey (1991).

PYROXENE

Pyroxene is much less common than garnet in the samples studied. Where present, pyroxene is finer grained and less abundant than coexisting garnet. The pyroxene is diopsidic (fig. 6), with a persistent, but relatively minor, manganese component (MnO ranges from 1.5 to 3.0 weight percent). Titanium contents are negligible, and alumina varies from below detection limits to 0.5 weight percent Al_2O_3. Pyroxene compositions for Nambija samples overlap pyroxenes from other mineralized skarns but lack the enhanced Al_2O_3 and TiO_2 contents noted by Ettlinger

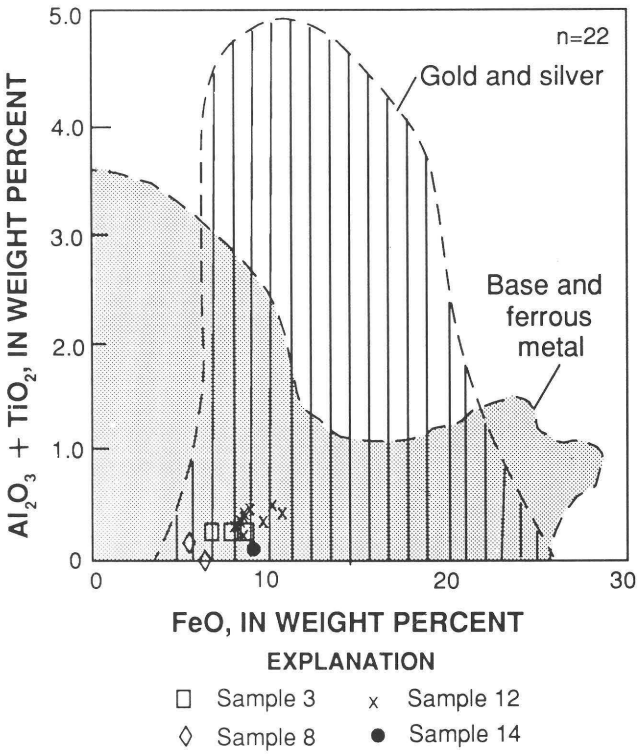

Figure 6. Pyroxene compositions, plotted in terms of weight percent $Al_2O_3 + TiO_2$ vs FeO. Fields for pyroxenes associated with gold and silver skarns and base- and ferrous-metal skarns from Etlinger and Ray (1989).

and Ray (1989) for pyroxenes from precious-metal-enriched skarns elsewhere.

CHLORITE

Chlorite is a relatively minor mineral in most of the calc-silicate-bearing samples studied, despite the extensive area mapped as chlorite skarn on figure 2. Chlorite clearly postdates garnet and tends to form clots of pale-green to brownish rosettes interstitial to garnet in samples of skarn. Chlorite compositions (table 2) are all relatively magnesian (Mg/(Mg+Fe) = 0.68 to 0.76). Cathelineau and Nieva (1985) described a chlorite solid-solution geothermometer based on an empirical correlation between observed authigenic chlorite compositions and temperatures measured in active geothermal systems (e.g., Salton Sea geothermal field, McDowell and Elders, 1980). Cathelineau (1988) refined this geothermometer and suggested that the method could be applied with caution to hydrothermal and metamorphic chlorites because the temperature-sensitive parameter, the tetrahedral aluminum content (Al^{IV}), appears to be independent of lithology or fluid composition. However, he noted that the presence of smectite intergrown with chlorite or chlorite replacing a preexisting layer silicate may invalidate the use of the method. Chlorite geothermometry was used in a study of a massive sulfide deposit by Krandidiotis and MacLean (1987), and Jowett (1991) reevaluated their conclusion that a correction is needed to account for variations in chlorite Fe/Mg ratios. Temperatures computed for Nambija chlorites (table 2) from Jowett's (1991) equation range from 165°C to 362°C. Relatively high concentrations of CaO and K_2O in analyses 2, 4, 6, and 7 (table 2) suggest that intergrown smectite or mica may be present. Temperatures computed for analyses containing these impurities are low (< 200°C for analyses 2, 4, and 6; table 2) relative to temperatures computed for other analyses. For two analyses from tuff sample NAM-10, a lower temperature is obtained for K-bearing analysis 7 (337°C; table 2) than for K-free analysis 8 (362°C; table 2); both temperatures are high, beyond the range of 150°–325°C for which Jowett's (1991) equation is applicable, and textures suggest that chlorite replaces biotite or other mafic silicate minerals in this rock. Similarly, the temperature computed for brown, K- and Ca-bearing chlorite in skarn sample NAM-7 (table 2, analysis 4) is lower than the temperature computed for purer green chlorite from the same rock. The Nambija chlorites are much more manganiferous than the chlorites from geothermal systems on which the geothermometers are based, and the assumption of low ferric iron content may be invalid. Chlorite in skarn samples such as the interstitial rosettes, represented by analysis 3 and analysis 5, which yield temperatures of 264°C and 288°C, respectively, are the most likely chlorites to record meaningful temperatures in the data set because textures are compatible with growth from a fluid, and Ca and K contents are negligible. Although it would be presumptuous to attach any significance to the individual absolute temperatures, the range of temperatures for chlorite overlaps the temperature range (220°–320°C) of fluid inclusions in chlorite-dominant skarn at the Tomboy-Minnie gold skarn deposit (Theodore and others, 1986).

Johnson (1991) applied chlorite geothermometry to hydrothermally altered sedimentary rocks, including skarn, in the New World gold-copper district, Montana, to examine district-wide temperature gradients and fluid-flow paths. His study, with caveats on the application of such methods to different hydrothermal systems, showed a general pattern of temperature decrease away from postulated fluid conduits such as sills and dikes, fault zones, and lithologic contacts. Most of the calculated temperatures fell in the range 226°–321°C. Nambija may be an excellent mining district for similar studies, especially if coupled with fluid-inclusion work. Unfortunately, the available data set for Nambija is as yet too limited in distribution and number of samples to rigorously evaluate trends in chlorite temperatures.

OTHER MINERALS

Feldspars in all rock types are nearly pure albite or orthoclase. Intermediate plagioclase compositions (Ab_{62}) are only observed in phenocryst cores in altered tuff sample NAM-10; rims are albite. Partial analyses of apatite indicate a fluorine-rich variety, containing less than 0.2 weight percent chlorine. Barite, micron-size blebs of galena, pyrrhotite, sphalerite, and an unidentified telluride mineral were detected in coarse-grained pyrite in sample NAM-3. Calcite fluoresces blue or red under the microprobe beam and appears to be relatively pure based on energy dispersive analyzer (EDS) spectra.

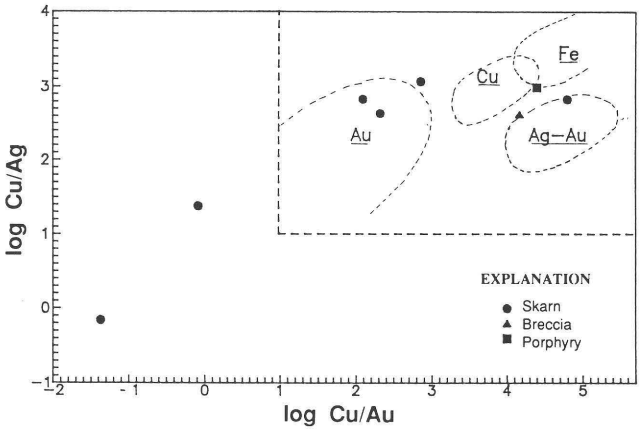

Figure 7. Metal ratios for Nambija rock samples. Fields for gold, silver-gold, copper, and iron skarns from Ettlinger and Ray (1989).

GEOCHEMISTRY

Analytical data (table 3) for samples representative of the various lithologies at Nambija show that gold contents range from below detection limits (0.002 ppm) to 47 ppm and that the highest values are present in skarn. Au/Ag ratios are greater than 1 for most samples. No particular elemental correlations are apparent in the overall data set, nor does the spatial distribution of elemental abundances indicate any zoning pattern. Tellurium ranges from below detection levels (0.05 ppm) to 2.80 ppm. Bismuth was sought, but not detected, at the 10 ppm level. Arsenic is present in most samples ($\leq$ 48 ppm), and both tungsten and arsenic are relatively enriched in skarn sample NAM-8. Copper ranges from 2 to 745 ppm; molybdenum values are all < 8 ppm, and most values are below detection limits (< 2 ppm). Fe/Mg ratios are greater than 1 for all samples; Na/K ratios are highly variable.

In their discussion of problems in classifying precious-metal-enriched skarns, Ettlinger and Ray (1989) note that such skarns are commonly present in geological settings that host iron and copper skarns and copper porphyry deposits. They proposed a skarn classification diagram using Cu/Au and Cu/Ag ratios that could be used with assay data as well as production data. Ratios for the Nambija data set are plotted on such a diagram in figure 7. Points are plotted for the eight samples for which gold, silver, and copper are all present above detection levels. Two of the Nambija skarn samples plot outside of the fields defined by Ettlinger and Ray (1989) on the basis of a worldwide skarn data set; these extremely high gold values undoubtedly reflect nugget effects in sampling. Three Nambija skarn samples plot in or near the gold skarn field; one plots in the silver-gold skarn field; and none plot in the copper or iron skarn fields. The scatter in the data points reflects the heterogeneity of the Nambija deposit and the unusually gold-rich nature of the mineralization. Neither the arsenic, tellurium, and (or) bismuth signature that is commonly associated with gold skarn deposits (as well as with other intrusion-related gold deposits (Sillitoe, 1991)) nor the antimony-arsenic-mercury chemical signature that is typical of some epithermal gold deposits are present in the samples studied here.

DISCUSSION

Meinert (1989), Theodore and others (1991), and Ettlinger and Ray (1989) compiled characteristics of a number of gold-bearing skarn deposits and summarized features that may be useful in exploration (table 4). Distinctive mineralogic characteristics of gold skarns noted by Meinert (1989) include garnet of intermediate grossular-andradite composition, high modal pyroxene/garnet ratios, relatively iron-rich (> Hd_{50}) pyroxene compositions, enhanced aluminum contents of pyroxene, and sulfide assemblages dominated by arsenopyrite, pyrrhotite, and marcasite. The presence of these minerals reflects the overall reducing environment that characterizes distal, gold-rich skarns (e.g., Fortitude, Nevada) that form the most attractive targets for exploration. Many proximal, copper-rich skarns commonly associated with porphyry copper systems also have significant quantities of gold, but these are characterized by a more oxidized, garnet-rich prograde assemblage and a dominant pyrite-chalcopyrite sulfide assemblage (Theodore and others, 1991; Meinert, 1989). The place of gold deposition in the complex spatial and temporal evolution of most skarn deposits from initial thermal metamorphism through prograde to retrograde metasomatism is not well understood. In many such deposits, gold appears to be deposited with sulfides late in the retrograde stages that develop best along structures permeable to hydrothermal fluids. In other cases, however, gold is associated with either paragenetically late quartz in skarn where prograde minerals such as garnet and pyroxene are

preserved or with a late quartz-pyrite overprint. The available data for the Nambija deposits (McKelvey, 1991; Salazar, 1988; this study) show that Nambija exhibits some of the characteristics of a relatively oxidized gold skarn, as indicated by garnet and pyroxene compositions, the presence of epidote, and the nature of the sulfide minerals (pyrite > pyrrhotite). More reduced mineral assemblages may lie at depth, and the gold observed in quartz within preserved prograde skarn assemblages may represent gold that was deposited or remobilized late in the history of the system. The protolith, albeit a diverse assemblage, appears to be dominated by volcaniclastic material rather than a relatively pure carbonate protolith. Neither copper, bismuth, arsenic, nor tellurium appear to be present in anomalous concentrations in the reconnaissance sample suite (table 4), although a Te-bearing mineral has been identified in pyrite. Gold/silver ratios are high, and copper/gold ratios for the Nambija samples appear to be extremely low compared to most gold skarn systems (McKelvey and Hammarstrom, 1991). Mineralization appears to be concentrated along major structures; however, the extensive alteration present in all of the samples studied from the area (notably alkali metasomatism of intrusive porphyry, igneous clasts in breccia, and skarn and extensive quartz veining) document the effects of a large magmatic-hydrothermal system, perhaps associated with an unidentified, possibly buried, porphyry (gold-copper) system.

Table 4. Characteristics of gold skarn deposits.

[Based on Theodore and others, 1991; Meinert, 1989; and Ettlinger and Ray, 1989]

- Clastic or volcaniclastic rock component in skarn protolith
- Relatively reduced, mafic calcalkaline/subalkalic plutons
- Anomalous contents of As, Bi, and (or) Te
- Gold enriched in distal skarn
- Gold deposited in retrograde skarn, together with sulfides
- Dominant skarn minerals:
  [Reduced type]
  Pyroxene (hedenbergitic, Al rich) > garnet (andradite-grossular)
  Narrow, Al-rich zones in pyroxene and garnet
  [Oxidized type]
  Garnet (andradite-grossular) > pyroxene (diopside rich)
- Reverse zoning and multiple generations of garnet
- Dominant sulfides:
  [Reduced type]
  Pyrrhotite, arsenopyrite, marcasite
  [Oxidized type]
  Chalcopyrite, pyrite
- Other gangue minerals:
  K-feldspar, biotite, prehnite, idocrase, scapolite, apatite, sphene, cuspidine, epidote (replaces garnet), actinolite or hornblende (replaces pyroxene), chlorite, quartz, calcite

ACKNOWLEDGMENTS

Greg McKelvey initiated this study, provided samples, base maps, and geologic data, and graciously encouraged me to complete the study when he left the project. Paul Schruben assisted in map preparation. John Slack and Ted Theodore provided extremely helpful critical reviews.

REFERENCES CITED

Arbogast, Belinda, F., ed., 1990, Quality assurance manual for the Branch of Geochemistry, U.S. Geological Survey: U.S. Geological Survey Open-File Report 90–668, 184 p.

Barragán, Jorge, 1989, El potencial aurífero del Ecuador: Geomimet, v. 16, no. 158, p. 89–90.

Cathelineau, Michel, 1988, Cation site occupancy in chlorites andillites as a function of temperature: Clay Minerals, v. 23, p. 471–485.

Cathelineau, Michel, and Nieva, David, 1985, A chlorite solid solution geothermometer, the Los Azufres (Mexico) geothermal system: Contributions to Mineralogy and Petrology, v. 91, p. 235–244.

Crock, J.G., Lichte, F.E., and Briggs, P.H., 1983, Determination of elements in NBS geological reference materials SRM268 obsidian and SRM688 basalt by inductively coupled plasma–atomic emission spectroscopy: Geostandards Newsletter, v. 7, no. 2, p. 335–340.

Einaudi, M.T., Meinert, L.D, and Newberry, R.J., 1981, Skarn deposits, *in* Skinner, B.J., ed., Seventy-Fifth Anniversary Volume, 1905–1980, Economic Geology: New Haven, Conn., Economic Geology Publishing Company, p. 317–301.

Ettlinger, A.D., and Ray, G.E., 1989, Precious metal enriched skarns in British Columbia: An overview and geological study: British Columbia Ministry of Energy, Mines, and Petroleum Resources Paper 1989–3, 128 p.

Johnson, T.W., 1991, Geology, hydrothermal alteration, and Cu-Ag-Au skarn and replacement mineralization in the northern part of the New World district, Park County, Montana: Pullman, Washington State University, unpub. M.S. thesis, 326 p.

Jowett, E.C., 1991, Fitting iron and magnesium into the hydrothermal chlorite geothermometer [abs.]: Geological Association of Canada—Mineralogical Association of Canada—Society of Economic Geologists, Program with Abstracts, v. 16, p. A62.

Krandidiotis, P., and MacLean, W.H., 1987, Systematics of chlorite alteration at the Phelps Dodge massive sulfide deposit, Matagami, Quebec: Economic Geology, v. 82, p. 1898–1911.

Lichte, F.E, Golightly, D.W., and Lamothe, P.J., 1987, Inductively coupled plasma–atomic emission spectrometry: U.S. Geological Survey Bulletin 1770, p. B1–B10.

Mapa Geológico Nacional de la República del Ecuador, 1982, scale 1:1,000,000.

McDowell, S.D., and Elders, W.A., 1980, Authigenic layer silicate minerals in borehole Elmore 1, Salton Sea geothermal field,

California, USA: Contributions to Mineralogy and Petrology, v. 74, p. 293–310.

McKelvey, G.E., 1991, Interest shown in Nambija gold deposits, Zamora Province, Ecuador: Mining Engineering, v. 43, no. 12, p. 1412–1414.

McKelvey, G.E., and Hammarstrom, J.M., 1991, A reconnaissance study of gold mineralization associated with garnet skarn at Nambija, Zamora Province, Ecuador [abs.], *in* Good, E.E., Slack, J.F., and Kotra, R.K., eds., USGS Research on Mineral Resources—1991, Program and Abstracts: U.S. Geological Survey Circular 1062, p.55.

Meinert, L.D., 1989, Gold skarn deposits—Geology and exploration criteria, *in* Keays, R.R., Ramsay, W.R.H., and Groves, D.I., eds., The Geology of Gold Deposits: The Perspective in 1988: Economic Geology Monograph 6, p. 537–552.

Mining Magazine, November 1990, Campanilla gold mine, p. 322–323.

Mineral Resources Data System (MRDS) [computer database], 1991, U.S. Geological Survey, Branch of Resource Analysis, Record number TC00085 for the Nambija district, Ecuador. [Available from USGS, BORA, MS 920, 12201 Sunrise Valley Drive, Reston, VA 22092].

Motooka, J.M., 1988, An exploration geochemical technique for the determination of preconcentrated organometallic halides by ICP-AES: Applied Spectroscopy, v. 42, p. 1293–1296.

Salazar, Edgar, 1988, Nambija: Conacimiento geologico y mineralogico hasta la presente: INEMIN, Quito, 11 p.

Sillitoe, R.H., 1991, Intrusion-related gold deposits, *in* Foster, R.P., ed., Gold Metallogeny and Exploration: Glasgow and London, Blackie, p. 165–209.

Theodore, T.G., Blake, D.W., Loucks, T.A., and Johnson, C.A., 1992, Geology of the Buckingham stockwork molybdenum deposit and surrounding area, Lander County, Nevada, *with a section on* Potassium-argon and $^{40}Ar/^{39}Ar$ geochronology of selected plutons in the Buckingham area, by E.H. McKee, *and a section on* Economic geology, by T.A. Loucks and C.A. Johnson, *and a section on* Supergene copper deposits at Copper Basin by D.W. Blake, *and a section on* Mineral chemistry of Late Cretaceous and Tertiary skarns, by J.M. Hammarstrom: U.S. Geological Survey Professional Paper 798–D, 307 p.

Theodore, T.G., Howe, S.S., Blake, D.W., and Wotruba, P.R., 1986, Geochemical and fluid zonation in the skarn environment at the Tomboy-Minnie gold deposits, Lander County, Nevada, *in* Nichols, E.E., ed., Exploration for Ore Deposits of the North American Cordillera; Selected Papers of the Symposium of the Association of Exploration Geochemists held in Reno, Nevada, March 25–28, 1984: Journal of Geochemical Exploration, v. 25, nos. 1, 2, p. 99–128.

Theodore, T.G., Orris, G.J., Hammarstrom, J.M., and Bliss, J.D., 1991, Gold-bearing skarns: U.S. Geological Survey Bulletin 1930, 61 p.

CHAPTER L

GEOCHRONOLOGY AND GEOCHEMISTRY OF THE LADOLAM GOLD DEPOSIT, LIHIR ISLAND, AND GOLD DEPOSITS AND VOLCANOES OF TABAR AND TATAU, PAPUA NEW GUINEA

By JAMES J. RYTUBA,[1] EDWIN H. MCKEE,[1] *and* DENNIS P. COX [2]

INTRODUCTION

The Tabar-Feni chain of alkaline volcanoes extends for a distance of over 250 km off the east coast of New Ireland, Papua New Guinea (fig. 1). Several gold deposits and prospects are present within the volcanic chain, which extends southeastward toward Bougainville Island, the site of the Panguna porphyry copper–gold deposit. The world-class Ladolam deposit, on the island of Lihir, was discovered in 1982 (Davies and Ballantyne, 1987) and has proven reserves of 29.7 million oz (923.7 t) of gold at a cutoff grade of 1 g/t (0.029 oz per short ton) and a geological reserve of 43 million oz (1,330 t) (Getz and Ward, 1990). The deposit formed very recently and still has active hot-spring and solfatara activity within parts of the orebody. This paper presents new age and geochemical data for the Ladolam deposit and for volcanic units and gold deposits in the northern part of the Tabar-Feni volcanic chain on the islands of Simberi and Tatau.

REGIONAL GEOLOGY

Volcanoes within the Tabar-Feni chain have been regarded to range in age from Miocene to Holocene based primarily on their morphology and a few isotopic age determinations. The five K-Ar isotopic ages reported previously for the chain range from 1.5 to 0.18 Ma with no systematic age progression along the chain (Wallace and others, 1983). The volcanic chain is characterized by shoshonitic alkaline volcanism, and petrochemical studies of volcanic suites from the volcanic chain by Wallace and others (1983) demonstrate a broad range of

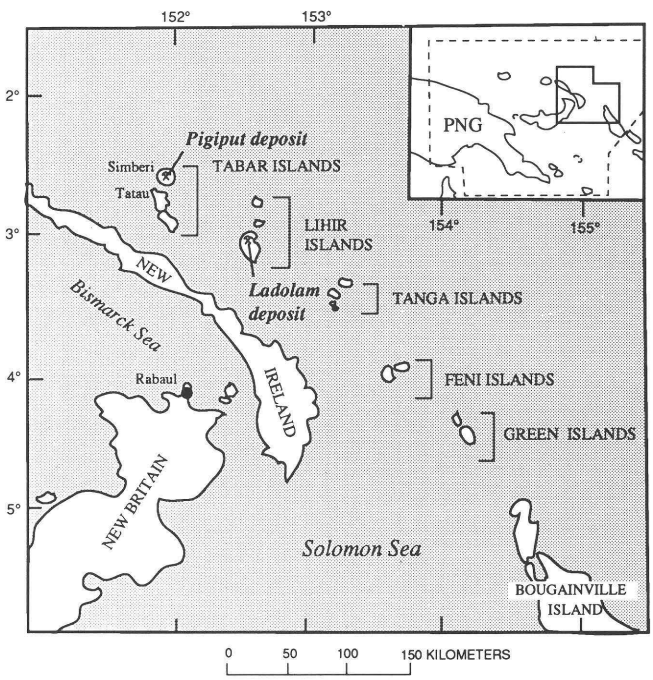

Figure 1. Location of Lihir and Tabar Islands and the Ladolam, Pigiput, Simberi, and Tatau gold deposits and prospects. PNG, Papua New Guinea.

[1]U.S. Geological Survey, Mail Stop 901, 345 Middlefield Road, Menlo Park, CA 94025.

[2]U.S. Geological Survey, Mail Stop 984, 345 Middlefield Road, Menlo Park, CA 94025.

Table 1. Data for samples collected from islands of Lihir, Simberi, and Tatau, Papua New Guinea.

[Constants used were $^{40}K/K=1.167\times10^{-4}$ mol/mol; $\lambda_\beta=4.962\times10^{-1}$/yr; $\beta_\epsilon+\beta_{\epsilon'}=0.581\times10^{-1}$/yr]

Sample no.	Locality	Sample type	Mineral	K_2O	$^{40}Ar_{rad}$ (mol/g$\times10^{-12}$)	$^{40}Ar_{rad}$ (percent of total)	Age (Ma)
DDHL53-427.7m	Lihir	Vein	Biotite	8.72	4.21927	9.01	0.34±0.03
DDHL63-424.8	Lihir	Porphyry	Biotite	9.39	4.89491	3.52	0.36±0.03
8531	Simberi	Trachyte	Whole rock	1.31	6.63084	43.9	3.5±0.2
8532	Simberi	Trachyte	Whole rock	1.14	6.0071	30.5	3.7±0.2
8533	Simberi	Basalt	Whole rock	0.65	2.16529	5.9	2.3±0.4
8534	Simberi	Basalt	Whole rock	0.44	1.98842	12.19	3.1±0.3
8537	Tatau	Trachybasalt	Whole rock	1.11	4.44735	22.1	2.8±0.2
8539	Tatau	Trachybasalt	Whole rock	3.97	1.11036	22.0	1.91±0.1
8527	Simberi	Vein	Alunite	0.28	5.21741	0.46	1.2±2.0
8528	Simberi	Vein	Alunite	0.88	3.57103	5.65	2.8±.6

nepheline-normative volcanic and intrusive rocks. The geochemical data, including radiogenic isotopic values, suggest similarities to an intraoceanic arc; however, the absence of andesitic volcanic rocks and the distinctly alkaline character of the volcanism makes the origin of the volcanism problematic (Plimer and others, 1988; Wallace and others, 1983; and Johnson, 1979). Johnson's (1979) hypothesis that the volcanism results from partial melting of mantle lithosphere previously modified by subduction is favored by recent studies.

K-Ar DATING

Six volcanic units and two mineral deposits on the islands of Simberi and Tatau and two samples from the Ladolam deposit on the island of Lihir were dated by K-Ar methods. The samples of volcanic units on Simberi and Tatau are representative of the volcanic edifices and also provide maximum-age constraints for the gold deposits and prospects on the two islands. Alunite samples from two gold deposits on Simberi directly date the mineralization (table 1). The two samples from the Ladolam deposit include biotite phenocrysts from the porphyry intrusion that is genetically related to the gold deposit and hydrothermal biotite from the mineralized stockwork part of the deposit (table 1).

METHODS

K-Ar analyses were performed using the standard isotope-dilution techniques similar to those described by Dalrymple and Lanphere (1969). Mineral concentrates were made by heavy-liquid, magnetic, electrostatic, and hand-picking procedures. Potassium analyses were by lithium-metaborate-flux-fusion flame photometry, the lithium serving as an internal standard (Ingamells, 1970). Argon analyses were done using a five-collector mass spectrometer for one sample (Stacey and others, 1981) and using a 15.2-cm-radius, Neir-type mass spectrometer for five samples. The precision of the data, shown as the "± value" (table 1), is the estimated analytical uncertainty at one standard deviation (Cox and Dalrymple, 1967). It represents uncertainties in the measurement of radiogenic ^{40}Ar and K_2O based on experience with hundreds of replicated analyses in the Menlo Park laboratories of the U.S. Geological Survey. Mass discrimination of the spectrometer is routinely determined on the basis of multiple analyses of purified air. The constants used in age determination are those recommended by the Subcommission on Geochronology (Steiger and Jaeger, 1977).

GEOLOGY OF THE LADOLAM DEPOSIT

The three stratovolcanoes that comprise the island of Lihir are Pleistocene in age and rest on a basement of Pliocene volcanic rocks (Plimer and others, 1988). The Ladolam gold deposit occurs within the Luise caldera, a 6-by-4-km summit caldera developed on a stratovolcano located on the east side of the island. The Ladolam deposit consists of several zones of gold mineralization within the floor of the Luise caldera (Davies and Ballantyne, 1987), and the deposit contains a geological reserve of 43 million oz Au (Getz and Ward, 1990).

Gold is hosted in a variety of breccias and is closely associated with a subvolcanic monzonite porphyry that also contains low-grade stockwork gold mineralization. The breccias are a mixture of collapse breccias derived from the oversteepened caldera walls, primary volcanic and intrusive breccias, and hydrothermal breccias that crosscut other breccia types. The highest gold grades are present within a subhorizontal breccia unit composed of volcanic and intrusive clasts, originally termed the "boiling zone" (Davies and Ballantyne, 1987). This breccia is

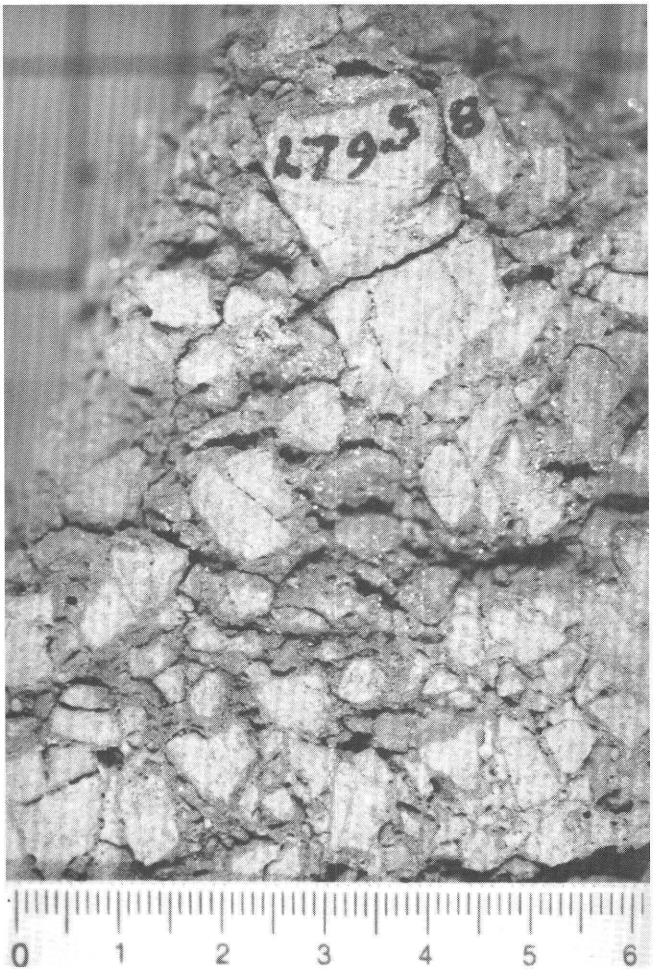

Figure 2. Core sample of high-grade gold ore from the Lienetz zone, Ladolam gold deposit. Open-space breccia (locally termed the "boiling zone") consists of monzonite clasts characterized by biotite alteration. Clasts are coated with fine-grained pyrite. Matrix has been leached from the rock.

characterized by an open-space texture in which the matrix has been leached (fig. 2). Clasts rich in secondary biotite are coated by fine-grained pyrite, giving the breccia a dark-black color. Gold forms grains that are < 20 μm in diameter within pyrite in the sulfide zone (Moyle and others, 1990).

Samples from the Leinetz ore zone, within the central part of the Ladolam deposit, were examined petrographically and with the scanning electron microscope (SEM). Breccia textures most common within the deposit consist of crackle breccias at depth, grading upward to clast-supported and finally matrix-supported breccias in the upper part (fig. 3). In general, rocks that appear as clasts in the breccias show a gradual transition in texture upward from fine- to medium-grained equigranular rocks beneath the "boiling zone" to hypabyssal porphyries with microaplitic groundmass and,

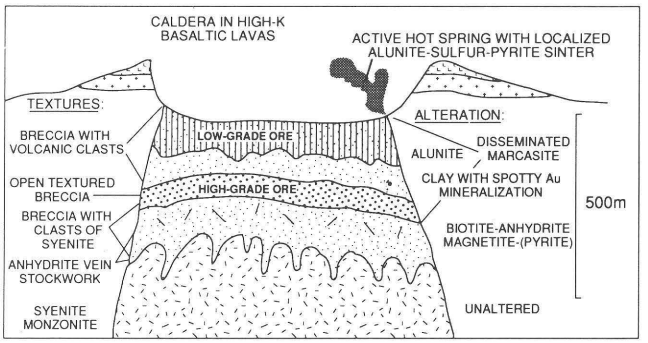

Figure 3. Idealized cross section through the Ladolam gold deposit, Lihir Island, showing distribution of breccia and textures and zoning of ore and alteration.

finally, to volcanic porphyries with flow-aligned groundmass feldspars in the upper alunite alteration zones.

Weakly altered intrusive rocks are of two types. The first type is a monzonite (DDH L63, 425 m) consisting of 1–2-mm-wide, radiating grains of plagioclase (An_{60}) and interstitial K-feldspar. Biotite forms large euhedral grains that poikilitically enclose plagioclase, and clinopyroxene is rare. Magnetite is abundant as small rounded grains and in clusters with biotite. The second type is a syenite (DDH L44, 344 m) composed of interlocking anhedral grains of K-feldspar, euhedral clinopyroxene, rare biotite, and abundant magnetite.

Grading upward from these weakly altered rocks into the ore zone (fig. 3), biotite alteration becomes prominent, but, except for anhydrite-calcite veins, stockwork veinlets typical of most porphyry systems are rare. However, narrow, widely spaced veinlets of clinopyroxene-magnetite-albite were noted in the syenite. Anhydrite-calcite veins are very abundant beneath the ore zone. They contain barite and irregularly distributed small grains of sphalerite, galena, chalcopyrite, and pyrite. Silver telluride was noted in one sample as a small inclusion in pyrite. A mineral rich in rare earth elements and phosphorous was detected by the SEM in several samples but was not found in thin section. Vapor-rich fluid inclusions are abundant in the veinlets, and many inclusions contain the daughter minerals celestite and barite. Chloride minerals (such as halite and sylvite), characteristic of fluid inclusions in porphyry systems, were not detected.

In the ore breccia, clasts of monzonite altered to biotite and white mica are surrounded by a matrix composed of biotite, anhydrite, and pyrite. The anhydrite is partially replaced by gypsum. Pyrite is abundant and is partially replaced by chalcopyrite. In addition to these minerals, PbS, ZnS, HgS, and the rare-earth phosphate were noted with the SEM. Bismuthian stibnite, similar to that present in the Paradise Peak deposit, Nevada (John and others, 1991), is also present.

Samples in which primary minerals were totally replaced by alunite retained their original texture so that breccia clasts and igneous rock textures could be observed. Pyrite is the most abundant sulfide, and marcasite is subordinate in abundance. Pyrite forms inclusion-filled grains surrounded by overgrowths of inclusion-free pyrite. It also occurs as fine wisps, atolls, and framboids. Magnetite was observed as inclusions in pyrite. Rarely, chalcopyrite replaces both pyrite and magnetite. Other inclusions in pyrite grains were identified by SEM methods as lead sulfide, molybdenum sulfide, and silver-gold telluride.

AGE AND GEOCHEMISTRY OF THE LADOLAM DEPOSIT

Biotite from phenocrysts in the fine-grained phase of the porphyritic monzonite at a depth of 424.8 m below the surface has an age of 360±30 ka (table 1). Veinlets that comprise the stockwork in the porphyry are characterized by an early phase of hydrothermal biotite intergrown with magnetite and overgrown by later anhydrite. Coarse-grained biotite from a vein containing 0.8 ppm Au at a depth of 427.7 m has an age of 340±30 ka (table 1). These ages are the same within analytical uncertainty and support a close genetic relationship between the porphyry and gold mineralization. However, the data are permissive of mineralization following emplacement of the porphyry by as much as 80,000 years.

Geochemical analyses of drill-hole and surface samples from the Lienetz zone of the Ladolam deposit (table 2) represent both porphyry and epithermal environments. Factor analysis was used to define elemental associations. The R-mode principal components analysis (Davis, 1986), using an orthogonal transformation solution, defines three factors with positive loading values of greater than 0.8. The elements in each factor are listed in order of decreasing loading and are summarized in table 3. Factor 1 consists of Au, Ba, Cs, As, Ag, and Rb. This elemental suite reflects the epithermal environment of precious metal mineralization. Factor 2 consists of W, U, Mo, Cu, Pb, and Cr and reflects mineralization associated with the porphyry environment. Factor 3 consists of Fe, Co, V, and Ce and reflects the original magmatic variation of these elements in the volcanic and plutonic host rocks.

GEOCHEMISTRY AND AGE OF GOLD DEPOSITS AND HOST ROCKS, SIMBERI AND TATAU

Simberi and Tatau form the northern two volcanoes of the Tabar group and occur at the northernmost part of the volcanic chain. The four volcanic units dated from Simberi represent the major geologic units on the island and span a short interval from 3.5 to 2.3 Ma. Based on the analytical uncertainty in the sample ages, the volcanic event could have lasted as little as 0.8 m.y. or as long as 2.0 m.y. (table 1). The alunite ages, 1.2±2.0 and 2.8±0.6 Ma, from the mineralized zones on Simberi are younger than the volcanic rocks, but because of the large analytical uncertainty in the ages, alunite could have formed during mineralization that occurred either during the last stage of volcanic activity or just after volcanism ended, at about 2.2 Ma.

Two volcanic units on the island of Tatau have ages of 2.8±0.2 and 1.9±0.1 Ma (table 1). The volcanic units provide a maximum age for the high-grade gold-quartz-adularia and base-metal veins present on Tatau. Volcanic activity on Tatau and Simberi overlap in part, and the similar ages for the end of volcanism suggest that the mineralizing event on Tatau occurred at the end of volcanic activity and at about the same time as on Simberi.

The Pigiput deposit on Simberi is hosted by volcanic breccias, flows, and associated plugs. Although air-photo analysis suggests circular structures on Simberi, the flat dips of the pyroclastic units observed in drilling suggest that the island is an erosional remnant of a tuff sheet rather than a remnant of a volcanic center (R. Rogerson, Papua New Guinea Geological Survey, oral commun., 1986).

Geochemical data of surface samples from the Pigiput deposit (table 2) were evaluated through correlation-coefficient and factor analysis. Gold has a strong correlation (> 0.8) with Ag, As, Fe, Mo, Sb, and V. Principal components factor analysis defines three significant elemental associations. The R-mode principal components analysis, using an orthogonal transformation solution, defines three factors with positive loading values of greater than 0.8 (table 3). Factor 1 consists of Fe, Mo, Sb, Au, As, V, and Ag; this elemental suite reflects precious metal mineralization. Factor 2 consists of Na, Cs, and Co and reflects the intense argillic alteration of the volcanic host rocks. Factor 3 consists of Sm, La, and Ce and reflects the magmatic fluid enrichment of light rare-earth elements (LREE) superimposed on the original LREE variation of these elements in the volcanic rocks (see Discussion section).

DISCUSSION

Geochronologic data presented in this paper and previously published ages (Wallace and others, 1983) indicate that the Tabar-Feni volcanic chain is Pliocene to Holocene in age, and there is no isotopic evidence for Miocene volcanism. Volcanic units from the Tabar

Table 2. Geochemistry of volcanic and plutonic rocks and mineralized samples from Lihir, Tatau, Simberi and Tabar Islands, Papua New Guinea.

[All values in ppm except gold (in ppb); iron and sodium in weight percent. Analysis by INNA except by atomic absorption for Cu, V, Pb, and Ag. Symbols: Feld, feldspar; Hb, hornblende; Py, pyrite; Por, porphyry; Bx, breccia; Bio, biotite; Stwk, stockwork; Q, quartz; Monz, monzonite]

Sample no.	Sample type	Location	Au	Ag	As	Ba	Ce	Cs	Cr	Cu	Co	Fe	La	Mo	Na	Pb	Rb	Sb	Sm	Sc	Th	U	V	W
LC1	Hb por flow	Luise caldera wall, Lihir	3	0.3	1	180	33	1	290	144	51	7.7	13	2	1.6	18	48	0.2	5.8	34	1.2	0.5	104	2
LC2	Basalt por flow	Luise caldera W. wall, Lihir	1	0.2	3	280	29	1	260	90	38	7.7	11	2	2	5	51	0.4	4.8	28	1.3	0.5	196	2
LC4	Flow	Luise caldera W. wall, Lihir	15	0.1	1	100	19	1	59	67	34	10	14	2	0.2	14	10	0.3	3	28	3.9	0.6	290	2
LC5	Flow	Luise caldera W. wall, Lihir	6	0.3	1	310	43	2	140	155	44	9.3	21	2	1.4	5	31	0.3	9.1	28	1.1	0.5	250	2
LC6	Basalt por flow	Kapit Creek	5	0.2	1	330	32	2	92	140	37	7.8	11	2	2	5	18	0.2	4.8	27	1.1	0.5	205	2
LC7	Basalt por flow	Luise caldera E. wall, Lihir	3	0.3	3	300	35	2	130	162	32	7.6	17	4	2.9	5	52	0.3	5.9	20	1.7	1.3	210	2
LC8	Mafic tuff	Luise caldera W. wall, Lihir	4	0.2	2	910	40	1	50	108	78	15	11	2	0.2	11	10	0.2	5.1	48	2.1	1.1	380	2
LC12	Mafic tuff	Luise caldera W. wall, Lihir	21	0.2	27	200	76	1	50	27	10	4.1	28	2	0.3	10	31	1.3	6.6	43	2.6	1.8	235	2
L16	Oxide ore	Lienetz ore zone, Lihir	504	0.6	10	1,200	110	1	260	26	10	1	46	84	0.2	5	18	8.6	8	24	2.5	2.2	72	8
L54-194.5	Sulfide ore	Lienetz ore zone, Lihir	30,000	7.8	1,460	30,000	100	6	210	137	14	5.2	110	246	0.2	420	150	162	8.4	16	1.9	3.6	210	8
L63-424.8	Bio monz stwk ore	Lienetz zone, Lihir	1,680	0.4	89	1,900	42	1	200	105	23	6.9	20	18	3	94	54	17	6	14	1	1.1	220	2
L63-568.2	Monzonite	Lienetz zone, Lihir	120	0.2	20	340	32	1	73	88	15	4.9	13	6	2.8	5	54	1.8	4.9	12	0.9	0.8	147	2
L71-177	Sulfide ore zone	Lienetz ore zone, Lihir	4,050	5.8	655	5,800	120	1	440	3,600	27	7.3	120	4,130	0.4	1,250	130	235	8.2	10	1.2	14	250	40
L87-411	Monzonite por	Lienetz ore zone, Lihir	22	0.2	9	480	30	1	67	27	10	4	14	6	3.4	53	80	0.7	4.4	6.9	1.9	1.5	122	2
M1	Lava	Makapena, Tatau	9	0.2	14	540	47	2	74	93	24	5.9	19	4	2.6	9	39	0.5	6.4	14	2	1.9	163	2
M2	Trachyte por	Makapena, Tatau	130	0.1	36	970	40	1	160	265	15	3.8	22	130	1.9	48	54	10	5.8	24	1.5	2.3	144	4
M3	Feld por, py-q veins	Makapena, Tatau	98	0.9	100	1,100	33	2	83	28	10	2.1	18	2	2.3	5	79	1.4	4.1	3.4	1.6	1.7	32	2
P1	Pumice tuff	Pigiput, Simberi	4,970	0.1	1,660	100	36	1	62	35	10	8.9	8	41	0.2	48	10	113	1.4	9.5	7.5	4.4	58	20
P2	Tuff	Pigiput, Simberi	390	0.1	1,110	100	10	1	50	191	10	4.6	5	2	0.2	8	74	12	1.1	9.2	7.7	3	106	4
P3	Vein, Mn and FeO	Pigiput, Simberi	9,020	0.2	4,100	540	360	1	86	90	19	11	160	43	0.1	37	60	162	67	15	5.7	5.4	240	9
P4	Por intrusive	Pigiput, Simberi	2,630	0.1	1,850	280	88	1	65	20	10	6	38	2	0.2	17	250	77	10	8.8	3.7	3.5	179	15
P5	Por intrusive	Pigiput, Simberi	3,070	0.2	2,470	100	71	3	94	132	15	8.2	26	17	0.2	12	150	68	11	19	4.7	4.3	260	27
S1A	Argillic zone	Samat, Simberi	67	0.2	39	640	58	8	120	108	24	5.7	24	2	2.2	2	32	1.3	8.2	26	1.9	2.6	168	2
S3	Oxide ore in flow	Samat, Simberi	140	0.2	181	260	93	1	50	20	10	3.6	35	8	0.3	4	140	37	6.8	11	2.5	3.1	145	8
S4	Oxide ore in flow	Samat, Simberi	1,230	0.8	418	290	72	1	120	1,700	10	5.5	29	4	0.2	8	180	13	8.5	40	2.9	5.3	215	2
S5	Oxidized vein ore	Samat, Simberi	30,000	1.5	11,800	510	220	1	190	265	10	44	130	221	0.3	10	57	572	31	47	2.7	6.2	645	2
TB1	Por mafic flow	Big Tabar	140	0.2	24	420	16	1	160	157	46	8.3	10	6	2	5	43	1.3	4.3	27	0.9	0.7	275	2
TB2	Vein, high grade ore	Big Tabar	11,500	0.1	746	410	45	1	50	170	22	8.8	20	15	2.2	8	67	34	6.3	20	1.3	1.5	305	2
8528	Alunite vein	Sorowar, Simberi	2,590	0.5	1,200	270	68	1	88	50	10	3	32	2	0.2	28	31	37	8.5	16	1.3	2.2	300	2
8531	Por mafic flow	Mt. Manambu, Simberi	1,370	0.1	87	170	52	1	230	80	39	8.7	19	2	1.3	20	21	7.2	7	46	1.3	0.8	220	2
8532	Mafic flow	Mt. Manambu, Simberi	140	0.1	44	310	50	3	260	70	31	6.6	22	3	1.6	17	10	3.9	8	36	1.9	1.7	175	2
8533	Por mafic flow	Asllawa, NE. coast Simberi	330	0.1	83	100	54	1	780	120	62	7.4	21	2	1.9	5	44	1.9	6.7	32	1.3	1.2	172	2
8534	Por mafic flow	Asllawa, NE. coast Simberi	480	0.2	34	170	53	1	300	156	39	7.3	19	3	1.8	5	14	1.8	6.2	35	1.6	0.9	188	2
8535	Hydrothermal Bx	Makopena	970	50	6,660	6,700	16	1	310	110	10	12	19	41	0.1	160	10	413	6.9	11	0.5	1	96	57
8537	Por mafic flow	Makopena	51	0.4	53	940	31	1	150	88	39	8.3	16	4	2.1	60	39	10	6	28	1.4	0.7	215	2
8538	Altered lava	Mt. Tiro prospect	180	26	1,310	3,100	62	4	110	192	140	10	8	6	0.2	23	150	35	5.3	29	1.9	1.4	255	5
8539	Por lava	Mt. Tiro prospect	25	1.1	10	670	45	2	120	157	32	6.3	17	2	1.2	31	71	5.7	6.5	20	1.4	1.2	230	2

Table 3. Array of orthogonal varimax loadings for three factors determined for the Ladolam and Pigiput deposits.

[Bold numbers indicate elements defining each factor. See text for definition of factors]

	Ladolam deposit, Lihir			Pigiput deposit, Simberi		
	Factor 1	Factor 2	Factor 3	Factor 1	Factor 2	Factor 3
Log (Au)	**0.989**	–0.038	0.001	**0.951**	–0.074	0.274
Log (Ag)	**0.848**	0.507	0.103	**0.888**	–0.078	0.033
Log (As)	**0.954**	0.262	0.093	**0.937**	–0.108	0.294
Log (Ba)	**0.989**	0.013	0.001	0.313	0.676	0.552
Log (Ce)	0.344	0.696	–0.233	0.328	–0.014	**0.940**
Log (Cs)	**0.979**	–0.145	–0.064	–0.123	**0.939**	–0.164
Log (Cr)	0.088	**0.853**	0.171	**0.836**	0.291	0.108
Log (Cu)	–0.017	**0.956**	0.281	0.017	–0.243	–0.135
Log (Co)	–0.053	0.548	**0.827**	–0.201	**0.847**	0.383
Log (Fe)	0.209	0.295	**0.883**	**0.985**	–0.015	0.158
Log (La)	0.652	0.719	0.040	0.499	–0.003	**0.861**
Log (Mo)	0.012	**0.966**	0.250	**0.972**	–0.045	0.167
Log (Na)	–0.455	–0.551	0.291	–0.069	**0.966**	–0.177
Log (Pb)	0.277	**0.917**	0.283	–0.099	–0.310	0.356
Log (Rb)	**0.808**	0.453	0.210	–0.267	–0.475	–0.020
Log (Sb)	0.572	**0.785**	0.230	**0.949**	–0.097	0.252
Log (Sm)	0.480	0.536	–0.087	0.239	0.025	**0.953**
Log (Sc)	0.020	–0.176	–0.341	0.722	0.165	–0.001
Log (Th)	0.175	–0.014	**–0.892**	–0.241	–0.404	–0.070
Log (U)	0.130	**0.975**	0.182	0.641	–0.396	0.439
Log (V)	0.418	0.399	**0.804**	**0.923**	0.007	0.248
Log (W)	0.067	**0.982**	0.155	–0.248	–0.338	–0.058

group in the northernmost part of the chain range in age from about 3.5 to 1.9 Ma. Within the Tabar group, volcanic units on Simberi and Tabar Island overlap in age. A previously reported age of 0.99±0.08 Ma (Wallace and others, 1983), for a quartz trachyte on Tabar Island, is considerably younger and may reflect an episode of younger volcanic activity separate from the mid-Pliocene event.

The Ladolam deposit on Lihir Island represents a unique gold deposit in many aspects. The deposit is the single largest gold orebody known and contains a geological reserve of 43 million oz (1,330 t) of gold (Getz and Ward, 1990). The close relationship of the gold deposit to a subvolcanic porphyry that intruded to very shallow levels of the volcanic edifice (within 400 m of the floor of the summit caldera) (fig. 3) demonstrates the transition from porphyry to hot-spring environment over a very telescoped interval. The age of the porphyry, about 360 ka, and the associated stockwork veining, about 340 ka, indicate a genetic relationship between the porphyry and the gold deposit. Biotite dated from coarse-grained biotite-magnetite-gold stockwork represents the older, high-density, hydrothermal fluid associated with the subvolcanic-porphyry style of mineralization. Mixing of the older, high-density fluid with meteoric water resulted in deposition of gold in the open-space breccia at depths of 50 to 200 m below the paleosurface. Near-surface argillic, advanced argillic, and phyllic alteration developed in the shallow hot-spring environment, and alunite from the advanced argillic zone has an age of 151±15 ka (Davies and Ballantyne, 1987). Detailed geochemical studies of REE demonstrates that boiling of the LREE-enriched magmatic fluids occurred at depth and resulted in condensation of vapor phases into the meteoric system, and this developed an acid-sulfate fluid in the near surface (Lottermoser, 1990). The presence of active hot-spring and solfatara activity within the deposit is indicative of this waning stage of acid-sulfate hydrothermal activity. The episode of porphyry intrusion, porphyry-style alteration and mineralization, and hot-spring gold deposition occurred over a remarkably short interval of about 360,000 years and demonstrates that long-lived hydrothermal systems are not necessary for the formation of world-class gold deposits. As Henley (1990) has noted, the Ladolam deposit demonstrates a clear continuum from magmatic-hydrothermal to the meteoric-water-dominated hydrothermal ore deposition.

Similarities and differences between Ladolam and typical porphyry copper–gold deposits are listed in table 4. These differences imply that the Ladolam deposit formed at a much higher level in the crust than is typical

Table 4. Comparison of Ladolam deposit to geologic features common to porphyry copper–gold deposits.

Characteristic	Ladolam	Porphyry Cu-Au
Intrusive rock texture	Equigranular, minor porphyry	Porphyry texture is predominant.
Alteration	Biotitic, argillic, and acid-sulfate	Porphyry texture is predominant.
Ore assemblage	Marcasite, pyrite, magnetite, gold.	Chalcopyrite, magnetite, (pyrite), gold.
Stockwork vein types	Anhydrite veinlets only	Biotite-K-feldspar, Quartz-magnetite-chalcopyrite.
Temperature	140–150°C and 200–220°C (Moyle and others, 1990).	400–700°C.
Fluid salinity	3.8 weight percent NaCl equivalent (Moyle and others, 1990).	30-75 weight percent NaCl equivalent.
Fluid inclusion daughter minerals	Sr and Ba sulfates in anhydrite	Na-K-Fe chlorides.
Breccia types	Phreatic and primary volcanic	Hydrofracturing.

of porphyry systems. The pressure quench that produces a porphyry texture did not occur during the late magmatic phase of intrusion nor did the evolution of a high-pressure fluid capable of hydrofracturing the intrusion to produce stockwork veins. Breccia, more characteristic of phreatic explosive activity, became the important ore-trapping structure. The anhydrite stockwork, as pointed out by Moyle and others (1990), probably formed during invasion by marine water. This conclusion is supported by the presence of strontium sulfate as the important daughter mineral in the fluid inclusions.

Ladolam differs from epithermal deposits mainly in its high content of hydrothermal biotite. It differs from epithermal, alunite-rich deposits in the low abundance of enargite or luzonite. It differs from gold telluride deposits associated with alkalic igneous rocks (Cripple Creek, Colorado, and Emperor, Fiji) in its low abundance of gold or silver tellurides. Although vanadium content is high at Ladolam, the green vanadium mica typical of gold telluride deposits has not been observed.

In conclusion, it is difficult to find similarities between Ladolam and any known type of deposit. Moreover, it does not resemble any of the known prospects in the Tabar-Feni island chain. Until other similar deposits are discovered, Ladolam must be considered unique.

ACKNOWLEDGMENTS

We wish to express out gratitude to Kennecott Exploration (Australia, Ltd.) for providing access to the deposits on Lihir, Tatau, and Simberi. In particular we wish to thank Rod Davies, Peter Morrissey, and John Wier for providing information and ideas as well as samples from each of the deposits. Our appreciation goes to Rick Rogerson of the Papua New Guinea Geological Survey for logistical help and discussions during our field work.

REFERENCES CITED

Cox, Alan, and Dalrymple, G.B., 1967, Statistical analysis of geomagnetic reversal data in the precision of potassium-argon dating: Journal of Geophysical Research, v. 72, no. 110, p. 2603–2614.

Dalrymple, G.B., and Lanphere, M.A., 1969, Potassium-Argon Dating: San Francisco, W.H. Freeman, 258 p.

Davies, R.G., and Ballantyne, G., 1987, Geology of the Ladolam gold deposit, Lihir Island, Papua New Guinea: Proceedings, Pacific Rim Congress, 1987, Gold Coast, Queensland, Australia Institute of Mining and Metallurgy, p. 943–949.

Davis, J.C., 1986, Statistics and Data Analysis in Geology: New York, John Wiley, 646 p.

Getz, A.J., and Ward, R.J., 1990, Western Pacific precious metals projects updated: Mining Engineering, v. 42, no. 9, p. 1067–1070.

Henley, R.W., 1991, Epithermal gold deposits in volcanic terranes, *in* Foster, R.P., ed., Gold Metallogeny and Exploration: Glasgow and London, Blackie, p. 133–164.

Ingamells, C.O., 1970, Lithium metaborate flux in silicate analysis: Analytica Chimica Acta, v. 52, p. 323–334.

John, D.A., Nash, Thomas, Clark, C.W., and Wolftange, W.H., 1991, Geology, hydrothermal alteration, and mineralization at the Paradise Peak gold-silver deposit, Nye County, Nevada, *in* Geology and Ore Deposits of the Great Basin: Reno, Nevada, Geological Society of Nevada, p. 1020–1049.

Johnson, R.W., 1979, Geotectonics and volcanism in Papua New Guinea—A review of the late Cainozoic: Bureau Mineral Resources, Journal of Australian Geology and Geophysics, no. 4, p 181–207.

Lottermoser, B.G., 1990, Rare-earth element and heavy-metal behavior associated with the epithermal gold deposit on Lihir Island, Papua New Guinea: Journal of Volcanology and Geothermal Research, v. 40, p. 269–289.

Moyle, A.J., Doyle, B.J., Hoogvliet, H. and Ware, A.R., 1990, Ladolam gold deposit, Lihir Island, *in* Hughes, F.E., ed., Geology of the Mineral Deposits of Australia and Papua New Guinea: Australia Institute Mining and Metallurgy Monograph No. 14, v. 2, p. 1793–1805.

Plimer, I.R., Andrew, A.S., Jenkins, R., Lottermoser, B.G., 1988, The geology and geochemistry of the Lihir gold deposit, Papua New Guinea: Melbourne, Geological Society of Australia, Extended Abstracts and Programs, Bicentennial Gold 88, p. 139–143.

Stacey, J.S., Sherrill, N.D., Dalrymple, G.B., Lanphere, M.A., and Carpenter, N.V., 1981, A five-collector system for the simultaneous measurement of argon isotopic ratios in a static mass spectrometer: International Journal of Mass Spectrometry and Ion Physics, v. 39, p. 167–180.

Steiger, R.H. and Jaeger, E., 1977, Subcommission on geochronology—Convention on the use of decay constants in geo- and cosmochronology: Earth and Planetary Science Letters, v. 36, p. 359–362.

Wallace, D.A., Johnson, R.W., Chappell, B.W., Arculus, R.J., Perfit, M.R., and Crick, I.H., 1983, Cainozoic volcanism of the Tabar, Lihir, Tanga, and Feni Islands, Papua New Guinea; geology, whole rock analyses and rock forming mineral composition: Bureau Mineral Resources, Geology and Geophysic Australia Report, 243 p.

CHAPTER M

VOLATILES IN CLAY MINERALS FROM SEDIMENTARY AND HYDROTHERMAL ENVIRONMENTS: A POTENTIAL PETROLOGIC AND MINERALS-ASSESSMENT TOOL?

By GENE WHITNEY[1] *and* GARY P. LANDIS[2]

ABSTRACT

Clay samples from two different geochemical environments were examined using quadrupole mass spectrometric analysis of gases evolved during heating to determine whether systematic differences in gas compositions can be used as petrologic-geochemical indicators of geologic environment. An illitic, interstratified illite/smectite was collected from the Shannon Sandstone Member of the Upper Cretaceous Steele Shale in the Powder River Basin, Wyoming. This rock currently serves as a petroleum reservoir rock and contains oil. A suite of clay samples also was collected from a fossil acid-sulfate geothermal system at Alum Mountain, New Mexico, for comparison. These samples include illitic clays, nearly pure smectite, nearly pure kaolinite, and a mixture of kaolinite, smectite, and illite—the samples typify clay alterations in hydrothermal ore systems. Comparison of the volatile species liberated and the temperatures at which they are released provide information about the abundance and residence of the gases in the clays. This information may be used to infer compositions of fluids in which the clays reacted.

All samples were heated from 60°C to 1,060°C at 5°C/min while 20 mass/electric charge (m/e) channels were analyzed by mass spectrometer. This technique permits the evaluation of volatile composition and the specification of the temperature at which various volatiles were released from the clay samples. Preliminary results show dramatic differences in volatile compositions of clays from the two geochemical environments. The petroleum-reservoir clay bears a distinctive organic signature, even after particle size separation and dispersal, whereas the geothermal clays show more distinctive characteristics related to sulfide and sulfate volatiles. Mineralogically similar samples from the two environments show roughly similar water-evolution profiles but dramatically different behavior for other gases. For example, the profiles for organic species, CO_2, and sulfur gases are entirely different for illitic clays from the two environments. On the other hand, samples with different mineral compositions from the same geochemical environment also showed distinctly different gas-evolution profiles: kaolinite and smectite from the fossil geothermal system exhibit entirely different profiles for HF, HCl, and sulfur gases. These data suggest that volatile composition and evolution profiles for clay minerals may be useful for fingerprinting geochemical fluids in which the clays formed; volatile composition and evolution profiles may be quantifiable with additional basic research on siting and partitioning of volatiles in clays and clay-rich rocks. Site-specific characterization of gas species in clays may prove a valuable tool in mineral resource assessment studies by quantifying the degree to which ore-forming fluids have interacted with host rocks.

INTRODUCTION

Clay minerals may form and react in a variety of aqueous fluids but are usually too fine grained to contain useful fluid inclusions. Do these fine-grained minerals retain traces of the fluids (including volatile components)

[1]U.S. Geological Survey, Mail Stop 904, P.O. Box 25046, Denver Federal Center, Denver, CO 80225.

[2]U.S. Geological Survey, Mail Stop 905, P.O. Box 25046, Denver Federal Center, Denver, CO 80225.

in which they reacted? Volatiles released from heated clay minerals have been identified and measured by mass spectrometry and by analysis of the condensed gases (Keller, 1986; Heller-Kallai and others, 1988; Gibson and Johnson, 1972; Gibson, 1973; Wicks and Ramik, 1990; Morgan and others, 1988; Müller-Vonmoos and others, 1977; Heller-Kallai and others, 1989). Important volatile species identified include H_2O, CO_2, O_2, NH_3, Ar, He, H_2, nitrates, sulfates, and a variety of additional organic and inorganic compounds. Although these volatiles have been identified, there has been little attempt to relate the volatile content of clay minerals to details of crystal chemistry or to the geochemistry of the environment in which the clays formed, despite the fact that the composition of selected evolved volatiles has been successfully used as a petrologic tool in igneous and metamorphic environments (Matson and others, 1984, 1986; Garcia and others, 1980). The goal of the present research is to measure the variations in abundance and composition of clay volatiles as a function of clay mineralogy and crystal chemistry and to relate the volatile chemistry of clays to their environment of formation. The work presented here is preliminary but provides some measure of the usefulness of this technique. It also points to the need for further research, especially in specific ore-forming environments.

VOLATILES AND THE CLAY MINERAL STRUCTURE

Volatiles in clay minerals are potentially important indicators of geologic processes because clays form in a wide variety of diagenetic and hydrothermal environments, and clay minerals themselves exhibit a range of composition and structure. Volatiles derived from clay minerals during heating may be released from different sites within the clay sample. These sites fall into three general categories: surface sites, interlayer sites, and structural sites (fig. 1). Surface sites are external sites on the clay particle onto which neutral or charged species may be adsorbed. Surface sites in clays do not differ, in a qualitative sense, from surface sites on other minerals. The strength of attraction between the volatile species and the mineral surface may vary greatly, depending upon the charge and polarity (if any) of the volatiles, the nature of the mineral surface, and the medium in which attachment occurs. The strength of attachment ranges from very weak (simple adsorption of a neutral species on a neutral surface) to very strong (chemisorption of a charged species on a charged surface). Clays differ from other minerals primarily in their unusually fine grain size and associated large surface area. Thus, clays may retain volatiles in large quantities simply by virtue of available surface area. In addition, certain clays bear a layer charge, which, if

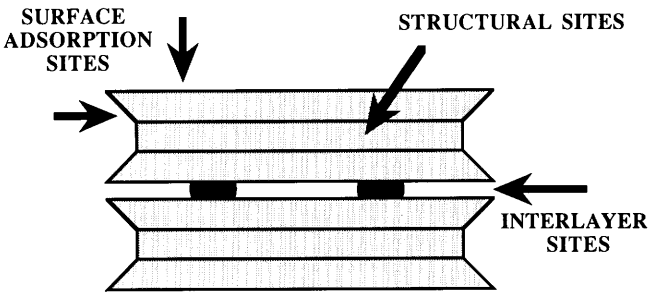

Figure 1. Schematic diagram of clay mineral structure showing possible sites of volatile species in clays.

unsatisfied on surfaces or edges, may facilitate pronounced adsorption-chemisorption phenomena (Yariv and Cross, 1979). Because of high surface area and structural layer charge, clays often contain substantial amounts of adsorbed or chemisorbed atmospheric gases that are driven off by heating at low to moderate temperatures.

The second site potentially occupied by volatile components is the interlayer space of clay minerals. Clays are comprised of stacks of silicate sheets. Clay minerals with a net negative charge on the silicate layers (smectites, vermiculite, mica) contain cations between layers to balance that charge (fig. 1). In the expandable clays (smectite and vermiculite), these interlayer cations are exchangeable and frequently hydrated. Thus, expandable clays usually contain large amounts of free molecular water. This expandable characteristic also permits the interchange of other molecules and ions between the surrounding medium and the interlayer space. For example, polar organic molecules may be associated with interlayer cations in expandable clays (Lagaly, 1984). Mica is a nonexpandable structure, and the interlayer cation is not exchangeable. Therefore, there is little interchange of ions or molecules after crystallization between the interlayer space of mica and the surrounding medium. However, volatile species that occupy the interlayer space of mica (such as Ar and NH_3) may be released during heating. Ordinarily, mica must be heated to a temperature sufficient to disrupt the silicate-sheet structure before these interlayer species are liberated.

The third site for volatiles in clay minerals is in structural cation and anion sites in the silicate layers. Substitution of volatiles for structural *cations* is relatively unusual in the clay structure, but anion substitution is common. The most abundant structural volatile in clay minerals is hydroxyl. When clays are heated (in vacuum) to a temperature sufficient to dehydroxylate the silicate layers, some free hydrogen and hydroxyl is released and combines to form molecular water, leaving a dehydrated oxide structure. Substitution of F^- or Cl^- for structural hydroxyl is common in small amounts, and when the mineral reaches its dehydroxylation temperature, much of the F^- and Cl^- also may be released. The structural sites

are the most restrictive because the silicate layer structure will accommodate only a few species that do not disrupt the crystal structure because of charge and ionic-radius constraints. Therefore, nitrates, sulfates, carbonates, and organic species must reside in the interlayer space or on surface sites: they cannot be accommodated in the silicate layer structure.

The range of species that may occupy the three different sites in clay minerals, and the temperatures at which they are likely to be liberated, varies greatly for the three types of sites. Surface sites may be occupied by any volatile species that exists in the environment that will attach to the mineral. These volatiles are generally loosely bound and are released at relatively low temperatures (~ 100°C), though chemisorption may cause some species to be retained until heating to 300°C or above (Adamson, 1982). Interlayer species are somewhat more restricted and are likely to be released at temperatures of 100°C to 300°C (Wicks and Ramik, 1990). Structural volatiles are limited almost exclusively to anions that may occupy hydroxyl sites. These species are released at temperatures from 450°C to 1,200°C, depending upon the specific clay and its structure (Mackenzie, 1970, 1972). Adsorbed molecular water and structural hydroxyl are consistently the most abundant volatiles released from clays upon heating. Nevertheless, it may be minor volatile species that reveal the composition of formation fluids or the presence of hydrocarbons or other distinctive volatiles in a particular geologic environment.

SAMPLES AND EXPERIMENTAL METHODS

In order to systematically investigate the ability of clay minerals to retain volatiles from their environment of formation, two suites of well-characterized samples were selected for preliminary analysis (table 1). The first set consists of authigenic clay minerals from core samples of petroleum reservoir sandstones in the Powder River Basin, Wyoming (Hansley and Whitney, 1991). The second set of samples is from outcrop samples of a fossil acid-sulfate geothermal system at Alum Mountain, New Mexico (Northrop and Whitney, 1987). The intent of sample selection was to check the variation in volatile composition of different clay minerals from the same environment, and the same (or similar) minerals from different environments, in order to assess how well the volatiles reflected the environment of formation and whether particular clay minerals tend to collect particular volatile species. Only selected samples from each suite are described here.

The laboratory preparation for all samples was the same. Each whole-rock sample was disaggregated ultrasonically in distilled water and the fine-size fractions were separated by centrifugation. Size separates were oriented on glass slides using the technique of Drever (1973), and clay mineral composition was determined by X-ray diffraction. Air-dried, ethylene-glycol-saturated, and heated (550°C) mounts of each sample were X-rayed for mineral identification. Separate aliquots of each sample were dried in Teflon beakers at 60°C for subsequent thermal and volatile analysis.

Table 1. Description of samples selected for this study.

Sample number	Mineralogy and description
PRB3	Authigenic interstratified illite/smectite (15 percent expandable) from Upper Cretaceous Shannon Sandstone Member of the Steele Shale, Powder River Basin, Wyoming. Sample contains < 10 percent chlorite as the only identifiable impurity. Particle size < 0.2 μm.
B2408G	Illite from the Alum Mountain fossil geothermal system. Contains trace amounts of kaolinite, K-feldspar and calcite(?). Particle size < 1.0 μm.
GW-86-53	Illitic clay from Alum Mountain fossil geothermal system. Contains < 15 percent kaolinite and a trace of jarosite. Particle size < 1.0 μm.
GW-86-44	Kaolinite from Alum Mountain fossil geothermal system. Contains a trace of natroalunite or jarosite. Particle size < 1.0 μm.
GW-86-40	Smectite from Alum Mountain fossil geothermal system. Contains a trace of kaolinite. Particle size < 1.0 μm.
GW-86-33	Mixture of smectite, kaolinite, and illite from Alum Mountain fossil geothermal system. May contain a trace of sulfate mineral. Particle size < 1.0 μm.

Each sample was subjected to thermogravimetric analysis using a Perkin-Elmer TGS-2 programmable analyzer. Ten milligrams of each sample were heated at 10°C/min from ambient to 1,000°C in a flowing-nitrogen atmosphere at approximately 1 bar (10^5 Pa) pressure. Weight loss and first derivative of weight loss were recorded with a computer-aided data-acquisition system consisting of MacADIOS interface hardware and LabVIEW II data-collection and analysis software on an Apple Macintosh computer.

Analysis of volatile species was performed by placing a separate 20 mg aliquot of each sample in a quartz tube (7 mm inside diameter) located in a muffle furnace and connected to the mass spectrometer. The quartz sample tube was evacuated, and the sample was heated stepwise from 60°C to 1,060°C at 5°C/min under high vacuum (10^{-8} torr). Samples were routinely baked out at 60°C or 100°C prior to analysis. Evolved volatiles were analyzed

with a Balzers 511 quadrupole mass spectrometer automated with a DEC PDP-11/83 data-collection system (Landis and Hofstra, 1991). Twenty masses (m/e) were measured every 12 seconds during the temperature ramp and recorded digitally.

RESULTS: BACKGROUND AND REPRODUCIBILITY TESTS

We performed a set of analyses designed to test the sample-preparation and analytical techniques and to establish background and reproducibility for a variety of volatiles. Of particular concern is the adsorption of atmospheric gases by fine-grained clay samples. It is important to distinguish geologically important gases from those adsorbed from the atmosphere during the sample-preparation process. In addition, we wanted to detect any gases being given off by the quartz sample tubes (or leaked gases) during heating.

The first test measured the amount of gas released by the quartz sample tubes, attributable to either adsorption of atmospheric gases or the presence of gas bubbles within the quartz that makes up the tubes. Figure 2 shows a direct comparison of the empty quartz sample tubes heated after exposure to the atmosphere and then reheated without exposure to the atmosphere. This test determines what gases are from the atmosphere and what gases are from the quartz. Detectable amounts of atmospheric gases are clearly present on the opened tubes, whereas the quartz tubes kept under vacuum show virtually no extraneous gases. The rise in background of both opened and unopened tubes must represent virtual leakage into the mass spectrometer at the higher temperatures from vacuum-system surfaces. It is important to note that the gas release "events" exhibited by the opened tube actually constitute very low level background compared to the amounts of gas released by samples (fig. 3, for comparison).

The second test utilized quartz powder (clear, euhedral crystals ground and elutriated to a 20- to 54-μm grain size and acid treated to remove hyperfine particles) to determine amounts of volatiles released by surface processes alone. (In order to measure the effects of surface adsorption for an "inert" solid, the solid must release only surface species and no volatiles from its own structure.) For the quartz powder used in this test, CO_2 and H_2O exhibit sudden release events near 200°C, 290°C and 520°C, suggesting that the quartz may contain microinclusions that burst at those temperatures (fig. 3*A*). Nevertheless, the amounts of gases released are roughly two orders of magnitude smaller than the amounts of these gases released during a typical clay analysis (fig. 3*B*). Aside from these small events from the quartz, no significant amounts of volatiles are released, suggesting that simple surface adsorption of atmospheric gases will not play a significant role in the analysis of clay volatiles.

The third test measured the reproducibility for multiple analyses of a single sample. Figure 4 shows duplicate runs of sample GW-86-44 for three species. The temperatures at which volatiles are released are reproducible within the precision of the temperature-measurement technique. The absolute amounts of volatiles released varied somewhat from run to run, but these changes may be attributable to sample size and different surface areas, and to sample inhomogeneity.

RESULTS AND PRELIMINARY INTERPRETATION: VOLATILE COMPOSITIONS OF NATURAL CLAYS

1. PETROLEUM RESERVOIR CLAYS

The first clay sample analyzed was an authigenic interstratified illite/smectite (I/S) from the Upper Cretaceous Shannon Sandstone Member of the Steele Shale in the Powder River Basin, Wyoming. This sandstone has served as a petroleum reservoir and still contains petroleum (Hansley and Whitney, 1991). Thermogravimetric (TGA) analysis (in N_2 at 1 atmosphere pressure) of the <0.2-μm fraction of this reservoir clay reveals the loss of adsorbed volatiles at 100°C and dehydroxylation and structural modification of the clay at about 570°C (fig. 5). The evolution of water during heating (under vacuum) in the furnace attached to the quadrupole mass spectrometer produced a peak at around 450°–500°C (fig. 6*A*). In both the TGA and the mass spectrometer pyrolysis analyses, the water-loss events are composed of multiple peaks, but it is not certain what each of these peaks indicates. The lower temperature at which dehydroxylation occurs in the mass spectrometer is attributable to the vacuum because gas-release reactions are accelerated under high vacuum. Virtually all of the adsorbed water on the clay had been lost during the 100°C bakeout prior to the analysis.

In addition to the release of structural water, several other species were released from this petroleum-reservoir clay in significant amounts during the water-release event. For example, HF (m/e = 20) and HCl (m/e = 36) mimic the water-release event exactly, as would be expected for anion species that substitute for structural hydroxyl. Other species that cannot substitute for structural anions, such as H_2S (m/e = 34) and Ar (m/e = 40), also exhibit events at the dehydroxylation temperature (fig. 6*B*, 6*C*), suggesting that they occupy interlayer spaces of the clay and are only released during the structural breakdown of the mineral. On the other hand, several volatiles were released that show no correlation whatsoever with the dehydroxylation event of the clay. These include several organic species or

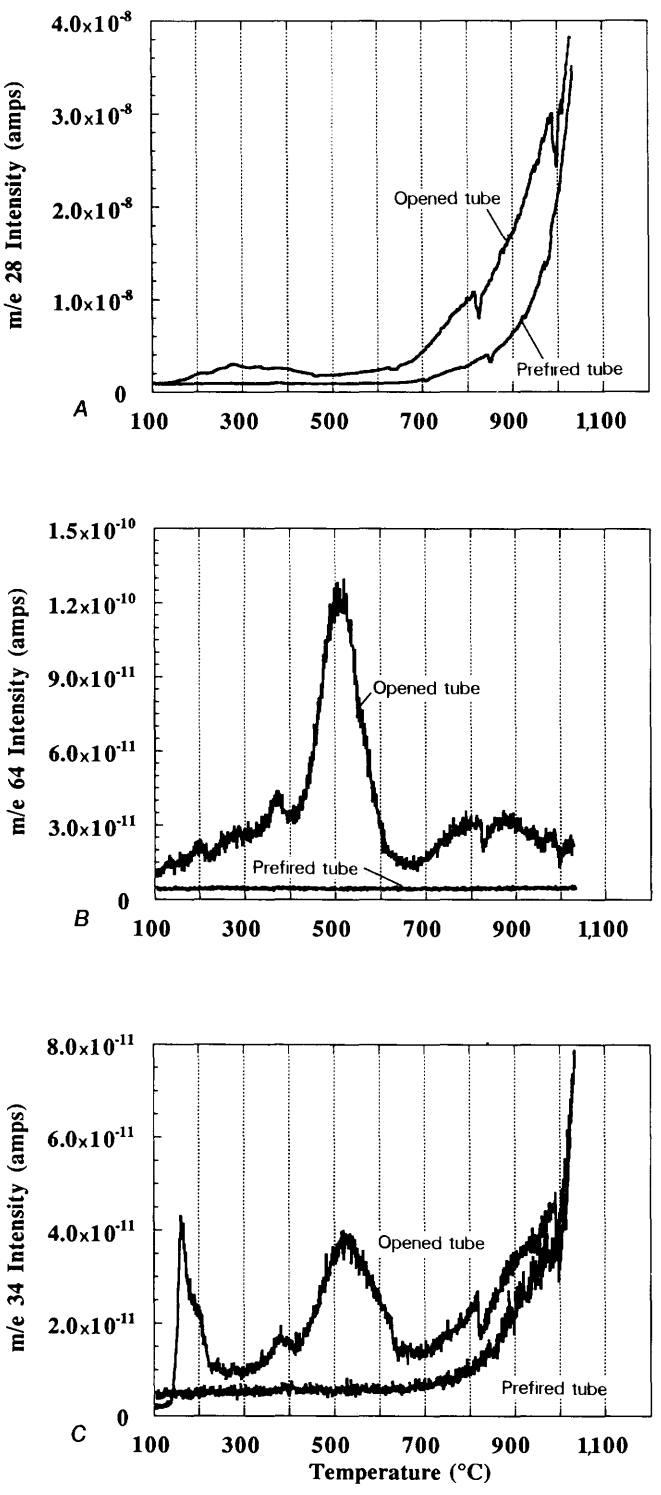

Figure 2. Background test. Comparison of the gas evolution profiles (for m/e = 28, 34, 64) for a quartz sample tube exposed to the atmosphere (opened) compared to the same quartz sample tube reanalyzed without exposure to the atmosphere (prefired). Volatiles released are clearly attributable to adsorption of atmospheric components. *A*, m/e = 28, attributable to N_2 and the CO ion fragment from CO_2; *B*, m/e = 64, attributable to SO_2; *C*, m/e = 34, attributable to H_2S.

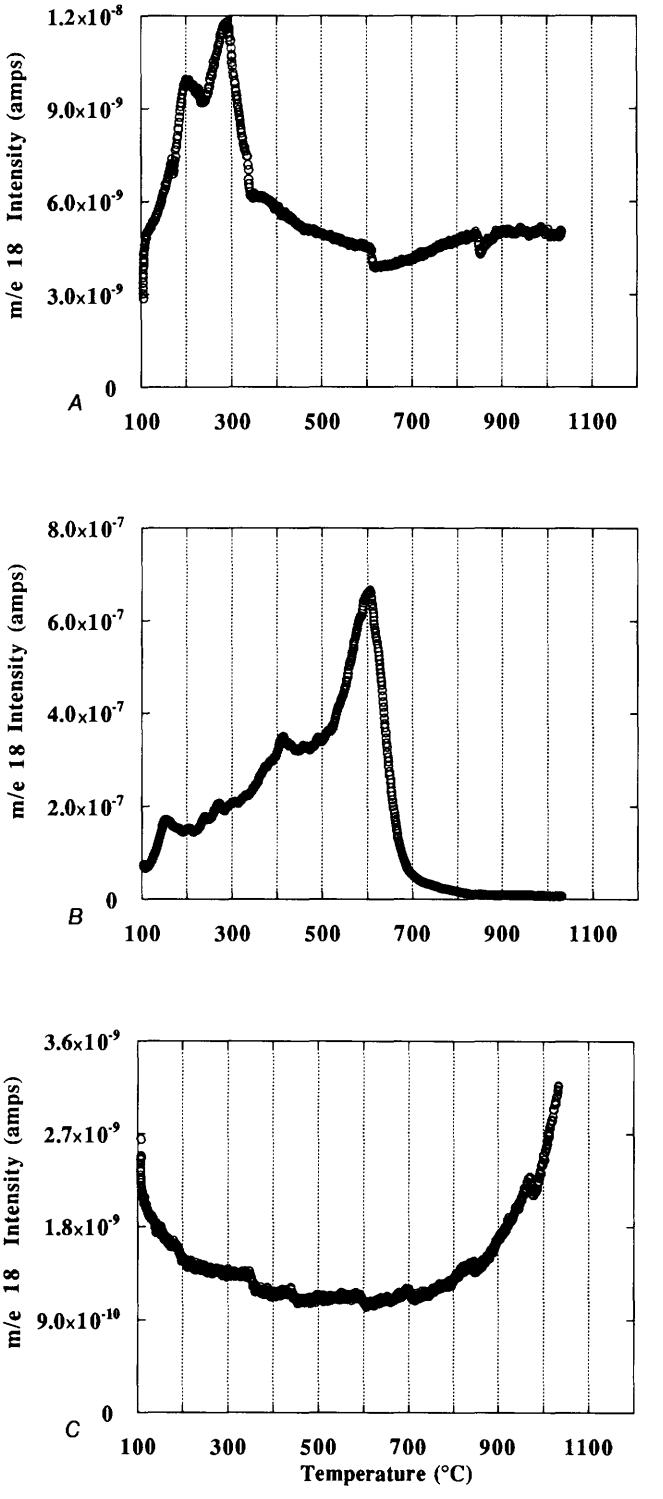

Figure 3. Background test for the sample tube and an "inert" substance (in this case quartz powder) illustrating the relative amounts of water (m/e = 18) adsorbed and then released from exposure to atmosphere versus that of sample (smectite clay). *A*, release from quartz powder in opened vacuum furnace tube; *B*, release from typical clay sample, smectite; *C*, release from prefired vacuum furnace tube. Although the quartz powder exhibits some evolution of water, the concentrations are at least two orders of magnitude lower than during a clay analysis and occurs at lower temperatures.

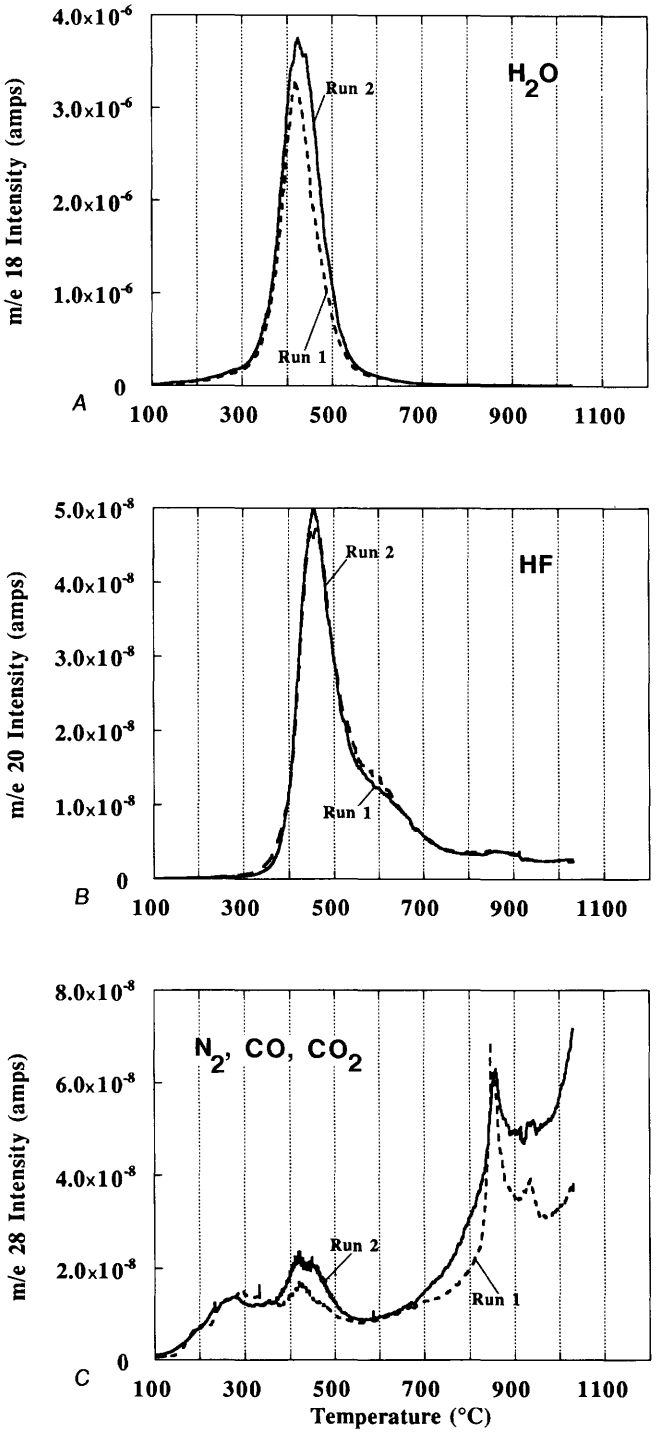

Figure 4. Duplicate analyses of the same material, analyzed two weeks apart. *A*, m/e = 18, the major peak of water; *B*, m/e = 20, a minor peak of water and the major peak of HF; *C*, m/e = 28, the major peak of N_2 and CO and ion-fragment peak of CO_2.

fragments with m/e = 27, 28, and 29 (fig. 7*A*, *B*, *C*). These events probably represent thermal pyrolysis of organic matter that is associated with the clay but is not contained structurally in the clay.

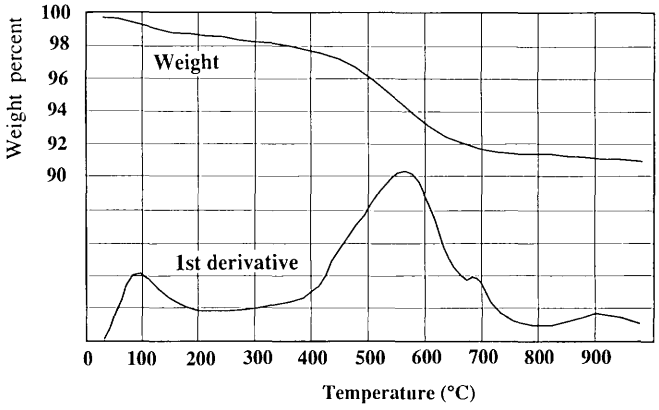

Figure 5. Thermogravimetric analysis of sample PRB3, showing major dehydroxylation peak at 570°C under 1 atm, N_2 gas flow. Upper trace is gravimetric response and lower trace is first derivative.

2. FOSSIL ACID-SULFATE GEOTHERMAL SYSTEM CLAYS

Analysis of several samples with different clay-mineral compositions from a fossil acid-sulfate geothermal system permits evaluation of how volatile retention varies as a function of mineralogy and permits qualitative analysis of gas species present. Five samples from the Alum Mountain fossil geothermal system were selected (table 1). These samples come from different alteration zones within the geothermal system (Northrop and Whitney, 1987), so each mineral or assemblage may have formed in contact with fluids with slightly (but systematically) different compositions. Such variations of fluid composition within a geothermal system is an additional variable to consider when examining differences among samples.

Some variation in thermal behavior as a function of mineralogy is seen in the m/e = 18 profiles. The main event for each sample is the loss of structural water (dehydroxylation). For kaolinite (fig. 8*A*), dehydroxylation occurs as a simple, symmetric event near 420°C under high vacuum. There is little evidence for adsorbed water or for any other minerals with different breakdown temperatures in this sample. The illitic samples (fig. 8*B*, 8*C*) exhibit more complex dehydroxylation events, but both occur near 430°–450°C. The smectite (fig. 8*D*) dehydroxylates at 600°C but shows water evolution almost continually from 100°C to 600°C. In fact, both the smectite sample and the illitic samples (which contain a small proportion of smectitic layers) exhibit low-to-moderate-temperature gas evolution. This effect probably reflects retention of water in the interlayer space of these clays that is greater than simple adsorption (Sposito, 1984; Sposito and Prost, 1982). As would be expected, a sample consisting of mixtures of these minerals exhibits volatile evolution curves that are composites of the individual

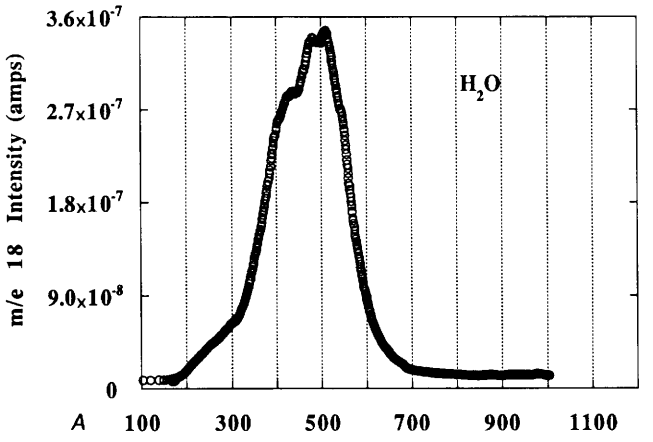

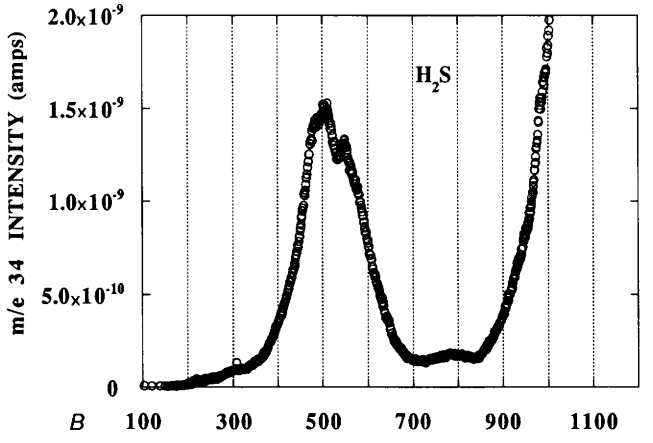

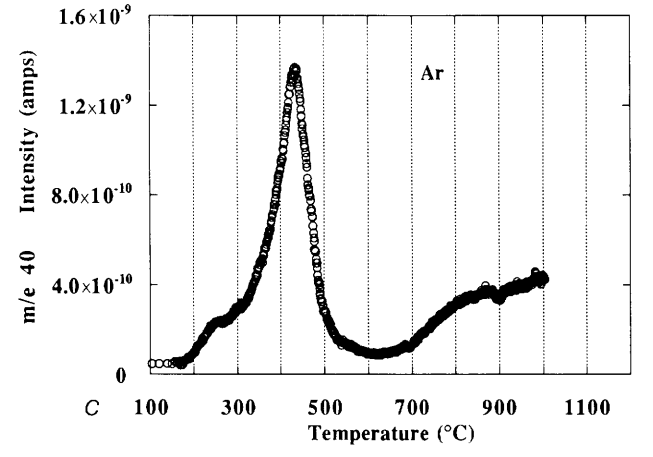

Figure 6. Gas-evolution profiles for sample PRB3. Both structural and nonstructural volatile species are evolved over a narrow temperature range. *A*, water, m/e = 18; *B*, hydrogen sulfide, m/e = 34; *C*, argon, m/e = 40.

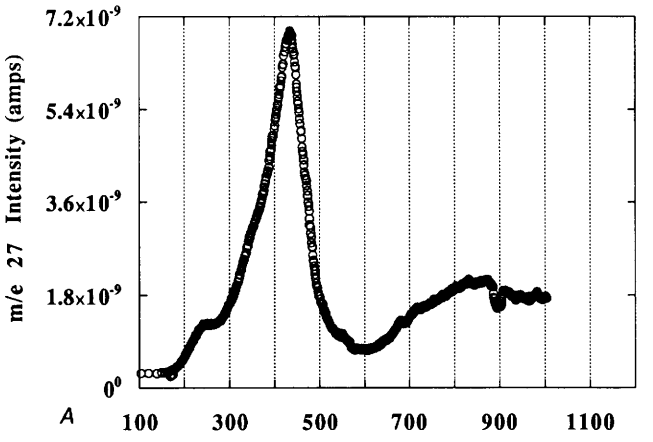

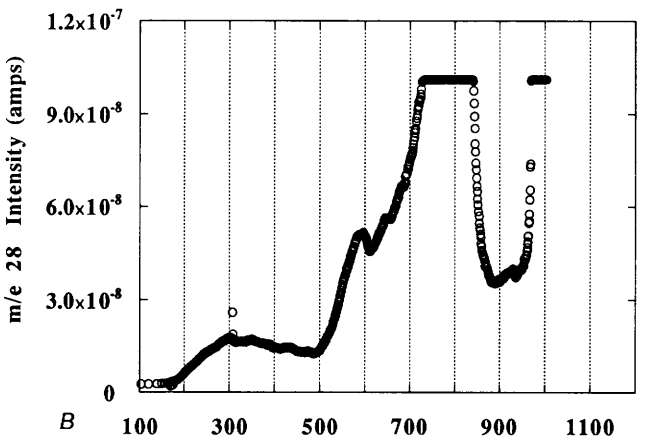

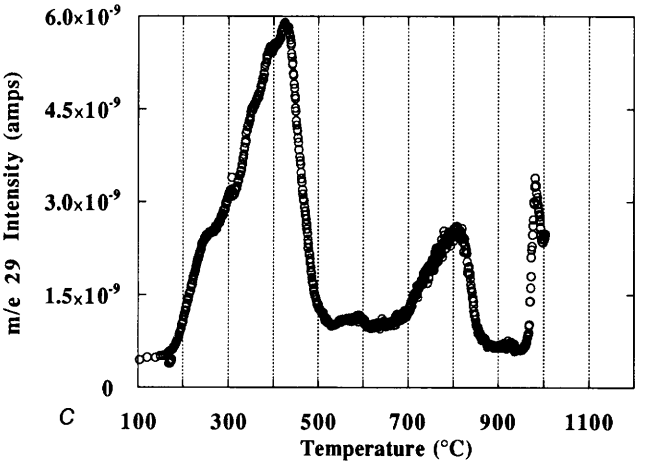

Figure 7. Gas-evolution profiles for organic species or ion fragments in sample PRB3 (m/e = 27, 28, 29). The m/e = 28 peak (part *B*) saturates the electrometer at 1×10^{-7} amps from the major nitrogen peak at the same m/e as organic-species ion fragments.

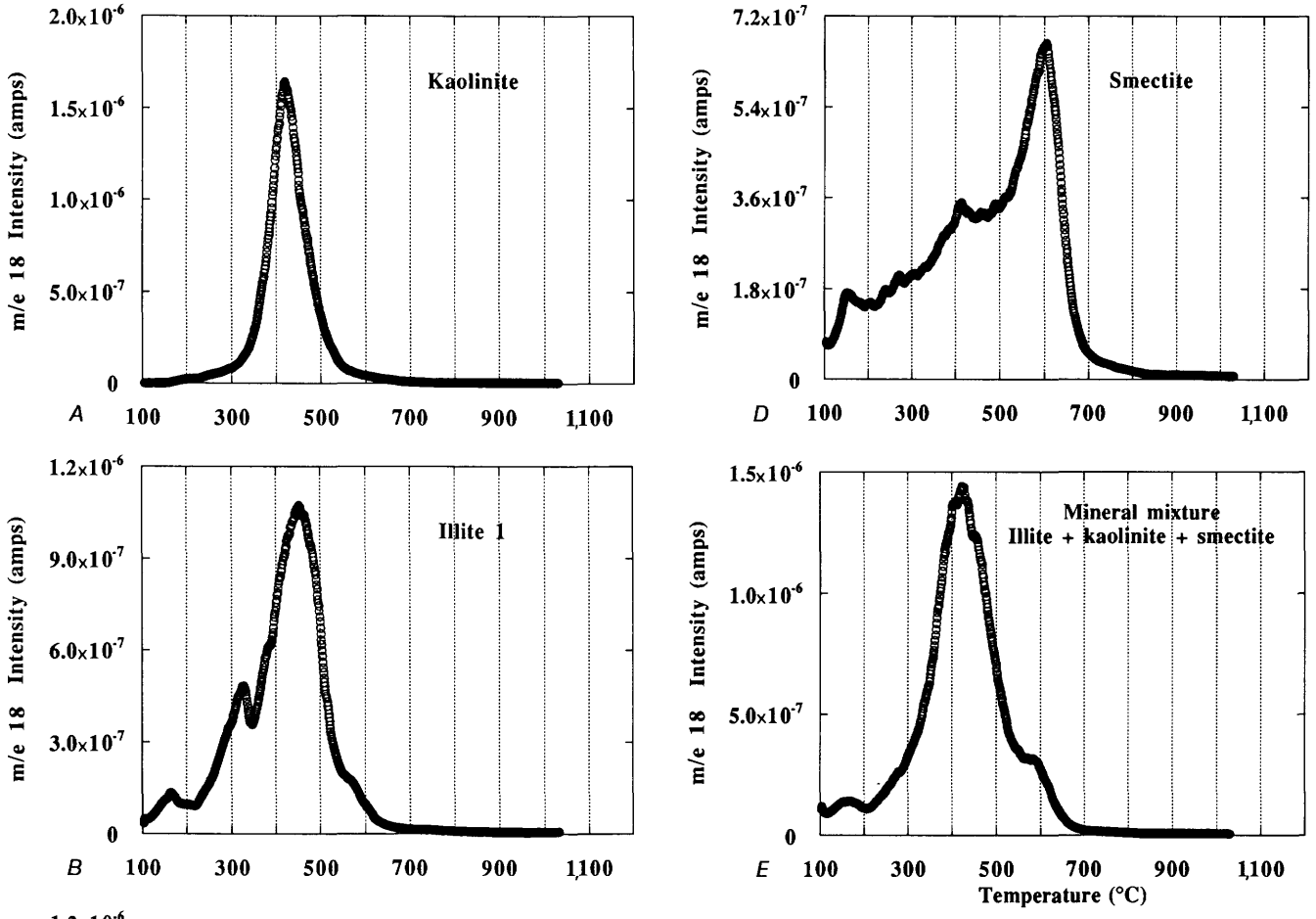

Figure 8. Water-release profiles (m/e = 18) for several samples with different mineral compositions from the Alum Mountain fossil geothermal system—this demonstrates mineralogical differences for a single volatile species from a single geologic environment. *A*, kaolinite, <1-μm size; *B*, illitic clay, 0.5- to 5-μm size; *C*, illitic clay, <1-μm size; *D*, smectite; *E*, mixed illite–kaolinite–smectite clay, <1-μm size.

components, in proportion to the amount of each mineral present (fig. 8*E*).

Because this suite of samples formed in a sulfur-bearing system, the behavior of sulfide and sulfate volatiles is of interest. For m/e = 34 (representing H_2S), there are several distinctive features of the gas-release curves. All of the samples exhibit some H_2S release between 400°C and 500°C that is roughly correlative with clay water-release events (fig. 9). The kaolinite sample exhibits an H_2S doublet at 200°C and 250°C that is not observed in any other sample (fig. 9*A*). All of the samples release H_2S above 700°C, but no two samples exhibit the same temperatures or patterns of gas release. It is likely that these high-temperature events are not related to structural changes in the clays but represent calcining of sulfide minerals present in amounts too small to detect with X-ray diffraction (as much as a few percent). They may also represent intracrystalline H_2S that is released when some thermal threshold is reached. This hypothesis is supported by the behavior of SO_2, which also shows patterns of liberation that seem to be unrelated to dehydroxylation or other thermally induced changes in the clay minerals (fig. 10). For example, both the kaolinite sample and one of the illitic samples exhibit a sharp SO_2 peak at 850°C. Such a similarity cannot be easily explained in terms of clay crystal chemistry because the two minerals are structurally and chemically different.

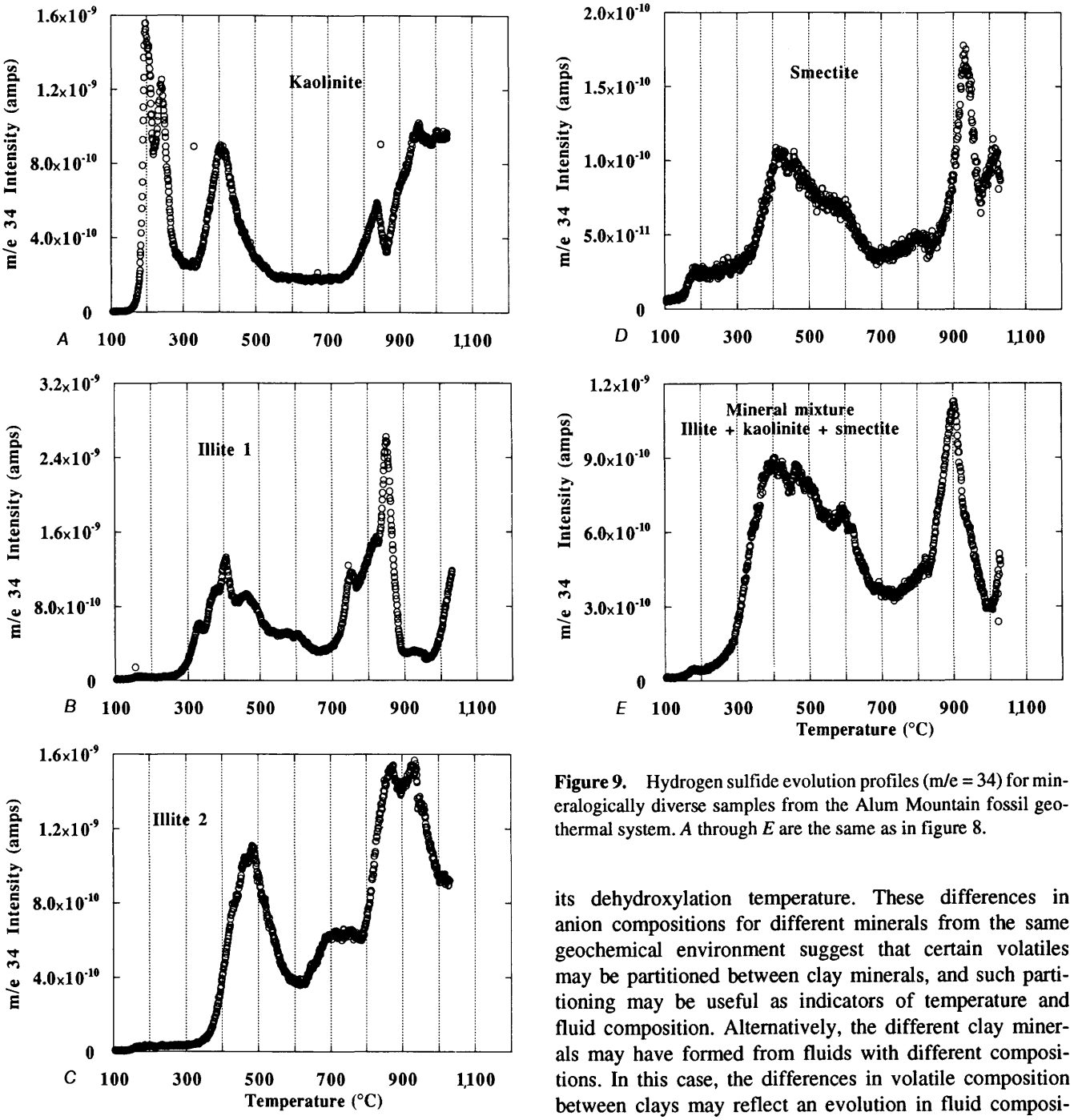

Figure 9. Hydrogen sulfide evolution profiles (m/e = 34) for mineralogically diverse samples from the Alum Mountain fossil geothermal system. *A* through *E* are the same as in figure 8.

Gas-evolution patterns for several other species are potentially useful for crystal chemical and geochemical interpretations. For example, the release pattern of HF (m/e = 20) follows that of water for both the smectite and kaolinite samples (fig. 11), reflecting normal anionic substitution of F^- for OH^- in the clay structure. However, despite the fact that Cl^- also may substitute for OH^-, the smectite sample displays no Cl^- (measured as HCl, m/e = 36) release at the dehydroxylation temperature (fig. 11*D*), whereas the kaolinite sample shows a strong Cl^- peak at its dehydroxylation temperature. These differences in anion compositions for different minerals from the same geochemical environment suggest that certain volatiles may be partitioned between clay minerals, and such partitioning may be useful as indicators of temperature and fluid composition. Alternatively, the different clay minerals may have formed from fluids with different compositions. In this case, the differences in volatile composition between clays may reflect an evolution in fluid composition with time.

3. COMPARISON OF PETROLEUM RESERVOIR AND GEOTHERMAL CLAYS

Besides the variation in volatile content for different clays from the same environment, it is instructive to examine the differences and similarities in the general volatile composition of clays from the two different environments. Because various clay minerals incorporate several volatiles

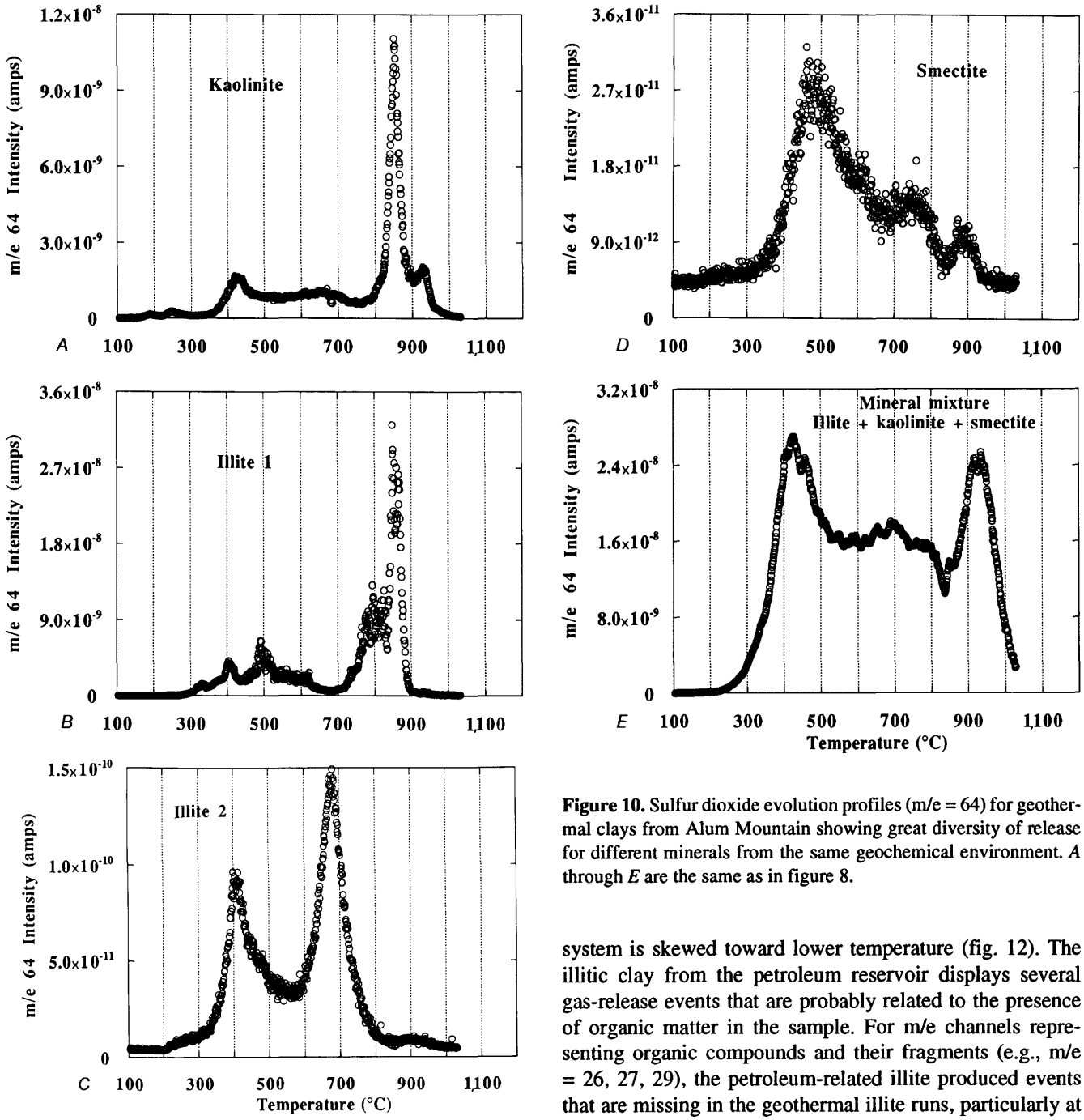

Figure 10. Sulfur dioxide evolution profiles (m/e = 64) for geothermal clays from Alum Mountain showing great diversity of release for different minerals from the same geochemical environment. *A* through *E* are the same as in figure 8.

in different ways related to their structure, it is perhaps most important to compare structurally similar minerals from the two environments. The clay from the petroleum reservoir rock is a highly illitic, interstratified, illite/smectite and is compared with an illitic clay from the geothermal system. As expected for two mineralogically similar samples formed in aqueous environments, the dehydroxylation behavior for the two samples is similar, but the water-release event for the illite from the geothermal system is skewed toward lower temperature (fig. 12). The illitic clay from the petroleum reservoir displays several gas-release events that are probably related to the presence of organic matter in the sample. For m/e channels representing organic compounds and their fragments (e.g., m/e = 26, 27, 29), the petroleum-related illite produced events that are missing in the geothermal illite runs, particularly at about 430°C (fig. 13). In addition, the petroleum reservoir clay released carbon dioxide and related fragments (m/e = 12, 28, 44) at 590°C, an event that is not seen in the geothermal illite (fig. 14). Similarly, H_2S (m/e = 34) and SO_2 (m/e = 64) were released from the petroleum clay at 500°–550°C and, again, there were no similar release events from the geothermal illite (fig. 15). Conversely, the geothermal illite released several of these species between 750°C and 850°C, with no parallel events in the petroleum-related illitic material. It is not yet clear what these high-temperature events represent, but they must represent accessory minerals (e.g., carbonates and sulfides) present

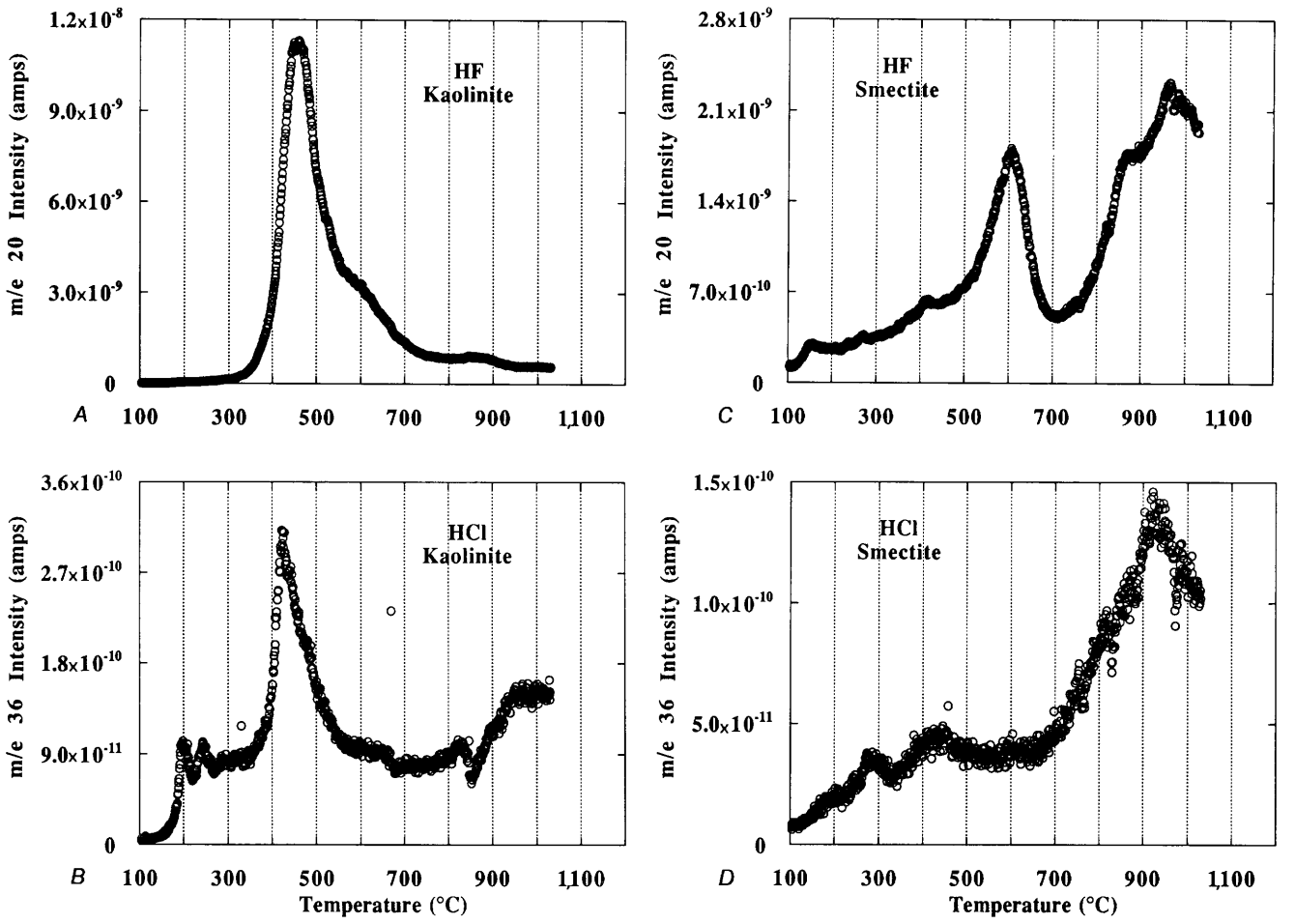

Figure 11. Comparison of HF (m/e = 20) and HCl (m/e = 36) liberation behavior for smectite and kaolinite from the Alum Mountain fossil geothermal system. *A*, kaolinite HF; *B*, kaolinite HCl; *C*, smectite HF; *D*, smectite HCl.

in very small amounts or volatiles trapped within clay particles as intracrystalline molecular species. In either case, it is clear that these mineralogically similar samples from two diverse geochemical environments produce distinctly different gas spectra during thermal ramping.

DISCUSSION AND FUTURE WORK

The purpose of the present study was to determine whether clay minerals formed in different geochemical environments might retain some "memory" of the composition of formation fluids as volatiles adsorbed on their surfaces, trapped in interlayer spaces of clays, or incorporated within structural sites in the silicate layers of the clay. Although a great deal of systematic study is still required, it is apparent that the gas chemistry of mineralogically similar clays from a petroleum environment and a geothermal-hydrothermal environment give strikingly different gas-evolution profiles when heated. Further,

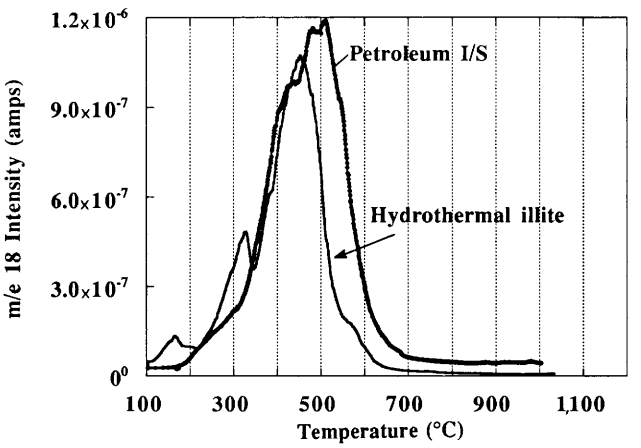

Figure 12. Dehydroxylation profiles of mineralogically similar illitic samples from both the petroleum reservoir (PRB3) and geothermal (B2408) systems. Although the geothermal sample (illite) has more low-temperature activity than the petroleum-reservoir sample (I/S), comparable dehydroxylation behavior is achieved from the same basic mineralogy.

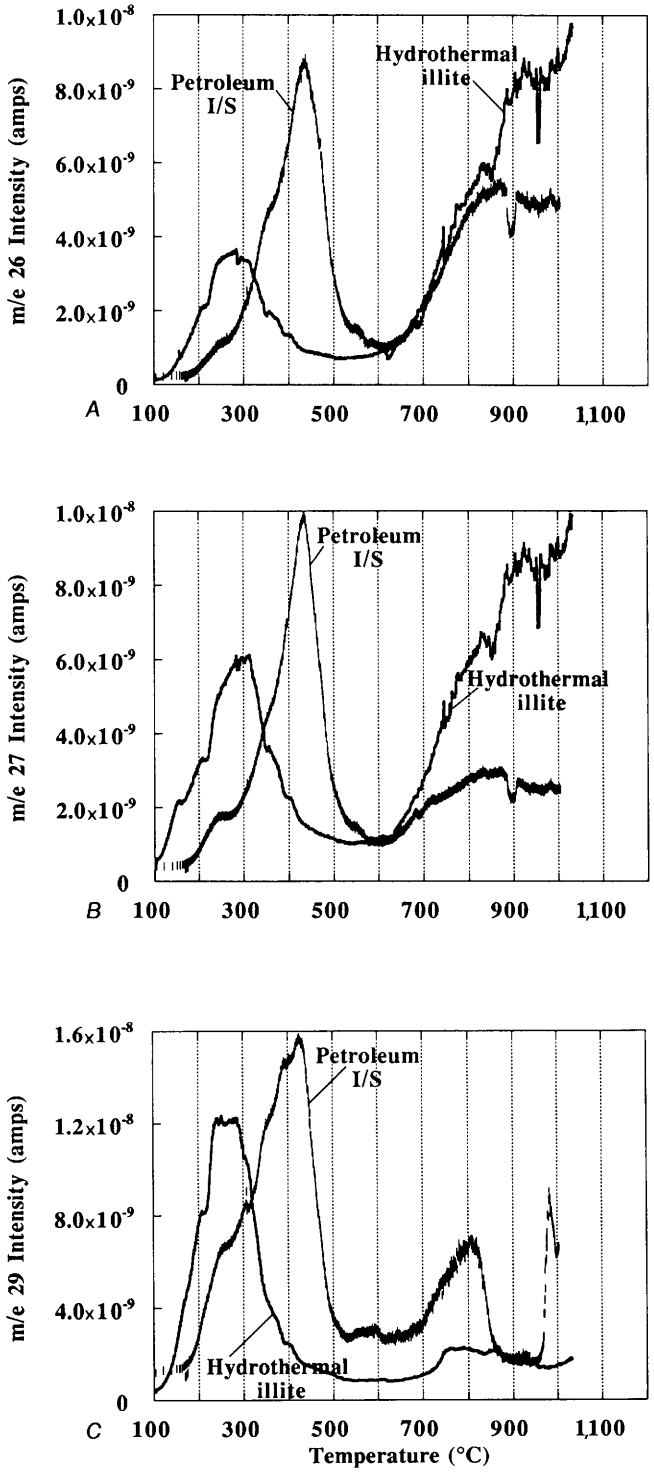

Figure 13. Comparison of the organic-species and ion-fragment (m/e = 26, 27, 29) evolution for illitic samples from both environments. Despite their mineralogic similarity, there is almost no correlation between the evolution of these species. The geothermal system (illite) and petroleum reservoir (I/S) are labeled on the diagrams for *A*, m/e = 26; *B*, m/e = 27; and *C*, m/e = 29.

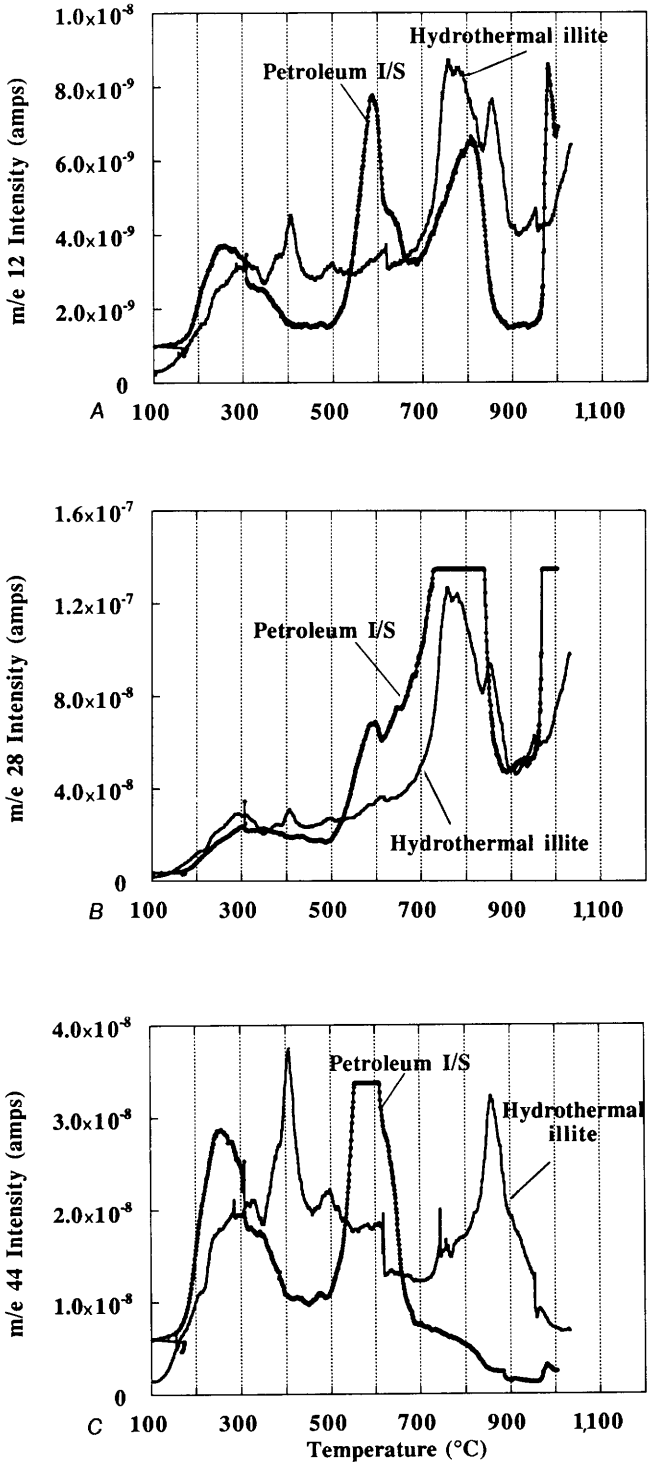

Figure 14. Carbon dioxide gas release. Comparison of the evolution of C^+ (m/e = 12), CO^+ (m/e = 28), and CO_2^+ (m/e = 44) ion fragments for the illitic clay sample from the petroleum reservoir (I/S) and for the illitic clay sample from the geothermal system (illite). *A*, m/e = 12; *B*, m/e = 28; *C*, m/e = 44.

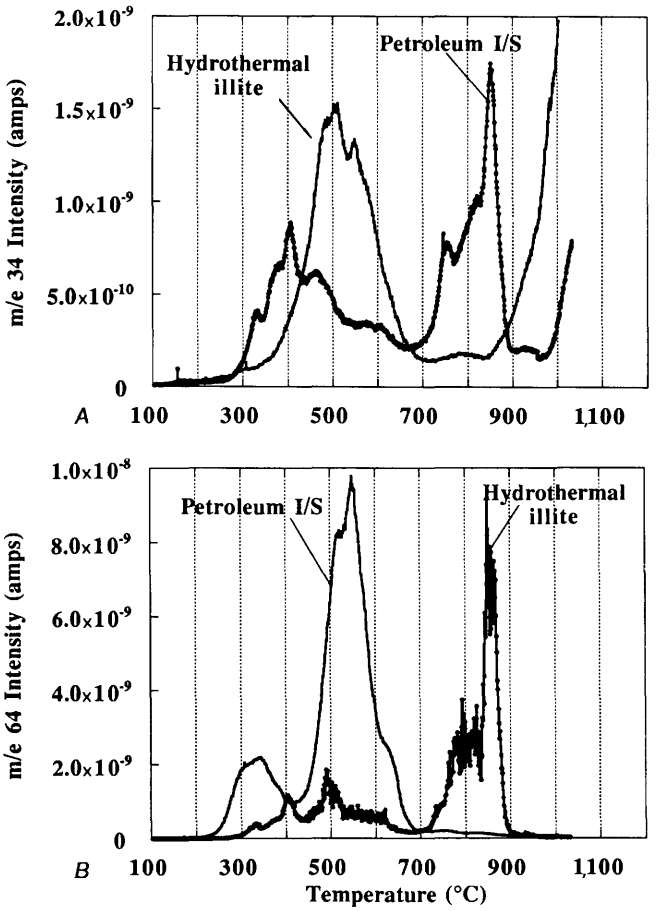

Figure 15. Sulfur gas release. *A*, The H_2S (m/e = 34); and *B*, SO_2 (m/e = 64) profiles for the illitic samples from the petroleum reservoir (I/S) and the geothermal system (illite).

these different gas compositions are consistent with the contrasting geochemical environments of the clays.

Based on these preliminary data, several specific areas of research are now required to permit a more rigorous interpretation of these differences in volatile chemistry.

First, natural samples must be analyzed chemically and mineralogically in order to detect very small amounts of secondary phases. Evolution of CO_2, H_2S, and SO_2 from accessory minerals undetectable by X-ray diffraction must be distinguishable from these gases held on clay mineral surfaces or within the interlayer space of expandable minerals. This work must be performed in conjunction with the characterization of the volatiles evolved by pure samples of the candidate phases.

Second, if certain volatiles are present as surface species adsorbed or chemisorbed on mineral surfaces, then the effects of sample-preparation technique must be assessed. For example, if organic compounds are present in the petroleum reservoir rock as grain coatings or interlayer species, then ultrasonic disaggregation or washing samples with organic solvents may alter the compositions drastically. Are any adsorbed species retained during sample preparation or are they replaced by different species from preparation solutions or from the atmosphere? A systematic analysis of samples during the course of sample separation and preparation would help answer this question. A corollary to this question is the effect of particle size. Small particles have a higher surface area per unit mass than larger particles and would therefore retain a higher concentration of adsorbed species. On the other hand, small particles have less volume for the retention of interlayer or intracrystalline species and would contain a lower concentration of these volatiles. Thus, a detailed analysis of particle-size effects for a uniform gas-mineral combination would be beneficial.

Third, and most critically, the quantitative incorporation of volatiles into a particular mineral, and their exact location within the mineral sample, must be determined. For example, if kaolinite evolves significant amounts of Cl^- during dehydroxylation but smectite does not, does that imply that Cl^- occupies basal hydroxyl sites in the kaolinite (sites that do not exist in smectite)? If anion partitioning occurs between different structural sites within clay minerals, then there is a potential for quantifying such partitioning in terms of temperature and fluid composition. On the other hand, if the Cl^- is present simply as an intracrystalline inclusion, then its presence simply reflects crystallographic contiguity and will tell us nothing about specific temperatures. This problem is probably best approached using experimental syntheses of clay minerals in solutions of precisely known compositions.

In conclusion, this preliminary study has shown that there are significant differences in the composition of retained volatiles in clay minerals formed in different geochemical environments. Volatiles for mineralogically similar samples from a petroleum reservoir rock and from a fossil geothermal system are distinctly different in composition and thermal evolution profiles. In addition, mineralogically different samples from the same geothermal system exhibit dramatically different gas-evolution profiles. By systematically determining the abundance and sites of volatiles in clay minerals and how these volatiles are incorporated into the clays during formation, we may be able to use composition and thermal evolution of volatiles from clays as petrologic tools to interpret temperatures and fluid chemistry of the clay-forming environment.

ACKNOWLEDGMENTS

This research was funded by the U.S. Geological Survey Development of Assessment Techniques (DAT) Program.

REFERENCES CITED

Adamson, A.W., 1982, Physical Chemistry of Surfaces: New York, John Wiley & Sons, 664 p.

Drever, J.I., 1973, The preparation of oriented clay mineral specimens for X-ray diffraction analysis by a filter-membrane peel technique: American Mineralogist, v. 58, p. 553–554.

Garcia, M.O., Muenow, D.W., and Liu, N.W.K., 1980, Volatiles in Ti-rich amphibole megacrysts, southwest U.S.A.: American Mineralogist, v. 65, p. 306–312.

Gibson, E.K., Jr., 1973, Thermal analysis–mass spectrometer computer system and its application to the evolved gas analysis of Green River shale and Lunar soil samples: Thermochimica Acta, v. 5, p. 243–255.

Gibson, E.K., Jr., and Johnson, S.M., 1972, Thermogravimetric–quadrupole mass spectrometric analysis of geochemical samples: Thermochimica Acta, v. 4, p. 49–56.

Hansley, P.L., and Whitney, C.G., 1991, Petrology, diagenesis, and sedimentology of the Upper Cretaceous Shannon Sandstone Member of the Steele Shale in the Powder River Basin, Wyoming: U.S. Geological Survey Bulletin 1917–B, 33 p.

Heller-Kallai, L., Miloslavski, I., and Aizenshtat, Z., 1989, Reactions of clay volatiles with n-alkanes: Clays and Clay Minerals, v. 37, p. 446–450.

Heller-Kallai, L., Miloslavski, I., Aizenshtat, Z., and Halicz, L., 1988, Chemical and mass spectrometric analysis of volatiles derived from clays: American Mineralogist, v. 73, p. 376–382.

Keller, W.D., 1986, Compositions of condensates from heated clay minerals and shales: American Mineralogist, v. 71, p. 1420–1425.

Lagaly, G., 1984, Clay-organic interactions: Philosophical Transactions of the Royal Society of London, v. A311, p. 315–332.

Landis, G.P., and Hofstra, A.H., in press, Fluid inclusion gas chemistry as a potential minerals exploration tool—Case studies from Creede, CO, Jerritt Canyon, NV, Coeur d'Alene district, ID and MT, southern Alaska mesothermal veins, and mid-continent MVT's: Journal of Geochemical Exploration, v. 42.

Mackenzie, R.C., 1970, Differential Thermal Analysis, Volume 1—Fundamental Aspects: London, Academic Press, 775 p.

Mackenzie, R.C., 1972, Differential Thermal Analysis, Volume 2—Applications: London, Academic Press, 607 p.

Matson, D.W., Muenow, D.W., and Garcia, M.O., 1984, Volatiles in amphiboles from xenoliths, Vulcan's Throne, Grand Canyon, Arizona, U.S.A.: Geochimica et Cosmochimica Acta, v. 48, p. 1629–1636.

Matson, D.W., Muenow, D.W., and Garcia, M.O., 1986, Volatile contents of phlogopite micas from South Africa kimberlite: Contributions to Mineralogy and Petrology, v. 93, p. 399–408.

Morgan, D.J., Warrington, S.B., and Warne, S.St.J., 1988, Earth sciences applications of evolved gas analysis—A review: Thermochimica Acta, v. 135, p. 207–212.

Müller-Vonmoos, M., Kahr, G., and Rub, A., 1977, DTA-TG-MS in the investigation of clays—Quantitative determination of H_2O, CO and CO_2 by evolved gas analysis with a mass spectrometer: Thermochimica Acta, v. 20, p. 387–393.

Northrop, H.R. and Whitney, G., 1987, Clays and associated minerals in the Alum Mountain fossil geothermal system near Gila Hot Springs, Grant County, New Mexico, *in* An Excursion to Selected Zeolite and Clay Deposits in Southwestern New Mexico and Eastern Arizona: Brockport, New York, International Committee on Natural Zeolites, p. 1–12.

Sposito, G., 1984, The Surface Chemistry of Soils: New York, Oxford University Press, 234 p.

Sposito, G., and Prost, R., 1982, Structure of water adsorbed on smectites: Chemical Reviews, v. 82, p. 553–573.

Wicks, F.J., and Ramik, R.A., 1990, Vacuum thermogravimetric analysis and evolved gas analysis by mass spectroscopy, *in* J.W. Stucki, D.L. Bish, and F.A. Mumpton, eds., Thermal Analysis in Clay Science: Boulder, Colorado, The Clay Minerals Society Workshop Lectures, v. 3, p. 160–189.

Yariv, S., and Cross, H., 1979, Geochemistry of Colloid Systems: New York, Springer-Verlag, 450 p.

CHAPTER N

MAPPING MINERALS WITH IMAGING SPECTROSCOPY

By ROGER N. CLARK,[1] GREGG A. SWAYZE,[1] *and* ANDREA GALLAGHER[1]

Imaging spectroscopy is a new mapping tool and represents the next generation in remote-sensing technology. The narrow spectral channels of an imaging spectrometer form a continuous reflectance spectrum of the Earth's surface—this contrasts with the 4 to 7 channels of the previous generation of imaging instruments, like the Landsat Thematic Mapper (TM) and Multispectral Scanner (MSS) instruments. Although systems like Landsat can distinguish general brightness and slope differences in the reflectance spectrum of the surface, imaging spectroscopy not only does that but also resolves absorption bands in the spectrum that can be used to identify specific species. Spectroscopic analysis of imaging-spectroscopy data allows any material (mineral, vegetation, man-made, water, snow, etc.) with unique absorption features in the measured spectral region to be mapped.

NASA is now flying the "Advanced Visual and Infra-Red Imaging Spectrometer" (AVIRIS) instrument. AVIRIS acquires data in the spectral range from 0.4 to 2.45 m in 224 spectral channels. The instrument is flown in an ER-2 aircraft (a modified U-2 spy plane) at an altitude of 19,800 m (65,000 ft). The ground resolution is 20 m; the swath width is about 11 km (614 pixels); and the swath length can be up to about 1,000 km. After initial poor performance in 1987 and 1989, the AVIRIS instrument now produces superb signal-to-noise data.

In 1989, we developed a new analysis algorithm that uses a digital spectral library of known materials and a fast, modified-least-squares method of determining if a single spectral feature for a given material is present (Clark and others, 1990). We have made a major advance in the mapping algorithm: now multiple minerals using multiple spectral features are mapped simultaneously. This is done by a modified-least-squares fit of spectral features from data in our digital spectral library to corresponding spectral features in the image data. The algorithm does not force a detection as do many other algorithms in use. For example, many algorithms take a set of curves and best fit them to the observed data, often requiring a set of parameters (like mineral fraction) to sum to one. Our algorithm only produces values indicating the presence of those minerals we choose to map. If the minerals do not exist in that area, the algorithm produces zeros, indicating they are not detected.

Our mapping algorithm produces, for each pixel in the image, a spectral feature depth (correlated to abundance) and a fit number (least-squares correlation coefficient) to the reference spectra (giving a measure of confidence in the result) for each mineral mapped. The depth values for each pixel and each mineral form a set of images of the minerals correlating to abundance. The fit values form a set of images corresponding to the confidence level of the identification. We combine single-mineral fit and depth images from several minerals, assigning a color to each mineral map. In this way, we produce multi-mineral maps. For example, red might be assigned to hematite; shades of red (from bright red to dark red) show relative abundance of hematite, brighter red indicating a stronger spectral signature. In these maps of minerals, black indicates none of the given set of minerals were detected at that location.

We have used the algorithm on AVIRIS data of Cuprite, Nevada, to illustrate some of the mapping possibilities with the new generation of sensors. The geologic and alteration maps are shown in figures 1 and 2. A false-color image of Cuprite (like one that might be produced by broad-band remote-sensing instruments) is shown in image A (all "image" figures are shown at the end of this chapter). An example minerals map is shown for iron-bearing minerals (image B). A color mineral map of clays and sulfates is shown in image C.

[1]U.S. Geological Survey, Mail Stop 964, P.O. Box 25046, Denver Federal Center, Denver, CO 80225.

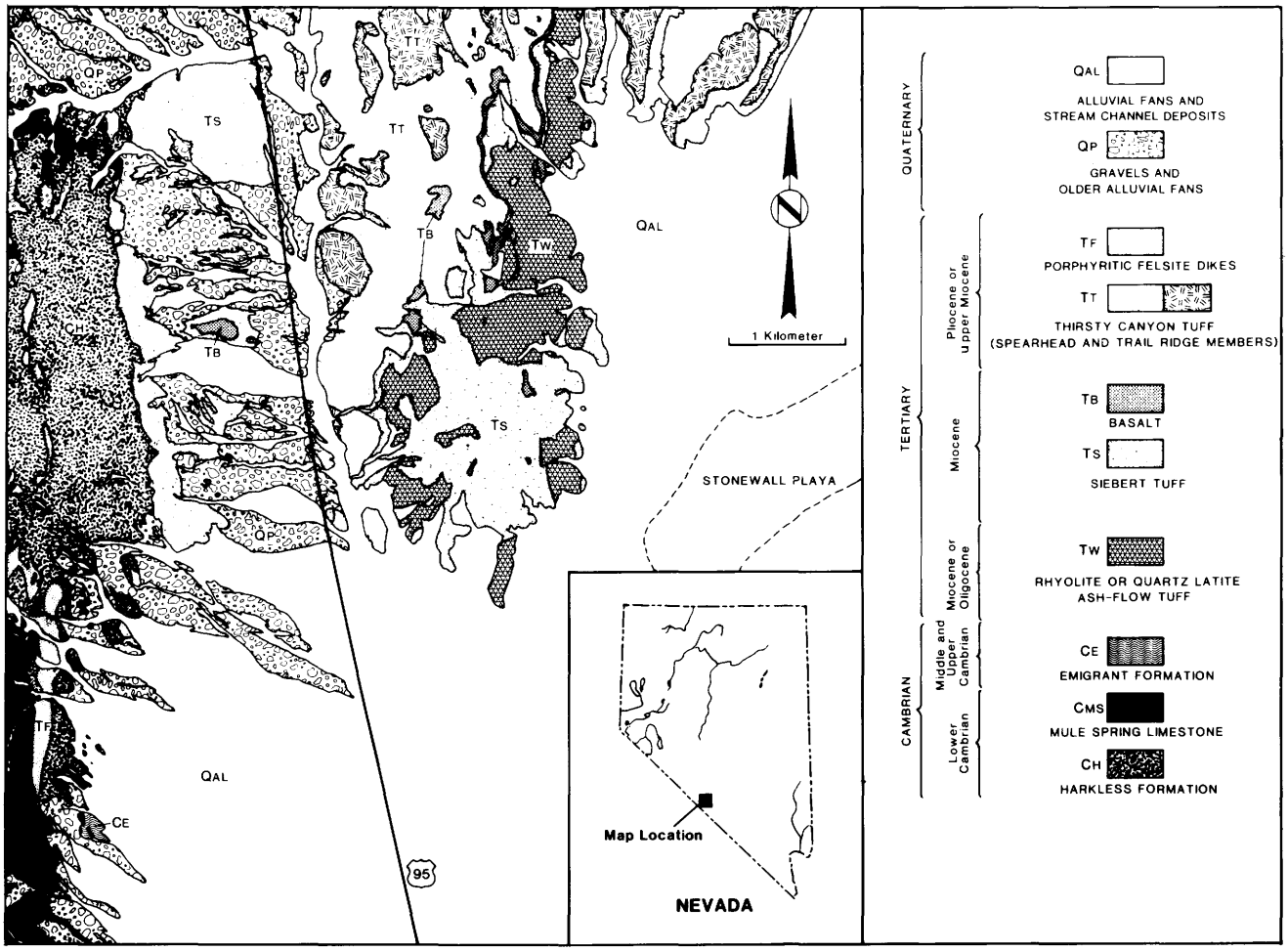

Figure 1. Geologic map of the Cuprite, Nevada mining district. The map was produced by conventional field work combined with remote-sensing TM data. From Abrams and Ashley (1980) and R.P. Ashley and R.C. Evarts (unpub. data, 1976) as modified by Hook (1990).

We can detect very subtle spectral differences, like degrees of kaolinite crystallinity (see image D), the difference between Na-montmorillonite versus Ca-montmorillonite (see image C), and individual members of the Na-K alunite solid-solution series (images E1 and E2). At Cuprite, maps of these subtle differences depict the alteration zone remarkably well. For example, poorly crystalline kaolinite or halloysite seems to be a general weathering product that occurs throughout the image, but as one moves closer to alteration zones, the kaolinite becomes progressively more crystalline. The highly crystalline kaolinite occurs just outside of the alunite zones. Alunite zones can be subdivided spectrally into areas where K-alunite occurs at the center and is surrounded by Na-alunite (see images E1 and E2).

These mineral maps have the potential to be extraordinary tools for mineral exploration because they show variations in mineral chemistry and, hence, pressure, temperature, and chemcal gradients in areal detail never seen before. Coupled with further geochemical research, detection of spectral variations in mineral solid solution series may provide a means to map temperature gradients on a large scale in a matter of hours. This information can also be used to locate areas where critical relationships need investigation. The applications seem boundless.

We have developed our methodology of calibration and mapping analysis to be a near-routine method. Imaging spectroscopy could now be used in U.S. Geological Survey (USGS) projects, and we believe the results illustrated here show that imaging spectroscopy could greatly enhance mineral mapping by the USGS. We also feel the method could be used for environmental problems because the spectral mapping algorithm will work on any material having diagnostic spectral absorption or emission features. Imaging spectroscopy could also be used in laboratory analysis of hand samples or in the field for investigating small areas.

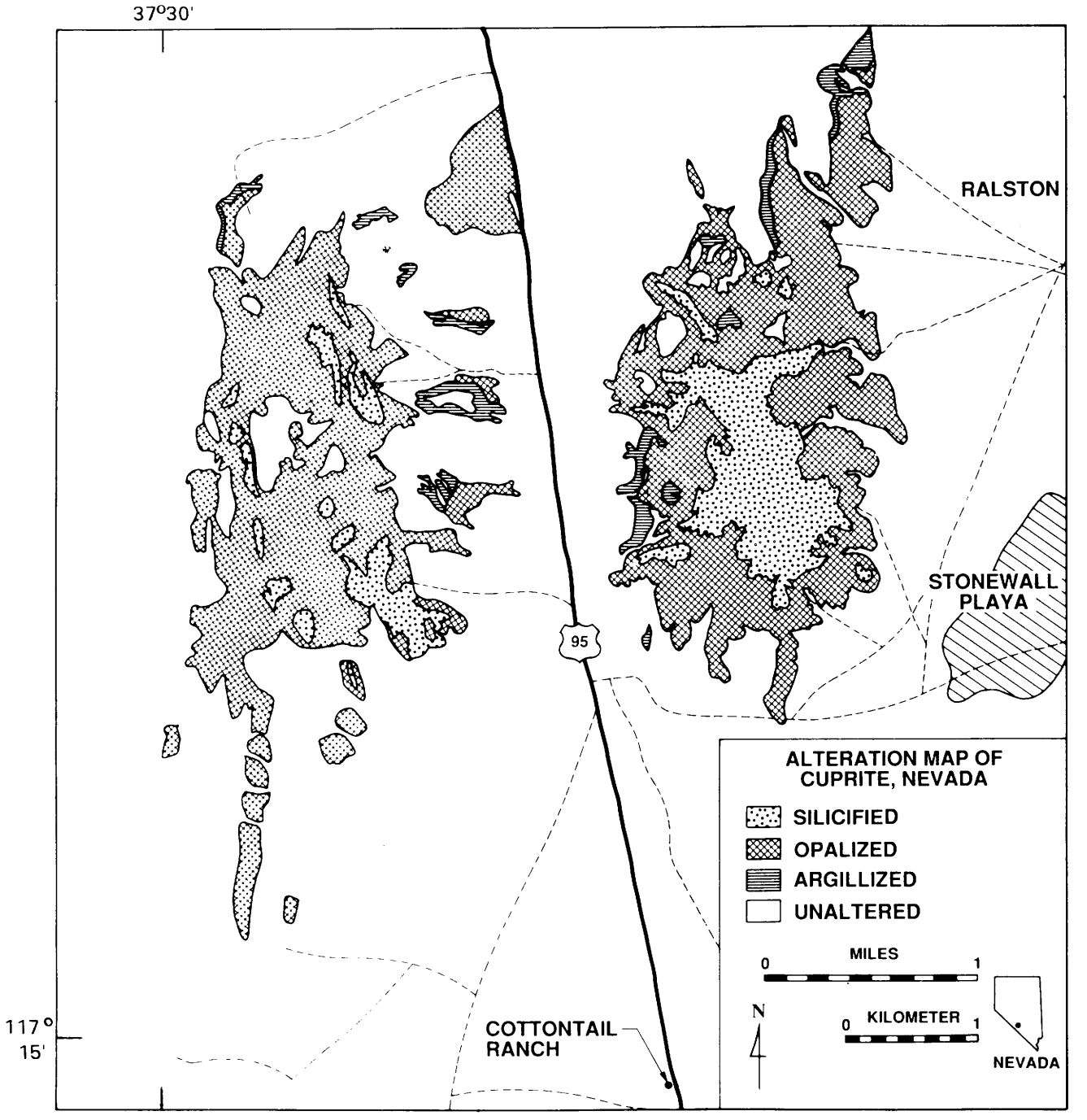

Figure 2. Alteration map of the Cuprite, Nevada mining district. The map was produced by conventional field work combined with remote-sensing TM data. From Abrams and Ashley (1980) and R.P. Ashley and R.C. Evarts (unpub. data, 1976) as modified by Hook (1990).

REFERENCES CITED

Abrams, M.J., and Ashley, R.P., 1980, Alteration mapping using multispectral images—Cuprite Mining district, Esmeralda County, Nevada: U.S. Geological Survey Open-File Report 80–367, 17 p.

Clark, R.N., Gallagher, A.J., and Swayze, G.A., 1990, Material absorption band depth mapping of imaging spectrometer data using a complete band shape least-squares fit with library reference spectra: Proceedings of the 2nd Airborne Visible Infrared Imaging Spectrometer (AVIRIS) Workshop, Jet Propulsion Laboratory, Publication 90–54, p. 176–186.

Hook, S.J., 1990, The combined use of multispectral remotely sensed data from the short wave infrared (SWIR) and thermal infrared (TIR) for lithological mapping and mineral exploration: Fifth Australasian Remote Sensing Conference, Proceedings, Oct., 1990, v. 1, p. 371–380.

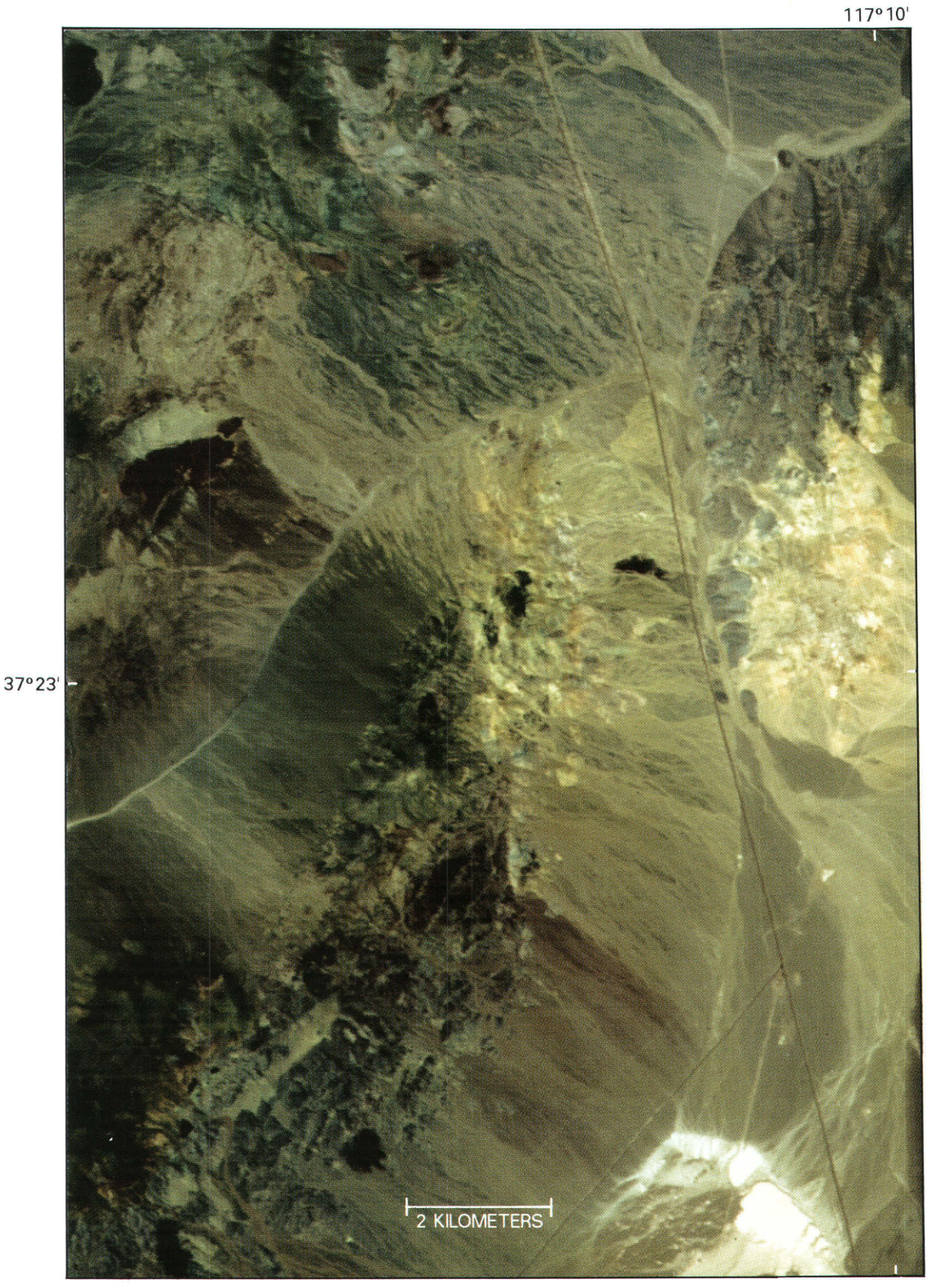

Image A. A color infrared image of Cuprite, Nevada from AVIRIS data. North is up in this 11-km-wide by 14-km-long scene. Ground resolution is 20 m. The linear feature running north-south to the right of center in the image is Highway 95. The area to the east of the road is the well-studied Cuprite mining district. This area consists of hydrothermally altered volcanic rocks and contains an intensely altered central silica cap surrounded by less altered zones of opalized and argillized rock. The area west of the highway consists of altered volcanic rocks and Cambrian siltstones and limestones. It also contains silicified, opalized, and argillized zones. Altered siltstones comprise most of the altered rocks in the northern part of the Cuprite Hills.

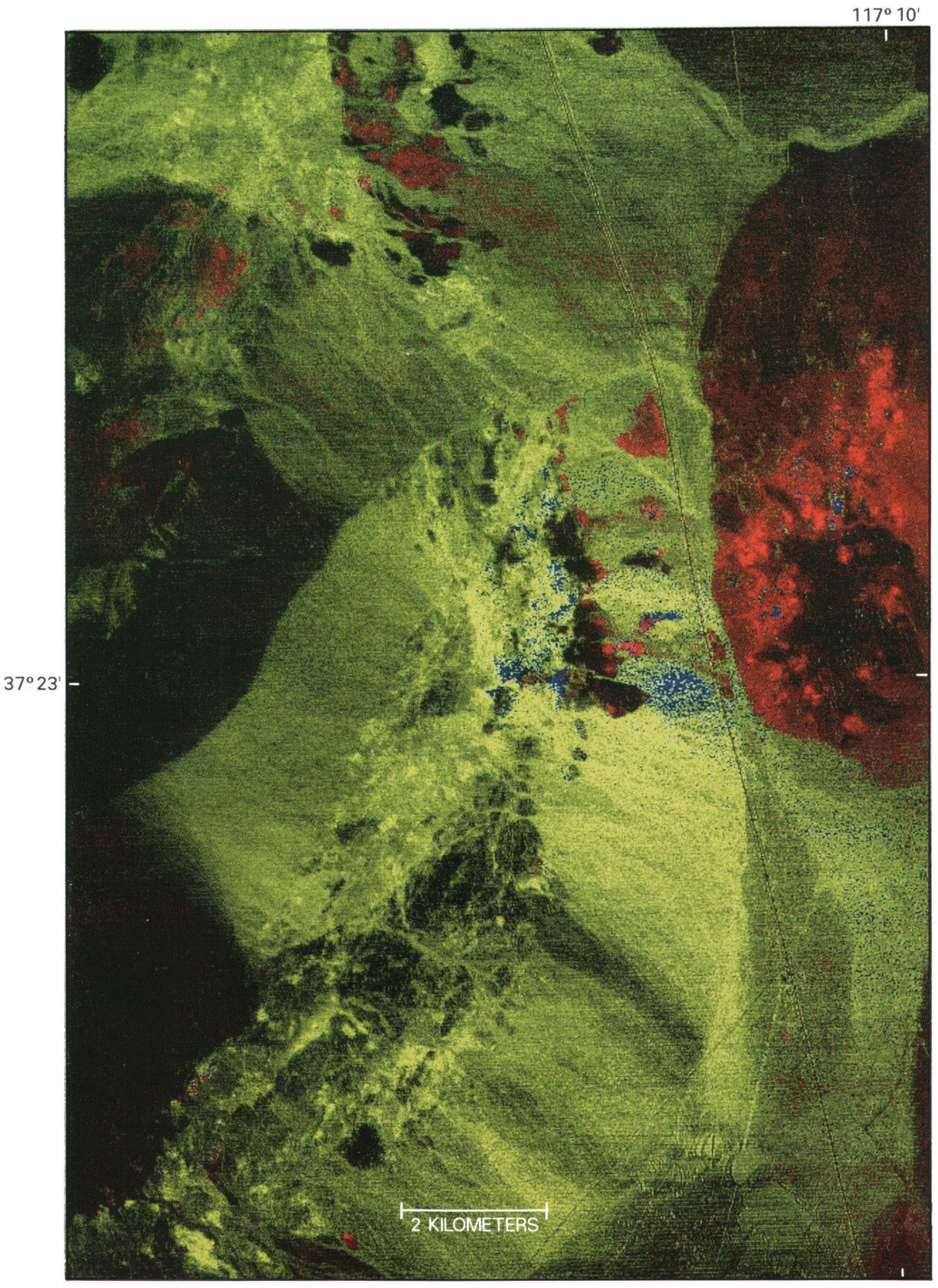

Image B. A color mineral map of iron-bearing minerals for Cuprite, Nevada. Hematite is red and is restricted to the opalized and argillized volcanic rocks on both sides of the highway. Goethite is green and is probably a weathering product (it is a common soil component). Jarosite is blue and occurs in the opalized zones on both sides of the highway; the largest occurrences are west of the highway.

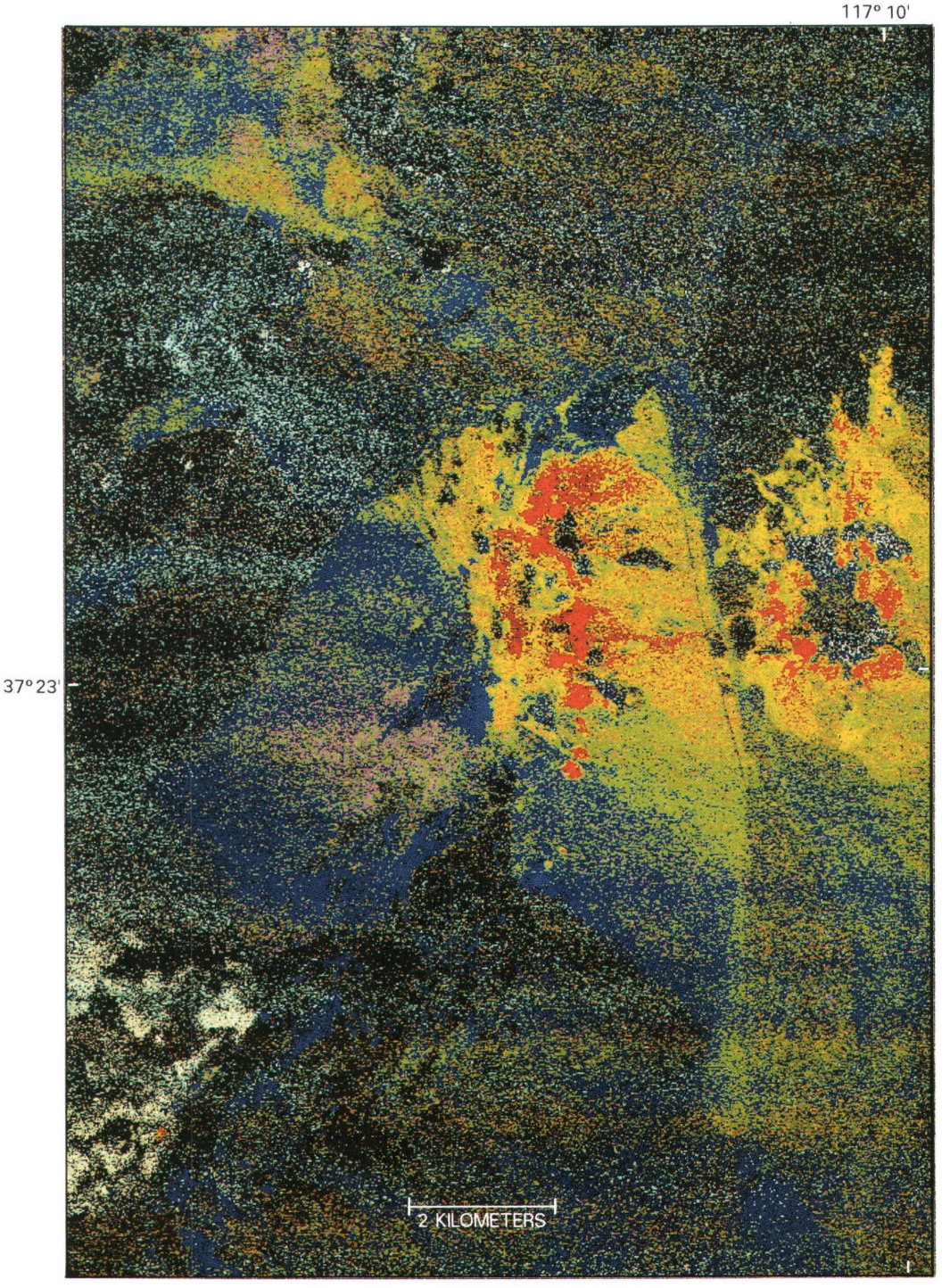

Image C. A color mineral map of clays and sulfates for Cuprite, Nevada. Alunite is red and occurs in opalized and argillic zones on both sides of the highway. Dickite is orange and is closely associated with kaolinite in the altered zones. Kaolinite (well crystallized) is yellow. Kaolinite (medium crystallized) is yellow green. Kaolinite (poorly crystallized) is green. (Halloysite and poorly crystallized kaolinite are spectrally indistinguishable at 2.2 μm.) Ca-montmorillonite is light blue and occurs in the northeastern portion of the scene. Na-montmorillonite is blue and occurs in rock units and as loess accumulations on alluvial fans and in playas. Some muscovites have a similar spectral signature and are also mapped as montmorillonite (with further research, these minerals may be separated). Buddingtonite is purple and is located only in a few pixels east of the highway. Buddingtonite can be better seen in white on the expanded image E2. Paragonite is magenta and occurs mostly in the lower left center of the image. Chlorite occurs as an intimate mixture with the paragonite. Opalized tuff is white and occurs in the lower left corner as well as in the central region of the Cuprite alteration zone.

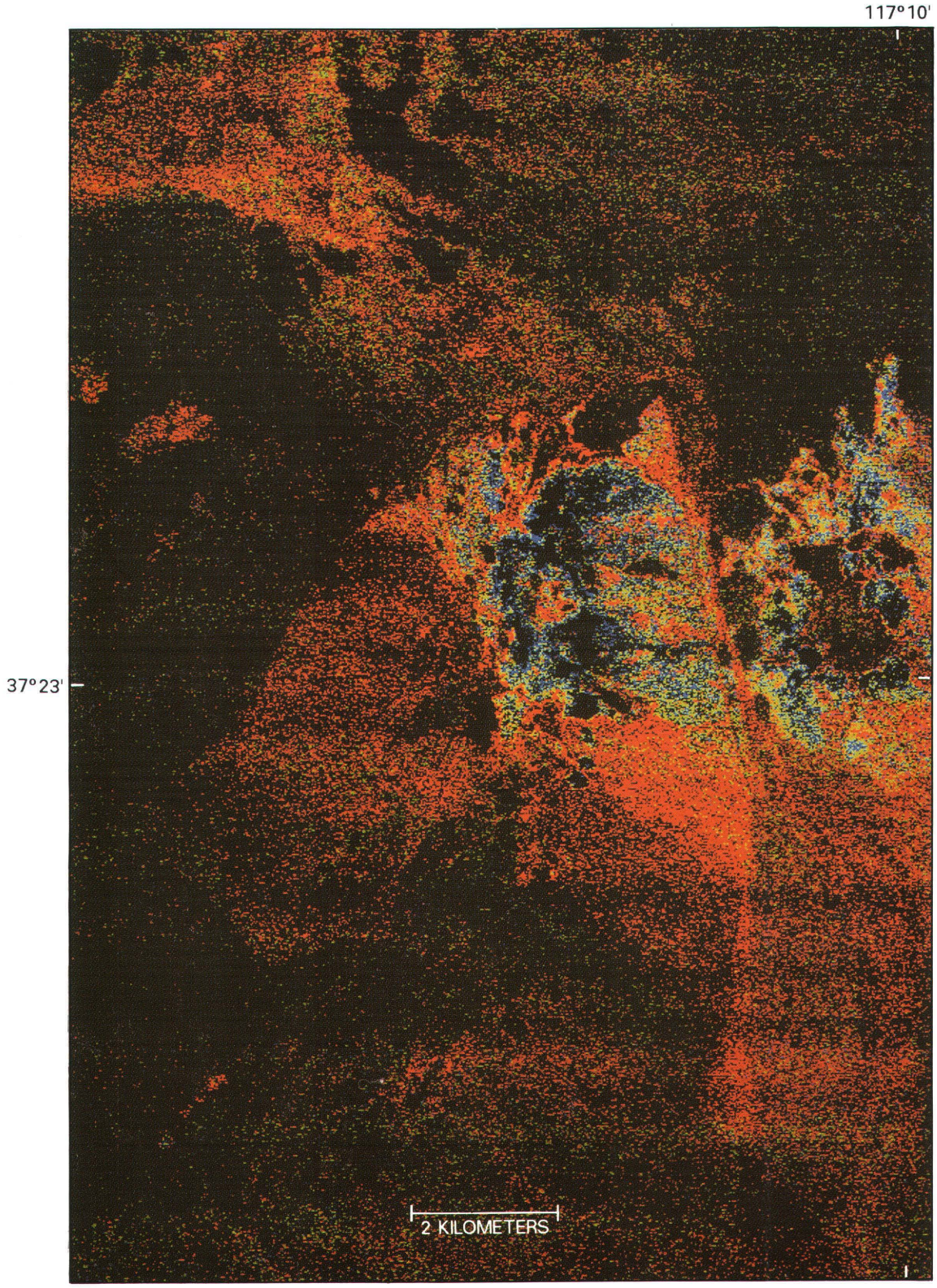

Image D. A color mineral map of kaolinite crystallinity for Cuprite, Nevada. Well crystallized kaolinite is blue and occurs near the outer margins of the alunite areas (which are black in this image). Medium crystallized kaolinite is green and occurs between the highly crystallized and poorly crystallized kaolinite. Poorly crystallized kaolinite is red and occurs farthest from the alunite areas. Poorly crystallized kaolinite or halloysite may be due to weathering processes. (Halloysite and poorly crystallized kaolinite are spectrally indistinguishable at 2.2 μm.)

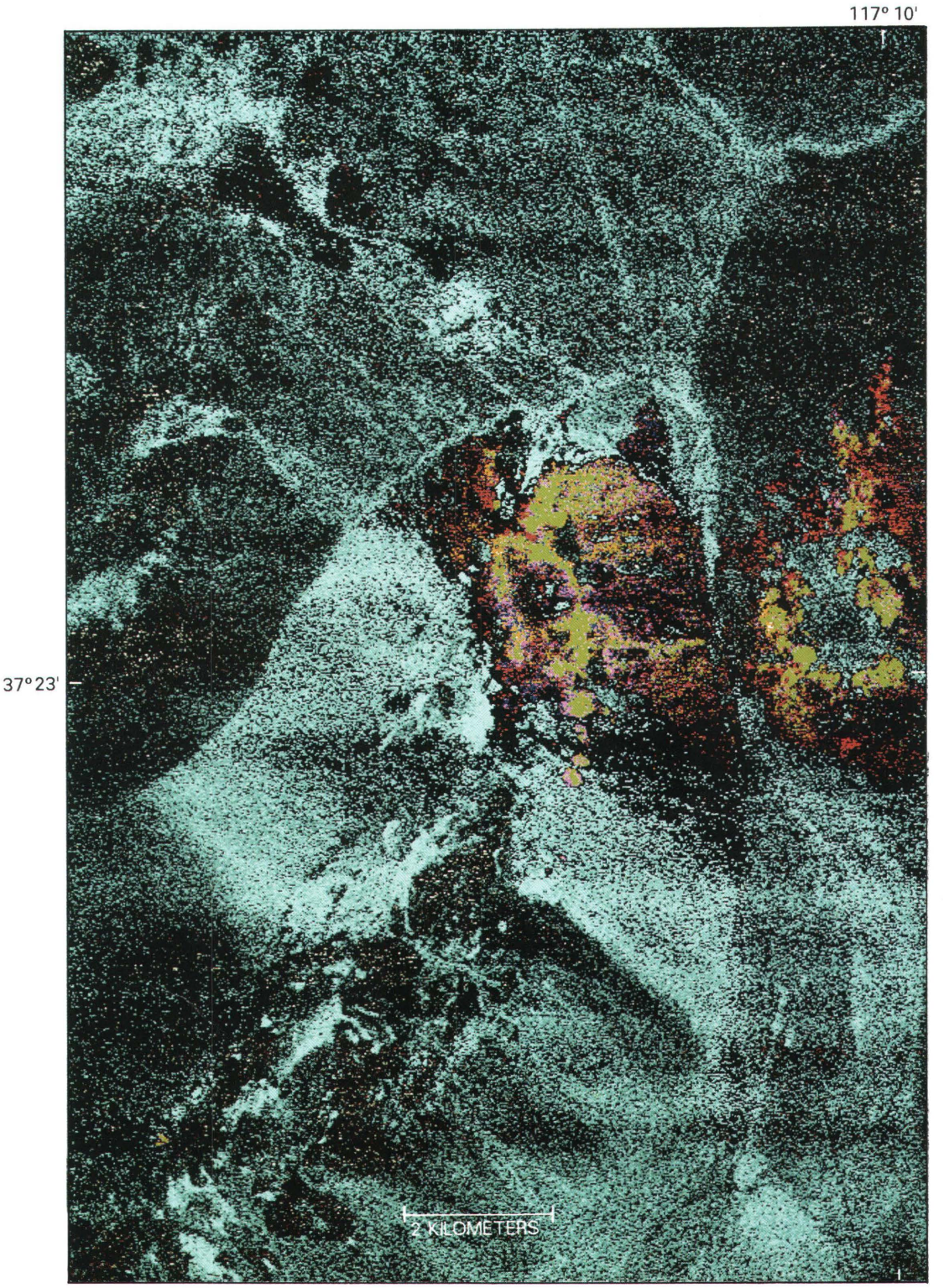

Image E1. A color mineral map of the alunite-natroalunite solid solution series, ammonium minerals, and two clays for Cuprite, Nevada. Potassium alunite is green and occurs in opalized and argillic zones on both sides of the highway. Natroalunite (Na mole fraction 0.65) is magenta and occurs next to potassium alunite, mostly to the west of the highway. Natroalunite (Na mole fraction 0.80) is blue and occurs with other natroalunites, mostly to the west of the highway. Buddingtonite is white and is located in a few pixels east of the highway and in a few small areas west of the highway. Ammonium illite-smectite is yellow and occurs in the alteration zones near alunite and buddingtonite. Kaolinite (well crystallized) is red and occurs near alunites in the alteration zones. Na-montmorillonite is cyan and occurs in rock units and loess accumulations on alluvial fans and in playas.

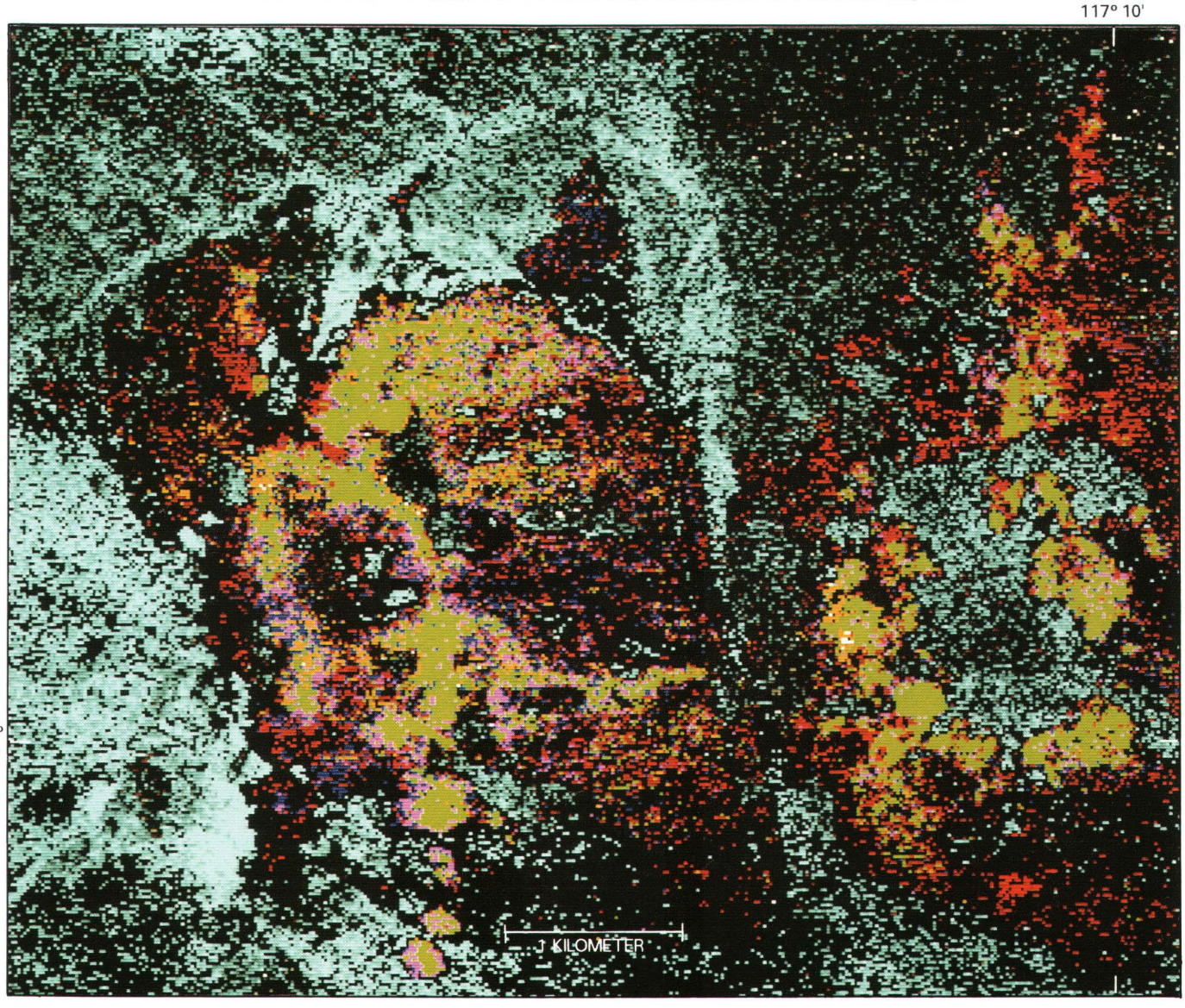

Image E2. An enlarged color mineral map of the alteration zones. This is an enlargement of the east-central part of image E1 and includes the alunite-natroalunite solid solution series, ammonium minerals, and two clays for Cuprite, Nevada. Potassium alunite is green and occurs in opalized and argillic zones on both sides of the highway. Natroalunite (Na mole fraction 0.65) is magenta and occurs next to potassium alunite, mostly to the west of the highway. Note how this natroalunite surrounds many of the potassium alunite zones (in green). Natroalunite (Na mole fraction 0.80) is blue and occurs with other natroalunites, mostly to the west of the highway. Buddingtonite is white and is located in a few pixels east of the highway and in a few small areas west of the highway. Note that buddingtonite is surrounded by ammonium illite-smectite. A few buddingtonite localities occur west of the highway. Ammonium illite-smectite is yellow and occurs in the alteration zones near alunite and buddingtonite. Note how the ammonium illite-smectite occurs at the edges of potassium alunite (green) zones. Kaolinite (well crystallized) is red and occurs near alunites in the alteration zones. Na-montmorillonite is cyan and occurs in rock units and loess accumulations on alluvial fans and in playas.

CHAPTER O

SATELLITE IMAGE PROCESSING FOR ENHANCED SPECTRAL DISCRIMINATION AND INTERPRETABILITY

By DANIEL H. KNEPPER, JR.[1]

BACKGROUND

Landsat Thematic Mapper (TM) satellite digital image data have been successfully applied to mapping hydrothermally altered rocks, lithologic units, and geologic structures in numerous CUSMAP, preassessment, and wilderness studies; the data have also been used by several U.S. Geological Survey (USGS) cooperative, international, mineral resource assessment projects. For the immediate future, at least until the end of this decade, TM data will be the only digital satellite data with worldwide coverage and spectral bands for detecting minerals with absorption features in the 2.2–2.3-μm region (mostly hydroxyl-bearing clay minerals and carbonates). Consequently, it is in the interest of the USGS to explore new methods of processing TM digital data to optimize the capability for extracting geologic information and to increase the interpretability of the digital-image products.

Color-ratio composite (CRC) images prepared from ratios of TM bands are commonly used to map areas of hydrothermally altered rocks and to discriminate rock units based on the presence of clay, carbonate, and iron-oxide minerals (Knepper, 1989; see also selected bibliography in Knepper, 1989). Two new image-processing techniques for preparing more useful CRC images were tested in the Geophysics Environmental and Minerals Demonstration Area (Watson and others, 1989), centered around Canon City in south-central Colorado. The two techniques are used in combination with standard processing procedures to increase the contrast between spectrally dissimilar materials and to display the TM band ratios in a more interpretable form. Spectral contrast is enhanced by a process called iterative ratioing (Crippen, in press a). Improved image presentation is obtained by combining three spectral components (band ratios) with a topographic component (average image) in a four-component display (Crippen, in press b) of the CRC image data. Encouraging results from this study prompted the application of the methods to additional test areas in the Altiplano of Bolivia, the Wind River Basin, Wyoming, and southern California with equally successful results.

[1]U.S. Geological Survey, Mail Stop 964, P.O. Box 25046, Denver Federal Center, Denver, CO 80225.

ITERATIVE RATIOING

The signal reaching the TM sensor is composed of light that is reflected from the ground surface and light that is scattered by the atmosphere. Iterative ratioing is a visually guided technique for removing the atmospheric scattering component from the signal measured by the TM sensor in each band. When band ratios are prepared, the iterative ratio correction provides a better measure of the actual spectral contrast between different materials and is based on the TM data alone without the need to apply complicated atmospheric models or to collect ground measurements.

Conceptually, iterative ratioing is a process of testing estimated atmospheric correction factors by visually evaluating the degree of topographic expression that remains in a test-band-ratio image after applying an estimated correction factor. Spectral-band-ratio values of a surface should be independent of the slope of the surface relative to solar illumination direction. However, in low illumination conditions, such as shadows, the dominant signal detected by the TM sensor is an additive term due to atmospheric scattering. Consequently, ratios of uncorrected bands in these shadowed areas are not the same as in full illumination, and they express an aspect of topography. The degree of

topography remaining in a test ratio is a measure of how well the estimated atmospheric correction factor removes the scattered-light component from the band data. If topographic expression remains, then the correction constant is too small; if the topographic expression is reversed (shadows are white), then the correction factor is too large.

Operationally, the test-ratio image is formed using one TM band for which the atmospheric correction factor is known (numerator) and one band for which the correction factor is to be determined (denominator). TM band 7 is the longest wavelength band of the TM data (2.08–2.35 μm) and is the least affected by atmospheric scattering. Removing an atmospheric correction factor of 2 data numbers (DN) from TM band 7 provides good correction for most TM scenes. Correction factors for any of the remaining TM bands can be determined by: (1) applying an estimated correction factor to the band, (2) forming a ratio image between the corrected TM band 7 (numerator) and the band with the estimated correction factor applied (denominator), (3) evaluating the degree of topography remaining in the test-ratio image, and (4) adjusting the correction factor and repeating steps (2), (3), and (4) until the amount of topography in the test-ratio image is minimized.

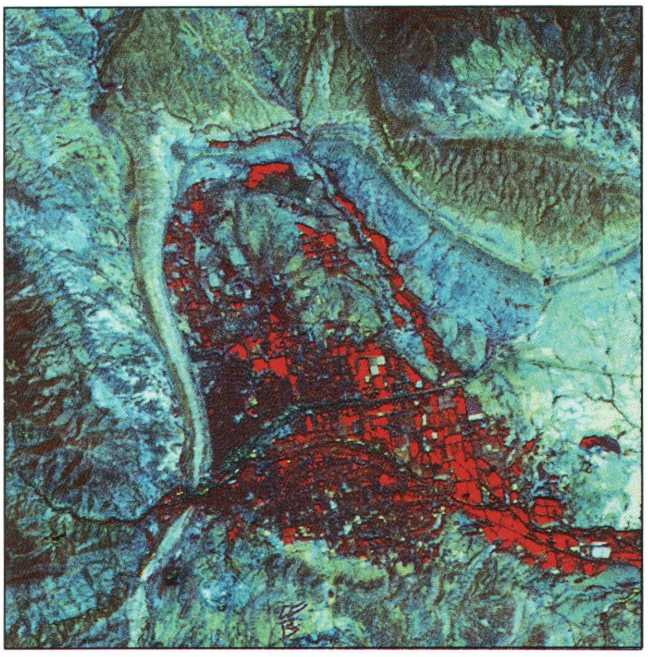

Figure 1. Standard Landsat TM color-ratio composite image of the Canon City area, Colorado, made without atmospherically correcting the band-image data. Image has been contrast stretched for display. Image area is approximately 10 miles across.

FOUR-COMPONENT DISPLAY

Atmospherically corrected TM band-ratio images display a minimum of topographic information, and color-ratio composite (CRC) images prepared from three atmospherically corrected band ratios are often difficult to interpret in the appropriate geologic and geomorphic context. In addition, potentially important spectral anomalies are difficult or impossible to accurately locate on maps. Selected amounts of topographic information can be merged into the CRC image by multiplying each of the band-ratio images by an image containing suitable topographic expression. An average image composed of the average of two or more single bands works well. The average image can be edge enhanced to increase the sharpness of tonal boundaries reflecting shadowing before merging with the band ratios. Alternatively, the spectral information from the TM band ratios can be merged with higher spatial resolution images, such as SPOT or digital radar image data, after resampling the TM band ratios to the same pixel size as the higher resolution data and registering the two data sets.

By carefully adjusting the means of the band ratios and the average image before merging, a CRC image can be prepared that provides a topographic reference for the spectral information in the band ratios without significantly affecting the hues of the colors depicting the spectral information. Crippen (in press b) provides a simple mathematical relationship that allows the mean adjustments to be made in a straightforward and consistent manner. The resulting CRC image can be visually interpreted and confidently used for photogeologic mapping.

DISCUSSION

Figure 1 is a standard TM CRC image centered on the Canon City, Colorado, area—this area lies in the center of the south-plunging (top to bottom) Oil Creek syncline, which is outlined by prominent hogbacks of Cretaceous sedimentary strata. Some topographic expression is apparent in the image because no atmospheric corrections were applied to the bands of TM data, but there is an overall subduing of most topographic features. The colors on the image indicate compositional variations of surface materials: red represents vegetation, magenta represents materials containing clays and (or) carbonate minerals, green represents minerals containing reduced (ferrous) iron minerals, and blue represents iron-oxide (ferric) minerals. Figure 2 is a four-component TM CRC image in which the individual TM bands have been atmospherically corrected using the iterative ratioing process. Color hues on the image are basically the same as on figure 1, although some differences are apparent because the atmospheric corrections provide a better (and different) measure of the actual spectral differences

Figure 2. Four-component Landsat TM color-ratio composite image of the Canon City area, Colorado, prepared from atmospherically corrected bands using iterative ratioing and merged with an edge-enhanced average image prepared from TM bands 3, 4, 5, and 7. Image has been contrast stretched for display. Image area is approximately 10 miles across.

between materials. The addition of the topographic component to the image clearly enhances the interpretability of TM CRC data.

The software necessary to produce atmospherically corrected, four-component Landsat TM CRC images is relatively simple and should be available in most image-processing packages. The functions that are necessary are: (1) adding, subtracting, multiplying, and dividing images and constants to images, (2) contrast stretching, (3) image statistics (mean and standard deviation), and (4) edge enhancement (although this can be accomplished with a simple boxfilter program and the arithmetic functions listed in (1) above). Programs contained in REMAPP-PC (Livo and Gallagher, 1991) were used to prepare figures 1 and 2. Details of the image-processing procedures are contained in Crippen (in press a, in press b).

REFERENCES CITED

Crippen, R.E., in press a, The iterative ratioing method of determining atmospheric corrections for scenes with rugged terrain: Photogrammetric Engineering and Remote Sensing.

———in press b, Image display of four components of spectral data: Remote Sensing of Environment.

Knepper, Daniel H., Jr., 1989, Mapping hydrothermal alteration with Landsat Thematic Mapper data, *in* Lee, Keenan, ed., Remote Sensing in Exploration Geology: 28th International Geological Congress Field Trip Guidebook T–182, p. 13–21.

Livo, K.E., and Gallagher, A.J., 1991, REMAPP-PC—Remote sensing image processing software for MS-DOS personal computers, Version 2.00: U.S. Geological Survey Open-File Report 91–449, 81 p.

Watson, Kenneth, Knepper, D.H., Jr., Clark, R.C., Pitkin, J.A., Labson, V.F., Campbell, D.L., Rowan, L.C., Kruse, F.A., Lee, Keenan, and Livo, K.E., 1989, Plans for integrated airborne geophysical study of the Geophysics Environmental and Minerals Demonstration Area, south-central Colorado [abs.]: USGS Research on Mineral Resources—1989, 5th Annual V.E. McKelvey Forum on Mineral and Energy Resources, Program with Abstracts, U.S. Geological Survey Circular 1035, p. 77–78.

CHAPTER P

$^{40}Ar/^{39}Ar$ STUDIES OF FLUID INCLUSIONS IN VEIN QUARTZ FROM BATTLE MOUNTAIN, NEVADA

By EDWIN H. MCKEE,[1] JAMES E. CONRAD,[1] BRENT D. TURRIN,[1]
and TED G. THEODORE[1]

ABSTRACT

Fluid inclusions in vein quartz from the Buckingham stockwork molybdenum deposit and from leucogranites north of the Buckingham deposit yield $^{40}Ar/^{39}Ar$ isochron ages that agree well with K-Ar and $^{40}Ar/^{39}Ar$ radiometric ages of phenocrysts from these rocks. (The Buckingham deposit is Late Cretaceous in age, and the leucogranites north of the Buckingham deposit are late Eocene to early Oligocene in age.) The younger period of igneous activity (late Eocene to early Oligocene) is clearly defined by three isochrons at about 38 Ma. The Late Cretaceous age is recognized by three isochrons, one well defined at 75.5±1.1 Ma, one that is 55.1±3.7 Ma, and one that is 51.2±16.3 Ma. All samples had inherited excess ^{40}Ar in amounts that equal about 30 percent of the total argon. Because of the excess argon, individual age determinations are highly variable and cannot be interpreted—isochrons based on several analyses are necessary to yield a meaningful age. Samples with small amounts of potassium proved unusable; sufficient potassium must be present to produce enough radiogenic ^{40}Ar to mask the excess ^{40}Ar.

INTRODUCTION

Igneous activity and associated mineralization in the Battle Mountain district, Nevada (fig. 1), occurred during the Late Cretaceous and again in late Eocene to early Oligocene time. These age designations are based on many K-Ar and $^{40}Ar/^{39}Ar$ age determinations (Theodore and others, 1973; McKee, 1992). The purpose of this study was to determine the radiometric ages of quartz veins from the Cretaceous Buckingham stockwork molybdenum deposit and nearby Eocene and Oligocene quartz veins in this district using single-grain laser-fusion $^{40}Ar/^{39}Ar$ methods. The fluid-inclusion-derived ages from this well-dated district are compared with existing K-Ar and $^{40}Ar/^{39}Ar$ dates to test the feasibility of obtaining usable geochronology from fluid inclusions. Vein quartz can be dated using argon produced by radioactive decay of potassium-bearing phases in fluid inclusions. All argon from quartz should be derived from fluid inclusions because there is no other site possible for the large K atom in the SiO_2 structure of quartz. Argon is present as a component of paleohydrothermal fluids trapped in fluid inclusions. As the data were gathered, however, it became evident that excess argon is present within the vein quartz. Only by constructing isochrons from a number of individual quartz grains is it possible to evaluate the amount of excess argon present. The ages determined by this technique confirm those derived by K-Ar and $^{40}Ar/^{39}Ar$ total fusion and incremental heating of potassium-bearing minerals from the Buckingham deposit (McKee, 1992).

The presence of argon in fluid inclusions in quartz was first demonstrated by Wahler (1956). Subsequently, excess Ar and He in beryl, cordierite, and tourmaline, which were assumed to come from fluid inclusions, was reported by Damon and Kulp (1958). The presence of Ar, Kr, and Xe in gas from gas inclusions in sylvite from the Bereznikovsk mine in Russia was reported by Nesmelova (1959). Excess ^{40}Ar in several quartz and fluorite samples was documented by Rama and others (1965), and they pointed out the difficulties that this presents for

[1]U.S. Geological Survey, Mail Stop 901, 345 Middlefield Road, Menlo Park, CA 94025

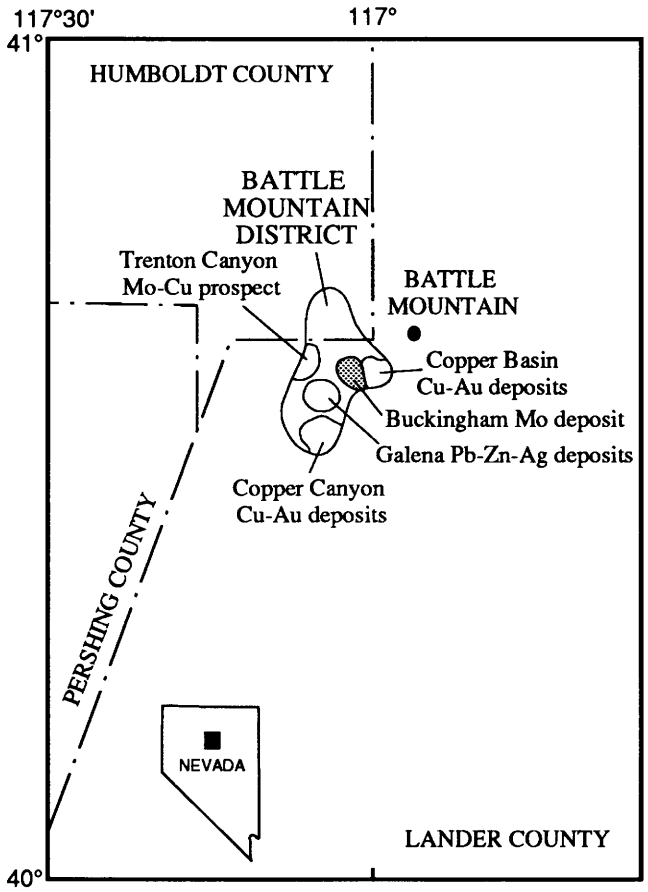

Figure 1. Map of north-central Nevada, showing Battle Mountain district and mineral deposits within it.

K-Ar dating. Little work has been published on K-Ar or $^{40}Ar/^{39}Ar$ dating of fluid inclusions since these studies.

Recently, Kelly and others (1986) examined, by incremental heating $^{40}Ar/^{39}Ar$ techniques, the Ar isotopes of fluid inclusions in quartz veins associated with granite-hosted tungsten mineralization in southwestern and northern England. In this study, the authors noted that argon in the fluid inclusions is released during incremental heating in amounts that correlate with the potassium and chlorine content of fluid inclusions. The argon in the potassium-correlated component is derived primarily from in situ decay of potassium in solid phases in the inclusions. Argon from the chlorine-correlated component is associated with brines that constitute the liquid phase of the inclusions. Inherited argon from the original magmatic fluid was not noted.

METHODS

Samples 79C103 and 79C104 were irradiated in the U.S. Geological Survey TRIGA reactor (Denver, Colo.) for a period of 60 h. Irradiation flux was monitored by use of the MMhb-1 hornblende standard, which has an age of 513.9 Ma. Sample handling techniques and corrections for Ca- and K-derived isotopes used in the Menlo Park laboratory are as described by Dalrymple and Lanphere (1971, 1974). Samples 1471-760, 1471-173, 79C77, and 81TT121 were irradiated in the Berkeley TRIGA reactor (University of California, Berkeley) for a period of 10 h. Irradiation flux was monitored by use of standards MMhb-1 (hornblende), GHC 305 (biotite, with an age of 103.76 Ma), and P-207 (muscovite, with an age of 82.1 Ma). Potassium and calcium corrections for the Berkeley TRIGA reactor were determined using optical grade CaF_2 and a laboratory potassium glass.

The $^{40}Ar/^{39}Ar$ analyses were conducted at the U.S. Geological Survey, Menlo Park, California, and at the Berkeley Geochronology Center using similar laser-fusion microextraction systems to analyze single grains of vein quartz that were approximately 0.5–1.0 mm in size. An on-line, ultrasensitive mass spectrometer was used for argon analyses.

GEOLOGIC SUMMARY

The Buckingham stockwork molybdenum deposit in north-central Nevada, about 10 km southwest of the town of Battle Mountain (fig. 1), contains one of the largest known resources of molybdenum in the United States. However, under present (1991) economic conditions, the relatively low molybdenum grades of the deposit make it uneconomic. The Buckingham deposit is a calc-alkaline, stockwork-molybdenum-bearing system located on the east flank of the Battle Mountain mining district (fig. 1). The deposit contains an estimated 1,000 million tons of mineralized rock, averaging approximately 0.10 percent molybdenum (as MoS_2). The deposit also contains small amounts of silver, tungsten, copper, and gold (Theodore and others, 1992). Molybdenum mineralization is related to emplacement of a Late Cretaceous composite porphyry system that intruded surrounding Paleozoic rocks and altered much of the country rock to hornfels.

Two periods of plutonism have been recognized in the Battle Mountain area (Theodore and others, 1992). The older period, represented by monzonites at Buckingham and the granodiorite of Trenton Canyon (on the west edge of the mining district and about 9.5 km due west of the Buckingham system), has been dated at about 86 Ma (McKee, 1992) (table 1, fig. 2). The younger period includes at least six Tertiary intrusive bodies in the Buckingham vicinity, ranging in age from 41.1 to 37.3 Ma (Theodore and others, 1973) (table 1, fig. 2).

Table 1. K-Ar and $^{40}Ar/^{39}Ar$ ages of Buckingham stockwork system and nearby intrusive rocks.

[σ, standard deviation. Modified from McKee (1992)]

Rock type	Mineral dated	Apparent age (Ma $\pm \sigma$)
Samples from the Buckingham stockwork system		
Monzogranite porphyry	Muscovite	61.3 ± 1.5
Monzogranite porphyry	Muscovite	61.7 ± 1.5
Monzogranite porphyry	Biotite and chlorite	65.1 ± 1.6
Monzogranite porphyry	Muscovite	68.6 ± 1.5
Aplite	Whole rock	70.3 ± 1.7
Monzogranite porphyry	Muscovite	75.7 ± 1.6
Monzogranite porphyry	Muscovite	77.4 ± 1.6
Monzogranite porphyry	Muscovite	85.5 ± 1.9
Monzogranite porphyry	Biotite	85.7 ± 0.4[1]
Monzogranite porphyry	Muscovite	86.1 ± 2.0
Monzogranite porphyry	Muscovite	88.0 ± 2.0
Samples of intrusive rocks north and southwest of the Buckingham stockwork system		
Rhyolite	Biotite	37.3 ± 1.1
Leucotonalite	Hornblende	37.7 ± 1.4
Monzogranite	Biotite	38.8 ± 1.1
Monzogranite	Hornblende	39.0 ± 1.1
Monzogranite	Hornblende	39.3 ± 1.0
Rhyolite	Biotite	39.1 ± 1.0
Sample of intrusive rock northeast of and cutting the Buckingham stockwork system		
Granodiorite porphyry	Hornblende	35.4 ± 1.1

[1] Age from the two greatest release steps from an incremental heating $^{40}Ar/^{39}Ar$ experiment.

CRETACEOUS MONZOGRANITES OF THE BUCKINGHAM AREA

The age of emplacement of the Buckingham system is based on evaluation of one incremental-heating $^{40}Ar/^{39}Ar$ determination and 10 K-Ar age determinations (McKee, 1992) (table 1). The ages range from 88.0±2.0 to 61.3±1.5 Ma; four of the K-Ar ages and the major argon release steps of the incremental heating experiment cluster around 86 Ma. This age (86 Ma) is considered to represent the initial time of cooling of the porphyry system.

Eight major intrusive phases identified in the Buckingham system were intruded sequentially from south to north across a distance of several kilometers. The present configuration of the intrusive center is an east-west alignment of two stocks (each a composite of several porphyries) and several outlying intrusive bodies (fig. 2). All eight intrusive phases underwent molybdenum mineralization. The two oldest intrusions form border phases, and the youngest, an outlying intrusion, produced relatively little molybdenum mineralization. The main Buckingham molybdenum deposit, formed by five igneous phases associated with the main part of the two stocks, developed umbrella-shaped shells of molybdenite mineralization that drape over the stocks (Theodore and others, 1992). Approximately one-half of the Buckingham deposit is hosted in metamorphosed and intensely veined rocks belonging to the Upper Cambrian Harmony Formation. Secondary, partially chloritized biotite is pervasive throughout the Buckingham porphyry and yields a K-Ar age significantly younger (by 10 to 15 percent) than the 86-Ma age that is considered to be the age of initial cooling of the pluton. This younger age is interpreted to result from partial loss of argon from the 86-Ma porphyry (McKee, 1992).

The argon release pattern from the incremental-heating $^{40}Ar/^{39}Ar$ experiment support the partial-argon-loss model, indicating a complex thermal history. The secondary thermal event, although not pervasive enough to completely reset the K-Ar clock, is clearly recognized in the release pattern (fig. 3). Heat and hydrothermal activity generated by the late Eocene and early Oligocene igneous events show varying amounts of intensity at different places throughout the Buckingham system. Almost all samples from the western part of the system yield ages that are variably reset, although none of them are completely reset to the approximate 38-Ma age of the younger, nearby plutons.

TERTIARY GRANITIC AND RHYOLITIC INTRUSIVE ROCKS

The six small monzogranite, granodiorite porphyry, and rhyolite stocks and dikes in the vicinity of the Buckingham deposit (fig. 2) yield K-Ar ages on biotite and hornblende of about 38 Ma (table 1). These bodies are mostly satellites of the main Cretaceous monzogranite porphyry of the Buckingham deposit. A system of granodiorite porphyry dikes, dated at about 35 Ma, cut the Buckingham porphyry (table 1, fig. 2). Hydrothermal alteration and mineralization related to late phases of this pervasive middle Tertiary period of igneous activity are recognized south of the Buckingham deposit, at Copper Canyon, and at many other places in the Battle Mountain mining district. The thermal effect of late Eocene and early Oligocene intrusive events manifests itself in the Cretaceous Buckingham system as partially reset K-Ar ages.

STRUCTURE

Deformation of the Buckingham system during the middle Tertiary included significant brittle-type faulting that is manifested primarily along three major, low-angle, normal faults. This Tertiary extensional tectonism progressed from east to west during Oligocene and possibly

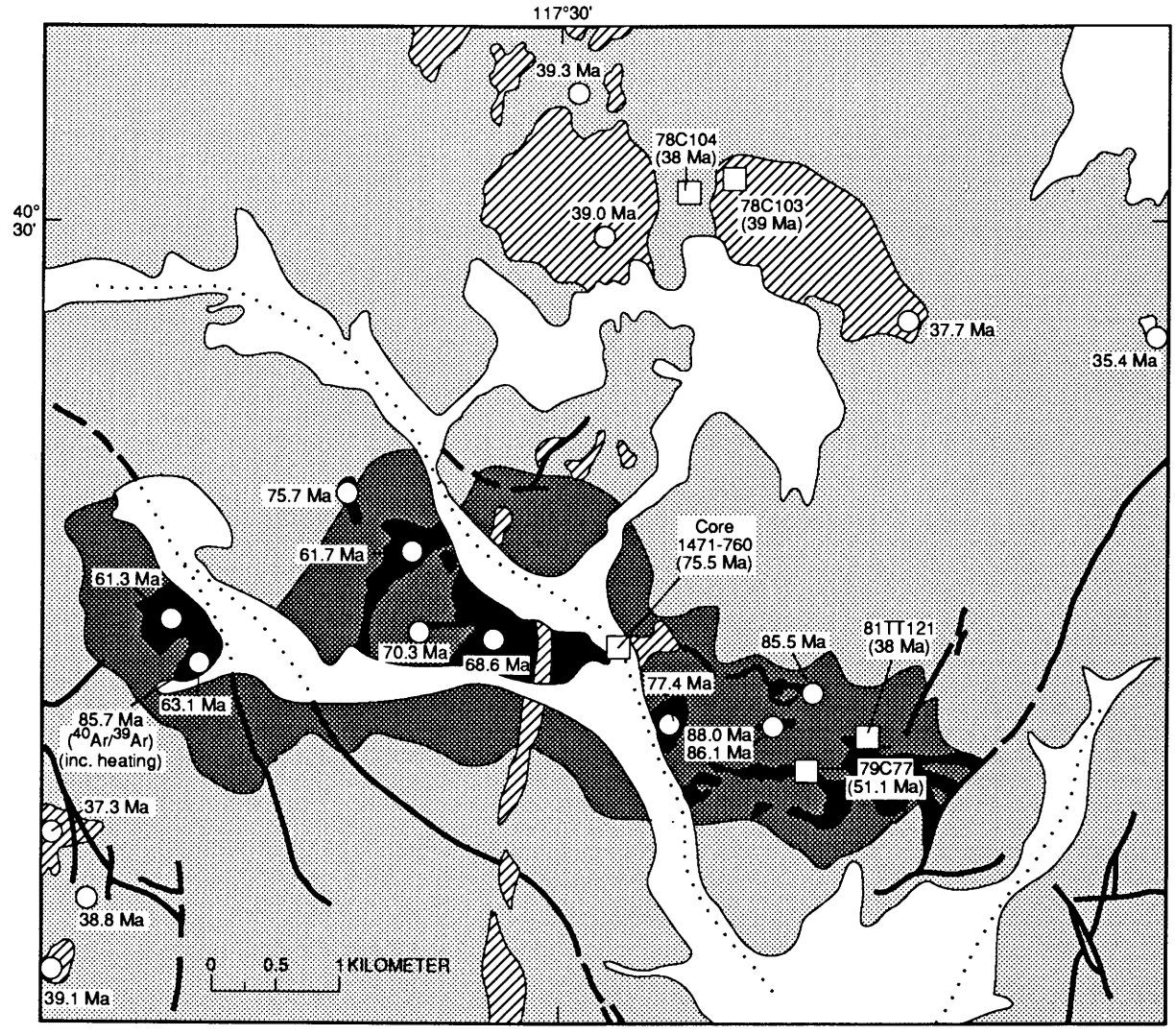

EXPLANATION

- **Quaternary alluvium**
- **Tertiary igneous rocks**
- **Cretaceous Buckingham stockwork system**—includes monzogranite (black)
- **Paleozoic sedimentary and metasedimentary rocks**
- 38.8 Ma — **K-Ar or $^{40}Ar/^{39}Ar$ sample locality**—showing age determinations from McKee (1992)
- 75.5 Ma — **$^{40}Ar/^{39}Ar$ quartz vein, fluid-inclusion sample site and age**
- **Fault**—dotted where concealed

Figure 2. Geologic map of the Buckingham stockwork molybdenum deposit and surrounding area. Sample sites for this report are represented by squares; K-Ar sample sites and one $^{40}Ar/^{39}Ar$ incremental-heating-age sample site represented by circles.

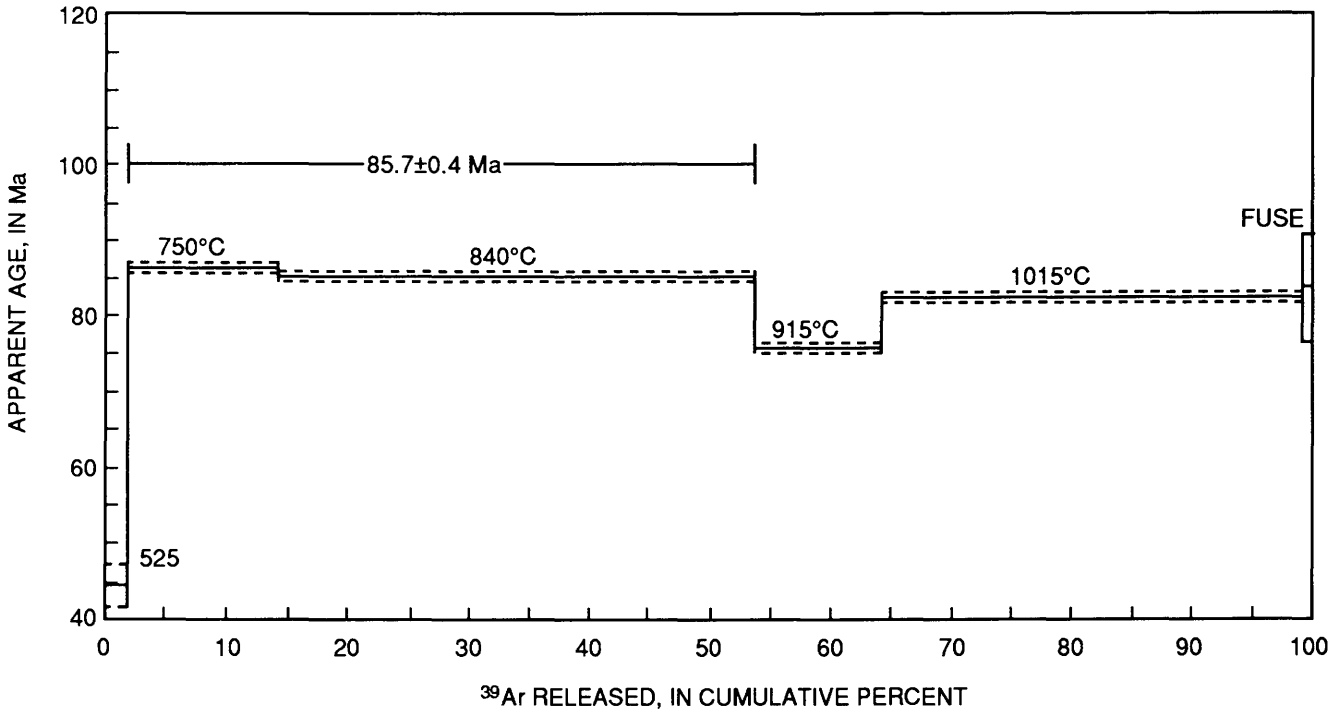

Figure 3. $^{40}Ar/^{39}Ar$ age spectra for a biotite from the Buckingham stockwork system (monzogranite porphyry). The six heating steps (and thus temperature in °C) are shown as horizontal bars. This release pattern is similar to patterns produced from minerals with disturbed thermal histories. The most likely age calculated using the two oldest steps (which produced more than 50 percent of the Ar) is 85.7±0.4 Ma (from McKee, 1992).

Miocene time (Theodore and others, 1992). Imbricate, down-to-the-east, listric-normal faults merge into a single, flat-lying dislocation east of the Buckingham porphyry system. In addition, major reverse dislocations in the hanging wall of the major fault probably reflect development of antithetic reverse faults in the toe region of a rigid-body glide block (Theodore and others, 1992).

FLUID INCLUSIONS

Hydrothermal fluids in the Buckingham system show complex histories that reflect successive influxes of fluids from newly injected magma into loci of earlier emplaced igneous phases (Theodore and others, 1992). In distal parts of the system, fluid inclusions in andradite-diopside suggest temperatures of about 300°C at extremely low mole fractions of CO_2. In proximal parts of the system, where the bulk of the quartz stockworks and molybdenite was deposited, fluids were relatively low-density, low-salinity NaCl brines that included variable amounts of CO_2. These early-stage fluids established an ascending plume of fluid that was considerably less saline than fluids associated with most porphyry copper systems in the southwestern United States. The magmas at the Buckingham deposit did not evolve large volumes of very dense, NaCl-rich fluids. High in the system, very sparse halite-bearing fluid inclusions formed through condensation from an earlier, higher temperature saline fluid. In the western part of the system, the high-temperature and high-saline halite-bearing fluid inclusions, having salinities as much as 65 weight percent NaCl equivalent and homogenization temperatures as high as 500°C, probably reflect ponded magmatic fluids from a deep source. Overall distribution of veins associated with such fluids appears to be restricted. Although a fluid-immiscibility model is probably applicable to some porphyry molybdenum systems where the exposed parts of the system are above a buried concentration of molybdenum, the geometry of the molybdenite-enriched shells and their proximity to the igneous source at the Buckingham deposit argue against this model. These shells are tightly constrained to the flanks and apical parts of the two mineralized stocks, and the shells show a genetic relationship to a quartz–potassium feldspar porphyry phase in the core of the stocks. Furthermore, an approximately 1-km-long composite vertical section through the Buckingham system is available for study in the three tectonically offset blocks, and nowhere is there widespread occurrence of hypersaline fluids. The bulk of the moderately saline, H_2O-NaCl-CO_2 mineralizing fluids associated with this deposit is related to quartz–potassium feldspar porphyry and slightly deeper

Table 2. Temperature and salinity data for vein quartz samples used for fluid inclusion studies.

[Locations of samples used for $^{40}Ar/^{39}Ar$ analyses shown on fig. 2; salinity ranges given in weight percent NaCl equivalent; --, not determined]

Sample no.	Host rock[1]	Homogenization temperature range (°C)[2]	Fluid-inclusion types[3]	Salinity range[2]	Comments
			Outcrop samples		
79C77	Km	--	I,II, IV	--	Quartz veins on Vail Ridge associated with Buckingham system.
81TT121	Km	229–324	I, IV	0–11.6	Quartz veins in upper copper-rich part of Buckingham system.
78C103	Ch	--	I, II, III, IV	--	Quartz stockworks near Tertiary leucogranite.
78C104	Ch	--	I, II, III	--	Quartz stockworks in pendant within Tertiary leucogranite.
87TT215A	Chg	175–550	I, II, III	1.3–48.5	Quartz stockworks near Tertiary leucogranite.
87TT215B	Chg	250–600	I, II, III	3.0–62	Quartz stockworks near Tertiary leucogranite.
			Samples from diamond drill core		
1453-259.8	Km	261–328	I, II	7.8–10.8	Drill hole collared in east stock of Buckingham system.
1471-173	Km	--	I, II, IV	--	Drill hole collared in Vail block part of Buckingham system.
1471-760	Km	292–345	I, II, IV	--	Drill hole collared in Vail block part of Buckingham system.

[1] Km, Cretaceous monzogranite; Ch, Upper Cambrian Harmony Formation hornfels; Chg, garnet skarn developed in Upper Cambrian Harmony Formation and related genetically to 38-Ma leucogranite (see text).

[2] From Theodore and others (1992); Theodore and Hammarstrom (1991).

[3] At 22±2°C: I, low vapor volume, mostly liquid H_2O; II, high vapor volume, mostly liquid H_2O; III, halite bearing, commonly with other daughter minerals; IV, mostly CO_2 vapor with some liquid CO_2, mostly H_2O liquid (see text).

equivalent igneous phases. A summary of fluid-inclusion types recognized in the Buckingham stockwork system is shown in figure 4, and temperature and salinity data for the fluid inclusions is in table 2.

In this study, $^{40}Ar/^{39}Ar$ values from fluid inclusions were measured on 29 approximately 1-mm grains from four samples of vein quartz from three localities (including a drill core) that are associated genetically with the Cretaceous Buckingham stockwork molybdenum system (table 2). These four samples were not found to include any of the type-III fluid inclusions (fig. 4), i.e., the daughter-mineral-bearing variety; nonetheless, it is possible that some sylvite and (or) other potassium-bearing minerals may have been present in the quartz fragments selected for argon analysis because other samples from the system contain some sylvite-bearing fluid inclusions. In addition, $^{40}Ar/^{39}Ar$ measurements were made from fragments of vein quartz associated with the 38-Ma leucogranite. These samples are from two localities (fig. 2): one vein (78C104) intrudes the Harmony Formation about 500 m west of a relatively large body of leucogranite, and the other (78C103) intrudes the leucogranite. In contrast with the samples from the Buckingham system, the vein quartz associated with the 38-Ma leucogranite contains abundant concentrations of type III, daughter-mineral-bearing fluid inclusions (fig. 4). Many of these type-III fluid inclusions contain sylvite (Theodore and others, 1992; Theodore and Hammarstrom, 1991).

$^{40}Ar/^{39}Ar$ ANALYSIS OF FLUID INCLUSIONS

$^{40}Ar/^{39}Ar$ analyses on fluid inclusions in quartz from the Battle Mountain district show a wide range of ages. Apparent ages of individual quartz grains are from about 40 Ma to about 1,747 Ma (table 3, no. 101-6). These ages are interpreted to represent the product of inherited excess ^{40}Ar from magmatic sources trapped in fluid inclusions plus the component of radiogenic ^{40}Ar derived from the decay of potassium-bearing fluids and solids trapped in fluid inclusions. This interpretation is supported by the association of the younger ages with a relatively high release of ^{39}Ar and a corresponding increase in age with lower ^{39}Ar releases. Fluid inclusions containing essentially no potassium

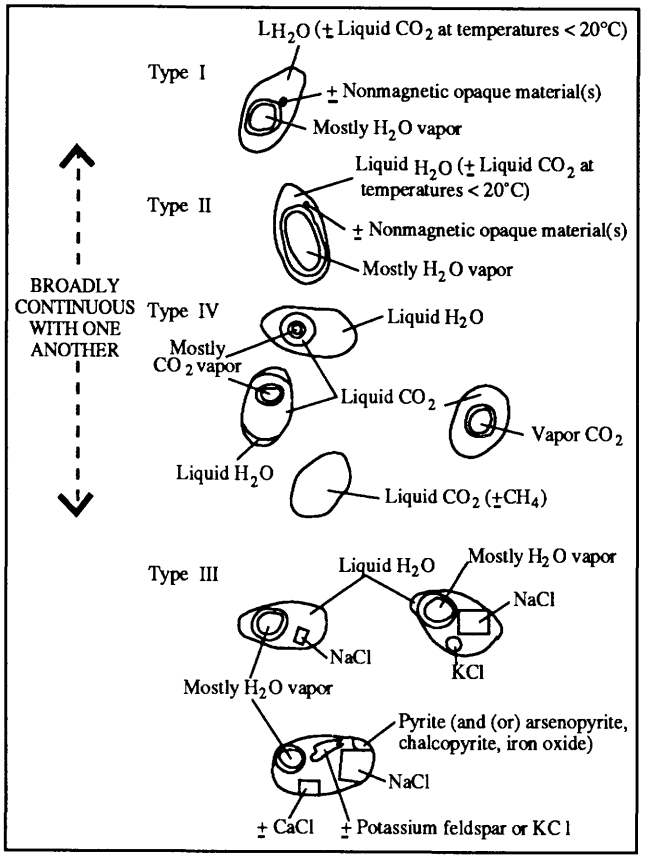

Figure 4. Types of fluid inclusions recognized in the Buckingham stockwork molybdenum system (modified from Theodore and others, 1992).

therefore give anomalously old $^{40}Ar/^{39}Ar$ ages, whereas fluid inclusions with high potassium content can produce enough radiogenic ^{40}Ar to almost entirely mask the presence of the excess ^{40}Ar component.

The ages determined from individual grains of samples of the Buckingham quartz stockwork are extremely variable and give no indication of the age of the fluid inclusions, assuming that they are Cretaceous as is indicated by previous studies (McKee, 1992). As noted, samples with very little potassium give anomalously old ages with analytical precision values as great or greater than the age. For instance, two grains from sample 79C77 (fig. 2) that contain very little potassium yield ages of 1,748±1,306 Ma and 1,314±660 Ma (table 3). Grains with greater amounts of potassium, however, provide points on a $^{40}Ar/^{36}Ar$ versus $^{39}Ar/^{36}Ar$ diagram from which an isochron can be drawn that defines the age of the fluid inclusions in the total sample (broken to produce the individual grains). The isochron also gives a measure of the amount of excess argon in the sample (intercept on the ordinate with a value greater than 295.5). Samples 1471-760, 1471-173, and 79C77 define isochrons (figs. 5, 6, and 7) that are interpreted to be between about 60 and 76 Ma. This is similar to the range of K-Ar and $^{40}Ar/^{39}Ar$ incremental heating ages from biotite, muscovite, and whole-rock samples from the Buckingham stockwork system (McKee, 1992) (table 1).

Sample 81TT121, which was expected to give a Late Cretaceous age (60 to 76 Ma), yielded a well-constrained isochron of 37.2±5.3 Ma (fig. 8). This late Eocene or early Oligocene age is the same as many of the small igneous bodies in the Battle Mountain district (McKee, 1992) (table 1). We assume that this age represents either almost complete replacement of the bulk of the fluid in older Cretaceous quartz by middle Tertiary fluid or that the quartz vein is a late Eocene to early Oligocene vein that is not recognized as such in the Cretaceous Buckingham stockwork system. The former alternative is more likely. The fluid-inclusion population hosted by the quartz vein in sample 81TT121 differs in many aspects from that near the fringes of the system. Firstly, the overwhelming bulk of the fluid inclusions, mostly type I (fig. 4), are secondary relative to vein quartz, and they are concentrated in dense swarms along annealed microcracks oriented at high angles to the walls of the veins (Theodore and others, 1992). These fluid inclusions must have been repeatedly trapped mostly during circulation of fluids associated with a widespread and locally intense, late-stage, argillic overprint that has affected these rocks. Nonetheless, almost all these veins still show relict potassic-alteration assemblages along their selvages that suggest that initial emplacement of veins occurred during potassic-alteration stages of the system. Although the overwhelming bulk of the fluid inclusions in the veined porphyry are the type I variety, these veins also seem to show a slightly increased abundance of halite-bearing, type-III-variety fluid inclusions relative to veins at the fringes of the system. Furthermore, liquid-vapor homogenization tests of fluid inclusions from these quartz veins in the monzogranite porphyry yield a plot significantly different from that derived from quartz veins that are minimally affected by postpotassic alteration. This difference results in a 100°C difference between medians for the two temperature-of-homogenization plots (380°C for the potassic-alteration assemblage, compared with 280°C for veins showing intense development of the intermediate argillic overprint). Thus, the apparent preferred concentration of fluid inclusions that homogenized to vapor at the high-temperature end of the distribution plot for samples of veined porphyry in the general area of sample 81TT121 suggests that these high-temperature fluid inclusions may be largely relict from early potassic stages (Theodore and others, 1992). In addition, circulation of fluids during the middle Tertiary in this part of the Cretaceous porphyry system is probably related to small bodies of Tertiary intrusive rocks not shown on figure 2.

Of the samples that produced Cretaceous isochron ages, number 1471-760 (760 ft depth in core hole shown

Table 3. Summary of single-grain laser-fusion $^{40}Ar/^{39}Ar$ analyses of quartz from the Battle Mountain district.

[Ages calculated using λ_ϵ=0.581×10^{-10} yr^{-1}, λ_β=4.962×10^{-10} yr^{-1}, $^{40}K/K_{total}$=1.167×10^{-4} moles/mole. Errors are estimates of the standard deviation (σ) of analytical precision]

Sample no.	Experiment no.	$^{40}Ar/^{39}Ar$	$^{38}Ar/^{39}Ar$	$^{37}Ar/^{39}Ar$	$^{36}Ar/^{39}Ar$	^{40}Ar rad (×10^{-14} moles)	^{40}Ar rad/ ^{39}Ar	^{40}Ar rad (percent)	Apparent age (±1σ) (Ma)
Quartz veins from the Buckingham stockwork system									
1471-760[1]	100-1	143.36	0.17742	1.0008	0.29231	3.1992	57.085	39.81	268.4±46.2
(fig. 5)	100-2	542.86	0.65356	0.93087	1.6314	6.8823	60.881	11.21	284.9±18.1
	100-3	17.762	0.021477	0.050199	0.008106	50.853	15.363	86.49	76.24±0.59
	100-4	184.32	0.54344	0.54672	0.19733	0.78051	126.07	68.39	547.1±113.0
	100-5	17.213	0.019658	0.000707	0.005415	21.353	15.604	90.65	77.42±0.73
	100-6	874.42	1.6889	0.48291	1.4799	0.87615	437.22	49.99	1,445±1,022
	100-7	1183.2	1.5772	0.38085	2.7903	0.91207	358.75	30.32	1,257±1,343
1471-173[1]	114-1	175.69	0.27240	0.025152	0.31226	4.5563	83.411	47.48	379.9±60.0
(fig. 6)	114-2	29.938	0.047228	0.35130	0.03736	27.980	18.922	63.20	93.46±2.77
	114-3	33.953	0.057976	0.38035	0.05322	9.6808	18.253	53.75	90.23±6.63
	114-4	183.46	0.46293	5.2656	0.21180	1.5298	121.52	66.14	530.0±312.0
79C77[1]	101-1	168.64	0.28784	0.058985	0.36945	12.585	59.465	35.26	278.8±28.7
(fig. 7)	101-2	470.22	0.83678	0.29027	1.1120	19.681	141.64	30.12	604.4±65.0
	101-3	167.31	0.39749	0.022914	0.23509	2.7926	97.837	58.47	438.2±75.9
	101-4	1077.0	3.5915	0.19807	2.3541	1.8709	381.39	35.41	1,314±659
	101-5	22.366	0.024696	0.003383	0.02698	19.424	14.387	64.32	71.50±1.92
	101-6	1272.3	3.4560	0.32611	2.3367	1.7346	581.86	45.73	1,747±1,306
81TT121[1]	99-1	11.777	0.021847	0.012340	0.012292	25.827	8.1376	69.10	40.79±5.57
(fig. 8)	99-3	21.739	0.025867	0.000779	0.036843	14.269	10.844	49.88	54.15±2.42
	99-4	17.261	0.024701	0.003130	0.010519	54.165	14.145	81.94	70.31±0.89
	99-5	21.742	0.013739	0.000925	0.026141	0.97164	14.009	64.43	69.65±22.58
	99-6	238.79	1.0214	0.019467	0.55847	0.36695	73.750	30.89	339.8±276.8
	99-7	44.022	0.11787	0.001111	0.091029	1.4932	17.115	38.88	84.74±16.84
	99-8	321.18	1.3810	1.1708	0.62517	0.89309	136.58	42.51	586.0±287.1
	99-9	16.615	0.021366	0.000136	0.020051	7.6325	10.682	64.29	53.35±2.24
Quartz veins associated with late Eocene to early Oligocene igneous event									
79C103[2]	89Z0245	5.0156	0.12399	0.22852	0.0031478	9.4073	4.0745	81.22	45.51±0.28
(fig. 9)	89Z0246	8.5362	0.38236	0.067216	0.011091	1.4048	5.2356	61.33	58.27±0.48
	89Z0247	10.825	0.47548	1.5676	0.015082	0.67411	6.4626	59.64	71.66±0.85
	89Z0248	7.5420	0.36763	1.1612	0.010515	0.70169	4.4961	59.57	50.15±0.58
	89Z0249	5.1823	0.16034	1.2324	0.004525	1.0897	3.9112	75.41	43.71±0.38
	89Z0250	3.8967	0.037980	0.35426	0.0011497	2.8827	3.5556	91.22	39.78±0.25
79C104[3]	89Z0240	4.6007	0.20468	0.008856	0.0028211	7.4874	3.7393	81.27	41.68±0.25
(fig. 10)	89Z0242	8.3961	1.5301	0.029108	0.012850	0.49378	4.5726	54.46	50.83±0.76
	89Z0243	7.2386	0.7508	2.1875	0.010203	0.41811	4.3639	60.20	48.54±0.82
	89Z0244	3.9638	0.075151	0.055961	0.0013574	10.673	3.5385	89.27	39.46±0.24
	89Z0251	3.7181	0.031822	0.50783	0.0005269	0.47926	3.5728	96.06	39.84±0.59
	89Z0252	5.2010	0.54699	0.31335	0.0038603	0.23390	4.0559	77.97	45.16±1.27

1 Reactor corrections: $^{40}Ar_K/^{39}Ar_K$=0.0086, $^{39}Ar_{Ca}/^{37}Ar_{Ca}$=0.0003, and $^{36}Ar_{Ca}/^{37}Ar_{Ca}$=0.0003. J=0.00281.
2 Reactor corrections: $^{40}Ar_K/^{39}Ar_K$=0.0285, $^{39}Ar_{Ca}/^{37}Ar_{Ca}$=0.000671, and $^{36}Ar_{Ca}/^{37}Ar_{Ca}$=0.000251. J=0.00627.
3 Reactor corrections: $^{40}Ar_K/^{39}Ar_K$=0.0285, $^{39}Ar_{Ca}/^{37}Ar_{Ca}$=0.000671, and $^{36}Ar_{Ca}/^{37}Ar_{Ca}$=0.000251. J=0.00625.

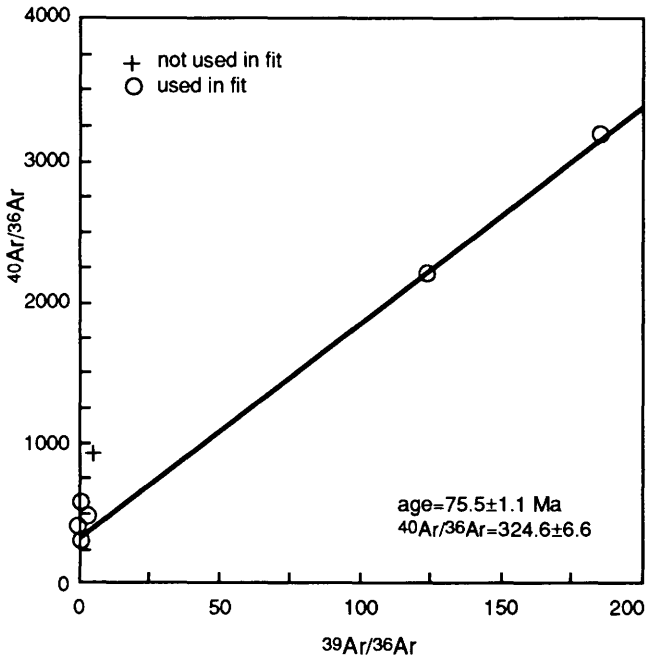

Figure 5. $^{40}Ar/^{36}Ar$ versus $^{39}Ar/^{36}Ar$ diagram with isochron plot for sample 1471-760. Isochron age is 75.5±1.1 Ma.

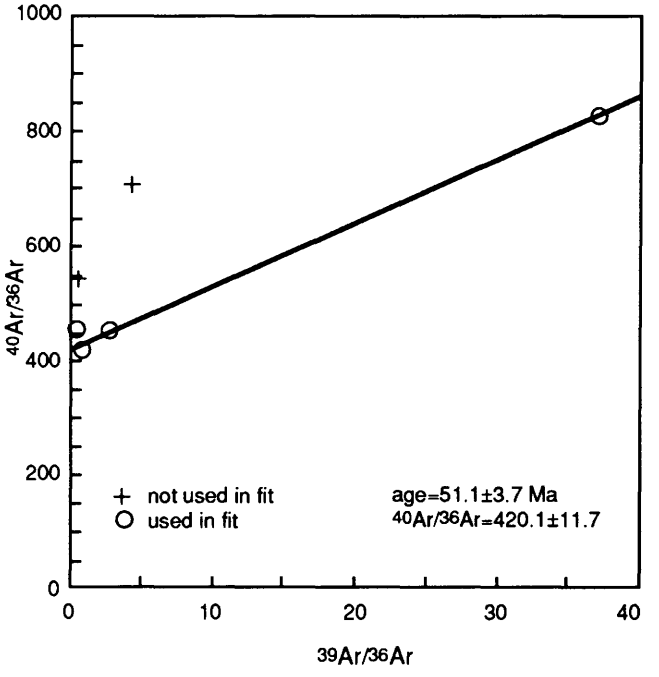

Figure 7. $^{40}Ar/^{36}Ar$ versus $^{39}Ar/^{36}Ar$ diagram with isochron plot for sample 79C77. Isochron age is 55.1±3.7 Ma.

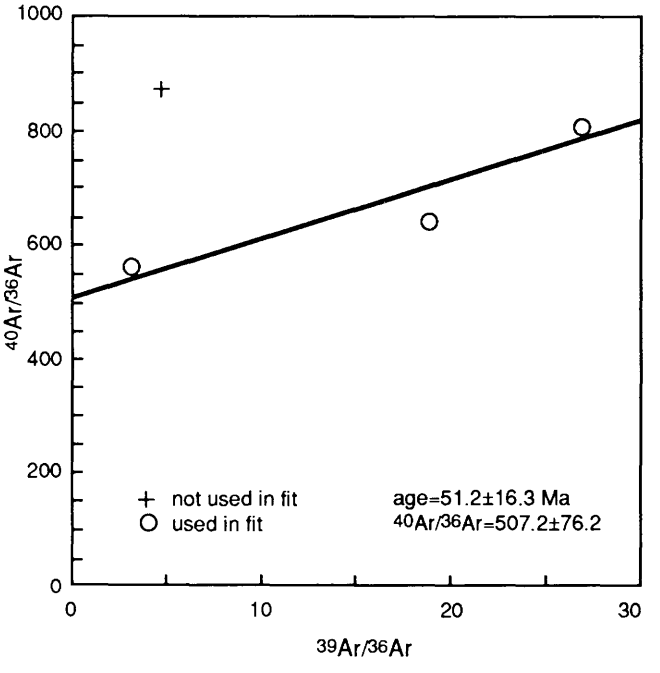

Figure 6. $^{40}Ar/^{36}Ar$ versus $^{39}Ar/^{36}Ar$ diagram with isochron plot for sample 1471-173. Isochron age is 51.2±16.3 Ma.

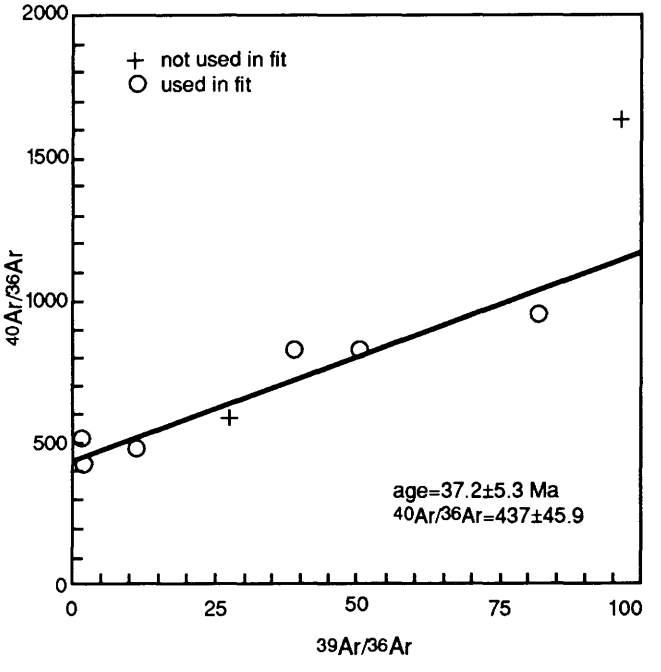

Figure 8. $^{40}Ar/^{36}Ar$ versus $^{39}Ar/^{36}Ar$ diagram with isochron plot for sample 81TT121. Isochron age is 37.2±5.3 Ma.

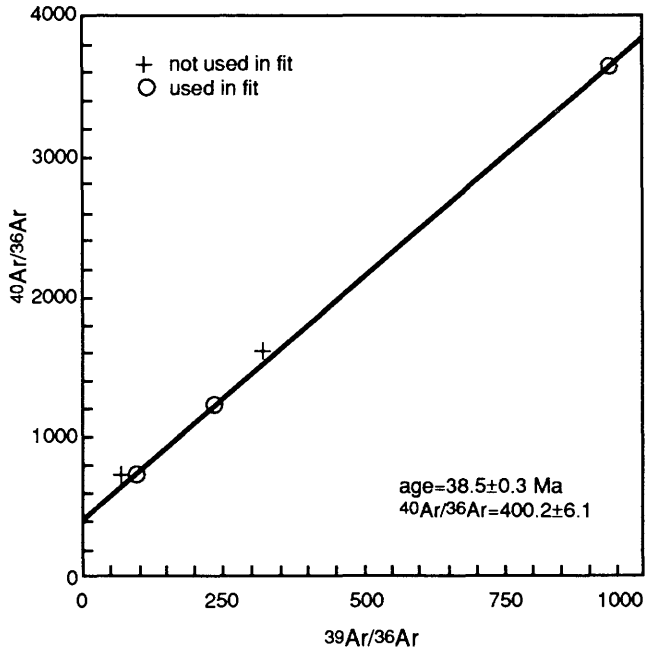

Figure 9. $^{40}Ar/^{36}Ar$ versus $^{39}Ar/^{36}Ar$ diagram with isochron plot for sample 78C103. Isochron age is 38.5±0.3 Ma.

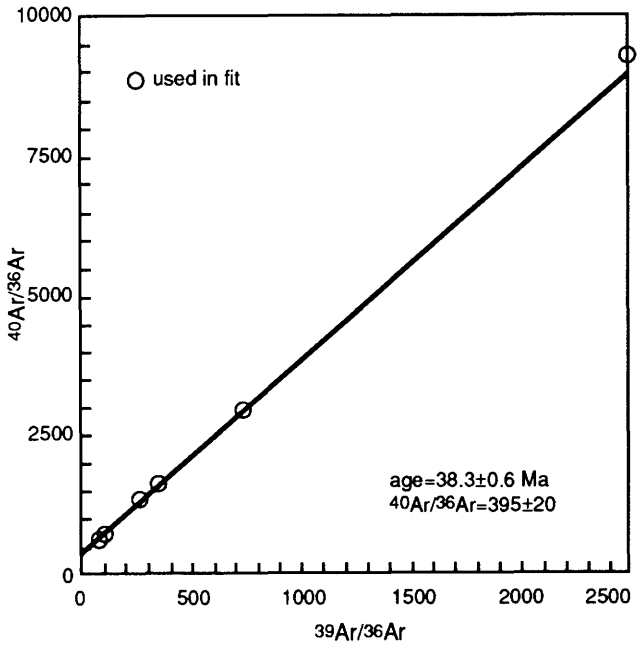

Figure 10. $^{40}Ar/^{36}Ar$ versus $^{39}Ar/^{36}Ar$ diagram with isochron plot for sample 78C104. Isochron age is 38.3±0.6 Ma.

on fig. 2) gives the best data for drawing an isochron because two analyzed grains had relatively large amounts of potassium (fig. 5). The influence on the isochron by samples with a high value of $^{39}Ar/^{36}Ar$ (an indication of the amount of potassium) is a significant factor because the points plot far from the ordinate on the $^{40}Ar/^{36}Ar$ versus $^{39}Ar/^{36}Ar$ diagram and have relatively more leverage in drawing the best line fit between the plotted points. Six grains define an isochron that is 75.1±1.1 Ma (fig. 5).

A second sample from the drill hole, 1471-173, also yields an isochron that can be interpreted as Late Cretaceous in age (fig. 6). It is much less well constrained, however, and has a much larger uncertainty due to the small amount of potassium in the six grains analyzed. The isochron age of 51.2±16.3 Ma, based on three points, is of little value in determining the age of the quartz fluid inclusions.

Sample 79C77 presented the same problems as sample 1471-173 (see above). Because of very small amounts of potassium and consequently small amounts of ^{39}Ar, the analysis is heavily biased by the excess ^{40}Ar in the fluid of the inclusion. The isochron drawn through four points defines an age of 55.1±3.7 Ma (fig. 7). The slope of the line is strongly influenced by one analysis with the highest $^{40}Ar/^{39}Ar$ value (101-5, table 3); the other three analyses cluster near the ordinate and near the 425 ratio, indicating about 30 percent excess argon.

Two samples (78C103 and 78C104, fig. 2) of vein quartz associated with a 38-Ma leucogranite north of the Buckingham quartz stockwork system produce well-defined isochron ages of 38.5±0.3 Ma and 38.3±0.6 Ma, respectively (figs. 9 and 10). The leucogranite bodies have K-Ar ages on hornblende and biotite of 37.7±1.4 Ma, 38.8±1.1 Ma, and 39.0±1.1 Ma (table 1); this is identical to the fluid-inclusion ages. The trapping of fluid in the quartz must have taken place at the time of cooling of these igneous bodies, and there has been no subsequent modification of the igneous system.

A summary $^{40}Ar/^{36}Ar$ versus $^{39}Ar/^{36}Ar$ diagram (fig. 11) shows the data points from all the analyses used from the four samples of quartz from the Buckingham quartz stockwork. The age is shown above or below each line. This figure emphasizes the fact that samples with low potassium (and, hence, a low $^{39}Ar/^{36}Ar$ ratio) cluster near the ordinate and limit the construction of an isochron if grains that have a higher potassium content are not available. Ideally, a wide variation of potassium content would produce the best isochrons. Samples 78C103 and 78C104 (figs. 9 and 10) are examples in which isochrons are controlled by a wide spread of $^{39}Ar/^{36}Ar$ values. They are not plotted on figure 11 because they have points an order of magnitude higher on the $^{39}Ar/^{36}Ar$ axis than the other samples.

CONCLUSIONS

$^{40}Ar/^{39}Ar$ dating of fluid inclusions in igneous minerals has promise as a means of dating the fluid and, hence,

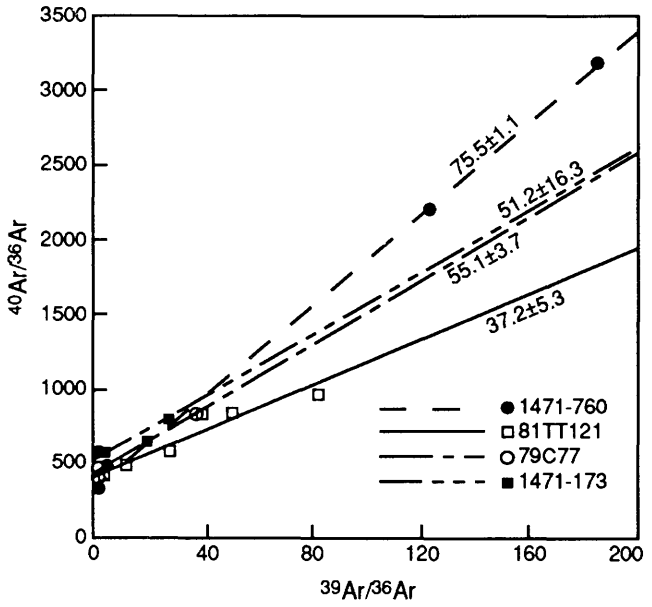

Figure 11. $^{40}Ar/^{36}Ar$ versus $^{39}Ar/^{36}Ar$ diagram with isochron plots from all Buckingham stockwork samples from the Battle Mountain district.

the age of mineralization (assuming that the two are related and nearly synchronous). Several limiting factors are apparent from the quartz samples from the Battle Mountain mining district, Nevada.

1. Excess inherited ^{40}Ar may be present, and should be expected, in the trapped fluid. Because of this, a number of analyses are needed to provide points on a $^{40}Ar/^{36}Ar$ versus $^{39}Ar/^{36}Ar$ diagram from which an isochron can be drawn. The slope of the isochron gives the age, and the intercept on the ordinate ($^{40}Ar/^{36}Ar$ axis) indicates the amount of excess argon (if the value is above 295.5 or the $^{40}Ar/^{36}Ar$ ratio of air).
2. Samples with small amounts of potassium that yield proportionally small amounts of ^{39}Ar on irradiation are difficult to analyze with good precision. These samples produce points on a $^{40}Ar/^{36}Ar$ versus $^{39}Ar/^{36}Ar$ diagram that cluster near the $^{40}Ar/^{36}Ar$ axis and are of little value in describing an isochron. Samples containing small amounts of potassium proved nearly unusable in this study.
3. Areas with several periods of igneous activity, such as Battle Mountain (Late Cretaceous and late Eocene to early Oligocene), probably produce several populations of fluid inclusions. At Battle Mountain, the youngest period of igneous activity (late Eocene to early Oligocene) proved datable with reasonable confidence. The Late Cretaceous event was evident but obscure. The mechanism for partial argon loss from fluid inclusions and for multiple periods of fluid entrapment in minerals is poorly understood but has a great effect on dating of mixed populations of fluid inclusions by the $^{40}Ar/^{39}Ar$ technique.

REFERENCES CITED

Dalrymple, G. B., and Lanphere, M.A., 1971, $^{40}Ar/^{39}Ar$ technique of K-Ar dating: A comparison with the conventional technique: Earth and Planetary Science Letters, v. 12, p. 300–308.

———1974, $^{40}Ar/^{39}Ar$ age spectra of some undisturbed terrestrial samples: Geochimica et Cosmochimica Acta, v. 38, p. 715–738.

Damon, P.E., and Kulp, J.L., 1958, Excess helium and argon in beryl and other minerals: American Mineralogist, v. 43, p. 433–459.

Kelley, S., Turner, G., Butterfield, A.W., and Shepherd, T.J., 1986, The source and significance of argon isotopes in fluid inclusions from areas of mineralization: Earth and Planetary Science Letters, v. 79, p. 303–318.

McKee, E.H., 1992, Potassium-argon and $^{40}Ar/^{39}Ar$ geochronology of selected plutons in the Buckingham area, *in* Theodore, T.G. and others, 1992, Geology of the Buckingham Stockwork Molybdenum Deposit and Surrounding Area, Lander County, Nevada: U.S. Geological Survey Professional Paper 798–D, p. D36–D98.

Nesmelova, Z.N., 1959, Gases in potassium salts of the Bereznikovsk mine: Trudy Vsesoyuznogo Nauchno-issledovatel'skogo Instituta Galurgii, n o. 35, p. 206–243.

Rama, S.N.I., Hart, S.R., and Roedder, Edwin, 1965, Excess radiogenic argon in fluid inclusions: Journal of Geophysical Research, v. 70, p. 509–511.

Theodore, T.G., Silberman, M.L., and Blake, D.W., 1973, Geochemistry and potassium-argon ages of plutonic rocks in the Battle Mountain mining district, Lander County, Nevada: U.S. Geological Survey Professional Paper 798–A, 24 p.

Theodore, T.G., and Hammarstrom, J.M., 1991, Petrochemistry and fluid-inclusion study of skarns from the northern Battle Mountain mining district, Nevada, *in* Aksyuk, A.M., ed., Skarns—Their Genesis and Metallogeny: Athens, Theophrastus Publications, S.A., p. 497–554.

Theodore, T.G., Blake, D.W., Loucks, T.A., and Johnson, C.A., 1992, Geology of the Buckingham stockwork molybdenum deposit and surrounding area, Lander County, Nevada: U.S. Geological Survey Professional Paper 798–D, 318 p.

Wahler, William, 1956, Über die in Kristallen eingeschlossenen Flüssigkeiten und Gose: Geochimica et Cosmochimica Acta, v. 9, p. 105–135.

CHAPTER Q

HEAVY MINERALS AT THE FALL ZONE— A THEORETICAL MODEL OF GRAIN SIZE, DENSITY, AND GRADIENT

By CURTIS E. LARSEN[1]

ABSTRACT

Placers are concentrations of heavy minerals sorted by density and shape through fluvial, littoral, and (or) eolian processes. A mineral's specific gravity and hydraulic equivalence relative to quartz determines the type of sedimentary deposit in which it is found. For example, a grain of gold or a titanium mineral such as ilmenite or rutile in the very fine sand range (0.06–0.12 mm) tends to concentrate in dissimilarly sized deposits. Gold of this size occurs with very coarse quartz sand (1.0–2.0 mm) or gravel. Very fine grained titanium minerals, as well as zircon and monazite, are deposited with fine-grained quartz sand (0.13–0.25 mm).

The size of sediment carried and subsequently depostied by a river depends on its discharge, slope, depth, and velocity. Sediments with limiting grain sizes that host placers are deposited in predictable reaches of the system where slope and velocity decrease. In the southeastern U.S., rivers draining the eastern Appalachians commonly decrease in gradient and velocity until they reach the outer edge of the Piedmont. Gradients of streams flowing across the Piedmont steepen where crossing structural or lithologic boundaries and then flatten abruptly at the Fall Zone, where rivers enter the Coastal Plain. The abrupt change in river dynamics preferentially deposits coarse-grained sediments near the Fall Zone and medium- and fine-grained sand at the inner edge of the Coastal Plain. Depending on upstream source terranes, the Fall Zone may be targeted for exploration for placer gold, whereas the inner edge of the Coastal Plain has potential as the site for monazite, zircon, rutile, and ilmenite accumulations.

Upper Cretaceous fluvial sediments near the Fall Zone in Georgia and South Carolina contain small concentrations of monazite, as well as zircon, rutile, and ilmenite. Fine-grained Cretaceous sands and silts of the upper delta and delta facies concentrate less dense, but hydraulically equivalent, heavy mineral suites that are characterized by staurolite, kyanite, amphiboles, pyroxenes, epidote, and rutile. A similar gradation of heavy minerals is also present within the Cenozoic fluvial facies of the Coastal Plain.

Although a qualitative relationship between certain heavy mineral suites and the inner Coastal Plain fluvial deposits has been known for some time, the role of stream gradient has not been examined critically. Detailed geomorphological and stratigraphic research in the Fall Zone region will allow development of more effective predictive models of placer mineral occurrence. Drainage basin analysis utilizing stream discharge, gradient, and channel width and depth, can be linked with geologic studies of favorable source terranes to identify for exploration specific river reaches that contain sediment sizes that are conductive to specific heavy mineral suites. Such studies allow the extensive database of stream flow characteristics in the southeastern U.S. to be coupled with economic geologic knowledge to refine heavy mineral prospecting techniques in the Fall Zone region.

INTRODUCTION

The inner edge of the Atlantic Coastal Plain has been successfully targeted for heavy mineral exploration at various sites in the southeastern U.S. The availability of favorable source terranes clearly influences the placement

[1]U.S. Geological Survey, Mail Stop 954, 12201 Sunrise Valley Drive, National Center, Reston, VA 22092

of heavy mineral deposits, but differential sorting by facies in fluvial systems is another important determinant of their location and is an effective guide to exploration. This paper examines heavy mineral occurrences near the inner edge of the Coastal Plain of southeastern U.S. and their relationship to stream gradients and fluvial facies. It is focused on the Deep River–Cape Fear River system of North Carolina to model downstream changes in heavy mineral location.

River systems draining the eastern flank of the Appalachian Mountains commonly decrease in gradient until they reach the outer edge of the Piedmont Upland. Gradients are commonly abruptly steeper at structural or lithologic boundaries in crystalline rocks and then decrease at the inner edge of the Coastal Plain, where rivers cross Mesozoic and Cenozoic sediments. Coastal Plain rivers are graded to sea level. Zones of rapids near the contact between the crystalline rocks of the Piedmont and the sediments of the Coastal Plain have historically been termed the Fall Line or, more accurately, the Fall Zone (Fenneman, 1938).

A change in river dynamics takes place near the Fall Zone. Rivers flowing through constricted channels in the crystalline terranes of the Piedmont carry the bulk of discharge from their drainage basins along with the suspended and entrained sediment load. Upon entering the more erodable sediments of the Coastal Plain, channels widen, causing a related decrease in stream velocity. As a result, river systems tend to deposit coarse-grained sediments near the Fall Zone, and they tend to deposit medium- and fine-grained sand in the fluvial-deltaic facies downstream.

Heavy mineral species are closely allied with the grain size of their host sediments. Partially as the result of hydraulic equivalence, grain shape, and bed roughness, heavy minerals supplied to the fluvial system are differentially sorted by decreasing specific gravity. Although source terrane is critical, differentiation by sorting is also a critical control on the location of deposits. Stratigraphic studies by Sohl and Owens (1991), Owens (1989), and Owens and Gohn (1985) have indicated qualitative relationships between heavy minerals and sedimentary facies in the Cretaceous sediments of the Coastal Plain, but the concept of linking facies with grain size to evaluate the heavy mineral potential of the Coastal Plain has not previously been attempted.

The Cape Fear River system of North Carolina is an example of discharge and gradient changes conductive to preferred deposition of heavy mineral suites. The Fall Zone, marking the approximate inland boundary between the Atlantic Coastal Plain and Piedmont Uplands, suggests a representative model for preferential heavy mineral deposition at gradient changes along rivers draining the Carolina slate belt. This river system provides a model for gradient and grain-size changes along former river courses draining the same source terranes, and it may have localized undiscovered paleoplacers.

HEAVY MINERAL EQUIVALENCE

The formation of heavy mineral placers is a function of weathering of primary source terranes, transport of detrital material, and deposition in suitable environments. Concentration of heavy minerals in placers results from differential sorting by specific gravity and shape through fluvial, littoral, and (or) eolian processes. The relationship is complex but is controlled by density differences between heavy minerals and other minerals (quartz, feldspar) and their host deposit.

The weight equivalence and hydraulic-equivalent settling velocity relative to quartz (Rubey, 1933; Rittenhouse, 1953; Tourtelot, 1968; Pettijohn and others, 1973) bear directly on the type of sedimentary deposit in which it is found. For example, a 1-mm diameter sphere of quartz (specific gravity 2.65) is *weight equivalent* to a gold sphere (specific gravity 18.0) of 0.528-mm diameter, less than one phi-size interval smaller than the quartz. On the basis of settling velocities in water, the *hydraulically equivalent* size variation between gold and quartz is different. The same 1-mm diameter sphere of quartz is hydraulically equivalent to a gold sphere of 0.15-mm diameter, approximately 2.5 phi sizes smaller than the quartz equivalent. Less dense heavy minerals such as ilmenite (specific gravity 4.75) settle at velocities nearer to that of quartz. In terms of size, ilmenite spheres tend to concentrate with equivalent-size quartz that are from 0.75 to 1.0 phi size larger.

Particle shape further complicates simple weight equivalence. Flakes settle far less rapidly than spheres. A flake with a diameter 10 times its thickness tends to settle at only about one quarter the rate of a sphere of similar diameter (Tourtelot, 1968). This translates to less than a one-phi size difference.

Where sediments enter the fluvial system, laminar and turbulent flow in channels dominate heavy mineral sorting and deposition. Laminar flow at low discharge periods relegates sediment to entrained transport movement of grains along stream beds by saltation. As velocity increases, turbulent flow captures saltating grains and carries them as suspended load to where velocity decreases. Differential-density settling velocity returns grains to the sediment entrained in the bed load (Friedman and Sanders, 1978). The heavy minerals are the first to be returned to the bed load, where they begin to be concentrated. Slingerland (1977, 1984) studied the relative movement and concentration of magnetite as entrained grains in bed load in laboratory experiments. He demonstrated that heavy mineral concentration within a sandy bed load is less dependent on the hydraulic equivalency of grains than on

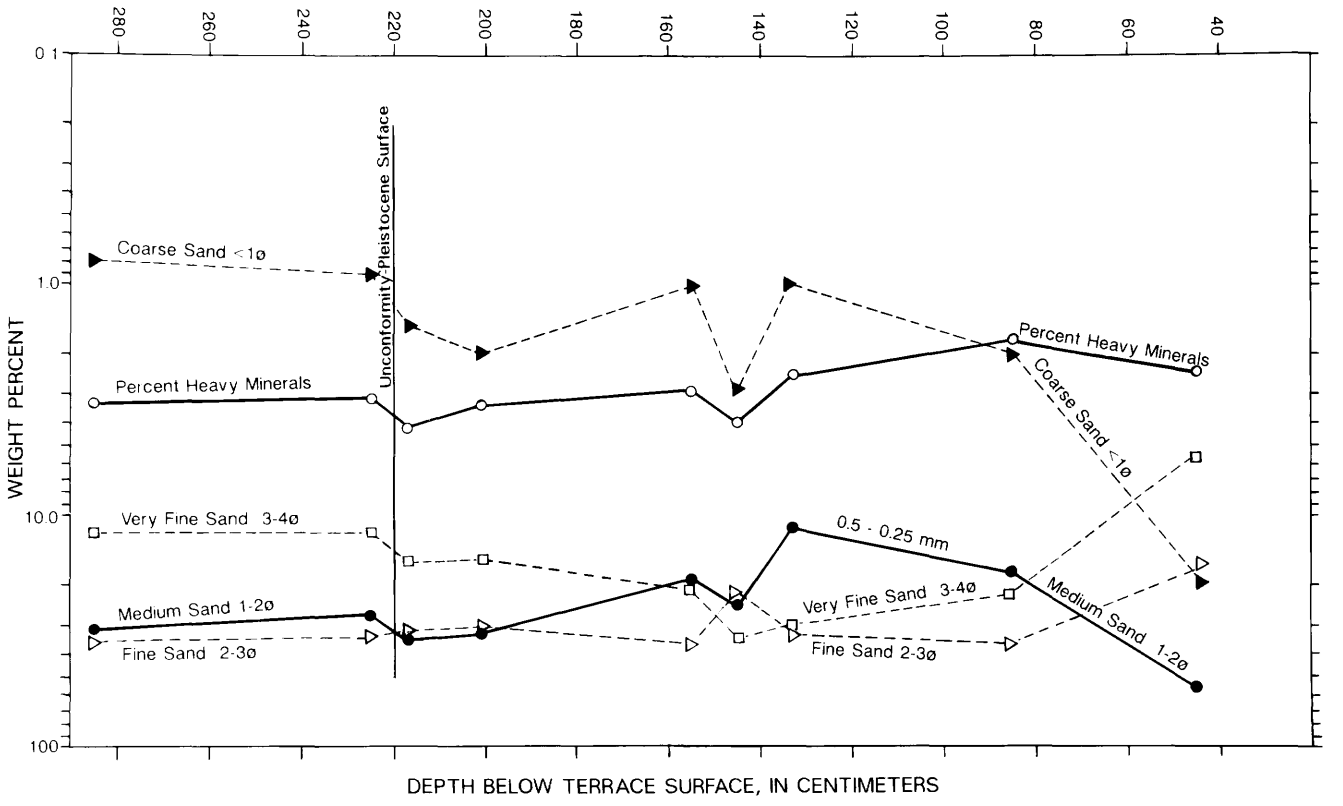

Figure 1. Grain size and heavy mineral distributions in stratified Holocene alluvial fill, Richard B. Russell Reservoir, Savannah River, Georgia.

the coarseness of the bed load itself. Increasing bed roughness corresponds to a greater heavy mineral concentration. Heavy minerals tend to nest in the interstices of larger grains.

Studies of heavy mineral deposition in glaciolacustrine deltas by Force and Stone (1990) examined grain-size differences and heavy mineral species in natural settings. They noted that the grain size of the host bed was the only variable correlating well with the percentage of heavy minerals. Each species showed maximum concentration at a particular grain size of the host bed. In general, the more equant-shaped heavy mineral grains studied, ranging in composition and density from magnetite (specific gravity 5.18) to tourmaline (specific gravity 3.25), showed median grain sizes from 0.5 phi to 1 phi size finer than the total sample mode.

Similar relationships between grain size of the heavy mineral species and the host are evident in alluvial deposits as well. Figure 1 shows an example of a stratigraphic analysis of Holocene, overbank, floodplain deposits along the Savannah River in the Richard B. Russell Reservoir. The weight percent of the total heavy mineral content of each sample is plotted with the percentage of the individual sand fractions. Weight percent is plotted logarithmically, but depth is shown arithmetically on the x-axis. This plotting technique identifies potential ratios among the variables shown by similarity between curves. Figure 1 shows greatest similarity between the *total* heavy mineral suite and the medium-sand fraction of each sample. Total heavy minerals are in ratio with the medium-grained sand. These curves are emphasized with solid lines. The comparison indicates that the heavy minerals present in each sample are dominantly found within this size fraction. Heavy mineral species for the same samples are shown on figure 2. Epidote and the amphiboles, the least dense of the suite (specific gravity 3.0–3.5), are the most abundant species. Epidote and, to a lesser extent, the amphiboles account for the pattern of the total heavy mineral curve on figure 1. As mineral species of greater density are considered, the similarity with the medium-grained fraction becomes less distinct, and higher density minerals tend to track with the fine- and very fine grained fractions. Differentiation by grain size and density is apparent.

The relationship between density and grain size of the host deposit is clearly illustrated on figure 3, which plots Rittenhouse's (1943) data on heavy mineral suites from fluvial samples as adapted by Pettijohn and others (1973). Heavy mineral species are plotted as the log of specific gravity versus the difference in phi size between the size of heavy minerals and the size of the host quartz grains in the deposit. Species with specific gravities

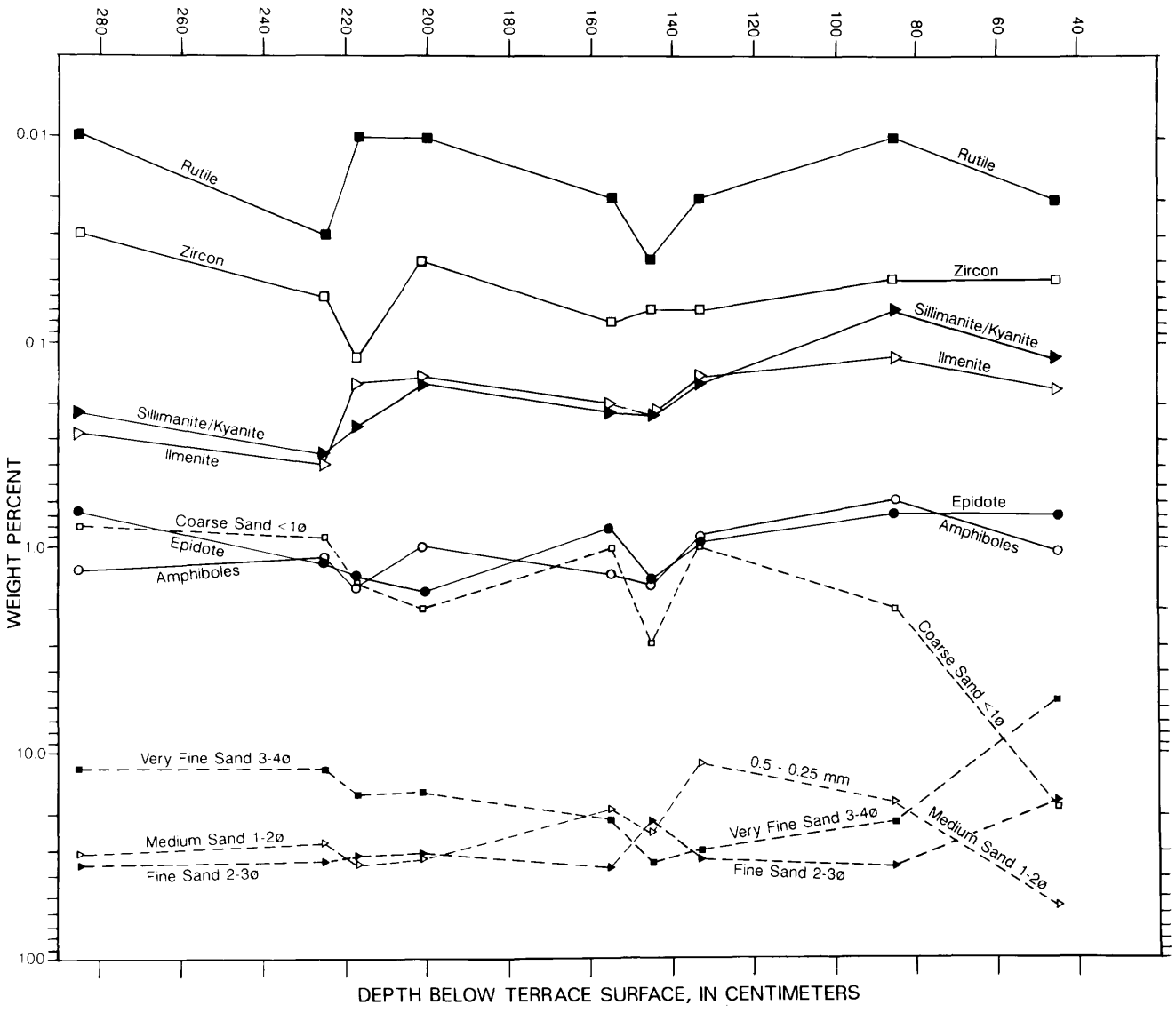

Figure 2. Distribution of heavy mineral species and grain size in stratified Holocene alluvial fill, Richard B. Russell Reservoir, Savannah River, Georgia.

between 2.8 and 5.0 tend to correlate with host quartz sands that are as much as 1.2 phi units coarser. The original work (Pettijohn and others, 1973) has been adapted here by extending the curve to include higher density minerals, such as cassiterite, silver, the platinum-group elements, and gold. Whereas the relationship shown between heavy mineral grains and their quartz equivalents on figure 3 is simplified and applies to equant-shaped grains, it is useful for assessing the heavy mineral potential of sand bodies on the basis of grain size.

Weight equivalency and hydraulically equivalent settling velocities as described by Rubey (1933) and Tourtelot (1968) are based on ideal shapes and conditions. Fluvial experiments by Slingerland (1977, 1984), on the other hand, rely on mathmatical expressions to explain complex relationships between heavy minerals and the grain size of entrained deposits in bed load. Observations by Force and Stone (1990) are useful for understanding heavy mineral concentrations in a single natural setting. None of these techniques alone, however, specifically addresses heavy mineral resource potential. Figure 3 presents a testable procedure for identifying and assessing the heavy mineral resource of fluvial sand bodies on the basis of grain size.

STREAM GRADIENT AND SEDIMENT SIZE

The relationship between the slope of a stream channel and the size of its sediment load is complex. As early as 1877, Gilbert (1877) tried to relate decrease in stream gradient with the quantity of stream discharge. Sternberg,

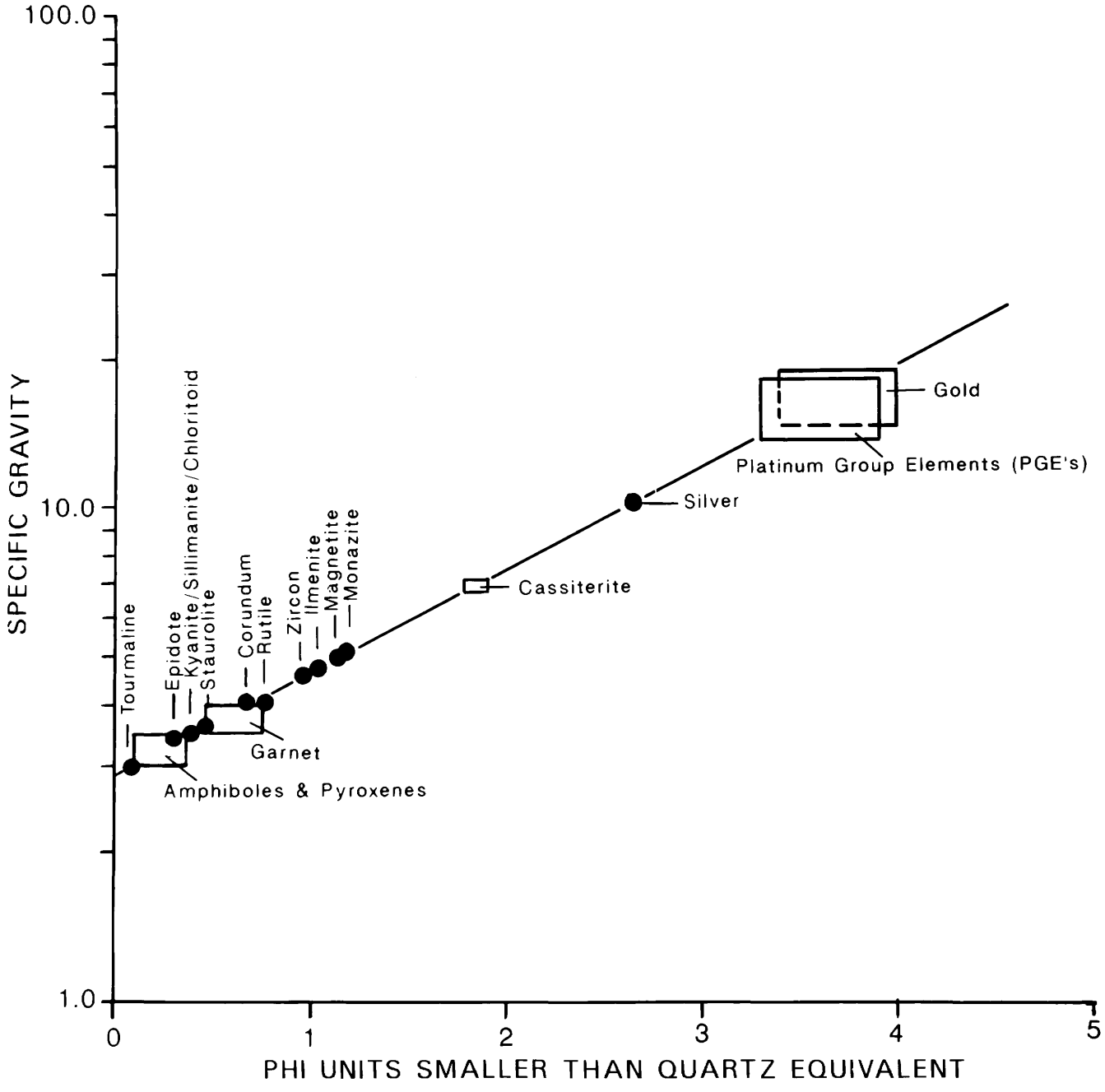

Figure 3. Relationship of heavy mineral grains to hydraulically equivalent quartz grains in a fluvial environment (adapted from Pettijohn and others, 1973; Rittenhouse, 1943).

on the other hand, (cf. Woodford, 1951, p. 813) believed that the slope of the stream channel is directly related to the size of the bed load. Rubey (1933) analyzed stream slopes using data from Gilbert's (1914) classic flume studies. He concluded that, if the depth-to-width ratio of the channel was constant, the graded slope decreased with a decrease in sediment load or particle size or with an increase in discharge. Hence, a stream might be adjusted to an increase in particle size by an increase in depth (relative to width) or an increase of slope.

Hack (1957) attempted to clarify this relationship. He noted that stream discharge is important in controlling slope, but it was difficult to measure as a quantity. On the other hand, stream discharge relates to its drainage area. He was able to show a direct relationship with the slope of a stream and the mean diameter of the bed material when drainage area was taken into account. For example, a clear relationship was present between slope and the ratio of mean sediment size to drainage area, and sediment size clearly decreased with a downstream decrease in

slope. In general, perennial streams show concave profiles, with coarse debris associated with steep slopes and fine debris with gentle slopes.

The complexity of the relationship between sediment size and slope in stream channels was pointed out by Leopold and others (1964). They showed that slope, channel roughness (size of bed load), depth, and velocity are interrelated through stream discharge. As discharge increases downstream by the entrance of tributaries, a channel may respond by an increase in width, depth, or velocity. With perennial streams, the response is normally an adjustment through increased width and depth of the downstream channel; concomitantly, velocity decreases. Expressed somewhat differently, the rate of change in depth increases with a decrease in the rate of change in slope. The rate of change in velocity decreases with the increase in depth and decrease in slope. Roughness decreases with slope and velocity as well (Leopold and others, 1964, p. 257). All the variables adjust to overall changes in discharge, such as those caused by increased precipitation. The processes of differential sorting of sediments by shape, size, and density takes place within this fluvial framework. Stream velocity and channel form are key factors in sediment transport and deposition. Turbulent and laminar flow within reaches of river systems influence the size and concentration of sediment carried by saltation as bed load, or by suspension. Changes in slope and channel form, however, determine where such sediments are deposited. This is of major importance in the study of heavy mineral placers because it serves as an aid in the location of specific economic deposits.

Slope or stream gradient, with respect to drainage area, has been shown by Hack, (1957, fig. 21) to have a predictable relationship with the median size of bed material. Hack showed the interrelationship with the equation:

$$S = 18\left(\frac{M}{A}\right)^{0.6}$$

where

S is the channel slope in ft/mi,

M is the median size of bed material in mm,

A is the drainage area in mi^2, and

18 is a constant determined for the units of measurement.

Tourtelot's (1968) presentation of hydraulic-equivalent grain sizes for heavy minerals can be adapted to Hack's geomorphic presentation. This is useful because the drainage basin is already used as a common unit to define stream-sediment sampling sites in mineral resource assessment studies.

Channel form displays similar controls on the grain size of deposits and the associated heavy minerals. Stream velocity, together with turbulent and laminar flow conditions, is a key factor in sediment transport and sorting and is related to channel depth and width. Particles of a certain size are transported at a given velocity and set of flow conditions. They will be deposited where the flow conditions are no longer able to carry them as saltating or suspended grains. Particles transported along confined channels are commonly not deposited along river reaches until the channels are no longer restricted and channel width can increase. As the channel width varies, a concomitant decrease in velocity results. Particles carried in suspension in the higher velocity flow of the confined channels are subsequently deposited as overbank deposits where channel constriction is removed. These are left as alluvial deposits of predictable grain size. Examples might include local areas of abrupt lithologic variation between resistant and less resistant rock types that allow locally wider channels due to differential erosion. Similarly, down-faulted or subsiding basins may exert geologic control on channel width as well as gradient. Using hydraulic equivalence as a guide and adjacent source terranes as a requirement, anticipated heavy mineral suites may be sought in such areas on the basis of the predicted grain size of deposits.

Figure 4 presents a longitudinal profile of the Deep River–Cape Fear River system superimposed on the underlying geologic controls of the Carolina slate belt, Deep River Mesozoic Basin, and the Atlantic Coastal Plain. The profile of the Haw River, the major tributary of the Cape Fear River is also shown. Gaging stations along the profile are plotted as well. The profile shows a strong geologic control with steep gradients associated with felsic volcanic rocks and gentler gradients corresponding with the metamudstone, argillite, siltstone, and shale. The lowest gradients occur with the sediments of the Coastal Plain. Table 1 presents the calculated median grain size for this river system on the basis of drainage area and slope from Hack' s equation above. Downstream from the confluence of the Deep River and Haw River, grain size of the Cape Fear River bed load decreases with increasing discharge and decreasing slope. The most pronounced change in grain size is between the Fall Line, near Lillington, N.C. (Md = 129 mm), and Huske Lock (Md = 6.65 mm). Although the abrupt decrease in grain size downstream from the Fall Line is partially attributable to the grain size of the underlying Cretaceous sediments, the change in slope also contributes to this variation.

Abrupt gradient changes along stream systems also offer controls on the preferential deposition of sediment and associated heavy minerals. Although influenced by channel depth and width, locally or regionally steepened gradients coincide with increased stream velocities and larger diameter particles as bed or suspended loads. Changes to less steep slopes have the opposite effect, with finer sized grains deposited rapidly along the channel as an adjustment to a decrease in stream velocity.

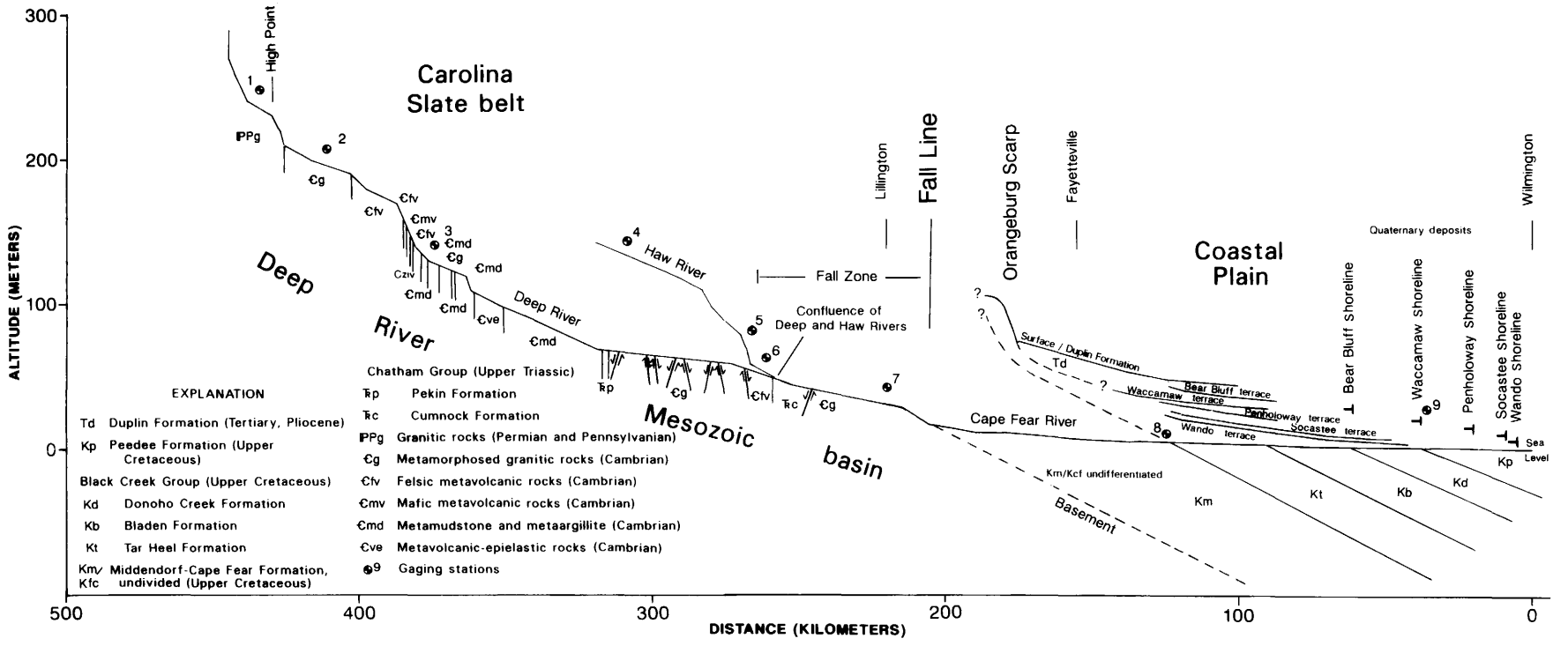

Figure 4. Longitudinal profile of the Cape Fear River system, North Carolina.

Table 1. Calculated median grain size for the Cape Fear River system bed load as a function of cumulative drainage area and slope.

[Gaging station numbers are shown on figs. 4 and 7]

	Gaging station	Cumulative drainage area (mi^2)	Slope (ft/mi)	Median grain size (mm)
1.	Deep River near High Point, N.C.	46.9	13.1	27.6
2.	Deep River near Randelman, N.C.	125.0	4.5	12.4
3.	Deep River near Ramseur, N.C.	349.0	10.5	142.1
4.	Haw River at Haw River, N.C.	596.0	5.0	70.5
5.	Haw River near Pittsboro, N.C.	1,310.0	7.9	332.0
6.	Deep River at Moncure, N.C.[1]	1,434.0	3.7	102.7
7.	Cape Fear River at Lillington, N.C.	3,464.0	2.5	129.0
	Fall Line			
8.	Cape Fear River at Huske Lock	4,810.0	0.34	6.7
9.	Cape Fear River at Lock No. 1	5,220.0	0.12	1.3

[1]Confluence of Deep River and Haw River: Head of Cape Fear River.

Hydraulic equivalency of heavy minerals in natural settings is coupled with the composite array of variables that influence stream velocity and particle size in fluvial systems. The relationship is complex and resists simple explanation. In a general sense, however, specific reaches along river channels may be highlighted as having the greatest potential for differential deposition of specific heavy mineral suites as a response to settling velocities and stream flow. Two clear examples are geologic boundaries that (1) allow for abrupt widening of channels in areas downstream from confined channels, and (2) abrupt changes to less steep gradients. Lithologic changes from resistant to less resistant rock types, either locally or regionally, can contribute to both types of preferred depositional settings.

LATE MESOZOIC AND CENOZOIC PLACER POTENTIAL AT THE FALL ZONE

The Fall Line is loosely associated with the inner edge of the Coastal Plain in the southeastern U.S., where it originally implied an imaginary line drawn through the downstream location of falls on major river systems that formed a barrier to navigation (McGee, 1888). Fenneman (1938) broadened the definition to represent a zone, 5–10 mi wide, that denoted a transition from the crystalline rocks of the Piedmont to unconsolidated sediments of the Coastal Plain. The term "Fall Line" was used instead to mark the point where Piedmont rocks passed beneath the sediments of the Coastal Plain. In this respect, the term became a boundary between physiographic provinces rather than a fluvial attribute. Hack (1982) returned to a fluvial definition. He showed that major breaks in modern stream gradients occurred within the Fall Zone and that these were often found within the Piedmont rather than the Coastal Plain. Thus, there is ambiguity in the use of the term. In this paper, "Fall Line" denotes the contact between Piedmont rocks and Coastal Plain sediments exposed along modern stream beds. Fall Zone, on the other hand, incorporates the steepened reaches upstream from the Fall Line to the inner edge of Coastal Plain sediments. In this respect, the changing position of the contact between the Piedmont and Coastal Plain can be taken into account as major stream systems were incised or alluviated during the post-Mesozoic history of tectonically and eustatically induced base-level changes. Fall Zone, in this view, incorporates the innermost deposits of the Coastal Plain but recognizes the potential proximity of former "Fall Line" positions with the contemporaneous fluvial facies of inner Coastal Plain deposits.

On the basis of past and present stream gradient changes, similar in pattern to those of the modern system, the inner Coastal Plain is preferentially suited for heavy mineral deposition and presents its own placer potential. Here again, the gradient change of streams draining the Piedmont played the major role.

The Late Mesozoic and Cenozoic rocks of the Coastal Plain form a complex wedge of fluvial and marine sediments that rises in altitude inland until pinching out against the crystalline rocks of the Piedmont. Upper Cretaceous strata rest unconformably on the weathered surface of the crystalline rocks. This relationship is common for the Atlantic Coastal Plain from New Jersey to Georgia (Frazier, 1979; Gohn and others, 1979; Owens and Gohn, 1985; Sohl and Owens, 1991). The basal Cretaceous units are sometimes weathered, both in outcrop and in subsurface, and consist of very coarse to fine-grained sand. At their basal contact they often incorporate coarse clasts of crystalline rocks. The basal Cretaceous formations include the Tuscaloosa Formation in Georgia, the Cape Fear and Middendorf Formations in the Carolinas, and the Potomac Group in the Middle Atlantic area. All are fluvial sediments related to ancestral river systems that once drained the Piedmont. They are upper delta plain sediments correlative with contemporaneous shoreline positions that lie east of the present coastline (Sohl and Owens, 1991). The Lower Cretaceous sediments are overlain by Upper Cretaceous deltaic and shelf deposits.

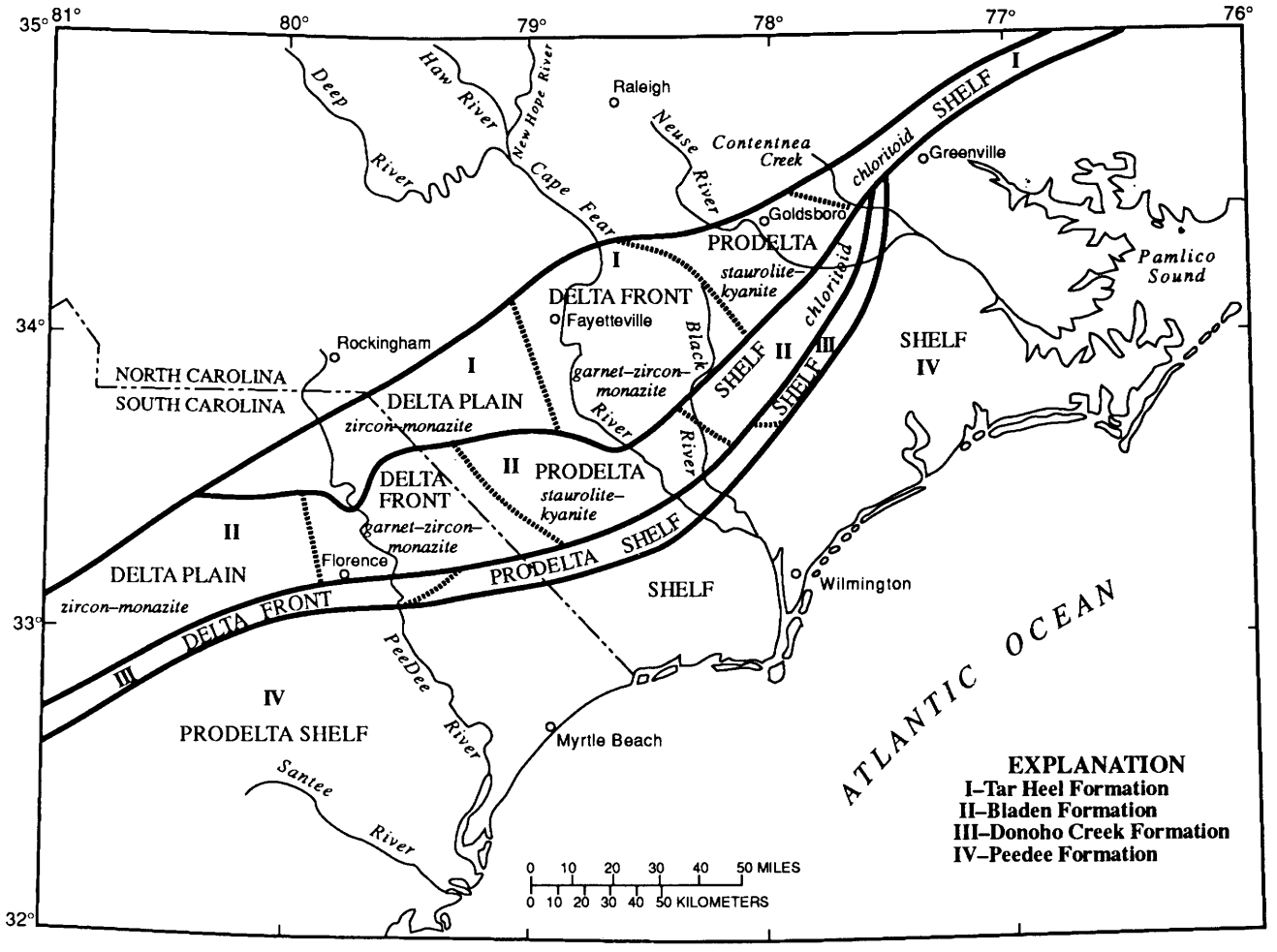

Figure 5. Generalized paleoenvironmental facies analysis of the Black River Group and lower Peedee Formation between Columbia, South Carolina, and Greenville, North Carolina.

The crystalline "basement" is an eastward subsurface extension of rocks of the Piedmont Province. From the inner edge of the Coastal Plain, the surface of the "basement" slopes eastward at about 3.4–3.8 m/km to where the surface is about 450 m below sea level at the present coastline. In the southeastern U.S., the surface is tectonically deformed by the Cape Fear arch in the Carolinas and by the Georgia uplift in Georgia and Florida. The Salisbury Embayment lies northeast of the Cape Fear arch and the Southeast Georgia Embayment lies to the southeast. Both are basins with thick sedimentary sequences that show Cretaceous and Cenozoic deformation.

Along the axis of the Cape Fear arch, the slope of the basement surface beneath the inner Coastal Plain is 2.0 m/km for 100 km downstream from the Deep River Mesozoic Basin. Farther east, however, the slope of the basement surface is comparable to steeper areas both north and south of the arch (3.8 m/km). The slope of the basement below the Coastal Plain is similar to that of the present Piedmont surface and suggests continuity of this surface through time, although river systems have changed. As an example, the modern gradient of the Deep River in the eastern Piedmont is approximately 1.7 m/km (fig. 5). This compares with the slope of the basement below the adjacent inner Coastal Plain of 2.0 m/km. By contrast, the modern gradient of the Cape Fear River across the Coastal Plain is approximately 0.28 m/km (Soller, 1988). Thus, Cenozoic deposition, complicated by tectonism and sea-level changes, has built up the Coastal Plain surface and decreased stream gradients relative to the eastern edge of the Piedmont. The change in gradient at the inner edge of the Coastal Plain represents a hydraulic break conducive to preferential heavy mineral deposition.

The Piedmont–Coastal Plain transition zone was identified by Mertie (1958, 1975) as a favorable location for accumulations of detrital monazite and zircon. He found these minerals within the heavy mineral suites of basal Cretaceous sediments deposited on Piedmont crystalline rocks in the Carolinas and Georgia. Mertie attributed the monazite-zircon concentrations in Cretaceous rocks of the inner Coastal Plain to simple heavy mineral dispersal from source terranes in granitic rocks at the eastern edge

of the Piedmont. Detrital heavy mineral concentrations decreased rapidly downstream from the source deposits because they were diluted by mineral suites supplied by nearby sources (Pettijohn, 1957, p. 566–567). Grain-size, hydraulic-equivlance, and sedimentary-facies relationships received less coverage in Mertie's reports. Nonetheless, he identified reworked sediments of Cretaceous and Tertiary age at the Fall Zone as potential sites for placers of monazite and zircon. Following a dispersal model, he sought out enriched fluvial placers for monazite and zircon along specific secondary stream drainages that drained basal Cretaceous formations.

HYDRAULIC SORTING WITHIN CRETACEOUS FLUVIAL-DELTAIC DEPOSITS

The dispersal model was limited by the outcrop area of basal Cretaceous rocks. There was little knowledge of the heavy mineral suites of subsurface rocks—not much was known of their grain size, stratigraphy, or depositional environments. Recent work by Sohl and Owens (1991) on the Cretaceous stratigraphy of the Carolina Coastal Plain provides insights into the heavy mineral suites. Here, the basal Cretaceous is represented by the Cape Fear Formation, which rests unconformably on the "basement." The Cape Fear Formation, consists of poorly sorted, fine- to coarse-grained fluvial sand. Sohl and Owens point out that the heavy mineral suite in the outcrop area along the Cape Fear River consists of ilmenite, zircon, tourmaline, rutile, and significant monazite. To the northeast, along the Tar River, monazite is subordinate to staurolite and kyanite. In subsurface deposits, the heavy minerals at Charleston, S.C., are more varied but contain zircon, rutile, and monazite. The coarse- to fine-grained fluvial sediments of the Cape Fear Formation represent deposits of the upper delta plain of a drainage system with a shoreline position near the present coastline.

The overlying Middendorf Formation displays different lithofacies and mineralological relationships from those of the Cape Fear. Both are of fluvial-deltaic origin however, and the lithofacies of each changes from upper delta plain to delta plain and delta front deposits from southwest to northeast along the strike of the outcrop area. The terrestrial facies grade into marine facies between the Pee Dee and Cape Fear Rivers. Prodelta and shelf deposits of the Middendorf are present in the subsurface near Charleston. A decrease in grain size accompanies the facies transition, as does an apparent hydraulically equivalent change in the heavy mineral suites. Zircon, rutile, and monazite are common in the upper delta plain deposits (Owens and Grosz, 1989), but are replaced by epidote, garnet, and andalusite along the delta front and prodelta.

Hydraulic sorting by grain size, density, and lithofacies is well defined, where appropriate grain-size data are available, in the overlying Black Creek Group. The Upper Cretaceous of the Carolinas was formerly thought to represent a single transgressive event with the Middendorf Formation, Black Creek Group, and Peedee Formation as lithofacies of the same unit that increased in altitude westward across the "basement" during transgression (Swift and Heron, 1969). Sohl and Owens' (1991) more reliable dating of lithofacies along the Cape Fear valley shows a series of transgressive and regressive events, each characterized by separate fluvial-deltaic facies.

As redefined by Owens (1989), the Black Creek Group includes the Tar Heel Formation, the Bladen Formation, and the Donoho Creek Formation. The Tar Heel Formation incorporates fluvial sediments once identified as Middendorf along the Cape Fear River. The group is overlain by shelf deposits of the Peedee Formation. Figure 5 shows the outcrop pattern and facies relationships of the Black Creek Group and Peedee Formation (Owens, 1989; Sohl and Owens, 1991). Changes from delta plain, and delta front, prodelta, to shelf are apparent from southwest to northeast and across the Cape Fear arch.

Heavy mineral suites in these formations reflect the facies changes. The coarse-grained Tar Heel Formation is a representative example. Along the Peedee River, the upper delta plain facies of the Tar Heel Formation contains abundant zircon and monazite. The delta front facies exposed along the Cape Fear valley has little monazite and less zircon, but garnet is abundant. In the prodelta facies that crops out along the Neuse River, garnet decreases with an increase of staurolite and kyanite. The shelf deposits contain chloritoid as the dominant heavy mineral species. The Bladen and Donoho Creek Formations are progressively finer grained than the Tar Heel but show similar heavy mineral suites and similar density sorting in the identified deltaic facies.

The theoretical relationship between heavy mineral suites, grain size, and deltaic facies is shown on figure 6, which illustrates grain-size changes of the Upper Cretaceous formations exposed along the Cape Fear valley from the Fall Line to the coast. This figure shows first percentile and median grain sizes analyzed and plotted by Swift and Heron (1969) to illustrate a downstream decrease grain size in a fluvial-marine depositonal system. Their data are adapted here to reflect the redefined facies mapped on figure 5. It should be noted that Sohl and Owens (1991) show downstream lithofacies in each formation of the Black Creek Group to progess from southwest to northeast along the strike of the outcrop rather than along the Cape Fear River. Nonetheless, sections exposed along the Cape Fear River show the same progression between individual facies, although, in this case, each facies represents a different formation. The grain-size data show a consistent decrease and are used here to model downstream heavy mineral distribution at the inner edge of the Coastal Plain or "Fall Zone."

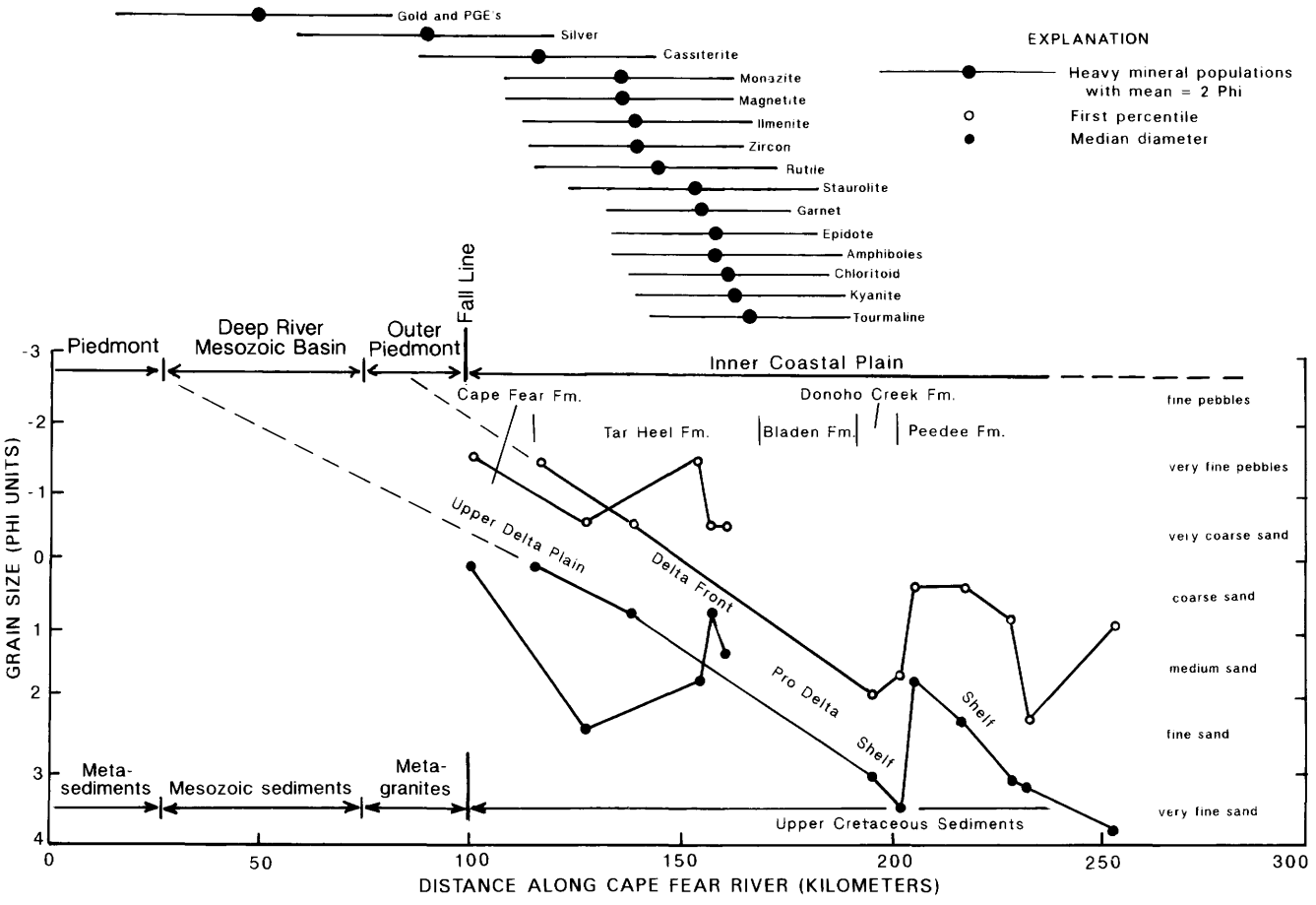

Figure 6. Grain size of Upper Cretaceous Formations exposed along the Cape Fear River (adapted from Swift and Heron, 1969). Median and first percentile grain size is plotted downstream from the Fall Line. Shown above are the theoretical ranges of heavy mineral species calculated from median grain size of the Cape Fear Formation and Black River Group along the Cape Fear River. Heavy mineral populations are calculated from an assumed mean grain size of 2 phi ± 1 phi unit. The ranges of heavy mineral species are from figure 3.

Grain size progressively decreases from delta plain facies through delta front facies in the Tar Heel to prodelta facies in the Bladen and finally shelf facies in the Donoho Creek. Anomalous, coarse grain sizes in the overlying Peedee Formation, a shelf deposit, reflects a basal concentration of reworked phosphatic clasts consisting of bored, subrounded cobbles, internal molds of mollusks, and bone and teeth material. Plotted above the grain size data on figure 6 are the calculated equivalent ranges for fine-grained heavy mineral species (± one phi size) shown on figure 3 and keyed to the median grain size data of Swift and Heron (1969). The heavy mineral suite characterized by monazite, ilmenite, zircon, and rutile plot within the delta plain and delta front facies suggested by Sohl and Owens (1991). The less dense heavy minerals staurolite, garnet, epidote, and the amphiboles plot farther downstream in the delta front and prodelta facies. The theoretical and observed heavy mineral identifications point to downstream sorting by density as a key factor in the location of specific heavy mineral suites.

The Cretaceous fluvial-marine distribution of heavy mineral suites provides a conceptual model for understanding the depositional context of heavy mineral deposits on the Coastal Plain. Figure 7 shows the heavy mineral ranges of figure 6 superimposed on the longitudinal profile of the Cape Fear River system (fig. 4) and plotted relative to the Fall Line. The monazite-ilmenite-zircon-rutile zone, characterized by the grain size of the delta plain and delta front facies of the Tar Heel Formation and the Cape Fear Formation, lies immediately downstream from the modern Fall Line in the vicinity of the Orangeburg Scarp and the inner edge of the Duplin Formation. The less dense staurolite-epidote-garnet-amphibole zone within the Cretaceous is anticipated farther downstream and beneath the Duplin surface and Quaternary alluvial deposits. Above the Fall Line the coarser grained upper delta plain sediments would be more conducive to gold and PGE deposition.

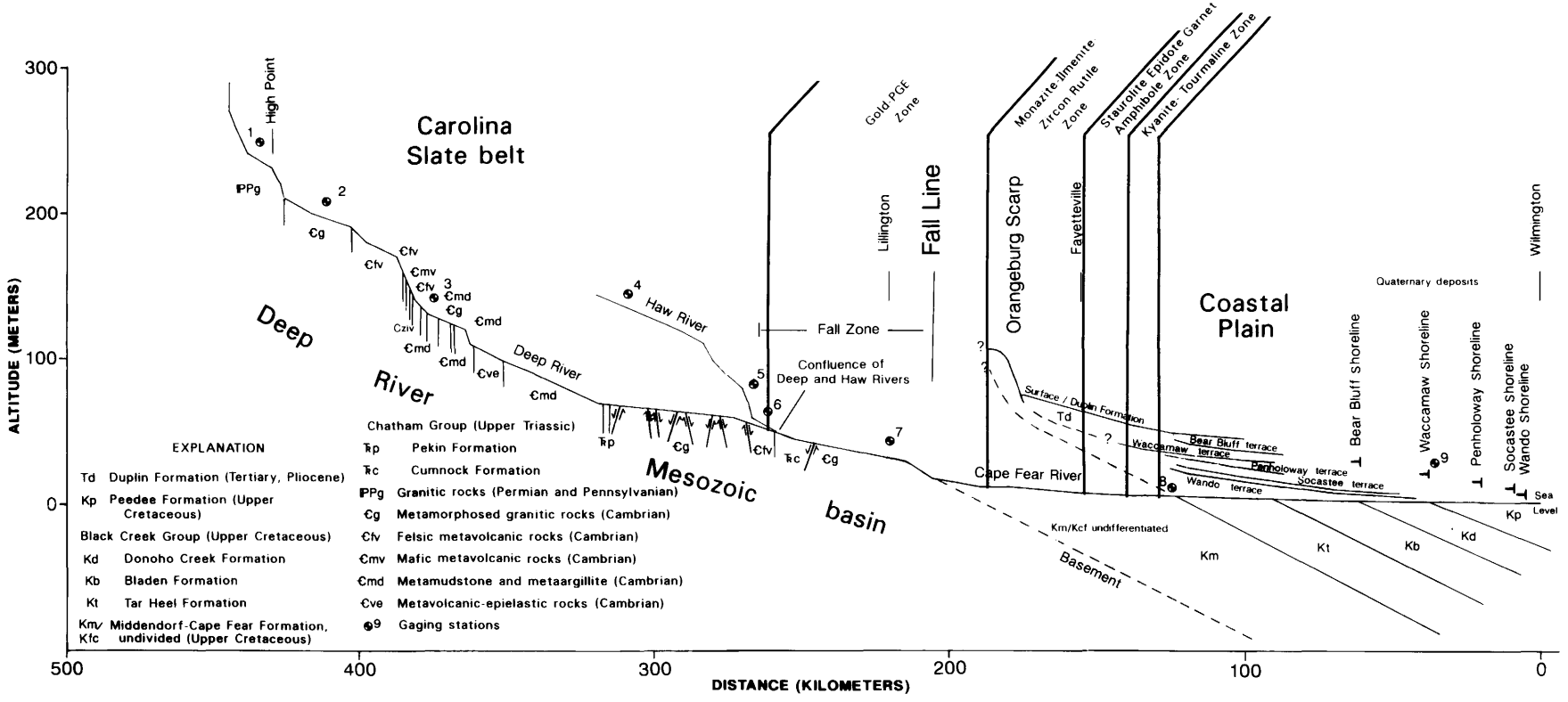

Figure 7. Theoretical Upper Cretaceous heavy mineral zonation along the Cape Fear River on the basis of figure 6.

CENOZOIC REWORKING OF THE INNER COASTAL PLAIN OF THE CAROLINAS

The surficial deposits of the Atlantic Coastal Plain are dominantly Cenozoic in age. Although lower Tertiary (Paleocene and Eocene) sediments are preserved at depth within the subsiding Southeast Georgia and Salisbury Embayments, they are commonly absent from the adjacent arches (Gohn and others, 1979; Owens, 1989). Instead, Miocene and lower Pliocene marine and coastal margin facies transgress the innermost Coastal Plain deposits from the Carolinas (Owens, 1989) to Virginia (Mixon and others, 1989). The transgressive events reworked the underlying Upper Cretaceous formations, as demonstrated by the Duplin Formation on figure 7, and incorporated equivalent heavy mineral suites within younger fluvial-deltaic and marine facies. Quaternary transgressive deposits occur at progressively lower altitudes eastward across the Coastal Plain to the present coast and are contemporaneous with alluvial fills along the major river systems.

The Cenozoic deposits of the Coastal Plain continue the fluvial-deltaic style of heavy mineral sorting demonstrated for the Cretaceous. Stream gradients across the Coastal Plain, however, decreased progressively through time relative to the Piedmont and the Fall Zone while a thickening wedge of sediment was deposited across the Mesozoic Coastal Plain. In effect, a rising base level adjusted to eustatic sea level and local tectonic and isostatic changes gave rise to lower gradient rivers across the Coastal Plain and emphasized the abrupt change to a lower gradient at the Fall Zone. As a consequence, finer grained fluvial facies were deposited across the Coastal Plain together with a suite of hydraulically equivalent "lighter" heavy minerals dominated by staurolite, kyanite, amphiboles, pyroxenes, and epidote. In contrast, the somewhat coarser grained facies nearer the Fall Zone produced concentrations of a high-density mineral suite: monazite, magnetite, ilmenite, zircon, and rutile. Thus using stream gradient and hydraulic equivalence as the dominant variables, the Coastal Plain Cenozoic deposits near the Fall Zone, as well as their Upper Cretaceous counterparts, tend to be the preferred setting for monazite, ilmenite, rutile, and zircon (Owens and Grosz, 1989). Subsequent reworking by coastal processes at the higher interglacial sea level stands further concentrated the inner Coastal Plain fluvial placers into barrier island beach and dune facies. These, in turn, resemble the classic economic coastal placer settings of southeastern Georgia and northern Florida.

CONCLUSION

The Fall Zone marks the transition between the crystalline terranes of the Piedmont and the sediments of the Atlantic Coastal Plain. Modern river systems like the Cape Fear drain the Piedmont and enter the Coastal Plain at the Fall Line, where stream gradients become gentle and the grain size of sediments often begins a pronounced downstream decrease. Although the position of the Fall Line has changed since the Mesozoic, the Coastal Plain sediments preserve a characteristic facies transition from upper delta plain, to delta front, prodelta, and shelf that begins at the edge of the Piedmont. A downstream decrease in grain size is accompanied by a related sorting of heavy mineral species by density and size. Coarser delta plain sediments near the Fall Line receive more dense heavy minerals like monazite, ilmenite, and zircon. Farther downstream the assemblage is more often comprised of staurolite, garnet, amphiboles, and epidote.

Low-gradient coastal plains offer a resource opportunity for concentrations of heavy minerals in suites governed by grain size and density that are dependent on upstream source terranes. With the Atlantic Coastal Plain of the southeastern U.S. as an example, and given appropriate source terranes, medium- to coarse-grained sand of the upper delta plain facies can be expected to concentrate a fine-grained heavy mineral suite characterized by magnetite, monazite, ilmenite, zircon, and subordinate rutile. The fine- to medium-grained sand of the delta front, on the other hand, has an anticipated heavy mineral suite dominated by very fine grained amphiboles, pyroxenes, staurolite, kyanite, epidote, and tourmaline with subordinate and even finer grained ilmenite, zircon, and rutile.

In short, coarse clastics are deposited in proximity to the Fall Zone, with grain size decreasing with distance downstream from the edge of the Piedmont. The contained heavy mineral suites are sorted accordingly by grain size, governed by hydraulic equivalence. A close relationship between heavy minerals and fluvial facies suggests that economic exploration should more closely investigate extant stratigraphic facies reconstructions for future economic studies.

REFERENCES CITED

Conley, J.F., 1962, Geology and mineral resources of Moore County, North Carolina: North Carolina Department of Conservation and Development Bulletin 76, 40 p.

Fenneman, N.M., 1938, Physiography of the Eastern United States: New York, McGraw-Hill, 714 p.

Force, E.R., and Stone, B.D., 1990, Heavy mineral dispersal and deposition in sandy deltas of glacial Lake Quinebaug, Connecticut: U.S. Geological Survey Bulletin 1874, 21 p.

Friedman, G.M., and Sanders, J.E., 1978, Principles of Sedimentology: New York, John Wiley & Sons, 792 p.

Frazier, W.J., 1979, Sedimentology and paleoenvironmental analysis of the Upper Cretaceous Tuscaloosa and Eutaw Formations in western Georgia, *in* Arden, D.D., Beck, B.F., and Morrow, E., eds., Proceedings, Second Symposium on the Geology of

the Southeastern Coastal Plain: Georgia Geologic Survey Information Circular 53, p. 39–52.

Gallagher, P.E. and Hoffman, C.W., 1990, Geology and heavy-mineral exploration of sedimentary deposits along the Fall Zone of Northampton, Halifax, Nash, and Wilson Counties, North Carolina: North Carolina Geological Survey Open-File Report 90–4, 16p.

Gilbert, G.K., 1877, Report of the geology of the Henry Mountains: U.S. Geographic and Geological Survey, Rocky Mountain Region, 160 p.

Gilbert, G.K., 1914, The transportation of debris by running water: U.S. Geological Survey Professional Paper 86, 259 p.

Gohn, G.S., Bybell, L.M., Christopher, R.A., Owens, J.P., and Smith, C.C., 1979, A stratigraphic framework for Cretaceous and Paleogene margins along the South Carolina and Georgia coastal sediments, *in* Arden, D.D., Beck, B.F., and Morrow, E., eds., Proceedings, Second Symposium on the Geology of the Southeastern Coastal Plain: Georgia Geologic Survey Information Circular 53, p. 64–74.

Hack, J.T., 1957, Studies of longitudinal stream profiles in Virginia and Maryland: U.S. Geological Survey Professional Paper 294–B, p. 53–63.

Hack, J.T., 1982, Physiographic divisions and differential uplift in the Piedmont and Blue Ridge: U.S. Geological Survey Professional Paper 1265, 49 p.

Leopold, L.B., Wolman, M.G., and Miller, J.P., 1964, Fluvial Processes in Geomorphology: San Francisco, W.H. Freeman, 522 p.

McGee, W.J., 1888, The geology of the head of the Chesapeake Bay, U.S. Geological Survey, 7th Annual Report (1885–1886), p. 537–646.

Mertie, J.B., Jr., 1958, Zirconium and hafnium in the Southeastern Atlantic States: U.S. Geological Survey Bulletin 1082–A, 25 p.

———1975, Monazite placers in the Southeastern Atlantic States: U.S. Geological Survey Bulletin 1390, 41 p.

Mixon, R.B., Berquist, C.R., Jr., Newell, W.L., and Johnson, G.H., 1989, Geologic map and generalized cross sections of the Coastal Plain and adjacent parts of the Piedmont, Virginia: U.S. Geological Survey Miscellaneous Investigations Series Map I–2033, 2 sheets.

Owens, J.P., 1989, Geologic Map of the Cape Fear region, Florence 1°×2° quadrangle and northern half of the Georgetown 1°×2° quadrangle, North Carolina and South Carolina: U.S. Geological Survey Miscellaneous Investigations Series Map I–1948–A, scale 1:250,000, 2 sheets.

Owens, J.P., and Gohn, G.S., 1985, Depositional history of the Cretaceous Series in the U.S. Atlantic Coastal Plain: Stratigraphy, paleoenvironments, and tectonic controls of sedimentation, *in* Poag, C.W., ed., Geological Evolution of the United States Atlantic Margin: New York, Van Nostrand Reinhold, p. 25–86.

Owens, J.P., and Grosz, A.E., 1989, Rare-earth resource potential—Monazite distribution in the Fall Zone Coastal Plain sediments of western South Carolina: U.S. Geological Survey Research on Mineral Resources—1989 Program with Abstracts, Fifth Annual V.E. McKelvey Forum on Mineral and Energy Resources: U.S. Geological Survey Circular 1035, p. 51.

Pettijohn, F.J., 1957, Sedimentary Rocks: New York, Harper & Row.

Pettijohn, F.J., Potter, P.E., and Siever, Raymond, 1973, Sand and Sandstone: New York, Springer Verlag, 618 p.

Rittenhouse, Gordon, 1953, Transportation and deposition of heavy minerals: Geological Society of America Bulletin, v. 54, p. 1725–1780.

Rubey, W.W., 1933, Settling velocities of gravel, sand, and silt particles: American Journal of Science, 5th series, v. 25, p. 325–338.

Slingerland, R.L., 1977, The effects of entrainment on the hydraulic eqivalence relationships of light and heavy minerals in sands: Journal of Sedimentary Petrology, v. 47, p. 753–770.

———1984, Role of hydraulic sorting in the orgin of fluvial placers: Journal of Sedimentary Petrology, v. 54, p. 137–150.

Sohl, N.F., and Owens, J.P., 1991, Cretaceous stratigraphy of the Carolina Coastal Plain, *in* Horton, J.W., Jr., and Zullo, V.A., eds., Geology of the Carolinas: University of Tennessee Press, p. 191–220.

Soller, D.R., 1988, Geology and tectonic history of the lower Cape Fear River valley, southeastern North Carolina: U.S. Geological Survey Professional Paper 1466–A, 60 p.

Swift, D.J.P., and Heron, S.D., Jr., 1969, Stratigraphy of the Carolina Cretaceous: Southeastern Geology, v. 10, p. 201–245.

Tourtelot, H.A., 1968, Hydraulic equivalence of grains of quartz and heavier minerals, and implications for the study of placers: U.S. Geological Survey Professional Paper 594–F, p. F1–F13.

Wilson, W.F., Carpenter, P.A., III, Burt, E.R., McDaniel, R.D., Coffey, J.C., and McKensie, B.J., 1978, Geology of the Raleigh 1°×2° quadrangle, North Carolina: U.S. Department of Energy, Grand Junction, Colo., Report no. GJBX–51.

Woodford, A.O., 1951, Stream gradients and Monterey Sea Valley: Geological Society of America Bulletin, v. 62, p. 799–852.

CHAPTER R

USE OF GEOCHEMICAL SURVEYS IN Ti-Hf-REE-Th-U PLACER EXPLORATION—A MID-ATLANTIC-STATES EXAMPLE

By ANDREW E. GROSZ[1]

ABSTRACT

Selected elements from the "hydrogeochemical and stream sediment reconnaissance" database of the National Uranium Resource Evaluation Program (NURE) are diagnostic and may predict the presence of commercially important heavy minerals. Titanium (Ti), hafnium (Hf), rare-earth elements (REE: Ce, Dy, Eu, La, Lu, Sm, Yb, Y), and thorium (Th) are among the elements analyzed and reported in the NURE database. Concentrations of these elements in samples from the Atlantic Fall Zone and Coastal Plain Province can predict the presence of commercially important heavy minerals such as ilmenite ($FeTiO_3$), rutile (TiO_2), zircon ($(Zr,Hf,U)SiO_2$), monazite ($(Ce,La,Y,Th,U)PO_4$), and xenotime (YPO_4). Ilmenite and rutile are the most commonly occurring Ti-bearing minerals in Fall Zone and Coastal Plain sediments. Zirconium and hafnium possess extraordinary geochemical affinity; thus, the presence of Hf (zirconium (Zr) was not analyzed) usually indicates the presence of zircon.

Known placer deposits of heavy minerals in (1) the North Carolina–South Carolina State-line region along the Fall Zone, (2) coastal South Carolina, and (3) at the base of the Fall Zone near the South Carolina–Georgia State line are outlined by the anomalies. The characteristic Ti-Hf-REE-Th-U signature is identified over unconsolidated Upper Cretaceous and Tertiary sediments along the Fall Zone and over North Carolina's Coastal Plain Province, particularly over Pliocene and Pleistocene fossil shoreline deposits. The geochemical data, therefore, may be used to locate other deposits.

A large area in North Carolina's Coastal Plain Province is outlined for Ti-Hf-REE-Th-U-bearing heavy minerals exploration. The Cape Fear arch is shown to have had a pronounced effect on the distribution of placer minerals and, therefore, on potential placer deposits in Coastal Plain sediments in North Carolina. Upper Cretaceous sediments in South Carolina and in North Carolina south of the Cape Fear arch constitute a REE-Hf-Th-U superprovince.

Other parts of the conterminous United States, particularly in the largely unexplored Central Plains, appear suitable for similar study. The potential for Ti-Hf-REE-Th-U-bearing deposits of heavy-mineral suites in the United States may be much greater than previously thought.

INTRODUCTION

Deposits of heavy minerals in unconsolidated sediments, both of the fluvial and beach-complex type, furnish most of the world's ilmenite and rutile (ores of titanium), zircon (ore of zirconium and hafnium), and monazite (ore of rare earths and thorium). Garnet, staurolite, tourmaline, and aluminosilicates (kyanite and sillimanite) are common byproducts of placer mining operations and are used as abrasives or minerals for refractories.

Exploration for deposits of heavy minerals has traditionally relied upon methods guided largely by geomrphologic and geologic rationale. Exploration commonly involves preliminary field sampling of surficial sediments followed by drilling on geomorphologically defined targets. Most commonly these are Quaternary(?) beach ridges and associated foredunes or their fossil equivalents in coastal plain sediments.

[1]U.S. Geological Survey, Mail Stop 954, 12201 Sunrise Valley Drive, National Center, Reston, VA 22092

More recently, airborne gamma-ray radiation and high-resolution magnetic surveys have been shown to be useful in outlining targets for sampling (Robson and Sampath, 1977; Force and others, 1982; Grosz, 1983; Grosz and others, 1989). Induced polarization is another promising technique for onshore and offshore placer exploration (Wynn and others, 1990).

This report details principles and techniques of placer deposits exploration by use of stream-sediment geochemical data and provides examples from the Carolinas that are applicable to the conterminous States and Alaska. The principles and techniques are applicable to a host of other deposit types, metallic and nonmetallic, in hard-rock and sedimentary settings. They may also prove useful in regional geologic mapping.

THE NURE-HSSR PROGRAM

The National Uranium Resource Evaluation (NURE) Program was established by the U.S. Department of Energy to gather data with which to evaluate uranium resources and to identify areas in the United States potentially favorable for uranium deposits (Averett, 1984). The "hydrogeochemical and stream sediment reconnaissance" (HSSR) was one element of the NURE program. The HSSR effort involved collection and analysis of samples of stream sediment, ground water, and surface water from the conterminous 48 States and Alaska to determine concentrations of uranium and other selected elements (Arendt and others, 1980). The data were expected to help outline geochemical provinces and to suggest favorable areas for more detailed studies. Tabulations of areas surveyed during the HSSR and the information that is available for those areas are given by Averett (1984).

Sampling and reporting in the HSSR were done on a quadrangle basis using the 1°×2° quadrangles of the National Topographic Map Series (NTMS) of the U.S. Geological Survey. HSSR data reports were issued for 330 (70.5 percent) of the 468 quadrangles in the 48 conterminous States and in 104 (68 percent) of the 153 quadrangles in Alaska. About 70 percent of the Nation has geochemical coverage. All samples were analyzed for uranium, and nearly all were also analyzed for up to 59 elements (Averett, 1984).

METHODOLOGY

The approach used in this study is based on the hypothesis that elements such as titanium (Ti) and hafnium (Hf) in stream-sediment samples reflect on the presence of common economic heavy minerals such as ilmenite ($FeTiO_3$) and rutile (TiO_2) in the case of Ti, and zircon ($(Zr,Hf)SiO_2$) in the case of Hf (Zr was not analyzed in HSSR). The rare-earth elements (REE) cerium (Ce), dysprosium (Dy), europium (Eu), lanthanum (La), lutetium (Lu), samarium (Sm), and ytterbium (Yb) are commonly associated with yttrium (Y), thorium (Th), and uranium (U) in heavy minerals such as monazite ($(Ce,La,Y,Th)PO_4$), xenotime (YPO_4), and allanite (epidote group: $(Ca,Ce,Y)_2(Al,Fe)_3(SiO_4)_3(OH)$)—other REE were not analyzed in HSSR. Because zirconium and hafnium possess extraordinary geochemical affinity, Hf usually indicates the presence of zircon (Vlasov, 1966). Although other commonly occurring heavy and light mineral species can carry these elements as well (for example Ti in amphiboles; Hf in pyroxenes; REE, U, and Th in apatite), they typically contain only trace abundances of these elements.

Mertie (1975), Overstreet (1967), Force and others (1982), and Owens and others (1989) show that monazite and zircon are present in the area of this report and that the sediments have undergone extensive weathering that removed much of the labile mineral component (amphiboles and pyroxenes, for example). Force and others (1982) and Owens and others (1989) also show that monazite (with its Th and U content) and zircon (with its U and Th content) control the aeroradiometric signature of surficially exposed heavy-mineral concentrations.

The HSSR database for each quadrangle contains all the sample types, their location coordinates, various descriptive fields, and their analytical data. The database for each of the quadrangles discussed in this report was searched for stream-sediment samples (sample type 50 in the database; –100 mesh (–149 micron) sieve fraction) having data for Be, Ce, Cr, Dy, Eu, Hf, La, Lu, Nb, P, Sm, Sn, Th, Ti, U, W, Y, and Yb by use of a query-by-example relational database program.

For the 10 1°×2° quadrangles used in this study, 10,093 stream-sediment samples met the search criteria. For any given sample, elemental data were: (1) a positive number (expressed as parts per billion (ppb)), (2) zero, (3) a negative number (signifying less than a given level of concentration; i.e., –2,000 ppb), or (4) no value (analytical data not available). In this study, only positive numbers were utilized for statistical analyses and graphic displays; data are discussed in percent format.

First, cumulative frequency plots for individual elements were constructed to identify anomalous outliers. As an example, figure 1 shows REE+Y for 8,174 samples. A maximum flexure in the curve near 7,600 on the abscissa indicates that the upper 9.3 percentile group (758 samples) has > 0.05 percent REE+Y. This group was plotted on a generalized geologic base map for North and South Carolina on which the Upper Cretaceous and Tertiary sediments (excluding those on the lower portions of the Coastal Plain) are shown as a single unit (fig. 2). The Fall Zone, at an average altitude of 240 feet, is generally coincident with the western edge of this unit. This

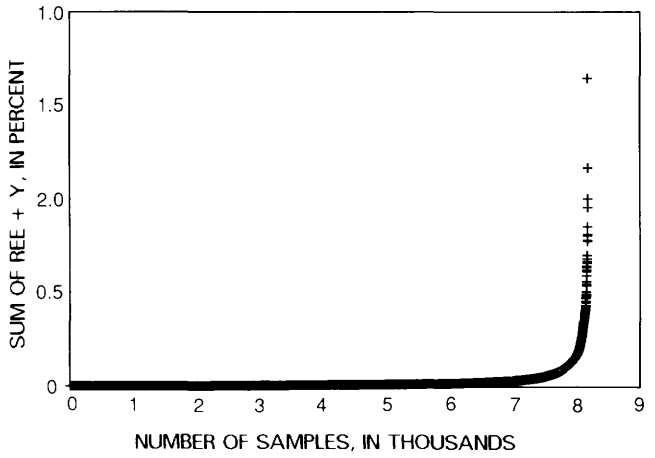

Figure 1. Cumulative frequency plot of 8,174 samples having REE+Y > 0.0 percent. Maximum flexure in the curve near 7,600 on the abscissa indicates that the upper 9.3 percentile group (758 samples) has > 0.05 percent REE+Y.

approach was followed for Hf, U+Th, and Ti. Other placer-mineral-indicating elements mentioned above were also plotted and showed patterns of distribution paralleling those shown in the figures.

Figure 3 displays linear relationships between the REE+Y and Th for the 758 samples having > 0.05 percent REE+Y. There appear to be at least two populations, distinguished by their Th to REE+Y ratios, that have not been intermixed to any great extent. The correlation of Th and REE+Y for both populations is expected for monazite; this is confirmed below. However, xenotime can be shown to be important locally by plots of the Y-subgroup (heavy REE) and the Ce-subgroup (light REE). Variability in the Th content of monazite (Overstreet, 1967) may also account for the two populations.

Zircon is a commonly occurring U-bearing mineral in terrigenous clastic assemblages. A plot of Hf versus U (fig. 4) for the group of Hf-bearing samples (60 percent of the total sample population) suggests that at least two incompletely mixed groups (end members) differing in their U/Hf ratios exist in the sample suite. Because the samples used for this plot span a broad spectrum of geologic units, compositional differences in zircons (for example, perhaps normal zircons and a metamict zircon population with low concentrations of U) may account for the scatter. However, other mineral species (for example Hf-rich pyroxenes) contributing to the scatter may be represented as well. Moreover, a plot of Th versus U for

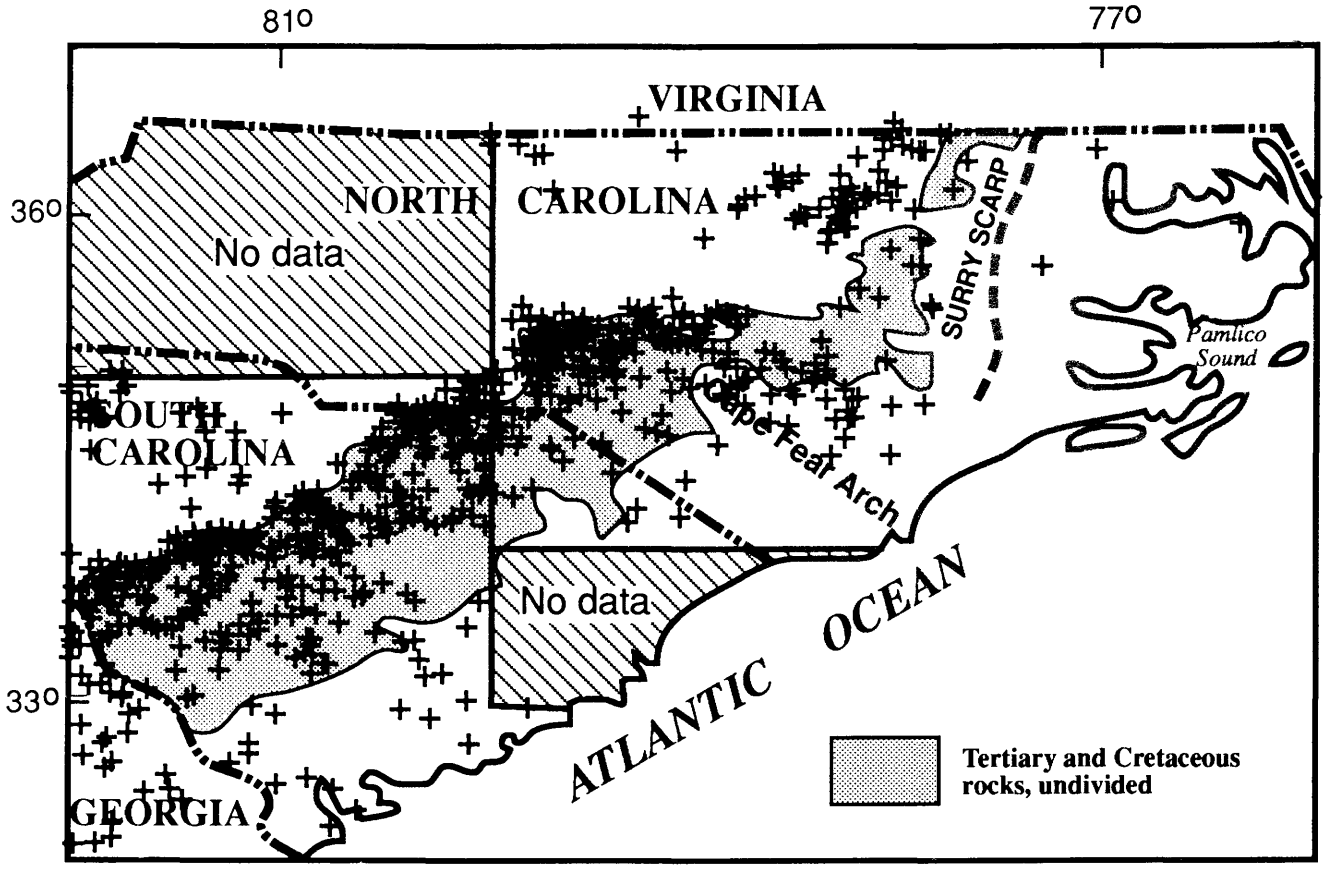

Figure 2. Locations of samples having > 0.05 percent REE+Y.

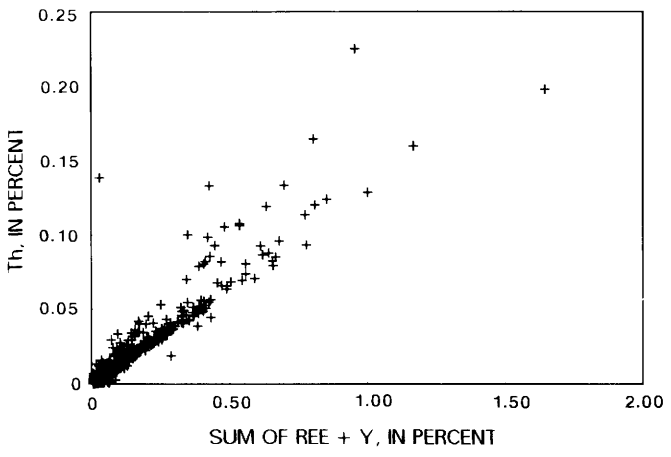

Figure 3. Plot of the sum of REE+Y against thorium for 758 samples having > 0.05 percent REE+Y (plotted on fig. 2).

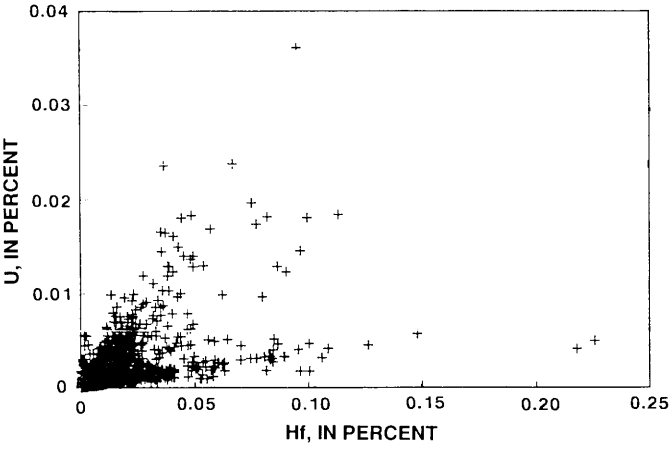

Figure 4. Plot of Hf against U for the Hf-bearing sample population (N = 6,102).

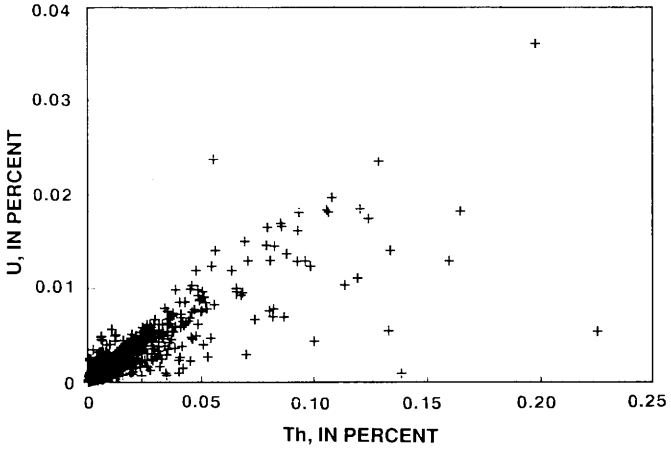

Figure 5. Plot showing the relationship between Th and U in samples having > 0.05 percent REE+Y.

samples having > 0.05 percent REE+Y (fig. 5) suggests that Th-rich monazite is an important source for both radioelements.

DISCUSSION

Samples from the locations shown on figure 2 contain more than 0.05 percent REE+Y and represent 758 (7.5 percent) of the total sample population. The greatest concentration of anomalous values follows the western boundary of the undifferentiated Upper Cretaceous and Tertiary sediments (the Fall Zone) with remarkable accuracy and persistence from the South Carolina–Georgia State line north to about central North Carolina. North of this central region, the anomalous REE+Y pattern continues approximately linearly onto Mississippian and Pennsylvanian intrusive and interlayered metasedimentary and metavolcanic rocks of Late Proterozoic and (or) Cambrian age in the Piedmont, lying to the west of the Cretaceous and Tertiary sediments.

An anomalous REE+Y site on the lower portion of the Coastal Plain near Pamlico Sound is approximately coincident with known REE+Y-bearing sedimentary phosphorite occurrences. To the south of the approximate axis of the Cape Fear arch, anomalous REE+Y locations extend to the lower reaches of the Coastal Plain, particularly along the Cape Fear and Cooper Rivers. Sedimentary phosphorite is also known to occur in this region (Force and others, 1982). Shoreward dispersal of monazite-bearing sediments by rivers seems to be an important mechanism only to the south of the Cape Fear arch. Anomalous REE+Y concentrations are also evident in the region of the Horse Creek deposit, located at the Fall Zone near the Georgia–South Carolina State line (Mertie, 1975). Staatz and Armbrustmacher (1979) defined a rare-earth province coincident with the Cretaceous and Tertiary trend because of the high monazite content of the sediments.

The locations shown on figure 6 contain more than 0.15 percent Ti and represent 671 (6.6 percent) of the total sample population and 11.4 percent of the Ti-bearing samples. The distribution pattern is significantly different from that of REE+Y, although no less remarkable in its persistence and localization over Fall Zone sediments in north-central North Carolina.

To the east, and parallel to the Fall Zone sediments, anomalous Ti concentrations in Coastal Plain sediments extend south to the vicinity of the northeastern flank of the Cape Fear arch. Many of these anomalous concentrations are approximately coincident with the late Tertiary to early Quaternary Surry Scarp (a major geomorphic feature), as shown by Blackwelder and Cronin (1981). South of the Cape Fear arch, anomalous Ti concentrations are much less common in Coastal Plain sediments than to the

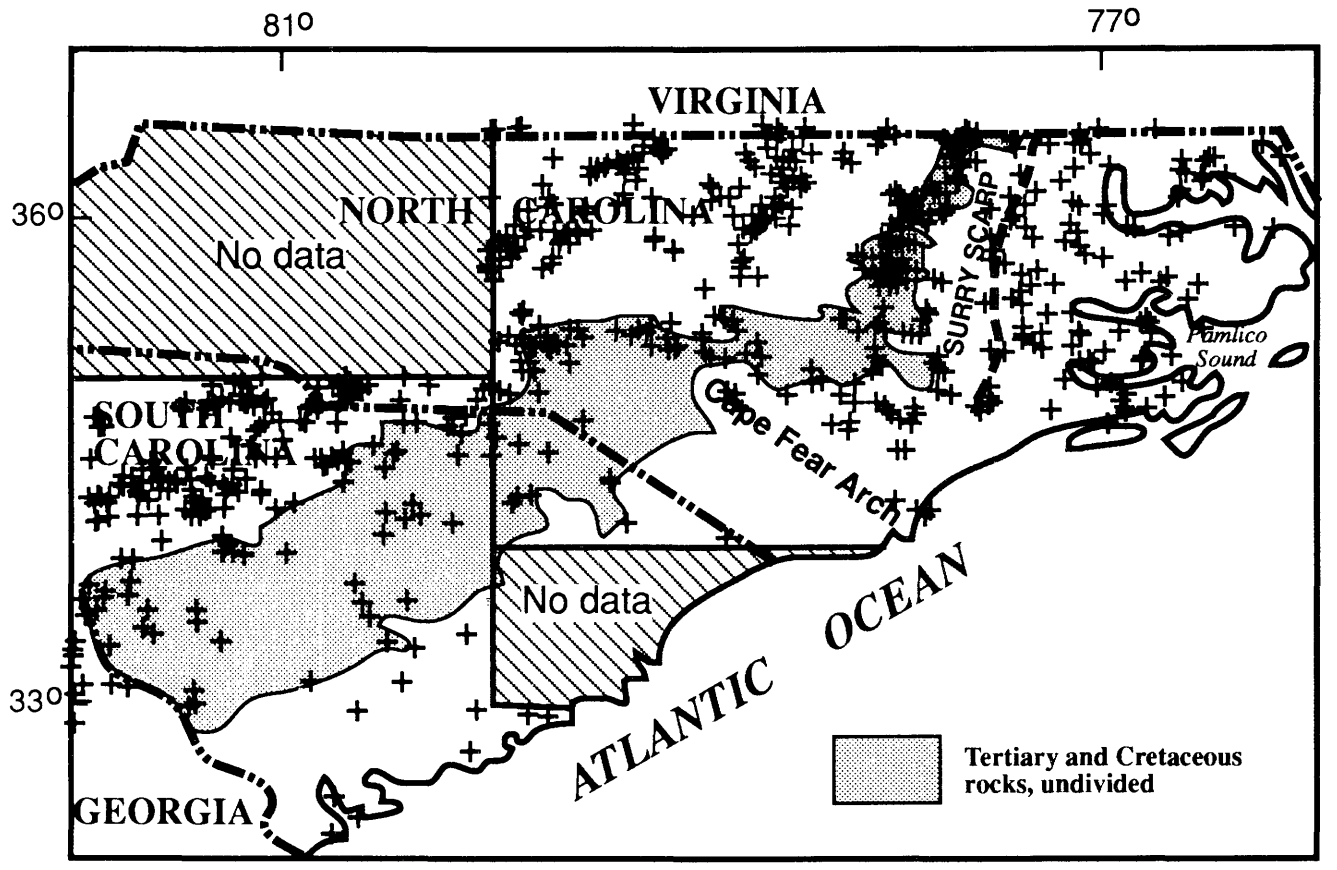

Figure 6. Locations of samples having > 0.15 percent Ti (N = 671).

north; the locations of samples containing anomalous concentrations of Ti shift westward onto crystalline rocks above the Fall Zone. In southern North Carolina, anomalous Ti values persist over the western edge of Upper Cretaceous sediments. In the North Carolina Piedmont, anomalous Ti concentrations occur in distinctive northeast-southwest-trending belts over Cambrian and Late Proterozoic metasedimentary, metavolcanic, and igneous rocks. The few anomalies over beach-complex sediments in coastal South Carolina are approximately coincident with heavy-mineral concentrations found by previous aeroradiometric surveys (Force and others, 1982).

Samples from the locations shown on figure 7 contain more than 0.015 percent Hf and represent 523 (5.2 percent) of the total sample population and 8.6 percent of the Hf-bearing samples. The distribution pattern shows more scatter than do the REE+Y and Ti distributions (compare fig. 7 with figs. 2 and 6). Over Fall Zone sediments in northern North Carolina, the Hf distribution closely resembles that of Ti, and over Coastal Plain sediments in South Carolina, the Hf pattern closely resembles that of Ti and REE+Y. The high cutoff value used to delimit anomalous Hf concealed subtle Hf anomalies that coincide with the Ti anomalies in coastal North Carolina, discussed above. South of the Cape Fear arch, anomalous Hf is remarkably persistent along the western boundary of Upper Cretaceous sediments. Crystalline rocks, specifically Silurian to Pennsylvanian intrusives appear to be important Hf (and REE+Y) sources in South Carolina.

Figure 8 shows the geographic distribution pattern of 631 (6.3 percent) of the total sample population and 8.8 percent of the samples that contain more than 0.01 percent U and Th combined. As predicted by figures 2, 3, and 4, the distribution pattern shown by these radioactive elements is remarkably consistent with that for REE+Y and much less so with that for Hf. This suggests that monazite may be the major control on both the U and Th distribution. Although less well defined because of large flight-line spacing, NURE spectral aeroradiometric surveys (Duval and others, 1989, 1990) also show anomalous U and Th signatures over many of these same areas. More closely spaced total-count aeroradiometric data are also in agreement (Force and others, 1982; Owens and others, 1989).

In contrast, the NURE-HSSR chemical data clearly outline the area of heavy-mineral deposits at the North Carolina–Virginia State line where gamma-ray radiation surveys do not. Thus, the NURE data may be used to find

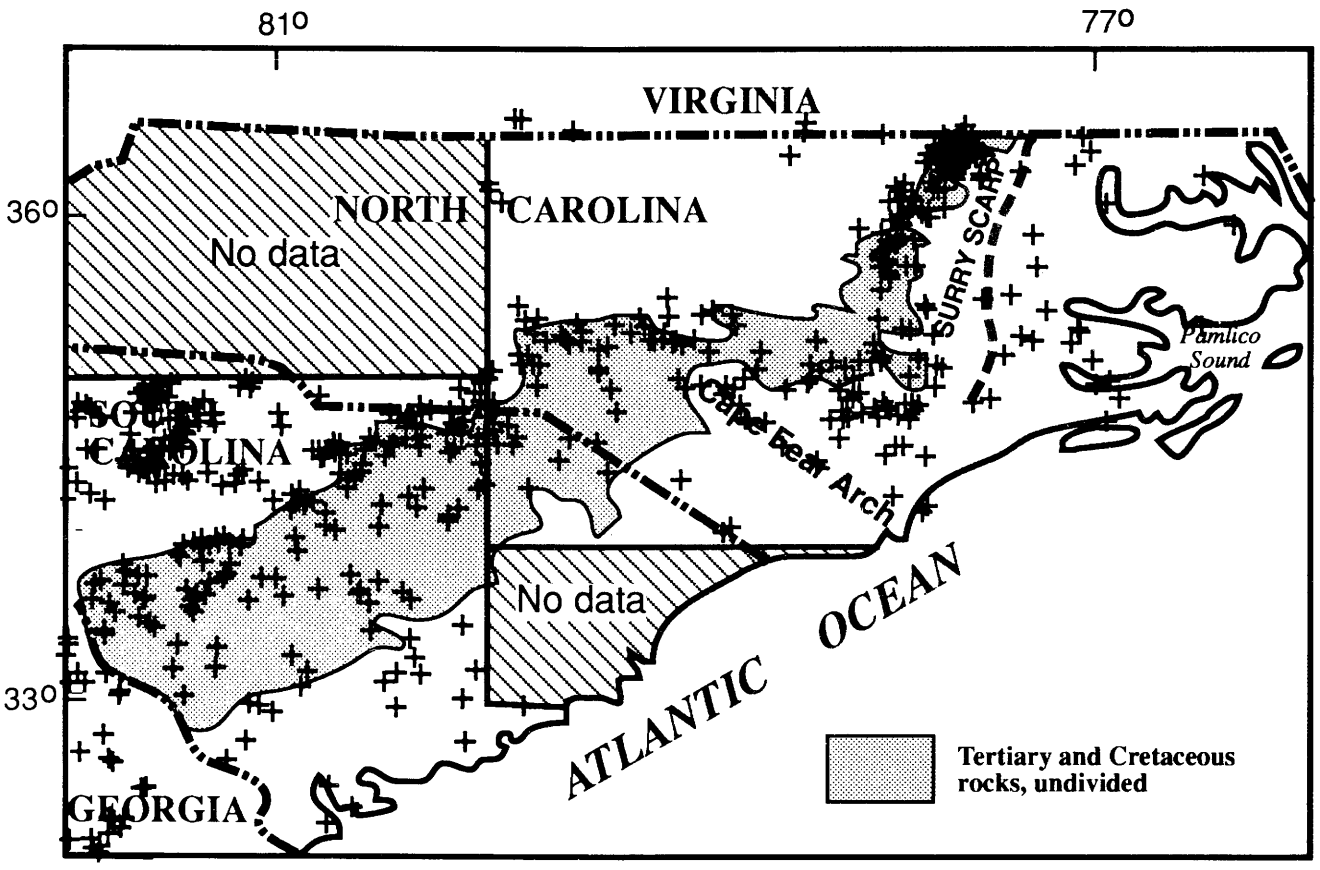

Figure 7. Locations of samples having > 0.015 percent Hf (N = 523).

Ti-bearing placer deposits that do not contain appreciable quantities of radioactive heavy minerals (i.e., monazite ± zircon). The congruence of a number of elements indicative of several placer minerals, therefore, is interpreted as an unambiguous indicator of the presence, and relative abundance, of commercially important heavy minerals.

Thus, in conjunction with geologic, topographic, and airborne geophysical information, the HSSR stream-sediment data can be used as a powerful exploration tool for placer deposits.

CONCLUSIONS

NURE-HSSR geochemical data is well suited for outlining small- to large-scale areas within the conterminous U.S. and Alaska permissive of Ti-Hf-REE-U-Th-bearing deposits of placer heavy minerals. The geochemical signature of known deposits of heavy minerals is identified over a large portion of North Carolina's Coastal Plain and Fall Zone regions. The Fall Zone region (generally coincident with exposures of Cretaceous and Tertiary sediments) in central Georgia, south-central Alabama, northeastern Mississippi, and western Tennessee shows a continuation of this geochemical pattern. Examination of only the most anomalous samples in the total sample population for any given element, as done in this paper, excludes much valuable information on potential large-volume/low-grade deposits of heavy minerals, particularly in coastal plain sediments where their geochemical expression is subdued. Examination of the 70 to 90 percentile group of the populations reveals persistent anomalies in Atlantic Coastal Plain sediments. The 50 to 90 percentile group over some midcontinent and western areas show similar geochemical signatures. Large areas in northeastern Kansas and eastern Nebraska, for example, may also have exploration potential for this mineral suite. The potential for Ti-Hf-REE-U-Th-bearing deposits of placer heavy minerals in surficially exposed sediments in the U.S. may be much greater than previously thought.

ACKNOWLEDGMENTS

Appreciation is extended to John C. Reed, Jr. for providing the digital geographic and geologic base map and to Terry L. Klein for reformatting the data. E. Force, J.

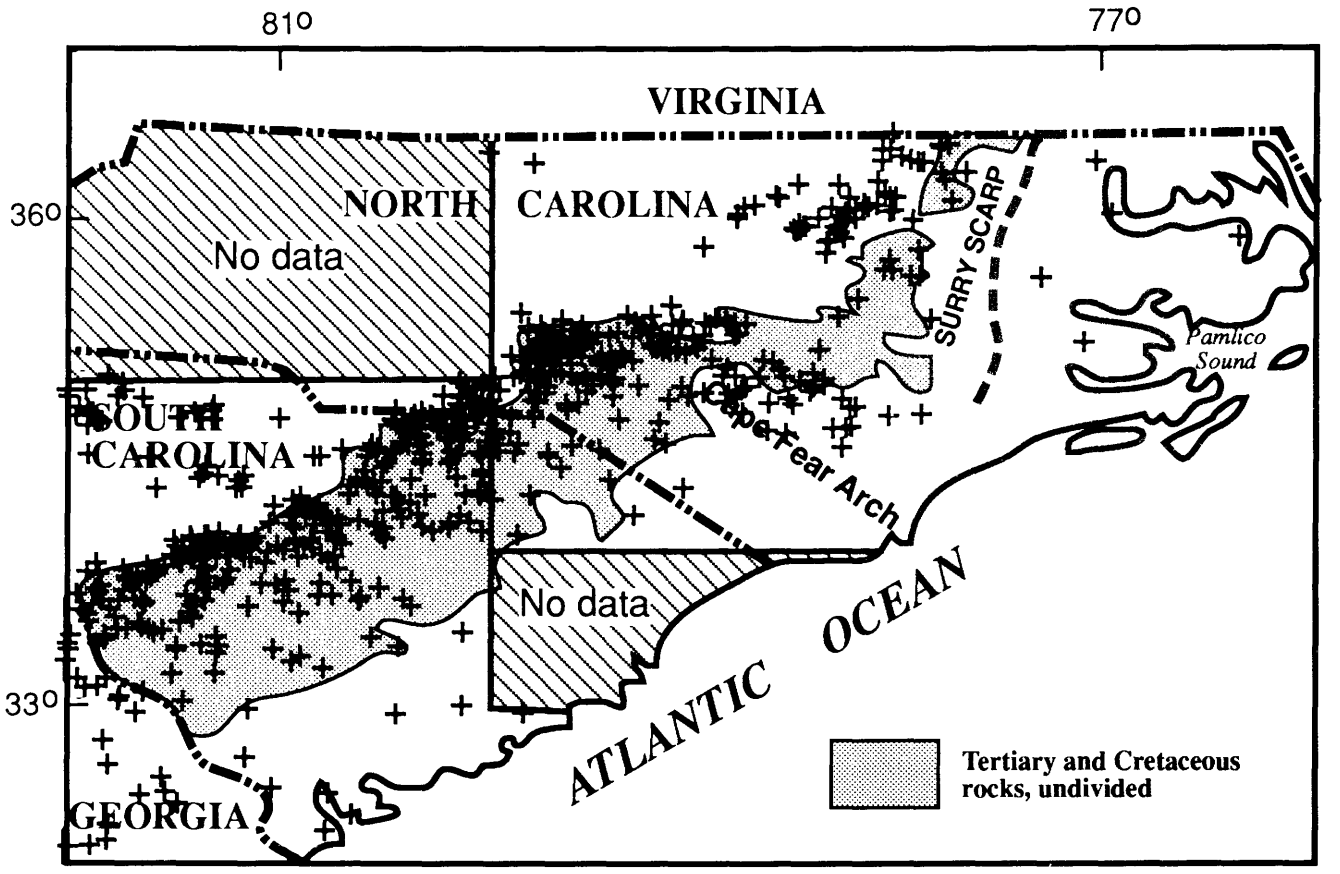

Figure 8. Locations of samples having > 0.01 percent U and Th combined (N = 631).

Philpotts, and K. Schulz provided thoughtful and constructive technical reviews.

REFERENCES CITED

Arendt, J.W., Butz, T.R., Cagle, G.W., Kane, V.E., and Nichols, C.E., 1980, Hydrogeochemical and stream sediment reconnaissance procedures of the uranium resource evaluation project: U.S. Department of Energy, GJBX–32(80), 53 p.

Averett, W.R., 1984, National uranium resource evaluation guide to data reports of the hydrogeochemical and stream sediment reconnaissance: U.S. Department of Energy, GJBX–5(84), 119 p.

Blackwelder, B.W., and Cronin, T.M., 1981, Atlantic Coastal Plain geomorphology illustrated by computer-generated block diagrams: U.S. Geological Survey Miscellaneous Field Studies Map MF–1242.

Duval, J.S., Jones, W.J., Riggle, F.R., and Pitkin, J.A., 1989, Equivalent uranium map of the conterminous United States: U.S. Geological Survey Open-File Report 89-478, 10 p., scale 1:2,500,000.

Duval, J.S., Jones, W.J., Riggle, F.R., and Pitkin, J.A., 1990, Potassium and thorium maps of the conterminous United States: U.S. Geological Survey Open-File Report 90-338, 16 p., scale 1:2,500,000.

Force, E.R., Grosz, A.E., Loferski. P.J., and Maybin, A.H., 1982, Aeroradioactivity maps in heavy-mineral exploration—Charleston, South Carolina, area: U.S. Geological Survey Professional Paper 1218, 19 p.

Grosz, A.E., 1983, Application of total-count aeroradiometric maps to the exploration for heavy-mineral deposits in the coastal plain of Virginia, *with a section on* Field-spectrometer-data reduction, by K.L. Kosanke: U.S. Geological Survey Professional Paper 1263, 20 p.

Grosz, A.E., Cathcart, J.B., Macke, D.L., Knapp, M.S., Schmidt, Walter, and Scott, T.M., 1989, Geologic interpretation of the gamma-ray aeroradiometric maps of central and northern Florida: U.S. Geological Survey Professional Paper 1461, 48 p.

Mertie, J.B., Jr., 1975, Monazite placers in the southeastern Atlantic States: U.S. Geological Survey Bulletin 1390, 41 p.

Overstreet, W.C., 1967, The geologic occurrence of monazite: U.S. Geological Survey Professional Paper 530, 327 p.

Owens, J.P., Grosz, A.E., and Fisher, J.C., 1989, Aeroradiometric map and geologic interpretation of part of the Florence and Georgetown 1°×2° quadrangles, South Carolina: U.S. Geological Survey Miscellaneous Investigations Series Map I–1948–B.

Robson, D.F., and Sampath, N., 1977, Geophysical response of heavy-mineral sand deposits at Jerusalem Creek, New South Wales: Bureau of Mineral Resources Journal of Australian Geology and Geophysics, v. 2, p. 149–154.

Staatz, M.H., and Armbrustmacher, T.J., 1979, Preliminary map of rare-earth provinces in the conterminous United States: U.S. Geological Survey Open-File Report 79-576-T.

Vlasov, K.A., ed., 1966, Geochemistry and mineralogy of rare elements and genetic types of their deposits [translated from Russian by Z. Lerman and Y. Brenner, Israel Program for Scientific Translations]: Jerusalem, Israel, 1633 p.

Wynn, J.C., Grosz, A.E., and Carlson-Foscz, V.L., 1990, Induced polarization response of some titanium-bearing placer deposits in the southeastern United States, *in* Fink, J.B., ed., Induced Polarization—Application and Case Histories: Tulsa, Oklahoma, Society of Exploration Geophysicists, Investigations in Geophysics No. 4, p. 280–303.

CHAPTER S

THE EFFECTS OF HYDROTHERMALLY ALTERED BEDROCK ON NATURAL FOREST VEGETATION IN THE SNOW CAMP–SAXAPAHAW AREA, NORTH CAROLINA, AND THE RESULTING EXPRESSIONS IN LANDSAT TM IMAGERY

By ALBA PAYÁS,[1] ROBERT G. SCHMIDT,[2] *and* ANDREU BONET[3]

ABSTRACT

Areas of intensely hydrothermally altered rocks in the Carolina slate belt are partially marked by anomalous patches of forest that are characterized by the forest community present and by the general condition of the canopy and understory. Parts of many of these hydrothermally altered areas are recognizable on processed satellite images and thus provide a useful exploration tool for locating unknown altered areas. The causative factors for the unusual forests and for their recognition on satellite images have been the subject of much speculation, but controlled data that may aid in identifying the factors have been difficult to obtain.

The Snow Camp–Saxapahaw area within the Carolina slate belt includes large masses of volcanic rocks that have been intensely altered by hydrothermal processes of the high-sulfidation type. Taxonomic and physiological studies of relevant forests and comparisons of soil analyses indicate that three factors are probably most important in influencing the distribution of satellite-detectable anomalous forest vegetation: (1) low amounts of available nutrients, especially Ca and Mg, in soils formed on the areas of most intense hydrothermal alteration, (2) rocky, relatively thin soils, and (3) south- or southeast-facing slopes. Both the second and third factors can be assumed to augment water stress during dry periods.

INTRODUCTION

The Snow Camp–Saxapahaw area chosen for this study is located within the Carolina slate belt, 20 km south of Burlington and 30 km west of Chapel Hill, in Alamance and Chatham Counties, North Carolina (fig. 1). Most of the study area is currently being mapped at a scale of 1:24,000. The 268-km^2 area is underlain by volcanic and volcaniclastic rocks of a wide variety of textures and compositions, from basaltic to rhyolitic. As in many other parts of the slate belt, these volcanic rocks are intruded by many plutons and small stocks of shallow intrusive rocks (also of diverse compositions, from gabbroic to granitic), many of which have associated strong hydrothermal alteration. Mineral potential of the area includes high-grade pyrophyllite, which has been quarried, and gold worked in various prospects and small-scale mines. Outcrops are locally abundant in the Snow Camp–Saxapahaw area, though for the most part, they are widely scattered, and in some of the area, they are rare.

Forest vegetation of the ridges and resistant hills in the Piedmont area have been described as more like that of the mountains farther west (Braun, 1950) and unlike the oak-pine association of the surrounding Piedmont (Milton and others, 1983). Because many of the intensely altered core zones form erosion-resistant ridges, there is a tendency for the forest communities on them to be different due to the topography alone; the effects of rock alteration are superimposed on that predictable variation.

[1]Servei Geológic de Catalunya, Barcelona, Spain

[2]U.S. Geological Survey, Mail Stop 954, 12201 Sunrise Valley Drive, National Center, Reston, VA 22092

[3]Botany Department, University of Barcelona, Barcelona, Spain

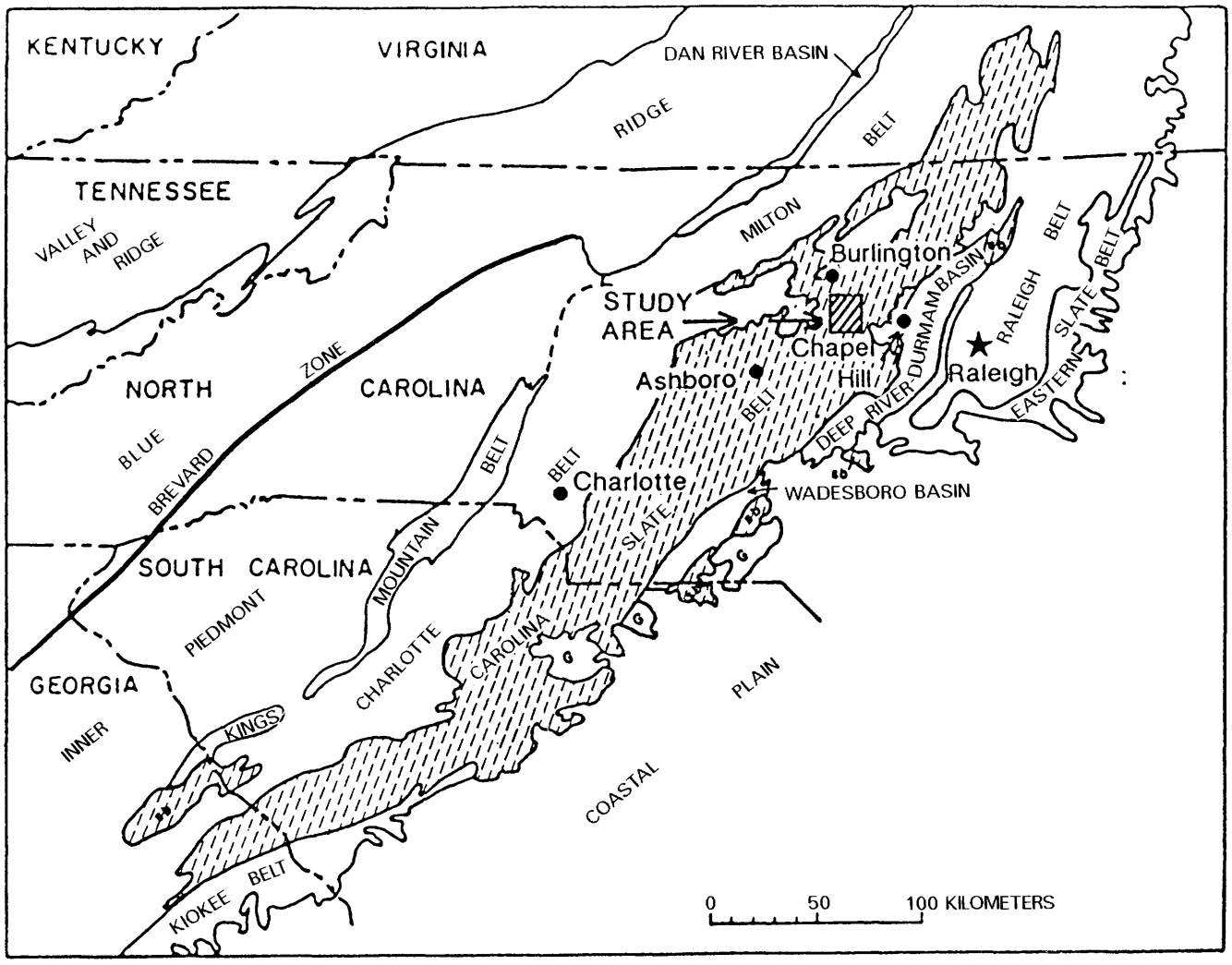

Figure 1. Index map showing the location of the Snow Camp– Saxapahaw study area (rectangle with diagonal line pattern) in the Carolina slate belt, North Carolina.

Identification of areas of hydrothermally altered rocks using processed Landsat images has been tested in the region with some success (Schmidt and Koslow, 1986; Schmidt and others, 1987).

Objectives.—The major objective of this study was to more precisely define the factors enabling discrimination on satellite images of forest areas that are present over bedrocks that have undergone intense hydrothermal alteration. We wanted to compare forest characteristics at approximately the same date, November 9, as that of our two image sets from previous years.

Field survey method.—Surveys were conducted November 1–10, 1989, to determine species present, size, tree density, canopy density, and foliage condition in areas with different slopes. Transects were run in areas of altered rocks and also on unaltered background areas; these transects were restricted to locations where we believed the geology to be well known. Transects were laid out using magnetic compass, and observation sites on the lines were spaced 20 m apart with a calibrated nylon rope. At each field observation point, the immediately surrounding area was divided into four equiangular quadrants measured from the compass bearing of the transect line. In each quadrant, the closest canopy tree (tree whose top is not shaded by another) was selected, the species and diameter 1 m above the base determined, and the distance from the observation point measured. Observation-site-to-tree distances were measured by tape and tree diameters by caliper. Identification of species was made in situ, and for a few less common trees such as *Carya*, only genus was determined. Four visual approximations of leaf abundance and greenness were made per 20 m interval by each of two observers, and the results were averaged. Relative greenness is a value obtained by estimating percent of chlorophyll retention ("G" values of 1 to 4 indicate: 1, 1–25 percent of leaves present are green; 2, 25–50 percent

are green; 3, 50–75 percent are green; and 4, 75–100 percent are green), and percent of leaves remaining on tree ("L" values of 1 to 4 indicate: 1, 0–25 percent of leaves remain on tree; 2, 25–50 percent remain; 3, 50–75 percent remain; and 4, 75–100 percent remain). The relative greenness was then derived by multiplying G times L, yielding index values of 1–16, which were subsequently normalized to 100. Percent canopy cover was determined by observers who used sighting frames (camera view finders) to estimate the amount of sky covered by tree canopy. Two observers each made four observations per site, and the results were averaged. From the data collected in this manner, graphs were prepared showing the abundance of *Quercus prinus* (chestnut oak), relative greenness, canopy density, and trees per hectare.

Soil samples for nutrient analysis were collected from points on the transects in March 1990 in the manner described in Milton and others (1983).

Time of data collection.—Our study was restricted to Landsat TM data sets already in hand, and these data sets were obtained during the normal time of leaf coloration and leaf fall (November 9, 1982, and November 9, 1988). These data sets gave good results in our study, but we do not know if a different time of year would have been better. Forest foliage changes rapidly from day to day during leaf senescence, and one assumes that conditions vary somewhat on the same calendar date from year to year. However, in applying Landsat data to forest studies, we are comparing one part of the forest to another in essentially an instant of time rather than comparing against any fixed standard. Certainly some of the foliage characteristics that we found significant may not be significant at other times of the year. The 1982 TM data gave much better discrimination of quartz-rich soils in tilled fields, perhaps as a result of dryer soil on the data-collection date.

Acknowledgments.—Our research was undertaken cooperatively by the U.S. Geological Survey, Branch of Eastern Mineral Resources, and the Servei Geológic de Catalunya, Barcelona, Spain. It has built upon earlier work in the area by the U.S. Geological Survey in cooperation with Instituto Tecnológico GeoMinero de España, Madrid.

Transportation and field expenses in North Carolina for Payás and Bonet were supported by NATO Collaborative Project No. 530/88. Images for field use were processed by the Institut Cartogràfic de Catalunya, Barcelona, Spain, which also transcribed Landsat TM data sets to floppy disks for further processing in the United States. We greatly appreciate discussions of methods and interpretations as well as help in the field by L.C. Rowan, N.M. Milton, C.M. Ager, M.S. Power, M.H. Podwysocki, Richard Brooks, Karl Shaffer, and E.M. Haskin. We are especially grateful to the North Carolina Department of Agriculture, Agronomic Division, Soil Testing Laboratory, Dr. D.W. Eaddy, Director, and M.R. Tucker, Chief, Soil Testing Section, for analyses of available nutrients in soils we collected from the study area.

GEOLOGY

The study area, in central North Carolina, is underlain by rocks that are generally typical of the Carolina slate belt in central and northern North Carolina. The slate belt consists of mostly arc volcanics of a variety of compositions, and they have been intruded by several generations of subvolcanic and plutonic rocks. These rocks and the hydrothermal alteration that has affected many of them have been discussed in greater detail by Schmidt and others (1990).

Volcanic and volcaniclastic rocks.—Roughly four-fifths of the area is underlain by volcanic and volcaniclastic rocks that are provisionally divided into two volcanic rock groups (fig. 2). The oldest group is a complex of small heterogeneous volcanic units within which only a few units could be mapped separately, and the younger is an extensive crystal-rich rhyodacite and dacite unit that rests unconformably upon the older group (Schmidt and others, 1990). Both groups are tentatively interpreted to correspond to 600–560-Ma rocks that have been dated in other parts of the slate belt. The basaltic to rhyolitic older group is mostly andesitic and dacitic but includes a flow-banded siliceous rhyodacite-rhyolite unit shown separately in figure 2.

Intrusive rocks.—Plutonic and subvolcanic rocks of several ages are very common in parts of the Snow Camp–Saxapahaw area. The largest plutonic bodies are granite, quartz diorite, or tonalite, in part forming intrusive complexes with masses and screens of hornfels and metavolcanic rocks. Fine-grained granophyric granite and quartz monzonite form plutons in the Cane Creek Mountains that probably connect to form one body at depth. Formed at shallow depth, these plutons are surrounded by somewhat silicified zones, their extent indicated by soils type. All of these pre-metamorphic intrusives may have been formed during a long span of time, but before about 320 Ma. The younger tonalite and quartz diorite are probably close to 300 Ma, the approximate age of several, dated "young plutons" of the slate belt. Areas mapped as little metamorphosed tonalite and quartz diorite also include considerable pre-metamorphism granitic rock into which masses of the younger rock have intruded. The youngest intrusive rocks are mafic dikes of Mesozoic age that are not shown on figure 2.

Metamorphism.—All of the volcanic rocks and perhaps three-fourths of the intrusive rocks in the area have undergone regional metamorphism, mostly to mid-greenschist facies, with local development of new actinolite or hornblende at a few sites. Open fractures and vugs have

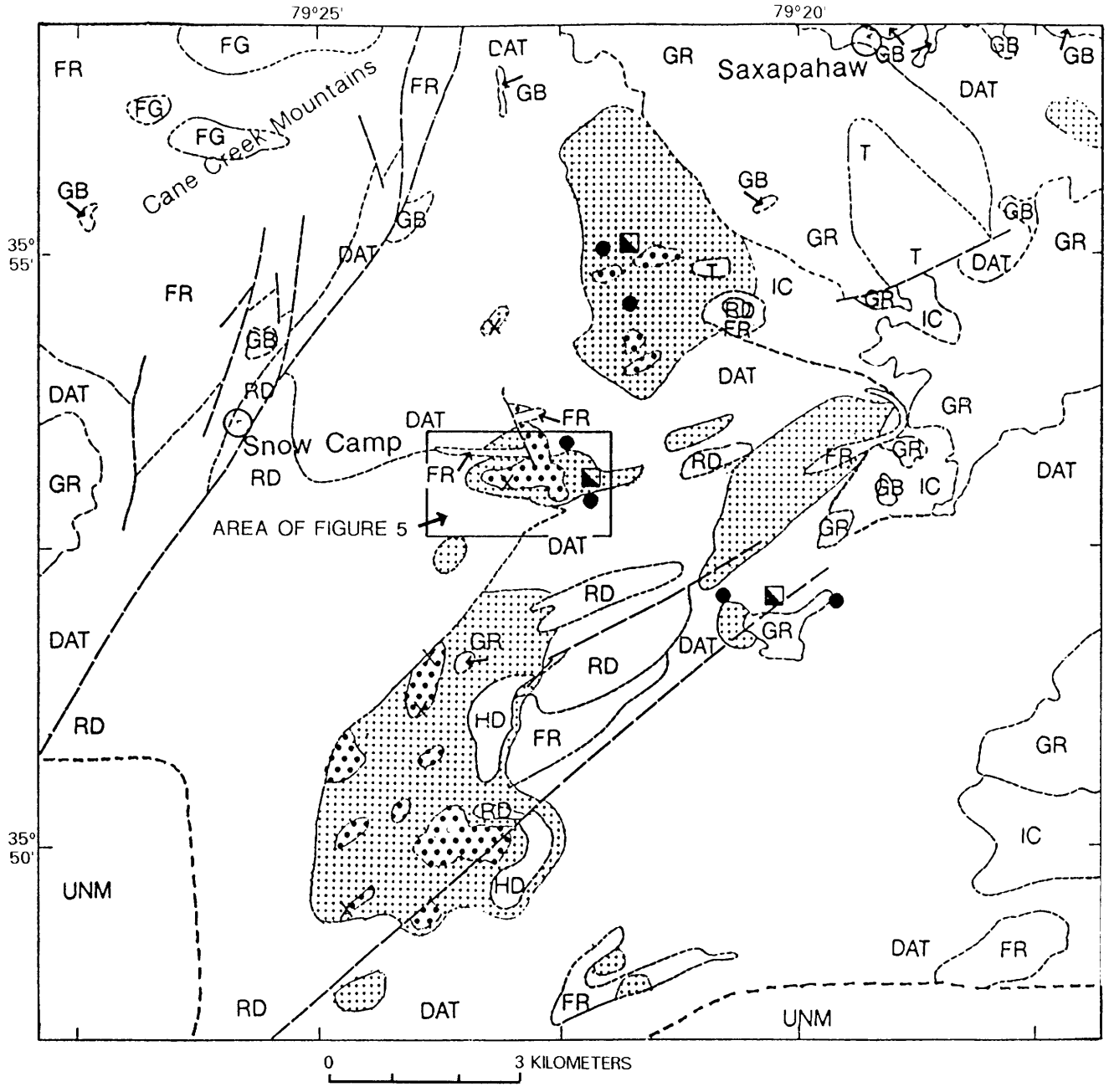

Figure 2 (above and facing page). Geologic map of the Snow Camp–Saxapahaw study area showing the distribution of hydrothermal alteration, former gold mines, and gold anomalies as determined by panning of stream sediments. Field mapping, 1985–1989, by Robert G. Schmidt, Elizabeth H. Hughes, Pablo Gumiel, Alba Payás, and Carmen Anton-Pacheco. Geologic units in southeast corner of map adapted from Wilkinson (1978).

been eliminated in the strongly altered rocks, thus changing their appearance substantially from that of unmetamorphosed equivalents as observed in other regions. The youngest plutonic and subvolcanic granitoid intrusives are essentially unmetamorphosed.

Structural geology.—Volcanic rocks of all of the Snow Camp–Saxapahaw area have open to tight folding, but recognizable layering is so rare that folding is not mappable. Straight, northeast-trending, linear features suggest faults and shear zones, and many of those checked in the field were found to be zones of sheared or brecciated rocks. A few north- and northwest-trending faults are suggested by offset alteration zones and rock units, but none of these were specifically identified in the field.

Hydrothermal alteration.—Extensive hydrothermal alteration has taken place in the volcanic and intrusive

EXPLANATION

VOLCANIC ROCKS

RD — Crystal-rich rhyodacite/dacite with many small inclusions, very uniform texture and composition throughout. Thin cobble-rich fragmental layer at base not shown separately here

UNCONFORMITY

DAT/FR — Heterogeneous mostly dacitic and andesitic tuffs, part fragment-rich; includes basaltic to rhyolitic units, includes distinctive lenses of flow-banded rhyodacite/rhyolite (FR) that are interpreted to thicken in northwest corner of area (Cane Creek Mountains)

HYDROTHERMALLY ALTERED ROCKS

Quartz-sericite-pyrite and quartz-paragonite rocks; also includes potassic and epidote-rich alteration near plutons. Protolith textures generally destroyed in central parts of zones

Intensely altered very siliceous central core zones and associated pods of pyrophyllite-andalusite-pyrite rock

OTHER AREAS

UNM — Areas unmapped in this study, mostly intermediate volcanic rocks

INTRUSIVE ROCKS

T — Tonalite and quartz-diorite, little metamorphosed. Mapped areas include some areas of pre-metamorphism plutonic rock as well

REGIONAL METAMORPHISM

IC — Quartz diorite/hornfels/volcanic rock injection complexes

HD — Hornblende granodiorite

GR — Granite, quartz diorite and tonalite, plagioclase oscillatory zoning destroyed by regional metamorphism

FG — Fine-grained granophyric granite and quartz-monzonite

GB — Gabbro, porphyritic gabbro, and hornblende gneiss

Geologic contact, dashed where inferred

Inferred fault

MINES AND PROSPECTS

● Pyrophyllite or sericite mines and prospects

Gold prospects and small mines

x Panned stream-sediment concentrate with visible gold

rocks, and it is most significant in the oldest units where alteration is of the high-sulfidation type as defined by White and Hedenquist (1990). The very large Snow Camp–Saxapahaw alteration systems make up a northeast-trending zone about 13 km long and up to nearly 4 km wide (Hughes, 1987). They share many characteristics with over 40 similar areas in the Carolina slate belt (Schmidt, 1985; Schmidt and Klein, 1985).

The most intensely altered parts of the systems, presumably innermost as the systems were formed, consist of large volumes of almost pure, fine-grained quartz rock. Near the edges of these cores are several smaller, in part minable, masses of pyrophyllite-quartz, including various amounts of pyrite and andalusite. These core zones are now mostly surrounded by extensive envelopes of quartz–white mica (sericite and paragonite) altered volcanic and subvolcanic rocks. Propylitic alteration probably formed a zone exterior to the quartz–white mica envelope, but we were not able to map it separately from the surrounding volcanic rocks that have undergone greenschist-facies metamorphism.

Metallic mineralization and pyrophyllite deposit.—Presently recognized gold and silver mineralizations are mostly in areas of strong quartz–white mica and probably propylitic alteration. Such mineralization is also found in some narrow zones along northeast-trending shears and is generally accompanied by quartz-sericite alteration (fig. 2) (D'Agostino and Schmidt, 1986; Schmidt and others,

Table 1. Nutrient elements available to plants in composite samples of A-horizon soils.

[Analyses by Soil Testing Section, Agronomic Division, North Carolina Department of Agriculture. The soil test indices and factors for conversion of indices to parts per million are used as defined in the Soil Testing Section, Standard Soil Test Report]

	Substrate		
	Unaltered rocks (2 samples)	Probably altered rocks (2 samples)	Strongly altered rocks (16 samples)
Cation exchange capacity (CEC, in meq/100 cm)	3.3, 4.4	3.3, 3.5	2.3–4.3 avg 3.3
Base saturation (percent of CEC)	36, 40	21, 28	7–20 avg 11.3
pH	4.5, 5	4.4, 4.4	3.8–4.6 avg 4.2
Phosphorus index × conversion factor (ppm)	1, 5	1, 4	1–5
Potassium index, converted to available K (ppm)	63, 35	70, 78	31–63 avg 44
Calcium (percent of CEC) converted to available Ca (ppm)	159, 181	60, 100	20–80 avg 28
Magnesium (percent of CEC) converted to available Mg (ppm)	62, 53	29, 29	10–20 avg 15
Manganese index (converted to ppm)	98, >100	30, 20	1–45 avg 5
Copper index (converted to ppm)	0.6, 0.4	0.2, 0.4	0.2–1.0 avg 0.4

1987). Several spotty occurrences of anomalous gold concentrations have been found in high-silica core-zone rocks as well. Pyrophyllite ore was extracted from one major quarry and two smaller pits in the area.

BEDROCK, SOILS, AND FOREST VEGETATION ASSOCIATIONS

General correlations of bedrock type, especially hydrothermally altered rocks, and forest tree communities have been understood in a general way and have been used in prospecting for pyrophyllite for many decades. By using Landsat remote-sensing techniques during geologic mapping in the region, we have been able to greatly expand the known areas of hydrothermal alteration because, to an important degree, forests of unique composition and condition can be recognized in processed Landsat TM imagery. At the same time, this application has greatly increased the need for better understanding of the processes involved.

The most common soil types in the area are the Herndon, Goldston, and Goldsboro silt loams. Although certain mapped soil types correlate well with specific mapped bedrock, the quartz-rich soil types associated with highly altered bedrock are also commonly present on other rock substrates.

Bedrock-controlled soil characteristics that strongly influence forest condition in this area include available nutrients, textures, and trace metals, as well as drainage, rockiness, soil depth, and slope direction.

We suspected intuitively that the core-zone soils lacked available nutrients because of the siliceous nature of the altered bedrock and the slow growth of trees on these sites, but standard total chemical analyses were inadequate to measure the soil nutrients available to growing plants. Consequently, 16 soil samples, each a composite of more than 10 subsamples taken within a 10 m circle, were obtained from the A horizon, below the organic layer, in areas of strongly hydrothermally altered bedrock, and 4 soil samples were obtained from areas of relatively weak alteration or unaltered rock. These were analyzed for a variety of constituents (table 1), and several distinct and consistent variations were found between areas of unaltered and highly altered bedrock; however, we recognize the limitations of our small data set for unaltered rock.

Soils and vegetation, areas of unaltered bedrock.—Most areas of volcanic and plutonic rocks in the Carolina slate belt are overlain by soils that support healthy natural forests with many species of deciduous and evergreen trees and understory trees and shrubs. We recorded 10–15 species on single transects in normal forests, and a total of 24 species were recorded in all transects on unaltered rocks, not including shrubs and understory trees. The canopy is generally closed, but when openings are present, they permit a dense second growth of canopy-tree saplings and understory species.

In five forest transects (252 trees observed) in areas of unaltered rocks, no species exceeds 19 percent (table 2). The seven most abundant species are: *Acer rubrum*, 19.0 percent; *Quercus alba*, 17.5 percent; *Q. stellata*, 10.0 percent; *Q. velutina*, 9.0 percent; *Carya sp.*, 6.0 percent; *Liquidambar styraciflua*, 4.8 percent; and *Liriodendron tulipifera*, 4.0 percent. Typical understory trees and shrubs include *Ilex*, *Vaccinium*, *Gaylussacia*, *Azalea*, *Rhododendron*, *Hamamelis*, and *Oxydendrum*.

Nutrient analyses in the normal forest, especially for calcium and magnesium, tend to be relatively low (table 1) but seem adequate to permit healthy forest growth. In normal forests (areas of unaltered rock) that were not on any transect, metals analyses ranged from below detection up to (in ppm), Cu = 120, Mo = 27, Pb = 39, and Zn = 73

Table 2. Tree species abundance related to bedrock type.

[All numbers, except total number of trees in sample, in percent. Rk, rock; sl, slopes]

Species	Underlying bedrock type and slope			
	Unaltered rk	Strongly altered rock		
	All slopes	All slopes	South, SE. sl	North, NW. sl
Quercus prinus	1.2	58.5	53.9	55.0
alba	17.5	10.3	14.4	10.6
falcata	3.6	2.4	1.1	3.3
velutina	9.1	5.8	5.6	6.1
marilandica	1.2	1.2	1.1	1.7
stellata	10.0	1.2	0.6	1.1
phellos	3.2			
Fraxinus sp.	3.6			
Prunus serotina	0.8			
Acer rubrum	19.0	6.0	8.3	5.6
Pinus virginiana	0.8	3.4	4.4	3.3
echinata	2.8	5.8	5.0	5.6
taeda	0.4			
Liriodendron tulipifera	4.0	0.4	0.6	
Liquidambar styraciflua	4.8			
Ulmus sp.	1.2			
Juniperus virginiana	2.4			
Cornus florida	3.6			
Oxydendrum arboreum	3.2	2.0	1.7	2.8
Nyssa sp.	0.4	1.2	1.1	2.2
Carya sp.	6.0	1.6	2.8	1.7
Fagus grandifolia	1.2	0.2	0.6	
Total	**100.0**	**100.0**	**100.0**	**100.2**
Total trees in sample	252	504	180	180

(all total element present) without observable effects on the condition of trees.

Soils and vegetation, areas of hydrothermally altered bedrock.—The forest community common on areas of intensely hydrothermally altered bedrock is noticeably less diverse than the surrounding forest (table 2, fig. 3). Somewhat fewer total species are present—4–11 on each of seven transects—and of these, a small number generally dominate. Only six species, *Quercus prinus*, *Q. alba*, *Q. velutina*, *Acer rubrum*, *Pinus virginiana*, and *P. echinata* make up 89.8 percent of the 504 trees sampled. However, the most noticeable difference is in the abundance of *Quercus prinus*, the chestnut oak. This species makes up most of the canopy forest over extensive areas at these sites and averages 58 percent of the forest for all of the altered area sampled (table 2). Furthermore, forests at these sites are characterized by a relatively open canopy and lack of a significant understory. Except on transect B, fewer species were present on the northwest-facing slope than on the sun-facing slope. The north slope of transect D had only four species (fig. 3). Because species composition of the forests on north and northwest slopes is much like that on the sunny slope and remains typical of forests on highly altered bedrock, the spectral reflectances in TM bands 4 and 5 are reduced there about 30 percent; band 3 is reduced about 20 percent; but band 2 is reduced only about 4 percent (fig. 4). Our estimates of greenness, admittedly somewhat subjective, indicate more chlorophyll remaining in the canopy on level and sun-facing slopes, which one would expect to reduce spectral reflectance there (fig. 4, transects L and D-1).

In soil analyses made to determine available nutrients, base-exchangeable Ca and Mg in hydrothermally altered areas were found to be only fractions (one-sixth and one-fourth) of the amounts present in forest soils formed on unaltered volcanic rock substrates (table 1), which are already relatively poor in Ca and Mg, thus suggesting a significant deficiency in these important nutrients. The relative amounts of other available nutrients determined do not seem significantly different from those in nearby forest soils over unaltered bedrock.

Maximum metal values within areas of strong hydrothermal alteration and anomalous forest vegetation ranged from below detection to the following (in ppm): Cu = 49, Pb = 30, Zn = 20, and Mo = 7.3. These contrast with the greater range (from below detection to greater amounts for each metal) in areas without anomalous vegetation. Thus, the distribution of these metals in the Snow Camp–Saxapahaw area does not appear to be a factor in the growth of the anomalous forests.

Although there seems to be no significant difference in tree species present on north and northwest slopes as compared with sun-facing slopes (table 2), visual examination of the forests indicates considerable difference in the condition of the trees in these two topographic situations. While the forest canopy in both tends to be relatively open and the understory vegetation very sparse despite the favorable light conditions, trees on the south-facing slopes are more spreading, slower growing, and some have many dead or weakened limbs. In contrast, trees on the north-facing slopes are of normal height and robustness. It would appear, therefore, that differences in the spectral response between the two slope environments recorded in Landsat data depend on forest condition—this may include tree structure that permits more sunlight on the sunny-slope forest floor, although this effect would be partly counteracted by more green leaf retention.

DATA ANALYSIS

Geobotanical data collected in the field were compared with bedrock geology and with spectral reflectance data collected by satellite (Landsat Thematic Mapper). Of 12 transects surveyed November 1–10, 1989, six were selected for final analysis on the basis of completeness of data and the representative nature of the forests.

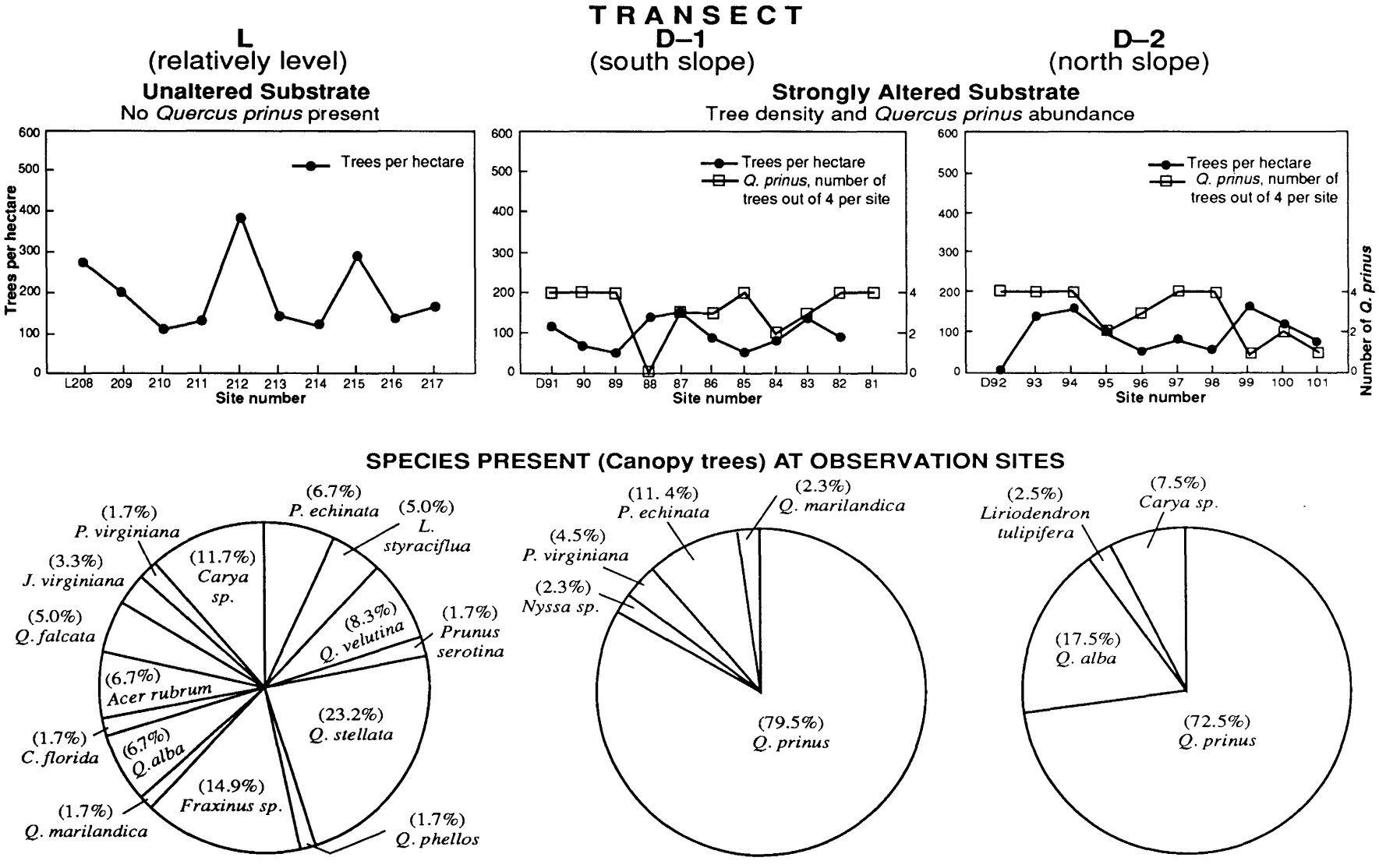

Figure 3. Trees per hectare and *Quercus prinus* distribution (top figures), and species abundance for three typical forest conditions. Transect L represents a forest on level ground and unaltered bedrock; transect D-1 represents a forest on a south-facing slope with highly altered bedrock, and transect D-2 is a continuation of D-1, with similar bedrock, on a north-facing slope. Some genera are abbreviated as follows: *C, Cornus; J, Juniperus; L, Liquidambar; P, Pinus; Q, Quercus.*

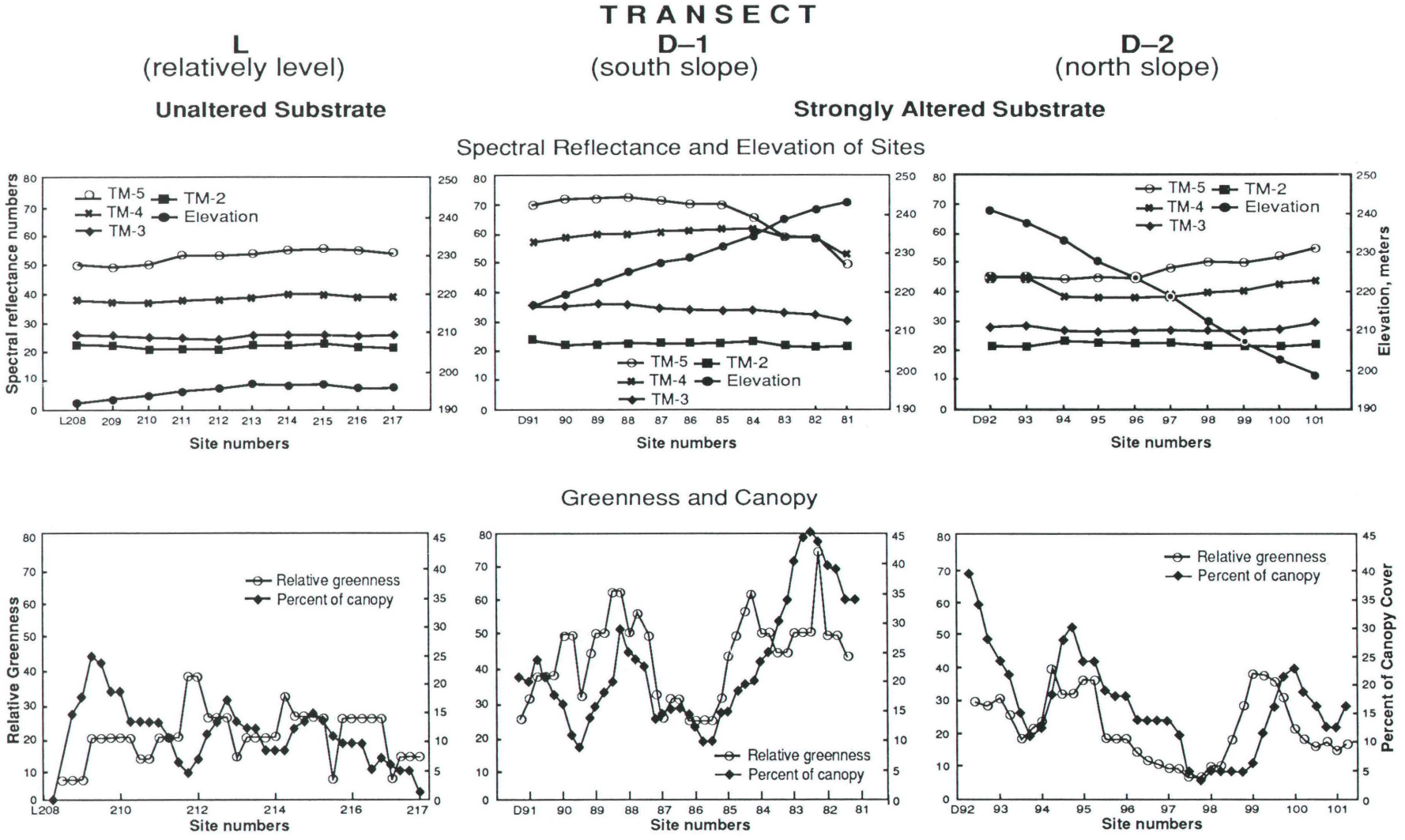

Figure 4. Site elevations, TM reflectance values, relative greenness, and percent of canopy cover for three typical forest conditions. Transect L represents a forest on level ground and unaltered bedrock, transect D-1 represents a forest on a south-facing slope with highly altered bedrock, and transect D-2 is a continuation of D-1, with similar bedrock, on a north-facing slope.

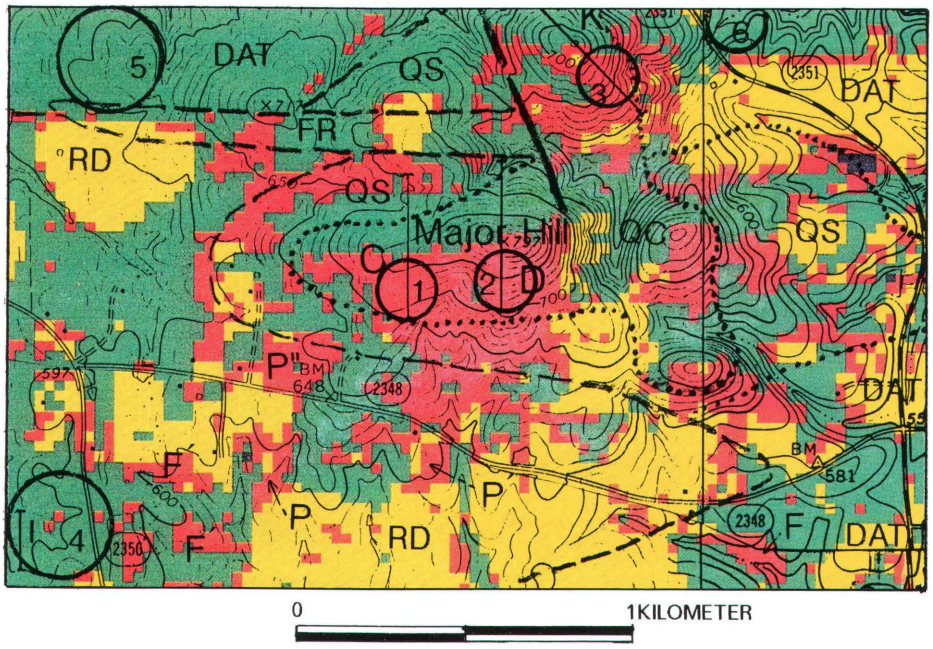

Figure 5. Detail of a digitally classified image of the Major Hill area superimposed on a standard topographic map. Green, ordinary forest; red, forest on high-silica or altered rock substrate; yellow, ordinary bare earth or stubble field or green, cropped field; dark blue, water. Geologic units are coded as follows: RD, crystal-rich rhyodacite/dacite; DAT, dacitic and andesitic tuffs; FR, flow-banded rhyodacite/rhyolite; QS, quartz-sericite-pyrite altered rock; QC, quartz-rich core zone. In our trials, a supervised classification using a maximum likelihood method resulted in images that most accurately represented forested areas above altered bedrock or highly siliceous bedrock and general cultural features. Some, if not most, of the areas that seem to be falsely classified as forest on altered or high-silica bedrock are mixed pixels of forest and field or grassed areas. These generally include pasture with scattered trees (probably areas P, P′, P″) or unusually open forest (F). Falsely classified forests marked F′ are not explained. C, D, K, and I are botanical transects. The image was generated on a 286-type personal computer using the Dragon Image Processing System and a maximum likelihood classifier. The circles show typical areas used to obtain characteristic TM reflectance values for hydrothermally altered rock (circles 1, 2, and 3) and normal forest (circles 4, 5, and 6). Statistical characteristics for the supervised classification of field and water areas were extracted in a similar manner.

Digital values for TM bands 2, 3, 4, and 5 along the transects were extracted by generating an enlarged portion of a classified image on a CRT screen and superimposing a topographic map on which the transect had been plotted in the field. Some inaccuracy in transect location is assumed because the 1:24,000 topographic maps are imperfect representations of minor land-surface details, and some areas lacked features that could be used as exact reference points. Digital numbers were extracted for each TM band for each pixel on the transect line and for one pixel on each side. Reflectance values that were finally used were moving averages on the center points of nine-point squares. Spectra for three typical transects are shown in figure 4.

Influence of slope direction on forest characteristics.—Digital classification of Landsat data can be used to identify forests growing on strongly altered rock substrates on level ground and sun-facing slopes but is much less reliable on north-facing slopes. Five transects were laid out on areas of highly altered rocks, each one including both south or southeast slopes and north- or northwest-facing slopes, but full data for greenness index and canopy were not collected for three of the transects. These slopes range from about 1:4.5 to 1:8. Transect D, the one judged to have the "most typical" forests throughout, is shown graphically in figures 3 and 4 and on a detailed segment of a classified image with topography superimposed (fig. 5). The abundance of *Quercus prinus* on the north slope is similar to that on the south slope (fig. 3); and the percentage of forest canopy is about the same, but there are significant differences in the relative greenness (table 3). Reflectance spectra of the north slope more closely resemble those of transect L and of other areas with unaltered bedrock than they do those of the south slope of transect D (fig. 4). We believe that the anomalous forests can be distinguished by their TM reflectance spectra where the

Table 3. Relative greenness of canopy forests on contrasting slope environments.

Group	Transect	Date of observation (Nov. 1989)	Mean relative greenness
Hydrothermally altered substrate			
SE. slopes	D-1	5	44.7
	K-2	8	26.1
Relatively level	F	6	35.1
	I	7	25.0
NW. slopes	K-1	8	29.1
	D-2	5	22.7
Unaltered substrate			
	E	5	24.6
	J	7	21.1
	L	9	20.0
	G	6	5.3

relatively open canopy combined with flat or sun-facing slope permit good illumination of the ground surface, irrespective of the measured greater greenness there. We also believe that more bare ground is exposed on the sun-facing slopes. Not surprisingly, spectra characteristic of anomalous forests are also obtained in open, forested pastureland and where individual pixels are made up of part forest and part field.

Digital classification.—Detailed results of a "maximum likelihood digital classification" of a small part of the area are shown in figure 5. Identification of anomalous forests growing on highly altered substrates is quite reliable on ridge crests and sun-facing slopes, but the similar forests on north and northwest slopes are generally not differentiated. "Anomalous bedrock" classifications in unaltered areas are believed to be related to very siliceous bedrocks, and some appear to be "edge effects" caused by pixels including more than one surface type. A few unexplained anomalous areas remain to be field checked.

CONCLUSIONS

Many areas of intensely hydrothermally altered rocks of the Carolina slate belt can be identified on processed Landsat TM imagery, thus providing a useful aid to mineral exploration. Our data confirm that forests in areas of intensely altered rocks are characterized by a diminished number of species and by dominance of *Quercus prinus*, the chestnut oak, as well as by differences in tree structure.

We believe that three main factors contribute to the forest conditions that can be recognized in Landsat TM data. These are: (1) seriously diminished available Ca and Mg in the soil, (2) a thin and (or) very rocky soil that accentuates moisture stress during dry periods, and (3) position of the forest on top of a dry ridge or on a south- or southeast-facing slope, causing additional moisture stress. The many ridge crests and south- or southeast-facing slope areas identified as "anomalous" by digital classification had all three factors present. Other anomalous ridges, generally with *Quercus prinus* forests, are underlain by siliceous rocks that are either unaltered or not more than moderately altered.

Metals present in the hydrothermally altered rocks do not appear to be a stress-causing factor in this study area.

Several areas have been identified where the species present reliably reflect the strongly altered rock substrate but where, due to a location on north- or northwest-facing slopes, water stress is presumably less and the forest floor less illuminated in mid-morning (the time of satellite data collection). These sites have reflectance spectra closer to those of a normal forest.

The Landsat data sets available to us were collected during periods of partial leaf coloration and leaf fall. All other experiments with which we are familiar using digital classification of images of southeastern Piedmont forests have used autumn or winter data sets. Obviously, data sets obtained earlier in the growing season need to be studied before we will know what part of the year gives the best images for these geologic purposes.

REFERENCES CITED

Braun, E.L., 1950, Deciduous Forests of Eastern North America: Philadelphia, Blakiston, 596 p.

D'Agostino, J.P., and Schmidt, R.G., 1986, Gold in panned concentrates from southern Alamance County, central North Carolina: U.S. Geological Survey Open-File Report 86–453, 5 p.

Hughes, E.H., 1987, The geology and alteration centers of the Snow Camp mine–Major Hill area, central Carolina slate belt, Alamance and Chatham Counties, North Carolina: U.S. Geological Survey Open-File Report 87–180, 29 p.

Milton, N.M., Collins, William, Chang, Sheng-Huei, and Schmidt, R.G., 1983, Remote detection of metal anomalies on Pilot Mountain, Randolph County, North Carolina: Economic Geology, v. 78, p. 605–617.

Schmidt, R.G., 1985, High-alumina alteration systems in volcanic rocks and their significance to mineral prospecting in the Carolina slate belt: U.S. Geological Survey Bulletin 1562, 59 p.

Schmidt, R.G., and Klein, T.L., 1985, High-alumina alteration systems and their role in mineral exploration, southeastern United States, *in* Krafft, Kathleen, ed., USGS Research on Mineral Resources—1985, Program and Abstracts: U.S. Geological Survey Circular 949, p. 47–48.

Schmidt, R.G., and Koslow, M.H., 1986, Preliminary map showing the occurrence of siliceous rocks in central North Carolina derived from enhanced principal component Landsat images: U.S. Geological Survey Miscellaneous Field Studies Map MF–1817.

Schmidt, R.G., Payás, Alba, Gumiel, Pablo, and D'Agostino, J.P., 1987, The Saxapahaw, North Carolina, gold occurrences—Search for a deposit model and new remote sensing techniques, *in* Sachs, J.S., ed., USGS Research on Mineral Resources—1987, Program and Abstracts: U.S. Geological Survey Circular 995, p. 62–63.

Schmidt, R.G., Gumiel, Pablo, and Payás, Alba, 1990, Provisional geologic map of the Snow Camp–Saxapahaw area, North Carolina: U.S. Geological Survey Open-File Report 90–417.

White, N.C., and Hedenquist, J.W., 1990, Epithermal environments and styles of mineralization: Variations and their causes, and guidelines for exploration: Journal of Geochemical Exploration, v. 36, p. 445–474.

Wilkinson, S.E., 1978, The geology of the northeast quarter of the Silk Hope quadrangle, Carolina slate belt, North Carolina: Chapel Hill, University of North Carolina, unpub. M.S. thesis, 56 p.

CHAPTER T

AEROMAGNETIC SURVEY OF NORTH-CENTRAL MINNESOTA

By ROBERT J. HORTON,[1] WARREN C. DAY,[2] and ROBERT E. BRACKEN[1]

INTRODUCTION

As part of the International Falls and Roseau Conterminous United States Mineral Assessment Program (CUSMAP) projects, the U.S. Geological Survey (USGS) conducted a detailed aeromagnetic survey over an extensive area in north-central Minnesota (fig. 1). Greater than 95 percent of the bedrock in the survey area is covered by Quaternary glacial deposits. Information from available drill holes (Klein and Day, 1989) and sparse outcrop data are inadequate for geologic mapping and resource assessment. The aeromagnetic data, therefore, played a crucial role in the interpretation of the bedrock geology for these CUSMAP projects.

AEROMAGNETIC SURVEY

The 60,000 line-kilometer survey was conducted from 1984 through 1986. The aeromagnetic data were collected using a Fairchild Heli-Porter research aircraft, operated by the USGS, Branch of Geophysics. For the north-central Minnesota aeromagnetic survey, the primary flight-line direction was north-south, with a flight-line spacing of about 380 meters. The survey altitude was radar controlled at about 91 meters above ground level. The magnetic field was measured using a Geometrics G-813 proton precession magnetometer, with a cycle time of 0.5 seconds and a sensitivity of 0.5 nanoTeslas. The average speed of the aircraft was 90 nautical miles per hour. The flight path recovery was accomplished using visual and electronic (LORAN and Mini-Ranger) methods.

The color shaded relief aeromagnetic map (fig. 2) was generated from a gridded data set (Bracken, 1991) that was produced from the flight-line data (Bracken and Petrafeso, 1991). The apparent relief is produced by computer-generated illumination from the southwest. The color-shading technique emphasizes subtle level changes in anomaly amplitude and enhances linear features such as faults and dikes that are aligned at oblique angles to the illumination direction.

GEOLOGY

The survey area is located in the Superior province of the Canadian Shield. Westward-thickening Quaternary deposits, ranging from less than 1 to greater than 60 meters thick, overlie most of the Precambrian bedrock within the survey area (Horton and others, 1989). Geologic mapping by Day and others (1990a, 1990b) has shown that this Late Archean terrane contains rocks of three subprovinces: the Wabigoon in the north, the Quetico in the central part, and the Wawa-Shebandowan in the south (fig. 1).

The Wabigoon subprovince is a granite-greenstone terrane composed of volcanic and coeval plutonic rocks and volcaniclastic, epiclastic, and chemical sedimentary rocks. The Quetico subprovince is composed of metasedimentary rocks, gneiss, and potassic granite. The Wawa-Shebandowan subprovince is a granite-greenstone terrane, composed of metavolcanic rocks, interlayered metasedimentary rocks, and granitoid intrusions. An Early Proterozoic dike swarm strikes northwest across the three older subprovinces (Southwick and Day, 1983).

MAGNETIC CHARACTERISTICS

The rocks of the Wabigoon subprovince have a wide range of magnetic characteristics. The granitic rocks of the

[1]U.S. Geological Survey, Mail Stop 964, P.O. Box 25046, Denver Federal Center, Denver, CO 80225

[2]U.S. Geological Survey, Mail Stop 905, P.O. Box 25046, Denver Federal Center, Denver, CO 80225

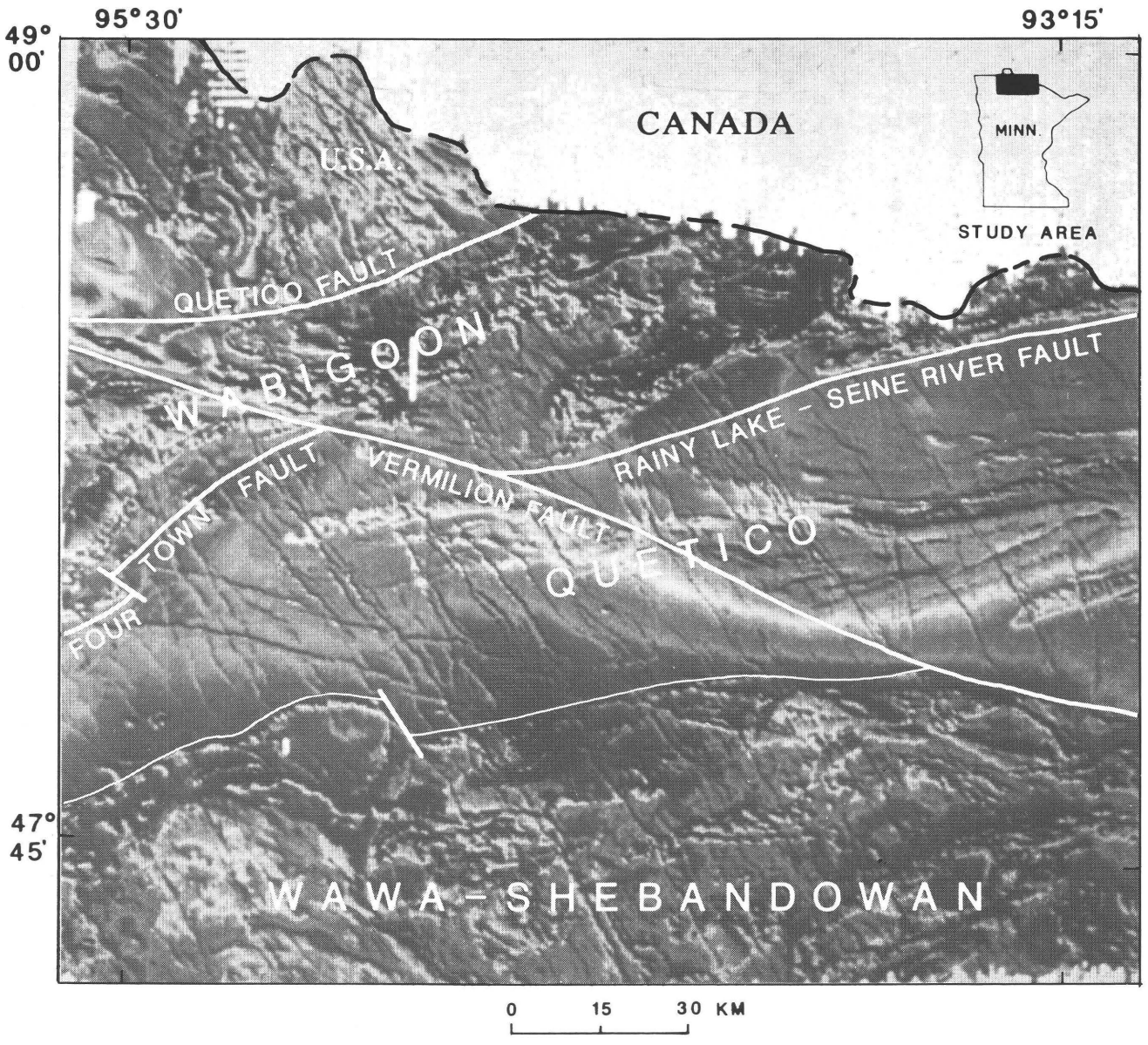

Figure 1. Diagram showing the location of the north-central Minnesota aeromagnetic survey and major lithotectonic terranes and structures.

Wabigoon generally produce broad, low-amplitude magnetic anomalies. The Wabigoon greenstone belts produce the relatively long, narrow, high-amplitude anomalies that are visible across the eastern third of the survey's northern border and along the west-central boundary of the survey area. Within these greenstone belts, iron formations produce the thin, highly magnetic anomalies. Mafic intrusive bodies produce two irregularly shaped, moderately high amplitude anomalies seen in the north-central portion of the survey area.

The metasedimentary rocks of the Quetico subprovince produce the low-gradient, low-amplitude magnetic terrane across the central portion of the survey area. Within this metasedimentary terrane, an east-west-striking magnetic high is produced by the migmatites of the Late Archean Vermilion Granitic Complex (Southwick and Sims, 1980), which are more magnetic than the metasedimentary units. Two prominent west-northwest-trending Archean dikes, located in the western portion of the Quetico subprovince, are offset by younger, northwest-trending Proterozoic dikes.

The rocks of the Wawa-Shebandowan subprovince also have a wide range of magnetic characteristics. As in the Wabigoon subprovince, the granitic rocks generally produce broad, low-amplitude magnetic anomalies, whereas the greenstone belts produce the relatively long,

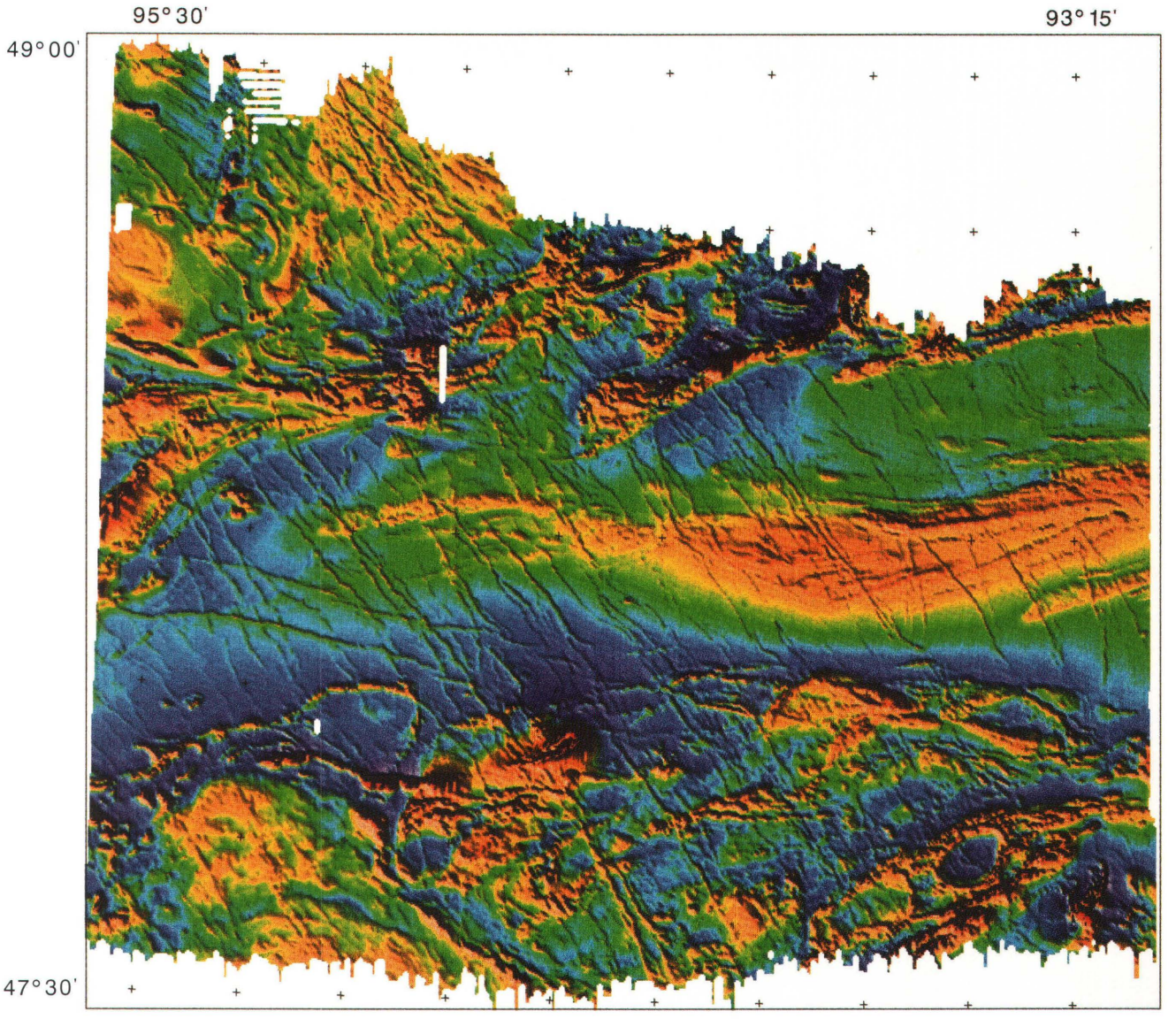

Figure 2. Color shaded relief aeromagnetic map of the north-central Minnesota survey. The color changes represent broad changes in magnetic field strength. The warm colors (red, orange, and yellow) represent areas of magnetic field highs, the cool colors (green, blue, and purple) represent magnetic field lows. The apparent relief is computer generated by illumination from the southwest. The illumination emphasizes subtle level changes in magnetic amplitude and enhances features that are aligned oblique to the illumination direction.

narrow, high-amplitude anomalies. Iron formations produce thin, high-amplitude magnetic anomalies. The large, broad feature in the southwestern corner of the survey area is produce by the Bemidji batholith. Numerous low-amplitude, subrounded anomalies are produced by granitoid intrusions. Many of these granitoid intrusions are partially, or wholly, encircled by narrow magnetic highs. These narrow, encircling magnetic features are usually caused by magnetic units within the enclosing greenstone terrain. However, in the southeastern corner of the subprovince, the magnetic ring around the elliptical anomaly (which is hosted within the northeast-trending magnetic high) is thought to be produced by a magnetic border phase within the pluton. In the extreme southeastern corner of the mapped area, the irregularly shaped, high-amplitude anomaly is produced by an iron formation deformed by faulting and intense folding.

Several prominent structural features are readily seen in the aeromagnetic map (figs. 1 and 2). The Vermilion fault strikes west-northwestward across the center of the survey area. Faults that separate the rocks of the Wabigoon and Quetico subprovinces (the Rainy Lake–Seine River and Four Town faults) lie within the high, northeast-tending gradients produced by the magnetic greenstone

terrane in contact with metasediments. The Early Proterozoic mafic dikes are readily apparent and can be seen cutting across major structural features and the three subprovince terranes—these dikes produce narrow, northwest-tending, linear anomalies.

SUMMARY

The north-central Minnesota airborne survey covered an extensive area where bedrock is buried by thick glacial deposits. Reliable geologic maps could not be produced based on the available outcrop and drill hole information; however, aeromagnetic data provided a means of mapping buried bedrock features, such as contacts and structures, by their magnetic characteristics. The high resolution of the survey generated data that is detailed enough to produce 1:24,000-scale aeromagnetic maps that greatly aid in geologic mapping. This survey demonstrates that aeromagnetic data, when used in conjunction with drill-core information, geochemical studies, and other geophysical methods, can be used to interpret bedrock geology and aid in mineral assessment in terranes with little or no bedrock exposure.

REFERENCES CITED

Bracken, Robert, 1991, Description of magnetic tapes containing gridded aeromagnetic anomaly data from north-central Minnesota: Sioux Falls, South Dakota, USGS–EROS Data Center, Data release serial no. D91-0597.

Bracken, Robert, and Petrafeso, Frank, 1991, Description of magnetic tapes containing north-central Minnesota aeromagnetic flight line data: Souix Falls, South Dakota, USGS-EROS Data Center, Data release serial no. D91-0439.

Day, W.C., Klein, T.L., and Schulz, K.J., 1990a, Preliminary bedrock geologic map of the Roseau 1°×2° quadrangle, Minnesota, U.S.A., and Ontario, Canada: U.S. Geological Survey Open-File Report 90–0544A and 90–0544B, scale 1:250,000.

Day, W.C., Southwick, D.L., Schulz, K.J., and Klein, T.L., 1990b, Bedrock geologic map of the International Falls 1°×2° quadrangle, Minnesota, U.S.A., and Ontario, Canada: U.S. Geological Survey Miscellaneous Investigations Map Series I–1965–B, scale 1:250,000.

Horton, R.J., Meyer, G.N., and Bajc, A.F., 1989, Reconnaissance Quaternary geology map of the International Falls 1°×2° quadrangle: U.S. Geological Survey Open-File Report 89–654, scale 1:250,000.

Klein, T.L., and Day, W.C., 1989, Tabular summary of lithologic logs and geologic characteristics from diamond drill holes in the western International Falls and Roseau 1°×2° quadrangles, northern Minnesota: U.S. Geological Survey Open-File Report 89–346.

Southwick, D.L., and Day, W.C., 1983, Geology and petrology of Proterozoic mafic dikes, north-central Minnesota: Canadian Journal of Earth Sciences, v. 20, no. 4, p. 622–638.

Southwick, D.L., and Sims, P.K., 1980, The Vermilion Granitic Complex—A new name for old rocks in northern Minnesota: U.S. Geological Survey Professional Paper 1124–A, p. A1–A11.

CHAPTER U

MINERALOGIC AND FLUID-INCLUSION STUDIES OF THE PEA RIDGE IRON–RARE-EARTH-ELEMENT DEPOSIT, SOUTHEAST MISSOURI

By GARY B. SIDDER,[1] WARREN C. DAY,[1] LAURENCE M. NUELLE,[2] CHERYL M. SEEGER,[3] *and* EVA B. KISVARSANYI[3]

ABSTRACT

Iron ore and reserves of rare-earth-element ore at the Pea Ridge mine occur in what is thought to be an eroded volcano-plutonic complex in the St. Francois Mountains of southeast Missouri. Middle Proterozoic rhyolitic tuffs host the iron ore. Rare-earth-element-bearing breccia pipes cut the iron ore and altered wallrocks. Comagmatic aplite dikes cut the deposit, which suggests that the mineralization was contemporaneous with the igneous activity in the St. Francois terrane.

The Pea Ridge deposit consists of four mappable zones: the amphib ole-quartz, magnetite, hematite, and silicified zones. Fluid-inclusion studies indicate that the deposit formed from highly saline, high-temperature, magmatically derived hydrothermal fluids. The mineralizing fluids are possibly related to rocks of an iron-rich trachyte suite, which is present regionally as ring intrusions associated with the volcano-plutonic complex. Halite homogenization in three-phase fluid inclusions in the amphibole-quartz, magnetite, hematite, and silicified zones indicate that temperatures varied from greater than 530°C to about 400°C during deposition and alteration associated with the magnetite ore. The rare-earth-element-bearing breccia pipes formed as late-stage fluids, derived from the magnetite ore system, that boiled. The breccia pipes were rapidly and explosively emplaced at a temperature of about 300°C.

INTRODUCTION

This study represents a contribution from the ongoing Midcontinent Strategic and Critical Minerals Program's Olympic Dam Project, which is a cooperative effort between the U.S. Geological Survey and the Missouri Geological Survey. The project is funded through the USGS Office of Mineral Resources. Research on the Pea Ridge deposit was an outgrowth of work by Sims and others (1987), who recognized that the Middle Proterozoic granite-rhyolite terranes in the Midcontinent may host Olympic-Dam-type copper-uranium-gold-silver deposits (Reeve and others, 1990).

A critical facet of the study of the Pea Ridge iron–rare-earth-element deposit is to establish the type, composition, and paragenesis of ore and alteration minerals. Detailed underground mapping combined with petrographic and electron microbeam analyses have documented the paragenesis in the Pea Ridge deposit and the nature of the ore and alteration minerals. This paper highlights new ore-petrography, mineral-chemistry, and fluid-inclusion data in an attempt to assess the conditions of ore formation. The reader is referred to Nuelle and others (1992) for a detailed description of the ore deposit, mineral paragenesis, and ideas on formation of the rare-earth-element-bearing breccia pipes.

[1]U.S. Geological Survey, Mail Stop 905, P.O. Box 25046, Denver Federal Center, Denver, CO 80225

[2]Doe Run Co., P.O. Box 500, Viburnum, MO 65566

[3]Division of Geology and Land Survey, Missouri Department of Natural Resources, P.O. Box 250, Rolla, MO 65401

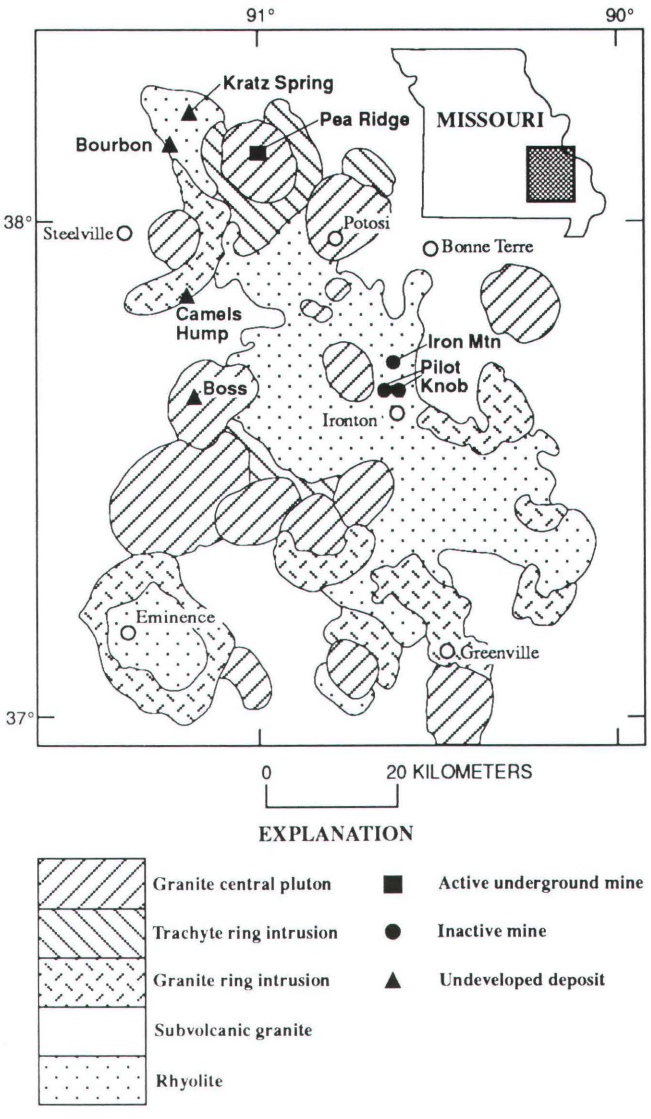

Figure 1. Geologic map of the Middle Proterozoic St. Francois terrane, southeast Missouri (from Kisvarsanyi, 1980).

GEOLOGIC SETTING

Middle Proterozoic rocks, 1,480–1,450 Ma (Bickford, 1988), of the St. Francois granite-rhyolite terrane in southeast Missouri host 32 known magnetite and hematite deposits and prospects that together form the Missouri iron metallogenic province (Kisvarsanyi and Proctor, 1967). The St. Francois terrane consists predominantly of rhyolite, which was intruded by coeval subvolcanic granite massifs (fig. 1). Later, granite porphyry and an iron-rich trachyte suite were emplaced as ring-dike intrusions around the margins of caldera complexes. Bodies of two-mica granite, which are enriched in fluorine, uranium, and thorium in addition to large-ion-lithophile elements (LILE), such as Sn, W, Nb, Y, Be, Li, Rb, and Ba, are inferred to form resurgent plutons within the central part of caldera complexes (Kisvarsanyi, 1980, 1981; Kisvarsanyi and Kisvarsanyi, 1989a).

The Missouri iron deposits belong to the family of Olympic-Dam- and Kiruna-type Fe, Cu, REE, and Au deposits (Oreskes and Einaudi, 1990; Reeve and others, 1990). The Missouri ores are predominantly magnetite and (or) hematite, with variable amounts of pyrite, chalcopyrite, and bornite. They are enriched in the LILE, and some are enriched in phosphorous. As is typical of this family of deposits, they are distinct from deposits associated with layered mafic intrusions in both mode of occurrence and by the fact that they have low titanium contents.

The Missouri iron deposits predominantly occur as intrusive or replacement bodies within volcanic rocks of the St. Francois terrane. Late-stage aplite or granitic dikes cut some of the deposits, which indicates that the mineralization was synchronous with igneous activity in the terrane (Day and others, 1989; Kisvarsanyi and Kisvarsanyi, 1989b).

THE PEA RIDGE DEPOSIT

The host rocks in the Pea Ridge deposit consist of crystal-rich, subalkaline, rhyolitic ash-flow tuffs that strike N. 80° W. and dip about 75° NE. Both the deposit and host rocks are interpreted to form a large "roof pendant" on top of a circular, 20-km-wide, central granite pluton (Nuelle and others, 1992) (fig. 1). This pluton was interpreted as the core of a buried caldera complex (Kisvarsanyi, 1981; Nuelle and others, 1991) on the basis of regional compilations of aeromagnetic and gravity data. The margin of the caldera complex is delineated by an iron-rich trachyte ring intrusion (fig. 1). The Pea Ridge ore system may have evolved as immiscible fluids from the source or a derivative magma of the iron-rich trachyte suite (Kisvarsanyi and Kisvarsanyi, 1981; Day and others, 1991).

The tabular Pea Ridge iron orebody discordantly cuts its host rhyolitic rocks (fig. 2). The orebody strikes N. 55°–60° E. and dips 75° SE. to nearly vertical (Husman, 1989). Replacement and open-space fill textures characterize the deposit (Nuelle, Seeger, and others, 1989), and cross-cutting, replacement, and alteration relations define four mappable zones (Nuelle and others, 1992). They are, from earliest to latest: (1) the amphibole-quartz zone; (2) the magnetite ore zone, with massive magnetite and magnetite-cemented breccia ore; (3) the hematite zone; and (4) the silicified zone (fig. 2). Quartz veins, mafic dikes, and aplite dikes cut the four main zones. REE-bearing breccia pipes cut rocks of the footwall and the eastern margin of the deposit (Marikos, Nuelle, and Seeger, 1989; Nuelle and others, 1992).

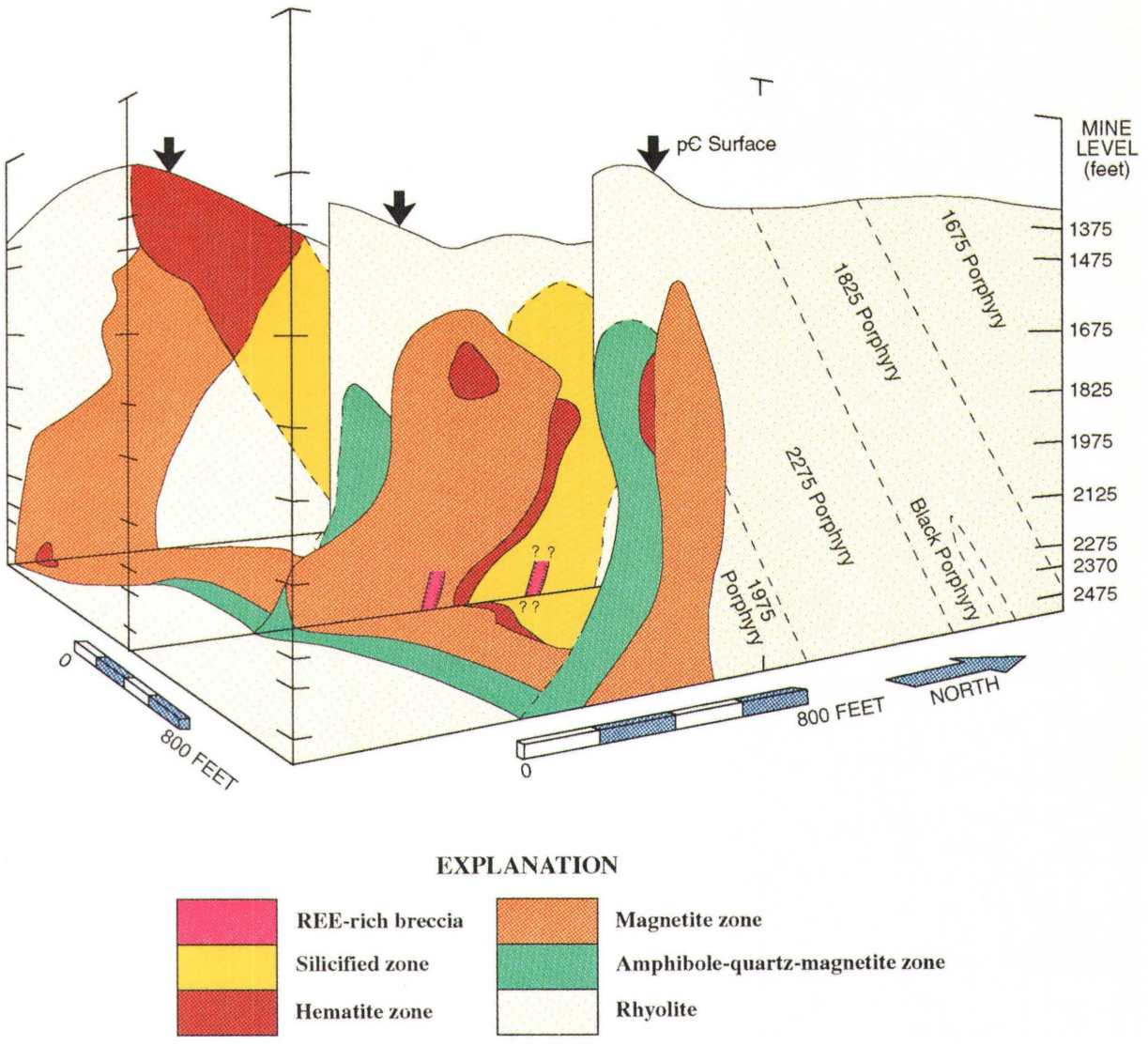

Figure 2. Isometric view of the Pea Ridge deposit. View looking northwest.

AMPHIBOLE-QUARTZ ZONE

The amphibole-quartz zone occurs on both the hanging wall and footwall of the deposit. This zone thins from about 40 m wide on the eastern edge of the hanging wall westward into host rock with fractures that are filled with amphibole and have silicified walls (Emery, 1968). The footwall amphibole-quartz zone is less brecciated and contains fewer quartz pods than that of the hanging wall. Contacts between the amphibole-quartz zone and host rhyolite wallrock are generally gradational; some wallrock exhibits only incipient replacement by actinolite (Nuelle and others, 1992).

The amphibole-quartz zone consists of massive, coarse-grained actinolite with interstitial quartz, apatite, magnetite, pyrite, chalcopyrite, and calcite (fig. 3). Actinolite forms crystals as much as 5 cm long with seams and disseminations of magnetite and sulfides. Fluorine content in actinolite ranges from about 0.20 to 0.90 weight percent, whereas chlorine concentration is less than 0.05 weight percent. Quartz is present as both interstitial grains and as massive pods 1 to 50 cm in diameter.

The amphibole-quartz zone represents a metasomatic alteration front that preceded emplacement of the magnetite orebody and formed a skarn in the host rhyolitic rocks. Relict textures of rhyolite in the amphibole-quartz zone of the hanging wall and incipient replacement of rhyolite by actinolite confirm that rhyolite is the protolith of the amphibole-quartz zone (Nuelle, Marikos, and others, 1989; Nuelle, Seeger, and others, 1989; Nuelle and others, 1992).

Figure 3. Representative sample of the amphibole-quartz zone. Actinolite forms crystals as much as 5 cm long. Calcite fills interstices. Magnetite is disseminated in actinolite.

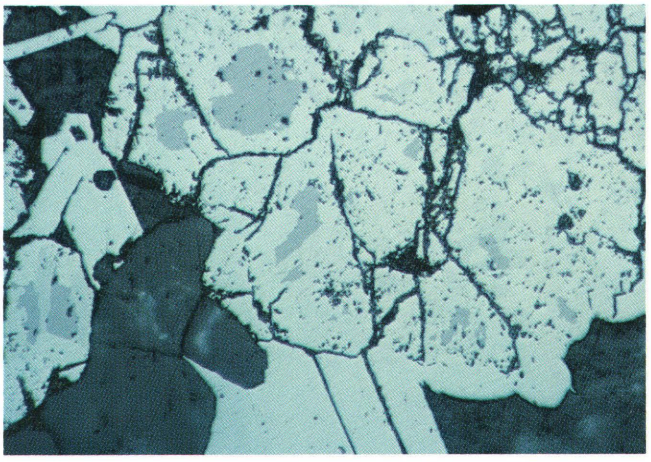

Figure 4. Photomicrograph of martite after magnetite in the magnetite zone. Relict magnetite in cores of grains is replaced by hematite. Some hematite formed as overgrowths on magnetite and as plates interstitial to magnetite. Field of view about 1.8 mm wide.

MAGNETITE ZONE

The magnetite ore zone consists of massive magnetite and, on its outer margins, completely assimilated rhyolite and magnetite-cemented breccias, known locally as pseudobreccia and heterolithic breccia (Nuelle and others, 1992). Magnetite comprises about 60 to 90 modal percent of the massive ore, with associated gangue minerals such as apatite, quartz, phlogopite, chlorite after phlogopite, pyrite, chalcopyrite, calcite, fluorite, barite, and potassium feldspar in decreasing abundance accounting for about 12 to 35 modal percent. Martite varies between less than 1 and about 13 modal percent throughout the magnetite ore zone. The texture of magnetite in the ore zone is generally massive, coarse to fine grained, and granular, with subconchoidal fracture. The gangue minerals form interstitial grains, net-textured veinlets, and pods within the massive magnetite.

Magnetite-cemented breccias contain variably altered fragments of rhyolite in a matrix of magnetite ± actinolite. Alteration of rhyolite varies towards the orebody from relatively minor in pseudobreccia to intense in heterolithic breccia. Locally, the contact between pseudobreccia and rhyolite is sharp. Between heterolithic breccia or pseudobreccia and massive magnetite is an ill-defined zone of rhyolite and (or) amphibole-quartz-zone rock that is massively replaced and assimilated by magnetite without any breccia texture or with only faint ghosts of magnetite-replaced fragments. This zone also contains a higher proportion of gangue minerals such as quartz and trace to minor amounts of apatite, actinolite, chlorite, calcite, pyrite, and chalcopyrite. These gangue minerals form seams, pods, and disseminations in magnetite. The pseudobreccia contains rhyolite fragments that are neither rotated nor displaced, and the breccia may be either matrix or clast supported. Heterolithic breccia is well developed along the hanging wall. It is predominantly a matrix-supported breccia that contains fragments of relatively unaltered rhyolite, chloritized rhyolite, and amphibole-quartz-zone rock in a magnetite matrix. Fragments in pseudobreccia are commonly angular to subangular, whereas those in heterolithic breccia are subangular to rounded due to resorption on the margins of fragments.

Magnetite throughout the ore zone is compositionally homogeneous and essentially pure Fe_3O_4. The titanium content in magnetite from the ore zone, as analyzed on the electron microprobe, ranges from < 0.01 to about 0.02 weight percent TiO_2, and the x'_{usp} (apparent mole fraction ulvospinel, Fe_2TiO_4 (Stormer, 1983)) for 20 grains is < 0.001. Other oxides of elements such as nickel, magnesium, chromium, manganese, silicon, aluminum, and zinc are present in total amounts < 0.40 weight percent.

Hematite (martite) in the massive magnetite zone is common as grains pseudomorphic after magnetite. The amount of replacement is variable from minor alteration on the rims of magnetite grains to complete replacement (fig. 4). The hematite zone on the top and footwall of the magnetite orebody (fig. 2) represents a zone of nearly complete replacement of magnetite by martite. Martite in the magnetite zone is virtually pure hematite, with x'_{ilm} (apparent mole fraction ilmenite, $FeTiO_3$ (Stormer, 1983)) < 0.001 and the sum of oxides of the trace elements < 0.25 weight percent.

Apatite and quartz are the most abundant gangue minerals in the magnetite zone. Both are present in amounts between about 1 and 10 modal percent. They occur most commonly as interstitial grains to magnetite as well as in pods and lining vugs. Semiquantitative analyses on the scanning electron microscope (SEM) and the electron microprobe indicate that apatite contains as much as 5 weight percent fluorine and less than 0.5 weight percent

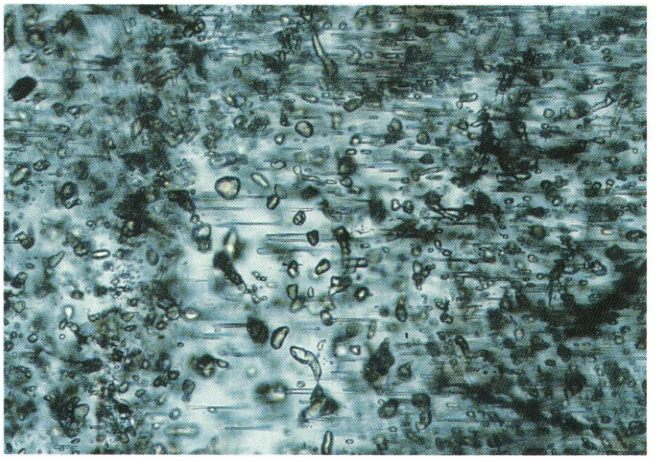

Figure 5. Photomicrograph of apatite with solid inclusions of monazite. Equidimensional inclusions of monazite are randomly oriented, whereas elongated crystals are crystallographically oriented. Field of view about 0.5 mm wide.

rare earth elements (REE). However, solid inclusions of REE-bearing minerals such as monazite, xenotime, and possibly britholite are abundant in apatite (Sidder, unpub. data; Whitten and Cornell, 1991). In contrast, quartz is distinctly free of solid inclusions. This is a key characteristic in distinguishing between quartz and apatite in polished thick sections. The mineral inclusions in apatite vary from equidimensional grains to elongated rods as much as 50 m in length. Although the former are oriented randomly, the long prismatic grains appear to be oriented crystallographically in the apatite (fig. 5). Moreover, the mineral inclusions in apatite appear to be zoned vertically through the deposit, with abundant inclusions in apatite at depth and inclusion-free apatite with associated, interstitial, discrete crystals of monazite at higher levels in the mine. These features suggest that the REE-bearing minerals included in apatite formed by exsolution. Åmli (1975) and McKeown and Klemic (1956) described similar inclusions in apatite in the Gloserheia granite pegmatite, Norway, and in the magnetite deposits in the Mineville district, New York, respectively. Åmli (1975) concluded that the REE-bearing minerals in apatite formed by exsolution, possibly accompanied by metasomatism.

Phlogopite or phlogopitic biotite is generally present in amounts of < 0.20 to 2.70 modal percent and rarely to as much as 12 modal percent. Phlogopite forms grains that are commonly intergrown with apatite interstitial to magnetite and as thin veinlets in magnetite. The mica varies in color from moderate reddish brown phlogopitic biotite to pale reddish brown and colorless phlogopite. This color variation appears to be related to the amount of TiO_2. Those grains that have recognizable color contain greater than 1.50 weight percent TiO_2, whereas those grains that are faintly colored to colorless have less than 0.50 weight percent TiO_2. The ratio Mg/(Mg+Fe) (assuming total iron as Fe^{2+}) also varies with color: darker grains have a ratio of about 0.80, and nearly colorless grains have a ratio greater than 0.80 and as much as 0.87. Fluorine abundance in phlogopite and phlogopitic biotite varies between about 0.7 and 1.8 weight percent, whereas chlorine is < 0.2 weight percent.

Chlorite commonly replaces phlogopite. Its abundance varies from < 0.50 to about 1 modal percent and rarely to 5 modal percent. Chlorite is typically pleochroic from light yellow to bluish or olive green, and it has low, first-order gray to anomalous Prussian blue birefringence. Its composition ranges from magnesian-rich chlorite (Mg/(Mg+Fe) ≥ 0.88), such as penninite or clinochlore, to iron-magnesium-rich chlorite (Mg/(Mg+Fe) between 0.55 and 0.76), such as pycnochlorite or prochlorite (ripidolite). This compositional variation is probably due to the compositional differences in phlogopite and phlogopitic biotite that it replaced.

Pyrite and chalcopyrite are the main sulfide minerals in the magnetite zone. Pyrite is present in amounts that vary from about 0.10 to as much as about 14 modal percent, whereas chalcopyrite varies from < 0.10 to about 1.50 modal percent. Pyrite occurs as disseminations in magnetite, as well as interstitial grains, seams, pods, and stringer veinlets in the magnetite ore. Chalcopyrite is sparsely disseminated in magnetite and is present as grains associated with pyrite interstitial to magnetite and as blebs in pyrite associated with pyrrhotite and possibly cubanite. Some pyrrhotite is nickeliferous, with about 4.0 weight percent nickel. Sulfide distribution is not zoned vertically or horizontally within the orebody. The composition of chalcopyrite approximates ideal stoichiometry without any trace elements. Pyrite also is stoichiometric; however, cobalt is a common trace metal in pyrite; and nickel, arsenic, silver, copper, manganese, and zinc are rarely present in amounts less than about 0.70 weight percent total. The content of cobalt in pyrite in the magnetite zone is generally zoned from as much as 5.00 weight percent in the core of grains to about 0.50 weight percent on the rim. This is in contrast to later pyrite that is associated with blades of hematite in the magnetite and hematite zones and contains < 0.50 weight percent cobalt.

Melonite ($NiTe_2$), coloradoite (HgTe), and cassiterite are present in trace amounts in the magnetite zone. They form inclusions in pyrite and chalcopyrite (fig. 6). Melonite forms euhedral grains as much as 85 μm in diameter and is disseminated in pyrite and associated with chalcopyrite that is interstitial to magnetite and apatite. A peanut-shaped grain of coloradoite about 18 μm long has been recognized in cassiterite within pyrite (fig. 6*E*). Other telluride minerals have not been distinguished in the magnetite ore. Altaite (PbTe) is the predominant telluride mineral in the REE-bearing breccia pipes. One sample of magnetite ore with both melonite and coloradoite is the

only one that contains detectable amounts of gold (400 ppb).

Calcite, fluorite, barite, calcium sulfate, and potassium feldspar are rare (< 1 modal percent) gangue minerals in the magnetite zone. Calcite, fluorite, and barite occur mostly in pods and vugs associated with apatite and quartz within massive magnetite. Electron microprobe and SEM analyses have detected calcium sulfate (gypsum or anhydrite) interstitial to apatite and chalcopyrite in magnetite ore (figs. 6*A*, *C*).

HEMATITE ZONE

The hematite zone irregularly mantles the margins of the magnetite orebody (fig. 2). The hematite zone separates the silicified zone from the magnetite orebody along the footwall and host rhyolite from the magnetite zone along the eastern edge of the deposit. Contacts are generally gradational, with irregularly distributed patches of magnetite in the hematite zone and hematite in the magnetite zone. Hematite is also localized along faults and fractures in the magnetite zone (Emery, 1968; Nuelle and others, 1992).

Hematite varies in abundance throughout the deposit from < 1.0 modal percent in the magnetite zone to about 80 modal percent in the hematite zone. In general, hematite decreases in abundance with depth. Most hematite is an alteration product of magnetite and, where massive replacement is present, forms fine-grained massive martite. However, some hematite in the magnetite and hematite zones is platy or bladed (fig. 7), and some hematite forms overgrowths on magnetite (fig. 4) as well as occurring in veins and pods in the magnetite zone. Some of the martite and hematite may have formed at high temperature in response to an increased fugacity of oxygen in the mineralizing fluids. As noted previously, martite after magnetite is relatively pure Fe_2O_3. Platy hematite is slightly more variable in composition, with x'_{ilm} varying between < 0.001 and 0.031 and containing as much as 1.58 weight percent TiO_2 and a total of 0.20 weight percent zinc, silicon, aluminum, manganese, and chromium oxides.

Quartz, apatite, pyrite, and calcium sulfate are the most common gangue minerals associated with hematite. Pyrite interstitial to and included within plates of hematite (fig. 7) is notably low in cobalt (< 0.60 weight percent) in contrast to early pyrite in the magnetite zone. Calcium sulfate (gypsum or anhydrite) is typically included within the plates of hematite (fig. 7).

SILICIFIED ZONE

Massively silicified rhyolite with extensive potassium feldspar alteration is developed in part of the footwall. This silicified zone is present between the hematite zone and host rock on the north side of the deposit and between magnetite ore and host rock on the west (Husman, 1989; Seeger and others, 1989). Massive white to light-gray quartz that variably replaces rhyolite and fills open spaces characterizes this zone (fig. 8). Potassium feldspar flooding, or potassic alteration, has converted the gray to reddish-brown host volcanic rocks to moderate reddish orange rock (Nuelle and others, 1992). Locally within the silicified zone, quartz and orthoclase form pegmatitic pods and veins. Sericite, muscovite, biotite, fluorite, barite, tourmaline, epidote, calcite, pyrite, chalcopyrite, hematite, rutile, apatite, monazite, zircon, calcium sulfate, and topaz are accessory minerals in the silicified zone (Husman, 1989; Nuelle and others, 1992). Sericite, fluorite, and tourmaline typically coat fractures, joints, and fragment surfaces in the silicified zone (Seeger and others, 1989; Nuelle and others, 1992), and calcite is common in veinlets, whereas the other accessory minerals occur as disseminations in quartz and orthoclase. Quartz and (or) orthoclase veins that cut other zones of the orebody were in part contemporaneous with massive silicification. These veins also contain minor amounts of barite, calcite, fluorite, chalcopyrite, monazite, xenotime, and rutile (fig. 8) (Nuelle, Seeger, and others, 1989). A uranium-lead date of 1.46 Ga on xenotime from a quartz vein (W.R. Van Schmus, University of Kansas, written commun., 1988) confirms the age of the Pea Ridge deposit to be contemporaneous with regional igneous activity.

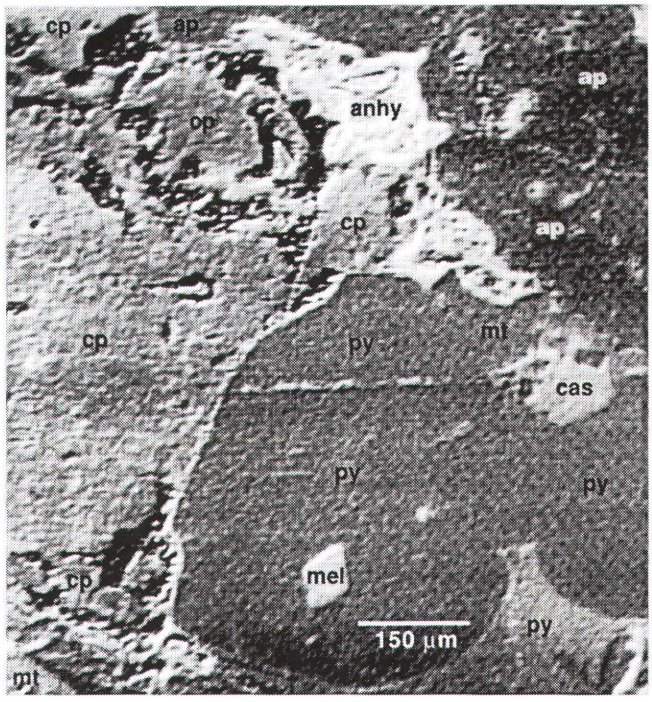

Figure 6*A*. Enhanced SEM image of telluride-bearing magnetite ore. Mt, magnetite; py, pyrite; cp, chalcopyrite; ap, apatite; anhy, calcium sulfate; cas, cassiterite; mel, melonite.

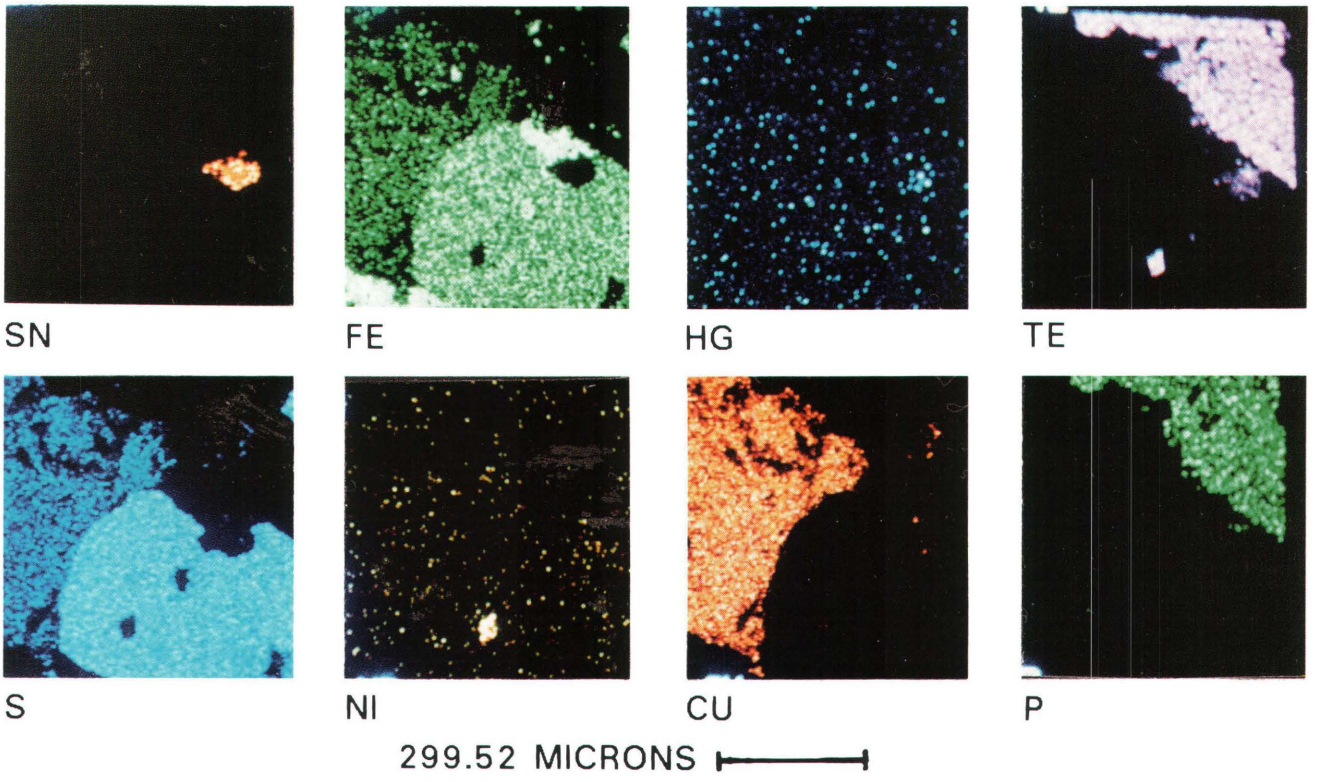

Figure 6*B*. Element maps of sample in 6*A*. Elements are, left to right, Sn, Fe, Hg, and Te on top, and S, Ni, Cu, and P on bottom.

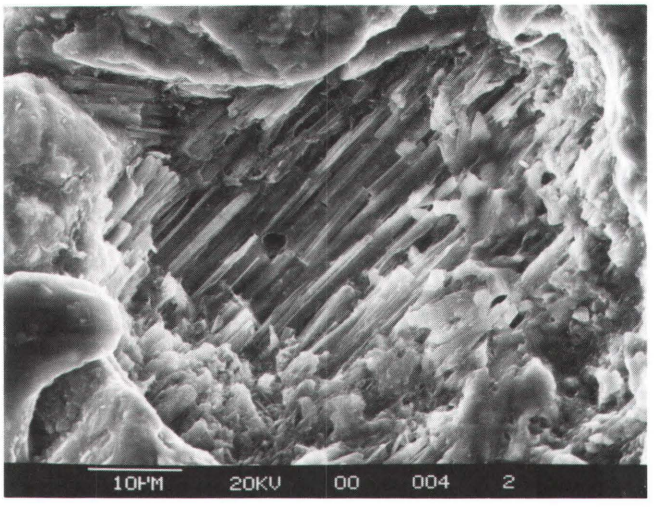

Figure 6*C*. SEM photomicrograph of calcium sulfate shown in 6*A*.

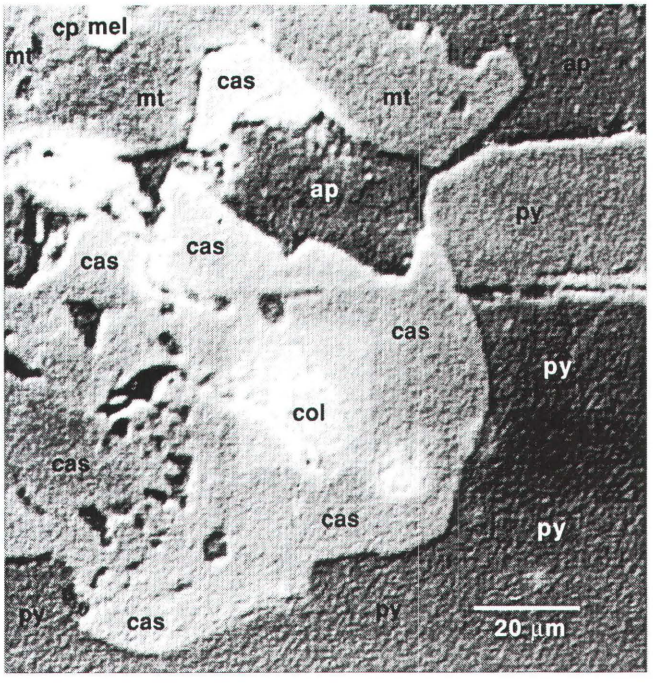

Figure 6*D*. Expanded view of area in 6*A* that contains cassiterite. Mt, magnetite; py, pyrite; cp, chalcopyrite; ap, apatite; cas, cassiterite; mel, melonite; col, coloradoite.

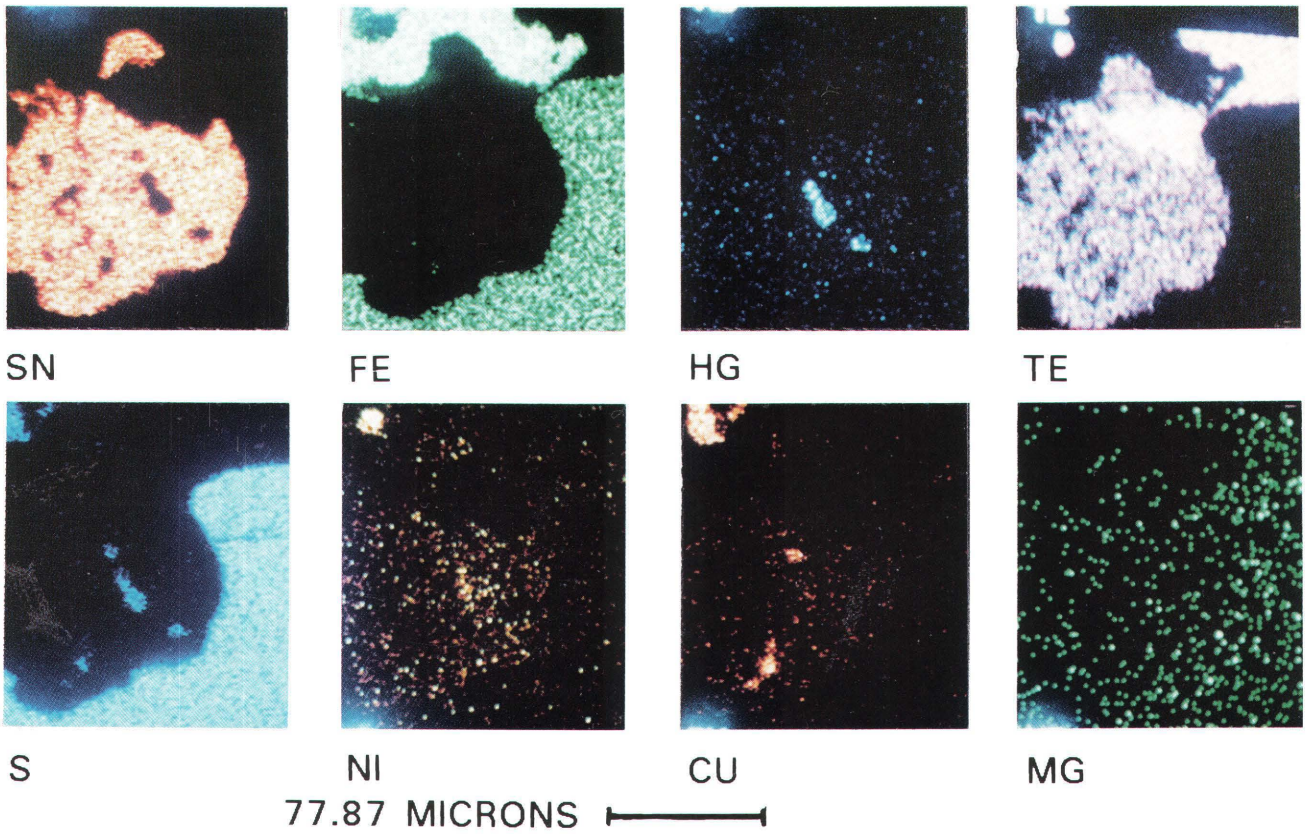

Figure 6*E*. Element maps of sample in 6*D*. Elements are, left to right, Sn, Fe, Hg, and Te on top; S, Ni, Cu, and Mg on bottom.

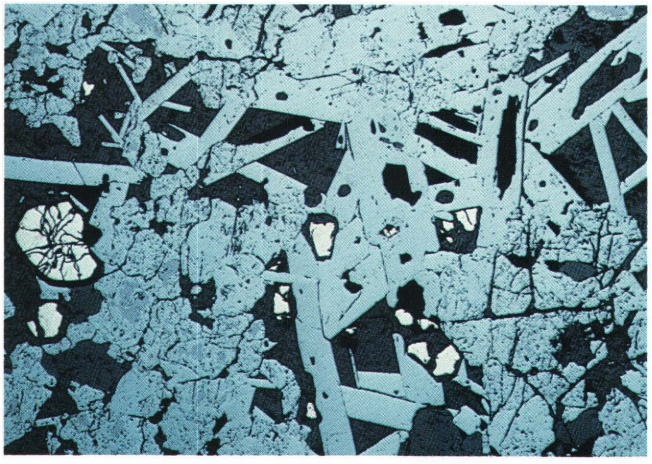

Figure 7. Photomicrograph of martite and hematite with interstitial pyrite and quartz in the hematite zone. Magnetite has been completely replaced by martite. Hematite plates enclose pyrite and quartz. Field of view about 4.8 mm wide.

Mapping of underground workings indicates that silicification postdated the emplacement of magnetite ore (Nuelle and others, 1992). For example, underground workings show silicified magnetite ore and pseudobreccia where both the rhyolite fragments and magnetite cement are silicified (fig. 8). However, in contrast, some drill core displays pseudobreccia with fragments of silicified rhyolite and quartz in unsilicified magnetite cement, which suggests that some silicification occurred before emplacement of the magnetite ore. Alternatively, magnetite emplacement and silicification may have overlapped in space and time. The diverse assemblage of minerals in the silicified zone and its ambiguous paragenetic relation with the magnetite zone suggest that the conditions of deposition, such as temperature, pH, and the fugacities of oxygen, sulfur, and carbon dioxide, changed through time. Work is in progress to document more closely mineral paragenesis in the silicified zone and to distinguish between relict textures and minerals in altered and replaced rhyolite versus secondary minerals introduced with quartz and potassium feldspar.

RARE-EARTH-ELEMENT-BEARING BRECCIA PIPES

At least four REE-bearing breccia pipes cut the iron ore and altered rhyolite wallrocks in the Pea Ridge deposit at or near the contacts between the different zones of the deposit. For example, one pipe is along the contact

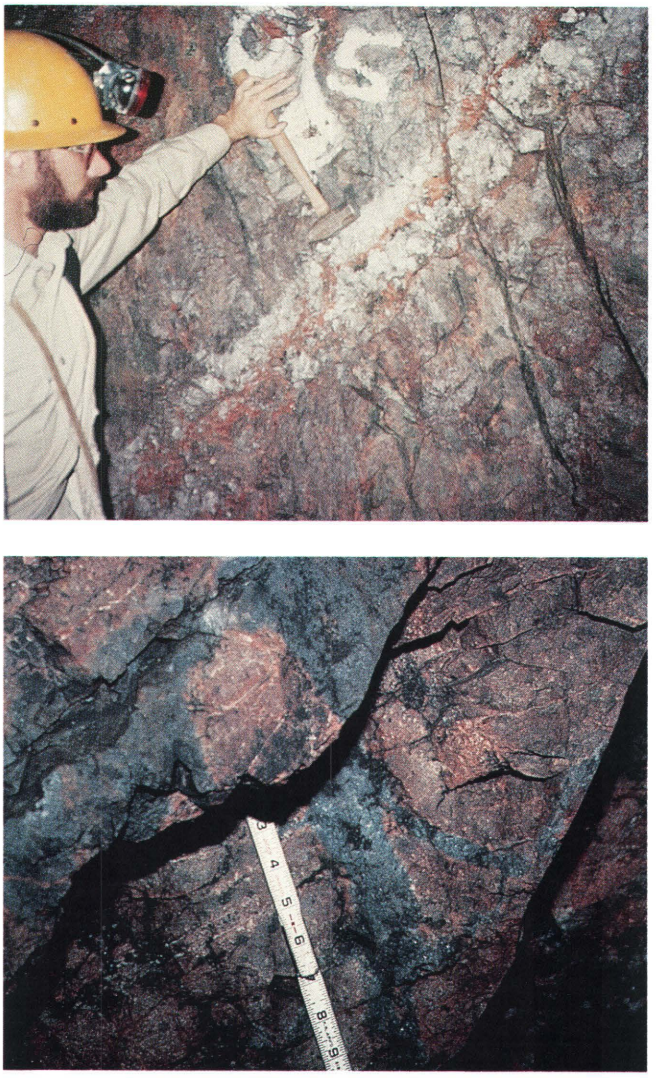

Figure 8. Photographs, taken underground, of the silicified zone. *Top*, Zone of massive silicification. *Bottom*, Silicified pseudobreccia.

between the silicified and magnetite zones, and another is between the silicified and hematite zones. Locally, apophyses of breccia pipes protrude into adjacent rocks (Nuelle and others, 1992). Three pipes are relatively soft and friable, whereas one is hard and indurated.

The temporal relation between the silicified zone and the REE-bearing breccia pipes is apparently ambiguous. Fragments of silicified wallrock and massive quartz from the silicified zone in the friable, soft, REE-bearing breccia pipes clearly indicate that silicification preceded emplacement of the breccia pipes, whereas the hard pipe is apparently silicified (Marikos, Seeger, and Nuelle, 1989). However, the hardness of the latter is probably related to a greater abundance of primary quartz in the pipe and is not an overprint due to secondary quartz introduced into the breccia pipe after its emplacement. The matrix of the hard breccia pipe is not silicified.

The forms of the hard and soft breccia pipes are similar. The pipes dip > 60° and are elongate to ovoid in plan view (Nuelle and others, 1992). They range in length from several meters to as much as 60 m and in width from < 1 to about 15 m. Their maximum vertical extent is not known, but at least one pipe is exposed over a distance of about 120 m.

Fragments of rhyolite, magnetite- and hematite-rich ore, and silicified-zone rocks in the breccia pipes range in diameter from < 1 mm to several meters and document the late-stage emplacement of the pipes. Some minerals such as sanidine, quartz, and barite form megacrysts or possibly phenocrysts (Nuelle and others, 1991). These breccias are both matrix and clast supported (Nuelle and others, 1992). The matrix of the breccias consists predominantly of rock flour, potassium feldspar (predominantly orthoclase), chlorite, barite, monazite, xenotime, quartz, apatite, allanite, and calcite (Marikos, Seeger, and Nuelle, 1989). Other accessory minerals present in trace quantities include other REE-bearing minerals, altaite, chalcopyrite, pyrite, hematite, galena, thorite, and cassiterite.

Monazite is the predominant REE-bearing mineral in the breccia pipes. Lesser amounts of xenotime and uncommon bastnaesite ($(Ce,La)CO_3(F,OH)$), britholite ($(Ca,Ce)_5(SiO_4,PO_4)_3(OH,F)$), allanite, and possibly tengerite ($CaY_3(CO_3)_4(OH)_3 \cdot 3H_2O$) and synchisite ($(Y,Ce)Ca(CO_3)F_2$) have also been observed (Husman, 1989; Whitten and Cornell, 1991; Sidder, unpub. data, 1991). These minerals generally occur as small crystals that are < 4.0 mm in diameter in the matrix, as fill in cracks in barite and sanidine megacrysts that are > 2 cm long, and as disseminations in rock fragments. Allanite forms euhedral tablets in acicular groups within the matrix of the hard breccia pipe. Total REE-oxide (REO) concentrations from grab samples range from about 5 to 38 weight percent, with an average of 20 weight percent. Grades from bulk samples range from about 7 to 25 weight percent REO and average about 12 weight percent (Nuelle and others, 1992). Ore reserves of about 600,000 tons at 12 weight percent REO have been estimated for the hard breccia pipe at Pea Ridge (Whitten and Yancey, 1990).

Thorium and uranium are present in minor quantities in the breccia pipes. The thorium concentration in grab samples averages about 3,320 ppm, and the uranium content averages about 190 ppm (Nuelle and others, 1992). Thorite has been identified as grains disseminated in the REE-bearing breccia pipes associated with altaite (PbTe), monazite, and other REE-bearing minerals (Husman, 1989; Sidder unpub. data, 1991). Radioactivity imparted by thorium and uranium serves as an exploration guide for the breccia pipes.

Precious metals are distributed erratically in the breccia pipes. Gold and silver are present in trace amounts, with 58 grab samples of breccia pipe material averaging about 0.9 ppm gold and 1.2 ppm silver (L.J. Tucker, Pea

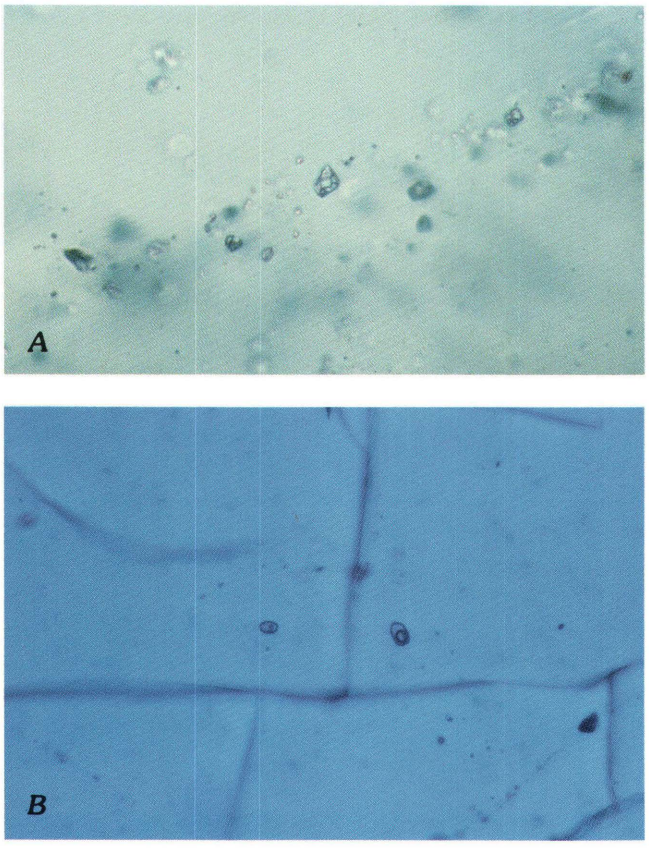

Figure 9. Photomicrographs of fluid inclusions in quartz (field of view about 0.5 mm wide). *A*, Three-phase fluid inclusions in quartz in the rare-earth-element-bearing breccia pipes. *B*, Two-phase fluid inclusions in the rare-earth-element-bearing breccia pipes. Note the different proportion of vapor and liquid in the inclusions.

Ridge Iron Ore Co., oral commun., 1989). The hard breccia pipe is apparently enriched in precious metals relative to the soft pipes (Husman, 1989). Precious-metal-bearing minerals tentatively identified include hessite (Ag_2Te), sylvanite ($AuAgTe_4$), and electrum (Husman, 1989). Altaite is the most common telluride mineral in the breccia pipes.

FLUID-INCLUSION STUDIES

Quartz in all zones of the Pea Ridge deposit is the only fluid-inclusion-bearing mineral identified thus far. Fluorite and barite do not contain fluid inclusions, and apatite contains only mineral inclusions, as mentioned previously. Primary fluid inclusions in quartz in the amphibole-quartz, magnetite, hematite, and silicified zones consist of three or more phases, with liquid, vapor, halite, and one or more other daughter minerals (fig. 9*A*). Those on the same plane within a given sample have similar proportions of the three phases. The inclusions range in size from less than 5 μm to as much as 16 μm. Fluid inclusions in the REE-bearing breccia pipes contain only liquid and vapor (fig. 9*B*). However, rock and mineral fragments from other zones in the breccia pipes make study of the fluid inclusions in the breccia pipes more difficult. Secondary fluid inclusions in all zones are recognized readily by their alignment along fractures. They are generally smaller (< 7 μm in diameter) than the primary inclusions, consist predominantly of liquid and vapor only, and homogenize at temperatures less than 250°C.

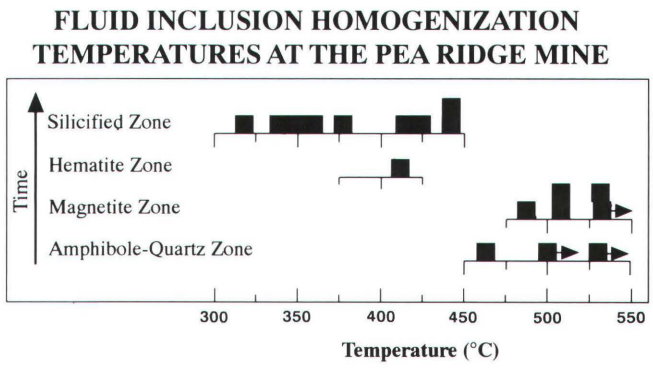

Figure 10. Histogram of homogenization temperatures of three-phase (L + V + H) fluid inclusions in the Pea Ridge deposit. All inclusions are in quartz and homogenize by halite disappearance.

All three-phase inclusions homogenize by halite dissolution after vapor disappearance. Homogenization temperatures of three-phase liquid + vapor + halite fluid inclusions in quartz within the amphibole-quartz zone indicate that these inclusions were trapped at temperatures as great as or greater than 530°C (fig. 10). Halite in some inclusions had shrunk in size and become rounded during heating, but had not dissolved by 530°C, at which point the heating run was terminated. Salinities calculated using the method of Potter and others (1977) for the inclusions in the amphibole-quartz zone range from about 52 to > 56 equivalent weight percent NaCl. Preliminary oxygen isotope data for quartz-magnetite pairs suggest that this zone may have formed at temperatures as high as 680°C (Sidder and others, 1991).

Gangue quartz interstitial to magnetite in the ore zone contains characteristic, but relatively rare, three-phase liquid + vapor + halite fluid inclusions. These inclusions generally homogenize at temperatures between about 480°C and 530°C; however, halite in some inclusions did not disappear by 530°C (fig. 10). Salinities in the magnetite zone range from about 54 to > 60 equivalent weight percent NaCl. A quartz-magnetite pair yields a calculated temperature from oxygen-isotope data of 480°C (Sidder and others, 1991).

Three-phase liquid + vapor + halite fluid inclusions are rare in quartz interstitial to hematite plates in the hematite zone (fig. 7). Preliminary heating studies indicate that these inclusions homogenize by halite dissolution at

about 410°C (fig. 10), and a quartz-hematite pair yields a calculated temperature of 395°C (Sidder and others, 1991). The calculated salinity in the hematite zone is about 47 equivalent weight percent NaCl.

Multi-phase fluid inclusions are abundant in the silicified zone. Liquid + vapor + halité inclusions are most common, but some inclusions contain additional daughter minerals. Some of these daughter minerals include hematite, recognized by its orangish color; an opaque mineral; and tabular or rounded translucent crystals, some of which are birefringent. These inclusions all homogenize by halite dissolution, although some of the other daughter minerals do not disappear before halite. The temperature of homogenization in the silicified zone ranges from about 320°C to 430°C, and the salinity ranges from about 39 to 49 equivalent weight percent NaCl.

Two-phase liquid-and-vapor fluid inclusions with variable liquid-to-vapor proportions coexist in quartz within the matrix of the breccia pipes. Such coexisting populations of vapor- and liquid-rich fluid inclusions are commonly indicative of entrapment of fluids that underwent boiling (Cunningham, 1978). Because of the variable proportion of liquid and vapor in these inclusions, temperatures of disappearance of the vapor or liquid are not necessarily representative of the trapping temperature. The temperature calculated from the sulfur isotope composition of barite and pyrite in the breccia pipes yielded 305°C (Sidder and others, 1991).

CONCLUSIONS

The Pea Ridge iron and rare-earth-element orebody is a high-temperature, magmatic-hydrothermal deposit. The ore was emplaced within what is thought to be an eroded caldera complex at a relatively shallow level (< 2 km) of the crust. The deposit consists of four mappable zones, the amphibole-quartz, magnetite, hematite, and silicified zones, which formed paragenetically in succession as temperature decreased from greater than 530°C to about 300°C. Ambiguous relations between the silicified and magnetite zones indicate that their period(s) of deposition may have overlapped in part of the deposit. Fluids interstitial to magnetite in the iron orebody may have escaped, boiled, and caused brecciation during rapid and explosive emplacement of the REE-bearing breccia pipes. The magnetite deposit (and the REE-bearing breccia pipes by direct association and geologic relations such as the presence of sanidine as a phenocryst phase) formed from highly saline, high-temperature, magmatically derived hydrothermal fluids. It is possible that the mineralizing fluids are genetically associated with rocks of the iron-rich trachyte suite and that they formed as immiscible fluids.

REFERENCES CITED

Åmli, Reidar, 1975, Mineralogy and rare earth geochemistry of apatite and xenotime from the Gloserheia granite pegmatite, Froland, southern Norway: American Mineralogist, v. 60, p. 607–620.

Bickford, M.E., 1988, The formation of continental crust: Part 1. A review of some principles; Part 2. An application to the Proterozoic evolution of southern North America: Geological Society of America Bulletin, v. 100, p. 1375–1391.

Cunningham, C.G., 1978, Pressure gradients and boiling as mechanisms for localizing ore in porphyry systems: U.S. Geological Survey Journal of Research, v. 6, no. 6, p. 745–754.

Day, W.C., Kisvarsanyi, E.B., Nuelle, L.M., Marikos, M.A., and Seeger, C.M., 1989, New data on the origin of the Pea Ridge iron-apatite deposit, southeast Missouri—Implications for Olympic Dam–type deposits [abs.]: Geological Society of America, Abstracts with Programs, v. 21, no. 6, p. A132.

Day, W.C., Sidder, G.B., Rye, R.O., Nuelle, L.M., and Kisvarsanyi, E.B., 1991, The Middle Proterozoic rhyolite-hosted Pea Ridge iron and rare-earth element deposit—A magmatic source for Olympic Dam–type deposits in the Midcontinent region of the United States [abs.], *in* Chappell, B.W., ed., Second Hutton Symposium on Granites and Related Rocks: Canberra, Australia, Sept. 1991, Abstracts with Program, p. 30.

Emery, J.A., 1968, Geology of the Pea Ridge iron orebody, *in* Ridge, J.D., ed., Ore Deposits of the United States, 1933–1967: New York, American Institute of Mining, Metallurgical, and Petroleum Engineers, Inc., The Graton-Sales Volume, v. 1, p. 359–369.

Husman, J.R., 1989, Gold, rare earth element, and other potential by-products of the Pea Ridge iron ore mine: Missouri Department of Natural Resources, Division of Geology and Land Survey, Contributions to Precambrian Geology No. 21, Open File Report OFR-89-78-MR, 18 p.

Kisvarsanyi, E.B., 1980, Granitic ring complexes and hotspot activity in the St. Francois terrane, Midcontinent region, United States: Geology, v. 8, p. 43–47.

Kisvarsanyi, E.B., 1981, Geology of the Precambrian St. Francois terrane, southeastern Missouri: Missouri Department of Natural Resources, Division of Geology and Land Survey, Report of Investigations No. 64, 58 p.

Kisvarsanyi, E.B., and Kisvarsanyi, Geza, 1989a, Alkaline granite ring complexes and metallogeny in the Middle Proterozoic St. Francois terrane, southeastern Missouri, U.S.A.: Geological Association of Canada Special Paper 38, 14 p.

Kisvarsanyi, Geza, and Kisvarsanyi, E.B., 1981, Genetic relationship of Kiruna-type apatitic iron ores to magnetite trachyte and syenite in the St. Francois terrane, Missouri [abs.]: Geological Society of America, Abstracts with Programs, v. 13, p. 488.

———1989b, Precambrian geology and ore deposits of the southeast Missouri iron metallogenic province, *in* Brown, V.M., Kisvarsanyi, E.B., and Hagni, R.D., eds., "Olympic Dam-Type" Deposits and Geology of Middle Proterozoic Rocks in the St. Francois Mountains Terrane, Missouri: Society of Economic Geologists Guidebook Series, v. 4, p. 1–40.

Kisvarsanyi, Geza, and Proctor, P.D., 1967, Trace element content of magnetites and hematites, southeast Missouri iron metallogenic province, U.S.A.: Economic Geology, v. 62, p. 449–471.

Marikos, M.A., Nuelle, L.M., and Seeger, C.M., 1989, Geology of the Pea Ridge Mine, *in* Brown, V.M., Kisvarsanyi, E.B., and Hagni, R.D., eds., "Olympic Dam-Type" Deposits and Geology of Middle Proterozoic Rocks in the St. Francois Mountains Terrane, Missouri: Society of Economic Geologists Guidebook Series, v. 4, p. 41–54.

Marikos, M.A., Seeger, C.M., and Nuelle, L.M., 1989, REE-mineralized breccia pipes in the Pea Ridge deposit of southeast Missouri [abs.]: Geological Society of America, Abstracts with Programs, v. 21, no. 6, p. A34.

McKeown, F.A., and Klemic, Harry, 1956, Rare-earth-bearing apatite at Mineville, Essex County, New York: U.S. Geological Survey Bulletin 1046–B, p. 9–23.

Nuelle, L.M., Day, W.C., Sidder, G.B., and Seeger, C.M., 1992, Geology and mineral paragenesis of the Pea Ridge iron ore mine, Washington County, Missouri—Origin of the rare-earth-element- and gold-bearing breccia pipes, *in* Day, W.C., and Lane, D.E., Strategic and Critical Minerals in the Midcontinent Region, United States: U.S. Geological Survey Bulletin 1989, Chapter A, p. A1–A11.

Nuelle, L.M., Kisvarsanyi, E.B., Seeger, C.M., Day, W.C., and Sidder, G.B., 1991, Structural setting and control of the Pea Ridge magnetite deposit, Middle Proterozoic St. Francois terrane, Missouri [abs.]: Geological Society of America, Abstracts with Programs, v. 23, no. 5, p. A292.

Nuelle, L.M., Marikos, M.A., Seeger, C.M., and Day, W.C., 1989, Hydrothermal aspects of amphibole and magnetite emplacement in the Pea Ridge Fe-REE deposit, Washington County, Missouri [abs.]: Geological Society of America, Abstracts with Programs, v. 21, no. 6, p. A248.

Nuelle, L.M., Seeger, C.M., Marikos, M.A., and Day, W.C., 1989, Mineral assemblages of the Pea Ridge Fe-REE deposit: Implications of an Olympic Dam–type variant in southeast Missouri [abs.]: Geological Society of America, Abstracts with Programs, v. 21, no. 6, p. A34.

Oreskes, Naomi, and Einaudi, M.T., 1990, Origin of rare earth element-enriched hematite breccias at the Olympic Dam Cu-U-Au-Ag deposit, Roxby Downs, South Australia: Economic Geology, v. 85, p. 1–28.

Potter, R.W., II, Babcock, R.S., and Brown, D.L., 1977, A new method for determining the solubility of salts in aqueous solutions at elevated temperatures: U.S. Geological Survey Journal of Research, v. 5, no. 3, p. 389–395.

Reeve, J.S., Cross, K.C., Smith, R.N., and Oreskes, Naomi, 1990, Olympic Dam copper-uranium-gold-silver deposit, *in* Hughes, F.E., ed., Geology of the Mineral Deposits of Australia and Papua New Guinea: Australasian Institute of Mining and Metallurgy, Monograph no. 14, p. 1009–1035.

Seeger, C.M., Nuelle, L.M., and Marikos, M.A., 1989, Massive silicification and late stage quartz veining in the Pea Ridge Fe-REE deposit, southeast Missouri [abs.]: Geological Society of America, Abstracts with Programs, v. 21, no. 6, p. A34.

Sidder, G.B., Nuelle, L.M., Day, W.C., Rye, R.O., Seeger, C.M., and Kisvarsanyi, E.B., 1991, Paragenesis and conditions of formation of the Pea Ridge iron and rare-earth element deposit, Missouri [abs.]: Geological Society of America, Abstracts with Programs, v. 23, no. 5, p. A292.

Sims, P.K., Kisvarsanyi, E.B., and Morey, G.B., 1987, Geology and metallogeny of Archean and Proterozoic basement terranes in the northern midcontinent, U.S.A.—An overview: U.S. Geological Survey Bulletin 1815, 51 p.

Stormer, J.C., Jr., 1983, The effects of recalculation on estimates of temperature and oxygen fugacity from analyses of multicomponent iron-titanium oxides: American Mineralogist, v. 68, p. 586–594.

Whitten, C.W., and Cornell, W.L., 1991, Rare earth occurrences in the Pea Ridge tailings: American Institute of Mining Engineers Preprint, 20 p.

Whitten, C.W., and Yancey, R.J., 1990, Characterization of the rare earth mineralogy at the Pea Ridge deposit: U.S. Bureau of Mines, Report of Investigations 9331, 15 p.

CHAPTER V

MINERAL RESOURCE POTENTIAL OF THE WHITE RIVER NATIONAL FOREST AND THE DILLON RANGER DISTRICT OF THE ARAPAHO NATIONAL FOREST, COLORADO

By MARGO I. TOTH,[1] ANNA B. WILSON,[2] THERESA M. COOKRO,[3] VIKI BANKEY,[4] GREG K. LEE,[5] *and* JOHN S. DERSCH[6]

ABSTRACT

The mineral resource potential of the White River National Forest and Dillon Ranger District of the Arapaho National Forest (referred to as "the Forest" in this report) was evaluated by the U.S. Geological Survey (USGS). Geological, geochemical, and geophysical data were compiled and compared to characteristics of known and inferred deposits within or close to the Forest. Models for 14 locatable commodities and five leasable commodities were identified and evaluated. For locatable commodities, the Forest contains 751 mi^2 of high resource potential, 535 mi^2 of moderate resource potential, 83 mi^2 of low resource potential, and 6 mi^2 of unknown resource potential. For leasable commodities, the Forest contains 433 mi^2 of high resource potential and 85 mi^2 of low resource potential.

[1]U.S. Geological Survey, Mail Stop 922, P.O. Box 25046, Denver Federal Center, Denver, CO 80225.

[2]U.S. Geological Survey, Mail Stop 905, P.O. Box 25046, Denver Federal Center, Denver, CO 80225.

[3]U.S. Geological Survey, Mail Stop 937, P.O. Box 25046, Denver Federal Center, Denver, CO 80225.

[4]U.S. Geological Survey, Mail Stop 964, P.O. Box 25046, Denver Federal Center, Denver, CO 80225.

[5]U.S. Geological Survey, Mail Stop 973, P.O. Box 25046, Denver Federal Center, Denver, CO 80225.

[6]U.S. Forest Service, U.S. Department of Agriculture, 11177 W. 8th Avenue, P.O. Box 25127, Lakewood, CO 80225.

INTRODUCTION

The assessment of the mineral resource potential of the White River National Forest and Dillon Ranger District of the Arapaho National Forest, Colorado (fig. 1), was made to assist the U.S. Forest Service in fulfilling the requirements of Title 36, Chapter 2, part 219.22, Code of Federal Regulations and to supply resource information and interpretations so that the mineral resources of the Forest could be considered, along with other resources, in land-use planning. The Dillon Ranger District of the Arapaho National Forest was included in the report on the White River National Forest because the two areas are administered by the staff of the White River Forest and are included in a single planning document. For simplicity, only figure 1 distinguishes or outlines the Dillon Ranger District; in all other figures the district is included within the Forest boundary. The identified, or known, resources of the Forest were studied by the U.S. Bureau of Mines (Brown, 1990); the potential for undiscovered mineral and energy resources was studied by the U.S. Geological Survey (Toth and others, in press). This report is an abbreviated summary of Toth and others (in press).

The Forest encompasses about 2.4 million acres in central and northwestern Colorado in two separate parcels: a southern parcel that is elongate in an east-west direction and a northern, square-shaped parcel. Eight distinct mountain ranges and parts or all of ten counties are within the Forest. The entire Forest is on the western side of the Continental Divide, which forms the eastern boundary of parts of the Forest in many places. Except for some water diversion projects, the Forest watershed drains into the

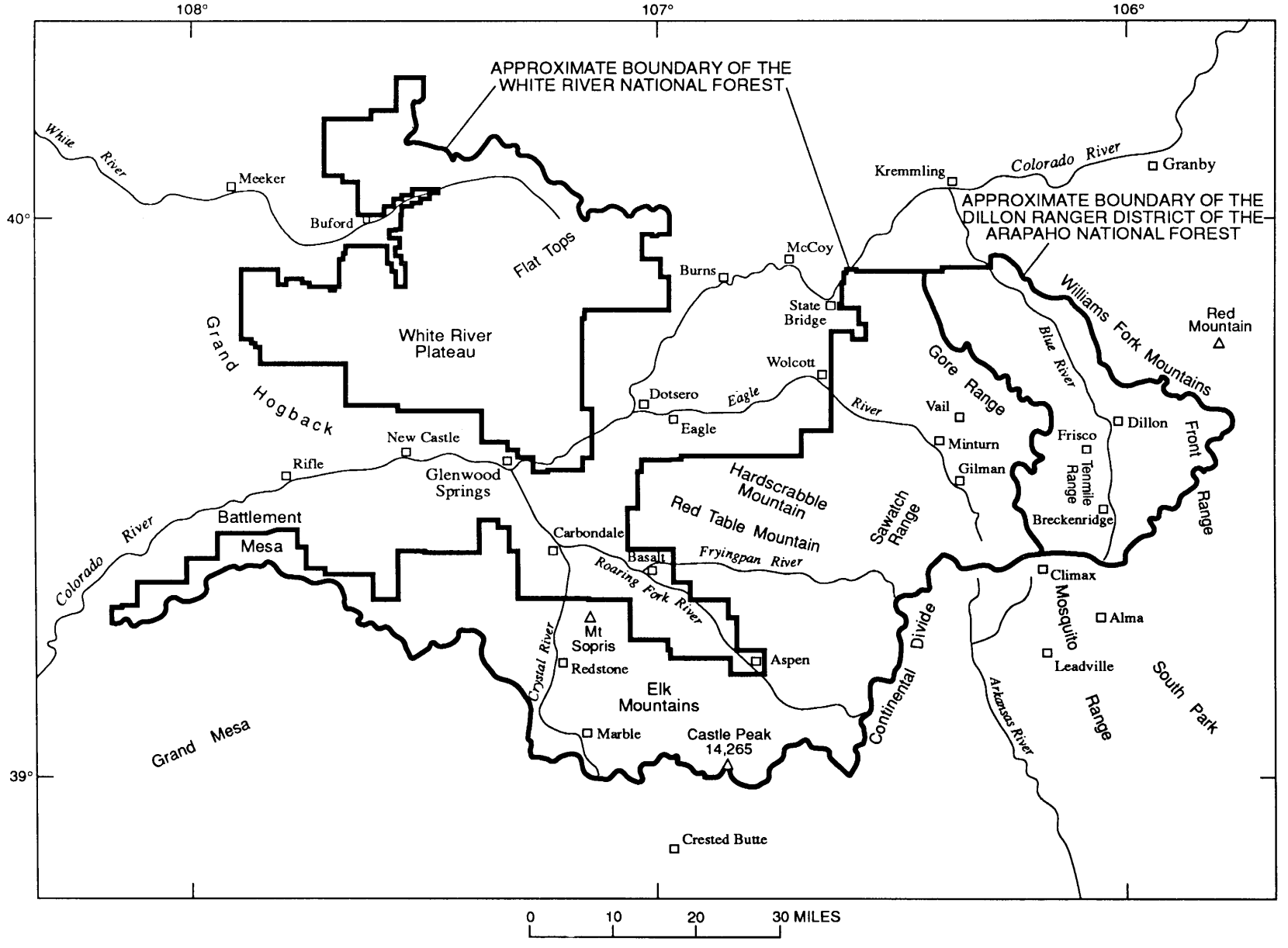

Figure 1. Index map showing the location of the White River National Forest and Dillon Ranger District of the Arapaho National Forest, Colorado.

Colorado River, which flows southwestward through central and western Colorado. Interstate Highway 70 traverses east-west through the central part of the Forest, and numerous other State and county highways extend through or to the Forest. Improved and unimproved roads and jeep trails provide access throughout the Forest. The major communities within and near the Forest are Aspen, Breckenridge, Dillon, Frisco, Vail, and Glenwood Springs.

GEOLOGIC HISTORY

Discussions of the geologic and tectonic history of central and northwestern Colorado are summarized in Tweto (1980), Wallace (1990), Mutschler and others (1987), and Toth and others (in press). The geologic history recorded in the Forest spans more than 1.8 billion years. The major structural and rock-forming events are as follows: Early Proterozoic accretion and metamorphism of volcanic and sedimentary rocks, and intrusion of granitic plutons; early to middle Paleozoic deposition of marine and nonmarine sedimentary rocks during repeated epeirogenic movements; late Paleozoic and early Mesozoic erosion and deposition related to the formation of two highlands, separated by a narrow basin; Late Cretaceous through early Eocene uplift during the Laramide orogeny, along with volcanism and emplacement of granitic plutons; middle Tertiary tectonic quiescence, accompanied by volcanism and emplacement of granitic plutons; late Cenozoic magmatism, block faulting in an extensional regime, formation of a bimodal suite of basalt and rhyolite and emplacement of related plutons; and Pleistocene to Holocene glaciation and erosion. The simplified geology and a few of the major structural features in the Forest are shown on figure 2.

Within the Forest, Proterozoic crystalline rocks are exposed in mountain ranges in the eastern part of the Forest and in some of the deeper canyons in the northwestern part of the Forest. Paleozoic sedimentary rocks flank the Proterozoic rocks on the western, northern, and eastern sides and are also exposed in the northwestern part of the Forest. Mesozoic sedimentary rocks are located principally in the northeastern part of the Forest and along the western boundary of the Forest, including exposures along the Grand Hogback monocline. To the west of the monocline, Tertiary sedimentary rocks are exposed in the Piceance Basin. Tertiary basalt flows are mostly in the northwestern part of the Forest, where they overlie Paleozoic sedimentary rocks. Laramide and younger plutons are concentrated along a northeast-trending zone through the southern and eastern parts of the Forest. Mineral deposits are also concentrated along this zone, known as the Colorado Mineral Belt (Tweto and Sims, 1963) (fig. 3).

GEOCHEMISTRY

The geochemical contributions to the mineral resource assessment of the White River National Forest were derived from data that include analyses for 2,661 rock, 637 stream-sediment, 820 heavy-mineral-concentrate, and 1,856 National Uranium Resource Evaluation (NURE) stream-sediment samples from the U.S. Geological Survey Branch of Geochemistry databases—altogether this represents 5,513 sample locations. The NURE data were combined from digital copies of analyses listed for the Leadville (Planner and others, 1981), Grand Junction (Langfeldt and others, 1981), Montrose (Broxton and others, 1979), Craig (Bolivar and others, 1979), and Denver (Shettel and others, 1981) 1°×2° quadrangles. Included in the geochemical information produced by the USGS were published and unpublished data previously generated for mineral resource appraisals of Wildernesses, Wilderness Study Areas, Primitive Areas, and Roadless Areas (Wallace and others, 1989; Van Loenen and others, 1989; Freeman and others, 1985; Ludington and Ellis, 1981; Tweto and others, 1970; Mallory and others, 1966; Soulliere and others, 1985a, 1985b, 1986; Theobald and others, 1983).

Analyses for 39 elements were included in the data and, of these, 15 were selected for primary use in the geochemical contribution to the assessment of resource potential in the Forest. These elements are silver, arsenic, gold, cobalt, chromium, copper, molybdenum, nickel, lead, antimony, tin, uranium, vanadium, tungsten, and zinc. The distributions of boron, barium, bismuth, beryllium, chromium, iron, manganese, and thorium were also examined but were determined to be less significant than the 15 elements mentioned above for use in the evaluation.

To combine the data from different sample media and analytical methods, a series of mathematical operations was performed on the data sets. Standardized data sets were created by performing various mathematical operations, resulting in numeric values that represented the number of standard deviations that the original value deviated from mean. Values between 2 and 3 in the transformed data were considered to represent slightly anomalous concentrations; values of 3 to 5 were treated as moderately anomalous; and values above 5 were considered highly anomalous. Interpretations were derived from graphical displays that could simultaneously include all available data.

These data were spatially interpolated, and contour plots were produced to provide areal representations of anomalous concentrations of various elements in the study area. Point plots of element suites were also generated to give a detailed accounting of the sample-site locations for the anomalous areas as well as a view of associations of elements that are thought to be likely constituents of various mineral-deposit types. In the Forest, samples containing

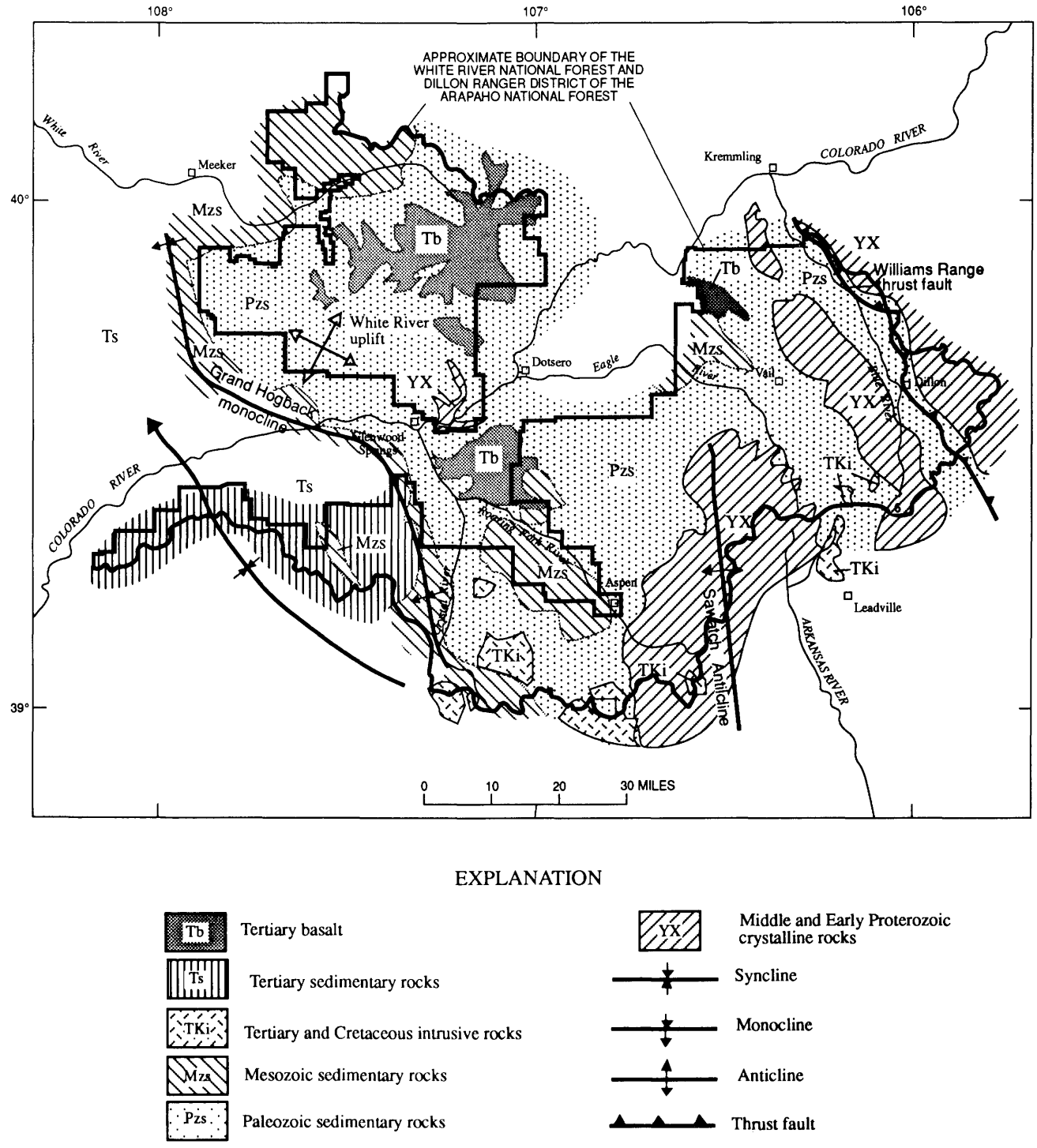

Figure 2. Map showing simplified geology and some of the major structural elements within or close to the White River National Forest and Dillon Ranger District of the Arapaho National Forest, Colorado.

anomalous concentrations of base and precious metals and related elements occur mostly in the proximity of known mining districts and mineral-deposit occurrences (Toth and others, in press). However, many areas of isolated anomalies of base and (or) precious metals were not found to be related to any known occurrences.

GEOPHYSICS

Three sets of geophysical data (gravity, aeromagnetic, and radiometric) were compiled and interpreted for the Forest (Toth and others, in press; Bankey, this volume). Sources of data include studies of six Forest Service and

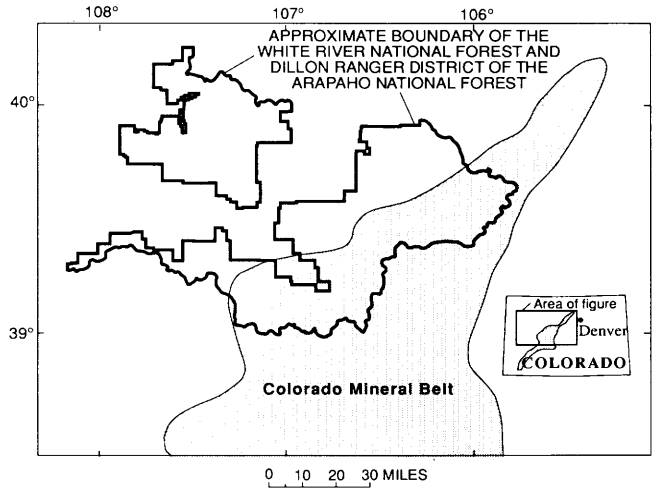

Figure 3. Map of the Colorado Mineral Belt. Modified from Tweto and Sims (1963).

BLM Wilderness Study Areas within the Forest (Campbell, 1981, 1985; Campbell and Wallace, 1986; Van Loenen and others, 1989; Tweto and others, 1970; and Moss and Abrams, 1985). Geophysical studies to support mineral resource studies in the Colorado Mineral Belt were made by Case and Tweto (Case, 1965, 1966, 1967; Tweto and Case, 1972). Other related geophysical studies include ones by Behrendt and Bajwa (1974) and Isaacson and Smithson (1976).

A complete Bouguer gravity anomaly map was produced using edited gravity data from 6,500 stations collected over the past several decades (Toth and others, in press). A derivative gravity map was calculated from the Bouguer gravity grid using the program FFTFIL (Hildenbrand, 1983) to remove or filter anomaly wavelengths longer than 30 mi. This derivative map emphasizes anomalies produced by shallow sources and suppresses the longer wavelength anomalies (> 30 mi) related to deep sources, such as regional gradients in the Colorado Plateau, in the White River uplift, and in the Colorado Mineral Belt gravity low.

A magnetic anomaly map was compiled showing regional magnetic anomalies (Toth and others, in press). The horizontal gradient of the pseudogravity field was calculated using the method of Cordell and Grauch (1985). This method calculates "pseudo" gravity anomalies caused by assumed density contrasts of bodies causing magnetic anomalies, and it is used because gravity anomalies are simpler to analyze than magnetic anomalies. Maximum gradient trends of the pseudogravity field were plotted on a contour map as long, partially discontinuous lines.

Gamma-ray-spectrometer data for the Forest are from airborne NURE surveys. Measurements detected near-surface (shallower than 20 inches) abundances of the radioelements uranium, potassium, and thorium. The contractor-interpreted amounts of K (in percent), "equivalent" uranium (eU, in ppm), and "equivalent" thorium (eTh, in ppm) were contoured and analyzed (Toth and others, in press).

MINING HISTORY

The White River National Forest and Dillon Ranger District of the Arapaho National Forest have a wealth of mineral resources. Mining and mineral exploration have played a central role in the history of this area and are still important. The Forest contains 26 mining districts and mineralized areas (fig. 4).

Most of the mining districts and major orebodies in the Forest had been discovered by the late 1800's. In 1859, gold placers in the Breckenridge district were the first deposits to be worked, and gold placers were discovered a year later a few miles south of the Forest, at Leadville. These two areas include some of the richest placer deposits in Colorado.

Base- and precious-metal lode deposits were discovered a few years after the gold placers. The first silver vein was discovered in the Forest in the Montezuma mining district in 1864. During the next decade, lode deposits were discovered and exploited throughout the Colorado Mineral Belt (Tweto and Sims, 1963). In 1878, bonanza silver deposits were discovered in the Kokomo-Tenmile district; silver-lead ore was found at Gilman and in the Aspen district the next year.

The Gilman district, known for its copper and zinc, is the State's largest producer of metals. The Eagle mine was the major producer, and it consolidated many older mines and workings into a single operating unit in 1918. Next in overall production in the Forest are the Aspen, Breckenridge, and Kokomo-Tenmile districts, respectively. Other districts and mines in the Forest had less significance in terms of total production.

The Eagle mine in the Gilman district ceased production in 1981. No large-scale mining has taken place in the Forest since that time; current mineral activity consists of annual assessment work on unpatented mining claims, prospecting, and small-scale mining, mostly in the Breckenridge area.

MINERAL RESOURCE POTENTIAL

Mineral resource potential information is given in terms of mineral-deposit types. The deposit types are based on geological, geochemical, and geophysical characteristics of known and inferred deposits within or close to the Forest and similarities to deposits described in Cox and Singer (1986). Most of the deposit types are represented by type localities at a mine or within mining districts.

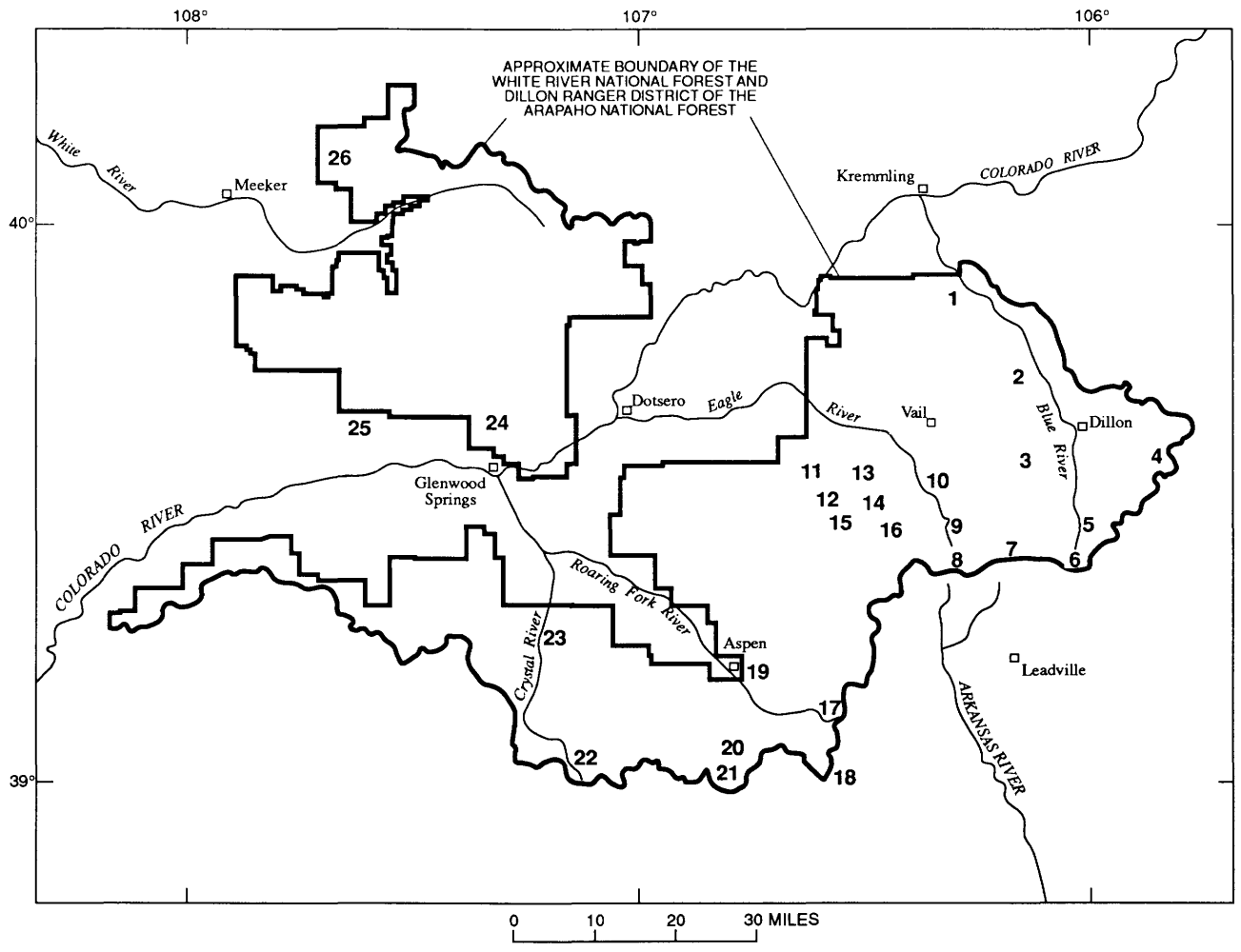

Figure 4. Index map showing mining districts within or close to White River National Forest and Dillon Ranger District of the Arapaho National Forest, Colorado. Numbers on map are keyed to mining districts as follows: 1, Green Mountain; 2, North Rock Creek; 3, Frisco; 4, Montezuma; 5, Breckenridge; 6, Upper Blue River; 7, Kokomo-Tenmile; 8, Tennessee Pass; 9, Eagle; 10, Gilman; 11, Fulford; 12, New York Lake; 13, East Lake Creek; 14, East Lake Creek–Cross Creek; 15, Middle Mountain; 16, Holy Cross City–Cross Creek; 17, Independence; 18, Lincoln Gulch; 19, Aspen; 20, Columbia-Ashcroft; 21, Taylor Peak, 22, Crystal River; 23, Spring Butte; 24, Carbonate; 25, Rifle Creek; 26, Uranium Peak. Map modified from Brown (1990).

All available information was assembled and analyzed according to procedures outlined by Shawe (1981) and Taylor and Steven (1983). The assessment of mineral resource potential in this summary is divided into three parts: locatable, leasable, and salable commodities. Table 1 summarizes the total size of areas of high, moderate, low, or unknown resource potential for locatable and leasable minerals, and figures 5–10 show areas of resource potential for all commodities except salable minerals. For simplicity, only the areas of high and moderate resource potential are shown on the figures, although areas of low or unknown potential may be mentioned in the text. Where areas of differing resource potential overlap, only the highest degree is shown (i.e., high instead of moderate). The reader is referred to Toth and others (in press) for more detail.

LOCATABLE COMMODITIES

A. Stockwork molybdenum.—Formed in the carapaces of highly differentiated granitic plutons and in the adjacent country rocks; valuable mainly for molybdenum but also contain tungsten, tin, and bismuth. Plutons occur in the southern part of the Forest. Three small areas have high resource potential, and three small areas have moderate resource potential (fig. 5).

B. Stockwork copper-molybdenum.—Formed in granite bodies; valuable mainly for copper and molybdenum, but can also contain gold, tungsten, tin, silver, lead, zinc, and bismuth. One small area in the southern part of the Forest has high resource potential (fig. 5); a small area just outside the southeastern part of the Forest has high resource potential; and two small areas have low resource potential.

Table 1. Resource potential of lands in the White River National Forest and Dillon Ranger District of the Arapaho National Forest classified according to type of deposit.

[The White River National Forest and Dillon Ranger District of the Arapaho National Forest contain a total of 3,928 mi^2. Figures in columns under each category of resource potential in mi^2 and rounded to the nearest mi^2. Letters in parentheses preceding the deposit type indicate the deposit type as discussed below. --, no area of resource potential for that category of resource potential]

Type of deposit	Mineral resource potential			
	High	Moderate	Low	Unknown
Locatable resources				
(A) Stockwork Mo	1	14	--	--
(B) Stockwork Cu-Mo	11	--	--	--
(C) Skarn	1	1	27	--
(D) Polymetallic replacement	82	111	1	--
(E) Sherman-type Pb-Zn-Ag	7	37	--	--
(F) Polymetallic vein	382	245	--	--
(G) Vein U	1	1	1	--
(H) Vein W	--	18	--	--
(I) Sandstone Cu	2	--	--	--
(J) Sandstone U-V	54	--	44	--
(K) Placer gold	33	6	8	--
(L) Stratabound sulfides	--	--	2	6
(M) Limestone	175	17	--	--
(N) Gypsum	2	85	--	--
Total locatable resources	751	535	83	6
Leasable resources				
(O) Oil and gas	332	--	--	--
(P) Coal	38	33	--	--
(Q) Methane	38	33	--	--
(R) Oil shale	--	52	--	--
(S) Geothermal energy	30	--	--	--
Total leasable resources	438	118	--	--

C. Polymetallic skarn.—Formed at the contact between intrusive igneous rocks and chemically reactive host rocks, such as limestone; valuable mainly for copper, lead, zinc, silver, tungsten, manganese, and iron, but may also contain trace amounts of gold. An area of high resource potential occurs south of Aspen, where an iron skarn was previously mined. Two small areas of moderate resource potential (fig. 5) and two small areas of low resource potential are in the southeastern part of the Forest.

D. Polymetallic replacement.—Formed by hydrothermal solutions traversing limestone and dolomite; contain copper, lead, zinc, silver, and manganese, but many also contain tungsten and gold. The principal area of high resource potential is along the flanks of the Sawatch Range where the Leadville Limestone is present (fig. 6*A*). Three other small areas have high resource potential, and two have moderate resource potential; these areas are usually associated with polymetallic vein deposits.

E. Sherman-type Pb-Zn-Ag.—Formed by the infilling of solution-collapse structures in the Leadville Limestone; contain lead, zinc, and silver. The Leadville Limestone has a high resource potential in a small area along the southwestern flank of the Sawatch Range and in a small area along the eastern flank. The remaining outcrops of Leadville Limestone have moderate resource potential (fig. 6*B*).

F. Polymetallic veins.—Related to Laramide and Tertiary igneous intrusions; contain lead, zinc, copper, silver, gold, and manganese; likely byproducts are tin, antimony, and arsenic. Principal areas of high resource potential are in the Carbonate, Crystal River, Independence and Lincoln Gulch, Fulford, New York Lake, East Lake Creek, Cross Creek, Middle Mountain, Holy Cross City, Gilman, Breckenridge, Montezuma, North Rock Creek, and Green Mountain mining districts (figs. 4, 7); three large areas of moderate resource potential are along the southern and southeastern parts of the Forest.

G. Vein uranium.—Formed from hydrothermal solutions associated with igneous intrusions; containing uranium and trace amounts of gold, silver, antimony, lead, zinc, and molybdenum. One small area, northeast of Aspen, has high resource potential (fig. 7); two small areas have moderate resource potential.

H. Vein tungsten.—Formed from hydrothermal solutions associated with igneous intrusions; contain tungsten, gold, silver, and zinc. Two small areas in the eastern part of the Forest, near Frisco, have moderate resource potential (fig. 7).

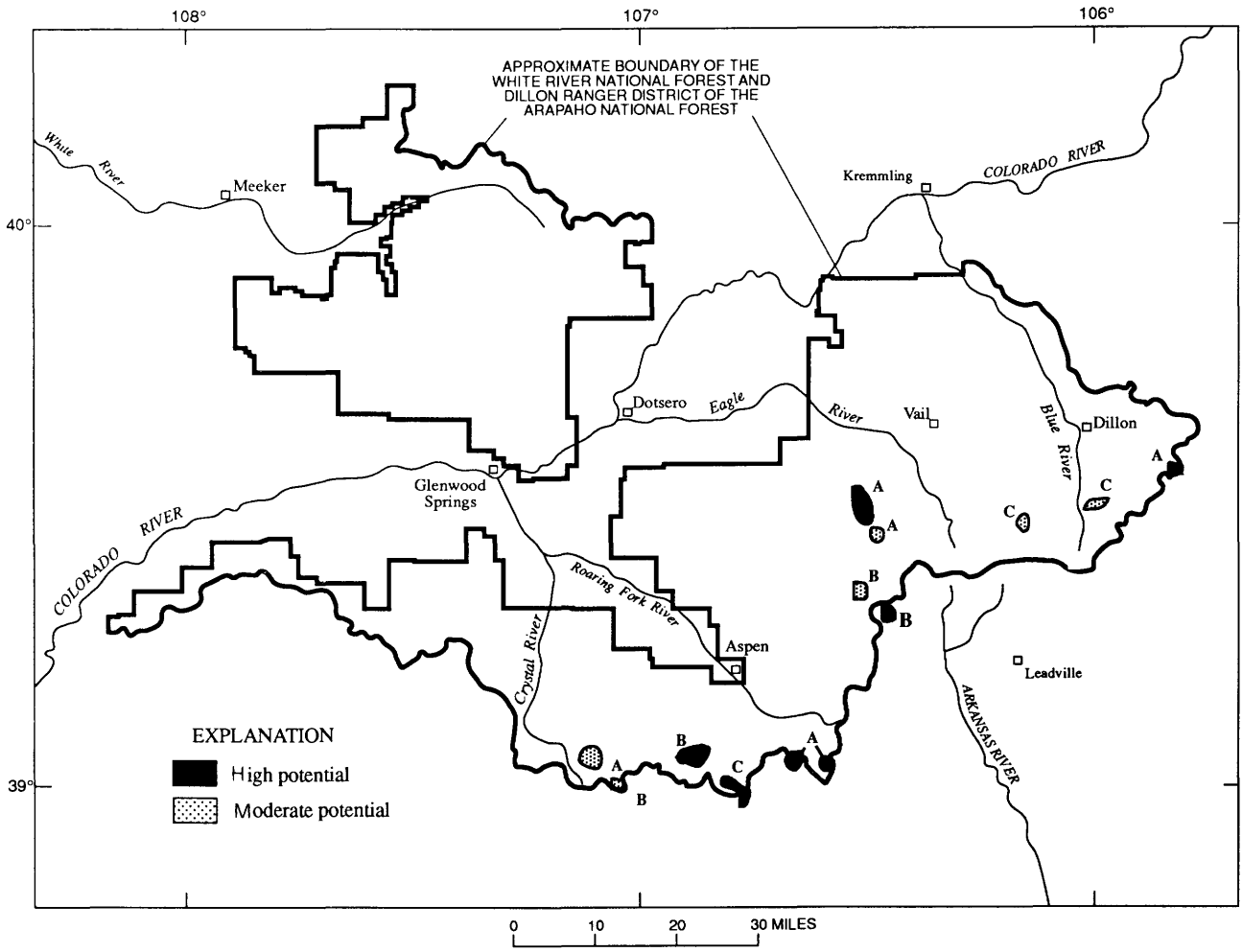

Figure 5. Mineral resource potential map for stockwork molybdenum (deposit type A), stockwork copper-molybdenum (deposit type B), and polymetallic skarn deposits (deposit type C) in the White River National Forest and Dillon Ranger District of the Arapaho National Forest, Colorado.

I. Sandstone copper.—Formed where copper-rich solutions encountered reducing environments in sandstone layers; contain copper and uranium, with byproducts silver and vanadium. One small area in the Forest, southwest of Vail, has high resource potential, and another small area, just west of Aspen, has high resource potential (fig. 8).

J. Sandstone uranium-vanadium.—Formed during diagenesis in locally reducing environments in sandstone; contain uranium, vanadium, and trace amounts of copper. Two small areas in eastern part the Forest and one large area in the northwestern part of the Forest have high resource potential (fig. 8).

K. Placer gold.—Deposited by streams that traversed and eroded gold-bearing rock; contain gold and minor quantities of silver and bismuth. One large area near Breckenridge, along the upper Blue River, has high resource potential. Seven small areas of moderate resource potential (fig. 8), in the southeastern part of the Forest, are downstream from known mining districts.

L. Stratabound sulfide deposits in Proterozoic rocks.—Formed where exhalatives from mafic volcanic rocks interacted with sea water to form brines; deposited in volcanic and sedimentary rocks in a submarine environment in Proterozoic time; contain copper, lead, zinc, gold, and silver. Three small areas in the eastern part of the Forest have low resource potential; several outcrops in the west-central part of the Forest and two small areas in the eastern part of the Forest have unknown resource potential.

M. High-calcium limestone.—Formed in shallow-water marine environment in Mississippian time. Areas on the flanks of the Sawatch Range, in the southeastern part of the Forest, and south of the Flat Tops, in the northwestern part of the Forest, that are underlain by the Leadville Limestone have high resource potential (fig. 9). Areas with moderate resource potential in the southeastern part of the Forest are underlain by Leadville Limestone that has been mineralized.

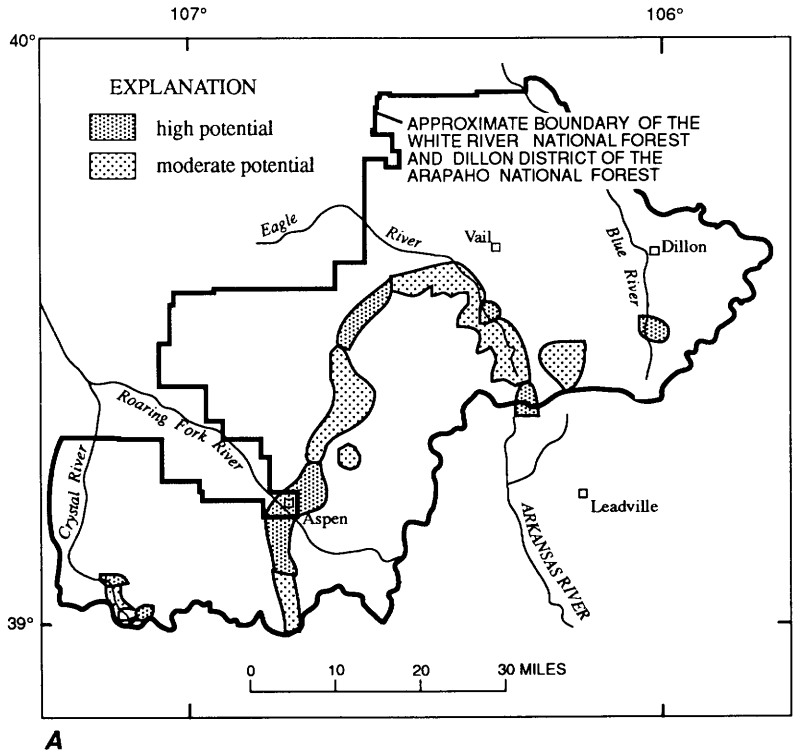

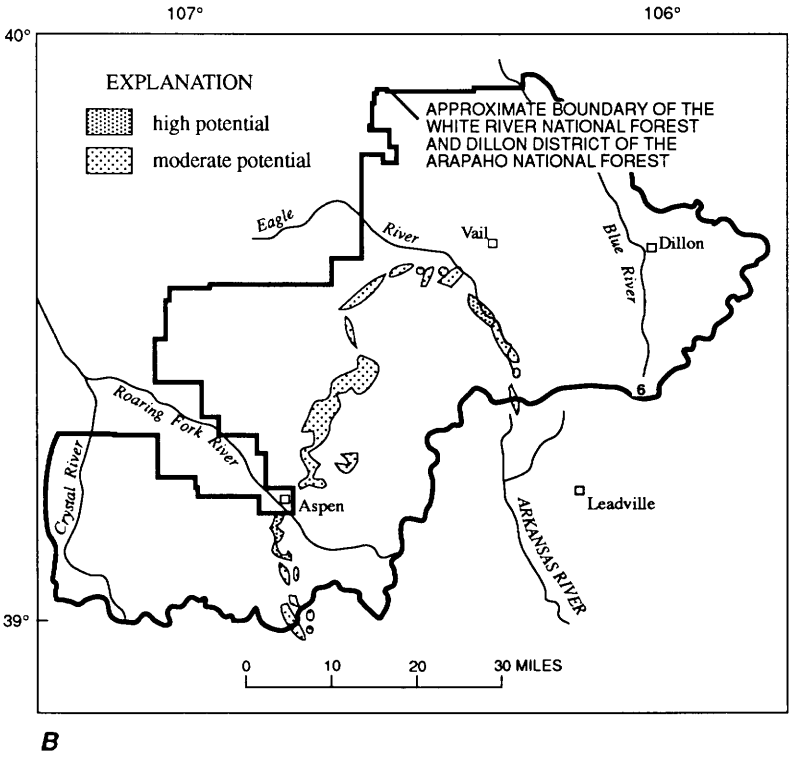

Figure 6. *A*, Mineral resource potential map for polymetallic replacement deposits (deposit type D), and *B*, mineral resource potential map for Sherman-type Pb-Zn-Ag (deposit type E) in the White River National Forest and Dillon Ranger District of the Arapaho National Forest, Colorado. Where areas of differing potential overlap, only the area of high potential is shown.

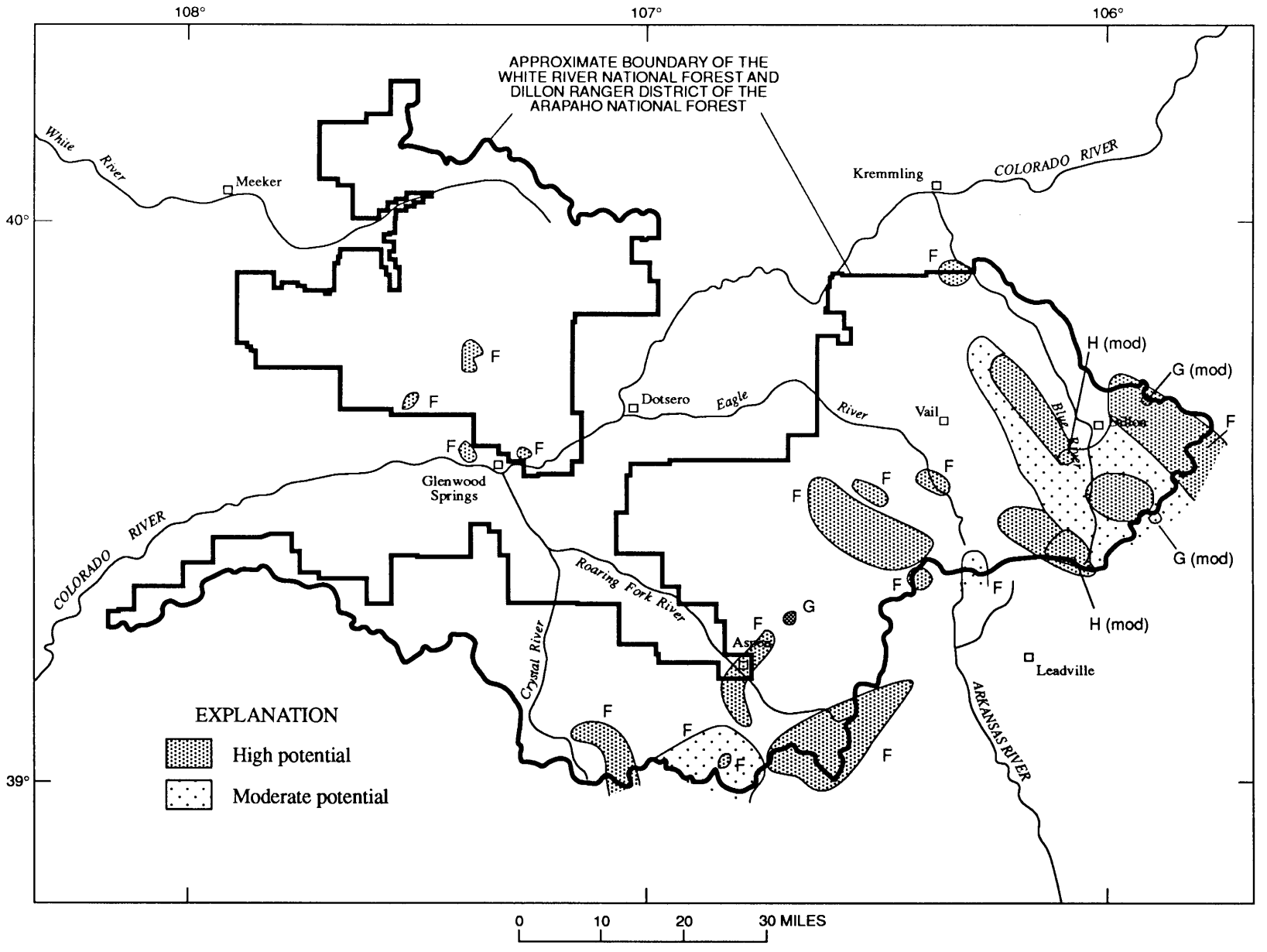

Figure 7. Mineral resource potential map for polymetallic vein (deposit type F), vein uranium (deposit type G), and vein tungsten (deposit type H) deposits in the White River National Forest and Dillon Ranger District of the Arapaho National Forest, Colorado. Where areas of potential overlap, the area of high potential is shown; the area of moderate potential is indicated by "(mod)."

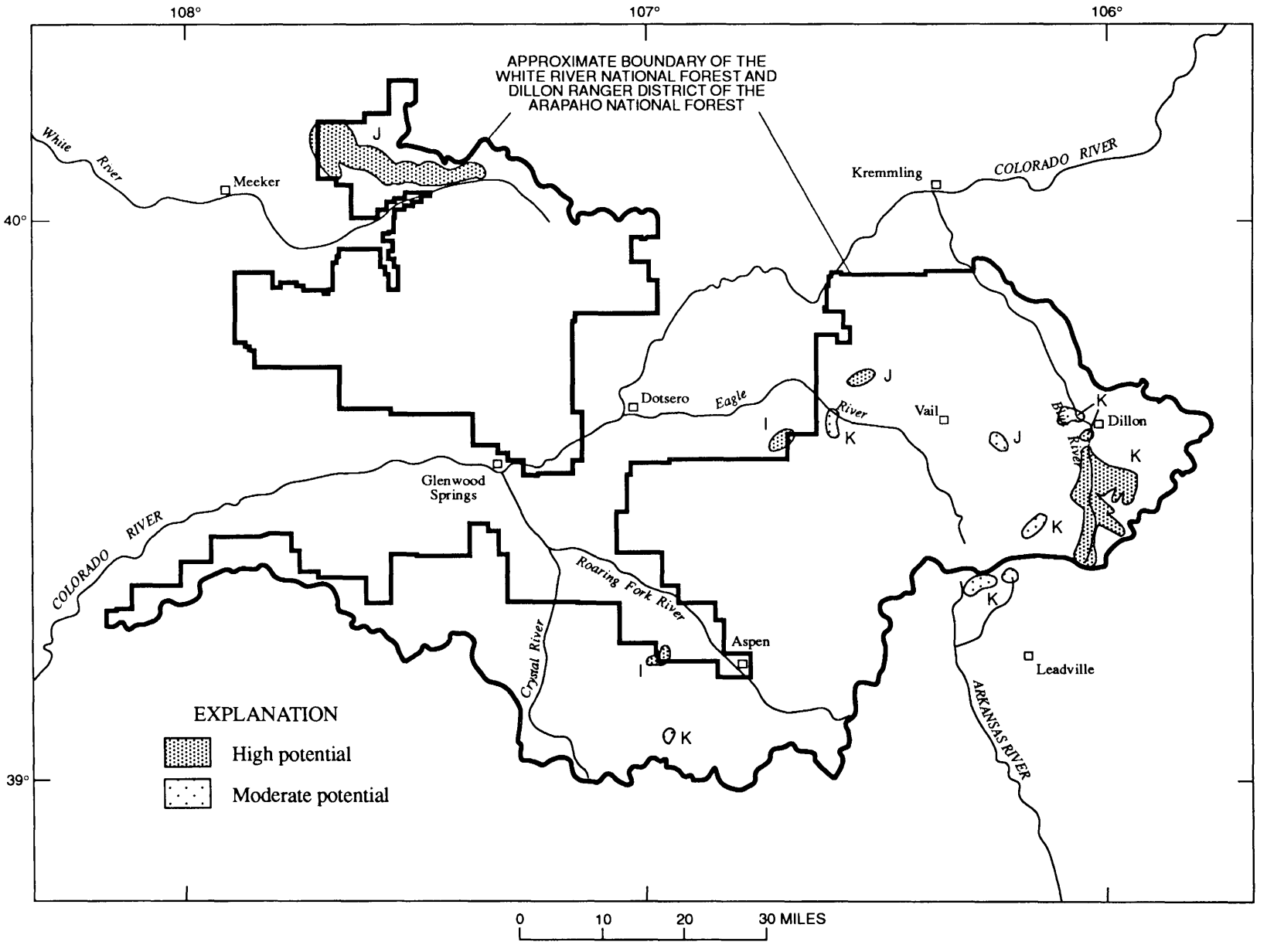

Figure 8. Mineral resource potential map for sandstone copper (deposit type I), sandstone uranium-vanadium (deposit type J), and placer gold (deposit type K) deposits in the White River National Forest and Dillon Ranger District of the Arapaho National Forest, Colorado. Where areas of different potential overlap, only the area of high potential is shown.

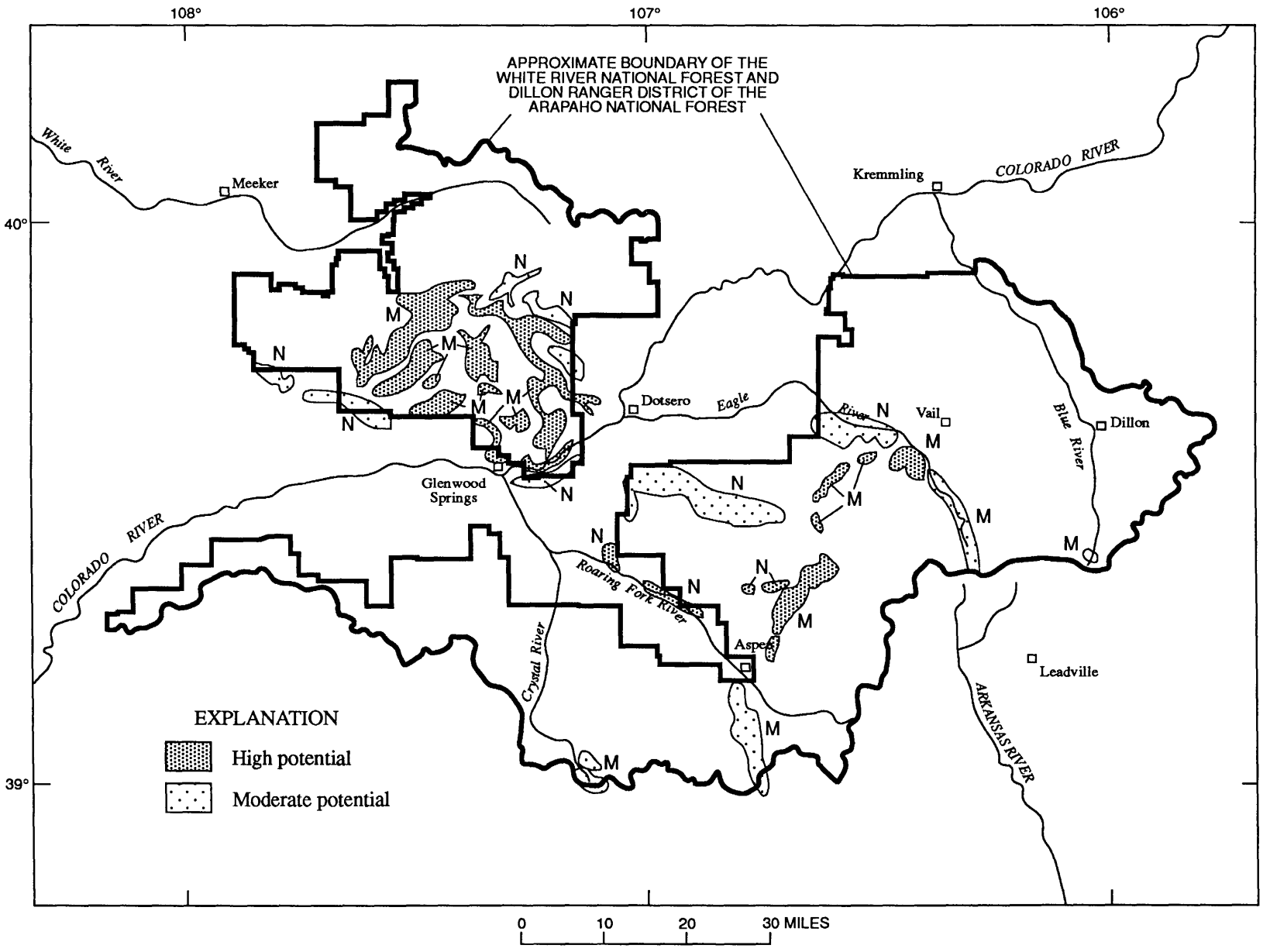

Figure 9. Mineral resource potential map for high-calcium limestone (deposit type M) and gypsum in evaporite deposits (deposit type N) in the White River National Forest and Dillon Ranger District of the Arapaho National Forest, Colorado. Where areas of different potential overlap, only the area of high potential is shown.

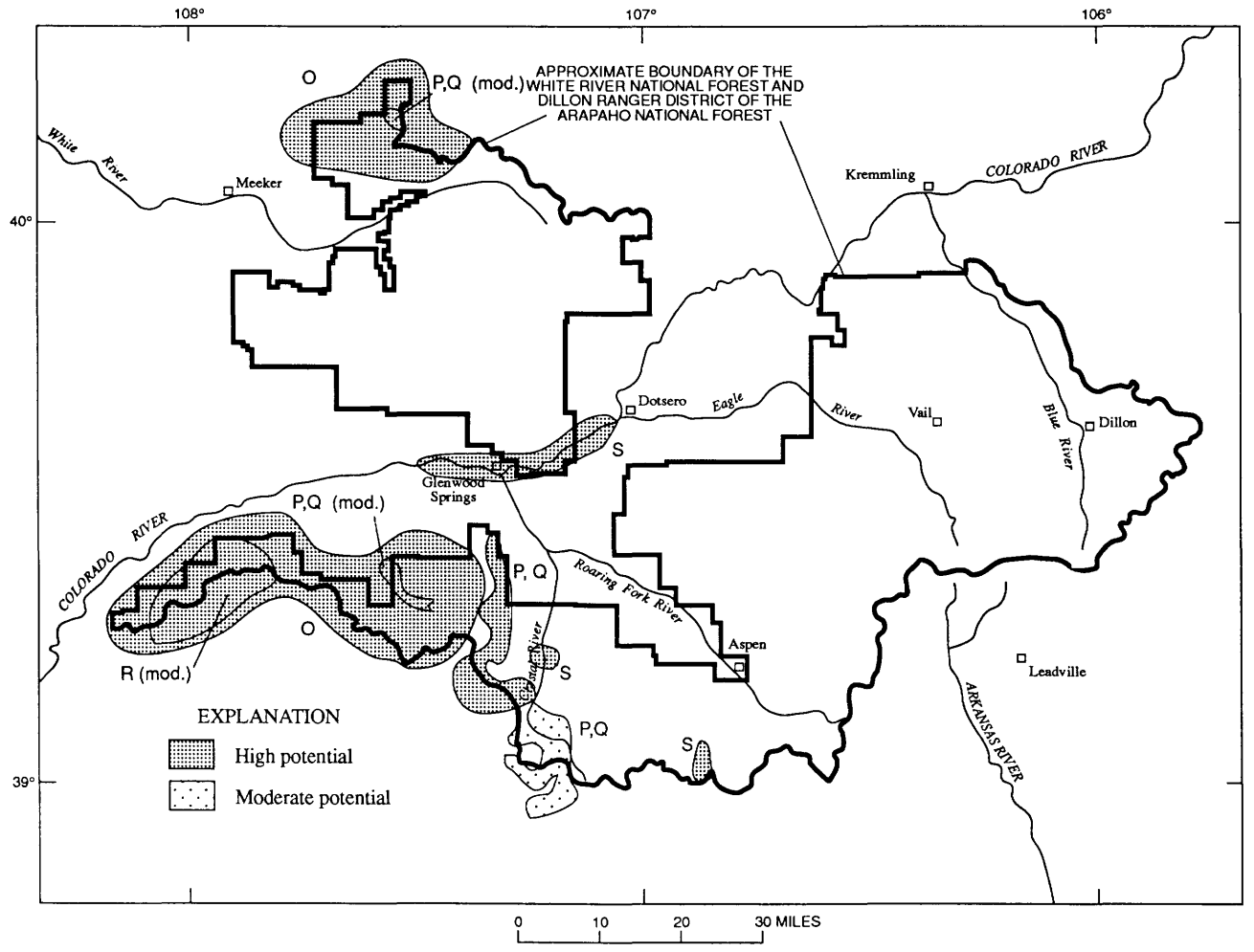

Figure 10. Mineral resource potential map for oil and gas (deposit type O), coal (deposit type P), coalbed methane (deposit type Q), and oil shale (deposit type R), and geothermal resources (deposit type S) in the White River National Forest and Dillon Ranger District of the Arapaho National Forest, Colorado. Where areas of different potential overlap, the area of high potential is shown; the area of moderate potential is indicated by "(mod)."

N. Gypsum in evaporite deposits.—Formed in shallow-water marine environment. Resource potential is high north of Aspen, where thick and relatively pure beds of evaporite are present; resource potential is moderate in several areas in the northwestern and central parts of the Forest (fig. 9).

LEASABLE COMMODITIES

O. Oil and gas.—Formed in a near-shore and coastal-plain environments. Two large areas of high resource potential are along the western part of the Forest (fig. 10).

P. Coal.—Formed in a deltaic system from the decomposition and alteration of organic remains. One area in the southwestern part of the Forest has high resource potential; one area in the northwestern part of the Forest and two areas in the southwestern part of the Forest have moderate resource potential (fig. 10).

Q. Coalbed methane.—Generated in the maturation process of coal. One area in the southwestern part of the Forest has high resource potential; one area in the northwestern part of the Forest and two areas in the southwestern part of the Forest have moderate resource potential (fig. 10).

R. Oil shale.—Formed in a large, shallow lake and on broad playa fringes. One large area in the southwestern part of the Forest has moderate resource potential (fig. 10).

S. Geothermal energy.—Resource areas consist of thermal springs located along fault zones. One large area near Glenwood Springs has high resource potential and two smaller areas in the south-central part of the Forest have high resource potential (fig. 10).

Table 2. Quantitative estimates of undiscovered resources of stockwork molybdenum, polymetallic vein, polymetallic replacement, and placer gold deposits in the White River National Forest and Dillon Ranger District of the Arapaho National Forest.

[Values, except number of deposits, in metric tonnes unless indicated as troy ounces (oz). Percentages in column headings refer to confidence levels for estimates of undiscovered deposits occurring in the Forest]

Metal	90%	50%	10%	Mean
Stockwork molybdenum				
Mo	0	230,000	1,200,000	430,000
Total mineralized rock	0	130,000,000	620,000,000	220,000,000
Number of deposits	0	1	1	
Polymetallic veins				
Pb	57	4,600	55,000	20,400
Zn	0	1,300	39,000	14,000
Cu	0	53	370	330
Ag	16,400 oz	1,029,000 oz	14,468,000 oz	8,037,500 oz
Au	0	612 oz	41,800 oz	22,800 oz
Total mineralized rock	350	56,000	840,000	280,000
Number of deposits	0	3	5	
Polymetallic replacement				
Pb	0	29,000	510,000	220,000
Zn	0	14,000	620,000	250,000
Cu	0	0	21,000	9,800
Ag	0	1,896,900 oz	67,515,400 oz	26,041,500 oz
Au	0	0	147,900 oz	99,600 oz
Total mineralized rock	0	6,200,000	12,000,000	4,100,000
Number of deposits	0	1	1	
Placer gold				
Au	180 oz	3,100 oz	23,000 oz	7,000 oz
Total mineralized rock	1,500	130,000	1,000,000	330,000
Number of deposits	0	1	2	

SALABLE COMMODITIES

Sand and gravel.—Numerous deposits of sand and gravel are located within major drainages in the Forest and are exploited for concrete and structural aggregate materials, road fill, mortar, and other uses. Fifty-three sites that have produced sand and gravel are on Forest land.

Dimension stone.—Sources in the Forest include marble and moss rock. White marble has been mined south of Marble, near Yule Creek, and black marble has been mined south of Aspen, in Conundrum Creek. Numerous moss-rock sites are in the Forest, and the potential resources are essentially unlimited.

Crushed and lightweight aggregate.—Crushed aggregates usable for roadway materials and general construction are derived from limestone, basalt, and granite sources. Rock quarries are scattered around the Forest where topography does not inhibit excavation. Lightweight aggregates include volcanic ash, pumice, and scoria. These are scattered around the Forest in limited quantities and contain varying amounts of impurities.

Clay.—Clay resources can be found in the Dakota Sandstone, south of Dillon Reservoir. Where clays have been sampled, they are not of refractory-brick quality.

ASSESSMENT OF METAL ENDOWMENT USING GEOLOGIC AND GRADE-TONNAGE MODELS

At the request of the U.S. Forest Service, the USGS provided a quantitative assessment of the undiscovered mineral resources that might exist in the Forest. Based on the geology, geophysics, and geochemistry of known deposits in the Forest, deposit types were defined and compared to other similar deposits worldwide. Using a computer program entitled MARK3, tonnages for undiscovered deposits in the Forest were estimated from known tonnages and grades of deposits worldwide. The results are presented in table 2. Note that these estimates do not imply that the resources would be economic to produce. Such a determination would require a complete analysis of both the costs of discovery and engineering feasibility, and would require an economic evaluation of production.

Only four deposit types have sufficient grade and tonnage information to assess them using the MARK3 program: stockwork molybdenum, polymetallic replacement, polymetallic vein, and placer gold deposits. All

remaining deposits that are known or predicted for the Forest lack sufficient data, or the deposit type is too poorly defined for quantitative assessment.

REFERENCES CITED

Behrendt, J.E., and Bajwa, L.Y., 1974, Bouguer gravity map of Colorado: U.S. Geological Survey Geophysical Investigations Map GP–895, scale 1:500,000.

Bolivar, S.L., Hill, D.E., Bunker, M.E., Cheadle III, J., Minor, M.M., Sandoval, W., Talcott, C.L., Trujillo, L., and Waterbury, G.R., 1979, Uranium hydrogeochemical and stream sediment reconnaissance data release for the Craig NTMS quadrangle, Colorado, including concentrations of forty-three additional elements: U.S. Department of Energy Open-File Report GJBX–76(79), 238 p., 5 plates.

Broxton, D.E., Morris, W.A., Bolivar, S.L., Apel, C.T., Gallimore, D.L., George, W.E., Hensley, W.K., McInteer, C., Minor, M.M., and Zelezny, W.F., 1979, Uranium hydrogeochemical and stream sediment reconnaissance data release for the Montrose NTMS quadrangle, Colorado, including concentrations of forty-three additional elements: U.S. Department of Energy Open-File Report GJBX–125(79), 255 p., 5 plates.

Brown, S.D., 1990, Mineral appraisal of the White River National Forest, Colorado: U.S. Bureau of Mines Open-File Report MLA 9–90, 378 p.

Campbell, D.L., 1981, Aeromagnetic and complete Bouguer gravity anomaly maps of the Hunter-Fryingpan Wilderness area, Pitkin County, Colorado: U.S. Geological Survey Miscellaneous Field Studies Map MF–1236–C, scale 1:50,000.

Campbell, D.L., 1985, Gravity and aeromagnetic maps of the Maroon Bells–Snowmass Wilderness and additions, Pitkin and Gunnison Counties, Colorado: U.S. Geological Survey Miscellaneous Field Studies Map MF–1647–B, scale 1:100,000.

Campbell, D.L., and Wallace, A.R., 1986, Aeromagnetic map of the Holy Cross Wilderness area, Eagle, Lake, and Pitkin Counties, Colorado: U.S. Geological Survey Miscellaneous Field Studies Map MF–1841–B, scale 1:100,000.

Case, J.E., 1965, Gravitational evidence for a batholithic mass of low density along a segment of the Colorado Mineral Belt [abs.]: Geological Society of America Special Paper 82, p. 26.

———1966, Geophysical investigations over Precambrian rocks, northwestern Uncompahgre Plateau, Utah and Colorado: American Association of Petroleum Geologists Bulletin, v. 50, p. 1423–1443.

———1967, Geophysical ore guides along the Colorado Mineral Belt: U.S. Geological Survey Open-File Report 67–039, 13 p.

Cordell, Lindrith, and Grauch, V.J.S., 1985, Mapping basement magnetization zones from aeromagnetic data in the San Juan Basin, New Mexico, *in* Hinze, W.J., ed., The Utility of Regional Gravity and Magnetic Anomaly Maps: Society of Exploration Geophysics, p. 181–197.

Cox, D.P., and Singer, D.A., 1986, Mineral deposit models: U.S. Geological Survey Bulletin 1693, 379 p.

Freeman, V.L., Campbell, D.L., King, H.D., Weisner, R.C., and Bieniewski, C.L., 1985, Mineral resource potential of the Maroon Bells–Snowmass Wilderness and additions, Gunnison and Pitkin Counties, Colorado: U.S. Geological Survey Miscellaneous Field Studies Map MF–1647–A, scale 1:100,000.

Hildenbrand, T.G., 1983, FFTFIL—A filtering program based on two-dimensional Fourier analysis on geophysical data: U.S. Geological Survey Open-File Report 83–237, 61 p.

Isaacson, L.B., and Smithson, S.B., 1976, Gravity anomalies and granite emplacement in west-central Colorado: Geological Society of America Bulletin, v. 87, p. 22–28.

Langfeldt, S.L., Youngquist, C.A., D'Andrea, Jr., R.F., Zinkl, R.J., Shettel, Jr., D.L., Broxton, D.E., Hansel, J.N., McInteer, C., and Minor, M.M., 1981, Uranium hydrogeochemical and stream sediment reconnaissance data release for the Grand Junction NTMS Quadrangle, Colorado/Utah: U.S. Department of Energy Open-File Report GJBX–264(81), 142 p., 7 plates.

Ludington, Steve, and Ellis, C.E., 1981, Mineral resource potential of the Hunter–Fryingpan Wilderness area and the Porphyry Mountain Wilderness Study Area, Pitkin County, Colorado: U.S. Geological Survey Miscellaneous Field Studies Map MF–1236–D, scale 1:50,000.

Mallory, W.W., Post, E.V., Ruane, P.J., Lehmbeck, W.L., and Stotelmeyer, R.B., 1966, Mineral resources of the Flat Tops Primitive Area, Colorado: U.S. Geological Survey Bulletin 1230–C, 30 p.

Moss, C.K., and Abrams, G.A., 1985, Geophysical maps of the Vasquez Peak Wilderness Study Area and the Williams Fork and St. Louis Peak Roadless Areas, Clear Creek, Grand, and Summit Counties, Colorado: U.S. Geological Survey Miscellaneous Field Studies Map MF–1588–D, scale 1:50,000.

Mutschler, F.E., Larson, E.E., and Bruce, R.M., 1987, Laramide and younger magmatism in Colorado—New petrologic and tectonic variations on old themes, *in* Drexler, J.W., and Larson, E.E., eds., Cenozoic Volcanism in the Southern Rocky Mountains Revisited: A Tribute to Rudy C. Epis—Part 1: Colorado School of Mines Quarterly, v. 82, no. 4, p. 1–47.

Planner, H.N., Apel, C.T., Fuka, M.A., George, W.E., Hansel, J.M., Hensley, W.K., and Pirtle, J., 1981, Uranium hydrogeochemical and stream sediment reconnaissance data release for the Leadville NTMS quadrangle, Colorado, including concentrations of forty-two additional elements: U.S. Department of Energy Open-File Report GJBX–13(81), 185 p., 1 plate.

Shawe, D.R., 1981, U.S. Geological Survey workshop on non-fuel mineral-resource appraisal of Wilderness and CUSMAP areas: U.S. Geological Survey Circular 845, 18 p.

Shettel, Jr., D.L., Langfeldt, S.L., Youngquist, C.A., D'Andrea, Jr., R.F., Zinkl, R.J., Bolivar, S.L., Garcia, S.R., George, W.E., and Hanks, D., 1981, Uranium hydrogeochemical and stream sediment reconnaissance data release for the Denver NTMS Quadrangle, Colorado: U.S. Department of Energy Open-File Report GJBX–263(81), 153 p., 17 plates.

Soulliere, S.J., Arnold, M.A., Kluender, S.E., and Zelten, J.E., 1985a, Mineral resources of the Eagle Mountain Wilderness Study Area, Pitkin County, Colorado: U.S. Geological Survey Bulletin 1717–B, 9 p.

Soulliere, S.J., Arnold, M.A., Kluender, S.E., 1985b, Mineral resources of the Hack Lake Wilderness Study Area, Garfield County, Colorado: U.S. Geological Survey Bulletin 1717–A, 5 p.

Soulliere, S.J., Arnold, M.A., Hassemer, J.R., Martin, R.A., Kluender, S.E., and Zelten, J.E., 1986, Mineral resources of the

Bull Gulch Wilderness Study Area, Eagle County, Colorado: U.S. Geological Survey Bulletin 1717–C, 12 p.

Taylor, R.B., and Steven, T.A., 1983, Definition of mineral resource potential: Economic Geology, v. 78, no. 6, p. 1268–1270.

Theobald, P.K., Bielski, A.M., Eppinger, R.G., Moss, C.K., Kreidler, T.J., and Barton, H.N., 1983, Mineral resource potential map of the Vasquez Peak Wilderness Study Area, and the Williams Fork and St. Louis Peak Roadless Areas, Clear Creek, Grand, and Summit Counties, Colorado: U.S. Geological Survey Miscellaneous Field Studies Map MF 1588–A, scale 1:50,000.

Toth, M.I., Wilson, A.B., Cookro, T.M., Bankey, Viki, Lee, G.K., and Case, J.E., in press, Mineral resource potential and geology of the White River National Forest and the Dillon Ranger District of the Arapaho National Forest, Colorado, *with a section on* Salable commodities, by J.S. Dersch: U.S. Geological Survey Bulletin 2035.

Tweto, Ogden, 1980, Tectonic history of Colorado, *in* Kent, H.C., and Porter, K.W., eds. Colorado Geology: Denver, Rocky Mountain Association of Geologists, p. 5–9.

Tweto, Ogden, and Case, J.E., 1972, Gravity and magnetic features as related to geology in the Leadville 30-minute quadrangle, Colorado: U.S. Geological Survey Professional Paper 726–C, 31 p.

Tweto, Ogden, and Sims P.C., 1963, Precambrian ancestry of the Colorado Mineral Belt: Geological Society of America Bulletin, v. 74, p. 991–1014.

Tweto, Ogden, Bryant, Bruce, and Williams, F.E., 1970, Mineral resources of the Gore Range–Eagle's Nest Primitive Area and vicinity, Summit and Eagle Counties, Colorado: U.S. Geological Survey Bulletin 1319–C, 127 p.

Van Loenen, R.E., Lee, G.K., Campbell, D.L., and Thompson, J.R., 1989, Mineral resource appraisal of the Mount Massive Wilderness, Lake County, Colorado: U.S. Geological Survey Bulletin 1636, 18 p.

Wallace, A.R., 1990, Regional geologic and tectonic setting of the central Colorado Mineral Belt, *in* Beaty, D.W., Landis, G.P., and Thompson, T.B., eds., Carbonate-Hosted Sulfide Deposits of the Central Colorado Mineral Belt: Economic Geology Monograph No. 7, p. 19–28.

Wallace, A.R., Lee, G.K., Campbell, D.L., Lundby, William, and Brown, S.D., 1989, Mineral resources of the Holy Cross Wilderness Area, Eagle, Pitkin, and Lake Counties, Colorado: U.S. Geological Survey Bulletin 1879, 22 p.

CHAPTER W

GEOPHYSICAL STUDIES OF THE WHITE RIVER NATIONAL FOREST, NORTHWESTERN AND CENTRAL COLORADO

By VIKI BANKEY[1]

INTRODUCTION

The U.S. Geological Survey (USGS) is undertaking a multidisciplinary study to assess the mineral resource potential of the White River National Forest and part of the Arapaho National Forest (referred to in this report as "the Forest"; fig. 1). The results of this study are summarized elsewhere in this volume (Toth and others). Twenty-six mining districts or mineralized areas are found within or adjacent to the Forest boundaries and include some of the largest concentrations of metallic mineral deposits in the Rocky Mountain region, notably in the Gilman, Leadville, and Climax districts. Most of these deposits formed within a zone of hydrothermal mineralization that characterizes the Colorado Mineral Belt in the southeastern part of the Forest (figs. 1 and 2). The deposits of the Colorado Mineral Belt are associated with Late Cretaceous to late Tertiary felsic to intermediate intrusive and volcanic rocks that were localized by numerous northeast-trending basement shear faults (Toth and others, this volume). A prominent 30–50 milliGal (mGal) gravity low is centered over the Colorado Mineral Belt and is produced by a low-density, silicic, batholithic mass that underlies a large part of the area (Case, 1965; Tweto and Case, 1972; Isaacson and Smithson, 1976). The outline of this gravity low is shown on figures 1 and 2. Many of the mapped intrusions and related mineralized areas probably formed as apophyses from the top of this massive batholith.

Gravity and aeromagnetic anomaly maps were compiled and interpreted for the White River National Forest area as part of the assessment study. The present work builds on previous geophysical studies made for the Leadville 1°×2° quadrangle (Wallace and others, 1988) and for six Wilderness Study Areas (Campbell, 1981, 1985; Campbell and Wallace, 1986; Moss and Abrams, 1985; and Van Loenen and others, 1989). Geophysical studies to support mineral resource evaluations of the Colorado Mineral Belt were made by Case and Tweto (Case, 1965, 1966, 1967; Tweto and Case, 1972), Behrendt and Bajwa (1974), and Isaacson and Smithson (1976).

Gravity and magnetic data contribute significantly to the understanding of geologic features associated with mineral deposits. Some of these features include Proterozoic faults and shear zones, sometimes characterized by offsets in gravity or magnetic anomalies or both, that provided conduits for Phanerozoic intrusive magmas and mineralizing fluids that formed the metallic mineral deposits of the Colorado Mineral Belt. Gravity anomalies may distinguish low-density porous sandstones (which may host copper, silver, uranium, or vanadium deposits in the Forest) or Paleozoic evaporites (host to gypsum, halite, and potassium salts, and oil and gas reservoirs) or high-density limestones (which are host to many of the significant metallic ore deposits in the area (Toth and others, in press)).

GRAVITY STUDIES

Gravity anomalies occur from the juxtaposition of rocks having measurable density contrasts, which result from structural or geologic features such as faults, folds, downwarps, intrusions, basin fill, lithologic contacts, or facies changes. The number and quality of gravity stations limits the accuracy of anomaly definition, especially in mountainous areas where station spacing is often sparse. However, on a regional scale, gravity mapping is a useful tool for locating structural breaks and folds and for delineating shallow, buried pediments.

[1]U.S. Geological Survey, Mail Stop 964, P.O. Box 25046, Denver Federal Center, Denver, CO 80225.

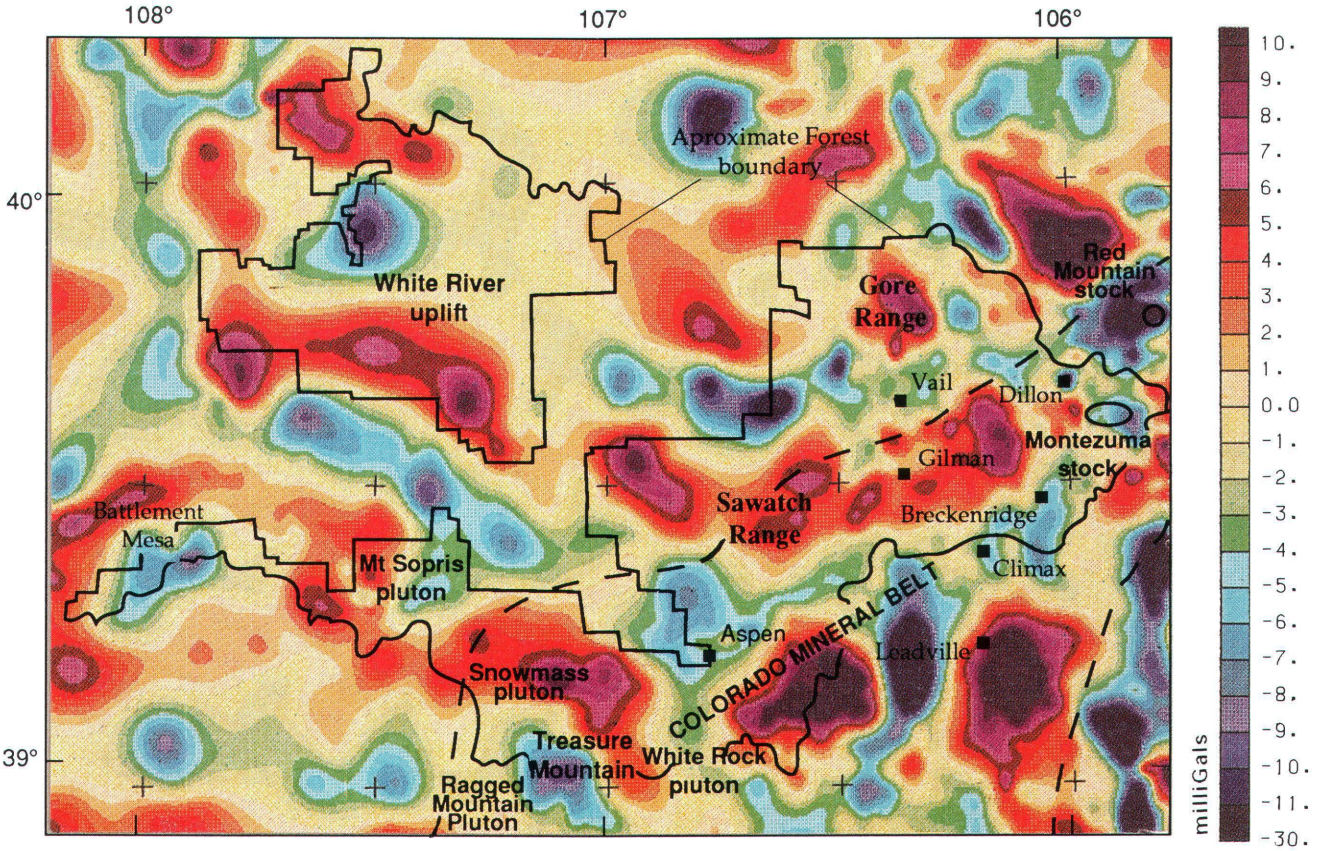

Figure 1. High-pass filtered residual gravity map of the White River National Forest. The map shows the Bouguer gravity field with broad, presumably deep, features removed and shallower features emphasized. Bouguer gravity mapping (Behrendt and Bajwa, 1974) shows a broad gravity low (hachured outlines) over the low-density batholith underlying the Colorado Mineral Belt.

In the Colorado Mineral Belt, gravity mapping has defined a broad area that is underlain by a low-density batholith that is the presumed source of mineralization (Behrendt and Bajwa, 1974). A shallow intracrustal origin for the low, having an apex within a few thousand feet of the surface, a depth extending 40,000 ft below sea level, and a width averaging 15–20 mi, has been demonstrated by gravity models (Case, 1966; Tweto and Case, 1972; Isaacson and Smithson, 1976). The broad, deep gravity low resulting from the batholith masks gravity anomalies resulting from smaller, shallower, and more mineralogically significant intrusions and hydrothermally altered areas. To minimize the gravity effect of the deep batholith, a mathematical filter was applied to a 1.2 mi (2 km) gridded data set of complete-Bouguer gravity data that was produced using gravity data from 6,500 stations. This filter removes wavelengths longer than about 30 mi from the Bouguer gravity grid (Hildenbrand, 1983). The resulting high-pass residual gravity map emphasizes anomalies due to shallow sources by suppressing long-wavelength anomalies caused by broad, often deep, regional features, such as the Colorado Mineral Belt, Colorado Plateau, and the White River uplift.

AEROMAGNETIC STUDIES

Aeromagnetic anomalies are caused by rocks that contain significant amounts of magnetic minerals; these anomalies reflect variations in the amount and type of magnetic material and the shape of the body. In general, igneous and metamorphic rocks contain enough magnetic minerals to generate magnetic anomalies, whereas sedimentary rocks are commonly virtually nonmagnetic.

Aeromagnetic anomaly maps are important tools in mapping surficial and buried igneous rocks. Aeromagnetic data can be used to locate and estimate depths to igneous intrusions that may be related to possible mineral deposits. For example, magnetic highs are caused by magnetic plutons in the Elk Mountains. High-intensity magnetic lows may indicate igneous rocks that acquired their magnetic properties during a period of magnetic field reversal, such as the magnetic lows associated with some outcrops of basaltic rocks in the White River uplift. Rings of magnetic highs with central or reentrant lows may indicate porphyry systems in which hydrothermal alteration has destroyed preexisting magnetic minerals. Local magnetic highs may exist where hydrothermal alteration has created secondary

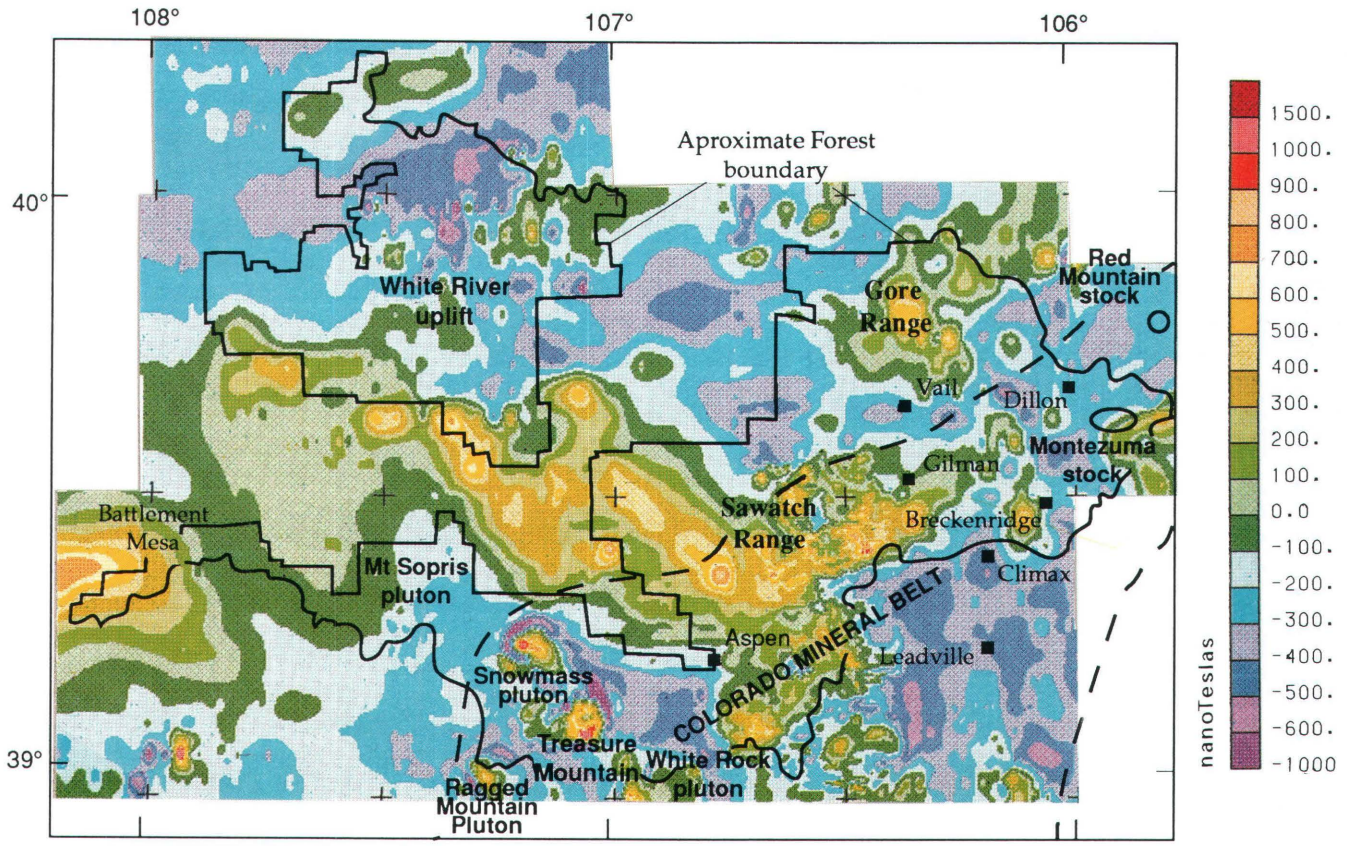

Figure 2. Aeromagnetic anomaly map of the White River National Forest and vicinity. The aeromagnetic maps of the area were digitally merged to generate this aeromagnetic compilation map.

magnetic minerals; for example, in a magnetite-bearing skarn. Small magnetic lows may occur where less magnetic Tertiary stocks have intruded more magnetic Proterozoic rocks.

Nine aeromagnetic surveys were flown over separate parts of the Forest, with flight-line spacing ranging from 0.5 to 3 mi apart. These aeromagnetic data sets were separately gridded and digitally merged to a common datum to produce the map in figure 2.

GEOPHYSICAL INTERPRETATIONS

The Forest has been divided into three geophysical provinces for this report: the Colorado Mineral Belt and Gore Range in the eastern and southern Forest; the White River uplift in the northern Forest; and the Battlement Mesa area in the western Forest.

In the Colorado Mineral Belt, residual gravity lows may indicate the presence and subsurface extent of shallow apophyses of the low-density, silicic, batholithic mass of Cretaceous to Tertiary age that is presumed to underlie a large part of the belt. One such string of gravity lows occurs on a northeast trend from the stocks at Climax to Montezuma to Red Mountain (fig. 1), suggesting that these features are related. Because buried batholiths play such an important role as a source of mineralizing fluids and heat in this area, this trend of gravity lows may be significant.

Among aeromagnetic anomalies of interest to mineral assessments are the high-amplitude, high-frequency anomalies associated with the mid-Tertiary outcrops of the Mt. Sopris, Snowmass, and White Rock plutons that are in the Elk Mountains in the south-central part of the Forest. These three plutons are connected at depth, as suggested by the gravity high that encompasses the area and demonstrated in models by Campbell (1985). However, these plutons are separated from the Ragged Mountain pluton to the southwest by the geophysically distinct granite of Treasure Mountain. The gravity and magnetic anomalies show the subsurface extent of these mineralized plutons and indicate some occurrences of magnetic alteration.

In the Sawatch and Gore Ranges, Cretaceous and Tertiary intrusive rocks are commonly, but not always, associated with gravity and magnetic lows, whereas the Proterozoic schists, granites, and gneisses are characterized

by magnetic highs. Magnetic gradients, caused by contrasting lithologies or locally increased magnetization, mark Proterozoic shear zones and metamorphic layering and northwest-trending, uplift-related, high-angle faults of Laramide and younger age. These numerous zones of crustal weakness are often the location of mineral deposits (Toth and others, in press).

Between the Sawatch Range and the Gore Range lies an interesting east-northeast-trending zone of magnetic lows that corresponds to a residual gravity low. This zone, which extends from west of Vail to Dillon and crosses many north-northwest-trending topographic and structural features, may reflect a larger volume of Phanerozoic intrusive rocks.

The magnetic field in the area of the White River uplift is characterized by high-frequency, small, positive and negative anomalies over basalt outcrops, some of which formed during periods of reversed magnetization. Low residual gravity values occur where basalt becomes the major rock type at the surface. Because the basalt magmas intruded through evaporites, the potential exists for Noril'sk-type copper-nickel-platinum deposits (Toth and others, in press). The southern and southwestern margins of the uplift are flanked by four magnetic highs that are all similar in appearance, magnitude, extent, and depth-to-source. A broad, positive gravity anomaly is associated with these magnetic highs. Because of the location of these anomalies along the edge of the uplift, they are presumed to be structurally controlled and may be caused by locally exposed Proterozoic rocks that are found in the bottom of some canyons in the southern White River uplift.

Gravity lows east of the White River uplift are associated with evaporite facies rocks within the Eagle Valley Evaporite. These rocks are a source of gypsum, halite, and potassium salts and may also host oil and gas deposits (Toth and others, this volume).

The Battlement Mesa area, in the westernmost part of the Forest, is associated with a residual gravity low and a broad magnetic high that reflect a presumably deep source. However, the data are of poor resolution so that smaller, shallower sources are not represented well.

CONCLUSIONS

Analysis of geophysical features provide new insights into structural history and subsurface configurations and can help geologists target new areas for mineral exploration. Recognizable patterns of geophysical anomalies correspond to geological targets for mineral potential, such as Proterozoic shear zones and Phanerozoic faults that provided conduits for mineralizing fluids, Cretaceous and Tertiary intrusive rocks that provided the fluids and heat for hydrothermal systems, Paleozoic sedimentary rocks that serve as host rocks for metallic minerals, and evaporite-sequence rocks that are both host rocks for oil and gas deposits and source rocks for salts.

REFERENCES CITED

Behrendt, J.E., and Bajwa, L.Y., 1974, Bouguer gravity map of Colorado: U.S. Geological Survey Geophysical Investigations Map GP–895, scale 1:500,000.

Campbell, D.L., 1981, Aeromagnetic and complete Bouguer gravity anomaly maps of the Hunter-Fryingpan Wilderness area, Pitkin County, Colorado: U.S. Geological Survey Miscellaneous Field Studies Map MF–1236–C, scale 1:50,000.

———1985, Gravity and aeromagnetic maps of the Maroon Bells–Snowmass Wilderness and additions, Pitkin and Gunnison Counties, Colorado: U.S. Geological Survey Miscellaneous Field Studies Map MF–1647–B, scale 1:100,000.

Campbell, D.L., and Wallace, A.R., 1986, Aeromagnetic map of the Holy Cross Wilderness Area, Eagle, Lake, and Pitkin Counties, Colorado: U.S. Geological Survey Miscellaneous Field Studies Map MF–1841–B, scale 1:100,000.

Case, J.E., 1965, Gravitational evidence for a batholithic mass of low density along a segment of the Colorado Mineral Belt [abs.]: Geological Society of America Special Paper 82, p. 26.

———1966, Geophysical investigations over Precambrian rocks, northwestern Uncompahgre Plateau, Utah and Colorado: American Association of Petroleum Geologists Bulletin, v. 50, p. 1423–1443.

———1967, Geophysical ore guides along the Colorado Mineral Belt: U.S. Geological Survey Open-File Report 67–039, 13 p.

Hildenbrand, T.G., 1983, FFTFIL—A filtering program based on two-dimensional Fourier analysis on geophysical data: U.S. Geological Survey Open-File Report 83–237, 61 p.

Isaacson, L.B., and Smithson, S.B., 1976, Gravity anomalies and granite emplacement in west-central Colorado: Geological Society of America Bulletin, v. 87, p. 22–28.

Moss, C.K., and Abrams, G.A., 1985, Geophysical maps of the Vasquez Peak Wilderness Study Area and the Williams Fork and St. Louis Peak Roadless Areas, Clear Creek, Grand, and Summit Counties, Colorado: U.S. Geological Survey Miscellaneous Field Studies Map MF–1588–D, scale 1:50,000.

Toth, M.I., Wilson, A.B., Cookro, T.M., Bankey, Viki, Lee, G.K., and Case, J.E., in press, Mineral resource potential and geology of the White River National Forest and the Dillon Ranger District of the Arapaho National Forest, Colorado, *with a section on* Salable commodities, by J.S. Dersch: U.S. Geological Survey Bulletin 2035.

Tweto, Ogden, and Case, J.E., 1972, Gravity and magnetic features as related to geology in the Leadville 30-minute quadrangle, Colorado: U.S. Geological Survey Professional Paper 726–C, 31 p.

Van Loenen, R.E., Lee, G.K., Campbell, D.L., and Thompson, J.R., 1989, Mineral resource appraisal of the Mount Massive Wilderness, Lake County, Colorado: U.S. Geological Survey Bulletin 1636, 18 p.

Wallace, A.R., Ludington, Steve, Lovering, T.G., Campbell, D.L., Case, J.E., Grauch, V.J.S., and Knepper, Dan, 1988, A mineral preassessment of the Leadville 1°×2° quadrangle, Colorado: U.S. Geological Survey Open-File Report 88–074, 56 p.

CHAPTER X

LOCATING BURIED CONDUCTIVE MATERIAL ALONG THE GETCHELL TREND, OSGOOD MOUNTAINS, NEVADA: IMPLICATIONS FOR GOLD EXPLORATION AND THE CARBON-GOLD ASSOCIATION(?)

By V.J.S. GRAUCH[1] *and* DONALD B. HOOVER[1]

INTRODUCTION

The Getchell trend is an alignment of six sedimentary-hosted, disseminated gold deposits along the eastern side of the Osgood Mountains in north-central Nevada (fig. 1). In 1988, the U.S. Geological Survey conducted a multi-sensor airborne geophysical program in this area in order to demonstrate the utility of integrated airborne geophysical surveying for exploration or mineral assessment in covered terranes. The surveys included an airborne electromagnetic (EM) survey, flown using three different frequencies. Apparent resistivity maps were constructed for each frequency; these maps are standardly used to interpret lateral variations in subsurface resistivities. (The word "apparent" is used because there are some simplifying assumptions made about the Earth in order to make the resistivity computation from measured EM parameters.) In a preliminary assessment of the apparent resistivity maps for the Getchell-trend area, Hoover and others (1991) observed that all the exposed gold deposits are associated with linear conductive zones. Because EM surveys can map subsurface resistivities, apparent resistivity maps, thus, can be an important guide to locating buried conductive zones, which in turn may be associated with buried gold deposits.

Unfortunately, the geophysical signature of buried conductive material is commonly masked by the effect of overlying or neighboring rocks, making identification on apparent resistivity maps difficult. A step toward isolating this signature is to take the ratio of apparent resistivities calculated for two different frequencies (Pierce and Hoover, 1991). Analogous to a derivative, the ratio of apparent resistivity at a higher frequency divided by that for a lower frequency is a measure of how fast resistivity is changing with depth. Buried conductive material, which we define as rocks with very low resistivity underlying rocks with moderate to high resistivity, will then be represented by areas where resistivity is decreasing with depth. However, areas where highly resistive rocks overlie moderately resistive rocks also express decreasing resistivity and, yet, are areas of no interest. Thus, a better approach enhances areas where resistivity is decreasing with depth *and* the apparent resistivity is low. We call such an operation a buried-conductor enhancement.

The purpose of this report is two-fold: (1) to introduce a buried-conductor enhancement of resistivity data that pinpoints buried conductive material and thus can better isolate subsurface areas of interest; and (2) to argue that the primary conductive material reflected in the enhanced map is the carbonaceous matter that has a common association with deposits of this type. In addition, perhaps the conductive properties of the carbonaceous matter have some sort of indirect or direct, but as yet unknown, relationship to the gold mineralization.

GEOLOGIC SETTING

The Getchell trend lies along the eastern side of the Osgood Mountains, a structurally complicated range

[1]U.S. Geological Survey, Mail Stop 964, P.O. Box 25046, Denver Federal Center, Denver, CO 80225.

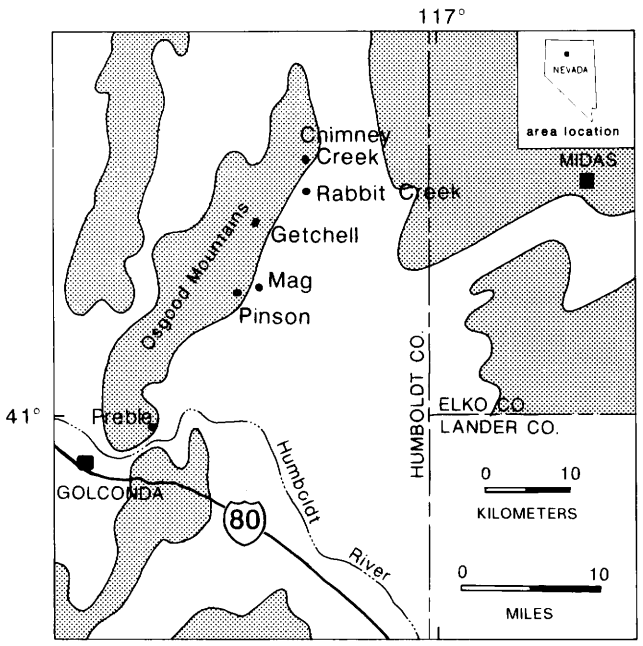

Figure 1. Location of the six sedimentary-hosted gold deposits that make up the Getchell trend along the east side of the Osgood Mountains. Stippling represents topographic ranges.

composed of Paleozoic sedimentary rocks, Cretaceous granodiorite, and Tertiary extrusive rocks (fig. 2). The Osgood Mountains host deposits of silver, tungsten, barite, and manganese as well as gold. The gold deposits are similar to the well-known Carlin deposit; disseminated, invisible gold is hosted in Paleozoic, thin-bedded, carbonaceous, calcareous siltstones and silty carbonates. Mineralization is controlled locally by the Getchell fault system at the Getchell, Pinson, and possibly Preble deposits (Bagby and Berger, 1985). Similar range-front faulting controls mineralization at the Chimney Creek (Osterberg and Guilbert, 1991) and Mag (Foster and Kretschmer, 1991) deposits. The Rabbit Creek deposit is more stratiform than fault controlled (Bloomstein and others, 1991).

Carbonaceous matter is abundant at all the Getchell-trend gold deposits; this association is typical of sediment-hosted, disseminated gold deposits in general, although no direct correlation between gold and organic carbon has been documented within the deposits themselves (Percival and others, 1988; Bagby and Berger, 1985). The carbonaceous matter may have originated as hydrocarbons that were partially remobilized by hydrothermal fluids along fractures and fault zones (Hausen and Park, 1986; Broili and others, 1988) and then heated to anthracite (Hausen and Park, 1986) or higher (Leventhal and Hofstra, 1990) coal rank. Studies at the Jerritt Canyon deposit in northeastern Nevada demonstrate that graphitization of the carbonaceous matter occurred prior to gold mineralization so that carbon was unavailable for gold transport (Leventhal and others, 1987). Only a few gold grains are spatially related to carbonaceous matter (Leventhal and others, 1987; Hausen and Park, 1986). In any case, the genetic relationship between the carbonaceous matter and gold mineralization, if any, remains unclear.

APPARENT RESISTIVITY DATA

Resistivity (or conductivity, its inverse) is primarily a function of the interconnected porosity of the rock, the amount and quality of contained water, and degree of saturation (Keller and Frischknect, 1966). Concentrations of electronically conductive minerals, such as metallic sulfides and graphite, can significantly lower resistivities locally but generally contribute little to bulk resistivities of rock units. Thus, bulk-earth resistivity is normally determined by ionic conduction through fluids contained in the pore spaces of rocks. As a rule of thumb, rocks with low porosity, such as igneous rocks, will have higher resistivities than rocks with high porosity, such as some clastic sedimentary rocks. On the other hand, a rock unit with moderate porosity in which the pores are filled with saline water instead of fresh water has an extremely low resistivity. In addition, large amounts of clay minerals decrease resistivities dramatically because of their ability to absorb water (Palacky, 1986).

The depth of exploration of an EM survey is dependent on the frequency of the EM measurements and the resistivity of the subsurface. Low-frequency measurements have greater exploration depths than high-frequency measurements, and the depth of exploration is greater in resistive terranes than in conductive ones. For example, at a given location, depth of exploration using 900 Hz is greater than for 7,200 or 56,000 Hz. Between locations, the 900-Hz depth of exploration is greater where subsurface resistivities are higher.

Apparent resistivity data for the Getchell-trend area were computed from data collected during an airborne EM survey flown in 1988 using a DIGHEM IV system. The

Figure 2 (facing page). Generalized geology of the Osgood Mountains and location of precious metal occurrences. Rock units adapted primarily from Willden (1964). Additional geologic names from Hotz and Willden (1964); ages from Erickson and Marsh (1974) and Silberman and others (1974). CC, Chimney Creek central pit; CN, Chimney Creek north pit; CS, Chimney Creek south pit; GC, Getchell central pit; GN, Getchell north pit; GS, Getchell south pit; HC, Hansen Creek mine; MA, Mag mine; PI, Pinson mine; PR, Preble mine; RC, Rabbit Creek pit (future outline); SCA, Summer Camp gold mine; SCO, Silver Coin silver mine; TR, Turquoise Ridge gold mineralization; 13, section 13 gold mineralization.

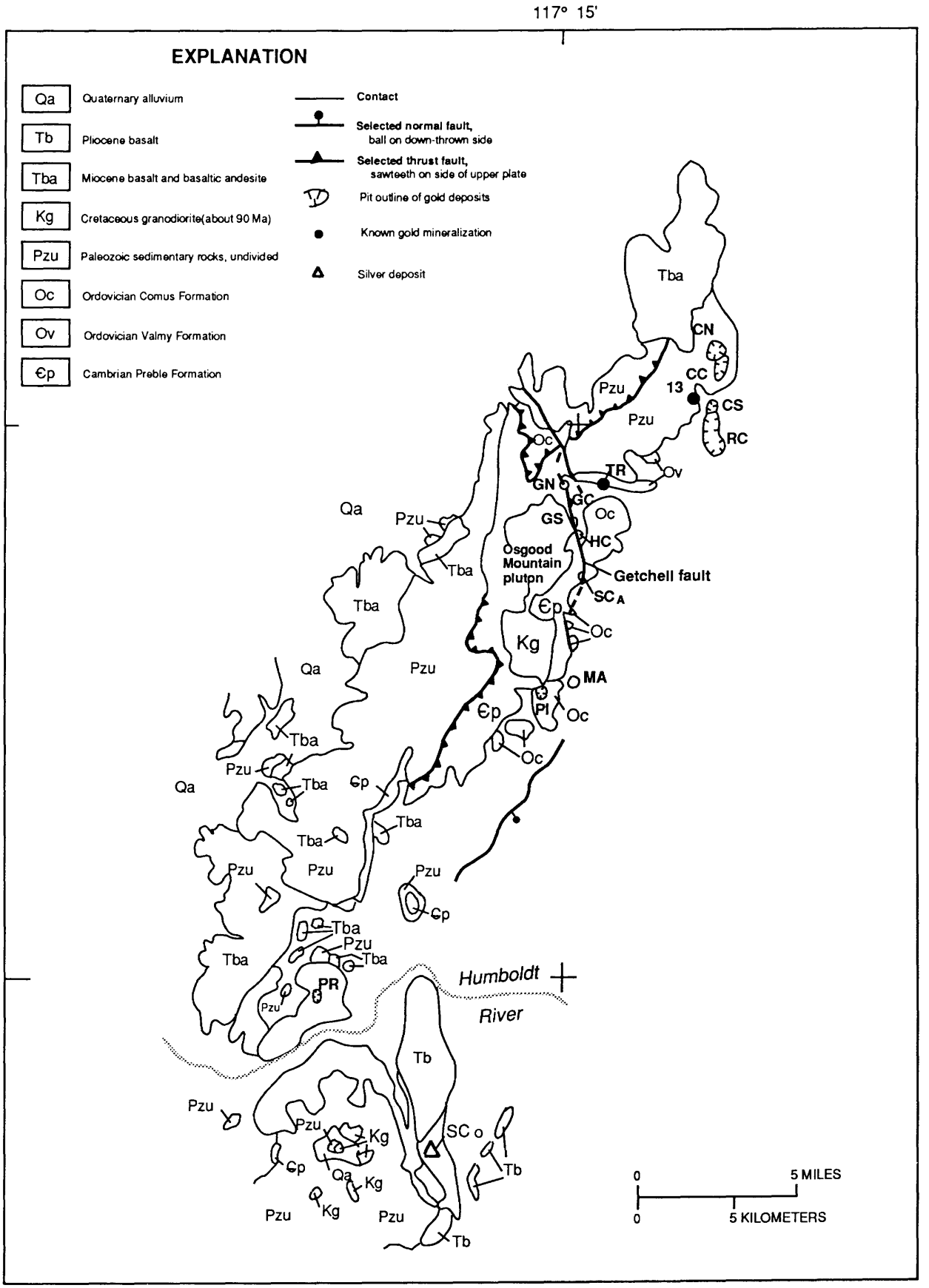
117° 15'
41° 15'
41° 00'
EXPLANATION
Qa Quaternary alluvium
Tb Pliocene basalt
Tba Miocene basalt and basaltic andesite
Kg Cretaceous granodiorite(about 90 Ma)
Pzu Paleozoic sedimentary rocks, undivided
Oc Ordovician Comus Formation
Ov Ordovician Valmy Formation
Ep Cambrian Preble Formation
Contact
Selected normal fault, ball on down-thrown side
Selected thrust fault, sawteeth on side of upper plate
Pit outline of gold deposits
Known gold mineralization
Silver deposit
Osgood Mountain pluton
Getchell fault
CN
CC
13
CS
RC
TR
GN
GC
GS
HC
SC A
MA
Pl
PR
SC o
Humboldt River
0 5 MILES
0 5 KILOMETERS

survey was flown 30 m (100 ft) above ground along northwest- and southeast-trending lines spaced 402 m (1/4 mile) apart (except over the gold deposits, where they were spaced 201 m (1/8 mile) apart). Data were acquired using frequencies of 56,000, 7,200, and 900 Hz, and apparent resistivities were calculated for each of these frequencies. Details of the data-acquisition system and the computation of apparent resistivity are described in Pierce and Hoover (1991).

The alluvial cover in the Getchell-trend area is typically fairly conductive, so that the depth of exploration using 900 Hz in those areas ranges from about 10 m (33 ft) to 100 m (330 ft). In areas of exposed rock, exploration depths are generally greater and, for most lithologies, range from about 100 m (330 ft) to 1,000 m (3,300 ft). Pierce and Hoover (1991) discuss the apparent resistivity results for the Getchell-trend area.

BURIED-CONDUCTOR ENHANCEMENT

As shown by Pierce and Hoover (1991), the logarithm of the ratio between apparent resistivities calculated for 7,200-Hz and 900-Hz frequencies, respectively, gives information about how resistivity changes with depth. Roughly speaking, where the ratio is greater than one (the logarithm is positive), resisitivity is decreasing with depth. Where it is less than one (the logarithm is negative), resistivity is increasing with depth. For the buried-conductor enhancement, this ratio is then multiplied by the logarithm of the 900-Hz apparent conductivity (the inverse of apparent resisitivity) after adding a constant to ensure only positive logarithms for the conductivity. The conductivity for the 900-Hz frequency is used because it represents the deepest looking frequency. In equation form, the results of the enhancement (E) can be written for each grid point as:

$$E = \left\{ \log \left(\frac{1}{\rho_{900}} \right) + k \right\} \log \left(\frac{\rho_{7,200}}{\rho_{900}} \right) \qquad (1)$$

where

ρ_{900} is the 900-Hz apparent resistivity (ohm-meters),

$\rho_{7,200}$ is the 7,200-Hz apparent resistivity (ohm-meters), and

k is a constant that ensures the left-hand side of the product will be positive for all grid points.

Note that k is usually chosen by inspection of the minimum value of $\log\left(\frac{1}{\rho_{900}}\right)$ for all grid points.

Because the negative values of E represent the uninteresting case where the resisitivities are increasing with depth, these values are neglected. Thus, the final plot of E has high values where the *product* of the 900-Hz apparent conductivity and the amount of decrease in resistivity with depth is great. The highest E values represent places where there is a large, probably abrupt, decrease in resistivity at depth. Moreover, the change in resistivity must occur at fairly shallow depths because the depth of exploration is diminished by the presence of the low resistivities in the subsurface.

RESULTS FOR THE GETCHELL-TREND AREA

The result of applying the above buried-conductor enhancement to apparent resisitivity data for the Getchell trend area is shown on figure 3. The highlighted features of the enhanced map are present on both the 900-Hz apparent resistivity and ratio maps of Pierce and Hoover (1991) as expected from equation (1), but there are many fewer targets on the enhanced map. The smaller number greatly facilitates follow-up investigations.

NATURE OF THE CONDUCTIVE MATERIAL

We surmise that the broad regions of slightly higher values on figure 3 are due to buried lithologies that are less resistive than the overlying lithology, whereas the high enhanced values that occur as spots, lines, or stringers are due to local concentrations of buried conductive material. In the case of the spot of high enhanced values near lat 41°02′N., long 117°17′W., the conductive material likely is a buried warm spring. In most other cases, we deduce that graphite primarily comprises the conductive material from the following observations: (1) Most of the highest enhanced spots where subsurface information is available correlate with rocks that contain large concentrations of carbonaceous matter, moderate to large amounts of clay or other argillaceous rock, and small amounts of

Figure 3 (facing page). Results of the buried-conductor enhancement applied to apparent resistivity data from an airborne survey over the Getchell-trend area. The dimensionless values increase as a function of the product of the decrease in resistivity with depth and the 900-Hz apparent conductivity (the inverse of resistivity). The enhancement is presented in color shaded relief, with false illumination from the east. Negative values represent the uninteresting case where resistivity increases with depth. Broad regions of slightly higher values are probably due to buried lithologies that are less resistive than the overlying lithology, whereas the high values that occur as spots, lines, or stringers are most likely caused by concentrations of buried conductive material that is composed partially or wholly of graphitized carbonaceous matter. Geologic contacts, pit outlines, and occurrence locations are from figure 2. Faults are not shown for clarity. Refer to figure 2 for names.

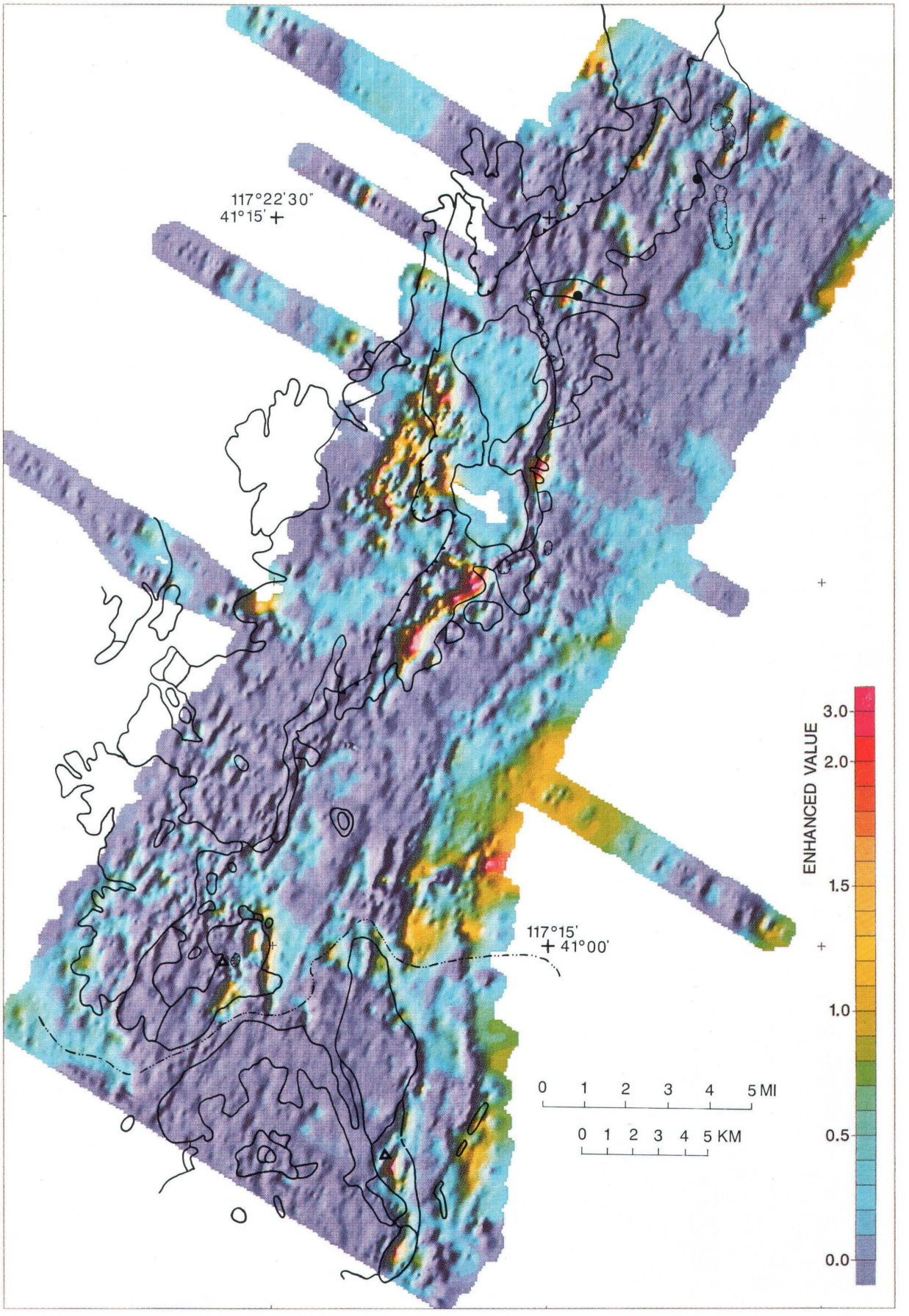
117°22'30"
41°15'
117°15'
41°00'
0 1 2 3 4 5 MI
0 1 2 3 4 5 KM
ENHANCED VALUE
3.0
2.0
1.5
1.0
0.5
0.0

sulfides; (2) occurrences of argillaceous rock without carbonaceous matter do not correspond to low resistivities on the apparent resistivity maps; (3) the amount of sulfides is not sufficient to produce the low resistivities measured; and (4) graphite can lower resistivies of rocks quite dramatically, even when present in small quantities (Nelson and others, 1982; Grant and West, 1965). Moreover, laboratory analyses of carbonaceous matter sampled from sedimentary-hosted disseminated gold deposits elsewhere in northern Nevada indicate cryptocrystalline graphite (Leventhal and Hofstra, 1990) with an anthracite or higher coal rank (Leventhal and Hofstra, 1990; Hausen and Park, 1986). Both anthracite coal and graphite are excellent electrical conductors. Moreover, if the cryptocrystalline graphite is localized along bedding or fault planes, as is carbonaceous matter at the Carlin deposit (Hausen and Park, 1986), the interconnectivity of the crystals would further increase conduction.

From these observations we infer that many, if not most, of the moderate to high values on the enhanced map reflect carbonaceous matter that is at least partially graphitized. Thus, the enhanced map can help determine the location and nature of buried carbonaceous matter in the Getchell-trend area.

Where known, the areas of highest enhanced values have no associated gold mineralization, although they commonly occur near or on line with precious-metal deposits (the two known silver deposits included). The high values to the west of the Osgood Mountains pluton are exceptions: no known gold mineralization occurs nearby. On the other hand, all but two of the gold occurrences that were detectable by the EM survey correspond to moderately enhanced values, which generally occur as lines or stringers. The two exceptions are at the central and south pits of the Getchell deposit, where the lack of enhancement may be explained by resisitivities that increase rather than decrease with depth (Pierce and Hoover, 1991). Here, the deposit and its associated conductive material are entirely exposed at the surface. The gold mineralization in section 13, the Chimney Creek south pit, and the Rabbit Creek deposit are deeper than the EM depths of exploration. The inadequate depth of exploration near the Rabbit Creek deposit implies that the large enhanced area to the south must reflect widespread, buried conductive material within the overburden, which may or may not be related to the deposit below (Pierce and Hoover, 1991).

STRUCTURE

Many faults are manifested on the enhanced map (fig. 3), either as lines or stringers, or as abrupt changes in value. For example, the northeasterly trending enhanced line about 3 km west of the central Chimney Creek pit coincides with part of a mapped thrust fault (Willden, 1964); carbonaceous rocks and some sulfide mineralization are present at depth (B. Berger, written commun., 1977). At the Pinson and Mag deposits, linear enhanced areas trend north and northeast, corresponding to Tertiary structure (E. Kretschmer, written commun., 1991). The north-south-trending linear enhanced area east of the Preble deposit is associated with the west edge of a graben-like feature that is interpreted from geophysical data (Hoover and others, 1991; Grauch and others, 1991) and corraborated by drilling (E. Kretschmer, oral commun., 1990). To the east, a more subtle linear area of low values on the enhanced map that trends northeast may represent the east edge of the graben. A northeasterly trend is suggested by connecting linear enhanced areas to the northeast and southwest of the Preble deposit. The trend may be a major fault related to the northerly trending fault mapped in the pit (Kretschmer, 1984).

Faults are also expressed by abrupt changes in character on the enhanced map, such as the two northeast-trending faults along the southeastern and northeastern edges of the study area. These faults are corraborated by other geophysical evidence (Hoover and others, 1991).

CONCLUSIONS

The buried-conductor enhancement applied to apparent resistivity maps can be a valuable tool for gold exploration in the Getchell-trend area. The high enhanced values are most likely explained by subsurface concentrations of graphite. Precious-metal mineralization may occur adjacent to areas that have the highest enhanced values, but it does not occur directly over these areas. Mineralized areas correspond better to low and moderately enhanced values that commonly follow faults. Possible explanations for these observations are: (1) Carbonaceous matter is moderately but not highly conductive in association with gold mineralization, implying that highly conductive carbonaceous matter and gold mineralization are mutually exclusive for a given area; (2) conductive cabonaceous matter is present in association with gold mineralization, but rocks overlying mineralized areas are less resistive than in nonmineralized areas; or (3) conductive carbonaceous matter is present in association with gold mineralization, but the resistive cover has been stripped off during mining. The last possibility does not explain the moderately enhanced values that occur near mines in areas where the cover has not been stripped off. The remaining two explanations both suggest that the resistivities of the rocks are somehow related to gold mineralization. Perhaps the gold mineralization event destroyed some of the conductive properties of the carbonaceous matter or increased the porosity of the overlying rocks. In situ electrical measurements near the Pinson mine suggest that carbonaceous

ore exhibits higher resistivities compared to carbonaceous non-ore (Hoover and others, 1987). This observation also suggests an interrelation between the conductive properties of carbonaceous matter and associated gold mineralization.

We predict that abundant carbonaceous material (partially or wholly graphitized) will be found at depth at the spots of highly enhanced values under the basalt south of the Silver Coin mine (fig. 2); under Paleozoic sedimentary rocks just to the northeast of Turquoise Ridge mineralization and near lat 41°7′30″N., long 117°22′30″W.; and under alluvium near the northern tip of the study area. In addition, faul ts containing conductive material that may have controlled hydrothermal fluid flow in the past occur along the southeastern edge of basalt northeast of the Silver Coin mine, along the contact between Preble Formation and alluvium 2 km west of Lone Butte, under alluvium about 1 and 2 km southeast of the Pinson mine, and possibly within the Paleozoic rocks west of the section 13 mineralization. Even if no gold is found in these areas, the buried-conductor enhancement does well in isolating conductive fault zones that may be related to mineralization. This technique may become extremely useful in studying the role of carbonaceous matter in sedimentary-hosted, disseminated gold deposits.

REFERENCES CITED

Bagby, W.C. and Berger, B.R., 1985, Geologic characteristics of sediment-hosted disseminated precious-metal deposits in the Western United States, *in* Berger, B.R., and Bethke, P.M., eds., Reviews in Economic Geology, Volume 2—Geology and Geochemistry of Epithermal Systems: El Paso, Society of Economic Geologists, p. 169–232.

Bloomstein, E.I., Massingill, G.L., Parratt, R.L., and Peltonen, D.R., 1991, Discovery, geology, and mineralization of the Rabbit Creek gold deposit, Humboldt County, Nevada, *in* Raines, G.L., Lisle, R.E., Schafer, R.W., and Wilkinson, W.H., eds., Geology and Ore Deposits of the Great Basin, Symposium Proceedings: Reno, Geological Society of Nevada, p. 821–845.

Broili, C., French, G. McN., Saddrick, D.R., and Weaver, R.R., 1988, Geology and gold minerali zation of the Gold Bar deposit, Eureka County, Nevada, *in* Schafer, R.W., Cooper, J.J., and Vikre, P.G., eds., Bulk Mineable Precious Metal Deposits of the Western United States Symposium Proceedings: Reno, Geological Society of Nevada, p. 57–72.

Erickson, R.L., and Marsh, S.P., 1974, Geologic map of the Golconda quadrangle, Humboldt County, Nevada: U.S. Geological Survey Geologic Quadrangle Map GQ–1174, scale 1:24,000.

Foster, J.M., and Kretschmer, E.L., 1991, Geology of the Mag deposit, Pinson mine, Humboldt County, Nevada, *in* Raines, G.L., Lisle, R.E., Schafer, R.W., and Wilkinson, W.H., eds., Geology and Ore Deposits of the Great Basin, Symposium Proceedings: Reno, Geological Society of Nevada, p. 845–856.

Grant, F.S., and West, G.F., 1965, Interpretation theory in applied geophysics: New York, McGraw-Hill, 584 p.

Grauch, V.J.S., Hoover, D.B., and Wojniak, W.S., 1991, Subsurface structure and lithology near the Getchell gold trend, Osgood Mountains, Nevada—Geophysical insights: U.S. Geological Survey Circular 1062, 34 p.

Hausen, D.M. and Park, W.C., 1986, Observations on the association of gold mineralization with organic matter in Carlin-type ores, *in* Dean, W.C., ed., Proceedings of the Denver Region Exploration Geologists Society Symposium on Organics and Ore Deposits: Denver Region Exploration Geologists Society, p. 119–136.

Hoover, D.B., Grauch, V.J.S., Pitkin, J.A., Krohn, M.D., and Pierce, H.A., 1991, An integrated airborne geophysical study along the Getchell trend of gold deposits, north-central Nevada, *in* Raines, G.L., Lisle, R.E., Schafer, R.W., and Wilkinson, W.H., eds., Geology and Ore Deposits of the Great Basin, Symposium Proceedings: Reno, Geological Society of Nevada, p. 739–758.

Hoover, D.B., Smith, B.D., Grauch, V.J.S., and Podwysocki, M.H., 1987, Geophysical studies in the vicinity of the Getchell fault system, Humboldt County, Nevada: U.S. Geological Survey Circular 995, p. 31–32.

Hotz, P.E., and Willden, Ronald, 1964, Geology and mineral deposits of the Osgood Mountains quadrangle, Humboldt County, Nevada: U.S. Geological Survey Professional Paper 431, 128 p.

Keller, G.V., and Frischknect, F.C., 1966, Electrical methods in geophysical prospecting: New York, Pergamon Press, 523 p.

Kretschmer, E.L., 1984, Geology of the Pinson and Preble gold deposits, Humboldt County, Nevada: Arizona Geological Society Digest, v. 15, p. 59–66.

Leventhal, Joel, and Hofstra, Albert, 1990, Characterization of carbon in sediment-hosted disseminated gold deposits, north central Nevada, *in* Hausen, D.M., Petersen, E.U., and Tafuri, W.J., eds., Gold '90, Symposium Proceedings: Littleton, Colorado, Society for Mining, Metallurgy, and Exploration, p. 365–368.

Leventhal, J.S., Hofstra, A.H., Vuletich, A.K., and Mancuso, T.B., 1987, Sediment-hosted disseminated gold mineralization at Jerritt Canyon, Nevada. III—Role of organic carbon [abs.]: Geological Society of America, Abstracts with Programs, v. 19, no. 7, p. 745.

Nelson, P.H., Hansen, W.H., and Sweeney, M.J., 1982, Induced-polarization response of zeolitic conglomerate and carbonaceous siltstone: Geophysics, v. 47, no. 1, p. 71–88.

Osterberg, M.W., and Guilbert, J.M., 1991, Geology, wall-rock alteration, and new exploration techniques at the Chimney Creek sediment-hosted gold deposit, Humboldt County, Nevada, *in* Raines, G.L., Lisle, R.E., Schafer, R.W., and Wilkinson, W.H., e ds., Geology and Ore Deposits of the Great Basin, Symposium Proceedings: Reno, Geological Society of Nevada, p. 805–820.

Palacky, G.J., 1986, Geological background to resistivity mapping: Geological Survey of Canada Paper 86–22, p. 19–27.

Percival, T.J., Bagby, W.C., and Radtke, A.S., 1988, Physical and chemical features of precous metal deposits hosted by sedimentary rocks in the Western United States, *in* Schafer, R.W., Cooper, J.J., and Vikre, P.G., eds., Bulk Mineable Precious

Metal Deposits of the Western United States Symposium Proceedings: Reno, Geological Society of Nevada, p. 11–34.

Pierce, H.A., and Hoover, D.B., 1991, Airborne electromagnetic applications—Mapping structure and electrical boundaries beneath cover along the Getchell trend, Nevada, *in* Raines, G.L., Lisle, R.E., Schafer, R.W., and Wilkinson, W.H., eds., Geology and Ore Deposits of the Great Basin, Symposium Proceedings: Reno, Geological Society of Nevada, p. 771–780.

Silberman, M.L., Berger, B.R., and Koski, R.A., 1974, K-Ar age relations of granodiorite emplacement and tungsten and gold mineralization near the Getchell mine, Humboldt County, Nevada: Economic Geology, v. 69, p. 646–656.

Willden, Ronald, 1964, Geology and mineral deposits of Humboldt County, Nevada: Nevada Bureau of Mines and Geology Bulletin 59, 154 p.

CHAPTER Y

GOLD IN DEVONIAN CARBONATE ROCKS AT CEDAR PEAK, SOUTHERN SNAKE MOUNTAINS, NORTHEASTERN NEVADA

By CHARLES H. THORMAN[1] *and* WILLIAM E. BROOKS[1]

ABSTRACT

A bedrock geochemical sampling program of the Oxley Peak and adjacent quadrangles shows anomalous gold concentrations in the Cedar Peak area, located 8 miles north of Wells, Nevada. Chemical analyses were obtained for 54 samples of unaltered bedrock and silicified and unsilicified fault zones throughout the study area and from zebra-banded Devonian dolomite and interbedded limestone at Cedar Peak. The Devonian zebra-banded dolomite and interbedded limestone occur within a west-northwest-trending structural block (Cedar Peak block). The Cedar Peak block is bounded on the north and south by west-northwest-trending high-angle faults and on the west by a west-dipping normal fault. Sixteen samples of dolomite and limestone contained from less than 0.002 to 0.150 parts per million gold; seven samples did not have detectable gold. Gold was not detected in the 31 samples collected from other locations in the area, including breccia from faults bounding the Cedar Peak block.

INTRODUCTION

Geologic mapping and geochemical sampling of fault zones and bedrock in the southern Snake Mountains were undertaken to study the history of deformation and mineralization of the range and to try to determine whether or not various deformational events and structures had different, and possibly characteristic, mineralization signatures and ages. Anomalous geochemical values, especially for gold, were found in the Cedar Peak study area in the Oxley Peak quadrangle (fig. 1), in the southern Snake Mountains. Two samples (88T04 and 88T06) were collected in 1988 from the Simonson Dolomite and Guilmette Formation during field mapping because of the unusual nature of the rocks. The presence of detectable gold prompted additional sampling of the section at Cedar Peak. The presence of gold and other metals in Devonian zebra-banded dolomites indicates that mineralizing fluids passed through these rocks, possibly several times.

GEOLOGIC SETTING

Northeastern Nevada is in the northern Basin and Range province and is underlain by rocks ranging in age from Archean orthogneiss to Holocene volcanic and basin-fill deposits. The stratigraphic column is comprised of three major sequences, separated by hiatuses representing the main orogenic events of the region. The oldest event was rifting of the Precambrian sialic(?) crystalline basement. Upon the rifted continental margin a second sequence was deposited, comprised of Proterozoic to Middle Jurassic strata. A major subdivision of the pre-Mississippian rocks in Nevada results from the recognition of two distinct sedimentary successions: an eastern or carbonate suite of miogeoclinal rocks deposited adjacent to the North American craton and a western or siliciclastic suite of eugeoclinal rocks deposited farther to the west. The transition from the eastern carbonate facies to the western siliciclastic facies rocks had a northerly trend and was located in central Nevada.

In western and central Nevada, several middle Paleozoic to early Mesozoic orogenic events have been recognized: the Late Devonian to Early Pennsylvanian Antler, Late Pennsylvanian Humboldt, and Late Permian to Early Triassic Sonoma orogenies. These events are mainly recorded in northeastern Nevada in the stratigraphic record rather than by structures. From Late Jurassic to early

[1]U.S. Geological Survey, Mail Stop 905, P.O. Box 25046, Denver Federal Center, Denver, CO 80225.

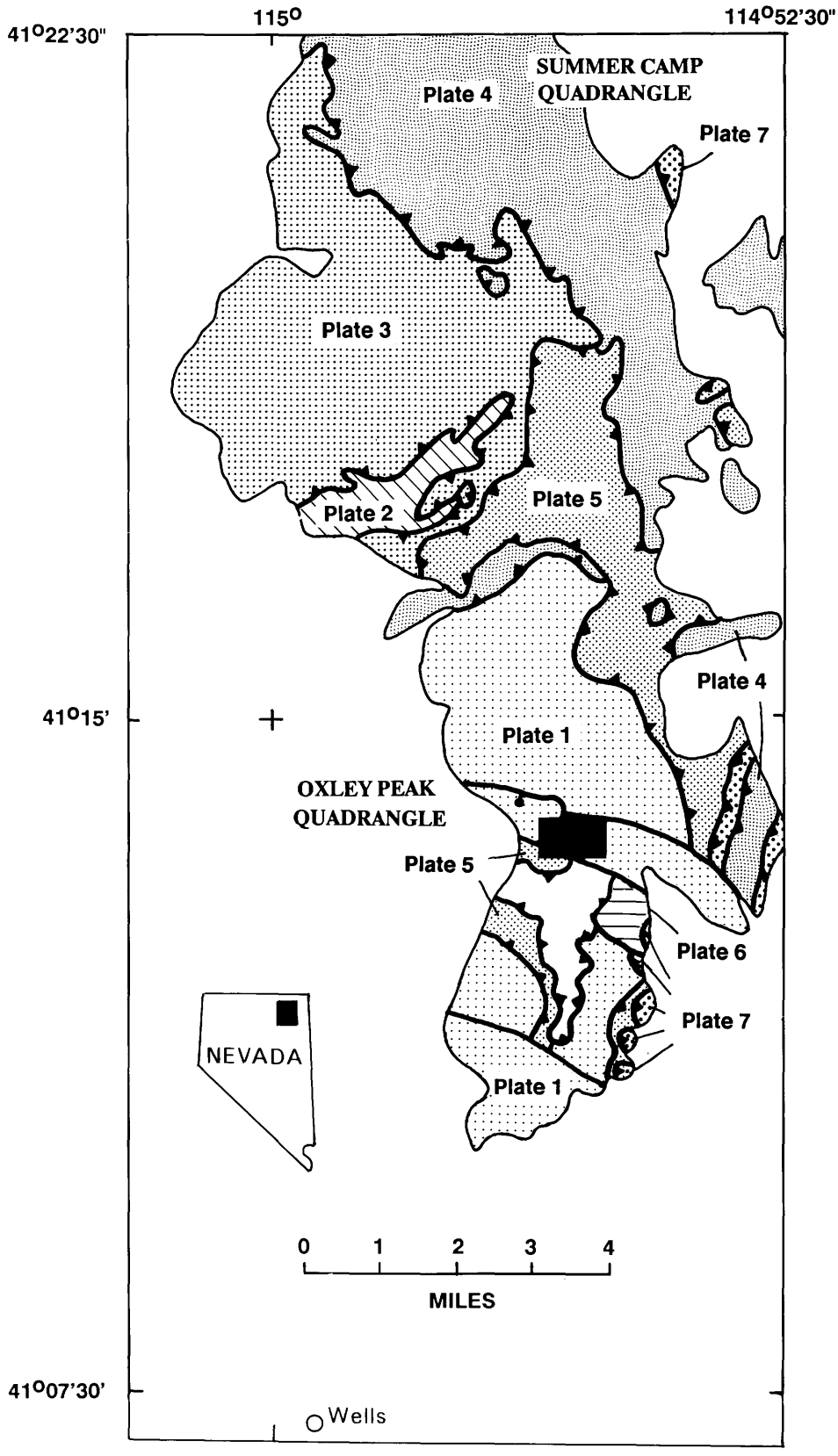

Figure 1. Map showing location of Cedar Peak study area (black rectangle) in the southern Snake Mountains and the principal structural plates (northern half of map modified after Smith and others, 1990).

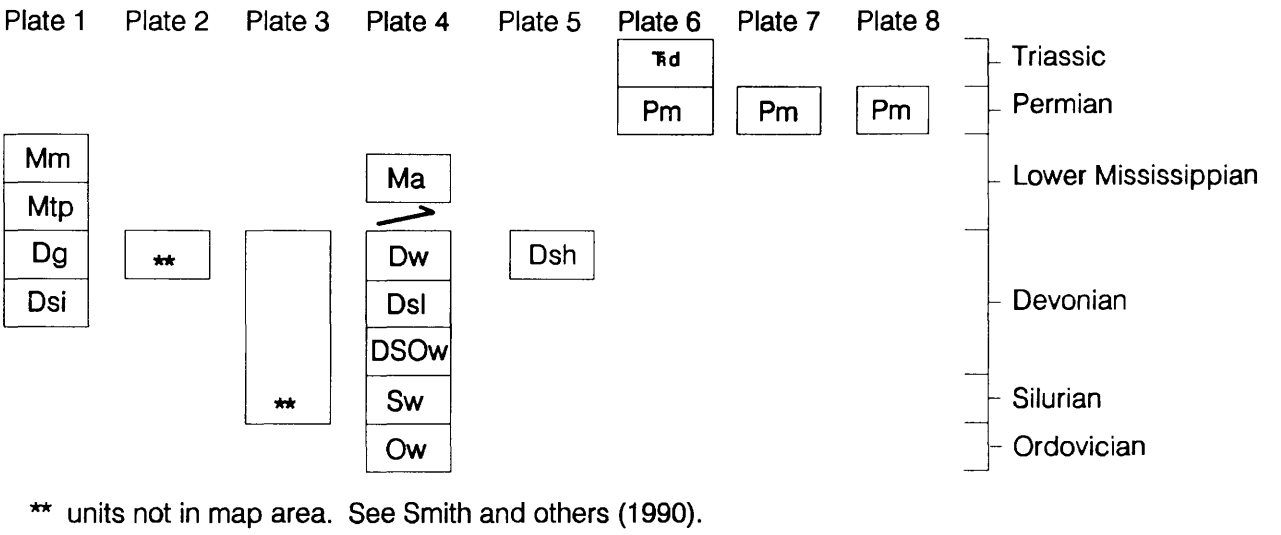

Figure 2. Distribution of pre-Tertiary rocks in thrust plates in the Oxley Peak quadrangle and adjacent quadrangles. Arrow between units Ma and Dw indicate subordinate thrust within plate 4. See appendix for description of map units.

Tertiary time, the area underwent two major compressional orogenic events, the Middle to Late Jurassic Elko orogeny (Thorman and others, 1991) and the Early Cretaceous to early Tertiary Sevier orogeny. These two orogenies resulted in regional metamorphism of miogeoclinal rocks, the formation of large-scale southeast- and east-directed structures, some extensional structures, plutonism, and regional uplift resulting in the shedding of enormous quantities of detritus into basins to the east. Sporadically preserved intermontane basinal deposits accumulated during this time (Vandervoort and Schmitt, 1990). The third major rock sequence was deposited after the Sevier orogeny; its age ranges from Eocene to Holocene. Rocks of this sequence accumulated during an extensional orogenic period that is still going on.

The southern Snake Mountains are underlain by a sequence of Paleozoic, Triassic, and Cenozoic sedimentary and volcanic rocks (Thorman and Brooks, 1988; Thorman and others, 1991; Smith and others, 1990). Direct and indirect evidence indicates that these rocks were deformed during the Antler, Humboldt, Sonoma, Elko, and Sevier orogenies and by Oligocene to Holocene basin-and-range extensional faulting. Compression and extension were oriented in the same general directions during these events and caused the reactivation of many faults, especially west-northwest-trending, high-angle faults. Pre-Tertiary rocks in the southern Snake Mountains range in age from Ordovician through Triassic and occur in a series of imbricate thrust plates (Thorman and Brooks, 1988; Thorman and others, 1991). The strata within the thrust plates strike subparallel to the bounding faults, which are subparallel to each other. Figure 2 shows the various units in these thrust plates; lithologic descriptions of the units are listed in the Appendix to this chapter. At Cedar Peak, facies of eastern, carbonate (miogeoclinal) rocks and western, siliciclastic (eugeoclinal) rocks of Ordovician through Devonian age are present in separate thrust plates that are bounded by both bedding-parallel and high-angle faults. The altered rocks discussed below are part of the eastern facies sequence. Tertiary rocks range in age from late Eocene (≈ 41 Ma) to Miocene and Pliocene and have undergone extensional deformation only.

STRUCTURES IN THE CEDAR PEAK BLOCK AREA

The Cedar Peak block (fig. 3) consists of east-dipping Middle Devonian Simonson Dolomite, Upper Devonian Guilmette Formation, Lower Mississippian Tripon Pass Limestone, and the Mississippian sandstone of Melandco (Thorman and Brooks, 1988). These rocks comprise the lowest thrust sheet, herein referred to as the Bishop Creek plate (plate 1 of Smith and others, 1990) in the Oxley Peak quadrangle—these rocks belong to the eastern (miogeoclinal) facies sequence of the Paleozoic miogeocline. The Finks Canyon plate (plate 5 of Smith and others, 1990) tectonically overlies the Bishop Creek plate and is comprised of Devonian limestone, shale, chert, and argillite, herein interpreted to be transitional between eastern (miogeoclinal) and western (eugeoclinal) facies strata. The Oxley Peak plate tectonically overlies both of these plates and consists of limestone, dolomite, chert, and siltstone of the Permian Murdock Mountain Formation.

Two types of faults dominate the structure at and near Cedar Peak: high-angle, west-northwest-trending faults (which probably have both lateral and vertical displacement) and faults that are subparallel or parallel to bedding

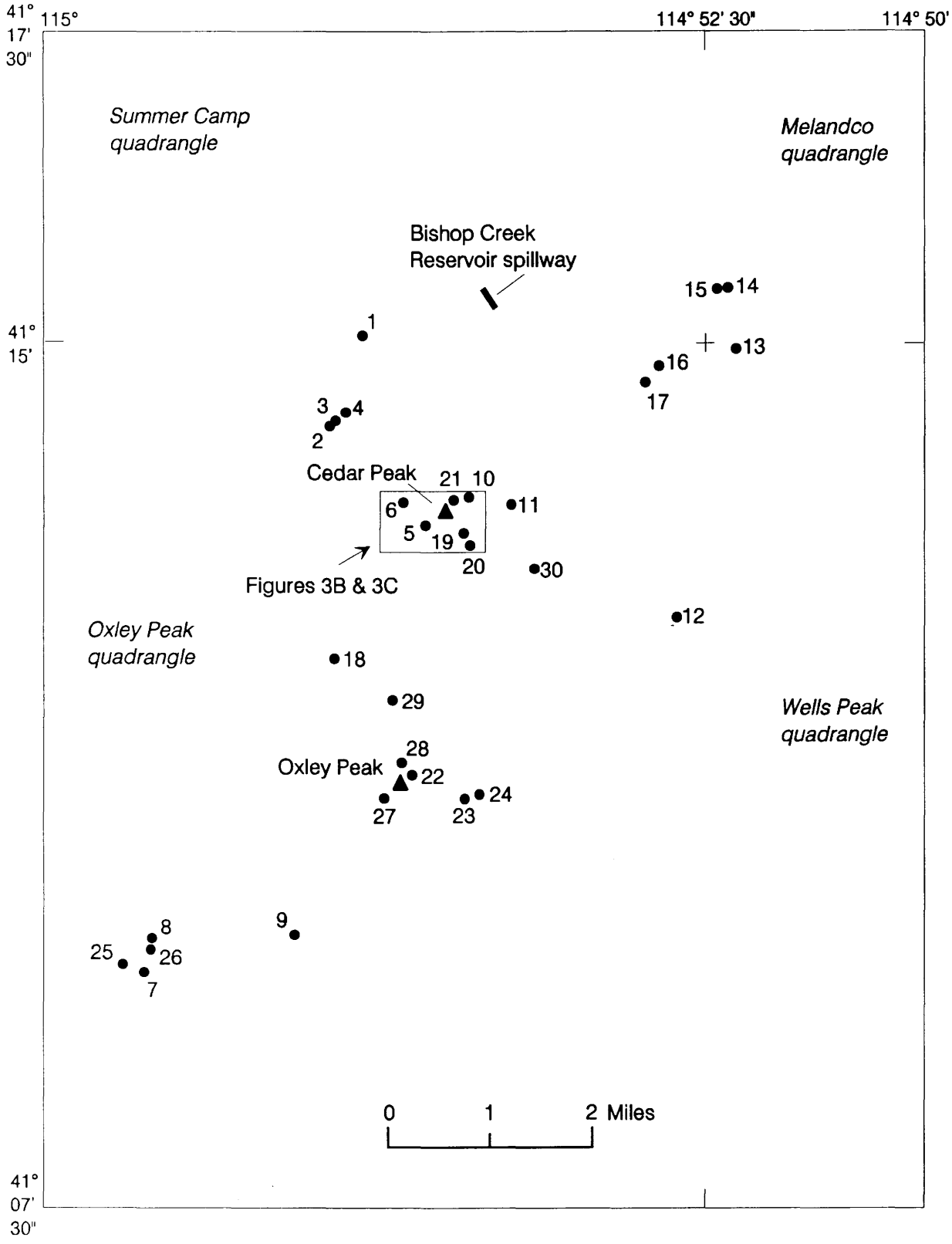

Figure 3A. Map showing samples sites 1 through 30 (see table 1) and location of areas shown in figures 3*B* and 3*C*.

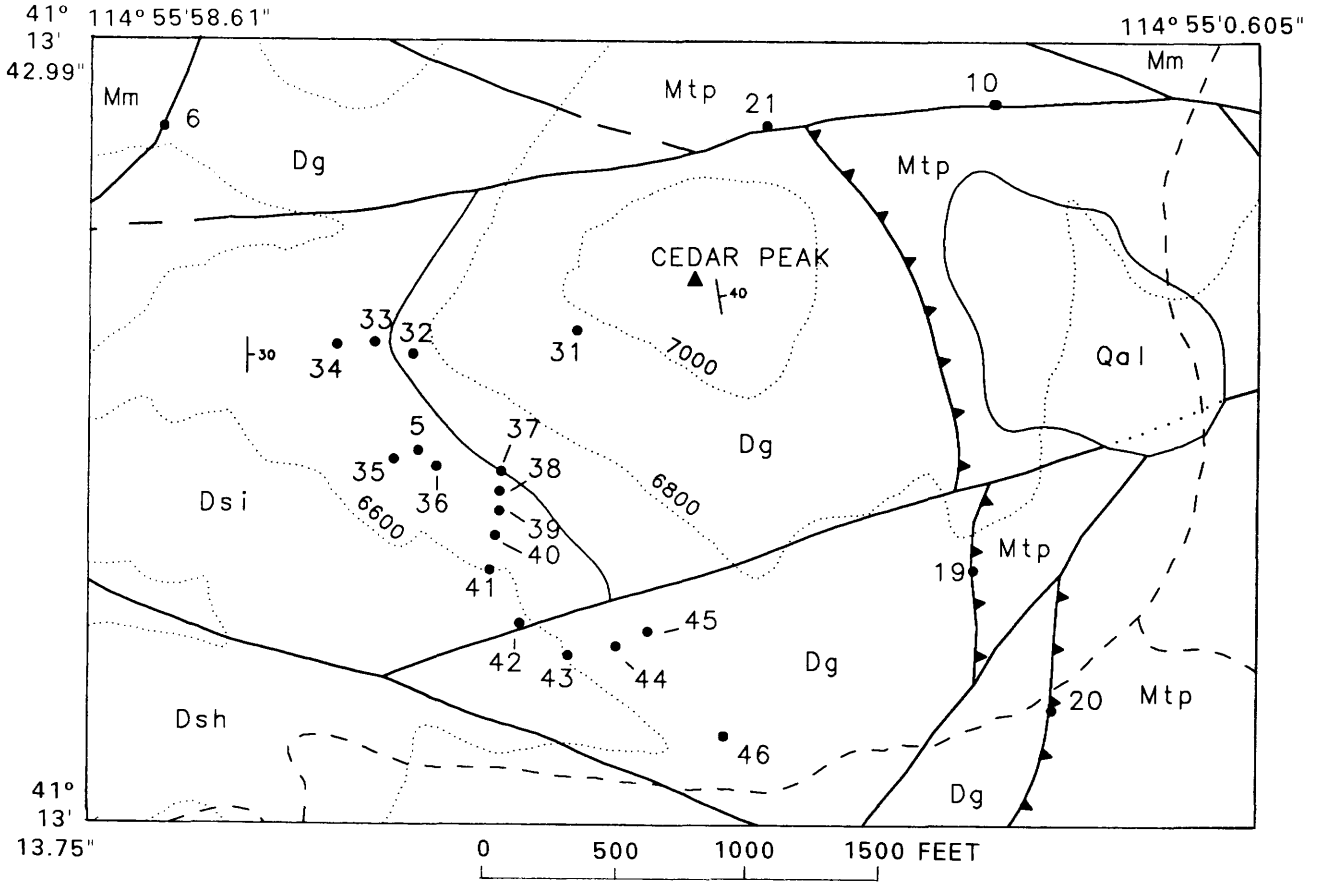

Figure 3B. Geologic map of the Cedar Peak block showing location of samples collected from the Simonson Dolomite, Guilmette Formation, and from fault zones. See tables 1 and 2. Topographic base digitized from Oxley Peak 7½-minute quadrangle. Location of figure shown on figure 3A. Dotted lines are contours; heavy solid lines are high-angle faults (dashed where inferred); heavy solid lines with teeth are low-angle to bedding-parallel faults with teeth on upper plate; light dashed lines are jeep trails. See Appendix for description of map units Dsi, Dg, Mtp, Mm, and Dsh.

(herein referred to as bedding-parallel faults). The bedding-parallel faults are of two types: those that bound major imbricate thrust sheets (both younger-over-older and older-over-younger relationships) and subordinate bedding-parallel faults within the thrust sheets that occur at boundaries between contrasting lithologies. In addition, northerly trending, down-to-the-west normal faults occur in the western portion of the range—the largest of these is at the western foot of the range.

The Cedar Peak block, a west-northwest-trending block about 0.7 miles wide comprised of middle Paleozoic miogeoclinal units, is bounded by high-angle faults that transect the Snake Mountains. The high-angle faults cut Paleozoic, Mesozoic, and Tertiary rocks. At least two periods of movement are interpreted to have taken place along these faults: one during late Mesozoic and the other during middle to late Tertiary. We consider the faults to be part of the Wells fault system, a Late Mesozoic west-northwest-trending right-slip fault system that extends across northeastern Nevada (Thorman and Ketner, 1979). Initial displacement is believed to have occurred in the Mesozoic, during either the Middle to Late Jurassic Elko or during the Late Cretaceous–early Tertiary Sevier orogenies. No data exist that may suggest (1) whether fault movement began during the Elko orogeny and was subsequently reactivated during the Sevier orogeny, or (2) whether fault movement occurred during only one orogeny or the other. At the eastern foot of the Snake Mountains, the high-angle faults juxtapose middle Miocene rhyolite flows against sandstone of Melandco in the Bishop Creek plate—this dates some of the faulting as middle Miocene or younger.

The northern bounding fault has left separation of about 0.7 miles and juxtaposes rocks of the Bishop Creek plate against higher plates on the eastern side of the range. The southern bounding fault has apparent down-to-the-south movement and juxtaposes the structurally higher Finks Canyon and Oxley Peak plates, on the south, against the Bishop Creek plate. It is not possible, at this time, to determine the amount and direction of the slip along these faults.

The bedding-parallel faults are interpreted to be pre-late-Eocene in age because 39-Ma to 40-Ma ash-flow tuffs

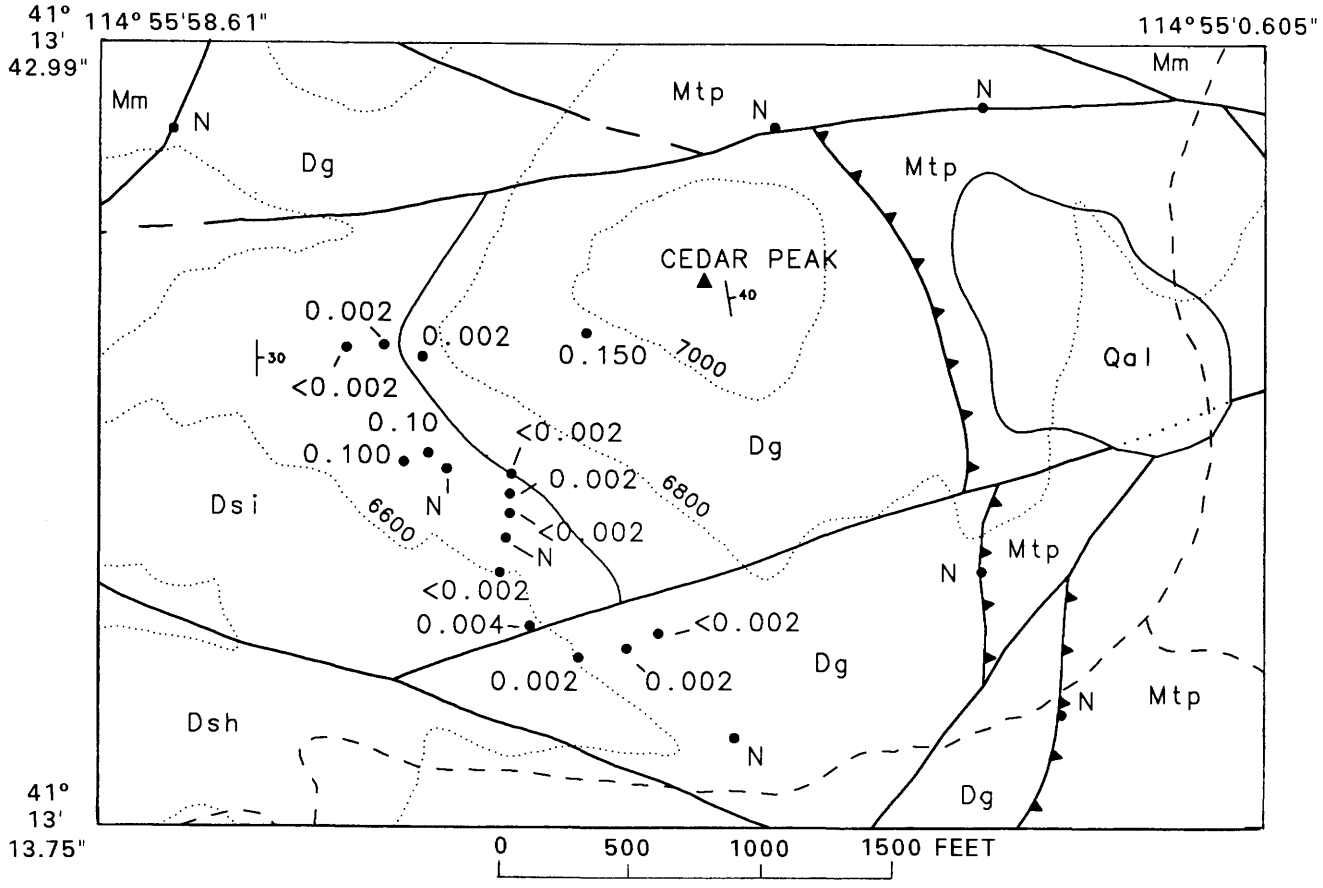

Figure 3C. Geologic map of Cedar Peak block showing gold values for sites shown in figure 3*B*. See Appendix for description of map units.

overlie these structures on the eastern flank of the range (Thorman and others, 1991). At Cedar Peak, west-northwest-trending, high-angle faults cut both types of bedding-parallel faults (see fig. 3).

STRATIGRAPHY OF GOLD-BEARING ROCKS AT CEDAR PEAK

The Simonson Dolomite in this part of northeastern Nevada typically is comprised of dolomite, locally with subordinate limestone. In contrast, the lower Guilmette is comprised of a lower unit of argillaceous, platy limestone approximately 100 ft thick that is overlain by several hundred feet of thin- to medium-bedded limestone with variable amounts of dolomite beds (generally less than 50 percent). Both the dolomite and limestone beds are characterized by laminated, medium-grained, medium- to dark-gray rocks (fig. 4). At Cedar Peak, the upper 400 ft of the Simonson Dolomite contains approximately 40–80 percent zebra-banded dolomite of an irregular, stratabound nature and forms a light-colored band on the hillside—this is in marked contrast to the otherwise dark-colored rocks in this portion of the stratigraphic section (fig. 5).

Two lithologies form the zebra-banded rock: a light-colored, bleached-looking, coarse-grained, massive dolomite and a darker, coarse-grained, weakly laminated dolomite (fig. 6). The darker rock is similar to the typical laminated Simonson Dolomite lithology but is much coarser grained. Discontinuous, flat, tabular fragments of the darker rock occur in a matrix of the light-colored dolomite, with the amount of light-colored dolomite ranging from zero to more than 95 percent. Some of the zebra-banded rock structure has the appearance of crossbedding (fig. 6); some has the appearance of edgewise conglomerate; and, in some beds, the dark fragments are randomly oriented. In the rocks that appear to be crossbedded or edgewise conglomerates, the light-colored dolomite crystals typically are oriented normal to the edges of the dark fragments, forming comb structure, commonly with open spaces. The upper Simonson Dolomite contains numerous irregular-shaped bodies of zebra-banded rock that are grossly stratabound, but in detail they cut across bedding and die out laterally. Small-scale collapse features within coarse-grained veinlets cut across bedding (fig. 7).

Figure 4. Typical exposure of weathered, laminated beds in the Simonson Dolomite.

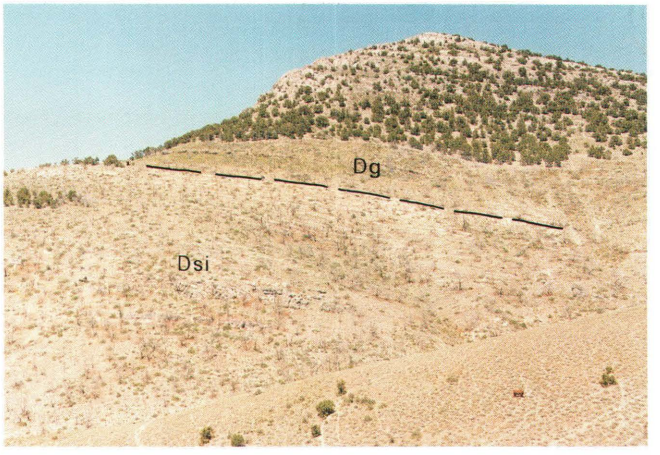

Figure 5. Looking northeast at Cedar Peak. Dashed line is contact between Simonson Dolomite (Dsi) and Guilmette Formation (Dg). Grassy slope with Dg label is basal unit of Guilmette. Light-colored beds below contact are zebra-banded dolomite beds in upper Simonson Dolomite.

Figure 6. Zebra-banded dolomite beds in upper Simonson Dolomite. Note cross bedded appearance and variation in amount of light and dark lithology.

Figure 7. Possible collapse structures in zebra-banded dolomite filled with light-colored dolomite matrix.

The origin of zebra-banded dolomite, or zebra rock, has been discussed by many workers. Two different processes considered to be essential to the formation of the basic zebra structure are: the development of stromatactis structure synchronous with carbonate sedimentation during which "episodic submarine lithification of the carbonate muds, which forms a series of crusts between which cavities (stripes) are eroded, cemented, and filled with rhombs, occurs near the sediment-seawater interface" (Landis and Tschauder, 1990, p. 340); or the development of zebra-banded dolomite "is best developed adjacent to karst channelways, and the zebra spar precipitated into voids created by karst dissolution" (Horton and De Voto, 1990, p. 86). Both models describe early-stage, low-temperature, light-colored (zebra spar) dolomite overgrown by late-stage dolomite of a higher temperature that is associated with ore deposition. We have not studied the small-scale features of the Cedar Peak zebra rock with regard to the origin of the zebra structure or with regard to how many generations of dolomite may be present.

NATURE OF MINERALIZED ROCKS

During mapping of the Oxley Peak quadrangle and adjacent areas, samples were routinely collected for geochemical analyses from altered rocks and from several black-shale-bearing western-facies units to determine their metal content. Samples were also collected from fault

Table 1. Samples collected in 1988 from the Oxley Peak, northwestern Wells Peak, southwestern Melandco, and southeastern Summer Camp quadrangles, northeast Nevada.

[See figure 3*A* for sample locations. Most of the samples were collected from fault zones; the other samples were from undeformed rocks to determine background geochemical characteristics. Abbreviations for formation names are presented in the Appendix; lower limits of detection for gold and mercury are 0.05 ppm and 0.02 ppm, respectively; n, not detected at limit of determination; H, greater than 36 ppm; V, high-angle fault; B, bedding-parallel fault; E-W, east-west-trending fault; N-S, north-south-trending fault; X, feature observed in sample; -, feature not observed in sample; /, separates symbols for map units in fault contact; ?, indicates uncertainty regarding nature of sample]

Map number	Field number	Formation names	Gold (ppm)	Mercury (ppm)	Fault	Brecciated	Silicified	Vein	Iron stained
1	88T01	Mtp	n	0.18	V-B	X	-	-	X
2	88T02	Mtp	n	0.42	V(E-W)	X	-	-	X
3	88T03	Mtp	n	0.68	V(E-W)	X	-	-	X
4	88T04	Dg	0.05	H	-	-	-	X	X
5	88T06	Dsi	0.10	n	Rock sample—zebra-banded dolomite				
6	88T07	Dg/Mm	n	0.02	V	X	X	-	X
7	88E07	Ttm	n	0.18	V(N-S)	X	X	-	X
8	88E08	Ttm	n	n	V(N-S)	X	X	-	X
9	88T10	Trau	n	n	-	-	X	-	-
10	88E12	Mtp/Mm	n	0.24	V(E-W)	X	X	-	X
11	88E13	Mm	n	0.08	V(E-W)	X	X	-	X
12	88T14	Pm/Dsl	n	0.02	B	X	X	-	X
13	88T17	DOw	n	0.18	Rock sample—black shale				
14	88T18	Sw	n	0.28	Rock sample—black shale				
15	88T19	Ow	n	0.02	Rock sample—basaltic? amygdaloidal pillow lava				
16	88T20	DOw	n	0.20	Rock sample—siltstone				
17	88T21	Msh	n	0.06	Rock sample—black shale				
18	88T26a	Dsh	n	0.34	Rock sample—black argillite				
18	88T26b	Dsh	n	0.22	Rock sample—black argillite				
19	88T27a	Dg/Mtp	n	0.04	B	?	X	-	X
19	88T27b	Dg/Mtp	n	0.12	B	?	X	-	X
20	88T28	Dg/Mtp	n	0.12	B	?	X	-	X
21	88T29	Dg/Mtp	n	0.04	V(E-W)	X	X	-	X
22	88T30	Pm/Mm	n	0.32	B	X	X	-	X
23	88T31	Pm/Dsh	n	n	B	X	?	-	-
24	88T32	Pm	n	0.16	B	?	X	-	X
24	88T33	Pm	n	0.04	B	X	X	-	X
25	88T34	Ttm	n	n	B(N-S)	X	X	-	X
26	88T35	Ttm	n	0.32	B(N-S)	X	X	-	X
27	88T52	Dsh	n	0.40	?	-	-	-	X
28	88T57	Pm	n	0.80	B	X	X	-	X
29	88T58	Dsh	n	0.40	Rock sample— dark siltstone with black chert and siliceous nodules				
30	88T80	Trp	n	n	V(E-W)	X	?	-	-

zones and veins of various types. Figure 3*A* shows the locations of samples collected in 1988. Figure 3*B* shows the locations of samples collected in 1989 and figure 3*C* shows the gold content detected from each sample in 1989. Tables 1 and 2 list the 54 samples collected in 1988 and 1989, respectively, and indicate formation name, gold and mercury content, structural setting, and nature of each sample (breccia, silicified, iron stained, high-angle or bedding-parallel fault). Tables 3, 4, and 5 list the samples according to the formation or structure sampled; table 3 lists samples from the Simonson Dolomite and Guilmette Formation; table 4 lists samples from fault zones; and table 5 lists samples collected for geochemical background data from black shales. Table 6 lists the latitude and longitude of the samples shown on figure 3*A* and listed in table 1.

The rocks of primary concern in this report are zebra-banded dolomites in the upper 440 ft of the Simonson Dolomite and lower 300 ft of the Guilmette Formation because they are the only rocks that contained detectable gold. However, various fault zones contain elevated concentrations of some metals, suggesting that some of the mineralizing fluids that deposited the gold may have passed through the fault zones.

Gold values in the zebra-banded rocks range from 0.02 to 0.150 ppm (parts per million); in some cases gold was detected but below the limit of detection (tables 1, 2, 3, and 4). Twenty-three samples were collected from these formations (tables 1 and 2), of which 14 were from the Simonson, 8 were from the Guilmette, and 1 was from an east-west-trending fault zone along which the Simonson

Table 2. Samples collected from the Simonson Dolomite (Dsi) and Guilmette Formation (Dg) at Cedar Peak in 1989 in the Oxley Peak quadrangle, northeast Nevada.

[See figure 3A for sample locations. Lower limits of detection for gold and mercury are 0.002 ppm and 0.02 ppm, respectively; n, not detected at limit of determination; <, detected but below limit of determination shown; /, separates map units in fault contact]

Map number	Field number	Formation names	Gold (ppm)	Mercury (ppm)	Sample description
31	89T24	Dg	0.002	n	Fine-grained, zebra-banded dolomite.
31	89T25	Dg	0.150	n	Coarse-grained, zebra-banded dolomite.
32	89T26	Dg	0.002	0.04	*Atrypa*-bearing, thin-bedded, argillaceous limestone.
33	89T27	Dsi	0.002	n	Medium-grained, mottled dolomite.
33	89T28	Dsi	n	n	Medium- to coarse-grained, zebra-banded dolomite.
33	89T29	Dsi	n	0.04	Dolomite breccia.
34	89T30	Dsi	<0.002	n	Medium-grained, zebra-banded dolomite.
34	89T31	Dsi	n	n	Medium-grained, zebra-banded dolomite.
35	89T32	Dsi	0.100	0.36	Medium-grained dolomite with intraformational breccia, some thin dolomite veins.
35	89T33	Dsi	n	0.04	Medium-grained dolomite with intraformational breccia.
36	89T34	Dsi	n	n	Medium- to coarse-grained, zebra-banded dolomite.
37	89T35	Dsi	<0.002	n	Medium- to coarse-grained, zebra-banded dolomite.
38	89T36	Dsi	0.002	0.20	Medium- to coarse-grained dolomite with fossil hash.
39	89T37	Dsi	<0.002	0.04	Medium- to coarse-grained, zebra-banded dolomite.
40	89T38	Dsi	n	n	Medium- to coarse-grained, zebra-banded dolomite.
41	89T39	Dsi	<0.002	n	Medium-grained, mottled dolomite.
42	89T40	Dsi/Dg	0.004	0.16	Silicified, brecciated, and iron-stained carbonate rock along E.-W. fault.
43	89T41	Dg	0.002	0.08	Brecciated and iron-stained limestone and dolomite.
44	89T42	Dg	0.002	0.08	Brecciated and iron-stained dolomite with calcite veinlets.
45	89T43	Dg	<0.002	0.16	Brecciated and iron-stained limestone and dolomite with calcite veinlets.
46	89T44	Dg	n	n	Brecciated and iron-stained limestone with calcite veinlets.

and Guilmette are juxtaposed. Eight samples from the Simonson, seven from the Guilmette, and the fault-zone sample contained detectable gold. We can see no difference in hand specimen between the gold-bearing and barren samples.

Distribution of several other metals in the Simonson and Guilmette show the following relationships: mercury generally occurs with gold but was not detected in two of the four samples with the highest gold values (88T06 and 88T25); antimony, arsenic, cadmium, copper, molybdenum, and zinc have distribution patterns similar to that of mercury. Silver was detected in only one sample at Cedar Peak (89T26), which also had anomalous amounts of zinc, antimony, gold, copper, molybdenum, and mercury.

In general, the following elements have higher concentrations in the faults than in the Simonson and Guilmette: zinc, mercury, lead, molybdenum, copper, antimony, cadmium, arsenic, zirconium, yttrium, vanadium, nickel, gallium, chromium, cobalt, beryllium, barium, boron, silver, titanium, phosphorous, and iron.

OBSERVATIONS

Conclusions regarding the zebra-banded dolomites and the alteration and distribution of gold and other metals are:

1. Gold appears to have been deposited primarily in the Cedar Peak block;
2. The zebra-banded beds occur primarily in the Cedar Peak block; Simonson Dolomite and Guilmette

Table 3. Analyses of samples collected from the Devonian Simonson Dolomite and Guilmette Formation in the Oxley Peak quadrangle, northeast Nevada.

[Analytical results are given in parts per million, except for Ca, Fe, Mg, Na, P, and Ti, which are given in percent. The column headings show the element analyzed, the method of determination, and the lower limit of determination (shown in parentheses in parts per million, except for Ca, Fe, Mg, Na, P, and Ti, which are in percent). Methods of determination are: s, emission spectrographic analyses; i-5 or i-10, 5- or 10-element inductively coupled plasma analyses, respectively; aag, graphite furnace atomic absorption analyses; aac, cold vapor atomic absorption; aaf, atomic absorption flame analysis. Other abbreviations are: n, not detected at the lower limit of determination; <, detected, but below the lower limit of determination; >, determined to be greater than the value shown]

Sample number	Ca	Fe	Mg	Na	P	Ti	Ag	As	Au	B	Ba	Be	Bi	Cd	Co	Cr	Cu	Ga	Ge	La	Mn	Mo
	s	s	s	s	s	s	s	s	s	s	s	s	s	s	s	s	s	s	s	s	s	s
	(0.05)	(0.05)	(0.02)	(0.2)	(0.2)	(0.002)	(0.5)	(200)	(10)	(10)	(20)	(1)	(10)	(20)	(10)	(10)	(5)	(5)	(10)	(50)	(10)	(5)
88T04	3	20	0.2	n	n	0.05	n	2,000	n	<10	3,000	20	n	n	30	n	30	50	15	n	300	50
88T06	20	0.1	10	0.2	n	0.002	n	n	n	n	n	n	n	n	n	n	20	n	n	n	300	< 5
89T24	> 20	< 0.05	> 10	n	n	0.002	n	n	n	n	<20	n	n	n	n	n	< 5	n	n	n	500	n
89T25	> 20	0.05	> 10	< 0.2	n	0.002	n	n	n	n	20	< 1	n	n	n	n	< 5	n	n	n	150	n
89T26	20	0.7	5	n	n	0.05	n	n	n	50	200	n	n	n	n	< 10	7	< 5	n	n	500	n
89T27	> 20	< 0.05	> 10	< 0.2	n	< 0.002	n	n	n	n	50	1	n	n	n	< 10	n	n	n	n	300	n
89T28	20	n	10	< 0.2	n	n	n	n	n	n	n	n	n	n	n	n	< 5	n	n	n	70	n
89T29	> 20	0.07	10	< 0.2	n	0.01	n	n	n	<10	50	n	n	n	n	< 10	5	n	n	n	200	n
89T30	> 20	n	> 10	< 0.2	n	< 0.002	n	n	n	n	<20	1	n	n	n	n	< 5	n	n	n	200	n
89T31	> 20	< 0.05	> 10	< 0.2	n	n	n	n	n	n	<20	1	n	n	n	n	n	n	n	n	100	n
89T32	> 20	0.15	> 10	n	n	0.005	n	n	n	n	30	n	n	n	n	n	10	n	n	n	500	n
89T33	> 20	< 0.05	> 10	n	n	0.003	n	n	n	n	n	n	n	n	n	n	n	n	n	n	500	n
89T34	> 20	n	> 10	< 0.2	n	0.003	n	n	n	n	<20	< 1	n	n	n	n	n	n	n	n	100	n
89T35	> 20	< 0.05	> 10	n	n	0.003	n	n	n	n	20	n	n	n	n	n	n	n	n	n	150	n
89T36	> 20	0.07	7	n	n	0.02	n	n	n	<10	30	n	n	n	n	n	< 5	n	n	n	100	n
89T37	> 20	0.05	10	< 0.2	n	0.002	n	n	n	n	200	1.5	n	n	n	n	< 5	n	n	n	300	n
89T38	> 20	< 0.05	> 10	< 0.2	n	0.003	n	n	n	n	100	1	n	n	n	n	< 5	n	n	n	300	n
89T39	> 20	0.05	> 10	n	n	0.005	n	n	n	n	20	n	n	n	n	n	10	n	n	n	300	n
89T40	20	1	7	n	n	0.02	n	n	n	10	5,000	< 1	n	n	n	n	5	n	n	n	200	n
89T41	> 20	< 0.05	0.5	n	n	0.005	n	n	n	n	300	n	n	n	n	n	< 5	n	n	n	150	n
89T42	> 20	0.07	0.5	n	n	0.005	n	n	n	n	200	n	n	n	n	n	< 5	n	n	n	150	n
89T43	20	0.1	7	n	n	0.005	n	n	n	n	2,000	n	n	n	n	n	< 5	n	n	n	200	n
89T44	> 20	0.05	0.7	n	n	0.01	n	n	n	n	150	< 1	n	n	n	< 10	< 5	n	n	n	50	n

Table 3. Analyses of samples collected from the Devonian Simonson Dolomite and Guilmette Formation in the Oxley Peak quadrangle, northeast Nevada—Continued.

[Analytical results are given in parts per million, except for Ca, Fe, Mg, Na, P, and Ti, which are given in percent. The column headings show the element analyzed, the method of determination, and the lower limit of determination (shown in parentheses in parts per million, except for Ca, Fe, Mg, Na, P, and Ti, which are in percent). Methods of determination are: s, emission spectrographic analyses; i-5 or i-10, 5- or 10-element inductively coupled plasma analyses, respectively; aag, graphite furnace atomic absorption analyses; aac, cold vapor atomic absorption; aaf, atomic absorption flame analysis. Other abbreviations are: n, not detected at the lower limit of determination; <, detected, but below the lower limit of determination; >, determined to be greater than the value shown]

Sample number	Nb s (20)	Ni s (5)	Pb s (10)	Sb s (100)	Sc s (5)	Sn s (10)	Sr s (100)	Th s (100)	V s (10)	W s (20)	Y s (10)	Zn s (200)	Zr s (10)	As i-5 (5)	Bi i-5 (2)	Cd i-5 (0.1)	Sb i-5 (2)	Zn i-5 (2)	Hg aac (0.02)	Au aaf (0.05)
88T04	n	100	< 10	200	< 5	n	n0	n	200	50	10	300	< 10	1300	< 2	2.9	96	160	H	0.05
88T06	n	< 5	< 10	n	n	n	n	n	< 10	n	n	< 200	< 10	< 5	< 2	< 0.1	< 2	< 2	n	0.10

Sample number	Nb s (20)	Ni s (5)	Pb s (10)	Sb s (100)	Sc s (5)	Sn s (10)	Sr s (100)	Th s (100)	V s (10)	W s (20)	Y s (10)	Zn s (200)	Zr s (10)	As i-10 (0.6)	Bi i-10 (0.6)	Cd i-10 (0.03)	Sb i-10 (0.6)	Zn i-10 (0.03)	Ag i-10 (0.045)	Cu i-10 (0.03)	Mo i-10 (0.09)	Pb i-10 (0.06)	Hg aac (0.02)	Au aag (0.002)
89T24	n	n	< 10	n	n	n	n	n	< 10	n	n	n	n	n	n	n	n	1.0	n	0.34	0.14	1.3	n	0.002
89T25	n	n	n	n	n	n	n	n	< 10	n	n	n	n	n	n	n	n	1.4	n	0.58	0.26	2.4	n	0.150
89T26	n	5	< 10	n	n	n	n	n	15	n	n	n	< 10	3.4	n	0.11	0.97	4.5	0.063	3.5	7.0	9.7	0.04	0.002
89T27	n	n	n	n	< 5	n	n	n	10	n	n	n	n	n	n	n	n	0.54	n	0.40	0.33	1.5	n	0.002
89T28	n	n	n	n	n	n	n	n	n	n	n	n	n	n	n	n	n	0.70	n	0.24	0.22	0.85	n	n
89T29	n	n	< 10	n	n	n	n	n	15	n	n	n	n	0.96	n	n	n	1.0	n	2.7	0.46	6.6	0.04	n
89T30	n	n	< 10	n	7	n	n	n	< 10	n	n	200	n	n	n	n	n	0.33	n	0.19	0.44	1.2	n	< 0.002
89T31	n	n	< 10	n	5	n	n	n	< 10	n	n	200	n	n	n	n	n	.030	n	0.26	0.20	0.74	n	n
89T32	n	n	100	n	n	n	n	n	10	n	n	300	n	2.1	n	1.5	n	380	n	3.9	1.3	81	0.36	0.100
89T33	n	n	< 10	n	n	n	n	n	< 10	n	n	n	n	n	n	0.11	n	51	n	0.85	0.23	7.2	0.04	n
89T34	n	n	< 10	n	n	n	n	n	< 10	n	n	n	n	n	n	n	0.60	0.80	n	0.29	0.17	0.82	n	n
89T35	n	n	n	n	n	n	n	n	< 10	n	n	n	n	n	n	n	n	1.0	n	0.96	0.19	1.6	n	< 0.002
89T36	n	n	n	n	n	n	n	n	15	n	n	n	n	1.8	n	n	0.93	2.5	n	2.2	0.57	5.5	0.20	0.002
89T37	n	n	n	n	< 5	n	n	n	< 10	n	n	n	n	n	n	n	n	1.6	n	1.3	0.094	1.4	0.04	< 0.002
89T38	n	n	< 10	n	< 5	n	n	n	< 10	n	n	n	n	n	n	0.043	n	5.1	n	0.97	n	1.7	n	n
89T39	n	n	15	n	n	n	n	n	< 10	n	n	n	n	2.1	n	0.033	2.0	6.5	n	6.3	2.2	15	n	< 0.002
89T40	n	< 5	n	n	n	n	n	n	10	n	n	n	< 10	40	n	0.067	7.6	4.8	n	3.2	3.0	4.5	0.16	< 0.004
89T41	n	n	n	n	n	n	< 100	n	< 10	n	n	n	n	1.1	n	0.033	n	2.4	n	0.87	0.37	1.7	0.08	0.002
89T42	n	n	n	n	n	n	n	n	< 10	n	n	n	n	4.8	n	0.071	0.72	11	n	4.0	0.18	4.3	0.08	0.002
89T43	n	n	< 10	n	n	n	n	n	< 10	n	n	n	n	12.0	n	0.068	1.8	17	n	1.9	1.3	5.9	0.16	< 0.002
89T44	n	n	< 10	n	n	n	200	n	10	n	n	n	n	0.60	n	0.049	n	1.3	n	1.2	0.26	2.8	n	n

Table 4. Analyses of samples collected from faults in the Oxley Peak quadrangle and adjacent quadrangles, northeast Nevada.

[Analytical results are given in parts per million, except for Ca, Fe, Mg, Na, P, and Ti, which are given in percent. The column headings show the element analyzed, the method of determination, and the lower limit of determination (shown in parentheses in parts per million, except for Ca, Fe, Mg, Na, P, and Ti, which are in percent). Methods of determination are: s, emission spectrographic analyses; i-5 or i-10, 5- or 10-element inductively coupled plasma analyses, respectively; aag, graphite furnace atomic absorption analyses; aac, cold vapor atomic absorption; aaf, atomic absorption flame analysis. Other abbreviations are: n, not detected at the lower limit of determination; <, detected, but below the lower limit of determination; >, determined to be greater than the value shown]

Sample number	Ca s (0.05)	Fe s (0.05)	Mg s (0.02)	Na s (0.2)	P s (0.2)	Ti s (0.002)	Ag s (0.5)	As s (200)	Au s (10)	B s (10)	Ba s (20)	Be s (1)	Bi s (10)	Cd s (20)	Co s (10)	Cr s (10)	Cu s (5)	Ga s (5)	Ge s (10)	La s (50)	Mn s (10)	Mo s (5)
North-south faults																						
88E07	0.05	1	0.1	0.2	<0.2	0.07	<0.5	n	n	50	200	3	n	n	n	<10	10	<5	n	n	100	50
88E08	0.1	1	0.1	0.2	<0.2	0.1	0.5	n	n	50	200	3	n	n	<10	<10	10	20	n	<50	100	10
88T34	0.1	1	0.15	0.2	<0.2	0.1	0.7	n	n	15	500	5	n	n	n	<10	7	20	n	n	30	15
88T35	0.05	1.5	0.05	0.2	<0.2	0.15	<0.5	n	n	50	300	2	n	n	n	n	5	5	n	<50	70	50
Bedding-parallel faults																						
88T14	0.1	0.3	<0.02	n	0.3	0.01	n	n	n	15	50	<1	n	n	n	30	5	n	n	n	20	n
88T27a	5	0.5	1	<0.2	<0.2	0.03	n	n	n	20	700	<1	n	n	<10	n	15	<5	n	n	200	n
88T27b	5	0.3	1.5	<0.2	n	0.02	n	n	n	15	300	<1	n	n	<10	n	7	n	n	n	300	<5
88T28	7	0.7	0.5	<0.2	0.2	0.05	n	n	n	50	300	<1	n	n	10	<10	15	<5	n	n	200	5
88T30	0.1	0.2	0.1	<0.2	0.2	0.15	n	n	n	100	500	<1	n	n	n	20	20	<5	n	<50	10	7
88T31	0.2	1	0.05	n	0.5	0.02	1	n	n	30	700	<1	n	n	<10	50	30	<5	n	n	70	5
88T32	0.07	0.3	0.1	<0.2	<0.2	0.07	n	n	n	70	500	<1	n	n	n	10	7	<5	n	n	50	<5
88T33	0.3	0.5	0.07	<0.2	0.5	0.07	n	n	n	70	700	<1	n	n	n	70	7	n	n	n	50	n
88T57	0.7	5	0.05	<0.2	1.5	0.07	0.5	300	n	100	2,000	<1	n	n	20	50	200	5	n	n	20	50
East-west faults																						
88T02	0.2	1.5	0.2	<0.2	0.2	0.2	<0.5	n	n	100	1,000	2	n	n	<10	30	50	10	n	n	50	n
88T03	1	1	0.2	<0.2	0.2	0.15	n	n	n	50	700	2	n	n	<10	30	20	<5	n	n	70	n
88E12	0.07	5	0.05	n	n	0.02	n	n	n	10	500	<1	n	n	n	n	10	<5	n	n	70	n
88E13	0.05	1.5	0.1	<0.2	0.2	0.1	<0.5	n	n	50	500	<1	n	n	10	30	20	<5	n	n	200	<5
88T29	1	0.5	0.2	<0.2	0.2	0.03	n	n	n	30	500	<1	n	n	<10	n	10	n	n	n	300	n
88T80	0.2	2	0.07	2	0.2	0.15	n	n	n	30	700	1.5	n	n	n	n	5	30	n	100	70	10
89T40	20	1	7	n	n	0.02	n	n	n	10	5,000	<1	n	n	n	n	5	n	n	n	200	n

Table 4. Analyses of samples collected from faults in the Oxley Peak quadrangle and adjacent quadrangles, northeast Nevada—Continued.

[Analytical results are given in parts per million, except for Ca, Fe, Mg, Na, P, and Ti, which are given in percent. The column headings show the element analyzed, the method of determination, and the lower limit of determination (shown in parentheses in parts per million, except for Ca, Fe, Mg, Na, P, and Ti, which are in percent). Methods of determination are: s, emission spectrographic analyses; i-5 or i-10, 5- or 10-element inductively coupled plasma analyses, respectively; aag, graphite furnace atomic absorption analyses; aac, cold vapor atomic absorption; aaf, atomic absorption flame analysis. Other abbreviations are: n, not detected at the lower limit of determination; <, detected, but below the lower limit of determination; >, determined to be greater than the value shown]

Sample number	Nb s (20)	Ni s (5)	Pb s (10)	Sb s (100)	Sc s (5)	Sn s (10)	Sr s (100)	Th s (100)	V s (10)	W s (20)	Y s (10)	Zn s (200)	Zr s (10)	As s (5)	Bi s (2)	Cd s (0.1)	Sb s (2)	Zn s (2)	Hg s (0.02)	Au s (0.05)
North-south faults																				
88E07	n	5	15	n	< 5	n	n	n	30	n	15	n	100	20	< 2	< 0.1	2	7	0.18	n
88E08	n	10	10	n	5	n	< 100	n	70	n	15	n	100	44	< 2	0.2	4	30	n	n
88T34	n	5	30	n	< 5	n	n	n	30	n	10	n	100	25	< 2	< 0.1	< 2	14	n	n
88T35	< 20	< 5	< 10	n	< 5	n	n	n	30	n	15	n	100	28	< 2	< 0.1	< 2	11	0.32	n
Bedding-parallel faults																				
88T14	n	5	n	n	n	n	n	n	10	n	< 10	n	< 10	< 5	< 2	< 0.1	< 2	27	0.02	n
88T27a	n	10	n	n	n	n	n	n	70	n	< 10	n	10	< 5	< 2	0.1	< 2	5	0.04	n
88T27b	n	7	n	n	n	n	n	n	50	n	n	n	< 10	7	< 2	0.2	< 2	< 2	0.12	n
88T28	n	20	< 10	n	< 5	n	n	n	100	n	10	n	50	13	< 2	0.2	< 2	20	0.12	n
88T30	n	5	< 10	n	< 5	n	200	n	150	n	< 10	n	70	< 5	< 2	< 0.1	2	2	0.32	n
88T31	n	20	n	n	n	n	300	n	50	n	< 10	200	50	44	< 2	0.7	3	110	n	n
88T32	n	7	n	n	< 5	n	n	n	100	n	< 10	n	50	< 5	< 2	0.1	< 2	6	0.16	n
88T33	n	5	n	n	n	n	200	n	30	n	20	n	100	19	< 2	0.4	< 2	30	0.04	n
88T57	n	100	30	n	< 5	n	200	n	200	n	10	500	70	170	< 2	4.2	9	160	0.80	n
East-west faults																				
88T02	n	50	20	n	< 5	n	n	n	200	n	15	< 200	100	23	< 2	< 0.1	8	67	0.42	n
88T03	n	30	20	n	< 5	n	n	n	150	n	< 10	< 200	100	33	< 2	< 0.1	8	44	0.68	n
88E12	n	10	< 10	n	n	n	n	n	20	n	n	n	10	12	< 2	< 0.1	< 2	26	0.24	n
88E13	n	20	n	n	< 5	n	n	n	100	n	10	n	100	9	< 2	< 0.1	< 2	27	0.08	n
88T29	n	15	n	n	< 5	n	n	n	30	n	< 10	n	50	10	< 2	0.2	< 2	24	0.04	n
88T80	< 20	< 5	50	n	< 5	n	n	n	20	n	30	n	200	11	< 2	0.1	< 2	48	n	n

Sample number	Nb s (20)	Ni s (5)	Pb s (10)	Sb s (100)	Sc s (5)	Sn s (10)	Sr s (100)	Th s (100)	V s (10)	W s (20)	Y s (10)	Zn s (200)	Zr s (10)	As i-10 (0.6)	Bi i-10 (0.6)	Cd i-10 (0.03)	Sb i-10 (0.6)	Zn i-10 (0.03)	Ag i-10 (0.045)	Cu i-10 (0.03)	Mo i-10 (0.09)	Pb i-10 (0.06)	Hg aac (0.02)	Au aag (0.002)
89T40	n	< 5	n	n	n	n	n	n	10	n	n	n	< 10	40	n	0.067	7.6	4.8	n	3.2	3.0	4.5	0.16	< 0.004

Table 5. Analyses of samples collected for geochemical background from the Oxley Peak quadrangle and adjacent quadrangles, northeast Nevada.

[Analytical results are given in parts per million, except for Ca, Fe, Mg, Na, P, and Ti, which are given in percent. The column headings show the element analyzed, the method of determination, and the lower limit of determination (shown in parentheses in parts per million, except for Ca, Fe, Mg, Na, P, and Ti, which are in percent). Methods of determination are: s, emission spectrographic analyses; i-5 or i-10, 5- or 10-element inductively coupled plasma analyses, respectively; aag, graphite furnace atomic absorption analyses; aac, cold vapor atomic absorption; aaf, atomic absorption flame analysis. Other abbreviations are: n, not detected at the lower limit of determination; <, detected, but below the lower limit of determination; >, determined to be greater than the value shown]

Sample number	Ca	Fe	Mg	Na	P	Ti	Ag	As	Au	B	Ba	Be	Bi	Cd	Co	Cr	Cu	Ga	Ge	La	Mn	Mo
	s	s	s	s	s	s	s	s	s	s	s	s	s	s	s	s	s	s	s	s	s	s
	(0.05)	(0.05)	(0.02)	(0.2)	(0.2)	(0.002)	(0.5)	(200)	(10)	(10)	(20)	(1)	(10)	(20)	(10)	(10)	(5)	(5)	(10)	(50)	(10)	(5)
88T17	< 0.05	0.5	0.07	< 0.2	< 0.2	0.05	n	n	n	50	2,000	< 1	n	n	< 10	n	7	n	n	n	30	20
88T18	0.05	0.15	0.1	n	< 0.2	0.1	n	n	n	150	1,000	n	n	n	n	70	70	< 5	n	n	< 10	n
88T19	2	2	2	0.5	0.5	0.7	n	n	n	15	5,000	< 1	n	n	50	150	50	50	n	100	200	n
88T20	0.05	5	0.5	n	< 0.2	0.15	n	n	n	100	2,000	n	n	n	< 10	50	50	5	n	n	500	n
88T21	0.05	7	3	1	n	0.2	n	n	n	300	700	n	n	n	30	100	30	30	n	n	300	10
88T26a	< 0.05	3	0.5	n	< 0.2	0.15	n	n	n	200	500	n	n	n	10	50	50	10	n	n	300	n
88T26b	0.05	2	0.5	n	0.2	0.15	n	n	n	200	1,000	n	n	n	< 10	50	50	7	n	n	1,500	n

Sample number	Nb	Ni	Pb	Sb	Sc	Sn	Sr	Th	V	W	Y	Zn	Zr	As	Bi	Cd	Sb	Zn	Hg	Au
	s	s	s	s	s	s	s	s	s	s	s	s	s	s	s	s	s	s	s	s
	(20)	(5)	(10)	(100)	(5)	(10)	(100)	(100)	(10)	(20)	(10)	(200)	(10)	(5)	(2)	(0.1)	(2)	(2)	(0.02)	(0.05)
88T17	n	7	10	n	< 5	n	< 100	n	100	n	n	n	20	14	< 2	< 0.1	4	9	0.18	n
88T18	n	20	< 10	n	n	n	n	n	70	n	n	n	50	< 5	< 2	0.8	< 2	32	0.28	n
88T19	50	100	< 10	n	20	n	500	n	150	n	20	n	100	< 5	< 2	0.5	< 2	64	0.02	n
88T20	n	20	10	n	< 5	n	n	n	200	n	10	n	200	6	< 2	< 0.1	< 2	110	0.20	n
88T21	n	70	15	n	10	n	n	n	150	n	15	n	50	6	< 2	0.2	< 2	100	0.06	n
88T26a	n	50	15	n	< 5	n	n	n	200	n	< 10	n	70	5	< 2	0.3	< 2	77	0.34	n
88T26b	n	50	10	n	< 5	n	n	n	200	n	< 10	n	50	5	< 2	0.4	< 2	90	0.22	n

Table 6. Latitude and longitude of samples collected in 1988 from the Oxley Peak, northwestern Wells Peak, southwestern Melandco, and southeastern Summer Camp quadrangles, northeast Nevada.

[See figure 3A for approximate location of sites: °, degrees;', minutes;", seconds]

Map number	Latitude (N.) °	'	"	Longitude (W.) °	'	"
1	41	15	3.615	114	56	23.894
2	41	14	17.839	114	56	46.319
3	41	14	19.503	114	56	42.497
4	41	14	24.923	114	56	35.122
5	41	13	27.386	114	55	41.468
6	41	13	39.200	114	55	55.500
7	41	9	39.371	114	58	50.592
8	41	9	57.495	114	58	45.659
9	41	9	58.143	114	57	10.107
10	41	13	41.661	114	55	11.577
11	41	13	38.195	114	54	42.945
12	41	12	40.665	114	52	49.871
13	41	14	57.050	114	52	9.674
14	41	15	28.296	114	52	15.430
15	41	15	27.854	114	52	22.300
16	41	14	49.131	114	53	2.724
17	41	14	40.360	114	53	10.935
18	41	12	19.840	114	56	41.922
19	41	13	23.209	114	55	14.119
20	41	13	17.039	114	55	11.087
21	41	13	40.482	114	55	21.010
22	41	11	20.089	114	55	51.012
23	41	11	7.838	114	55	15.456
24	41	11	9.631	114	55	4.826
25	41	9	43.009	114	59	5.427
26	41	9	50.053	114	58	47.307
27	41	11	8.160	114	56	9.024
28	41	11	26.136	114	55	57.187
29	41	11	58.150	114	56	1.897
30	41	13	5.368	114	54	27.235

Formation are exposed to the north of the block but contain few zebra-banded beds;

3. The distribution patterns for most metals in faults, both high and low angle, are similar, except that gold was not detected in any fault zone except one at Cedar Peak where Simonson and Guilmette are juxtaposed;
4. The siliciclastic units juxtaposed against the Simonson Dolomite and Guilmette Formation do not appear to be altered;
5. The youngest mineralizing event took place after about 14 Ma, the age of a rhyolite flow cut by east-west-trending, high-angle faults at the east end of the Cedar Peak block;
6. Several mineralizing events, separated in both time and space, may have occurred. The north-south-trending faults along the foot of the range are highly silicified, probably as the result of hot-spring activity at the range-front fault (which is currently active). This might explain the higher values for molybdenum and silver obtained from samples along these faults.

Geochemical anomalies have been noted from Middle and Upper Devonian rocks in the northern Pequop Mountains (approximately 20 miles east of Wells, Nevada) and in the Kings Canyon area, in the southern Confusion Range in western Utah. Zebra-banded dolomite in the Guilmette Formation, exposed along Interstate Highway 80 just west of Pequop Pass, contains anomalous concentrations of gold, mercury, lead, zinc, and barium (Erickson and others, 1966). These beds appear to be at or slightly above the stratigraphic position of the gold-bearing Guilmette beds at Cedar Peak. In the Kings Canyon area, samples from the Simonson and Guilmette contain anomalous concentrations of gold, silver, mercury, arsenic, antimony, fluorine, barium, copper, lead, and zinc (Zimbleman and others, 1990). These samples included jasperoid and breccia; bedrock samples for background concentrations were also collected.

Zebra-banded dolomites are not uncommon in Middle and Upper Devonian units in the eastern Great Basin according to F.G. Poole (oral commun., 1991). The importance of zebra-banded dolomite in minerals exploration is not clear, but the occurrences of anomalous concentrations of metal in them records the movement of metal-bearing fluids. A closer look at these types of rocks is needed to understand the origin of the zebra-banded structure, their contained metals, and the timing of fluid movement.

REFERENCES CITED

Erickson, R.L., Marranzino, A.P., Oda, Uteana, and Janes, W.W., 1966, Geochemical reconnaissance in the Pequop Mountains and Wood Hills, Elko County, Nevada: U.S. Geological Survey Bulletin 1198–E, 20 p.

Horton, H.A., Jr., and De Voto, R.H., 1990, Dolomitization and diagenesis of the Leadville Limestone (Mississippian), central Colorado, *in* Beaty, D.W., Landis, G.P., and Thompson, T.B., eds., 1990, Carbonate-Hosted Sulfide Deposits of the Central Colorado Mineral Belt: Economic Geology Monograph 7, p. 86–107.

Landis, G.P., and Tschauder, R.J., 1990, Late Mississippian karst caves and Ba-Ag-Pb-Zn mineralization in central Colorado—Part II. Fluid inclusion, stable isotope, and rock geochemistry data and model of ore deposition, *in* Beaty, D.W., Landis, G.P., and Thompson, T.B., eds., 1990, Carbonate-Hosted Sulfide Deposits of the Central Colorado Mineral Belt: Economic Geology Monograph 7, p. 339–366.

Smith, J.F., Jr., Ketner, K., Hernandez, G.X., Harris, A.G., Stamm, R.G., and Smith, M.C., 1990, Geologic map of the Summer Camp quadrangle and part of the Black Butte quadrangle, Elko County, Nevada: U.S. Geological Survey Miscellaneous Investigations Series Map I–2097, scale 1:24,000.

Thorman, C.H., and Brooks, W.E., 1988, Preliminary geologic map of the Oxley Peak quadrangle, Elko County, Nevada: U.S. Geological Survey Open-File Report 88–755, scale 1:24,000.

Thorman, C.H., and Ketner, K.B., 1979, West-northwest strike-slip faults and other structures in allochthonous rocks in central and eastern Nevada and western Utah, *in* Newman, G.W., and Goode, H.D., eds., 1979 Basin and Range Symposium: Rocky Mountain Association of Geologists, p. 621–636.

Thorman, C.H., Ketner, K.B., Brooks, W.E., Snee, L.W., and Zimmermann, R.A., 1991, Late Mesozoic–Cenozoic tectonics in northeastern Nevada, *in* Raines, G.L., Lisle, R.E., Schafer, R.W., and Wilkinson, W.H., eds., Geology and Ore Deposits of the Great Basin, Symposium Proceedings: Geological Society of Nevada, v. I, p. 25–45.

Vandervoort, D.S., and Schmitt, J.G., 1990, Cretaceous to early Tertiary paleogeography in the hinterland of the Sevier thrust best, east-central Nevada: Geology, v. 18, p. 567–570.

Zimbleman, D.R., Nutt, C.J., Hageman, Phil, Hill, R.H., Fey, D.L., Arbogast, B.F., and Bullock, J.H., Jr., 1990, Selected analytical results, sample locality map, and discussion of trace-element anomalies for rock samples near Kings Canyon, Confusion Range, Millard County, Nevada: U.S. Geological Survey Open-File Report 90–317, 16 p.

APPENDIX TO CHAPTER Y

DESCRIPTION OF MAP UNITS SHOWN ON FIGURE 2

EASTERN-FACIES UNITS

Trd Dinwoody(?) Formation (Triassic)—Shale and limestone. Interbedded greenish, gray, and "chocolate brown" thin-bedded to fissile shale with subordinate brownish, thin-bedded to platy, fine-grained limestone to shaley limestone.

Pm Murdock Mountain Formation (Permian)—Limestone, chert, and siltstone. Gray, medium- to thick-bedded, medium- to coarse-grained bioclastic limestone to dolomitic limestone; brachiopod valves and spines are common.

Mm Sandstone of Melandco (Lower Mississippian)—Sandstone, conglomerate, and shale. Brown to reddish-brown, medium- to thick-bedded, medium- to coarse-grained to gritty chert-quartz sandstone.

Mtp Tripon Pass Limestone (Lower Mississippian)—Gray, medium- to thin-bedded, fine- to medium-grained limestone with graded bedding. Locally becomes sandy, the grains being quartz and chert.

Dg Guilmette Formation (Upper Devonian)—Gray, medium- to thick-bedded, medium-grained limestone. Contains medium- to thin-bedded dolomite as interbeds in lower 3 to 6 m. Basal part of unit consists of thin-bedded, argillaceous, *Atrypa*-bearing limestone that forms a smooth slope. Formation is approximately 300 m thick.

Dsi Simonson Dolomite (Middle Devonian)—Gray, medium- to thick-bedded, fine- to medium-grained, laminated dolomite with minor interbeds of limestone. Base is not exposed. Thickness probably exceeds 450 m.

WESTERN-FACIES UNITS

Ma Argillite, shale, and chert (Mississippian)—Black siliceous argillite with chert-quartz arenite beds. Black shale and siltstone with scarce, bedded, black chert and bedded barite. Fine-grained sandy beds. Upper and lower contacts are low-angle faults. Thickness probably exceeds several hundred feet.

Dsh Shale, limestone, and chert (Devonian)—Dominant lithology is black to dark brownish gray, fissile to thin-bedded, locally weakly phyllitic shale. Contains interbedded, medium-gray, thin- to medium-bedded, medium-grained, in part bioclastic, limestone; locally beds contain well-rounded, frosted, medium-grained quartz. Black, thin-bedded chert is present locally as thin interbeds. Thickness of unit exceeds 250 m. Upper and lower contacts are low-angle faults. Contains four early Late Devonian conodont assemblages (B. Wardlaw, written commun., 1988). Equivalent to unit Dt of Smith and others (1990) in the Summer Camp quadrangle, where it ranges from Early to Late Devonian in age.

Dw Shale, limestone, and chert, undivided (Devonian)—Contains lithologies found in both units Dsh and Dsl.

Dsl Shale, limestone, and chert (Upper Devonian)—Contains more or less equal amounts of fissile, black shale; yellowish thin-bedded to platy, argillaceous, siliceous, fine-grained limestone; and black, thin-bedded, platy chert. Contains sparse bedded barite. Thickness is unknown, but probably exceeds 150 m. The lower and upper contacts are low-angle faults. Two conodont assemblages are middle Middle Devonian and Devonian to Early Mississippian in age (B. Wardlaw, written commun., 1988). Equivalent to unit DSOw of Smith and others (1983), which they determined to range in age from Ordovician to Devonian.

Sw Siltstone, chert, and argillite (Silurian)—Graptolite-bearing, yellow-weathering, greenish-gray, micaceous siltstone, chert, and argillite underlain by black, white, red, and green chert.

Ow Shale and chert (Middle to Upper Ordovician)—Black bedded chert containing sparse graptolites, underlain conformably by thick, graptolite-rich, black shale.

DSOw Shale, siltstone, chert, limestone, and argillite, undivided (Devonian, Silurian, and Ordovician)—Undifferentiated western-facies rocks, including units mapped separately as Dsl, Dw, Sw, and Ow. Thickness probably exceeds 200 m.

CHAPTER Z

OCCURRENCES OF NATIVE GOLD CONTAINING SILVER, MERCURY, COPPER, AND PALLADIUM IN LEMHI COUNTY, EAST-CENTRAL IDAHO

By GEORGE A. DESBOROUGH,[1] WILLIAM H. RAYMOND,[2] *and* JAMES NISHI[3]

ABSTRACT

Native gold grains collected from streams in Lemhi County, Idaho, range in chemical composition from pure gold to varieties containing up to 36.3 weight percent mercury, 30 weight percent silver, 4 weight percent copper, and 2 weight percent palladium—all of which are in solid solution with gold. Very fine grained (< 150 μm) native gold grains were recovered from stream-sediment samples and studied by scanning-electron-microscope (SEM) methods to determine their size, morphology, and chemical composition. Analyses of individual native gold grains show significant variations in chemical composition among grains in a single stream-sediment sample and also show distinct variations in compositions between samples from different localities. The chemical compositions of some of these grains are unique with regard to palladium or copper content when compared with published data for samples from other localities in the United States.

The chemical diversity in the compositions of the grains, locally and regionally, is significantly greater than compositional variations reported for native gold for most other regions of North America.

Most of the samples studied are from streams that drain areas of Middle Proterozoic strata; most samples from drainages underlain chiefly by Paleozoic sedimentary or Cenozoic volcanic rocks do not contain native gold grains. However, gold was found in samples from streams near large faults that juxtapose Cenozoic volcanics and Middle Proterozoic rocks.

The geochemical signatures of native gold reported here are sufficiently unique to warrant further studies with a higher density of samples in areas of the Lemhi Range that are currently being geologically mapped. This should allow delineation of potential lode sources. Additionally, regional studies east of the study area should aid in delineating the region that contains copper- and palladium-bearing gold. Because of the association, known from the literature, of copper- and palladium-bearing gold with mafic rocks, such sources in or beneath the Middle Proterozoic rocks should be considered.

INTRODUCTION AND METHODS OF STUDY

Most of the study area is composed of siltite and fine-grained feldspathic quartzite of Middle Proterozoic age that may be as thick as 19,000 m (J. Connor, written commun., 1991); metamorphism of these strata is in the greenschist facies. Proterozoic-age granite occurs in the Leesburg area (fig. 1). Minor amounts of Ordovician syenite are present in the northwestern part of the study area, and small localized areas of lower Paleozoic strata are present in the central and southern parts. Remnants of Cenozoic extrusive and lacustrine rocks are present in many areas, mainly in valleys and on mountain flanks, but are a small proportion of the exposed rocks.

The morphology, size, and chemical composition of native gold grains collected from streams in Lemhi County, Idaho, have been analyzed using scanning-

[1]U.S. Geological Survey, Mail Stop 905, P.O. Box 25046, Denver Federal Center, Denver, CO 80225.

[2]U.S. Geological Survey, Mail Stop 921, P.O. Box 25046, Denver Federal Center, Denver, CO 80225.

[3]U.S. Geological Survey, Mail Stop 917, P.O. Box 25046, Denver Federal Center, Denver, CO 80225.

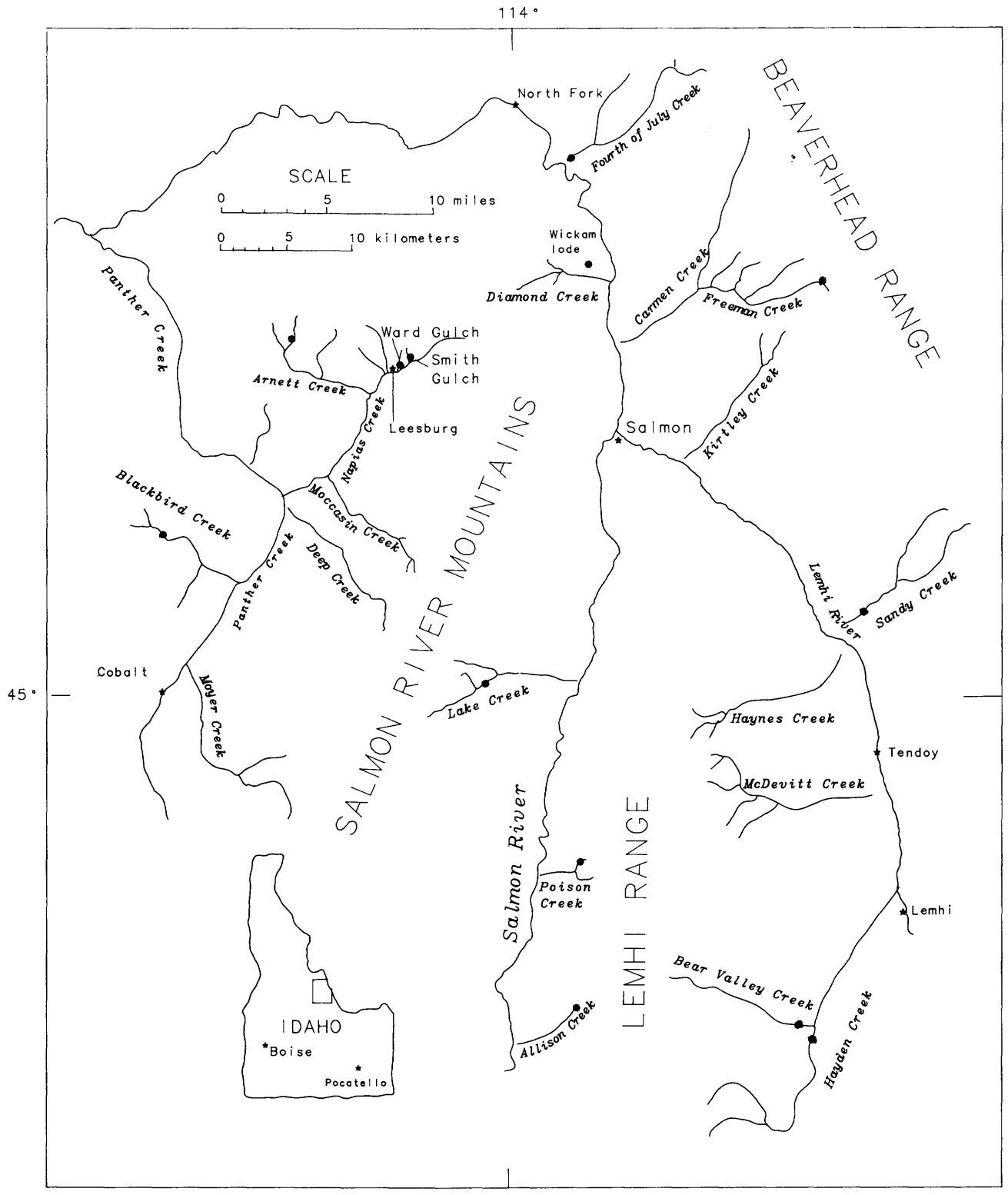

Figure 1. Drainages and sample localities (solid circles) in Lemhi County, Idaho.

electron-microscope (SEM) techniques coupled with simultaneous semiquantitative energy dispersive analysis. The results of these analyses are used to interpret the origin of the gold grains and included or attached minerals and to establish local and regional variations in the geochemistry of native gold.

Previous studies of gold in stream sediments from Lemhi County indicated that native gold grains are

abundant in areas that have little or no history of mining or prospecting (Desborough and others, 1990). These areas had been previously considered to be unfavorable for the occurrence of gold deposits. Native gold was concentrated in the laboratory from bulk stream-sediment samples.

The gold grains were examined with a binocular microscope (40× or 80×), and the sizes and masses of gold grains were estimated. Based on this examination, the number of gold grains per kilogram of bulk stream-sediment sample was reported, and estimated gold concentrations in parts per million (ppm) were reported.

For the present study, bulk samples collected in the field ranged from about 1 to 5 kg; the number of gold grains in these ranged from about 10 to 50 gold grains per kg. A large sample was selected in order to collect a minimum of about 20 gold grains for each locality. However, this was not achieved for several samples. Locations of samples studied and major drainages in the area are shown on figure 1.

Native gold grains in stream sediments were concentrated and isolated by laboratory mechanical-panning techniques (English and others, 1987). The size of the native gold grains range from about 20 to 800 μm; most grains were in the size range of 20 to 100 μm. Individual gold grains were hand picked with a single bristle on an artist's paint brush and mounted on sticky tape attached to SEM mounts that were then coated with carbon. Because of their small size and the difficulty of handling of each grain, about 10 to 20 percent of the grains were lost in transfer from the pan to the SEM mount.

Prior to chemical analysis (for Au, Ag, Cu, Pd, and Hg), the morphology of the native gold grains was examined. Most of the gold grains were relatively smooth; some were slightly porous and had amorphous or irregular shapes. Subhedral grains were sparse or rare, and euhedral shapes were virtually absent.

For this SEM study, detection limits of palladium and silver are about 0.1 weight percent. The detection limits for copper and mercury are estimated to be about 0.2 and about 1.0 weight percent, respectively. The high detection limit for mercury is due to interference by gold. These detection limits are about 100 times higher than those from the semiquantitative emission spectroscopy method and about 10 times higher than those from the electron microprobe, which requires a flat, polished surface.

RESULTS

A summary of the compositional data for grains from each locality studied is given in table 1.

Allison Creek.—Seven native gold grains from this locality range from about 40 to 80 μm in their largest dimensions. Pure gold, silver-bearing, mercury-bearing, and palladium-bearing grains were found. Copper-bearing grains were not found. The highest amount of palladium (2 weight percent) was found at this locality. The geochemical signature for this locality is similar to that of Poison Creek; both of these localities are along or near a large north-south-trending fault that juxtaposes Middle Proterozoic and Cenozoic rocks.

Arnett Creek.—This locality is upstream from the Haidee lode gold mine and is in the headwaters of Arnett Creek. Only 12 native gold grains, ranging up to 200 μm in average diameter, were analyzed. Grains from this locality contain all five elements for which samples were analyzed (table 1) and also contain the highest proportion of copper-bearing grains. The geochemical signature is similar to those from the four other sample localities in group 3 (figs. 1 and 2). Only traces of pyrite are present in the concentrate.

Bear Valley Creek.—This locality, near the mouth of the creek, has the largest native gold grain (800 μm in diameter) recovered and also has grains of the highest average purity. Two SEM mounts were made. Of 20 grains analyzed, 7 are pure gold. A SEM photo of 14 grains is shown on figure 3*A*. Palladium, copper and mercury were not detected. One gold grain has a pyrite inclusion; another has both quartz and a potassium-, iron-, magnesium-, aluminum-silicate inclusion with micaceous morphology that is presumed to be biotite. Both pyrite and chalcopyrite are present in the heavy-mineral concentrate. The geochemical signature is simple, but it is unlike the other samples studied (fig. 2).

Blackbird Creek.—This sample was collected less than 1 km downstream from the Blackbird cobalt mine. The largest of 23 grains studied is about 200 μm in diameter. Neither mercury nor copper was detected, and thus, this sample is similar to those from Allison Creek and Poison Creek (fig. 2).

Fourth of July Creek.——Seventeen grains ranging up to 250 μm in diameter were analyzed from the mouth of the creek. A SEM photo of these grains is shown on figure 3*B*. Palladium and copper are present, but mercury is not; this sample has the highest mean silver content of all samples (table 1). It is also from the mouth of a very large drainage basin (about 50 km^2), as is the Sandy Creek sample, which has a similar geochemical signature (fig. 2).

Freeman Creek.—Twenty-six grains from near the head of Freeman Creek were analyzed. Two SEM mounts, one of 21 grains and one of 19 grains were made. A SEM photo of the 19-grain mount is shown on figure 3*C*. In addition to gold, the concentrate contains abundant pyrite and minor galena and chalcopyrite. The locality is downstream from the Ore Cash gold mine, which ceased operations around 1900. A single grain was pure gold. The largest grain is about 200 μm in the largest dimension, but most grains are smaller than 100 μm (fig. 3*C*). The high proportion of mercury-bearing grains is thought

Table 1. Number of grains and percentage of native gold grains containing only gold, silver, palladium, copper, or mercury for localities in Lemhi County, Idaho.

[Number in parentheses is the percentage of grains containing that metal. Number in brackets is the range or amount of metal concentration(s). Number in bold print is mean silver content of silver-bearing grains]

Locality (no. of grains)	100% Au	Silver-bearing grains	Palladium-bearing grains	Copper-bearing grains	Mercury-bearing grains
Allison Creek (7)	1 (14)	6 (86) [0.8-15.1] **10.4**	1 (14) [2.0]	0	1 (14) [5.7]
Arnett Creek (12)	2 (17)	8 (66) [0.5-16.4] **5.1**	1 (8) 1.7	5 (42) [0.5-0.9]	2 (16) [5.4-14.2]
Bear Valley Creek (20)	7 (35)	13 (65) [0.2-1.8] **0.6**	0	0	0
Blackbird Bear Valley	8 (35)	13 (56) [0.3-30.0] **4.25**	5 (22) [0.5-0.9}	0	0
Fourth of July Creek (17)	1 (6)	16 (94) [0.5-29.2] **12.1**	3 (18) [0.4-0.6]	6 (35) [0.4-1.3]	0
Freeman Creek (26)	1 (4)	25 (96) [0.2-10.3] **5.5**	7 (27) [0.4-1.0]	1 (4) [4.0]	19 (83) [4.7-25.9]
Lake Creek (29)	0	29 (100) [1.2-7.4] **4.8**	6 (21) [0.4-0.9]	10 (34) [0.4-1.3]	4 (14) [4.8-16.4]
Poison Creek (44)	14 (32)	23 (52) [0.2-18.2] **3.8**	12 (27) [0.5-1.6]	0 [3.0-23.2]	4 (9)
Sandy Creek (20)	1 (5)	15 (75) [0.3-17.4] **6.4**	6 (30) [0.3-0.6]	7 (35) [0.5-1.0]	0
Smith Gulch (13)	0	12 (92) [2.4-13.0] **7.6**	3 (23) [0.6-0.9]	8 (62) [0.4-1.2]	0
Sourdough Gulch (21)	0	19 (90) [0.3-11.8] **5.2**	3 (14) [0.4-0.7]	2 (10) [0.5-0.6]	21 (100) [8.6-36.3]
Ward Gulch (26)	5 (19)	20 (77) [0.2-14.6] **7.0**	4 (15) [0.5-1.0]	7 (27) [0.5-1.8]	1 (4) [13.5]
Wickam lode (21)	3 (14)	11 (52) [0.3-3.0] **0.9**	3 (14) [0.7-0.9]	13 (62) [0.4-1.3]	0

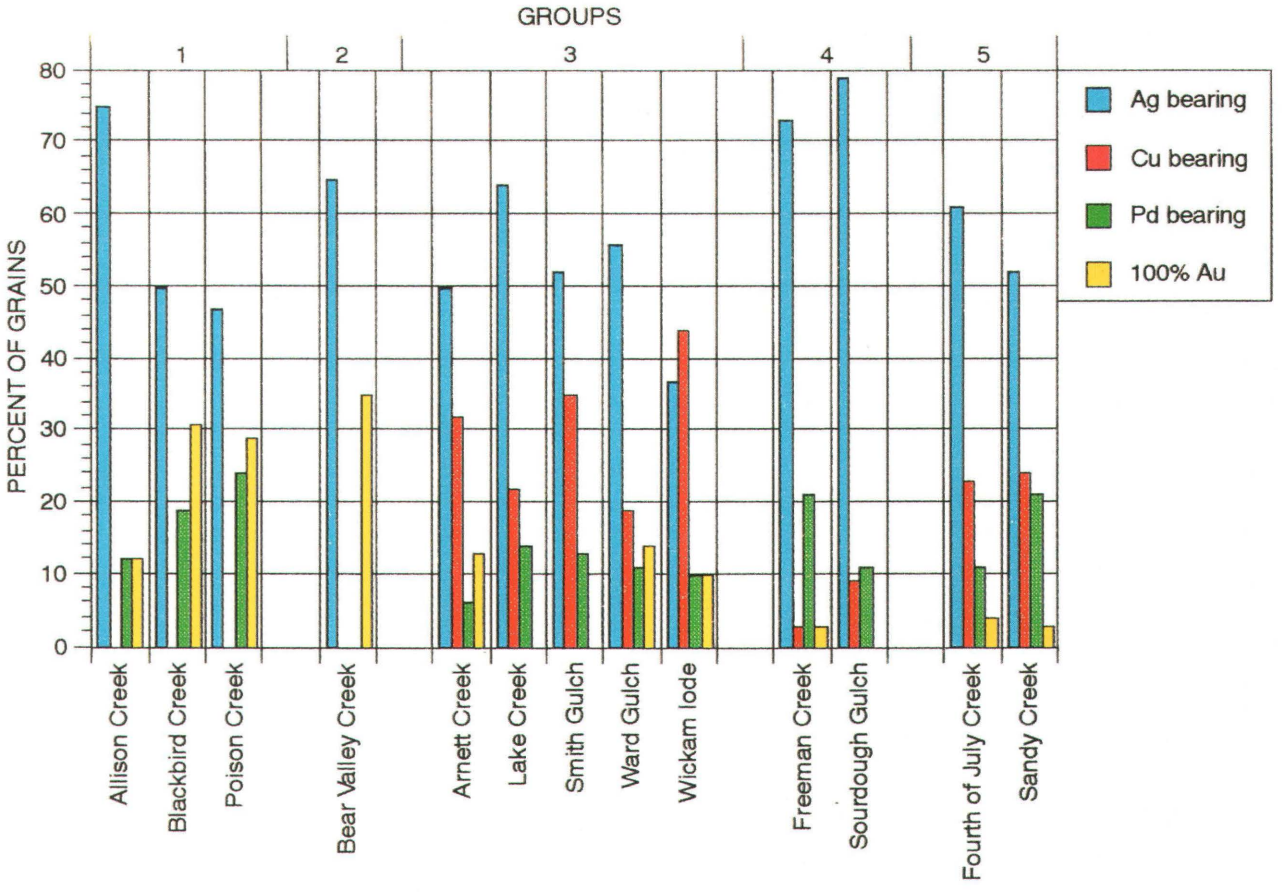

Figure 2. Percentages of gold grains that are silver bearing, copper bearing, palladium bearing, and pure gold for each locality studied. Five geochemical groups are tentatively recognized. Percentages were obtained by dividing the number of grains in each category by the total number of grains at each locality. These four parameters were normalized to 100 percent.

to be an artifact, and thus, the geochemical signature is placed with that of the Sourdough Gulch sample (fig. 2).

Hayden Creek.—A sample from above the Bear Valley Creek confluence contained two grains of gold-copper minerals. One grain has Au=70.5, Cu=22.0, Ag=5.0, and Zn=2.6 (all weight percent), corresponding to $Au_{0.425}Cu_{0.438}Ag_{0.058}Zn_{0.051}$, which is the mineral tetraauricupride (AuCu). The second grain has Au=58.6, Cu=37.8, and Ag=3.6 (all weight percent), corresponding to $Cu_3AuAg_{0.125}$, which is essentially the composition of th e mineral auricupride (Cu_3Au). Both grains are 40 to 50 µm in their largest dimension. No native gold was recovered from this sample site.

Lake Creek.—This sample was taken about 1.5 km upstream from Williams Lake. Twenty-nine grains were studied (fig. 3*D*). Pyrite is present in the concentrate. In addition to the grains shown on figure 3*D*, three coin-shaped grains of gold (mounted separately) appear to be of bacterial-replacement origin based on the ornate morphology observed at high magnification in SEM studies (J.R. Watterson, oral commun., 1991; Brooks and Watterson, in press). These three grains range from about 100 to 300 µm in diameter. A SEM photomicrograph of one of these grains (fig. 4) shows a gold-replaced bacterial colony at low and high magnifications. Only silver and gold were detected, and the silver content is 3.6 weight percent.

Poison Creek.—These gold grains range in size from about 20 to 250 µm; only five are 100 µm or larger (fig. 3*E*). Forty-three grains were analyzed (table 1). One grain is a complex intergrowth of gold and pyrite and an unidentified mercury mineral that could not be analyzed; another grain (not analyzed) is a finely intergrown mixture of biotite and gold. Pyrite is present in the concentrate as grains that are mostly smaller than 100 µm. A very small spherical grain ("a" on figure 3*E*) is an artifact (discussed later).

Sandy Creek.—Twenty grains analyzed from this locality range up to about 200 µm in maximum diameter (table 1). Mercury was not detected. Minor pyrite is present in the concentrate. This sample is from a large drainage area (about 30 km^2), and thus, the gold may be from many sources (fig. 1).

Smith Gulch.—This locality lies on the south side of the Beartrack gold deposit of Meridian Gold, Inc., near

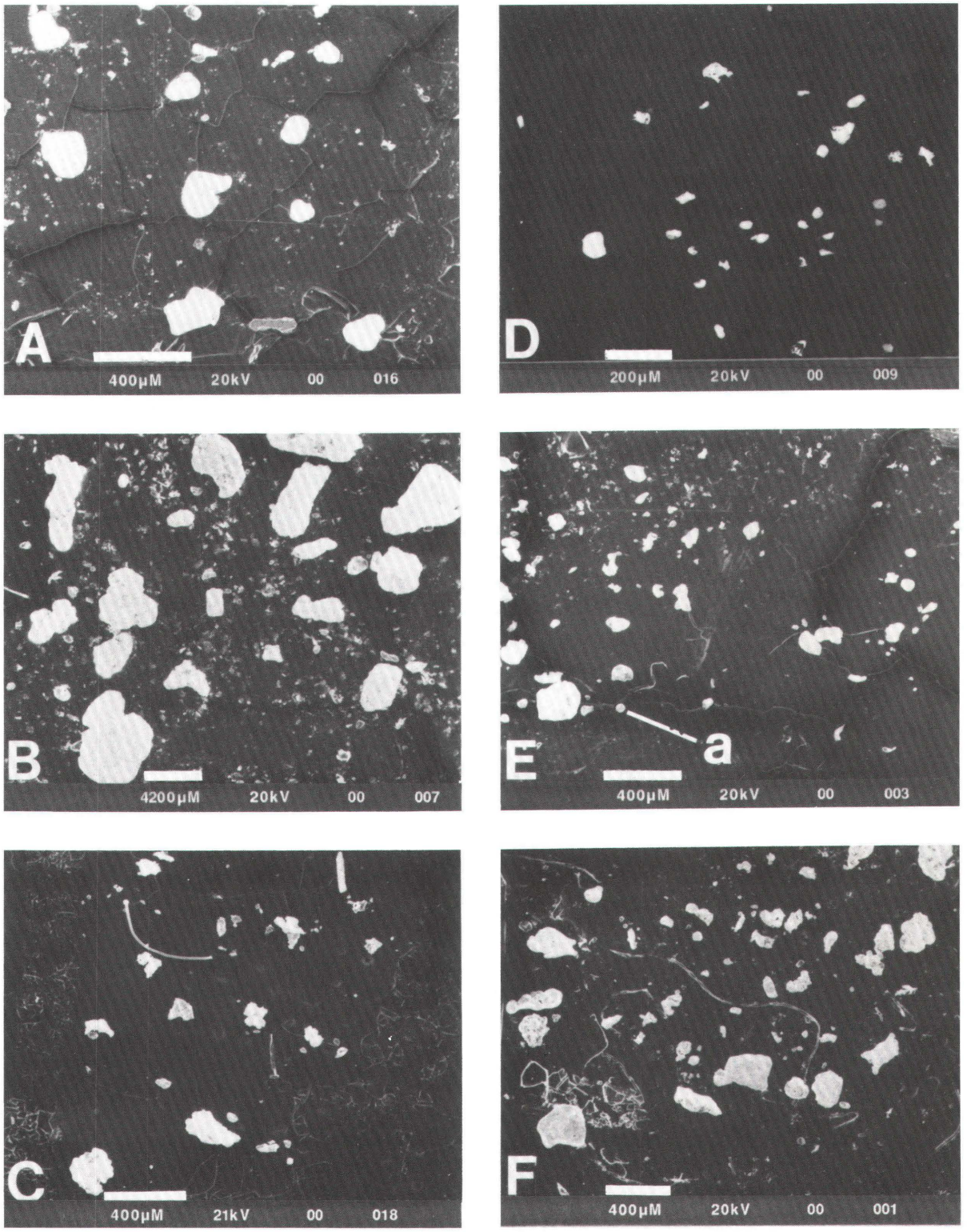

Figure 3. Scanning electron microscope photographs of native gold grains from six localities in Lemhi County, Idaho. Bar scales on each photo are in micrometers. Whitest grains are gold; gray grains present in some photos are other heavy minerals. Samples are from: *A*, Bear Valley Creek (14 gold grains); *B*, Fourth of July Creek (17 gold grains); *C*, Freeman Creek (19 gold grains); *D*, Lake Creek (29 gold grains); *E*, Poison Creek (44 gold grains); "a" is spherical artifact with 13 weight percent Cu and 5 weight percent Hg; *F*, Ward Gulch (43 gold grains).

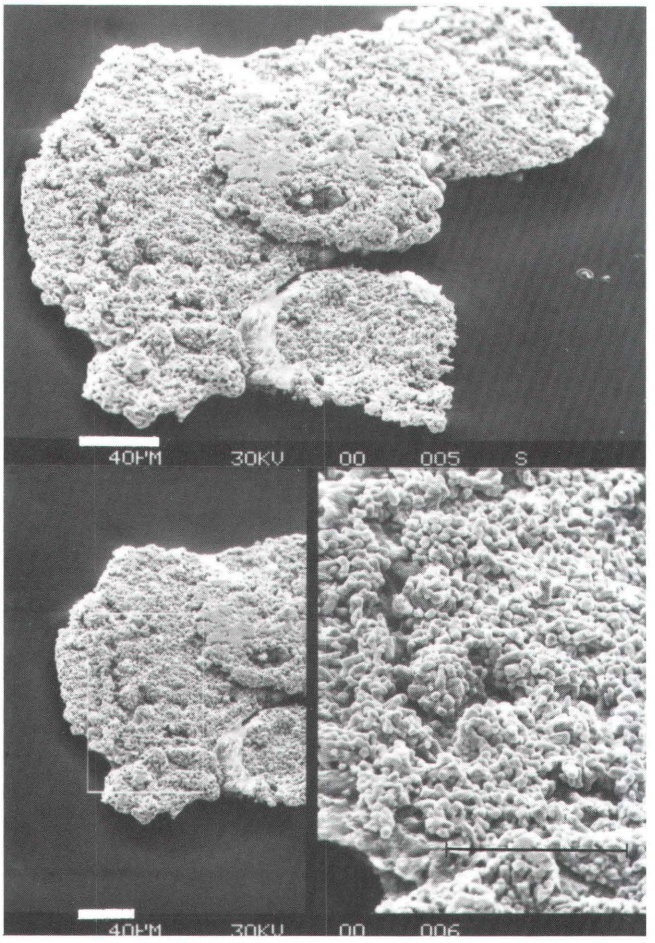

Figure 4. Scanning electron microscope photographs of a gold-replaced bacterial colony from Lake Creek. Bar scales in µm; black line in lower right photograph represents 40 µm. Photograph courtesy of John R. Watterson.

Leesburg (fig. 1). Only 13 grains were analyzed (table 1). The largest gold grain is about 200 µm in the largest dimension. Mercury was not detected, but copper and palladium are present, and thus, the geochemical signature is grouped with four other localities with similar compositions (fig. 2). Trace amounts of pyrite are present.

Sourdough Gulch.—This locality is about 3.5 km north of the abandoned mining camp of Gilmore. It is just southeast of the area shown on figure 1. The drainage basin is about 3 km long and contains Paleozoic sedimentary and Tertiary intrusive rocks (Ruppel and Lopez, 1988). Galena, pyrite, and thorite are abundant in the concentrate. Fine-grained gold (as much as 150 µm in diameter) is very abundant, amounting to about 50 gold grains per kg (0.05–0.1 ppm). Mercury is present on all grains analyzed (table 1) but is suspected to be an artifact because adits with wastepiles are present upstream from the sample site.

Ward Gulch.—This locality is near Smith Gulch, and this short drainage is on the south side of the Beartrack gold deposit. A SEM photograph of 43 gold grains from this locality is shown on figure 3*F*, and analytical results are given in table 1. The geochemical signature of the sample is similar to that of Smith Gulch, which is the adjacent drainage, 0.5 km to the east (figs. 1 and 2). Minor pyrite is present in the concentrate.

Wickam lode.—This sample is from gossan in an adit about 1 km north of Diamond Creek; the host rock is Proterozoic strata. It contains abundant native gold that was associated with sulfide prior to oxidation. Twenty-one grains, all smaller than 100 µm, were analyzed (table 1). This sample contains the highest proportion of copper-bearing grains, and mercury is absent (table 1). The geochemical signature is similar to four other localities that are west of the Salmon River (figs. 1 and 2).

GEOCHEMICAL SIGNATURES OF NATIVE GOLD—PRIOR STUDIES

The most extensive recent study of the geochemistry of native gold was done on Alaskan lode and placer deposits by emission spectroscopy. One hundred and ninety-one analyses for 28 lode occurrences and 2,438 analyses for 295 placer localities have been reported by several investigators (table 2). Maximum amounts of palladium, copper, and mercury are shown for lode deposits, and maximum amounts of palladium and copper for placer deposits are listed in table 2.

Desborough (1970), using electron microprobe methods, performed 3,000 quantitative analyses on about 300 individual gold grains from 24 placer localities in 6 Western States and Alaska; maximum copper concentrations (0.1–2.0 weight percent) were found in 18 grains from 3 localities. Desborough and others (1970), in a study of placer gold in the northeastern part of the Colorado Mineral Belt, analyzed 991 grains from 17 localities and found detectable copper (0.1–0.25 weight percent) in 44 grains. Of these 44 grains with detectable copper, 37 were from 4 large drainages near Boulder, Colorado. All of the copper-bearing grains analyzed in these studies contained 1 or more weight percent of silver. Desborough and others (1971), using the same method, analyzed 788 grains from 5 placer localities and 1 lode deposit in 5 Western States. The results show that 138 grains from Ninemile Creek, Montana, contained between 0.1 and 0.6 weight percent copper.

Thus, of 47 studied localities in the Western U.S. and Alaska, only 12 have native gold with more than 0.1 weight percent copper. In summary, prior geochemical studies of native gold in the Western United States and Alaska show that only 5 of 370 localities contain more than 1 weight percent copper in native gold; only 3 of 370 localities contain 2–10.2 weight percent copper in native gold.

Table 2. Summary of reported emission-spectrographic analytical data for copper, palladium, and mercury in native gold for Alaskan lode deposits and summary of copper and palladium in native gold for Alaskan placer deposits.

[Maximum palladium, copper, and mercury concentrations are shown in weight percent; conc., concentration. Mercury values reported for Alaskan placer gold are not given here because of possible introduction of mercury during commercial gold-recovery efforts. Detection limits are: Cu=0.0001 weight percent, Hg=0.002 weight percent, Pd=0.0005 weight percent (Mosier, 1975)]

Location	No. of analyses	No. of localities	Maximum palladium conc.	Maximum copper conc.	Maximum mercury conc.
Lode gold					
Fairbanks mining district plus others[1]	191	28	0.002	0.24	6.2
Placer gold					
Circle quadrangle[2]	476	51	0.002	0.85	
Livengood quadrangle[3]	247	21	0.002	0.2	
Various locations[4]	160	33	<0.0005	0.2	
Fairbanks mining district[5]	199	37	<0.0005	0.1	
Bonnifield mining district[6]	196	27	0.08	2.1	
Tolovana and Rampart mining districts[7]	48	5	0.04	0.3	
Fortymile mining district[8]	248	30	0.01	0.09	
Four districts in Tanana and Livengood quadrangles[9]	404	45	0.01	10.2*	
Koyukuk-Chandalar mining districts[10]	460	46	0.002	1.2	

* 11 grains; 1–10.2%.

1 Cathrall and others (1989a, 1988a, 1990, 1987).
2 Cathrall and others (1988b).
3 Cathrall and others (1988a).
4 Cathrall and others (1990).
5 Cathrall and others (1989b).
6 Cathrall and others (1989c).
7 Cathrall and others (1987).
8 Cathrall and others (1989a).
9 McDanal and others (1988).
10 Mosier and Lewis (1986); Mosier and others (1989).

An electron microprobe study of native gold and gold-rich alloys in the gold-bearing horizon of the Skaergaard intrusion, East Greenland (Bird and others, 1991, table 1, p. 1090), reports copper values of 1.5 and 11 weight percent, respectively, in 2 native gold grains (analyses 1 and 2); 3 other grains (analyses 3, 4, and 5) are the mineral tetraauricupride, which contains 23.2–25.5 weight percent copper, although the authors refer to all 5 analyses as representing "gold-rich alloys." In addition, the two copper-bearing native gold grains contain 0.8 and 5.8 weight percent palladium; the three tetraauricupride grains contain 0.15, 3.0, and 5.5 weight percent palladium and from 0.25 to 1.6 weight percent platinum (Bird and others, 1991, table 1).

Electron microprobe studies of precious-metal minerals in the Jijal layered ultramafic-mafic complex, Pakastani Himalayas (Miller and others, 1991, table 2, p. 1100), have revealed three gold- and copper-bearing minerals. Two grains contain 24 and 22.7 weight percent copper, respectively, and were identified as tetraauricupride. Another grain contains 5.3 weight percent copper and is a gold-silver alloy referred to as "electrum." The two tetraauricupride grains contain 6.1 and 6.3 weight percent palladium. The copper-bearing electrum grain contains 0.6 weight percent palladium.

CONTAMINATION, ARTIFACT, AND BACTERIAL GOLD

DiLabio and others (1988) conducted an interesting study of "the spherical form of gold," which investigated many aspects of the chemical signature of both natural and artifactual (e.g., jewelry-scrap gold) gold alloys. Laboratory

and sample contamination was shown to be significant in some cases. In our Poison Creek sample, 1 of 44 "native gold" grains analyzed was spherical and about 20 μm in diameter; it contained 13 weight percent copper, 5 weight percent mercury, and the balance is mostly gold and minor amounts of silver (grain "a," fig. 3*E*). This grain has a microcrystalline structure (incipient crystal growth or quenched crystal growth) on the surface like that shown by DiLabio and others (1988, fig. 1*E*), which is typical of quenched-liquid metals. We consider this grain to be a contaminant (artifact) and do not report the results as representing native gold. This aspect is discussed to illustrate our awareness of possible metal contamination problems.

Mercury-bearing gold grains present significant problems to interpretation because of the potential that mercury is an artifact. For some localities that have a history of mining and prospecting (e.g., Freeman Creek and Sourdough Gulch), abundant mercurian gold was expected (table 1); 77 percent of the mercury-bearing grains are from these 2 localities. However, localities at Allison Creek, Lake Creek, and Poison Creek have no evidence or history of mining or prospecting, yet mercury is present in native gold at these localities. We expect that some mercurian gold grains from the study area is of natural occurrence, but we cannot prove it. Mercury is present in 13 percent, or 40 of the 308 grains analyzed. Naturally occurring mercurian gold is known from many lode deposits and is reported in table 2 for Alaskan lode gold.

Brooks and Watterson (in press) and Watterson (1992) have only recently demonstrated that gold may be precipitated in, on, or by bacteria and (or) bacterial colonies and that native gold preserves the original morphologies of the organisms. The gold pseudomorphs after bacteria apparently form in near-surface environments such as streams, soils, or deeply weathered bedrock. This gold is of high purity and apparently contains less than about 5 weight percent silver. Gold concentrated by bacteria in this form has not yet been shown to be of economic significance. However, gold of bacterial-replacement origin is easily recognized by the delicate and microscopically ornate morphology identifiable in SEM studies (Brooks and Watterson, in press; Watterson, 1992). Only three disc-shaped native gold grains that we found in Lemhi County may have a bacteria-replacement origin (fig. 4). These are from a locality in Lake Creek (fig. 1) in which fine-grained native gold is very abundant (> 20 gold grains per kg).

PERSPECTIVE AND DISCUSSION

Our purpose is to try to understand the possible geochemical significance and the potential value to exploration that gold geochemical signatures may provide.

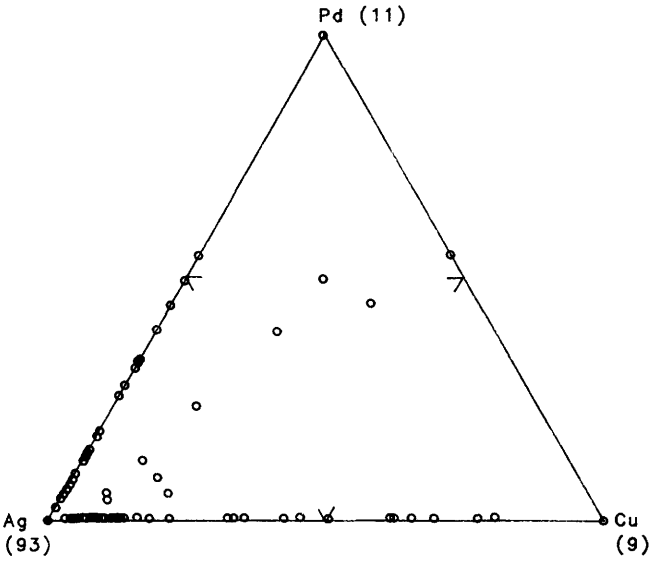

Figure 5. Ternary diagram of Ag-Pd-Cu showing the relative amounts of silver, palladium, and copper (weight percent) in mercury-free native gold grains from Lemhi County, Idaho. Numbers at apices indicate number of grains with only silver (93), only Pd (11), and only Cu (9).

Figure 5 shows a ternary plot of copper, silver, and palladium for 182 mercury-free grains. Only nine grains (5 percent) contain detectable amounts of all three elements. Ninety-three silver-bearing grains (51 percent) contain no copper or palladium; 11 palladium-bearing grains (6 percent) contain neither silver nor copper; and 9 copper-bearing grains (5 percent) contain neither silver nor palladium. Of these 182 grains, 32 (18 percent) contain silver and copper (without palladium), and 23 (13 percent) contain silver and palladium (without copper). These data are interpreted to indicate a general incompatibility of extensive solid solution of all three elements (Ag, Pd, and Cu) simultaneously in native gold under the conditions of deposition. With the exception of the nine gold grains containing all three elements, and the occurrence of auricupride and tetraauricupride in Hayden Creek, most gold grains are not similar in composition to native gold found in mafic and (or) ultramafic rocks (Bird and others, 1991; Miller and others, 1991).

The occurrence of minor amounts of copper and minor amounts of palladium in native gold in the study area is significant. If we include all gold grains (including those containing mercury): (1) Palladium occurs in 12 of 13 localities studied (92 percent), and palladium occurs in 54 of 308 gold grains analyzed (17 percent); (2) copper occurs in 9 of 13 localities studied (69 percent), and copper occurs in 59 of 308 gold grains analyzed (19 percent). When compared to the Alaskan native-gold data shown in table 2, these occurrences of both palladium and copper in native gold in Lemhi County, Idaho, must be considered

unusual. Differences and similarities in the populations of gold grains from each locality studied are shown on figure 2. The number of silver-bearing grains, copper-bearing grains, palladium-bearing grains, and pure gold grains was determined for each sample, and the relative percentage of each of these parameters was normalized to 100. On this basis, five compositional groups of native gold signatures are tentatively identified on figure 2. The first group has no copper-bearing grains and has a high proportion of pure gold grains. The second "group" of only one locality has neither copper- nor palladium-bearing grains but has a high proportion of pure gold grains. The third group has a high proportion of copper-bearing grains and also has palladium-bearing grains; all of these localities are west of the Salmon River (fig. 1). The fourth group has a very high proportion of silver-bearing grains and a low proportion of copper-bearing grains in comparison to the proportion of palladium-bearing grains. The fifth group has a modest percentage of copper- and palladium-bearing grains; this group might be better considered as part of the third group. However, the average silver content of the third group is 5.3 weight percent, whereas the average silver content of the fifth group is 9 weight percent. We hope that additional studies will determine whether or not these tentative groups of gold geochemical signatures will be distinct or not.

Based on the occurrences of native gold along post-Eocene faults, we infer that some of the gold was deposited during Cenozoic time. The extensive occurrence of gold in areas underlain chiefly by Proterozoic metasedimentary rocks (lower greenschist facies) and locally by Proterozoic igneous granitic rocks or thin mafic sills and dikes is inferred to indicate the strong possibility that some of the gold may have been deposited during Proterozoic time. We tentatively infer that some of the unusual compositions of the gold in this area may be related to Proterozoic mineralization. Another possibility is that some of the gold was deposited in Proterozoic rocks but was remobilized by later mineralizing events that may not have destroyed the Proterozoic geochemical signatures.

Further research on the native gold in the region should reveal whether or not the copper-bearing and palladium-bearing gold is geologically and (or) geographically limited to certain terranes. Focus will be placed on greater sample density in areas currently being geologically mapped.

REFERENCES CITED

Bird, D.K., Brooks, C.K., Gannicott, R.A., and Turner, P.A., 1991, A gold-bearing horizon in the Skaergaard intrusion, East Greenland: Economic Geology, v. 86, p. 1083–1092.

Brooks, R.R. and Watterson, J.R., in press, On the microbial biogeochemistry of noble metals, *in* Brooks, R.R., ed, Biological Systems and Noble Metals, Chapter 6: West Palm Beach, Florida, CRC Press.

Cathrall, J.B., Albanese, M., VanTrump, G., Mosier, E.L., and Lueck, L., 1989, Geochemical signatures, analytical results, mineralogical data, and sample locality map of placer and lode gold, and heavy-mineral concentrates from the Fortymile mining district, Eagle quadrangle, Alaska: U.S. Geological Survey Open-File Report 89–451, 32 p.

Cathrall, J.B., Antweiler, J.C., and Mosier, E.L., 1987, Occurrence of platinum in gold samples from the Tolovana and Rampart mining districts, Livengood quadrangle, Alaska: U.S. Geological Survey Open-File Report 87–300, 12 p.

Cathrall, J.B., Antweiler, J.C., VanTrump, G., and Mosier, E.L.,1989a, Gold analytical results and gold signatures from the Fairbanks mining district, Fairbanks and Livengood quadrangles, Alaska: U.S. Geological Survey Open-File Report 89–490, 23 p.

———1989b, Gold, platinum, and silver analytical results and gold signatures from the Bonnifield mining district, Fairbanks and Healy quadrangles, Alaska: U.S. Geological Survey Open-File Report 89–461, 23 p.

———1990, Gold analytical results and gold signatures from the Anchorage, Charley River, Healy, Iditarod, Juneau, Mt. Hayes, Mt. McKinley, Ophir, Ruby, and Talkeetna quadrangles, Alaska: U.S. Geological Survey Open-File Report 90–210, 25 p.

Cathrall, J.B., McDanal, S.K., VanTrump, G., Mosier, E.L., and Tripp, R.B., 1988, Analytical results, geochemical signatures, mineralogical data, and sample locality map of lode gold, placer gold, and heavy mineral concentrates from the Tolovana mining district, Livengood quadrangle, Alaska: U.S. Geological Survey Open-File Report 88–578, 32 p.

Cathrall, J.B., Tripp, R.B., McDanal, S.K., Mosier, E.L., and VanTrump, G., 1988, Analytical results, geochemical signatures, mineralogical data, and sample locality map of placer gold and heavy mineral concentrates from the Circle mining district, Circle quadrangle, Alaska: U.S. Geological Survey Open-File Report 88–676, 48 p.

Desborough, G.A., 1970, Silver depletion indicated by microanalysis of gold from placer occurrences, Western United States: Economic Geology, v. 65, p. 304–311.

Desborough, G.A., Raymond, W.H., and Iagmin, P.J., 1970, Distribution of silver and copper in placer gold derived from the northeastern part of the Colorado Mineral Belt: Economic Geology, v. 65, p. 937–944.

Desborough, G.A., Heidel, R.H., Raymond, W.H., and Tripp, J., 1971, Primary distribution of silver and copper in native gold from six deposits in the Western United States: Mineralium Deposita; v. 6, p. 321–334.

Desborough, G.A., Raymond, W.H., and Evans, K.V., 1990, Fine-grained gold in stream sediments of east-central Lemhi County, Idaho: U.S. Geological Survey Open-File Report 90–332, 9 p.

DiLabio, R.N.W., Newsome, J.W., McIvor, D.F., and Lowenstein, P.L., 1988, The spherical form or gold: Man-made or secondary: Economic Geology, v. 83, p. 153–162.

English, B.L., Desborough, G.A., and Raymond, W.H., 1987, A mechanical panning technique for separation of fine-grained gold and other heavy minerals: U. S. Geological Survey Open-File Report 87–364, 9 p.

McDanal, S.K., Cathrall, J.B., Mosier, E.L., Antweiler, J.C.,and Tripp, R.B., 1988, Analytical reseults, geochemical signatures, mineralogical data, and sample locality map of placer gold and heavy-mineral concentrates from the Manley Hot Springs, Tofty, Eureka, and Rampart mining districts, Tanana and Livengood quadrangles, Alaska: U.S. Geological Survey Open-File Report 88–443, 54 p.

Miller, D.J., Loucks, R.R., and Ashraf, M., 1991, Platinum-group element mineralization in the Jijal layered ultramafic-mafic complex, Pakastani Himalayas: Economic Geology, v. 86, p. 1093–1102.

Mosier, E.L., 1975, Use of emission spectroscopy for the semiquantitative analysis of trace elements and silver in native gold, *in* Ward, F.N., ed., New and Refined Methods of Trace Analysis Useful in Geochemical Exploration: U.S. Geological Survey Bulletin 1408, p. 97–105.

Mosier, E.L., Cathrall, J.B., Antweiler, J.C., and Tripp, R.B., 1989, Geochemistry of placer gold, Koyukuk-Chandalar mining district, Alaska: Journal of Geochemical Exploration, v. 31, p. 97–115.

Mosier, E.L. and Lewis, J.S., 1986, Analytical results, geochemical signatures, and sample locality map of lode gold, placer gold, and heavy-mineral concentrates from the Koyukuk-Chandalar mining district, Alaska: U.S. Geological Survey Open-File Report 86–345, 172 p.

Ruppel, E.T. and Lopez, D.A., 1988, Regional geology and mineral deposits in and near the central part of the Lemhi Range, Lemhi County, Idaho: U. S. Geological Survey Professional Paper 1480, 121 p.

Watterson, J.R., 1992, Preliminary evidence for the involvement of budding bacteria in the origin of Alaskan placer gold: Geology, v. 20, p. 315–318.

CHAPTER AA

THE IMPORTANCE OF SOURCE ROCKS IN FORMATION OF METALLIC-SULFIDE ORE DEPOSITS

By BRUCE R. DOE[1]

ABSTRACT

Knowledge of the source rocks for carbon is important in finding economic accumulations of oil and natural gas. Source rocks are also seriously considered for some other commodities like uranium, but they are yet to enter the mainstream of considerations in evaluations of metallic-sulfide ore deposits. Five factors need to be considered about source rocks: the abundance of metals in source rocks; the site of the metals (accessibility); the kinds of anions available (sulfur, chlorine, ammonia, carbon dioxide, methane, fluorine) and organic compounds present; accompanying metals involved (e.g., iron); and complex sources where metals, anions, and organic compounds may come from several geologic units. An appeal is made for information relating to the importance of source rocks in the formation of metallic-sulfide ore deposits.

INTRODUCTION

Although source rocks long have been considered vital to the formation of petroleum and natural gas accumulations, source rocks are generally considered to be unimportant to the formation of metallic mineral deposits with certain notable exceptions (e.g., Titley, 1987). In oil and gas evolution (Tissot and Welte, 1984), source rocks must contain more than a certain level of carbon in order to produce commercial crude oil (> 0.5 percent if the carbon is in the form of algal matter, the most favorable material). If the organic matter is composed of land plants, the prime product will tend to be natural gas; if marine plants, then oil most likely will be generated. At low temperatures, only biogenic gas will be produced. The temperature must reach about 50°C for crude oil to be produced, but, if it is greater than about 150°–200°C, the oil will break down into thermogenic gas. The temperature interval favorable for generation of crude oil is called the "oil window." Much can be learned about the economic potential of a sedimentary basin for oil or gas even from a "dry" well.

Initial efforts on various non-sulfidic ores (e.g., sedimentary uranium, phosphate, manganese, iron, etc.) give every indication that source rocks are important to the development of other natural resources as well. Development of a theory for the importance of source rocks in formation of metallic sulfide ore deposits is now timely. The goals of developing such a theory emphasize the bearing of source rocks on formation of super-large, super-rich metallic sulfide ore deposits and what might be learned from surface geology, geophysics, and "dry" holes.

DISCUSSION

A number of aspects need to be considered in evaluating the importance of source rocks in the formation of metallic sulfide ore deposits:

1. Metal-enriched sources.—The prime targets in oil exploration are the largest deposits or "supergiant" fields. Thus, shales are the prime source rock of interest because they can be carbon rich. Limestones may produce valuable quantities of oil, but shale should yield the largest deposits. For metallic sulfides, we can expect a similar relationship. Especially for ore deposits related to igneous processes (the magmatothermal case, where fluid amounts—either magmatic fluids or circulating hydrothermal cells—and

[1]U.S. Geological Survey, Mail Stop 923, 12201 Sunrise Valley Drive, National Center, Reston, VA 22092.

duration of hydrothermal systems are limited), formation of "supergiant" ore deposits should be favored by enriched sources. The reasoning is simple. At 1 ppm of an element, there are only 10,000 tons of an element in a cubic mile of rock. Therefore, 100 mi^3 of rock that contains this element at a concentration of 1 ppm would have to be extracted to get a deposit yielding 1 million tons of metal. But the largest deposits would require a considerably greater rock volume. Broken Hill, Australia, will produce more than 20 million tons (20 Mt) of zinc, which would require more than 2,000 mi^3 with only 1 ppm extraction. It stands to reason that formation of a "supergiant" ore deposit would be easier at the 10 or 100 ppm level than at the 1 ppm level. More subtle concentration fluctuations may also be paramount. For example, a parent magma that starts with twice the copper content of a "normal" magmatic system may yield a porphyry copper deposit of 0.45 percent rather than 0.23 percent. The former may well be economic to mine, the latter will not. Thus, we may have to look for small enrichments in concentrations.

In my experience, most people who feel that source rocks are not important in the generation of major ore deposits feel that way because they imagine that the source being considered is just a lower grade mineralization, i.e., a regeneration of older deposits (these people oppose the "geostill" hypothesis, where ore fluids are either directly derived from subducted, metal-rich, exhalative sediments or indirectly from magmas in which such sediments are a component). There is no doubt that nature does form some ores through a succession of enrichment stages (a "bootstrap" operation)—supergene enrichment of porphyry copper may be among the least controversial examples. Indeed, supergene enrichment is often more important for putting the metal into a form in which the ore may be economically processed (e.g., by heap leaching of oxides and carbonates rather than sulfides) than it is for enriching concentrations; however, element enrichment is also important (e.g., gossan gold). The importance of regeneration certainly needs to be considered.

2. *Site of the metals.*—In addition to the abundance of an element in the source rock, the location of the element—i.e., the accessibility of the element—within the rock can also be important. This factor is recognized as most important in the generation of uranium ore deposits. Uranium in a major uranium-bearing phase like zircon is relatively inaccessible to leaching, whereas much uranium is often in cryptic, easily-mobilized phases. In sediments containing normal concentrations of uranium, volcanic-glass shards, from which uranium is readily mobilized, have been proposed as the source of uranium in some major sandstone uranium deposits (Zielinski, 1983). Thus, unusual concentrations of an element may not be required if the element is readily available to the ore fluid.

3. *Anions.*—There is little doubt that anions can play a predominant role in ore formation. For metallic-sulfide ore deposits, a source of sulfur is clearly needed. Indeed, the reason that a major deposit has not been found in the Salton Basin that was deposited from the hot, metal-rich, chloride brines owes to a lack of sulfur. But other anions are also important (e.g., chlorine, carbon dioxide, ammonia, fluorine), and organic compounds are often mentioned as being important for ore formation. Chlorine can be of paramount importance in complexing metals to more soluble form. For example, hot, chloride-rich brines (e.g., Salton-Sea brine) can carry metals that are enriched in the 100–1,000 ppm range. These brines also are highly reactive: They will acquire the necessary concentrations of heavy metals even from metal-poor source rocks if the high solubility of these metals can be maintained either through remaining hot or through decreasing pressure (Hemley and others, 1992) over a long flow path. The source of chlorine in such brines seems to be some combination of connate water and evaporites because the sulfur isotopic composition ($\delta^{34}S$) is usually heavy (as expected for sulfur derived from anhydrite in evolved sea water and evaporites). Thus a "dry" hole in a sedimentary basin that shows the presence of evaporites might still be encouraging for the presence of mineral deposits.

Philip Candela and colleagues at the University of Maryland have stressed the importance of both water and chlorine in the source in order to produce certain kinds of ore deposits (e.g., Candela and Holland, 1986). They feel that a porphyry copper results from incorporating a hydrous source in the melt so that a chloride-rich fluid phase separates early in magmatic differentiation before copper, a compatible element, becomes too depleted in the melt. Paucity of water in a source, such that a fluid phase might form late in magmatic differentiation, might produce a different kind of mineralization for an incompatible element such as molybdenum (i.e., molybdenum porphyry). Thus, one might deduce that amphibolite in the lower crust may favor copper porphyry, and granulite may favor molybdenum porphyry. Firming up such deductions may not be beyond our abilities. In some cases, the nature of the lower crust may be deduced from surface geology, in other cases from seismology or isotopes.

4. *Accompanying metals.*—The metals accompanying those elements of economic interest may also play an important role in ore formation. The importance of the cationic elements not of economic interest (e.g., iron) is well known. Although copper is as abundant as zinc in most mafic source-rock candidates, the richest porphyry copper ores rarely reach 3.5 percent, whereas zinc deposits have "supergiant" representatives that average 17 percent (e.g., Broken Hill, Australia, and Red Dog, Alaska). These deposits also tend to contain greater ore grades for lead (about 5 percent) than the best copper ores, even though lead is almost certainly much less abundant in the source rocks. A part of this discrepancy may relate to discussions by Hemley and others (1992), who point out

that iron is relatively common in ore fluids. Iron readily combines with copper to form only a moderately rich copper mineral, chalcopyrite ($CuFeS_2$), rather than a richer equivalent, such a bornite (Cu_5FeS_4). Thus, an iron-poor source might favor richer copper deposits, such as the copper-rich Colorado Pipe in Mexico, although relations of sulfur and oxygen in the ore fluid can be important also.

5. Complex sources.—Although there are many analogies between petroleum and metallic-sulfide deposits, there are also clear differences. Metals may be acquired from several sources and from over the total path length of the ore fluid; yet, petroleum may have mixed sources too. Both require permeability and some sort of trap (structural control). Both may involve a large range of temperatures-of-generation (e.g., biogenic gas and thermal gas; red-bed copper deposits and Mississippi Valley Zn-Pb deposits; or porphyry copper deposits and massive sulfide Cu-Zn-Pb deposits). Both can be spoiled by "gangue," which for crude oil is the presence of hydrogen sulfide or carbon dioxide. Petroleum formation, however, has nothing similar to important controls on ore deposition, such as: concentration by solution cooling or neutralization; the need for two or more components such as metal and sulfur, which can be derived from separate sources; and perhaps some complexing agent such as chlorine that might come from yet a third source. The magmatic differentiation escalator, which can be important in enriching metals, is not involved in crude-oil generation. To what extent all these aspects can be sorted out remains to be seen.

There are no illusions about the difficulty of what is being undertaken. Many metallic-sulfide ore deposits, for example, are polymetallic without any economic abundances in any one metal taken by itself. Also, hot, chloride-rich brines will acquire metals from anything through which they pass, so the problem in forming a major ore deposit may be more one of acquiring the chloride and keeping the solubility up over long flow paths than the need for metal-rich sources. The author would like to hear from you concerning interesting references and any ideas you might wish to relate concerning the importance of source rocks in the formation of metallic-sulfide ore deposits. In return, he will send you a copy of his paper (Doe, 1991) upon request.

REFERENCES CITED

Candela, P.A., and Holland, H.D., 1986, A mass transfer model for copper and molybdenum in magmatic hydrothermal systems—The origin of porphyry-type ore deposits: Economic Geology, v. 81, p. 1–17.

Doe, B.R., 1991, Source rocks and the genesis of metallic mineral deposits: Global Tectonics and Metallogeny, v. 3, p. 13–19.

Hemley, J.J., Cygan, G.L., Fein, J.B., Robinson, G.R., and d'Angelo, W.M., 1992, Hydrothermal ore-forming processes in the light of studies in rock-buffered systems—I. Iron-copper-zinc-lead sulfide solubility relations: Economic Geology, v. 87, p. 1–22.

Tissot, B.P., and Welte, D.H., 1984, Petroleum formation and occurrence (2nd ed.): Berlin, Springer-Verlag, 699 p.

Titley, S.R., 1987, The crustal heritage of silver and gold ratios in Arizona ores: Geological Society of America Bulletin, v. 99, p. 814–826.

Zielinski, R.A., 1983, Tuffaceous sediments as source rocks for uranium—A case study of the White River Formation, Wyoming: Journal of Geochemical Exploration, v. 18, p. 285–306.

Published in the Central Region, Denver, Colorado
Manuscript approved for publication October 26, 1992
Edited by Richard W. Scott, Jr., Branch of Central Technical Reports
Graphics prepared by Dick Walker and M.A. "Marty" Simmons, Branch of Geochemistry; some author drafting used
Assistance with manuscript preparation by Margo Johnson and Barbara Ramsey, Branch of Geochemistry
Type composed by Shelly A. Fields, Branch of Central Technical Reports
Cover design by Art Isom, Branch of Central Technical Reports

☆ U.S. GOVERNMENT PRINTING OFFICE: 1992—774-049/66,044.REGION NO. 8

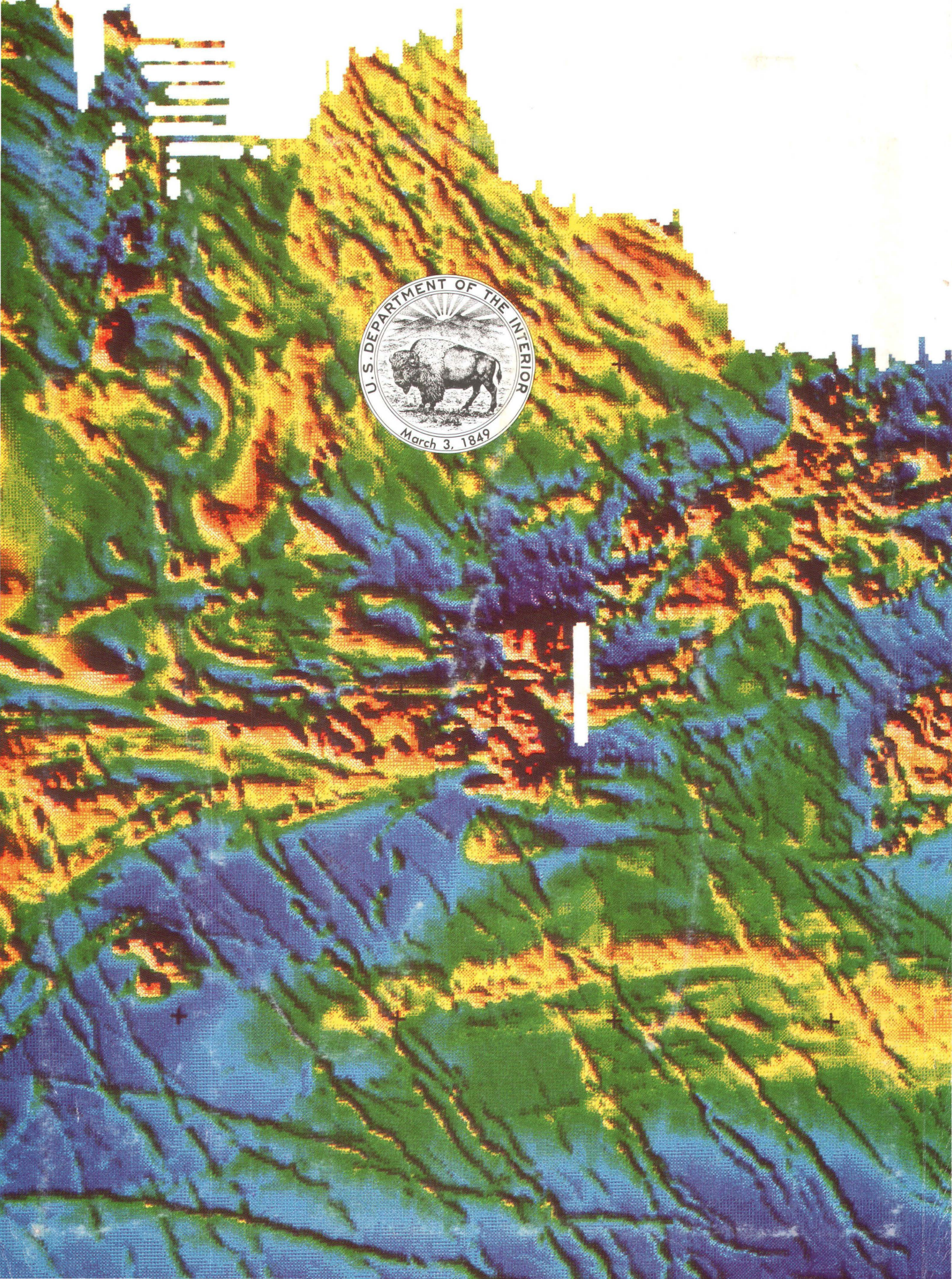
U.S. DEPARTMENT OF THE INTERIOR
March 3, 1849